

ALMA MATER STUDIORUM - UNIVERSITÀ DI BOLOGNA

DIPARTIMENTO DI FISICA E ASTRONOMIA

DOTTORATO DI RICERCA IN FISICA

CICLO XXXIV

**Search for Type-III SeeSaw heavy leptons in
leptonic final states using proton-proton
collisions at $\sqrt{s} = 13$ TeV with the ATLAS
detector.**

Candidato: Giuseppe Carratta

Coordinatore Dottorato:
Prof. Michele Cicoli

Supervisore:
Chiar.mo Prof. Maximiliano Sioli

Co-supervisor:
Dr. Antonio Sidoti
Dr. Matteo Franchini

Settore Concorsuale di afferenza: 02/A1

Settore Scientifico disciplinare: FIS/01

Esame Finale - Anno 2022

Sommario

Questa tesi analizza gli stati finali multi-leptonici per la ricerca della produzione di coppie di leptoni pesanti predetti dal meccanismo SeeSaw di Tipo-III. L'analisi usa i dati prodotti dalle collisioni protone-protone ad una energia del centro di massa di 13 TeV, corrispondenti ad una luminosità integrata di 139 fb^{-1} raccolti dall'esperimento ATLAS durante l'intero periodo Run 2 del Large Hadron Collider (2015-2018). La ricerca è focalizzata su stati finali con tre e quattro leptoni leggeri (elettroni e muoni) e con un'elevata energia rilasciata dalla collisione proveniente da tutti i possibili decadimenti dei leptoni pesanti attraverso bosoni elettrodeboli. Poiché non sono stati osservati eccessi di segnale rispetto alle predizioni del Modello Standard, sono stati posti dei limiti superiori e inferiori sulla sezione d'urto di produzione e sulla massa dei leptoni pesanti. Il limite inferiore di massa osservato è di 870 GeV al 95% di livello di confidenza considerando entrambi i canali con tre e quattro leptoni. In aggiunta, questo risultato è stato combinato per la prima volta con quello già pubblicato dalla collaborazione ATLAS nello stato finale con due leptoni e due jet. In questo caso, il limite inferiore di massa ottenuto combinando i canali con due, tre e quattro leptoni è di 910 GeV al 95% di livello di confidenza.

Abstract

This thesis analyzes multi-leptonic final states to perform a search for the pair production of heavy leptons as predicted by the Type-III SeeSaw mechanism. The analysis uses proton-proton collision data at a centre-of-mass energy of 13 TeV, corresponding to 139 fb^{-1} of integrated luminosity recorded by the ATLAS detector during the full Run 2 period of the Large Hadron Collider (2015-2018). The search is focused on final states with three and four light leptons (electrons and muons) and large energy produced by the collision coming from all the possible decays of the heavy leptons via intermediate electroweak bosons. As no significant excesses with respect to the Standard Model predictions are observed, upper and lower limits on the production cross-section and on the heavy lepton masses are set. The observed lower mass limit is 870 GeV at 95% of confidence level considering both three- and four-lepton channels. In addition, this result is combined for the first time with the ones already published by the ATLAS Collaboration in the two leptons plus two jets final state. In this case, the observed lower mass limit combining two, three and four lepton channels is 910 GeV at the 95% of confidence level.

Contents

Introduction	V
1 Theoretical Fundamenta	1
1.1 The Standard Model of Particle Physics	2
1.1.1 Fundamental interactions	4
1.2 Origin of neutrino mass	14
1.3 The SeeSaw Mechanisms	16
1.3.1 Type-III SeeSaw mechanism	17
1.4 Search at colliders	20
2 LHC and the ATLAS experiment	27
2.1 The Large Hadron Collider	28
2.1.1 Acceleration Chain	32
2.1.2 Physics requirements	34
2.2 The ATLAS detector	37
2.2.1 Tracking	40
2.2.2 Magnet system	45
2.2.3 Calorimetry	47
2.2.4 Muon system	52
2.2.5 Forward detectors	57
2.2.6 Trigger, readout, data acquisition and control systems	59
3 Object Reconstruction	63
3.1 Tracks and Vertices	64
3.1.1 Primary Vertex	66
3.2 Electrons	67
3.3 Muons	72
3.4 Jets	79
3.5 Missing Transverse Energy	84
3.5.1 Missing Transverse Energy Significance	86
3.6 Overlap Removal	87
3.7 Lepton Triggers	89

4	ATLAS Offline Software	93
4.1	Data Analysis Tools	93
4.2	Data Samples	103
4.3	Simulated Signal Samples	103
4.4	Simulated Background Samples	103
5	Search for Type-III SeeSaw heavy leptons	107
5.1	Analysis Strategy	108
5.1.1	Objects Definition	110
5.1.2	Analysis Regions	113
5.2	Background Estimation	127
5.2.1	Background from electron charge misidentification	127
5.2.2	Background from fake leptons	130
5.3	Systematic Uncertainties	160
5.3.1	Theoretical Uncertainties	160
5.3.2	Experimental Uncertainties	162
5.4	Signal Extraction Technique	164
5.4.1	Likelihood-based test	166
5.4.2	Hypothesis test	167
5.4.3	Background extrapolation and error propagation	169
5.5	Results	170
	Conclusions	189
A	Analysis details	191
A.1	Fake Lepton Composition	192
A.2	Systematics Tables	201
A.3	Post-fit distributions	210
A.4	Cutflows	226
A.5	Results for separated channels	236
A.6	Signal regions post-fit distributions Dilepton channel	243
A.7	Pull and ranking plots, and exclusion limit with toys for the combined fit with two-, three- and four-lepton channels	246
B	The LUCID Detector	251
B.1	Luminosity Measurement	252
B.2	The LUCID-2 Detector	256
B.2.1	The LUCID-2 Design	257
B.2.2	The Calibration System	259
B.2.3	LUCID Electronics	262
B.2.4	LUCID-3 Test and Installation	265

B.3	LUCID-3 Design	268
B.4	LUCID Simulations	270
B.5	Conclusions and perspectives	274
C	The ATLAS Inner Tracker	277
C.1	High-Luminosity LHC	277
C.2	The ITk Design	280
	C.2.1 ITk Pixel Detector	281
C.3	Database system	284
C.4	Conclusions	288
	List of Figures	313
	List of Tables	336

Introduction

During the past decades, the particle physics community has been devoted to describing the fundamental forces of Nature through a theoretical model called the Standard Model (SM) of particle physics. The Standard Model is the result of fundamental theories developed during the XXth century which has led to the discovery of many fundamental interactions and particles. The SM is up to-day the most advanced and complete theory describing the building blocks of matter and their interactions, strongly supported by experimental observations. Despite the extremely precise predictions of this framework, some phenomena are still under investigation, as the gravitational force which is not included in the theory, the amount of baryonic matter in the universe or the explanation of the non-zero mass of neutrinos. Several theoretical models have been developed to answer open questions necessary for a complete description of Nature introducing new physics processes.

To provide precise measurements of all the Standard Model particles properties, and to search for evidence of new physics phenomena, the largest particle accelerator in the world was built, the Large Hadron Collider (LHC). It is located at CERN laboratories in Geneva and it is designed to reach the un-precedented center-of-mass energy of $\sqrt{s} = 14$ TeV during proton-proton collisions. One of the biggest experiments at the LHC is carried on by the ATLAS Collaboration which exploits a multi-purpose detector, A Toroidal LHC ApparatuS (ATLAS), in order to perform searches for new physics signatures and measurements to prove the Standard Model predictions at higher precision.

Beyond the Standard Model theories aim to fill some of the gaps predicting new particles at different energy scales to explain the still open questions of the theory. However, these scales are not known but there are hints that they could be at the order of the TeV, within the energy reached by the LHC accelerator.

One of the most puzzling feature to be addressed in modern particle physics is represented by neutrinos masses. In the SM, neutrinos are massless, while observations provide evidence of non-zero mass for these neutral particles. Their

Introduction

extremely small masses compared to the ones of the other fermions appear unnatural in the theory. The Type-III SeeSaw mechanism provides an elegant way to give a very small mass value to each SM neutrino by introducing at least one extra heavy fermionic $SU(2)_L$ triplet field coupled to electroweak gauge bosons. These heavy neutral (N^0) and charged (L^\pm) leptons are expected to be produced by electroweak processes at the LHC energy.

In this thesis a search for the Type-III SeeSaw heavy leptons in final states containing three and four light leptons (electrons and muons) and large energy produced by the collision is presented. This analysis uses data collected by the ATLAS detector during the full Run 2 period (2015-2018) in LHC pp collisions at $\sqrt{s} = 13$ TeV with an integrated luminosity of 139 fb^{-1} . High leptons multiplicity channels provide key signatures for many new physics scenarios with a low contribution of Standard Model processes and have the advantage of carrying low systematic uncertainties associated with objects reconstruction.

The multi-leptonic final states are further divided into multiple regions of interest depending on the heavy leptons decay modes. Several kinds of background coming from SM events affect the different regions with a common contribution that arises from misreconstructed objects, such as leptons from wrongly reconstructed objects or electrons with wrong reconstructed charge. For the latter, an *ad hoc* data-driven technique is implemented for the estimation of this background source.

The signal strength in the three- and four-lepton channels is investigated through a statistical likelihood fit, first individually and then in a combination of these final states to search for possible excesses of signal events with respect to the Standard Model predictions. Exclusion limits on exotic particles cross-section and mass are set if no excesses are found. The results obtained with this analysis are combined with the ones already published by the ATLAS Collaboration for the Type-III SeeSaw search in the two leptons plus two jets channel, showing for the first time measurements on these heavy leptons considering all the most important decay channels.

This thesis is organized as follows. Chapter 1 presents the theoretical framework of the Standard Model, the origin of neutrino mass and the Type-III SeeSaw model. Chapter 2 describes the LHC collider and the ATLAS detector with all its sub-systems. Chapter 3 provides information on the objects reconstruction techniques and their performances. In Chapter 4 the ATLAS offline software tools, as well as the simulated and collision data samples used in the analysis are illustrated. Chapter 5 discusses the search for Type-III SeeSaw heavy leptons focusing on the analysis strategy and the systematic uncertainties, the background estimation, the signal extraction techniques with a final detailed description on

the obtained results. In Appendix [A](#) additional materials related to the analysis are reported, while activities performed for the LUCID and the ATLAS Inner Tracker detectors are shown in the Appendices [B](#) and [C](#), respectively.

Introduction

Chapter 1

Theoretical Fundamenta

1.1	The Standard Model of Particle Physics	2
1.1.1	Fundamental interactions	4
1.2	Origin of neutrino mass	14
1.3	The SeeSaw Mechanisms	16
1.3.1	Type-III SeeSaw mechanism	17
1.4	Search at colliders	20

The knowledge of the Universe's structure has always been a milestone of the human history. To describe the elementary particles, and their interactions, which compose it, the *Standard Model of Particle Physics* (SM) was formulated. The SM is a quantum field theory (QFT) developed in the second half of the 20th century in several stages, finalized in the 1970s with the experimental observation of the *quarks*. The last confirmation of the SM theory came in 2012 with the discovery of the *Higgs boson*, which is often regarded as the biggest success in the confirmation of the SM.

Though different experiments put the groundwork on this theory, several phenomena are not yet explained by the SM, then Beyond the Standard Model (BSM) theories are needed to give an alternative interpretation on this uncovered physics processes. One of the most puzzling features of particles physics is the origin of neutrino masses, which can be explained by the *Type-III SeeSaw* mechanism, discussed in detail in this thesis.

1.1 The Standard Model of Particle Physics

The Standard Model of particle physics describes elementary particles, called *fermions*, and their interactions, mediated by *gauge bosons*, in terms of *gauge theory* [1]. Although four fundamental forces are present in nature, only three of them are described in the SM: strong interactions, via *Quantum Chromodynamics* (QCD) [2]; electromagnetic and weak interactions which are combined in the electroweak interactions (EW) by the Glashow-Weinberg-Salam (GSW) model [3–5]. The gravitational force is not included in the SM theory since the *general relativity*, the canonical theory of gravitation, is not successfully explained in term of QFT.

The SM is defined by a *local gauge symmetry* of the group:

$$SU(3)_C \otimes SU(2)_L \otimes U(1)_Y \quad (1.1)$$

where $SU(3)_C$ describes, through a non-Abelian group, the strong interaction caused by the colour charge; $SU(2)_L \otimes U(1)_Y$ represents the GWS theory, where the special unitary group $SU(2)_L$ is associated to the weak isospin, while the unitary group $U(1)_Y$ is associated to the weak hypercharge. Each symmetry group will be fully described in the following sections.

Exploiting the properties of the Lie's Algebra groups¹, number of gauge bosons can be defined finding the number of generators for each group:

$SU(3)$: 8 generators, corresponding to the *gluons*;

$SU(2)$: 3 generators, corresponding to gauge fields, W_i ;

$U(1)$: 1 generator, corresponding to gauge field, B .

Through linear combinations of the gauge fields W_i and B , the ones associated to the *physical bosons* (W^\pm , Z^0 , γ) can be represented. The symmetry group in (1.1) requires that all bosons should be massless, however it is experimentally proved that the weak interaction mediators W^\pm and Z^0 have a mass of 80 GeV and 91 GeV respectively. The explanation for weak bosons and fermion masses was provided by three theorists: Higgs, Englert and Brout. They developed a new mechanism, *Spontaneous Symmetry Breaking* [6], that introduces a neutral scalar field, called Higgs field, giving mass to all of the SM fundamental particles. These *vector bosons* are particles following the Bose-Einstein statistics and have spin 1. As shown in Figure 1.1, only the weak force mediators are massive, for this reason weak interactions have a short interaction range, as reported in Table 1.1.

¹For a Lie group as $SU(n)$ there are $n^2 - 1$ generators, for $U(n)$ these are n^2 .

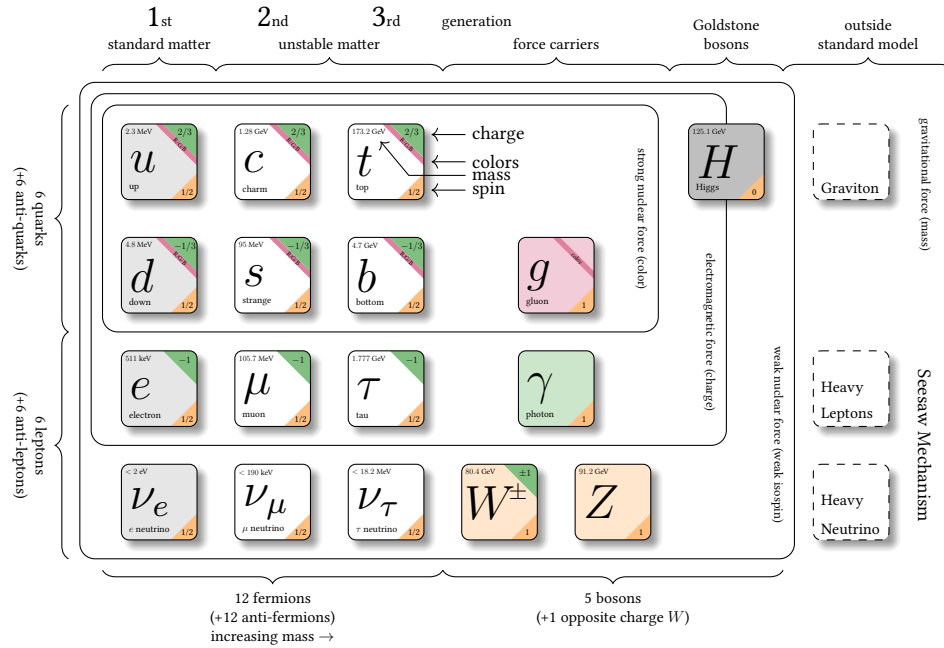


Figure 1.1: Constituents of the SM. Starting from left: fermions, divided into quarks (upper part) and leptons (bottom part), gauge bosons, including the Higgs boson, and particles outside the SM as the graviton or the heavy leptons predicted by the SeeSaw mechanism. Adapted from [7].

	Strong	Electromagnetic	Weak	Gravitational
Range(m)	10^{-15}	∞	10^{-18}	∞
Magnitude	1	10^{-2}	10^{-6}	10^{-39}

Table 1.1: Main characteristics of the fundamental forces at the EW scale [1].

Fermions are spin 1/2 particles following the Fermi-Dirac statistics, divided into *leptons* and *quarks*. Each kind of fermions is further split into three generations. Leptons are formalized in a doublet structure, each doublet corresponds to a flavour with the associates neutrino:

$$\begin{pmatrix} e \\ \nu_e \end{pmatrix} \begin{pmatrix} \mu \\ \nu_\mu \end{pmatrix} \begin{pmatrix} \tau \\ \nu_\tau \end{pmatrix}.$$

Each lepton family has a leptonic number with a value of +1 for the leptons and -1 for the anti-leptons, it is conserved under all the interactions. All leptons have a negative charge (positive for anti-leptons), and they can interact via electro-

magnetic or weak force. Neutrinos, being electrically neutral, are only sensitive to the weak interactions.

Quarks have six different flavours, categorized in the so called *up-type* (u, c, t) with a charge of $2/3$ and *down-type* (d, s, b) with a charge of $-1/3$:

$$\begin{pmatrix} u \\ d \end{pmatrix} \begin{pmatrix} c \\ s \end{pmatrix} \begin{pmatrix} t \\ b \end{pmatrix}$$

Quarks can interact via strong, electromagnetic and weak interactions. Hadrons are composed by quarks and have an integer charge resulting from quarks charge combination. Differently from the leptons, quarks are not directly observed, since they are always bound in hadrons as a consequence of the phenomenon called *confinement* [8]. Several quantum numbers are associated to the quarks:

- the flavour number, which is conserved under each interactions except the weak one;
- the colour number, corresponding to the strong interaction charge. This quantum number is characterized by the following values: *red*, *blue* and *green*. Colour is conserved by all interactions and it is the responsible for the confinement phenomenon since quarks can be observed only in a null-color combination;
- the barionic number, additive and conserved by all the three fundamental interactions included in the SM. Quarks (anti-quarks) have a barionic quantum number of $1/3$ ($-1/3$).

Fermions interact exchanging a field of quanta, corresponding to the photon (γ) for the electromagnetic interaction, the Z^0 and W^\pm bosons for the weak interaction and the *gluon* for the strong one. In the 1960s weak and electromagnetic interactions were unified in the *electroweak force* [9].

1.1.1 Fundamental interactions

The SM, as a quantum field theory, describes the fundamental interactions by coupling fields with particles. The SM includes all the fundamental forces except the gravitational one, since it is described by a quantum theory not renormalizable, but this does not modify the SM predictions due to its negligible contribution in particle physics, as shown in Table 1.1.

All of these interactions are included in the SM by a mathematical formalism called *gauge theory* based on the concept of *symmetry*. In a gauge theory, the potential generating the fields is not uniquely defined, then the *gauge invariance* lays the possibility to arbitrary choose the potential to describe the same field.

It means that the system Lagrangian is invariant under the transformation of a certain group of symmetry (i.e. rotation, translation, time). Symmetries are divided in two groups:

Global symmetry: Lagrangians are invariant under certain transformations changing by the same amount in every point of the space-time;

Local symmetry: Lagrangians transformations depends on a parameter locally defined which is different from point to point.

According to this theory the SM Lagrangian is invariant for both global and local transformations. Following the Noether's theorem, a continuous symmetry results in a conserved quantity.

Quantum Electrodynamics

The *Quantum Electrodynamics* (QED) describes the electromagnetic interaction in term of quantum field theory. QED is a formulation in quantomechanical and relativistic terms of the Maxwell's equations in absence of sources for the magnetic field \vec{B}

$$\text{div}\vec{B} = \vec{\nabla} \cdot \vec{B} = 0, \quad (1.2)$$

where the vector differential operator *nabla*, defined as:

$$\vec{\nabla} = \left(\frac{\partial}{\partial x}, \frac{\partial}{\partial y}, \frac{\partial}{\partial z} \right), \quad (1.3)$$

is used to write the magnetic field as:

$$\vec{B} = \text{rot}\vec{A} = \vec{\nabla} \times \vec{A} \quad (1.4)$$

with \vec{A} vector potential of the magnetic field. Introducing an arbitrary scalar function Φ , its gradient can be added to the vector potential:

$$\vec{A} \rightarrow \vec{A} + \vec{\nabla}\Phi \quad (1.5)$$

as the magnetic field does not change under this transformation, due to:

$$\vec{B} = \vec{\nabla} \times (\vec{A} + \vec{\nabla}\Phi) = \vec{\nabla} \times \vec{A}. \quad (1.6)$$

In absence of sources, the electric field \vec{E} is defined as:

$$\vec{\nabla} \times \vec{E} = -\partial\vec{B}/\partial t, \quad (1.7)$$

and using the (1.4), it can be written as:

$$\vec{\nabla} \times (\vec{E} + \partial\vec{A}/\partial t) = 0. \quad (1.8)$$

Identifying the scalar potential of the electric field \vec{E} with V , the following equation is valid:

$$\vec{E} + \partial\vec{A}/\partial t = -\vec{\nabla}V. \quad (1.9)$$

In order to have also the electric field invariant as well as (1.5), the following relation is needed:

$$V \rightarrow V - \partial\Phi/\partial t. \quad (1.10)$$

Using the covariant notation, the equation in (1.2) and (1.7) can be written as:

$$F^{\mu\nu} = \partial^\nu A^\mu - \partial^\mu A^\nu \quad (1.11)$$

where μ and ν are four dimensions indices running on the space-time coordinates, $\partial^\mu = (\frac{\partial}{\partial t}, \vec{\nabla})$, $\partial_\mu = (\frac{\partial}{\partial t}, -\vec{\nabla})$, and $F^{\mu\nu}$ is the Maxwell's electromagnetic tensor:

$$F^{\mu\nu} = \begin{pmatrix} 0 & E_1 & E_2 & E_3 \\ -E_1 & 0 & B_3 & -B_2 \\ -E_2 & -B_3 & 0 & B_1 \\ -E_3 & B_2 & -B_1 & 0 \end{pmatrix} = -F^{\nu\mu} \quad (1.12)$$

and A^μ is the four-vector potential

$$A^\mu = (V, \vec{A}). \quad (1.13)$$

$F^{\mu\nu}$ is invariant under gauge transformation, as described in the relation below:

$$A^\mu \rightarrow A^\mu - \partial^\mu\Phi. \quad (1.14)$$

The Maxwell's electromagnetic tensor (1.11) can be compactly expressed in covariant notation:

$$\partial_\mu {}^*F^{\mu\nu} = 0 \quad (1.15)$$

where ${}^*F^{\mu\nu}$ is obtained from $F^{\mu\nu}$, replacing $\vec{E} \rightarrow \vec{B}$ and $\vec{B} \rightarrow -\vec{E}$.

The other Maxwell's equations are:

$$\vec{\nabla} \cdot \vec{E} = \rho \quad (1.16)$$

$$\vec{\nabla} \times \vec{B} = \vec{J} + \frac{\partial\vec{E}}{\partial t}, \quad (1.17)$$

with ρ the electric charge density, \vec{J} the current density and $c = \frac{1}{\sqrt{\mu_0\epsilon_0}} = 1$ (μ_0 and ϵ_0 are respectively permeability and permittivity of the vacuum) corresponding to the speed of light.

Using the covariant notation, they can be expressed as:

$$\partial_\mu F^{\mu\nu} = -J^\nu \quad (1.18)$$

where the electromagnetic current J^ν is given by:

$$J^\nu = (\rho, \vec{J}). \quad (1.19)$$

Also these Maxwell's equations are invariant under the gauge transformation (1.14), therefore:

- the electromagnetic current is conserved:

$$\partial_\nu J^\nu = -\partial_\nu \partial_\mu F^{\mu\nu} = 0; \quad (1.20)$$

- the equation (1.18), in absence of sources and in a Lorenz gauge ($\partial_\mu A^\mu = 0$), satisfies the relation

$$\square A^\nu = 0 \quad (1.21)$$

where \square is the D'Alembert operator, meaning that each component of the vector potential (identified with the photon field) satisfies the Klein-Gordon equation for a massless particle.

The QED Lagrangian can be written as:

$$\mathcal{L}_{QED} = \bar{\Psi}(i\gamma^\mu \partial_\mu - m)\psi \quad \rightarrow \quad \textit{Propagation of free fermion} \quad (1.22)$$

$$- \frac{1}{4} F_{\mu\nu} F^{\mu\nu} \quad \rightarrow \quad \textit{Propagation of free photon} \quad (1.23)$$

$$- J^\mu A_\mu \quad \rightarrow \quad \textit{Interaction between gauge and matter field} \quad (1.24)$$

where the first line represents the Dirac Lagrangian for free particles of spin 1/2 composed by the wave function $\Psi(x)$ (with four complex components, a Dirac spinor) and the γ^μ are 4x4 matrices [1].

If a mass term would be added for the photon, it should have the form:

$$\mathcal{L}_\gamma = \frac{1}{2} m^2 A^\mu A_\mu \quad (1.25)$$

$$A^\mu A_\mu \rightarrow (A^\mu - \partial^\mu \alpha)(A_\mu - \partial_\mu \alpha) \neq A^\mu A_\mu \quad (1.26)$$

which violates the gauge invariance in 1.26. Therefore, the vector field associated to the photon is massless. As an example, some QED processes are shown in Figure (1.2).

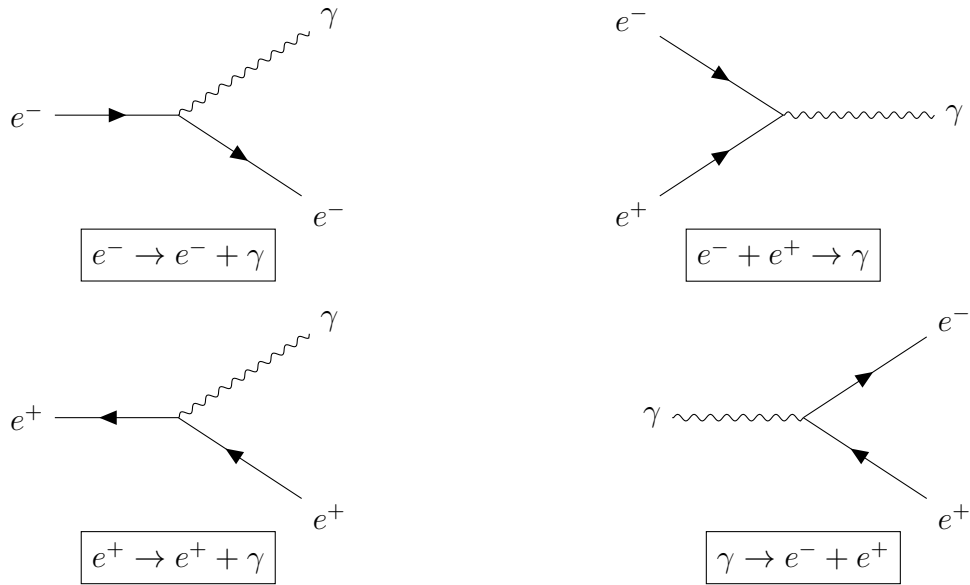


Figure 1.2: The diagrams illustrate basic processes that may occur in positron and electron interactions with a photon. They are: fundamental QED vertex (*top left*); electron-positron annihilation (*top right*); emission of a photon by a positron (*bottom left*); pair production by a photon (*bottom right*).

Weak interaction and electroweak unification

Each SM fermion is sensitive to weak interaction, which has a significantly small intensity compared to the strong and the electromagnetic ones at low energy.

The first theoretical explanation of the weak theory was given by Enrico Fermi in 1934 studying the β -decay [10], described by the process:

$$n \rightarrow p + e^- + \bar{\nu}_e$$

and shown in Figure 1.3. The weak interaction is described as a quantum field theory by the *Quantum Flavor-Dynamics* (QFD), which is symmetric for a gauge rotation of $SU(2)_L$. As described in the first section of this chapter, this group has 3 generators associated to the physical bosons W^\pm and Z^0 , which mediate charge current (CC) and neutral current (NC) interactions respectively. In Figure 1.3 some CC and NC interactions are reported.

This theory was developed by Fermi following the electromagnetic theory describing the weak interactions as a point-like vectorial (V) current interaction of four fermions. However, a parity violation was experimentally observed, and the introduction of an axial (A) term was needed to guarantee the Lorentz-invariance in the weak Hamiltonian. Writing separately the vectorial and the axial currents for the leptonic case (for the hadronic particles they are the same),

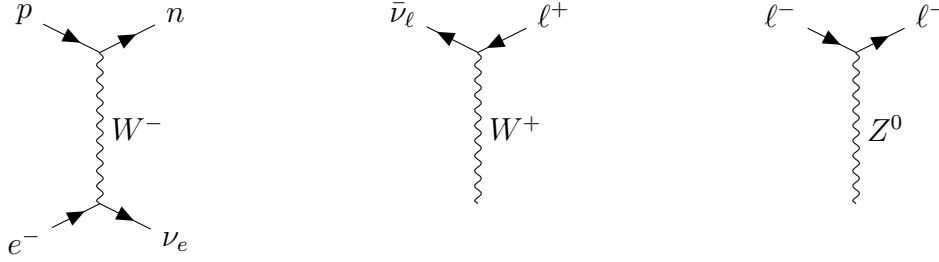


Figure 1.3: Feynman diagrams for: the β -decay (*left*); fundamental vertex of weak interaction in CC (*center*) and in NC (*right*).

the following relations are obtained:

$$J_V^\mu = \sum_l \bar{\Psi}_l(x) \gamma^\mu \Psi_{\nu l}(x) \quad (1.27)$$

$$J_A^\mu = \sum_l \bar{\Psi}_l(x) \gamma^\mu \gamma^5 \Psi_{\nu l}(x) \quad (1.28)$$

with the γ^5 chirality operator defined as $\gamma^5 = i\gamma^0\gamma^1\gamma^2\gamma^3$, and the “ β -decay” Hamiltonian with the V-A terms can be defined as:

$$H_{V-A} = \frac{G}{\sqrt{2}} \left[\bar{\psi}_p \gamma^\mu (1 - \gamma^5) \psi_n \right] \left[\bar{\psi}_e \gamma^\mu (1 - \gamma^5) \psi_\nu \right] \quad (1.29)$$

where G is the Fermi coupling constant. Defining the chirality projector operators:

$$\psi_L = \frac{1 - \gamma^5}{2} \psi \quad \rightarrow \quad \text{Left component} \quad (1.30)$$

$$\psi_R = \frac{1 + \gamma^5}{2} \psi \quad \rightarrow \quad \text{Right component} \quad (1.31)$$

it can be seen that the “left-handed” (LH) particles (or “right-handed” (RH) anti-particles) in a weak coupling are the only selected ones, due to the presence of the $(1 - \gamma^5)$ term. Consequently, in the weak sector, only the interactions between LH particles and RH anti-particles are allowed.

The study of a possible unification of the electromagnetic and weak interactions started in the 1960s by Glashow, Weinberg and Salam. The final results were reached in 1968 with the formulation of the *electroweak theory* (EW). This new theory is based on the $SU(2)_L \times U(1)_Y$ gauge symmetry group:

$SU(2)_L$: the electroweak symmetry group, whose algebra is generated by the *weak isospin* T ;

$U(1)_Y$: the weak hypercharge symmetry group, whose algebra is generated by the *weak hypercharge* Y .

The electrical charge Q is defined by these two quantum numbers according to the Gell-Mann-Nishijima formula:

$$Q = T^3 + \frac{Y}{2} \quad (1.32)$$

where T^3 is the third component of the weak isospin.

In the $SU(2)_L$ symmetry group, fermions fields can be written as:

$$\psi_1(x) = \begin{pmatrix} u_L \\ d_L \end{pmatrix} \quad \rightarrow \quad LH \text{ isospin doublet}, \quad (1.33)$$

$$\psi_2(x) = u_R \quad , \quad \psi_3(x) = d_R \quad \rightarrow \quad RH \text{ isospin singlets}, \quad (1.34)$$

where the notations in 1.33 and 1.34 are valid for both leptons and quarks.

To construct the EW Lagrangian, \mathcal{L}_{EW} , three vector gauge fields associated to $SU(2)_L$ ($W_\mu^a(x)$, with $a=1,2,3$) and one vector gauge field ($B_\mu(x)$) associated to $U(1)_Y$ are introduced. The covariant derivative for the electroweak interaction is defined as:

$$\mathcal{D}_\mu = \partial_\mu + ig \frac{\sigma_a}{2} W_\mu^a + ig' \frac{Y}{2} B_\mu \quad (1.35)$$

with σ_a Pauli matrices generating $SU(2)$, g and g' are the coupling constants for $SU(2)_L$ and $U(1)_Y$ respectively. Given the field strength tensors:

$$W_{\mu\nu}^a = \partial_\mu W_\nu^a - \partial_\nu W_\mu^a - g \epsilon^{abc} W_\mu^b W_\nu^c \quad (1.36)$$

$$B_{\mu\nu} = \partial_\mu B_\nu - \partial_\nu B_\mu \quad (1.37)$$

the EW Lagrangian can be finally derived:

$$\begin{aligned} \mathcal{L}_{EW} &= \sum_{j=1}^3 i \bar{\psi}_j(x) \gamma^\mu \mathcal{D}_\mu \psi_j(x) \quad \rightarrow \quad \text{Lepton propagation and interaction} \\ &\quad - \frac{1}{4} W_{\mu\nu}^a W_a^{\mu\nu} \quad \rightarrow \quad SU(2)_L \text{ fields free propagation} \\ &\quad - \frac{1}{4} B_{\mu\nu} B^{\mu\nu} \quad \rightarrow \quad U(1)_Y \text{ field free propagation} \end{aligned} \quad (1.38)$$

As previously explained, boson should be massless as predicted by the theory. Since experiments observed a non-null mass for the weak bosons mediators, a complex scalar field needs to be added in the model to introduce a mass:

$$\phi = \begin{pmatrix} \phi^+ \\ \phi^0 \end{pmatrix} = \frac{1}{\sqrt{2}} \begin{pmatrix} \phi_1 + i\phi_2 \\ \phi_3 + i\phi_4 \end{pmatrix}. \quad (1.39)$$

The field introduced in 1.39 is the so called *Higgs field*. The corresponding Higgs Lagrangian \mathcal{L}_{Higgs} is introduced in the SM in the form of:

$$\mathcal{L}_{Higgs} = (\mathcal{D}_\mu \phi)^\dagger (\mathcal{D}^\mu \phi) - \left(\mu^2 \phi^\dagger \phi + \lambda (\phi^\dagger \phi)^2 \right) \quad (1.40)$$

where the first term is related to the kinetic part, \mathcal{D}_μ is the covariant derivative in 1.35 and the second part of the Lagrangian is the *Higgs potential*, $V(\phi)$. The so called *vacuum expectation value (vev)* is the minimum value of the potential obtained for values $\mu^2 < 0$ and $\lambda > 0$:

$$|\phi^\dagger \phi| = -\frac{1}{2} \frac{\mu^2}{\lambda} \equiv \frac{1}{2} v^2. \quad (1.41)$$

This minimum can be defined requiring $\phi_1 = \phi_2 = \phi_4 = 0$ and $\phi_3^2 = -\mu^2/\lambda \equiv v^2$ breaking the symmetry of the weak interaction. This leads to the *spontaneous symmetry breaking*. The field can be rewritten with the following expression:

$$\phi(x) = \frac{1}{\sqrt{2}} \begin{pmatrix} 0 \\ v + h(x) \end{pmatrix} \quad (1.42)$$

where $h(x)$ is the small excitation above the minimum, representing the physical Higgs boson. The mass eigenstates for the other physical bosons of the weak and electromagnetic forces can be derived from 1.36 and 1.37 as:

$$W_\mu^\pm = \frac{(W_\mu^1 \mp iW_\mu^2)}{\sqrt{2}} \rightarrow W^\pm \text{ bosons} \quad (1.43)$$

$$Z_\mu = -B_\mu \sin(\theta_W) + W_\mu^3 \cos(\theta_W) \rightarrow Z^0 \text{ boson} \quad (1.44)$$

$$A_\mu = B_\mu \cos(\theta_W) + W_\mu^3 \sin(\theta_W) \rightarrow \text{Photon boson} \quad (1.45)$$

where θ_W is the Weinberg angle, equal to about 30° . It can be expressed in terms of the weak coupling constants shown in 1.35:

$$\theta_W = \frac{g}{\sqrt{g^2 + g'^2}}. \quad (1.46)$$

Due to the relation in 1.46, θ_W is also called *mixing angle* since it points out the unification between weak and electromagnetic interactions.

With the addition of the mass eigenstates (1.43 - 1.45) in the Higgs Lagrangian (1.40), the masses of the gauge bosons can be obtained:

$$m_{W^\pm} = \frac{1}{2}vg \quad (1.47)$$

$$m_{Z^0} = \frac{vg}{2\cos(\theta_W)} = \frac{m_{W^\pm}}{\cos(\theta_W)} \quad (1.48)$$

$$m_H = \sqrt{2\lambda}v. \quad (1.49)$$

In order to complete the electroweak theory, the quark sector is to be included. Differently with respect to the leptons, quarks can mix flavours, experimentally confirmed by the K -meson decay [11]:

$$K^0(d\bar{s}) \rightarrow \pi^- (d\bar{u})\ell^+\nu_\ell \quad (1.50)$$

involving a flavour variation due to an interaction between different quark families: $\bar{s} \rightarrow \bar{u}\ell\nu_\ell$. To explain this phenomenon, Cabibbo introduced the *mixing of quarks* describing the eigenstates of the weak interaction as a linear combination of the mass eigenstates [12]. This theory was generalized with a 3×3 unitary matrix, the *CKM*-matrix developed together with Kobayashi and Maskawa [13]:

$$\begin{pmatrix} d' \\ s' \\ b' \end{pmatrix} = \begin{pmatrix} V_{ud} & V_{us} & V_{ub} \\ V_{cd} & V_{cs} & V_{cb} \\ V_{td} & V_{ts} & V_{tb} \end{pmatrix} \begin{pmatrix} d \\ s \\ b \end{pmatrix} \quad (1.51)$$

Quantum Chromodynamics

Similarly to the interaction involved in the QED, quarks can exchange the mediator of the *strong* interaction: *gluons*. This force is described by the *Quantum Chromodynamics* (QCD) [14], based on the same gauge principles as QED. To explain the hadron structure, the colour charge is introduced with three possible values. This group has 8 generators defined by the Gell-Mann matrices. In this theory the colour charge is preserved since the QCD is invariant under global gauge transformations. Furthermore QCD is a non-abelian theory which implies that gluons carry colour charge and interact with each other.

Starting from the Dirac Lagrangian in 1.22, the $SU(3)$ Lagrangian can be derived:

$$\mathcal{L} = \bar{\psi}^\alpha (i\not{D}^{\alpha\beta} - m\delta^{\alpha\beta}) \psi^\beta. \quad (1.52)$$

Similar to the covariant derivative in 1.35, an additional derivative can be introduced to guarantee the local gauge invariance of the 1.52:

$$D_\mu^{\alpha\beta} = \delta^{\alpha\beta}\partial_\mu + ig_s A_{\mu a}(T^a)^{\alpha\beta} \quad (1.53)$$

where $\delta^{\alpha\beta}$ is the Kronecker function, g_s is the coupling constant of QCD, T^a are the group generators and A_μ is the gluonic propagator. The gluon field is then represented by a tensor field as:

$$F_{\mu\nu}^a = \partial_\nu A_\mu^a - \partial_\mu A_\nu^a + g_s f_{abc} A_\mu^b A_\nu^c \quad (1.54)$$

with f_{abc} the fine structure constants of the group and the indices a, b, c indicate a sum on the eight colour degrees of freedom of the gluon field. The last term of the field structure involves a non-commutative feature of the QCD generators, implying the gluons *self-interactions*. Finally the QCD Lagrangian can be written as:

$$\mathcal{L}_{QCD} = -\frac{1}{4} F_{\mu\nu}^a F_a^{\mu\nu} - \sum_{flavour} \bar{\psi}_f (\gamma^\mu D_\mu - m_f) \psi_f. \quad (1.55)$$

Fermion mass terms

The Higgs Lagrangian described in 1.40 generates the gauge boson masses leaving SM fermions massless, while experimentally fermions have a non-null mass. Fermion masses can be added to the Lagrangian, with the introduction of the *Yukawa interactions* coupling to the Higgs boson, preserving the local gauge invariance. The Yukawa Lagrangian for leptons can be written as:

$$\mathcal{L}_{Yukawa}^{Leptons} = -G \left[(\bar{\nu}_\ell, \bar{\ell})_L \begin{pmatrix} \phi^+ \\ \phi^0 \end{pmatrix} \ell_R + \bar{\ell}_R (\phi^-, \bar{\phi}^0) \begin{pmatrix} \nu_\ell \\ \ell \end{pmatrix}_L \right] \quad (1.56)$$

with the effect of the spontaneous symmetry breaking, leptons masses are obtained:

$$\mathcal{L}_{Yukawa}^{Leptons} = -\frac{G}{\sqrt{2}} \left[v (\bar{\ell}_L \ell_R + \bar{\ell}_R \ell_L) - (\bar{\ell}_L \ell_R + \bar{\ell}_R \ell_L) h \right] \quad (1.57)$$

with a value of $m_\ell = Gv/\sqrt{2}$. As pointed out in 1.33 and 1.34, RH (ℓ_R) and LH (ℓ_L) leptons are written as singlet and doublet terms respectively. While neutrinos, which do not have RH states, remain massless. Similarly, the Higgs interaction with quarks leads to the following Lagrangian:

$$\mathcal{L}_{Yukawa}^{Quarks} = -m_d^i \bar{d}_i \left(1 + \frac{h}{v} \right) - m_u^i \bar{u}_i \left(1 + \frac{h}{v} \right) \quad (1.58)$$

where i represents the number of quark doublets. Fermions masses derived in 1.57 and 1.58 are free parameters of the theory.

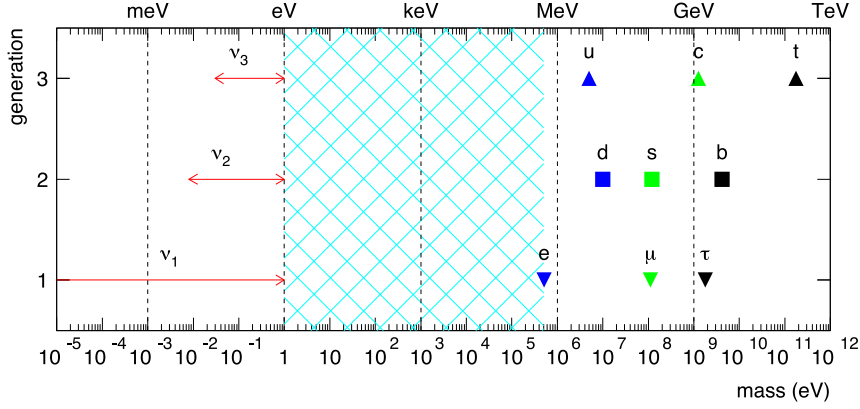


Figure 1.4: Masses of all known fundamental fermions. A normal mass-hierarchy has been assumed - $m^2\nu_1 < m^2\nu_2 < m^2\nu_3$ - together with a rather conservative upper bound $m^2\nu_i < 1 \text{ eV} \forall i = 1, 2, 3$. The light, hatched region indicates the six-orders-of-magnitude “desert” between the largest possible neutrino mass and the electron mass [18].

1.2 Origin of neutrino mass

Looking at the Lagrangian form in 1.57, in order to couple with the Higgs boson leptons need both their chirality components. Since only RH (LH) field was observed for neutrinos (anti-neutrinos), they cannot acquire mass via the Higgs mechanism in the SM. If ν_R would exist, their interaction with matter would require an additional term in the Lagrangian without changing the symmetry.

In 1958 Bruno Pontecorvo introduced the idea of neutrino oscillations [15]. Following this theory, if neutrinos oscillate between left- and right-handed states and also between different neutrino flavours, their masses must be non-null and not degenerate. Neutrino oscillations were observed experimentally [16], requiring a massive field for these particles. Furthermore, due to the huge difference with respect to the masses of the charged leptons (see Figure 1.4), the neutrino mass term in the Lagrangian could involve a *naturalness* problem for the theory [17].

The flavour oscillations of neutrinos was mathematically explained by Maki, Nakagawa and Sakata in analogy with the CKM theory of the quarks’ sector, introducing the PMNS matrix.

Since neutrinos are produced and detected in weak interactions, the weak eigenstates must be considered, instead of the mass ones, in order to correctly describe the oscillations. Considering for simplicity only two flavour eigenstates, using a matrix to describe an angular rotation² in the flavour space, a base trans-

²Because of the two eigenstates sets are orthonormal.

formation is possible:

$$\begin{pmatrix} \nu_e \\ \nu_\mu \end{pmatrix} = \begin{bmatrix} \cos(\theta) & \sin(\theta) \\ -\sin(\theta) & \cos(\theta) \end{bmatrix} \begin{pmatrix} \nu_1 \\ \nu_2 \end{pmatrix} \quad (1.59)$$

and weak eigenstate can be written as a linear combination of mass eigenstates:

$$|\nu_e\rangle = +\cos(\theta) |\nu_1\rangle + \sin(\theta) |\nu_2\rangle \quad (1.60)$$

$$|\nu_\mu\rangle = -\sin(\theta) |\nu_1\rangle + \cos(\theta) |\nu_2\rangle. \quad (1.61)$$

Since neutrino is a neutral particle, it may be either Dirac particle or neutral Majorana particle [19]. For the Dirac particles, the mass term provided by the theory is:

$$\bar{\nu}_L m_\nu^D \nu_R + h.c. \quad (1.62)$$

where m^D is a complex non-diagonal matrix, diagonalised using the PMNS matrix as in the 1.59. Looking at the 1.62, it is clear that the RH neutrino is required. This particle could only interact via gravitational force, being not sensitive to any of the fundamental interactions of the SM. Therefore this particle is called *sterile neutrino* [20].

A Majorana neutrino is defined as $\nu = \nu_L + \nu_L^c$ where ν^c is the charge conjugated field, $\nu^c = C\bar{\nu}_L^T$. Majorana neutrino mass term can be defined as:

$$\bar{\nu}_{L,R} m_{L,R}^M \nu_{L,R}^c + h.c. \quad (1.63)$$

where m^M is a complex non-diagonal matrix. A summary of the differences among Dirac and Majorana particles are provided in Table 1.2.

This Majorana mass term introduces the possibility to have massive neutrinos only considering the LH chiral component. Since ν_L field comes from the $SU(2)$ doublet (ν_L, ℓ_L) , the mass term in 1.63 would violate the isospin conservation, which is difficult to accommodate in the SM. To account this Majorana neutrino mass in the SM, a higher dimensional effective operator is needed, thus the Weinberg operator \mathcal{O}_5 is introduced:

$$\mathcal{O}_5 = (\bar{\phi}^\dagger \psi_L)^T C (\bar{\phi}^\dagger \psi_L) \quad (1.64)$$

where ϕ is the SM Higgs field. This \mathcal{O}_5 is a 5-dimensional not-renormalizable operator [21]. This problem can be solved interpreting \mathcal{O}_5 as an effective operator produced at low energies by new particles, coming from new physics mechanism at high energy scale.

In this context, the *SeeSaw mechanism* can fix the not-renormalizable problem of the Weinberg operator introducing Beyond the Standard Model leptons connecting the LH SM neutrino masses with the masses of new RH neutrino-like particles.

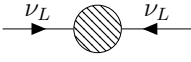
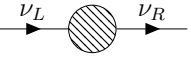
	Majorana	Dirac
Physical State	$\psi = \psi_L + \psi_L^c$	$\psi = \psi_L + \psi_R$
Mass term	$m^M \psi^T \psi = \frac{1}{2} m^M \psi_L^c \psi_L + \text{h.c.}$ 	$m^D \bar{\psi} \psi = m^D \bar{\psi}_R \psi_L + \text{h.c.}$ 
Lepton Number Variation	$\Delta L = 2$	$\Delta L = 0$
Required Scales	$m \sim y v^2 / \Lambda \rightarrow \Lambda \sim 10^{15} \text{ GeV}$	$m \sim v y \rightarrow y \sim 10^{-12}$
U_{PMNS} parameters	3 angles θ_{ij} 3 \mathcal{CP} phases δ, α, β	3 angles θ_{ij} 1 \mathcal{CP} phase δ

Table 1.2: Comparison of Dirac and Majorana mass terms. Λ is a new physics mass scale where Majorana neutrinos could acquire its mass, y the Yukawa Coupling, v is the vacuum expectation value (vev). PMNS matrix is the equivalent of CKM matrix for the leptonic sector.

1.3 The SeeSaw Mechanisms

The SeeSaw mechanism introduces new heavy particles to generate a tiny Majorana mass for the neutrinos, providing the coupling with lepton and Higgs doublets. This mechanism introduces heavy particles in a mass range of $10^2 - 10^{16}$ GeV. The neutrino mass introduced by the SeeSaw mechanism is given by:

$$m_v = y \frac{v^2}{M} \quad (1.65)$$

where y is the Dirac Yukawa coupling, v the vev and M the heavy particles mass. For very high values of M , y is the order of $\mathcal{O}(1)$, while for small values of M , $y \sim \mathcal{O}(10^{-6})$.

The Weinberg operator can be produced without the addition of extra gauge symmetries at high energies in three different ways:

Type-I introduces a *fermion singlet* N , that represents a RH sterile neutrino which couples to one lepton and one Higgs doublet [22];

Type-II introduces a *scalar weak triplet* $\Delta = (\Delta^{++}, \Delta^+, \Delta^0)$, which couples to two lepton doublets and two Higgs [23];

Type-III introduces a *fermion weak triplet* $\Sigma = (\Sigma^+, \Sigma^0, \Sigma^-)$, whose neutral lepton component is considered as a RH neutrino [24].

In the Type-I SeeSaw, the heavy right-handed Majorana neutrino is added to the Standard Model with a mass value higher than 10^{11} GeV, which is far too heavy to be probed experimentally at the LHC, while Type-II and Type-III provide mass scales able to lower the weak triplet masses up to the TeV scale. In Figure 1.5

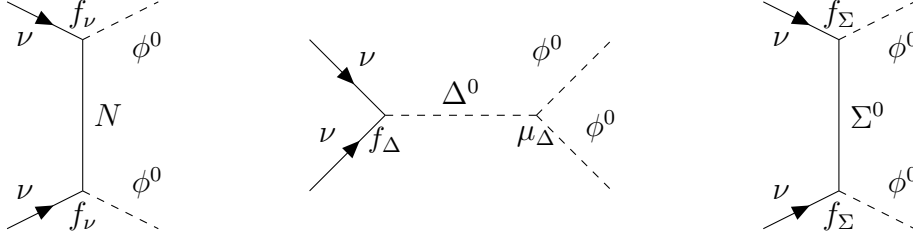


Figure 1.5: Generation of neutrino Majorana mass terms for the three versions of the SeeSaw mechanism.

the diagrams of the three SeeSaw models are shown, which give contributions to the Weinberg operator.

The study described in this thesis only includes the Type-III SeeSaw mechanism.

1.3.1 Type-III SeeSaw mechanism

The Type-III SeeSaw model introduces at least two new heavy fermionic triplets with zero hyper-charge in the adjoint representation of $SU(2)_L$. They couple to electroweak gauge bosons and generate neutrino masses through Yukawa couplings to the Higgs boson and neutrinos. Then, these new neutral and charged heavy leptons could be produced in electroweak processes in proton-proton collisions at the Large Hadron Collider (LHC) at observable rates [26]. A simplified model introducing only one fermionic triplet is considered for this thesis, since only the lighter states could be observed at the TeV scale.

The heavy fermionic triplet components are:

$$\vec{\Sigma} = \begin{pmatrix} \Sigma^1 \\ \Sigma^2 \\ \Sigma^3 \end{pmatrix}. \quad (1.66)$$

This triplet is coupled to the $SU(2)$ doublet as:

$$\Sigma = \vec{\sigma} \vec{\Sigma} = \frac{1}{\sqrt{2}} \begin{pmatrix} \sqrt{2}\Sigma^3 & \Sigma^1 - i\Sigma^2 \\ \Sigma^1 + i\Sigma^2 & -\sqrt{2}\Sigma^3 \end{pmatrix} = \begin{pmatrix} N^0 & L^- \\ L^+ & -N^0 \end{pmatrix} \quad (1.67)$$

where $\vec{\sigma}$ is the vector of Pauli's matrices. Thus, the $\vec{\Sigma}$ fields, corresponding to the physical particles, are defined as:

$$L^\pm = \frac{\Sigma_1 \mp i\Sigma_2}{\sqrt{2}} \quad , \quad N_0 = \Sigma_3 \quad (1.68)$$

where the charged Dirac fermions L^+ and L^- are, respectively, L_L and L_R , while the neutral Majorana fermion is $N_L = N^0 = N_R$. This nomenclature will be used in this thesis referring to these heavy leptons.

The Yukawa Lagrangian for the Type-III SeeSaw can be written as:

$$\mathcal{L} = i\bar{\vec{\Sigma}}_R \not{\partial} \vec{\Sigma}_R - \frac{1}{2} \bar{\vec{\Sigma}}_R M \vec{\Sigma}_R^c - \bar{\vec{\Sigma}}_R y_\Sigma (\tilde{\phi}^\dagger \vec{\sigma} \psi_L) + h.c. \quad (1.69)$$

which can be divided, after the electroweak spontaneous symmetry breaking, as:

$$\mathcal{L}_\nu = -\frac{1}{2} (\bar{\nu}_L \quad \bar{N}_L) \begin{pmatrix} 0 & \frac{v}{\sqrt{2}} y \\ \frac{v}{\sqrt{2}} y^T & M \end{pmatrix} \begin{pmatrix} \nu_R \\ N_R \end{pmatrix} + h.c. \quad (1.70)$$

$$\mathcal{L}_\ell = -(\bar{\ell}_L \quad \bar{L}_L) \begin{pmatrix} \frac{v}{\sqrt{2}} y^\ell & v y \\ 0 & M \end{pmatrix} \begin{pmatrix} \ell_R \\ L_R \end{pmatrix} + h.c. \quad (1.71)$$

Finally the generated masses can be derived as follow:

$$m_1 = v y_\ell = m_\ell^D \quad (1.72)$$

$$m_2 = -v^2 y_\Sigma^T |M|^{-1} y_\Sigma = m_\nu = m_\ell^M. \quad (1.73)$$

In this thesis, the minimal Type-III SeeSaw model is considered, assuming the heavy leptons are degenerate in mass.

Phenomenology

The Type-III SeeSaw heavy leptons, L^\pm and N^0 , could be produced in pp collision at the LHC through gauge couplings. They can be produced via $q\bar{q}$ interactions by Higgs, Z^0 and W^\pm bosons. Their possible decays modes are:

$$\begin{array}{ll} N^0 \rightarrow \nu H & L^\pm \rightarrow \ell^\pm H \\ N^0 \rightarrow \nu Z & L^\pm \rightarrow \ell^\pm Z \\ N^0 \rightarrow W^\pm \ell^\mp & L^\pm \rightarrow W^\pm \nu. \end{array}$$

Examples of the pair production of these heavy leptons decaying in final states with three and four leptons is shown in Figure 1.10a and 1.10b, respectively. In

the three-lepton channel, two opposite sign charge heavy leptons are produced via a virtual Z boson: one heavy lepton decays in a lepton and a real Z^0 boson which produces a pair of leptons; the other one decays in a neutrino and a real W^\pm boson producing a quark- anti quark pair. In the four-lepton channel, a virtual W^\pm boson produces both neutral and charged heavy leptons: N^0 decays in a lepton and a real W boson which produces a quark- anti quark pair; L^\pm produces a lepton and an opposite sign lepton pair via a Z^0 boson.

The L^\pm and N^0 total width and their decay BR into the SM leptons depend on the leptons mixing matrix elements, V_i ($i = e, \mu, \tau$). This matrix element only enters in heavy leptons decays, while the production is independent due to the coupling with the EW bosons. The BR is instead directly proportional to the mixing angles values as:

$$BR \propto \frac{|V_e|^2}{|V_e|^2 + |V_\mu|^2 + |V_\tau|^2}. \quad (1.74)$$

In Figure 1.6 the heavy neutrino branching ratios (BR) are reported as function of its mass. The analysis performed in this thesis assumes the same BR for all

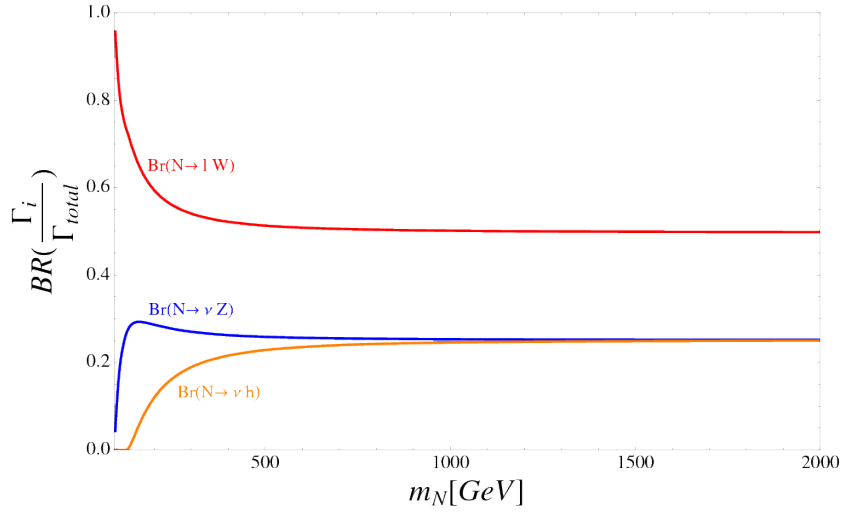


Figure 1.6: Branching ratios of the neutral component of the fermionic triplet as a function of its mass considering the following lepton mixing matrix elements: $V_e=V_\tau=0$ and $V_\mu=0.063$. Since the heavy leptons are assumed to be degenerate in mass, BRs into W , Z and H bosons are the same for the charged component [27].

the three lepton flavours, $BR_e = BR_\mu = BR_\tau = 1/3$, the so-called *flavour-democratic scenario*. Theory and experimental independent measurements provide the following values for the allowed combinations [28–30]:

$$\begin{aligned}
|V_e| &< 5.5 \cdot 10^{-2} & |V_e V_\mu| &< 1.7 \cdot 10^{-7} \\
|V_\mu| &< 6.3 \cdot 10^{-2} & |V_e V_\tau| &< 4.2 \cdot 10^{-4} \\
|V_\tau| &< 6.3 \cdot 10^{-2} & |V_\mu V_\tau| &< 4.9 \cdot 10^{-4}
\end{aligned} \tag{1.75}$$

These theoretical assumptions imply constraints on the heavy leptons production (via the minimal Type-III SeeSaw model) and decay modes (due to the flavour-democratic scenario). The degeneracy does not limit the results of the searches, since the theoretical calculations predict only a very fine mass-splitting due to radiative corrections and the possible decays among the heavy leptons are highly suppressed in the model [31]. On the other hand, the assumption of a flavour-democratic scenario leads, in principle, to the possibility to obtain small masses for the three generations of neutrinos inside the Standard Model. Due to the huge difference between neutrinos and heavy leptons masses, this consideration does not change the targeted phase-space.

1.4 Search at colliders

At the LHC several searches for Type-III SeeSaw heavy leptons considering different decay modes have already been performed. Using the LHC Run 1 (2010-2013) data sample at $\sqrt{s}=8$ TeV, ATLAS excluded heavy leptons with masses below 335 GeV in final states with two light leptons (electron or muon) and two jets [32]. Still in Run 1, the addition of the three-lepton final state improves the limit to 470 GeV [33].

Exploiting Run 1 data, CMS performed a search investigating three kind of branching ratio scenarios [34]: flavour democratic scenario, muon scenario ($BR_e = BR_\tau = 0, BR_\mu = 1$) and electron scenario ($BR_\mu = BR_\tau = 0, BR_e = 1$). Depending on the considered scenarios, lower limits are obtained on the mass of the heavy partner of the neutrino that range from 180 to 210 GeV. Each of these limits obtained with different BR scenarios is in agreement with the others inside the uncertainty bands.

In Run 2 (2015-2018) considering proton-proton collisions at $\sqrt{s}=13$ TeV, a search performed by the CMS Collaboration has excluded heavy lepton masses up to 880 GeV [35] in three- and four-lepton final states, while ATLAS focusing only on the two leptons plus two jets final states has excluded heavy lepton masses up to 810 GeV [36,37]. CMS and ATLAS exclusion limits are shown in Figure 1.7b and 1.7a respectively.

A more general overview on the heavy leptons searches at colliders is given by Figures 1.8 and 1.9, where the exclusion limits reported by several collaborations are shown [38]. These results bound the mixing between a neutrino and the heavy neutral lepton in the mass range 100 MeV - 500 GeV. In these figures two kinds of complementary energy frontiers can be identified: heavy-mass short-lived particles (upper-right part of the plots) and light-mass long-lived particles (lower-left side of the plots). Heavy leptons, as the ones predicted by the Type-III SeeSaw mechanism, require a different approach with respect to the searches for long-lived particles, which have a very different signature due to their macroscopic distances travelled before decaying inside the detector. These distances can range from order microns to several meters [39]. At the LHC, ATLAS [40], CMS [41] and LHCb [42, 43] experiments performed several searches for long-lived particles covering a large area of the phase-space to set exclusion limits on particles masses and lifetimes.

For heavy neutrino (HN) masses below 1 MeV, the mixing between electron neutrino and HN can be constrained by searches for *neutrinoless double β decay* and fine measurements of β -decay energy spectra [44]. For $1 \text{ MeV} < M_{HN} < 1 \text{ GeV}$, the mixing with both muon and electron neutrinos can be constrained by peak searches in leptonic decays of pions and kaons [44]. For mass values above the MeV scale, heavy leptons searches need to reach higher energy frontiers, such as the ones delivered by LHC.

Figures 1.8 and 1.9 summarize the state-of-the-art of heavy lepton searches in the mass range 100 MeV - 500 GeV, showing the most important constraints observed by collider experiments and some expected results from future experiments. The gray area labelled ‘BBN’ corresponds to an HN with a lifetime more than 1 second, that is disfavoured by Big Bang Nucleosynthesis (BBN) [45–47]. The brown contour labelled ‘Seesaw’ shows the mixing scale predicted by the canonical SeeSaw mechanism at the GeV-scale [38].

For the electron neutrino case (Figure 1.8), the following limits are reported:

- the dotted dark brown area ‘EWPD’ is the 90% CL exclusion limit from electroweak precision data [48];
- the contours ‘ $\pi \rightarrow e\nu$ ’ (solid yellow) [49–51] and ‘ $K \rightarrow e\nu$ ’ (solid black) [52] are excluded at 90% C.L. by peak searches;
- the zones ‘PS191’ (dot-dashed magenta) [53], ‘CHARM’ (dot-dashed dark blue) [54], ‘NA3’ (solid light yellow) [55] and ‘JINR’ (dashed dark red) [56] are excluded at 90% C.L. from beam-dump experiments;
- the solid cyan area ‘ $K \rightarrow ee\pi$ ’ is excluded at 90% CL from K -meson decay search using a detector size of 10 m [57];

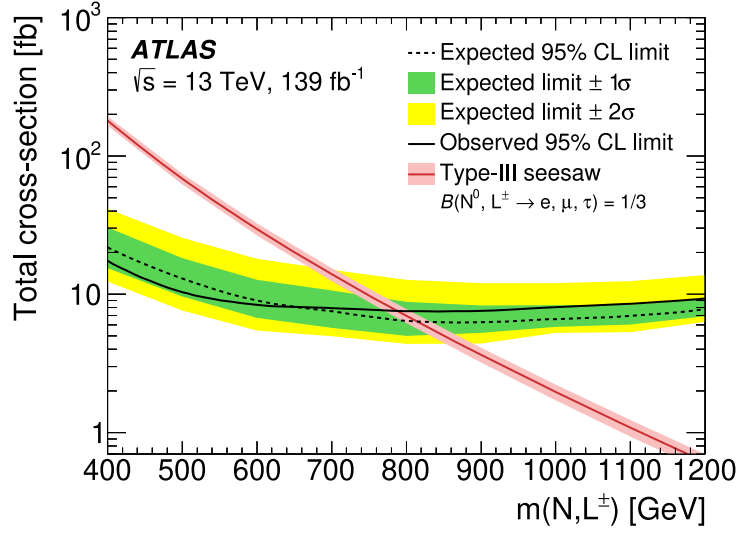
- the solid green region ‘Belle’ represents the exclusion limit at 90% CL reported by the Belle Collaboration for B -meson decay searches [58];
- the ‘L3’ (dashed pink) [59] and ‘DELPHI’ (dashed dark green) [60] contours are excluded at 95% CL performing a reanalysis of the LEP data;
- the solid red region ‘LEP2’ is excluded at 95% CL by direct searches for heavy leptons at LEP [61];
- the solid blue contour ‘ATLAS’ represents the exclusion limit obtained by performing direct searches at $\sqrt{s} = 8$ TeV using the ATLAS detector at the LHC [62];
- the ‘LHC 14’ contour (dashed blue) [44] is the expected exclusion limit using LHC data at $\sqrt{s} = 14$ TeV with 300 fb^{-1} while the ‘ILC’ region (solid purple) is the one obtained by using ILC data at $\sqrt{s} = 500$ GeV with 500 fb^{-1} [44, 63];
- the area ‘LBNE’ (solid light blue) is expected 5-year sensitivity of the LBNE near detector assuming a normal hierarchy of neutrinos [64];
- the solid dark green region ‘FCC-ee’ is the projected sensitivity at the future collider FCC-ee for 10^{12} Z -decays [65];
- the solid violet contour ‘SHiP’ is the projected reach of the proposed SHiP detector at 90% CL [66, 67].

Some of these observations are also used to set limits on the mixing between the muon neutrino and the HN (Figure 1.9), with in addition the following results:

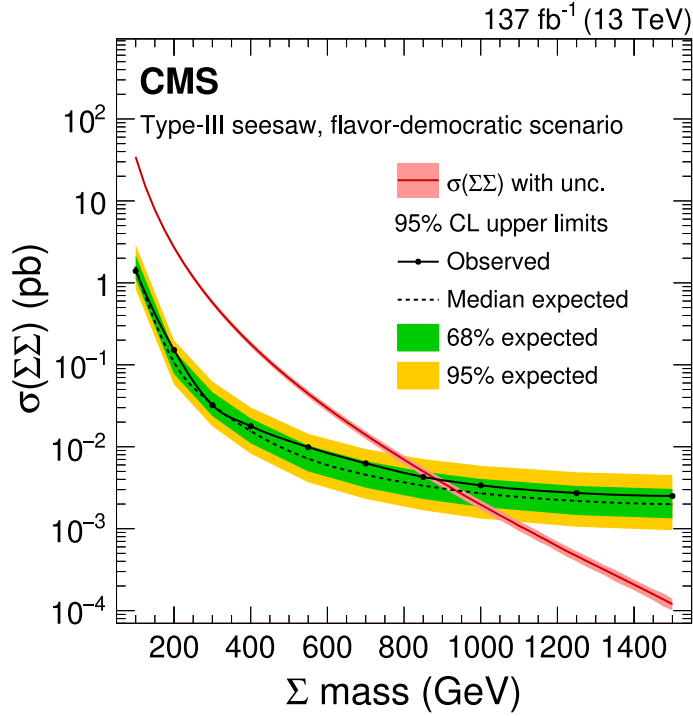
- the solid black contour ‘ $K \rightarrow \mu\nu$ ’ is excluded at 90% CL by peak searches [52, 68];
- regions ‘BEBC’ (dotted orange) [69], ‘FMMF’ (dashed light cyan) [70], ‘NuTeV’ (dashed purple) [71] are excluded at 90% CL from beam-dump experiments;
- the solid cyan area ‘ $K \rightarrow \mu\mu\pi$ ’ is excluded at 90% CL from K -meson decay search using a detector size of 10 m [57];
- the solid yellow contour represents the exclusion region at 95% CL from HN searches in B -meson decays at LHCb [72];
- the dot-dashed dark blue area ‘CHARM-II’ is excluded at 90% CL from the search for direct production with a wide-band neutrino beam at CERN [73];

- the solid red area ‘CMS’ is excluded at 95% CL from direct HN searches at $\sqrt{s} = 8$ TeV [74].

In this thesis the search for the Type-III SeeSaw heavy leptons in three- and four-lepton final states using the full ATLAS Run 2 dataset is presented. A combination with also the two leptons plus two jets channel will be given, showing for the first time the exclusion limit for the three most significant decay modes of the type-III SeeSaw heavy leptons.



(a)



(b)

Figure 1.7: Expected and observed 95% CLs exclusion limits for the Type-III SeeSaw process with the corresponding one- and two-standard-deviation uncertainty bands, showing the 95% CL upper limit on the cross-section. The theoretical signal cross-section prediction with its corresponding uncertainty band is also shown. Top: two-lepton channel plus two jets performed by ATLAS [36]. Bottom: three- and four-lepton channel performed by CMS [35].

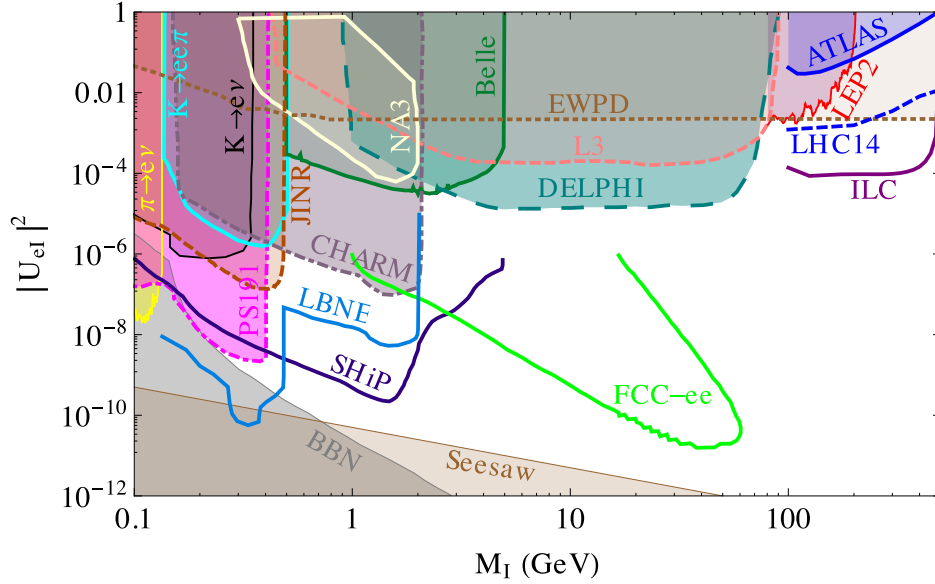


Figure 1.8: Limits on the mixing between the electron neutrino and a heavy neutral lepton in the mass range 100 MeV - 500 GeV [38].

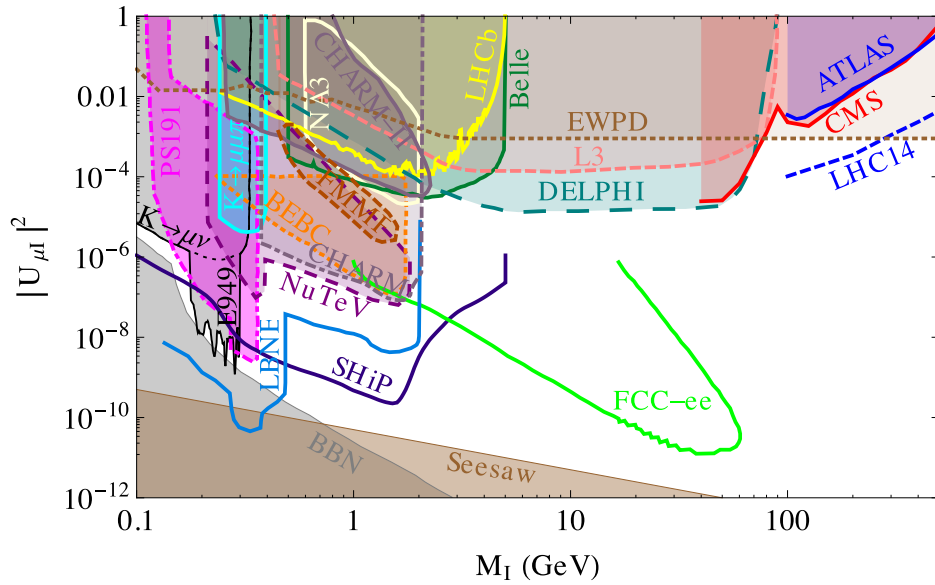


Figure 1.9: Limits on the mixing between the muon neutrino and a heavy neutral lepton in the mass range 100 MeV - 500 GeV [38].

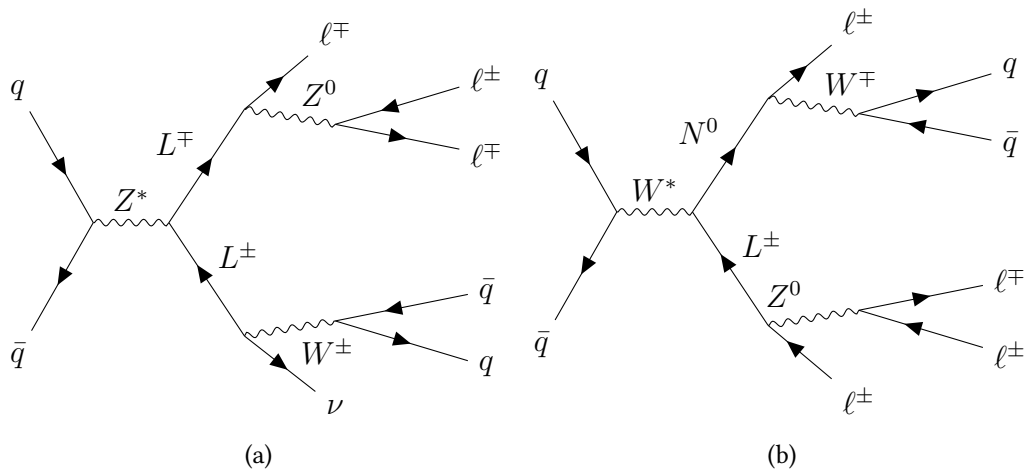


Figure 1.10: Example of Feynman diagrams for the considered Type-III SeeSaw heavy leptons pair production in the three- (a) and four-lepton (b) final states.

Chapter 2

LHC and the ATLAS experiment

2.1	The Large Hadron Collider	28
2.1.1	Acceleration Chain	32
2.1.2	Physics requirements	34
2.2	The ATLAS detector	37
2.2.1	Tracking	40
2.2.2	Magnet system	45
2.2.3	Calorimetry	47
2.2.4	Muon system	52
2.2.5	Forward detectors	57
2.2.6	Trigger, readout, data acquisition and control systems	59

The CERN (Conseil Européen pour la Recherche Nucléaire) is the world largest research center., founded in 1954. It sits astride the French-Swiss border near Geneva and now has 23 member states that cooperate to probe the fundamental laws of the Nature. Particle accelerators and detectors are used to reach this aim: beams of particles at very high energies are boosted into accelerators to collide with stationary targets or with other accelerated beams; detectors allow to record the results of each collision and observed them to perform every kind of studies.

The Large Hadron Collider (LHC) was built at CERN and represents the state-of-the-art of the particle accelerator. It is the newest CERN accelerator complex and it is the world's largest and most powerful particle accelerator. In 2010, it

started a long series of important data-takings. LHC is a circular accelerator, on its ring are placed four particle detectors: ATLAS, CMS, ALICE and LHCb.

2.1 The Large Hadron Collider

LHC is situated in the tunnel previously hosting the Large Electron-Positron Collider (LEP, 1989-2000), from 45 to 175 m under the ground of Geneva, as schematized in Figure 2.1. The collider ring is 26.7 Km long, it has superconducting magnets with radiofrequency cavities to increase the energy of the particles. The ring consists of eight arcs and of eight long straight sections (LSSs). LHC is designed to boost protons or heavy ions up to a center of mass energy $\sqrt{s}= 14$ TeV or $\sqrt{s}= 2.76$ TeV per nucleon, respectively. Particles travel in separate beam pipes in opposite directions in ultra-high vacuum (10^{-10} torr) colliding in eight Interaction Points (IP). The large particle physics experiments ALICE, ATLAS, CMS and LHCb are installed at IPs in the middle of four LSSs, while the other LSSs house the collimation (or beam cleaning) system, the radio-frequency system, the beam instrumentation and the beam dumping system.

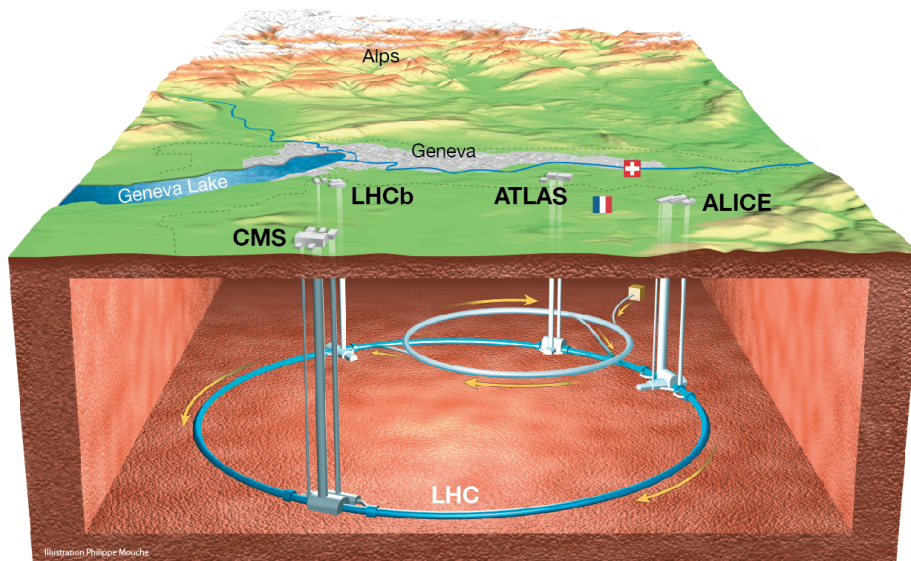


Figure 2.1: The LHC system in the underground of Geneva [75].

In order to boost the beam, 16 metallic chambers containing an electromagnetic field of 5.5 MV/m, known as radiofrequency cavities, are installed inside the accelerator. These cavities are placed in four cylindrical refrigerators called cry-

omodules, to work in a superconducting state. The two beams were structured in a maximum of 3564 bunch slots. At the maximum performance, during the Run-1 collisions took place every 50 ns, during the Run-2 every 25 ns. To keep the beams into circular trajectories, 1232 NbTi superconducting dipole magnets composed by coils of special electric cables, are used. They operate in superconducting state at 1.9 K, cooled by superfluid helium, and could generate a circulating current of 11.85 kA to endure a magnetic field of 8.4 T. The beams are focused by 392 superconducting quadrupole magnets producing a 6.8 T field each.

To measure the number of collisions that can be produced in a detector per cm^2 and per second, a fundamental quantity called *luminosity* \mathcal{L} is used. It is one of the most important parameters of an accelerator and it is defined only by machine parameters. Taking into account two identical beams, with a Gaussian shape and perfectly overlapping at the IP, the luminosity \mathcal{L} is defined as:

$$\mathcal{L} = f_r n_b \frac{N_1 N_2}{4\pi\sigma_x\sigma_y}, \quad (2.1)$$

with σ_x and σ_y are the transverse profiles of the beams, N_1 and N_2 the number of protons per bunch, n_b number of bunches, f_r the beam-revolution frequency. Generally, beams collide with a non-null crossing angle, then \mathcal{L} can be written as:

$$\mathcal{L} = f_r n_b \frac{N_1 N_2 \gamma}{4\pi\sigma_x\sigma_y\beta^* \epsilon_{xy}} \cdot F, \quad (2.2)$$

where ϵ_{xy} is the geometric emittance, γ the relativistic Lorentz factor and F is a geometric reduction factor given by [76]:

$$F = \frac{1}{\sqrt{1 + \frac{(\sigma_s \tan \phi)^2}{\epsilon_{xy}\beta^*}}} \quad (2.3)$$

where σ_s is the bunch length and ϕ half of the crossing angle.

Circulating along the LHC ring, beams lose intensity following the relation:

$$\mathcal{L} = \mathcal{L}_0 \cdot e^{-\frac{t}{\tau}} \quad (2.4)$$

where τ is a time constant which for LHC is ~ 15 h.

In the period 2015-2018, the so called Run-2, LHC performed the last data taking accelerating protons (and also heavy ions in dedicated runs) up to an energy of 6.5 TeV, producing collisions at a center-of-mass energy $\sqrt{s} = 13$ TeV at a maximum instantaneous luminosity of $L = 1.4 \times 10^{34} \text{ cm}^{-2} \text{ s}^{-1}$. In Figure 2.2, the scheduled periods of active work and technical stops together with the future plans of upgrades [77] are reported.

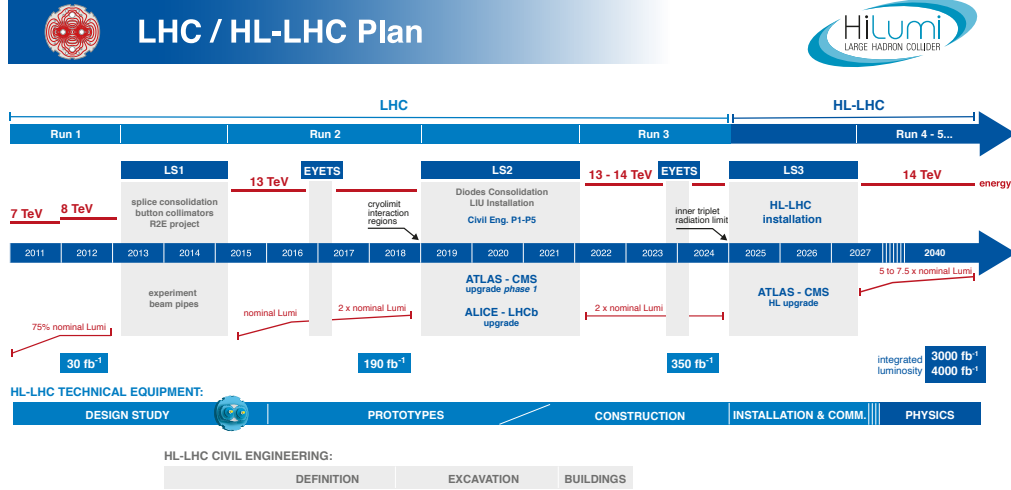


Figure 2.2: Time schedule of LHC, from Run-1 to last upgrade to High Luminosity LHC [77].

The most important luminosity-related parameters during the Run-1 and Run-2 periods are reported in table 2.1.

Parameter	2015	2016	2017	Design
Beam Energy (TeV)	6.5	6.5	6.5	7
Bunch spacing (ns)	25	25	25	25
Max number of bunches	2244	2220	2736	2808
Protons per bunch	$1.1 \cdot 10^{11}$	$1.1 \cdot 10^{11}$	$1.25 \cdot 10^{11}$	$1.1 \cdot 10^{11}$
Peak Luminosity ($cm^{-2}s^{-1}$)	$5 \cdot 10^{33}$	$1.1 \cdot 10^{34}$	$1.4 \cdot 10^{34}$	$1 \cdot 10^{34}$
Average Pile-up ($\langle\mu\rangle$)	~ 15	~ 25	~ 37	~ 20

Table 2.1: LHC performance during the operation of 2015-2017 compared to the machine design values [78].

In Figure 2.3a and 2.3b, the mean number of interactions per filled bunch crossing $\langle\mu\rangle$, called *pile-up* (μ), corresponding to the mean of the Poisson dis-

tribution on the number of interactions per crossing, is shown as a function of time, during pp collisions in 2015 [79] and 2018 [80].

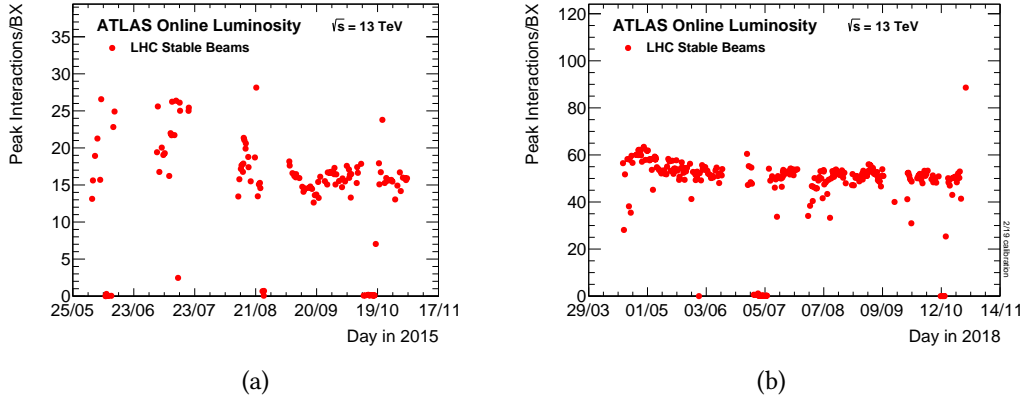


Figure 2.3: The mean number of interactions per filled bunch crossing per lumi-block versus day during the pp runs of (a) 2015 [79] and (b) 2018 [80]. For this calculation, the online luminosity measurement is used. Only the maximum value during stable beam periods is shown.

The recorded luminosity as function of the pile-up and the luminosity delivered to (green) and recorded by (yellow) the ATLAS detector, in 2015-2018, during stable pp beam collisions as a function of the time, are shown in Figure 2.4a and 2.4b, respectively. The recorded luminosity is evaluated during the fraction of time in which both the detector and the data acquisition system were active, with respect to the delivered luminosity which is provided in a safe standby mode. It is affected by the inefficiency of the data acquisition system, as well as the inefficiency of the so-called “warm start”: when the stable beam flag is raised, the tracking detectors undergo a ramp of the high-voltage and, for the pixel system, turning on the pre-amplifiers.

	Integrated Luminosity			
	2015 (pb^{-1})	2016 (fb^{-1})	2017 (fb^{-1})	2018 (fb^{-1})
Delivered	3.9	38.5	49.0	62.1
Recorded	3.6	35.5	46.4	60.0

Table 2.2: Delivered and recorded integrated luminosity \mathcal{L} in 2010 and 2011 ($\sqrt{s} = 7$ TeV), 2012 ($\sqrt{s} = 8$ TeV), 2015 and 2016 ($\sqrt{s} = 13$ TeV), by the ATLAS detector. [83]

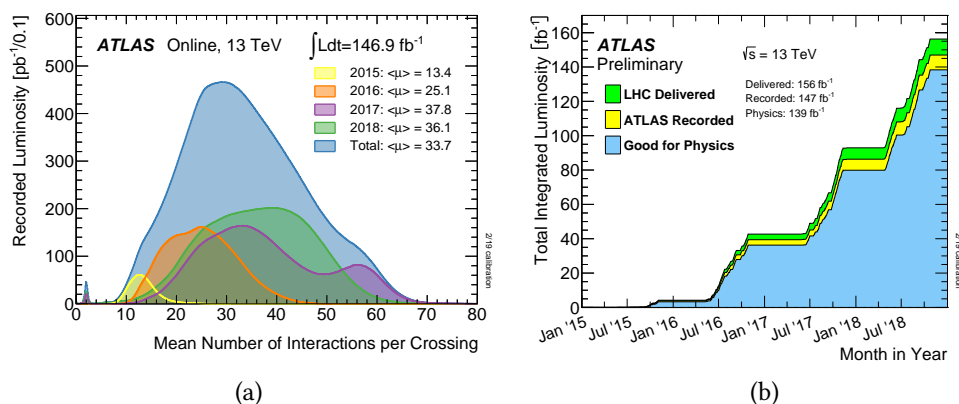


Figure 2.4: Left: Luminosity distribution as function of the mean number of interaction per crossing (pile-up) for the 2015-2018 pp collision data recorded by ATLAS at $\sqrt{s}=13$ TeV [81]. Right: Total integrated luminosity versus time delivered by LHC (green), recorded by the ATLAS detector (yellow) and certified to be good quality data (blue) during stable beams for pp collisions at 13 TeV centre-of-mass energy in 2015-2018 [82].

2.1.1 Acceleration Chain

The acceleration process in the LHC ring is only the final step of several acceleration processes performed by the CERN accelerators chain, as depicted in Figure 2.8.

Protons are obtained by a simple tank of hydrogen gas, ionised using an electric field to create plasma separating protons from electrons. Protons are then ready to be injected in an acceleration chain consisting of:

Linac2: linear accelerator to boost protons up to energy of 50 MeV (protons also gain 5% in mass). A system of quadrupole magnets is used to focus the beam. Protons (or heavy ions) are then injected to the Proton Synchrotron Booster (PSB), which took them to a higher energy.

PSB: is made up 4 superimposed synchrotron rings to accelerate protons up to 2 GeV for injection into the Proton Synchrotron (PS).

PS: was the first synchrotron at CERN, bending bend the beams round the circular trajectory. PS produces a proton bunch every 25 ns with 25 GeV of energy per proton. The beam is then sent to the Super Proton Synchrotron (SPS).

SPS: is a circular accelerator measuring 7 km in circumference. It operates at 450 GeV using 1317 electromagnets and 744 dipoles keeping the beams on a circular trajectory.

LHC: is the world's largest and most powerful particle accelerator, it is the last stage of the accelerator chain. Beams are transferred from SPS into two beam pipes at the LHC, one beam circulating clockwise and the other counter-clockwise. Particle beams travel close to the speed of light guided around the accelerator ring by two kind of superconducting magnets (both dipole and quadrupole) at -271.3°C (a temperature colder than outer space) cooled by a system of liquid helium. In 20 minutes each beam reaches its final energy of 6.5 TeV and collisions may start.

Along the LHC ring, the two beams are deviated to cross with each other in four interaction points in correspondence of the four experiments. They are:

ATLAS: (A Toroidal LHC ApparatuS) is a multi-purpose detector designed to work at high luminosity ($\mathcal{L} = 10^{34}\text{cm}^{-2}\text{s}^{-1}$) searching signatures of new physics and to perform precise Standard Model measurements;

CMS: (Compact Muon Solenoid) is a multi-purpose experiment which works at high luminosity. It pursues the same physics goals of ATLAS using different detector technologies;

LHCb: performs precise measurements in the flavour physics, focusing on the B mesons and CP violation observation. LHCb works at lower values of luminosity ($\mathcal{L} = 10^{32}\text{cm}^{-2}\text{s}^{-1}$), using an asymmetric design covering the forward direction along the beam pipe;

ALICE: (A Large Ion Collider Experiment) is designed to study the quark-gluon plasma state produced in heavy ion collisions (mainly ions). Using nucleus-nucleus collisions, it can work with a luminosity of $\mathcal{L} = 10^{27}\text{cm}^{-2}\text{s}^{-1}$.

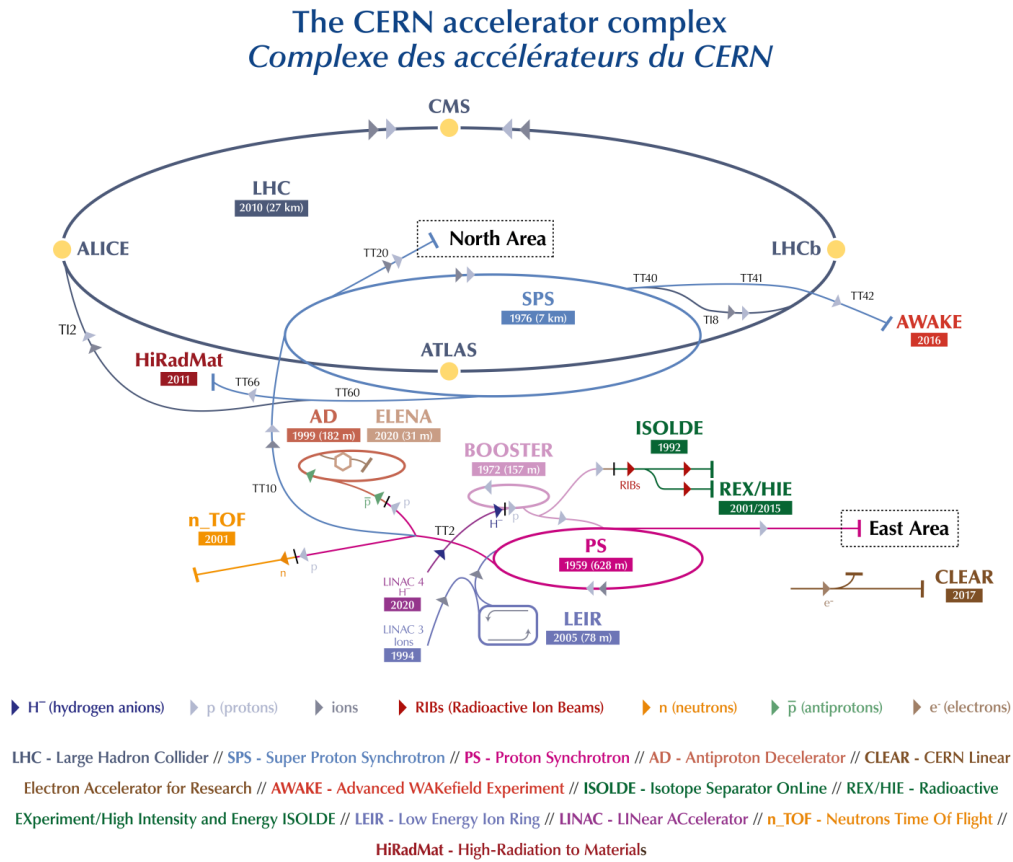


Figure 2.5: Scheme of the CERN accelerator complex [84].

2.1.2 Physics requirements

The LHC detectors were designed to observe rare physics processes in very challenging data taking conditions. The high luminosity and the large cross-sections available at the LHC allow high precision measurements of QCD, electroweak interactions and flavour physics. The severe conditions shown in Table 2.1 impose stringent requirements on the detector. Considering pile-up values in 2017, every 25 ns an average of 37 interactions per bunch-crossing must be recorded, and it is a hard challenge.

The nature of proton-proton collisions imposes another difficulty involving in multiple inelastic scatterings of hadrons constituents, namely *partons*, giving a non-null probability of multiple interactions even in a single collision. These events are referred to as *underlying events*. Rare processes from Beyond the Standard Model particles, such as the production of heavy leptons, doubly charged

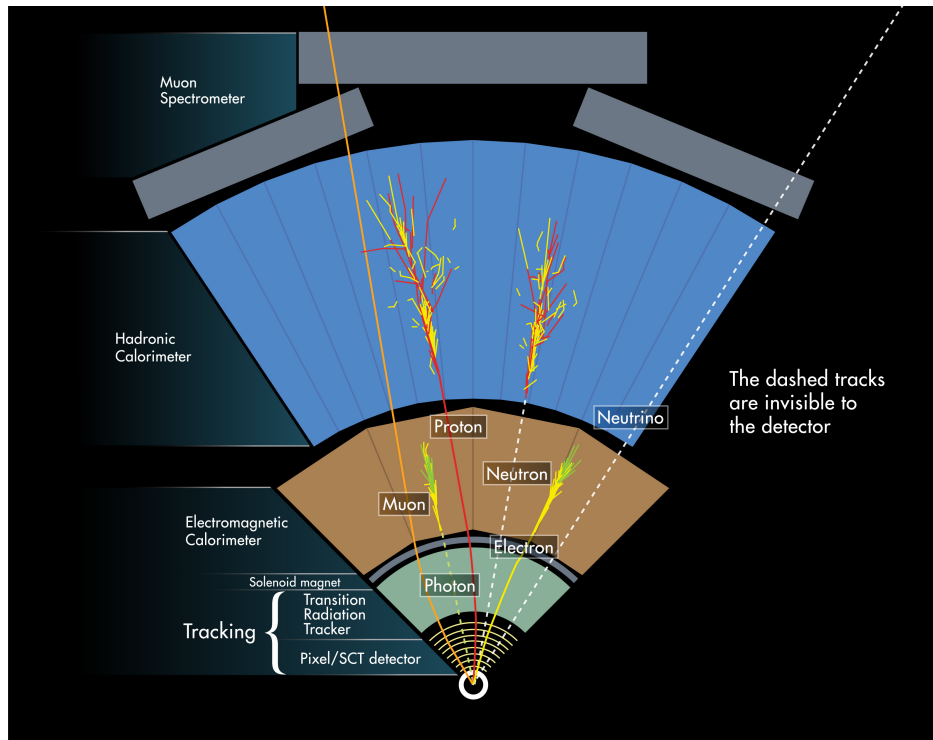


Figure 2.6: Different reconstruction of particles in ATLAS according to their different interactions with materials [85].

bosons or supersymmetric particles, require the identification of experimental signatures characteristic for these kind of processes., as E_T^{miss} , secondary vertex, or high- p_T objects. These final states imposes demand on the particle reconstruction capabilities for each detector and on the integrated luminosity needed. In Figure 2.6 the reconstruction of several particles in the ATLAS detector according to their different interactions with the detectors, is shown.

To identify and reconstruct physics phenomena, all the detectors must satisfy a general set of physical and technical requirements:

- radiation-hard electronics, sensor elements. Due to the high particle fluxes and the influence of overlapping events, a high detector granularity is needed;
- fast electronic response to limit the dead-time of the data acquisition system;
- large acceptance in pseudorapidity (η) and good azimuthal angle (ϕ) coverage for missing energy measurement and high efficiency particle detection;

- high resolution and full calorimetric and hadronic coverage for electron, photon, jets identification and energy measurements;
- good resolution on the secondary vertices to reconstruct τ -leptons and b -jets decays;
- tracking system with good charged-particle momentum resolution and reconstruction efficiency;
- good muon identification and momentum resolution over a wide range of momenta together with the determination of the charge for high p_T muons;
- efficient triggering system for both high- and low- p_T objects with good background rejection.

2.2 The ATLAS detector

The ATLAS detector shown in Figure 2.7 [86] is a multi-purpose particle detector placed approximately 100 meters underground at the Point-1 site along the LHC tunnel. It is 44 m long and it has a diameter of 22 m and has a cylindrical symmetry. Different sub-detectors compose ATLAS which are designed to reconstruct particles in pp collisions, such as electrons, photons, muons, jets and neutrinos (which are reconstructed in terms of E_T^{miss}). Starting from the IP, concentric layers of sub-detectors arranged around the beam pipe are placed in the following order: inner detector, the electromagnetic and hadronic calorimeters and the muon spectrometer. A magnetic system is also present to bend the trajectory of charged particles and allowing precise reconstruction of particle momenta.

The performance of the main sub-system are summarized in Table 2.3.

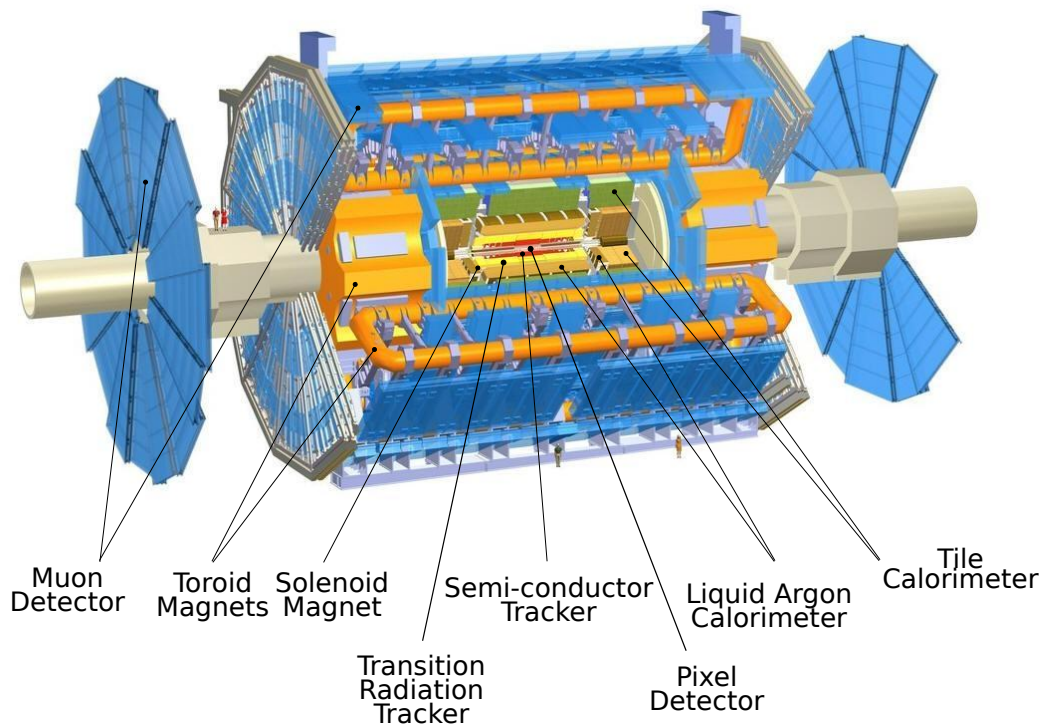


Figure 2.7: Cut-away view of the ATLAS detector. The dimensions of the detector are 25 m in height and 44 m in length. The overall weight of the detector is approximately 7000 tonnes. Adapted from [87].

Particles are detected inside the detector using the ATLAS coordinate system, taking the interaction point as the origin of the right-handed coordinate system with the beam direction defined on the z -axis and, consequently, the x - y plane

Detector component	Required resolution	Obtained resolution (2015)	η coverage	
			Measurement	Trigger
Tracking	$\sigma_{p_T}/p_T = 0.05\% p_T \oplus 1\%$	$\sigma_{p_T}/p_T = 0.038\% p_T \oplus 1.5\%$	± 2.5	
EM calorimetry	$\sigma_E/E = 10\%/\sqrt{E} \oplus 0.7\%$	$\sigma_E/E = 10\%/\sqrt{E} \oplus 0.2\%$	± 3.2	± 2.5
Hadronic calorimetry (jets)				
barrel (Tile) and end-caps (LAr)	$\sigma_E/E = 50\%/\sqrt{E} \oplus 3\%$	$\sigma_E/E = 50\%/\sqrt{E} \oplus 3\%$	± 3.2	± 3.2
forward (LAr)	$\sigma_E/E = 100\%/\sqrt{E} \oplus 10\%$	-	$3.1 < \eta < 4.9$	$3.1 < \eta < 4.9$
Muon spectrometer	$\sigma_{p_T}/p_T = 10\%$ at $p_T = 1$ TeV	$\sigma_{p_T}/p_T = 10\%$ at $p_T = 1$ TeV	± 2.7	± 2.4
combined with tracker	-	$\sigma_{p_T}/p_T = 7\%$ at $p_T = 1$ TeV	± 2.7	± 2.4

Table 2.3: General performance goals [86] and obtained resolutions in 2015 [88] of the ATLAS detector. If not indicated, the units for E and p_T are in GeV.

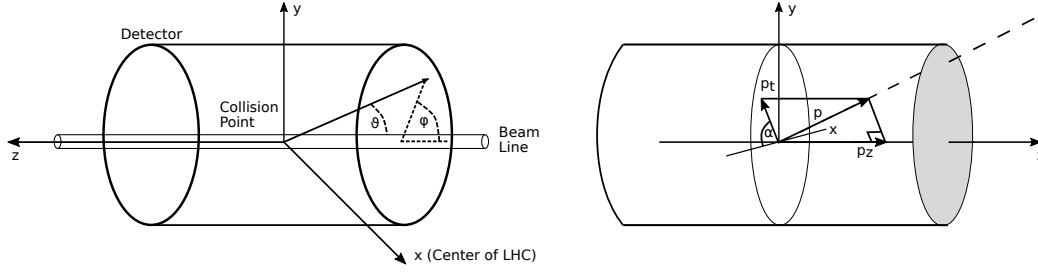


Figure 2.8: Left: ATLAS detector coordinate system. Right: Coordinate system in the transverse momentum plane.

is transverse to the beam direction. The x -axis points to the center of the LHC ring and the y -axis points up to the earth surface upwards. The z -axis divides the detector in two equal parts one on the side-A, for positive values of z , the other one on side-C, for the negative values. A transverse plane is defined in terms of r - ϕ coordinates, with ϕ measured from the x -axis, around the beam and r is the distance from the beam line. The polar angle θ is defined as the angle from the positive z -axis. Assuming negligible the initial transverse momentum (in the xy plane) of the proton beam, the final p_T can be written as:

$$\sum p_T \simeq 0, p_T = \sqrt{p_x^2 + p_y^2} \quad (2.5)$$

then it is useful to identify a set of Lorentz-invariant variables, such as the *rapidity* y :

$$y = \frac{1}{2} \ln \left(\frac{E + p_z}{E - p_z} \right), \quad (2.6)$$

where E and p_z are the energy and the z -axis momentum component of the par-

title. For objects with negligible mass with respect to the energy, it corresponds to the pseudorapidity η :

$$\eta = -\ln \left[\tan \left(\frac{\theta}{2} \right) \right] \quad (2.7)$$

The transverse momentum p_T , the transverse energy E_T and the missing transverse energy E_T^{miss} are defined in the x - y plane. In the η - ϕ space, ΔR distance can be introduced:

$$\Delta R = \sqrt{\Delta\eta^2 + \Delta\phi^2}. \quad (2.8)$$

The ATLAS detector has a forward-backward symmetry with respect to the IP. The magnet configuration comprises a thin superconducting solenoid surrounding the inner-detector cavity, and three large superconducting toroids (one barrel and two end-caps) arranged with an eight-fold azimuthal symmetry around the calorimeters; this choice has driven the design of the rest of the detector.

2 T solenoidal field. wraps the *inner detector* region. Combining the inner part, composed by high-resolution semiconductor pixel and strip detectors, and the outer part, with straw-tube tracking detectors with the capability to generate and detect transition radiation, momentum, trajectory, vertex measurements and pattern recognition are achieved.

Measurements of energy and position of electrons and photons can be provided by the high granularity *liquid-argon (LAr)* electromagnetic sampling calorimeters with excellent performances. The hadronic calorimetry is a scintillator-tile calorimeter which surrounds the *LAr* calorimeter, it is separated into a large barrel and two smaller extended barrel cylinders, one on either side of the central barrel.

The *muon spectrometer* surrounds the calorimeter and defines the overall dimensions of the ATLAS detector. A strong bending power is generated by the air-core *toroid system*, with a long barrel and two inserted end-cap magnets. For high- p_T muons, the muon-spectrometer performance (see table 2.3) is independent of the inner-detector system.

The proton-proton interaction rate at the design luminosity of $10^{34} \text{ cm}^{-2}\text{s}^{-1}$ is approximately 40 MHz (considering about 30 interactions per bunch crossing), while the event data recording, based on technology and resource limitations, is limited to about 1 kHz. The *Level-1 trigger* (L1) system uses a subset of the total detector information to make a decision on whether or not to continue processing an event, reducing the data rate to approximately 100 kHz (limited by the bandwidth of the readout system). The *high-level trigger* provides the reduction to a final data-taking rate of approximately 1 kHz.

2.2.1 Tracking

All the ATLAS tracking system detectors are schematized in Figures 2.9a and 2.9b.

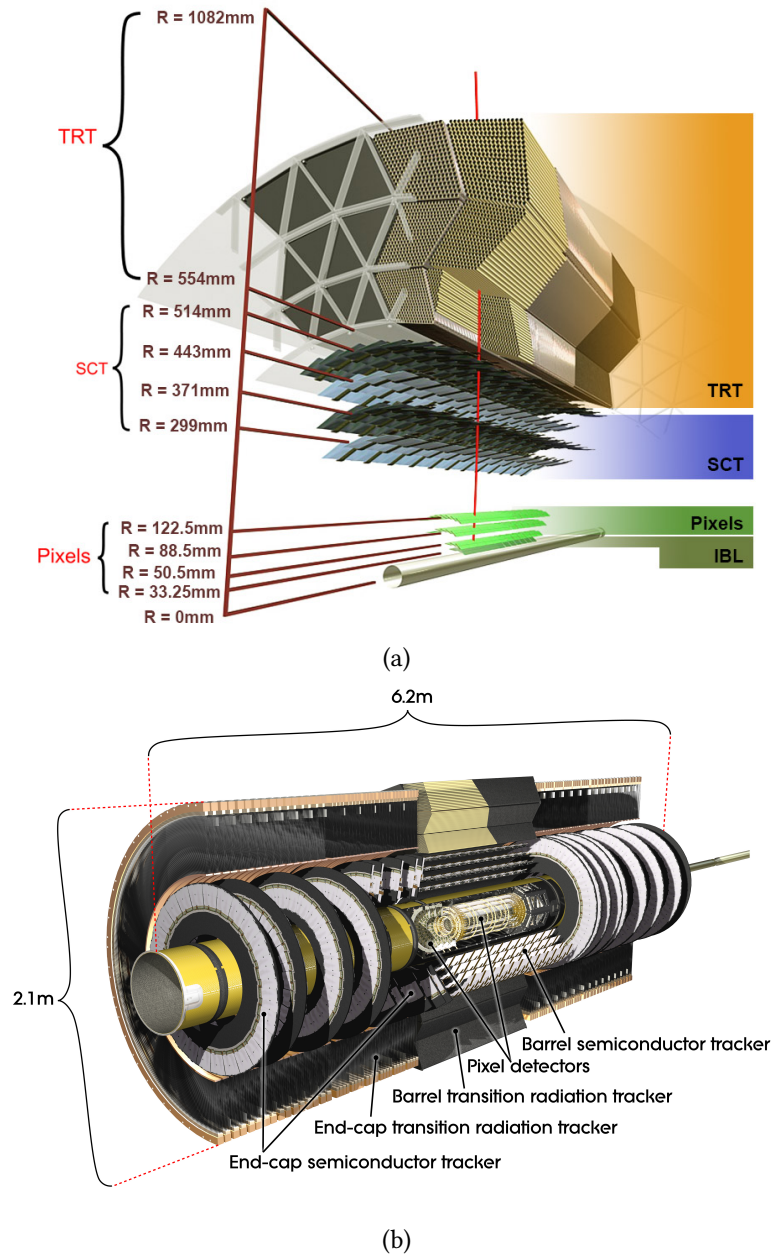


Figure 2.9: Top: Schematic layout of the Inner Detector including the new Insertable B-Layer [86]. The distances to the interaction point are also shown. Bottom: Cut-away view of the ATLAS inner detector [86].

From the collision point, every 25 ns within $|\eta| < 2.5$ a very large track density is generated in the detector with the production of about 1000 particles.

The **Inner Detector** (ID) placed close to the IP inside the central solenoid, and it is the first detector crossed by a particle produced inside a collision. It is immersed in a 2 T magnetic field generated by the central solenoid, which extends over a length of 6.2 m with a diameter of 2.5 m [86]. Bending particles by the magnetic field, the ID provides measurements of the charge and momentum. Interaction vertices are reconstructed by the extrapolation of tracks to their origin point in the beam pipe. The primary vertex corresponds to the vertex where pp collisions take place, while secondary vertices correspond to the position of heavy particle decay.

The ID is composed by the Insertable B-Layer (IBL), pixel and the Semi Conductor Trackers, covering the region $|\eta| < 2.5$ (see Figure 2.9a and 2.9b) and globally provides a transverse impact parameter resolution of $\simeq 35$ ($\simeq 10$) μm for pions with $p_T = 5$ (100) GeV and a transverse momentum resolution of about 4% for 100 GeV muons.

In the barrel region, the ID is arranged on concentric cylinders around the beam axis, in the end-cap regions it is located on disks perpendicular to the beam axis (the IBL is not present in this region). Around the vertex region, using silicon pixel detectors, the highest granularity is achieved.

The *Insertable B-Layer* (the 2015 upgrade of the ATLAS detector), the *Pixel* and the silicon microstrip of the *Semi Conductor Trackers* (SCT), used in conjunction with the straw tubes of the *Transition Radiation Tracker* (TRT) (see Figure 2.9b), allow to reach the required momentum and vertex resolution. The resolution of principal kinematic quantities are listed in table 2.4.

Parameter	p_T	η	Value
Momentum resolution	100 GeV	~ 0	3.8%
Momentum resolution	100 GeV	~ 2.5	11%
Transverse impact parameter resolution	1000 GeV	~ 0	11 μm
Transverse impact parameter resolution	1000 GeV	~ 2.5	11 μm
Identification efficiency for pions	1 GeV	-	84.0%
Identification efficiency for electrons	5 GeV	-	90.0%

Table 2.4: Main performance of the ATLAS tracking detector.

The inner detector system provides tracking, vertex and impact parameter

measurements in a range matched by the precision measurements of the electromagnetic calorimeter. The secondary vertex measurement performance is enhanced by the innermost layer of pixels and by the new IBL.

The combination of precision trackers at small radii with the TRT at a larger radius gives very robust pattern recognition and high precision in both R - ϕ and z coordinates.

The Insertable B-Layer

The IBL is the sub-detector closest to the beam pipe, it measures charged tracks at the smallest radius from the beam lines. The IBL is made of a single cylindrical layer of silicon pixel to give information on the decay vertices of short living particles and the impact parameter. It is placed between the thinner Beryllium beam pipe and the inner Pixel layer. Its layout is composed by a barrel layer consisting of 14 staves equipped with both planar and 3D silicon pixels along 332 mm on each side of the ATLAS detector. The total envelope of the IBL in radius is between 31 and 40 mm while the average radial distance of the sensitive area from the beam is 33 mm. The radiation length at $\eta = 0$ of the IBL is 1.54% of X_0 .

IBL guarantees a full ϕ coverage for high- p_T tracks with an intrinsic precision in the coordinate measurements of 23 μm . The silicon pixel size is 50 μm in the ϕ direction and 250 μm in the z direction in order to lower the occupancy at high luminosity.

The insertion of IBL into the ID closes proximity to the interaction point, improves the quality of the impact parameter and vertex reconstruction, increasing the b -tagging performance. For example, considering the b -tagging, the IBL reduces the probability of tagging the wrong particle type by a factor ~ 2 [90], while providing the same tagging efficiency.

Pixel detector

The pixel detector (PD), Figure 2.10, is composed by three layers of silicon pixels, placed at 50.5, 88.5 and 122.5 mm from the detector center. Due to the high particle density in this region, the PD has a thin granularity. All pixel sensors are identical and are 50 $\mu\text{m} \times 400 \mu\text{m}$. ($\phi \times z$) in size. The PD consists of 1744 pixel modules organized in the three barrel layers, containing approximately 67 millions of pixels. They are complemented by three end-cap disks on each side, containing 13 millions of pixels corresponding to about 80 million readout channels. The total area covered by the PD system is about 1.7 m^2 . Due to the effect of the Lorentz deviation, in the barrel region the pixel modules are tilted of 20° with respect to the cylinder's tangent.

The innermost barrel layer is placed at $R=51$ mm and the outer one at $R=123$

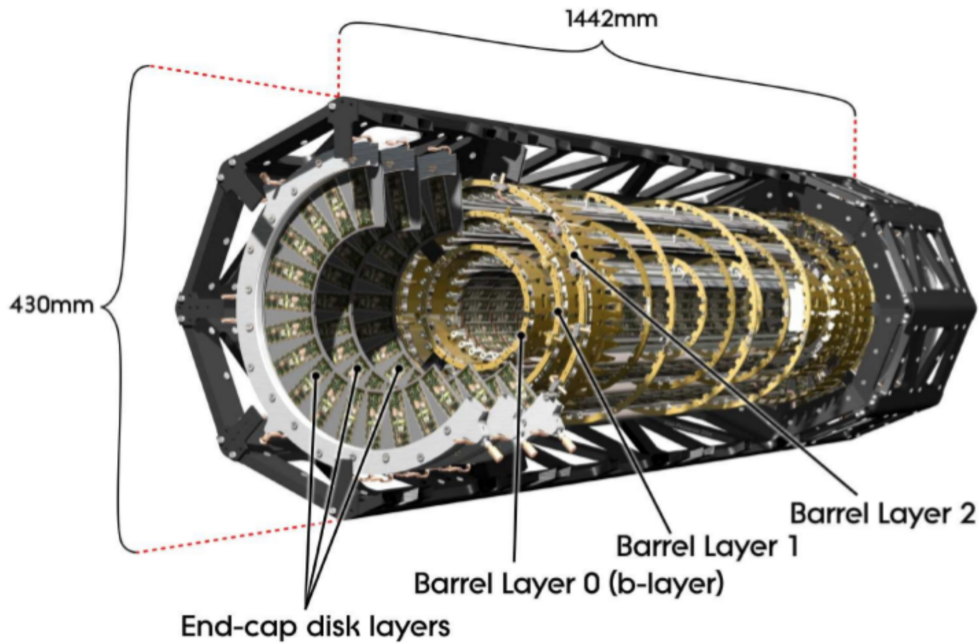


Figure 2.10: Cut-away view of the ATLAS pixel detector [86].

mm from the z -axis. The first end-cap disk is located at $|z|=495$ mm and the last at $|z|=650$ mm. The PD dimensions are chosen to maximize the probability that a particle cross all the three layers. The intrinsic precision in the coordinate measurements in the barrel is $10\ \mu\text{m}$ for the R - ϕ and $115\ \mu\text{m}$ for the z -coordinate, while in the end-caps is $10\ \mu\text{m}$ for the R - ϕ plane and $115\ \mu\text{m}$ R -coordinate.

The micro-strip detector

The layout of the detector is given in Figure 2.9b. The SCT system is designed to provide track precision measurements of momentum, impact parameter and vertex position in the intermediate radial range of the ID, where it is placed. The SCT uses the similar semiconductor technology as the PD, providing measurements with silicon microstrips of $120\ \text{mm} \times 60\ \text{mm}$ in $\phi \times z$ instead of pixels.

The SCT barrel section is composed of four layers of silicon microstrip modules placed at 300, 373, 447 and 520 mm from the beam pipe. This detector uses stereo strips with small-angle (40 mrad) to the position measurements. One set of strips is used in each layer parallel to the beam direction, to measure R - ϕ . The radiation length at $\eta = 0$ is approximately $0.1 X_0$. In the SCT approximately 6.3 million of readout channels are provided.

In the end-cap region, nine layers of silicon microstrip are located in the

region $850 \text{ mm} < z < 2730 \text{ mm}$. The detectors have a set of stereo strips at small-angle and a set of strips running radially.

Because of the pixel sensor geometry, they have good 2-dimension coverage, on the other hand microstrips have a better resolution along one coordinate. The spatial resolutions of the SCT in the barrel are $17 \mu\text{m}$ (R - ϕ) and $580 \mu\text{m}$ (z) and in the end-caps are $17 \mu\text{m}$ (R - ϕ) and $580 \mu\text{m}$ (R).

The straw-tube tracking detector

The TRT is the outer part of the ID, see Figure 2.9b. It is a combination of a Transition Radiation detector for the pattern recognition and a tracker based on the straw tubes. With the Transition Radiation detector, light and heavy particles can be discriminated through several layers of material with different refraction indices, producing transition radiation depending on the speed of the incident particle. The high relativistic particles (typically electrons) are recognised by the wider emitted radiation with respect to the other incident particles.

A xenon-based gas mixture of the straw tubes is used to enhance electrons identification capabilities by the detection of transition-radiation photons.

The detector is made by Polyimide drift (straw) tubes of 4 mm diameter containing the anodes: tungsten wires plated gold, connected to the front-end electronics and kept at ground potential. A mixture of gases (70% Xe, 27% CO₂ and 3% O₂) is used to fill the gap between the straw and the wire. Ionizing particle induces a low amplitude signal on the anodes. The passage through the polypropylene fiber stimulates transition radiation emission from ultrarelativistic charged particles causing X-ray emission, which contributes to ionization as a high energy signal. This process leads to an high signal in the TRT electronic that can be distinguished from ionization signal by the its amplitude. Signals are then amplified, shaped and discriminated according to the thresholds: a low-threshold (LT) of about 300 eV and a high-threshold (HT) of about 6-7 keV.

Figures 2.11a and 2.11b show events as a function of the HT fraction, defined as the ratio between the number of hits exceeding the HT and the total number of hits on the track. From the shape of the curve electrons and pions can be distinguished, as shown in the plots. The misidentification probability reaches a maximum of 12% in the $0 < |\eta| < 0.625$ region.

A large number of hits (typically 36 per track) is provided by the straw tubes of the TRT, which enables track-following up to $|\eta| = 2.0$. The TRT only provides R - ϕ information with a spatial resolution of $130 \mu\text{m}$ per straw. In the barrel region, the straws are located parallel to the beam pipe and are 144 cm long, their wires are divided into two halves, approximately at $\eta = 0$. In the end-cap region, the straws are arranged radially in wheels. The radiation length at $\eta = 0$ is approximately $0.2 X_0$.

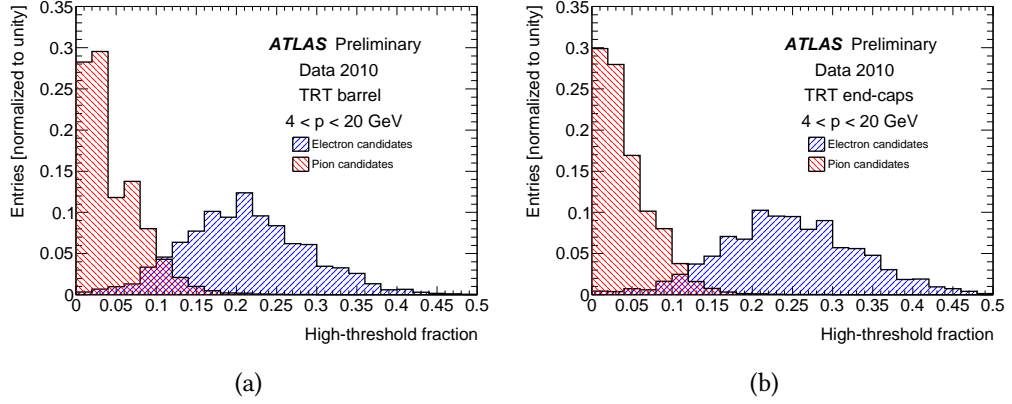


Figure 2.11: The HT fraction for electrons from photon conversions and pion candidates in the momentum range $4 \text{ GeV} < p_T < 20 \text{ GeV}$, in the barrel region (left) and in the end-cap region (right) [91].

The resolution of the ID is parameterized in terms of z_0 , defined as the longitudinal impact parameter, and d_0 , as the distance of closest approach to the beam-line:

$$\sigma(d_0) = 12 \oplus \frac{88}{p_T \sqrt{\sin(\theta)}} \mu\text{m} \quad (2.9)$$

$$\sigma(z_0) = 95 \oplus \frac{160}{p_T \sqrt{\sin^3(\theta)}} \mu\text{m} \quad (2.10)$$

where the track p_T is in units of GeV/c . In Figures 2.12a and 2.12b the impact parameters resolution $\sigma(d_0)$ and $\sigma(z_0)$ measured from data in 2015 at $\sqrt{s} = 13 \text{ TeV}$ are reported, respectively.

2.2.2 Magnet system

For accurate track reconstruction and momentum measurement, a strong magnetic field must be used to provide sufficient bending power.

The curvature radius ρ of a particle with a charge q and a momentum p travelling in a magnetic field B is derived using the Lorentz force:

$$\rho = \frac{|\vec{p}|}{q |\vec{B}|}. \quad (2.11)$$

Equation 2.11 increases with momentum and decreases at higher magnetic field values. The ATLAS magnetic system is 22 m in diameter and 26 m in length, with a stored energy of 1.6 GJ. The general layout is shown in Figure 2.13. The

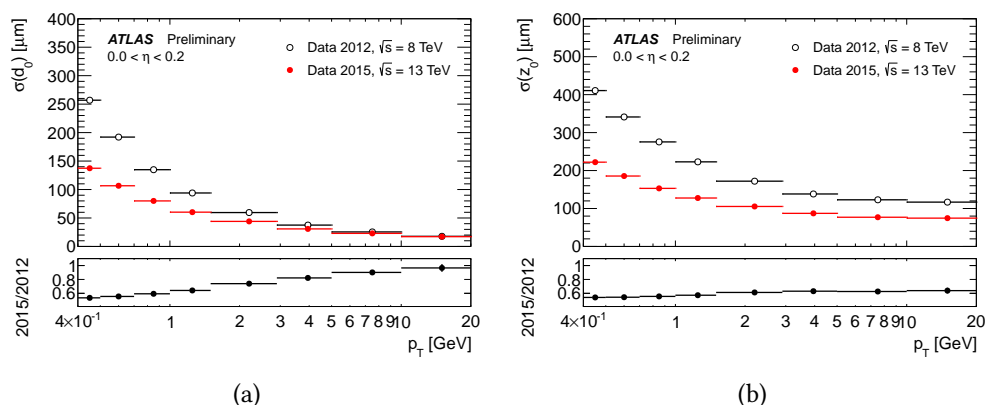


Figure 2.12: Unfolded transverse impact parameter resolution measured from data in 2015, $\sqrt{s} = 13$ TeV, with the Inner Detector including the IBL, as a function of p_T , for values of $0.0 < \eta < 0.2$, compared to that measured from data in 2012, $\sqrt{s} = 8$ TeV. The data in 2015 is collected with a minimum bias trigger. The data in 2012 is derived from a mixture of jet, tau and E_T^{miss} triggers. Figure 2.12a shows the distribution for $\sigma(d_0)$, while Figure 2.12b for $\sigma(z_0)$ [92].

four main layers of detectors and the four superconducting magnets provide the magnetic field over a volume of approximately 12000 m^3 .

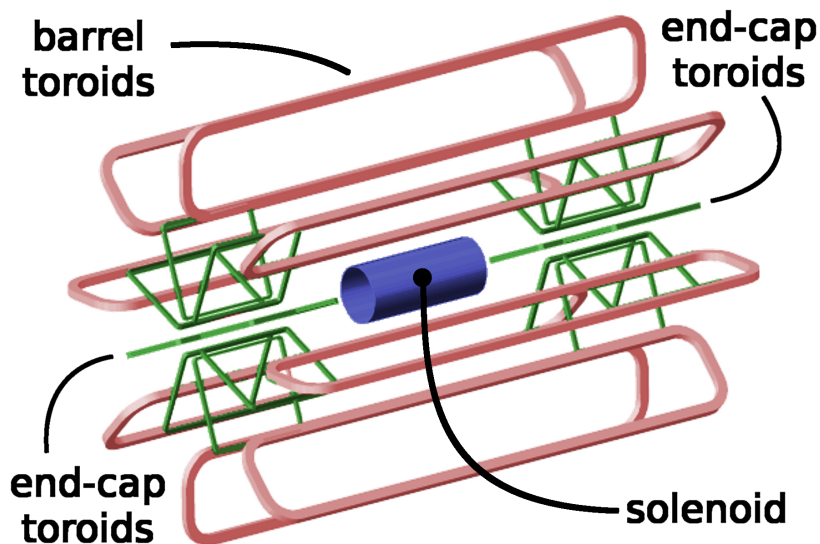


Figure 2.13: Geometry of magnet windings and tile calorimeter steel [86]. The eight barrel toroid coils, with the end-cap coils interleaved are visible. The solenoid winding lies inside the calorimeter volume.

The system consists of following superconducting magnets:

- a **solenoid**, 2.5 m of diameter and 5.3 m long, is aligned on the beam pipe axis and provides a 2 T axial magnetic field for the ID. The layout was designed to keep the material thickness in front of the calorimeter as low as possible. The solenoid assembly contributes to a total of $\simeq 0.66$ radiation lengths at normal incidence;
- a **toroid** system, provides a field orthogonal to the muon trajectories up to $\simeq 4$ T. As shown in Figure 2.13, it is composed by eight Barrel Toroids (BT) 25 m long, with an inner radius of 9.4 m and an outer diameter of 20.1 m, and two End-Cap Toroids (ECT) 5 m long (inner radius 1.64 m, outer diameter 10.7 m). The ECT coil system is rotated by 22.5° with respect to the barrel toroid coil system in order to optimise the bending power at the interface between the two coil systems and to provide radial overlap. Its field is orthogonal to the beam axis and deviates particles in the region $1.4 < |\eta| < 2.7$, while the BT provides the particle bending in the region $\eta < 1$. In the transition region $1.0 < |\eta| < 1.4$, the magnetic field is produced by both the BT and the ECT. The ATLAS magnetic system is cooled at liquid helium temperature (4.8 K).

2.2.3 Calorimetry

The calorimeter is designed to trigger and to measure destructively energy and position measurements of electrons, photons, jets, neutrons and missing E_T . It is designed to absorb most of the particles coming from a collision, forcing them to deposit all of their energy and stop within the detector.

A view of the ATLAS calorimetry system and its main characteristics are shown in Figure 2.14 and in Table 2.5 respectively. The calorimeters cover the range $|\eta| < 4.9$. On the η region matched to the ID, ($|\eta| < 2.5$), the high granularity of the EM calorimeter is designed for precision measurements of electrons and photons. The minor granularity in the rest of the calorimeter is sufficient to satisfy the physics requirements for jet reconstruction and E_T^{miss} measurements.

Several sub-systems are involved in the ATLAS calorimeter system, all of them placed in three cryostats, one barrel and two end-caps. The electromagnetic barrel calorimeter is contained in the barrel cryostat, while the electromagnetic end-cap calorimeter (EMEC), the hadronic end-cap calorimeter (HEC) and the forward calorimeter (FCal) are located each one in the two end-cap cryostats to cover the region closest to the beam. The FCal uses Liquid Argon (LAr) to provide both electromagnetic and hadronic energy measurements.

All the calorimeters need an active material to measure the particles energy. LAr has been chosen for its intrinsic radiation-hardness, its stability of response over time and its intrinsic linear behaviour. In the hadronic barrel scintillating

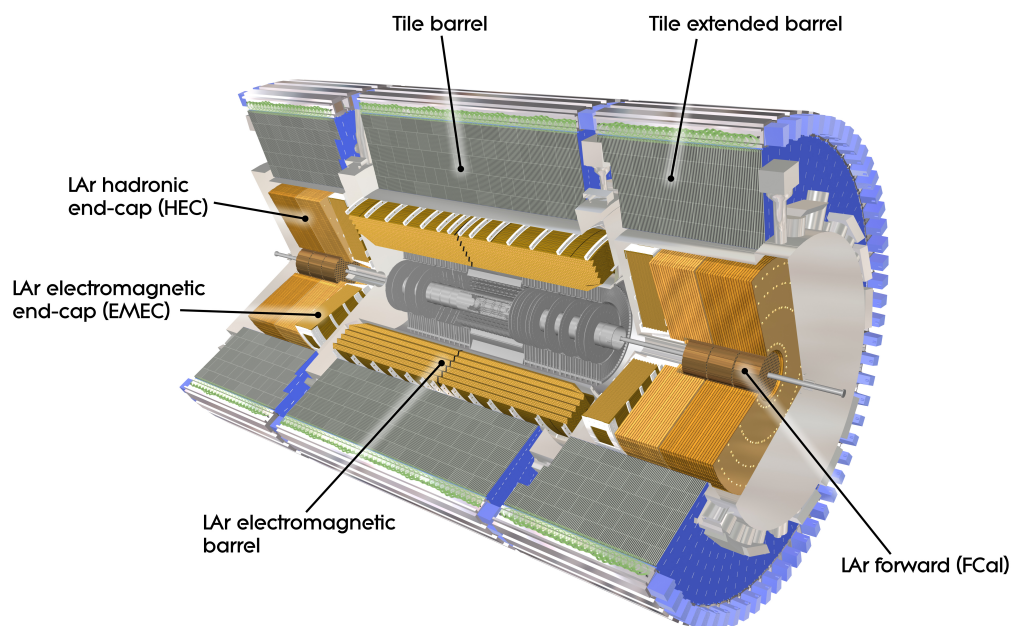


Figure 2.14: Cut-away view of the ATLAS calorimeter system [86].

Calorimeter Type	Active material	Passive material	X_0	λ	η coverage
EM LAr (barrel/end-cap)	LAr	Pb	22/24	2.2	$< 1.475 / 1.375 < \eta < 3.2$
Hadronic Tile	Scintillating tiles	Fe		9.7	$0.8 < \eta < 1.7$
Hadronic LAr end-cap	LAr	Cu		10	$1.5 < \eta < 3.2$
LAr Forward (EM/Hadronic)	LAr	Cu/W	27/91	2.7/3.7	$3.1 < \eta < 4.9$

Table 2.5: Main features of the sampling calorimeters of the ATLAS detector. The interaction (λ) and radiation (X_0) lengths values refer to $|\eta| = 0$ and $|\eta| = 3.2$ for the barrel and the end-cap regions respectively.

tiles are used to contain the shower of jets .

Calorimeters provide good transverse energy resolution taking advantage of its hermeticity and containing electromagnetic and hadronic showers. The calorimeters have enough thickness to achieve a good containment for jets to limit the punch-through into the muon system. The total thickness of the EM calorimeter is more than 22 radiation lengths (X_0) in the barrel and more than 24 X_0 in the end-caps. The Hadronic calorimeter in the barrel provides good resolution for high energy jets exploiting its 9.7 interaction lengths (λ) (10λ in

the end-caps). Considering also the 1.3λ from the outer support, the total thickness is 11λ at $\eta = 0$, which is enough to reduce punch-through well below the irreducible level of prompt or decay muons. Together with the large η -coverage, this thickness will also ensure a good E_T^{miss} measurement, which is important for many physics signatures and in particular for Beyond Standard Model searches as the one on the Type-III SeeSaw Heavy leptons. Secondary particles produce other particles by the same mechanism generating a cascade. The longitudinal size of an electromagnetic cascade is described in terms of the radiation length, X_0 , depending on the material itself, representing the average path the particle.

In Table 2.3 the required resolutions of both EM and Hadronic Calorimeter are reported.

LAr electromagnetic calorimeter

The EM calorimeter is a sampling calorimeter which uses LAr as active medium and lead as passive medium. Lead plates were chosen as passive medium because their large electromagnetic cross-section: high energy electrons and photons mainly interact via bremsstrahlung or pair production, generating an electromagnetic shower. The radiation length X_0 represents the average path a particle needs to travel to reduce its initial energy by a factor $1/e$. For example, calorimeters with $25 X_0$ thickness, has a shower leakage beyond the end of the detector less than 1%, up to electron energies ~ 300 GeV.

The EM calorimeter is composed by a barrel part and two end-cap components in the η region in $|\eta| < 1.475$ and $1.375 < |\eta| < 3.2$, respectively. In front of the calorimeter, in $|\eta| < 1.8$, an additional pre-sampler detector, made by an active layer of liquid argon of 1.1 cm thickness, provides a correction to the energy loss. The barrel part is divided into two half separated by a 6 mm gap at $z = 0$, whereas each end-cap is divided into two coaxial wheels: an outer one covering the region $1.375 < |\eta| < 2.5$ and an inner wheel covering $2.5 < |\eta| < 3.2$.

The accordion geometry of the EM calorimeter is shown in Figure 2.15. It has been chosen to provide a complete ϕ symmetry without azimuthal cracks. The total thickness of the EM calorimeter is larger than $24 X_0$ in the barrel and larger than $26 X_0$ in the end-caps. Because many physics analysis, both searches and measurements, require object in the region $|\eta| < 2.5$, the EM calorimeter is segmented into three longitudinal sections. For the end-cap inner wheel, the calorimeter is segmented in two sections in depth providing a lower lateral granularity than for the rest of the acceptance.

Figure 2.15 shows the the barrel calorimetry structure, arranged in three different layers:

Inner Layer: $4.3 X_0$ long, consists of strips with $\Delta\eta = 0.0031$ to discriminate charged and neutral pions;

Middle layer: $16 X_0$ long, is divided in squared towers $\Delta\eta \times \Delta\phi = 0.025 \times 0.025$;

Outer layer: made by towers with $\Delta\eta \times \Delta\phi = 0.050 \times 0.025$, was designed to measure showers of electrons and photons with energy $E > 50$ GeV.

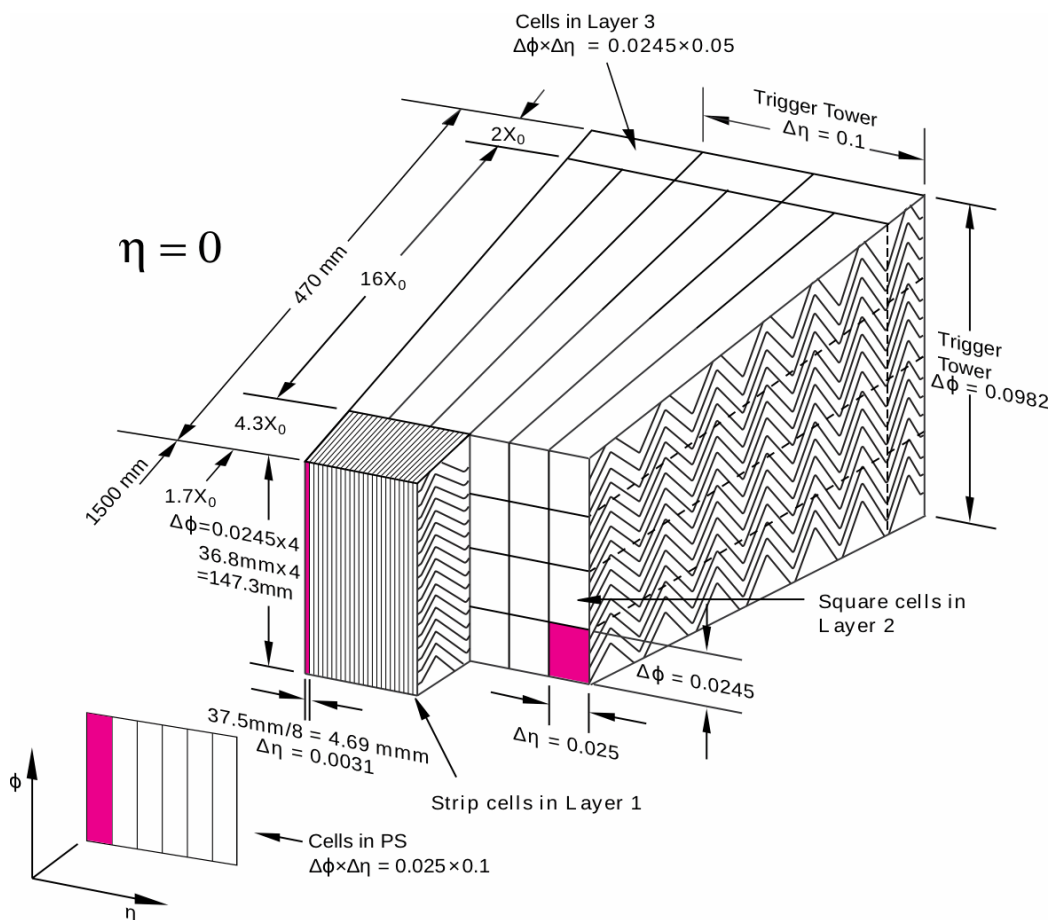


Figure 2.15: Sketch of a barrel module with the accordion geometry. The granularity in η and ϕ cells of each of the three layers and of the trigger towers is also shown [86].

The readout system is composed by an ADC system, shapers, analog pipelines and pre-amplifiers located outside the cryostats. The readout electrodes are located in the gaps between the lead absorbers and segmented in three conductive copper layers separated by insulating Polyimide sheets.

In Figures 2.16a and 2.16b, the energy resolution obtained using simulated single-particle MC samples for electrons and unconverted photons is shown, respectively. The resolution is defined as the interquartile range of $E_{\text{calib}}/E_{\text{gen}}$,

where E_{gen} is the true energy of the generated particle and E_{calib} is the reconstructed energy.

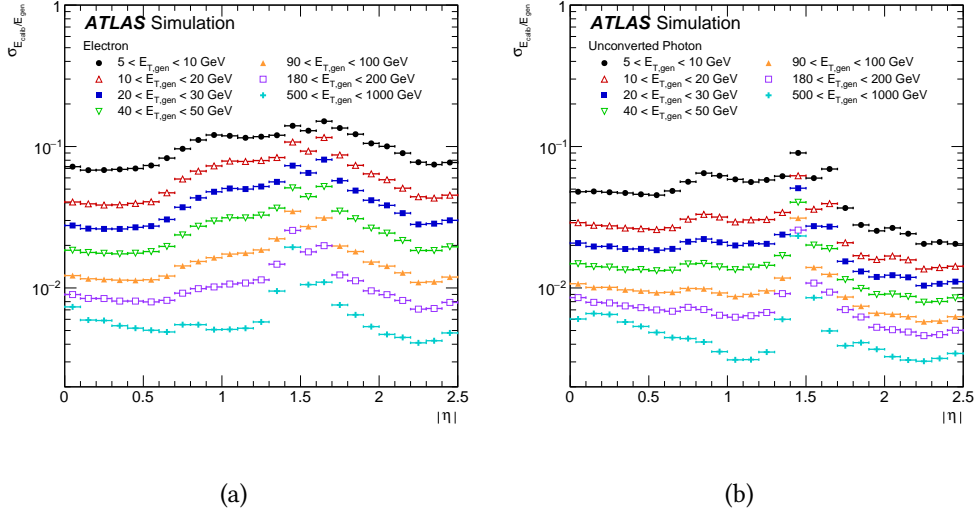


Figure 2.16: Energy resolution, $\sigma_{E_{\text{calib}}}/E_{\text{gen}}$, estimated from the interquartile range of $E_{\text{calib}}/E_{\text{gen}}$ as a function of $|\eta|$ for 2.16a electrons and 2.16b unconverted photons, for different E_{T} ranges [93].

Tile calorimeter

The tile calorimeter is a hadronic calorimeter designed to provide good measurements of hadron energy and to contain hadronic showers to avoid strong-interacting particles to reach the muon system. It is placed outside the EM calorimeter and it is composed by a barrel and two end-caps. It is a sampling calorimeter using iron as the absorber and scintillating tiles as the active material.

The barrel and extended barrels (in the η region between the barrel and the end-caps) are divided into 64 wedges, each 5.6 m and 2.6 m long respectively. They are consisting of three layers in depth, approximately 1.5, 4.1 and 1.8 interaction lengths (λ) thick for the barrel and 1.5, 2.6, and 3.3 λ for the extended barrel. The interaction lengths λ represents the mean free path of particle between two inelastic interactions. The total detector thickness at the outer edge of the tile-instrumented region is 9.7 λ at $\eta = 0$. To partially recover the energy loss between the two barrel regions, gap scintillators are located along the internal edge of the extended barrel, where the readout of the EM calorimeter is placed.

The tile calorimeter covers the region $|\eta| < 1.7$. It measures jet energies with a resolution:

$$\frac{\sigma(E)}{E} = \frac{50\%}{\sqrt{E}} \oplus 2.5\% \oplus \frac{5\%}{E}, \quad (2.12)$$

where the energy E is in GeV.

LAr hadronic end-cap calorimeter

The Hadronic End-cap Calorimeter cover the range $1.5 < |\eta| < 3.2$. It consists of two independent wheels per end-cap, placed directly behind the end-cap EM calorimeter. Each wheel is built from 32 identical wedge-shaped modules, and it is divided into two longitudinal segments, for a total of four layers per end-cap. The wheels in close proximity to the interaction point are made by parallel copper plates 25 mm long, as passive material, while those further away use 50 mm copper plates. The copper plates are separated with LAr gaps with 8.5 mm of size, providing the active medium for this sampling calorimeter. The energy resolution for the Hadronic End-cap Calorimeter is the same as in Equation 2.12.

LAr forward calorimeter

The Forward Calorimeter (FCal) is an electromagnetic and hadronic calorimeter. It is placed very close to the beam pipe covering the region $3.1 < |\eta| < 4.9$. The FCAL allows detection of hadronic jets at angles less than 1° from the beam-axis. It is approximately 10 interaction lengths long, and it is segmented in three modules, as shown in Figure 2.17, in each end-cap. The first has copper as passive material and it is optimised for electromagnetic measurements, the other two are instead used to measure predominantly the energy of hadronic interactions and they are provided with tungsten as passive material. Each module consists of a metal matrix, with regularly spaced longitudinal channels filled with the electrode structure consisting of concentric rods and tubes parallel to the beam axis. The LAr in the gap between the rod and the tube is the sensitive medium. This geometry allows for excellent control of the gaps, which are as small as 0.25 mm in the first section, in order to avoid problems due to ion buildup.

2.2.4 Muon system

The ATLAS Muon Spectrometer (MS) is designed to reconstruct muons and it is located in the outer part of the detector (see Figure 2.18) since they travel much more than other particles (neutrinos excepted) which not escape the hadronic calorimeter. Muons are then reconstructed combining information provided by

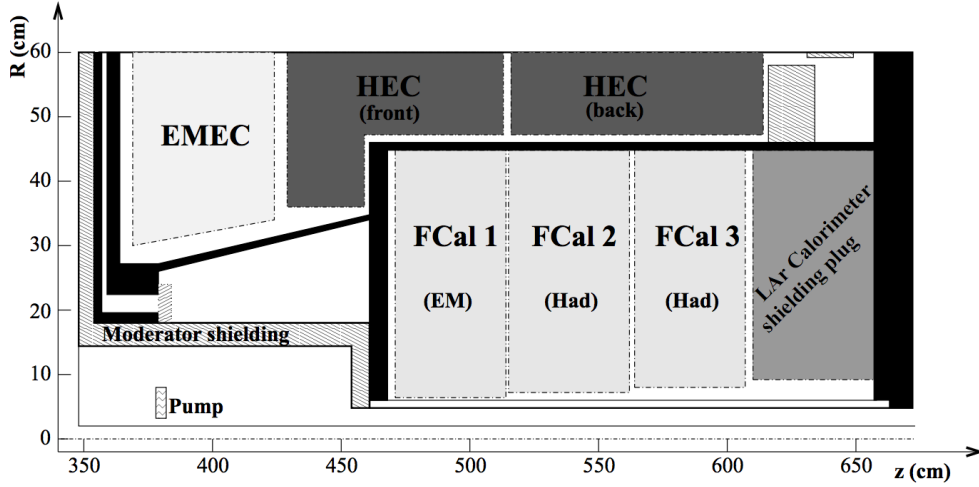


Figure 2.17: Schematic diagram showing the three FCal modules located in the end-cap cryostat [86]. The material in front of the FCal and the shielding plug behind it are also shown. The black regions are structural parts of the cryostat. The diagram has a larger vertical scale for clarity.

ID, energy deposits in the calorimeters and MS. The MS covers the region $|\eta| < 2.7$.

As muons fly out of the collision point, their tracks curve due to a surrounding toroidal magnetic field which bends them in the $R - z$ plane, to derive the muon's momentum. The MS allows independent measurements with respect to the one provided by the ID, since its trajectory is changed by the magnets. The spectrometer has an outer diameter of 22 m and it is composed by separate trigger and high-precision tracking chambers. In the barrel region, tracks are measured in chambers arranged in three cylindrical layers around the beam axis at a distance of ~ 5 m (inner station), 7.5 m (middle station) and 10 m (outer station); in the transition and end-cap regions, the chambers are installed in planes perpendicular to the beam, also in three layers at distances of $|z| \sim 7.4$ m, 10.8 m, 14 m and 21.5 m from the IP.

Over most of the η -range, a precision measurement of the track coordinates in the principal bending direction of the magnetic field is provided by *Monitored Drift Tubes* (MDT). At large pseudorapidities ($2 < |\eta| < 2.7$), the same measurements are performed by the *Cathode Strip Chambers* (CSC), the multiwire proportional chambers with cathodes segmented into strips.

The trigger system covers the pseudorapidity range $|\eta| < 2.4$ by the use of *Resistive Plate Chambers* (RPC) in the barrel and *Thin Gap Chambers* (TGC) in the end-cap regions. The trigger chambers for the muon spectrometer are used for

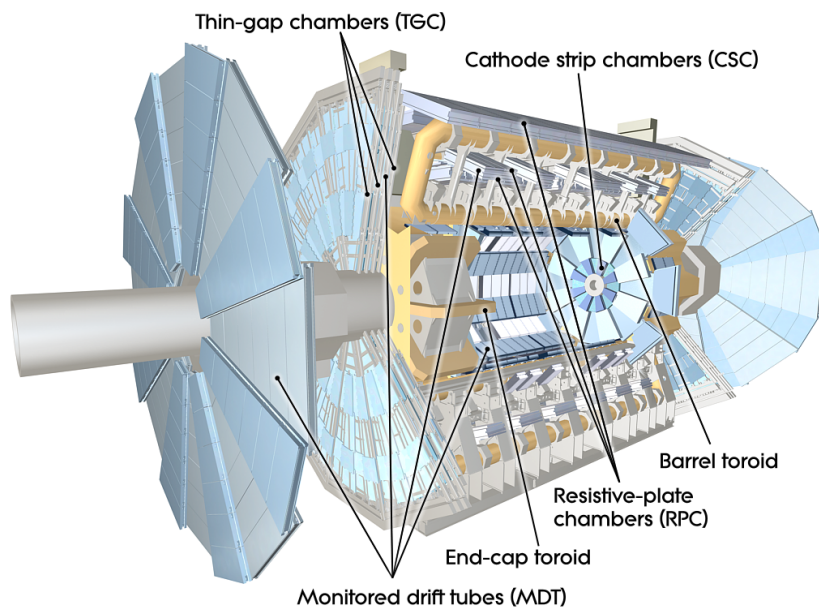


Figure 2.18: Cut-away view of the ATLAS muon system [86].

several other purposes as provide bunch-crossing identification, provide signals above chosen p_T thresholds, and measure the muon coordinate in the direction orthogonal to the one determined by the precision-tracking chambers.

All relevant parameters of the Muon Spectrometer's sub-detectors are summarised in Table 2.6.

Type	Chamber resolution in			Hit/track		Number of	
	z/R	ϕ	time	barrel	end-cap	chambers	channels
MDT	$35 \mu m (z)$	-	-	20	20	1088	339k
CSC	$40 \mu m (R)$	5 mm	7 ns	-	4	32	30.7k
RPC	10 mm (z)	10 mm	1.5 ns	6	-	544	359k
TGC	2-6 mm (R)	3-7 mm	4 ns	-	9	3588	318k

Table 2.6: Parameters of the four sub-systems of the muon detector [86]. The quoted spatial resolution (columns 2, 3) does not include chamber-alignment uncertainties. Column 4 lists the intrinsic time resolution of each chamber type, to which contributions from signal-propagation and electronics contributions need to be added.

Resistive Plate Chambers

In the barrel, the trigger system consists of the RPCs, made by three concentric cylindrical layers around the beam-axis covering the region $\eta < 1.05$. The low- p_T (below 10 GeV) trigger requires a coincidence in the middle RPC layers while the high- p_T (above 10 GeV) trigger requires a further coincidence of hits in the outer RPC layer, as shown in Figure 2.19.

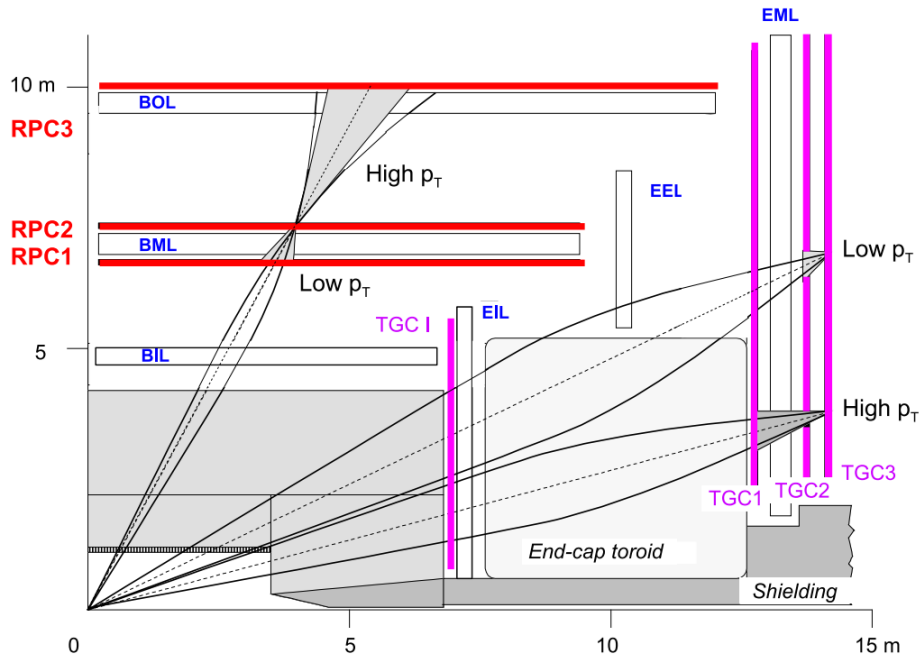


Figure 2.19: Schematics of the muon trigger system [86]. RPC2 and TGC3 are the reference (pivot) planes for barrel and end-cap, respectively.

Each station consists of two independent detector layers, each measuring η and ϕ . A track going through all three stations thus delivers six measurements in η and ϕ . This redundancy in the track measurement permits the use of a 3-out-of-4 coincidence in both projections for the low- p_T trigger (RPC1 and RPC2 stations) and a 1-out-of-2 OR for the high- p_T trigger (RPC3 station). This coincidence scheme rejects fake tracks from noise hits and greatly improves the trigger efficiency in the presence of small chamber inefficiencies.

The RPC is a gaseous parallel electrode-plate detector. The gas used is a mixture of $C_2H_2F_4$ /Iso- C_4H_{10} /SF₆ (94.7/5/0.3) which combines relatively low operating voltage, non-flammability and low cost, while providing a comfortable plateau for safe avalanche operation. Muons travelling the chamber produce primary ionization electrons which are multiplied into avalanches by a 4.5 kV/mm

electric field.

Thin Gap Chambers

TGCs are multi-wire proportional chambers segmented radially into one end-cap and forward region. The peculiarity of these chambers is that wire-to-cathode distance of 1.4 mm is smaller than the wire-to-wire distance of 1.8 mm., allowing very short drift time, less than 20 ns. The TGCs are filled with highly quenching gas mixture of CO₂ and n-C₅H₁₂ (n-pentane), to allow for operation in a quasi-saturated mode. The highly quenching gas prevents the occurrence of streamers in all operating conditions.

TGCs provide an azimuthal coordinate measurements complementing the one given by the MTDs in the bending (radial) direction. The TGCs need good time resolution to tag the beam-crossing with high efficiency ($\geq 99\%$) and fine granularity to provide a sufficiently sharp cut-off in the momentum of the triggering muon. To satisfy all the physics requirements on the momentum resolution, the size of the wire groups varies from 6 to 31 mm as a function of η , corresponding to a variation in width from 10.8 mm to 55.8 mm. The spatial resolution of the TGCs is 4 mm in the radial direction and 5 mm in the ϕ coordinate.

Monitored Drift Tubes

The MDT detector is formed by two multi-layer (3 or 4 layers) drift tubes, with diameter of 29.970 mm and aluminum walls, operating with gaseous mixture of argon and carbon dioxide, at a pressure of 3 bar. They cover the pseudorapidity region $|\eta| < 2.7$, except for the innermost end-cap layer which covers $|\eta| < 2.0$. The electrons resulting from ionisation are collected at the central wire with a diameter of 50 μm . The wire is held in position at the tube ends to guarantee the wire-tube concentricity with an accuracy of $\sigma < 10 \mu\text{m}$. The wire is also used for the gas transfer in and out of the tube.

The operating gas was selected because of the good ageing properties. Formation of polymers is rare since no hydrogen is present in the gas mixture. A disadvantage of this gas mixture is the non-linear space-drift time relation and the drift time of about 700 ns, longer than the typical gases such as Ar/CH₄. The non-linearity of the Ar/CO₂ gas reduces the spatial resolution at high counting rates since positive ions perturb the electric field.

Cathode-strip Chambers

The CSCs are multiwire proportional chambers with the wires oriented in the radial direction with respect to the beam-axis to provide muon momentum in the region $2 < |\eta| < 2.7$. Cathodes planes are segmented both perpendicular and

parallel to the wires to allow measurements in the longitudinal and transverse coordinate, respectively. The track position is obtained by the interpolation of the charges induced on neighbouring cathode strips. The CSC wire signals are not read out. Considering a readout pitch of 5.31 mm and 5.56 mm for the large and small chambers in the bending direction respectively, the CSC reaches a resolution of 60 μm per CSC plane in the ϕ direction and of the order of one cm in η . The time resolution is about 7 ns.

The CSCs are segmented into large and small chambers in ϕ with two disks with eight chambers each. Each chamber contains four CSC planes to provide four independent measurements in η and ϕ along the track.

In the first layer of the end-cap for $\eta > 2$, the MDTs are replaced by CSCs, which combine high spatial, time and double track resolution with high-rate capability and low neutron sensitivity.

2.2.5 Forward detectors

To detect particles also in the high rapidity region ($|\eta| < 4.9$), not covered by the central detectors, additional detectors are placed in the forward region. The whole ATLAS Forward Detector system is illustrated in Figure 2.20. As shown, the detector closest to ATLAS is LUCID (Luminosity measurement Using Cherenkov Detectors), followed by ZDC (Zero Degree Calorimeter), AFP (ATLAS Forward Proton) and ALFA (Absolute Luminosity For ATLAS).

The total pp interaction cross-section is the results of two main contributions given by the elastic and the inelastic cross-sections:

$$\sigma_{pp} = \sigma_{el} + \sigma_{inel}. \quad (2.13)$$

At the energies provided by the LHC, σ_{el} contributes for the 20% of the total σ_{pp} . The other 80%, is due to inelastic contribution including Single Diffractive dissociations (SD), Double Diffractive dissociations (DD), Central Diffractive production (CD) and non-diffractive processes.

The importance to instrument the forward part of ATLAS can be understood by inspecting the plots reported in Figure 2.21. Looking at the left plot, is clear that about 40% of the particles are produced outside the ATLAS central acceptance, while from the right one, that the energy released there is a tiny fraction with respect to the total.

The Forward detectors allow to detect and study particles and processes not detectable in the central region. The ATLAS Forward detector system is divided into:

- **LUCID** is a Cherenkov detector designed to measure the relative luminosity in the region $5.6 < |\eta| < 5.9$. It is placed at 17 meters from the IP.

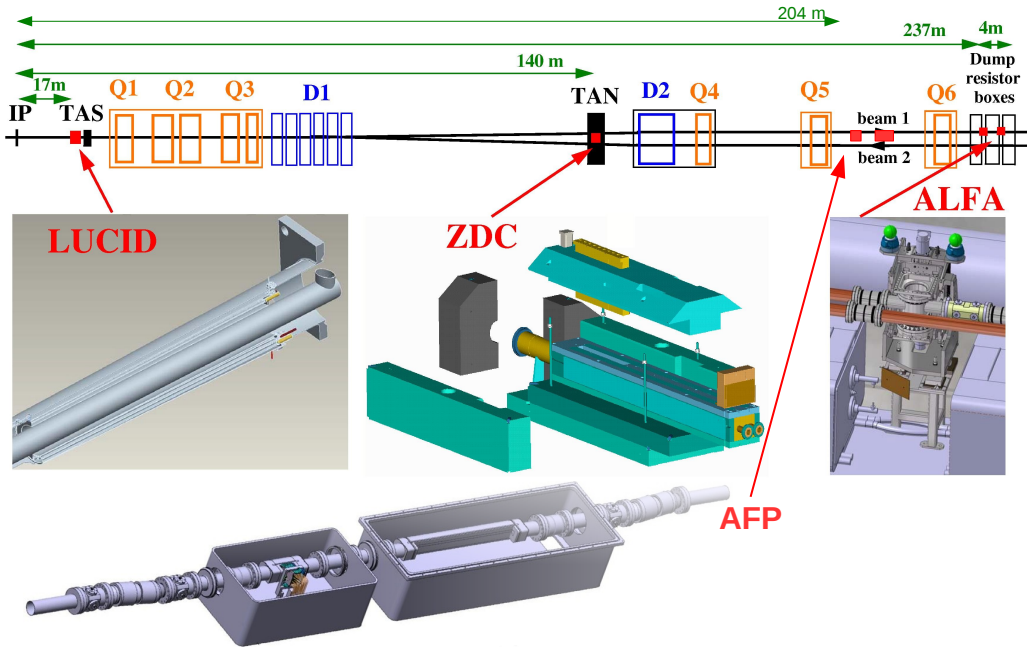


Figure 2.20: ATLAS Forward Detectors and their relative positions with respect to the IP [94].

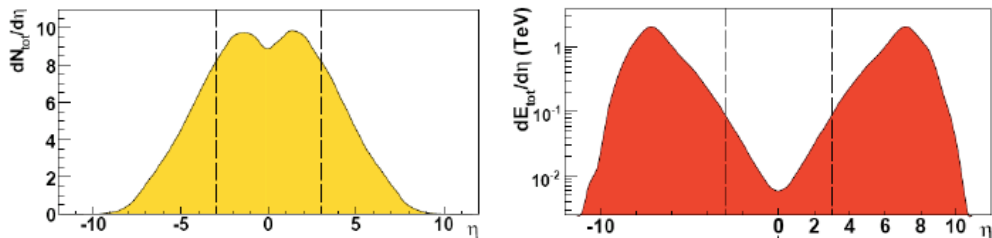


Figure 2.21: Particle flow (left) and energy flow (right) as a function of rapidity as obtained by DPMJET generator for pp interactions at \sqrt{s} 14TeV [95].

It provides the ATLAS official luminosity measurement. Since the LUCID detector is the core of my technical activity, it will be deeper discussed in the Appendix B.

- **MBTS** is designed to detect low momentum particles and to select collisions from low luminosity collisions. It is located at 356 cm from the IP and covers a region $1.9 < |\eta| < 3.8$.
- **BCM** is placed at a distance of 1.84 meters from the IP and covers the re-

gion $3.9 < |\eta| < 4.1$. It consists of diamond sensors revealing the passage of charged particles. The BCM provides a measurement of the instantaneous relative luminosity detecting signals of beam instability, measuring interaction rate and discriminating signals from background.

- **ZDC** is placed at ± 140 meters from IP where the beam pipe is divided into two separated tubes. It covers the region $|\eta| > 8.3$. Its time resolution is about 100 ps, allowing the determination of the IP with a 3 cm precision in z coordinate. Each side of the detector contains four modules: one electromagnetic and three hadronic calorimeters. They are made of quartz and tungsten and are designed for relative luminosity measurements during heavy ion runs. It measures the forward cross-section detecting neutral particles (mainly photons and neutrons) very close to the beam pipe.
- **ALFA** is located at ± 240 meters from the IP. It covers the region $10.6 < |\eta| < 13.5$, to detect small-angle scattered protons. It measures the proton cross section in elastic scattering collisions in the coulomb nuclear interference region, used to evaluate the absolute luminosity of ATLAS. Since the angle needed for this measure ($\sim 3 \mu\text{rad}$) is smaller than the beam divergence, special beam conditions (large values of the betatron function at the IP) are required. ALFA is made of scintillating fibre trackers and it is placed inside Roman Pots, which allow the sub-detectors to be as close as possible to the beam-axis ($\sim 1 \text{ mm}$). There are two Roman Pots on each side at 4 m from each other. The ALFA spatial resolution is $25 \pm 3 \mu\text{m}$.
- **AFP** was installed for the Run 2 data taking, to improve measurements of protons positions and directions. It consists of two stations per side: a tracker is located at 205 m and another tracker with a ToF (Time of Flight) detector is placed 217 m from the IP. The tracker achieves a high granularity by using pixels of $10 \mu\text{m} \times \mu\text{m}$ ($x - y$). The ToF detector provides measurements of the ToF of the colliding particles with a time resolution $\leq 30 \text{ ps}$.

2.2.6 Trigger, readout, data acquisition and control systems

The huge amount of data collected by LHC in each collision cannot be completely acquired and analyzed. ATLAS, through a complex Trigger and Data Acquisition (collectively TDAQ [96]) system, manages the selections of events, needed to reduce the information rate from $\sim 40 \text{ MHz}$ to approximately 1 kHz.

The TDAQ systems, the timing- and trigger-control logic, and the Detector Control System (DCS) are partitioned into sub-systems, typically associated with

each sub-detector, with the same logical components and building blocks.

Trigger system

The trigger system has two distinct levels: L1 and the High-Level Trigger (HLT). Each trigger level refines the decisions made at the previous level and, where necessary, applies additional selection criteria.

- The **L1 trigger** searches for high transverse-momentum muons, electrons, photons, jets, and τ -leptons decaying into hadrons, as well as large missing energy and total transverse energy. Its selection is based on information from a subset of detectors. High transverse-momentum muons are identified using trigger chambers in the barrel (RPC) and end-cap regions (TGC) of the spectrometer. Calorimeter selections are based on reduced-granularity information from all the ATLAS calorimeters. Results from the L1 muon and calorimeter triggers are processed by the central trigger processor, which combines the different trigger selections. Events passing the L1 trigger selection are transferred to the next stages of the detector-specific electronics and, subsequently, to the data acquisition via point-to-point links. In each event, the L1 trigger also defines one or more Regions-of-Interest (RoI), i.e. the geographical coordinates in η and ϕ , of those regions within the detector where its selection process has identified interesting features. The RoI data include information on the type of features identified and the criteria passed. This information is subsequently used by the high-level trigger. The diagram of the L1 operation is reported in Figure 2.22.

The maximum L1 accept rate which the detector readout systems can handle is 100 kHz, reduced from the initial 40 MHz.

- The **HLT** selection is seeded by the RoI information provided by the L1 trigger over a dedicated data path. The selections use, at full granularity and precision, all the available detector data within the RoIs and the offline analysis procedures. The system merges together the Run-1 two stage system (L2 and Event Filer) to a single farm in order to reduce the complexity and the duplication of CPU usage and network transfer. The configurations and thresholds are set to reduce the trigger rate approximately to 1 kHz.

Readout architecture and data acquisition

The front-end electronics sub-system includes different functional components [86]:

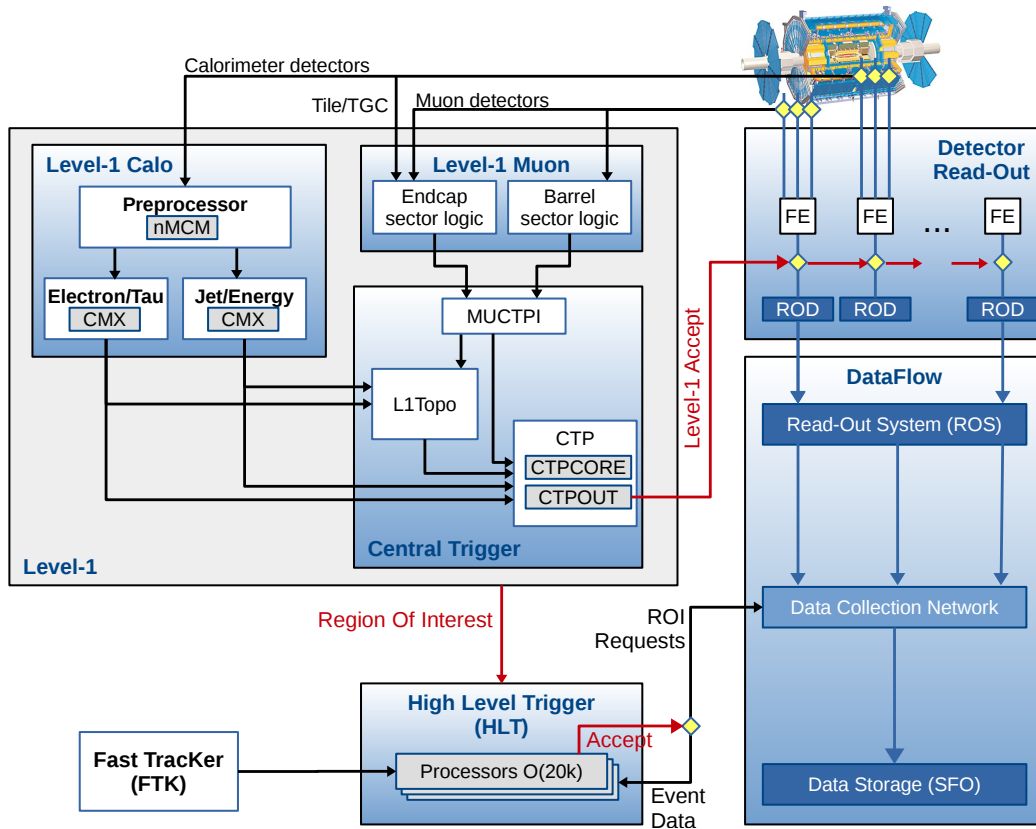


Figure 2.22: Block diagram of the L1 trigger. The overall L1 decision is made by the central trigger processor, taking input from calorimeter and muon trigger results. The paths to the detector front-ends, L2 trigger, and data acquisition system are shown from left to right in red, blue and black, respectively [97].

- the front-end analogue or analogue-to-digital processing;
- the L1 buffer in which the (analogue or digital) information is retained for a time long enough to accommodate the L1 trigger latency;
- the derandomising buffer in which the data corresponding to a L1 trigger accepted events are stored before being sent to the following level. This element is necessary to accommodate the maximum instantaneous L1 rate without introducing significant downtime (maximum 1%);
- the dedicated links or buses which are used to transmit the front-end data stream to the next stage.

After an event is accepted by the L1 trigger, the data from the pipe-lines are transferred off the detector to the *Readout Drivers* (RODs). The RODs are

detector-specific functional elements of the front-end systems, which achieve a higher level of data concentration and multiplexing by gathering information from several front-end data streams.

Digitised signals are formatted as raw data before being transferred to the DAQ system. The RODs follow some general ATLAS rules, including the definition of the data format of the event (changed significantly from Run-1 to Run-2), the error detection/recovery mechanisms to be implemented, and the physical interface for the data transmission to the DAQ system.

The first stage of the TDAQ, the readout system, receives and temporarily stores the data in local buffers. It is subsequently solicited by the HLT that performs the final selection. Selected events are moved to permanent storage at the CERN computer centre. In addition to the movement of data, the data acquisition system also provides for the configuration, control and monitoring of the hardware and software components which together provide the data-taking functionality.

The Detector Control System

The Detector Control System (DCS) permits the coherent and safe operation of the ATLAS detector hardware and serves as a homogeneous interface to all sub-detectors and to the technical infrastructure of the experiment. It controls, continuously monitoring and archiving the operational parameters, signals indicating any abnormal behaviour to the operator, and allows automatic or manual corrective actions to be taken. The DCS also enables bi-directional communication with the data acquisition system in order to synchronise the state of the detector with data-taking. It also handles the communication between the sub-detectors and other systems which are controlled independently, such as the LHC accelerator, the CERN technical services, the ATLAS magnets, and the detector safety system.

Chapter 3

Object Reconstruction

3.1	Tracks and Vertices	64
3.1.1	Primary Vertex	66
3.2	Electrons	67
3.3	Muons	72
3.4	Jets	79
3.5	Missing Transverse Energy	84
3.5.1	Missing Transverse Energy Significance	86
3.6	Overlap Removal	87
3.7	Lepton Triggers	89

Any ATLAS physics analysis is based on the reconstruction and the identification of the objects of interest, representing the observed characteristics of the particles produced by the pp interactions and travelling through the detector volume. These objects are typically electrons, muons, tau leptons, jets and missing transverse energy, reconstructed exploiting the technologies described in Section 2.2.

The first step in the reconstruction is related to objects representing individual particles, such as the tracks which are reconstructed in the Inner Detector from spacepoint hits and cells clusters formed in the calorimeters. Leptons, photons and jets are reconstructed from tracks and calorimeter clusters. All of these particles are then used to measure the total transverse energy, and via the energy balance, the so-called “missing transverse energy”, which is produced by undetected particles as the SM neutrinos.

In this work, leptons coming from IP are selected to be used in the analysis regions, from now called as *prompt leptons*. As explained in detail in the following sections, despite the exceptional performance provided by the ATLAS detector in the object reconstruction, the analysis are not background free. Leptons which are not originated in the IP but coming by secondary processes are referred to as *non-prompt* leptons. The object reconstruction provided by the ATLAS detector guarantees a high efficiency with a significant background rejection.

3.1 Tracks and Vertices

Tracks reconstruction is based on the particle interaction with the detector and it is also used to detect charged particles via the ID. The extrapolation of the track path to the beam line allows to locate *primary vertices* and to identify the particles produced in the collision.

Track reconstruction exploits information provided by pixel and SCT detectors, but it can be also extended with the TRT [98]. First, clusters are composed by grouping pixel and stripes which have a common corner or edge with the charge particle above a defined threshold. Particle path is built from three-dimensional measurements, called *space-points*, which corresponds to the point where the particle traversed the ID. In the pixel detector, each cluster equates to one space-point, while in the SCT, clusters from both sides of a strip layer must be combined to obtain a three-dimensional measurement.

In a dense environment with high pile-up, such as the ATLAS working conditions, multiple tracks might share one cluster. In this context, it is useful to introduce the several classes of clusters identified by either the “truth information”, only available in simulation and referring to information at Monte Carlo (MC) generator level, or reconstructed quantities in both collision data and MC simulation. Two kind of cluster are defined: single-particle clusters, created by charge deposits from one particle, and merged clusters, created by charge deposits from multiple particles. These definitions rely on truth information and both cases are illustrated in Figures 3.1a and 3.1b.

Track seeds are obtained considering sets of three space-points. This approach maximizes the possible number of combinations while allowing a first crude momentum estimation. In this case, a perfect helical trajectory in a uniform magnetic field is assumed. To ensure a good quality of the track reconstruction, ATLAS uses two different sequences: the main *inside-out* track reconstruction and a consecutive *outside-in* tracking, depending on the order in which space-points are considered to form tracks. In the inside-out method, track seeds of three space points in the silicon detectors (SCT and pixel detectors) form a triplet from which track candidates are reconstructed using a combina-

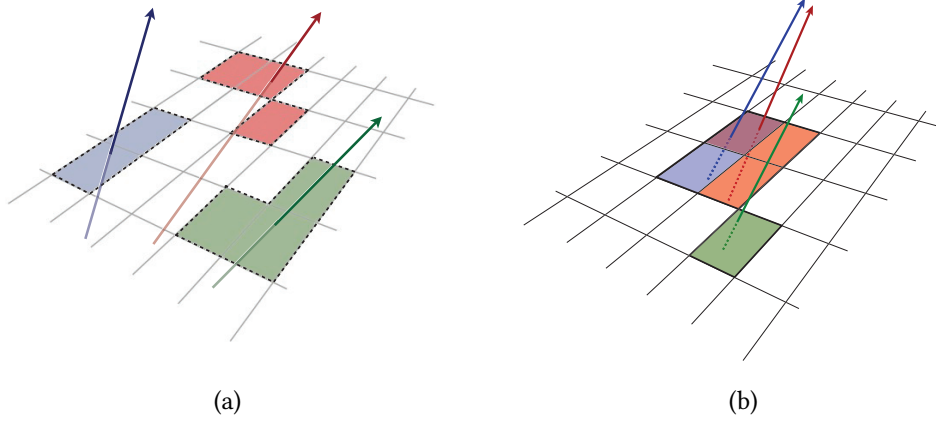


Figure 3.1: Illustration of (a) single-particle pixel clusters on a pixel sensor and (b) a merged pixel cluster due to very collimated charged particles. Different colours represent energy deposits from different charged particles traversing the sensor and the particles trajectories are shown as arrows [98].

torial Kalman filter [99]. Tracks passing an ambiguity resolver algorithm are then extrapolated outwards requiring coincident hits in the TRT. In the second sequence, the outside-in one, TRT hits are used to seed tracks and they are extended backward towards the IP to identify coincident silicon hits.

Since a track seed is a collection of space points, it does not provide a parametrisation of track parameters with respect to the origin. Then, the track is projected in the transverse plane following a circular trajectory uniquely described by three parameters: the transverse momentum (p_T), the transverse impact parameter (d_0) and the azimuthal angle (ϕ_0). In Figure 3.2, a sketch of the track obtained using three space points is illustrated.

It is useful to define the track impact parameters. The transverse impact parameter d_0 is the shortest distance between a track and the beam line in the transverse plane.. The longitudinal impact parameter z_0 corresponds to the difference along the beam line between the point where d_0 is measured and the primary vertex or the beam spot. Usually tracks are required to have: $|d_0| < 2.0$ mm and $|z_0 \sin(\theta)| < 3.0$ mm, with θ polar angle of the track.

Tracks are reconstructed with a resolution in the transverse momentum measurement:

$$\frac{\sigma p_T}{p_T} = 0.05\% \times \frac{p_T}{\text{GeV}} \oplus 1\%. \quad (3.1)$$

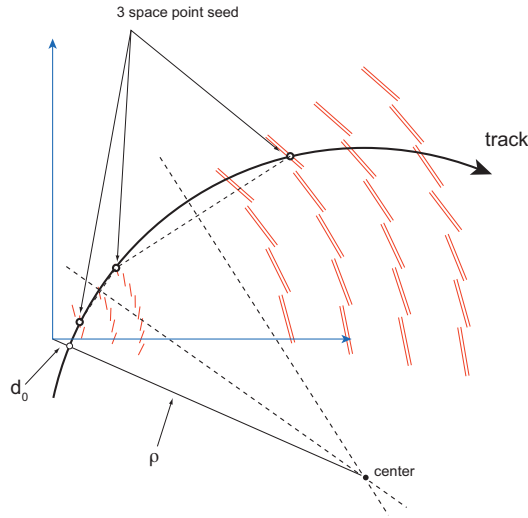


Figure 3.2: A sketch of the technique used to estimate the track parameters of the seeds [99].

3.1.1 Primary Vertex

Primary vertices are obtained by grouping all the selected tracks that pass the reconstruction requirements. Vertex candidate are generally reconstructed in two stage: *vertex finding* and *vertex fitting*. The vertex fitting step deals with reconstruction of the current vertex position and its covariance matrix [100]. The reconstruction strategy is a sequence of several steps: first a set of tracks passing the selection criteria is identified, then the seed position for the first vertex is selected as the one closest to the beam spot. The best vertex position is determined using an iterative χ^2 minimization applying in each iteration less compatible a down-weight and the vertex position is recomputed. After the vertex position is determined, the rejected tracks (incompatible with the vertex at 7σ) are considered as input for a new vertex finding iteration. This procedure is repeated for all the remaining tracks in the event. The vertex with the highest sum of squares of transverse momenta ($\sum p_T^2$) is defined as *primary vertex*, while the other ones are assumed to be pile-up vertices. In general, a primary vertex should contain at least two tracks. The reconstruction efficiency of a vertex has been measured using MC simulation: isolated vertices with 2 associated tracks has $\sim 85\%$, with 4 or more associated tracks is essentially 100%.

3.2 Electrons

In the ATLAS detector, electrons produced in pp collisions pass through the Inner Detector to end its travel in the Electromagnetic calorimeter. Electron reconstruction involves information from the ID, to define the angular direction at the interaction point, and from EM calorimeter, to measure their energy. [101] Travelling through the detector, an electron can lose energy due to bremsstrahlung when interacting with the material it traverses. The radiated photon produced in this process, may convert into an electron-positron pair which itself can interact with the material that surrounds it. As a result, a single electron produces multiple tracks generating an *electromagnetic shower*. The secondary particles produced in this phenomenon are usually emitted at a very small angle, and match with the same electromagnetic cluster. In Figure 3.3, a schematic illustration of the elements involved in the electron reconstruction is reported.

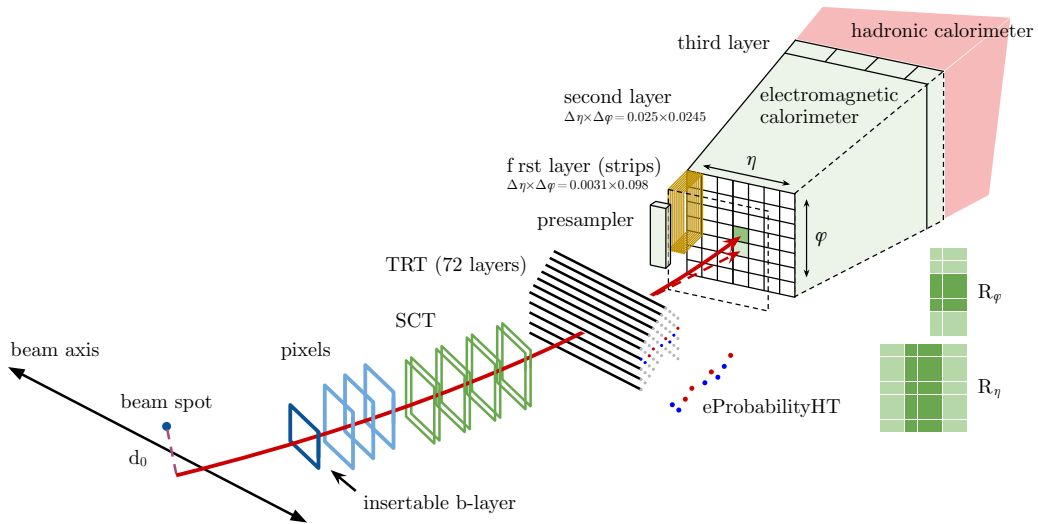


Figure 3.3: A schematic illustration of the path of an electron through the detector. The red trajectory shows the hypothetical path of an electron, which first traverses the tracking system (pixel detectors, then silicon-strip detectors and lastly the TRT) and then enters the electromagnetic calorimeter. The dashed red trajectory indicates the path of a photon produced by the interaction of the electron with the material in the tracking system [101].

Electron Reconstruction

Electron reconstruction is provided by ATLAS in the precision region of the detector, for $|\eta| < 2.47$. Three fundamental components of the electrons signature

characterise the reconstruction procedure: charged-particle tracks identified in ID, localised clusters of energy deposits into the EM calorimeter, and close matching of the tracks in $\eta \times \phi$ space, to the clusters to obtain the final electron candidates [102].

Clusters are built in the EM calorimeters using the intermediate section, divided into a grid of 200×256 towers with a granularity of $\Delta\eta \times \Delta\phi = 0.025 \times 0.025$. Electron cluster “seeds”, with transverse energy above 2.5 GeV, are searched as longitudinal towers. For each element, the energy of the cells in all the three calorimeter layers, as well as in the presampler, is summed to form the energy of the tower. Electromagnetic-energy cluster candidates are then formed around the seeds exploiting a clustering algorithm [103], removing also the duplicates. If two candidates are found within an area of $\Delta\eta \times \Delta\phi = 5 \times 9$ units of 0.025×0.025 , the one with the higher E_T is selected, assuming its transverse energy is at least 10% higher than the other cluster. If not, the cluster with the highest E_T central tower is kept. This process guarantees a reconstruction efficiency of 95% and more than 99% at $E_T = 7$ GeV and $E_T = 15$ GeV respectively, as can be seen in Figure 3.4a and Figure 3.4b.

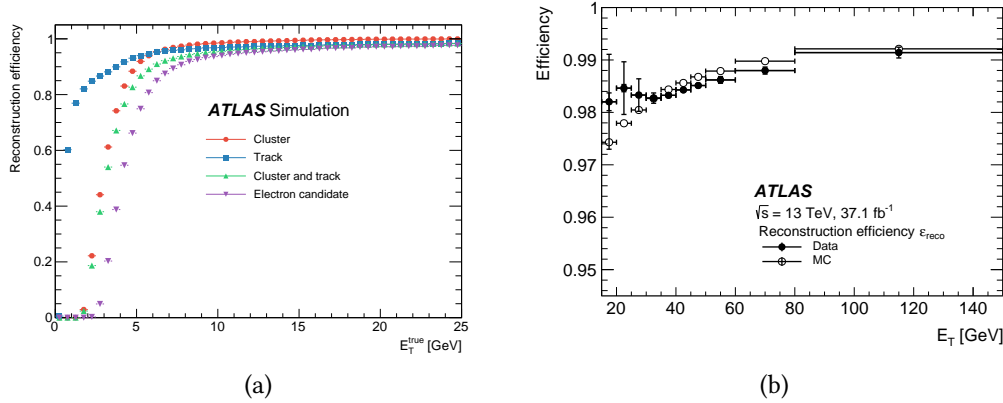


Figure 3.4: The total reconstruction efficiency for simulated electrons in a single-electron sample is shown in (a) as a function of the true (generator) transverse energy E_T for each step of the electron-candidate formation [104]. The reconstruction efficiency relative to reconstructed clusters, ϵ_{reco} , as a function of electron transverse energy E_T for $Z \rightarrow ee$ events is shown in (b) [102].

The track information provided by the ID is analysed in two steps, exploiting pattern-recognition and track fit. For the standard ATLAS pattern-recognition algorithm, the pion hypothesis is used for the model of energy loss from interactions of the particle with the detector material. To be selected, tracks seeds must have three hits in the IBL, PIX and SCT, with also a momentum higher than 1 GeV. If a track seed with $p_T > 1$ GeV cannot be successfully extended to a

full track of at least 7 hits in the silicon detectors but if falls in the electromagnetic cluster region of interest, a new attempt using electron hypothesis (instead of pion) is performed. This second attempt allows up to 30% energy loss due to bremsstrahlung. Tracks are fitted considering electron and pion hypothesis using the ATLAS Global χ^2 Track Fitter [105].

EM clusters and tracks are then matched considering the distance, in the $\eta-\phi$ space, between the position of the extrapolated track in the EM middle layer and the cluster barycentre. Tracks associated to electron clusters with a number of precision hits higher than 4 are fitted using an optimised Gaussian Sum Filter (GSF) [106] (based on a more general Kalman filter), which considers also the energy loss due to non-linear bremsstrahlung.

The final step of the electron reconstruction procedure is the matching of the GSF-track candidate to the candidate calorimeter seed cluster. This procedure is similar to the one described above with more stringent criteria.

If more than one track fulfil the matching criteria, only one is chosen as *primary* tracks using an algorithm taking into account the cluster-track distance R calculated using several momentum hypothesis, the presence of a hit in the first silicon layer and the number of pixel hits. Electron candidate with no pixel hits is removed and classified as a photon.

In Run-2, in order to reject the background from secondary particles and conversions, electron tracks must be compatible with the primary interaction vertex of the hard collision.

Electron Identification

To improve the purity of the selected electron, additional quality criteria called *identification selections* are used. The Particle IDentification (PID) algorithm is based on a large set of observables such as: track properties, calorimeter shower shapes, information from TRT, track-cluster matching related quantities and variables measuring bremsstrahlung effects to discriminate signal from backgrounds events. With the insertion of the IBL in the LHC Run-2, the number of hits in this innermost pixel layer is used to distinguish electrons from converted photons.

The baseline PID algorithm used in ATLAS, is the likelihood-based (LH) method. It is a multivariate (MVA) technique which evaluates simultaneously several electron properties when performing a selection decision. The LH procedure exploits the signal and background probability density functions (PDFs) of the discriminating observables defined above. An overall probability is then calculated for the signal and background objects based on the PDFs. These probability are combined into a discriminant $d_{\mathcal{L}}$ on which a requirement is applied:

$$d_{\mathcal{L}} = \frac{\mathcal{L}_S}{\mathcal{L}_S + \mathcal{L}_B}, \quad \mathcal{L}_{S(B)}(\vec{x}) = \prod_{i=1}^n P_{s(b),i}(x_i) \quad (3.2)$$

where \vec{x} is the vector of discriminating variable values and $P_{s,i}(x_i)$ is the value of the signal probability density function of the i^{th} variable evaluated at x_i . In the same way, $P_{b,i}(x_i)$ refers to the background probability function. The LH response $d_{\mathcal{L}}$ has often a sharp peak at 0 (background) and 1 (signal), which is inconvenient to select working points as it would require extremely fine binning. Then an inverse sigmoid function is used to transform the discriminant:

$$d'_{\mathcal{L}} = -\tau^{-1} \ln(d_{\mathcal{L}}^{-1} - 1), \quad (3.3)$$

where the τ parameter is set to 15 [107]. This MVA method guarantees a better background rejection for a given signal efficiency than a “cut-based” analysis that would use selection criteria sequentially on each variable.

Three fixed values of the LH discriminant are used to define three levels of identification working points (WPs) for electron PID. These WPs are, in order of increasing background rejection: *Loose*, *Medium* and *Tight*. Each WP uses the same variables to define the LH discriminant, but the selection on the discriminant is different. Electrons selected by Medium are all selected by Loose, and Tight electrons are all selected by Medium.

The distributions of electron shower shapes depend on the amount of material the electrons pass through, and therefore vary with the pseudorapidity of the electron candidates. In addition, significant changes to the shower shapes and track properties are expected with increasing energy. The PID operating points were consequently optimised in several bins in $|\eta|$ and E_T .

Considering standard electroweak processes, the target efficiencies of the PID WPs are, on average, 93%, 88% and 80% for Loose, Medium and Tight respectively, increasing from low to high E_T values. Medium and Tight operating points provide a reduced efficiency while guarantee an improved rejection of background processes by factors of about 2.0 and 3.5, respectively, in the range $20 \text{ GeV} < E_T < 50 \text{ GeV}$. In Figure 3.6a and 3.6b, the resulting efficiencies in data, as function of E_T and η , are shown. The discontinuity at $E_T \approx 15 \text{ GeV}$ is due to a known mismodelling of the observables used in the LH discriminant at low energies. Using simulated events, the discriminant is optimized leading to an higher efficiency in data, resulting in the rise at low E_T in the bottom panel in Figure 3.6a.

Electron Isolation

Further isolation criteria are implemented in most ATLAS physics analysis to improve the discrimination between signal and backgrounds. The isolation vari-

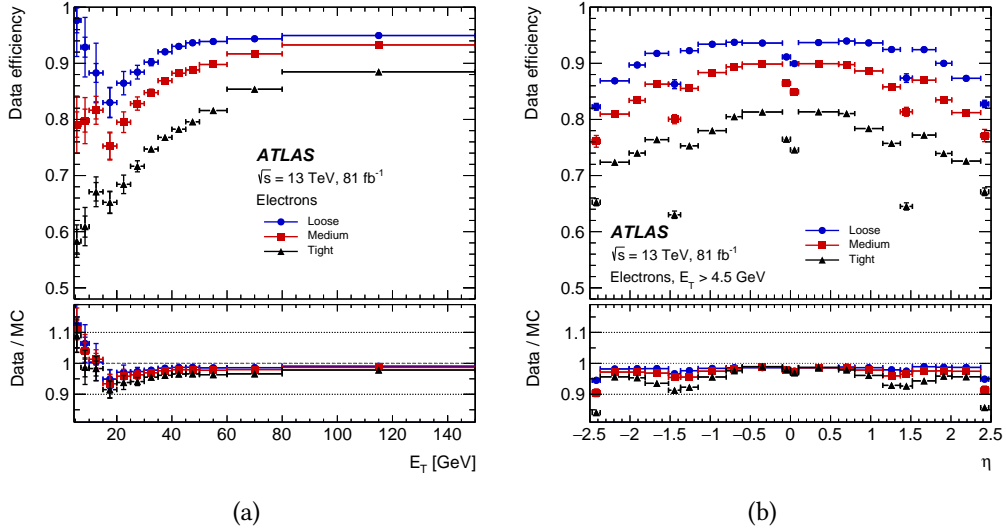


Figure 3.5: The electron identification efficiency in $Z \rightarrow ee$ events as a function of E_T (a) and as a function of η (b) for the Loose, Medium and Tight working points. The lower panels show the ratio of the efficiencies measured in data and in MC simulations. The total uncertainties include both statistical and systematic components. [104].

ables estimate the particle energy around the electron candidate and allow to distinguish prompt electrons (the ones coming from heavy resonances decays) from non-isolated electron candidates originated from heavy flavour hadron decays or from converted photons produced in hadron decays, and light hadrons misidentified as electrons.

Two classes of discriminating variables was designed for this purpose:

- a *calorimetric* isolation energy ($E_T^{cone0.2}$), defined as the sum of transverse energies of all topo-clusters in the EM calorimeters inside a cone with radius $\Delta R = 0.2$ around the electron cluster candidate. Only clusters with reconstructed positive energy are taken into account in this sum. A correction depending on E_T and η is applied to consider the electron energy leakage outside this cluster.
- a *track* isolation ($p_T^{varcone0.2}$), defined as the sum of transverse momenta of all tracks within a cone with radius $\Delta R = \min(0.2, 10 \text{ GeV} / E_T)$ around the electron track candidate., excluding the electron associated tracks. To further improve the track quality, additional requirements must be satisfied, such as $p_T > 1 \text{ GeV}$, $|\eta| < 2.5$, at least 7 hits in the silicon detector (Pixel + SCT) with at most 1 shared hit and not more than 2 and 1 missing hits in the silicon and pixel detectors respectively. Finally to minimize the

pile-up impact, the longitudinal impact parameter z_0 must have $|z_0 \sin \theta| < 3$ mm.

The isolation WPs are defined depending on the cuts on $E_T^{cone0.2}/E_T$ and $p_T^{varcone0.2}/p_T$. These operating points can be classified in two different ways, with fixed cuts on the isolation variables or targeting a fixed value of efficiency. The Gradient is designed to guarantee an efficiency about 90% at $p_T = 25$ GeV and 99% at $p_T = 60$ GeV. The other operating points, such as HighPtCaloOnly, Loose and Tight have a fixed requirements on the track isolation and/or on the calorimeter variables. In Table 3.1 the requirements for these different WPs are summarized.

Working Point	Calorimeter Isolation	Track Isolation
Gradient	$\epsilon = 0.1143 \times p_T + 92.14 \%$	$0.1143 \times p_T + 92.14 \%$
HighPtCaloOnly	$E_T^{cone0.2} < \max(0.015 \times p_T, 3.5 \text{ GeV})$	-
Loose	$E_T^{cone0.2}/E_T < 0.20$	$p_T^{varcone0.2}/E_T < 0.15$
Tight	$E_T^{cone0.2}/E_T < 0.06$	$p_T^{varcone0.2}/E_T < 0.06$

Table 3.1: Definition of the electron isolation working points and isolation efficiency ϵ . In the Gradient definition, the momenta is expressed in GeV [104].

In Figure 3.6a and 3.6b, the electron isolation efficiency measured in data recorded during 2017 is shown as function of E_T and η .

3.3 Muons

Muons are the most penetrating particles (except the non-detectable neutrinos) which travel from the interaction point, passing through the calorimeters without being absorbed, and reach the outermost part of ATLAS detector, the Muon Spectrometer.

Muon Reconstruction

In the MS, reconstruction starts searching for hit patterns in each of the muon chambers which are then grouped into short straight-line local track segments. In each MDT chamber and nearby trigger station, segments are identified by the Hough transform pattern recognition algorithm [109], which searches for hits

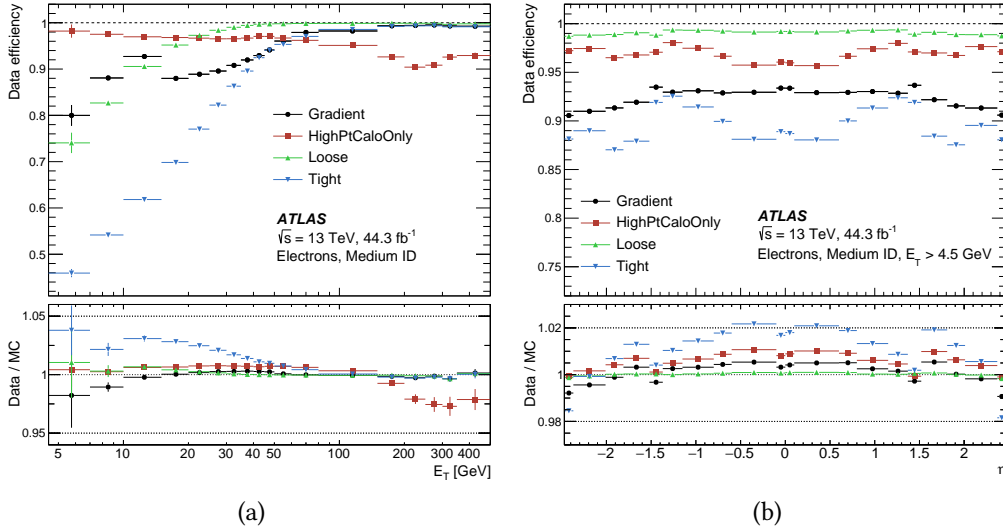


Figure 3.6: The electron isolation efficiency in $Z \rightarrow ee$ events as a function of E_T (a) and as a function of η (b) for different working points. The electrons are required to fulfil the Medium selection from the LH-based electron identification. The lower panels show the ratio of the efficiencies measured in data and in MC simulations. The total uncertainties include both statistical and systematic components [104].

aligned on a trajectory in the bending plane of the detector. The hits in the trigger chambers (RPC or TGC) are used to measure the coordinate orthogonal to the bending plane. Segments in CSC are reconstructed using a separate combinatorial search in the ϕ and η detector planes. These information are fitted together to create a three-dimensional track candidates choosing seeds from the middle layers and moving inwards and outwards. Finally, a global χ^2 fit of the muon trajectory is performed, accounting the effects of possible interactions in the detector material and possible misalignments between the different chambers.

Combining information from Inner Detector (described in Section 3.1) and Muon Spectrometer (as well as from the calorimeters), four types of muons can be defined, depending on which sub-detectors are used in reconstruction [110] (see Figure 3.7):

Combined (CB) muon : Muon track candidates are reconstructed independently in the ID and MS, then a combined track is obtained by a global fit that exploits information provided by the ID and the MS sub-detectors. Hits from MS can be added or removed to improve the fit quality. For $|\eta| > 2.5$, MS tracks can be combined with short track segments from hits in SCT and pixel detectors to form silicon-associated forward (SiF) muons.

Inside-out (IO) Combined : Muons are reconstructed using a complementary

inside-out algorithm, extrapolating ID tracks to MS requiring at least three loosely-aligned MS hits. This method has advantages for low- p_T muons (which lose a significant part of their energy in the calorimeter) and muons travelling in regions of limited MS coverage, recovering some efficiency.

Extrapolated and Standalone (ME) muons Are used when MS track cannot be matched to an ID track and its parameters are extrapolated to the beam-line. At least two layers of MS chambers in the barrel and at least three layers in the forward region must be traversed. ME muons are used to extend the acceptance outside that of the ID exploiting the whole MS coverage up to $|\eta| = 2.7$.

Segment-Tagged (ST) muon : ID tracks candidate are extrapolated to the MS requiring at least one reconstructed segment in MDT or CSC chambers. Muon parameters are taken directly from the ID track fit.

Calorimeter-Tagged (CT) muon : Tracks candidates from the ID are extrapolated through energy deposits in the calorimeters consistent with a minimum-ionising particle. This kind of muons are used to recover the acceptance in regions where the MS is only partially instrumented (due to cabling and other services) at $|\eta| < 0.1$. A $p_T > 5$ GeV is required to suppress the large background contamination at low p_T .

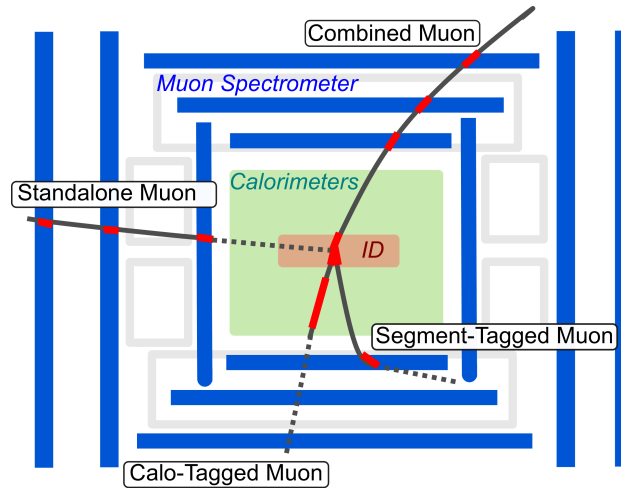


Figure 3.7: Schematic drawing of the detector parts used for muon reconstruction. Several muon types are defined depending on the detector parts used for the reconstruction [111].

In case of two muons types share the same ID track, preference is given to CB muons, then to ST, and finally to CT muons. The overlap with ME or IO muons

in the muon system is resolved by analysing the track hit content and selecting the one with the larger number of hits and better fit quality.

Muon Identification

After reconstruction, to further improve the muon quality, track candidates are selected by a set of requirements on the number of hits in the different ID sub-detectors and different MS chambers, on the track fit properties, and on variables which test the compatibility of the individual measurements in the two detectors. Several muon identification WPs are defined to suppress the background due to non prompt-muons (mainly originated from pion and kaon decays) and to select prompt muons with high efficiency and robust momentum measurement. Three standard selection WPs are designed to address the specific needs of different physics analyses. In order of increasing purity they are the *Loose*, *Medium*, *Tight*, where, as in the electron case, muon selected by Medium are all selected by Loose, and Tight muons are all selected by Medium. Two additional identification WPs are designed to cover extreme phase space regions: *High- p_T* and *Low- p_T* .

Loose : is designed to maximize reconstruction efficiency and provide good-quality muons. It was optimised for the reconstruction of the Higgs boson in the four-muon channel, which benefits from a higher efficiency while increasing systematic uncertainties and losing purity. All muon types are used: CT and ST are restricted to be in $|\eta| < 0.1$ region; in the region $|\eta| < 2.5$, about 97.5% of the Loose muons are CB or IO, 1.5% are CT and ST, and the last 1% are ST muons.

Medium : is the ATLAS standard WP for muons, providing appropriate efficiency and purity for most of the analyses, minimizing the systematic uncertainties associated with the prompt-muon efficiency while rejecting a small fraction of background. Only CB and IO tracks are used. CB and IO muon candidates must have at least 3 hits in more than 2 MDT layer, except for muons in the $|\eta| < 0.1$ region, where tracks with at least 1 MDT layer but no more than 1 MDT hole layer are allowed. ME and SiF muons are also selected in the $2.5 < |\eta| < 2.7$ region to extend the acceptance outside the ID geometrical coverage, requiring more than 3 MDT/CSC layers. About 98% of muons passing the Medium WP are CB muons.

Tight : is the purest WP which provides a substantial background rejection while losing a few percentage of efficiency compared to Medium. Only Medium CB and IO muons with at least two stations of the MS are taken into account. To remove pathological tracks and to guarantee a strong rejection of misidentified object with $p_T < 20$ GeV, the normalised χ^2 of

the combined track fit is required to be < 8 . Tight WP is used in analyses that are limited by background from non-prompt muons.

High- p_T : is used in searches for high-mass resonances to ensure an optimal momentum resolution for muons with $p_T > 100$ GeV. CB and IO muons satisfying the Medium requirements with at least 3 hits in three MS stations are selected. This WP reduces the reconstruction efficiency of about 20% while improving the p_T resolution of muons above 1.5 TeV by approximately 30%. High- p_T WP provides the best momentum resolution and guarantee an optimal rejection of poorly reconstructed tracks affected by large uncertainties.

Low- p_T : is the WP aimed to target the lowest- p_T muons which cannot be fully reconstructed in the MS and are identified based on MS segments. Only CB and IO muons with at least one hit in precision MS station are considered, except in the region $|\eta| > 1.3$, where muons with $p_T > 3$ GeV have enough energy to reach the second station, then at least two hits are required. At this energy, a large amount of backgrounds from non prompt-muons is present. The Low- p_T WP provides an optimal separation between prompt-muons and light-hadron decays guaranteeing an high efficiency and a good background rejection. Two kind of Low- p_T WP are developed: *cut-based* (C-B) selection to reduce the kinematic dependencies of the background efficiencies, and a multivariate WP to maximize the overall performance.

The muon reconstruction and identification efficiency for *Loose*, *Medium*, and *Tight* muons as measured in $J/\Psi \rightarrow \mu\mu$ and $Z \rightarrow \mu\mu$ events is shown in Figure 3.8a and 3.8b is shown.

The prompt muon efficiencies and light-hadron misidentification rates considering muons in the $|\eta| < 2.5$ region for different WPs in different p_T regions, are shown in Table 3.2.

Muon Isolation

As for the electrons, further isolation requirements can be imposed on muon candidates to improve their quality. Muons from prompt decays of SM bosons or predicted Beyond the Standard Model particles are produced isolated from other particles in the events while non-prompt muons are close to jets and generally surrounded by higher detector activity. If the contributions from light-hadron decays or hadrons misidentified as muons are efficiently suppressed by the identification requirements, for heavy-flavour hadron isolation criteria are needed to reject muons coming from their semi-leptonic decays.

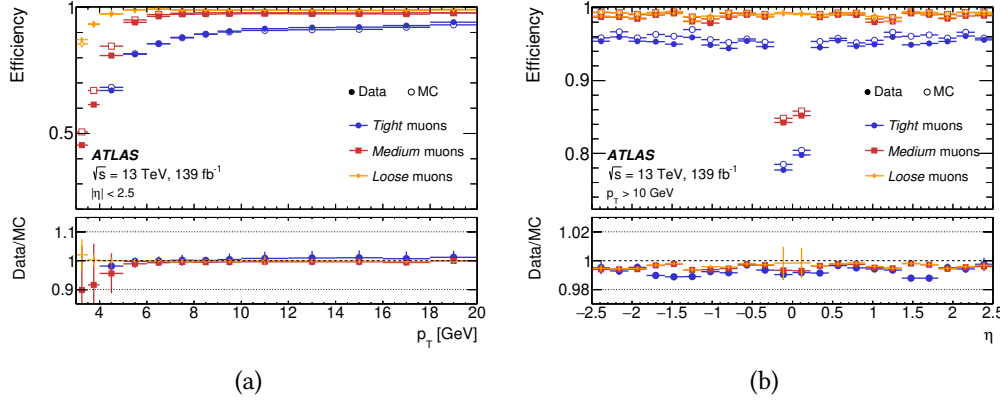


Figure 3.8: Muon reconstruction and identification efficiencies for the *Loose*, *Medium*, and *Tight* criteria. The efficiencies measured in $J/\Psi \rightarrow \mu\mu$ events as function of p_T and in $Z \rightarrow \mu\mu$ events as function of η are shown in (a) and (b) respectively. The predicted efficiencies are depicted as open markers, while filled markers illustrate the result of the measurement in collision data. When not negligible, the statistical uncertainty in the efficiency measurement is indicated by the error bars. The panel at the bottom shows the ratio of the measured to predicted efficiencies, with statistical and systematic uncertainties. [110].

Working Point	$3 < p_T < 5$		$5 < p_T < 20$		$20 < p_T < 100$		$100 < p_T$	
	ϵ_μ (%)	ϵ_{had} (%)	ϵ_μ (%)	ϵ_{had} (%)	ϵ_μ (%)	ϵ_{had} (%)	ϵ_μ (%)	ϵ_{had} (%)
Loose	90	1.17	98	1.06	99	0.25	98	0.12
Medium	70	0.63	97	0.85	97	0.17	97	0.07
Tight	36	0.15	90	0.38	93	0.12	93	0.04
Low- p_T (C-B)	86	0.82	95	0.71	97	0.17	97	0.07
Low- p_T (MVA)	88	0.73	96	0.66	97	0.17	97	0.07
High- p_T	45	0.34	79	0.60	80	0.13	80	0.05

Table 3.2: Prompt-muon identification efficiencies ϵ_μ and light-hadron misidentification rates ϵ_{had} for the different selection WPs, evaluated in $t\bar{t}$ MC samples in different p_T regions for $|\eta| < 2.5$. The p_T is expressed in GeV [110].

Three types of variables are used to assess isolation: using independently the information provided by the ID (track-based) or the the calorimeters (calorimeter-based), or a combination of the two (particle-flow-based).

Track-based isolation ($p_T^{*varconeex}$) is defined as the scalar sum of the transverse momenta of the ID tracks, excluding the muon track itself, in a cone of size ΔR around the muon track. Basing on the isolation selection criteria, ΔR can be either 0.2 (labelled as p_T^{cone20}), or $\min(10 \text{ GeV} / p_T^\mu, 0.3)$ (labelled as $p_T^{varcone30}$), with the latter optimised for topologies where jets or other leptons are close to an energetic muon. The minimum required p_T of tracks can be either 500 MeV or 1 GeV, depending on the isolation criterion. This isolation criterion is mostly independent of pile-up.

Calorimeter-based isolation ($E_T^{topoetcone20}$), is defined as the sum of the transverse energy of topological cell clusters in a cone of size $\Delta R = 0.2$ around the muon, after the energy subtraction of the muon itself and corrections due to pile-up effects. This technique tends to be more pile-up dependent than the track-based isolation.

Particle-flow-based isolation is defined as the sum of track-based isolation, using $p_T^{varcone30}$ for $p_T < 50$ GeV and p_T^{cone20} for $p_T > 50$ GeV, and the transverse energy of neutral particle-flow objects in a cone of size $\Delta R = 0.2$ around the muon (labelled as $E_T^{meflow20}$). In this case the latter is corrected for the pile-up effects and the contribution of energy deposit of the muon.

The efficiencies for prompt muons and muons from heavy-flavour hadronic decays are reported in Table 3.3, for tracks passing the Medium identification.

Working Point	$3 < p_T < 5$		$5 < p_T < 20$		$20 < p_T < 100$		$100 < p_T$	
	$\epsilon_\mu(\%)$	$\epsilon_{\text{HF}}(\%)$	$\epsilon_\mu(\%)$	$\epsilon_{\text{HF}}(\%)$	$\epsilon_\mu(\%)$	$\epsilon_{\text{HF}}(\%)$	$\epsilon_\mu(\%)$	$\epsilon_{\text{HF}}(\%)$
Loose	63	14.3	86	7.2	97	6.1	99	12.7
Tight	53	11.9	70	4.2	89	1.0	98	1.6
PflowLoose	62	12.9	86	6.8	97	5.0	99	9.1
PflowTight	45	8.5	63	3.1	87	0.9	97	0.8
HighPtTrackOnly	92	35.9	92	17.2	92	4.5	92	0.6
TightTrackOnly	80	19.9	81	7.0	94	3.2	99	3.3

Table 3.3: Prompt-muon isolation efficiencies ϵ_μ and heavy-flavour hadron semileptonic decays ϵ_{had} for the different isolation WPs, evaluated in $t\bar{t}$ MC samples in different p_T regions. The p_T is expressed in GeV [110].

3.4 Jets

In the ATLAS detector, a large variety of particles are produced. Quarks and gluons hadronise immediately, originating a shower of collimated particles with a momentum equal to the originating particle one. This shower of particles, called *jet*, is reconstructed in ATLAS using the particle-flow algorithm [112]. As explained in the muon isolation section, particle-flow technique combines momentum and energy measurements provided by both ID and calorimeter systems, respectively.

The particle-flow method exploits a cell-based energy subtraction algorithm to remove overlaps between momentum and energy measurements. A list of tracks and a list of topo-clusters containing both the original and the subtracted energy information are provided. Tracks reconstructed as described in the Track Section 3.1 are selected, then a match to a single topo-cluster (formed in the same way as for electron, outlined in Section 3.2) is attempted. The expected energy in the cell of the calorimeter is computed looking at the track momentum and the topo-cluster position. Since a single particle can release energy in more than one topo-cluster, the algorithm assigns, for each track and cluster, the probability that the particle energy was deposited in multiple clusters. Each topo-cluster is ranked depending on the distance metric $\Delta R'$ based on the distances $\Delta\phi$ and $\Delta\eta$ between the barycentre of the cluster and the track:

$$\Delta R' = \sqrt{\left(\frac{\Delta\phi}{\sigma_\phi}\right)^2 + \left(\frac{\Delta\eta}{\sigma_\eta}\right)^2} \quad (3.4)$$

where σ_ϕ and σ_η are the angular topo-clusters widths. The correct topo-cluster almost always lies at a small $\Delta R'$ relative to other clusters. If no topo-clusters are found in a cone of size $\Delta R' = 1.64$, it is assumed that the particle did not release energy in the calorimeter. Using a discriminant accounting the expected energy and the energy on the topo-cluster, single and multiple-topo cluster cases can be distinguished. Topo-clusters within a cone of $\Delta R = 0.2$ around the track position are considered to be matched to the track. The energy deposited in the calorimeters is then subtracted cell by cell from the set of matched clusters. Each cell is weighted depending on their closeness to the extrapolated track, favouring cells which are in proximity to the track. Finally, the remaining clusters which are compatible with the expected shower fluctuations of the signal of a single particle are removed.

The anti- k_t algorithm [113] is used to reconstruct particle-flow jets, recombining clusters with the following procedure:

- the distance d_{ij} is evaluated for each cluster i with respect to each other

cluster j :

$$d_{ij} = \min \left(p_{T,i}^{2k}, p_{T,j}^{2k} \right) \frac{\Delta R_{i,j}^2}{R^2} \quad (3.5)$$

where $\Delta R_{i,j}^2$ is the angular distance between clusters i and j in the $\eta - \phi$ space, R is the cone radius of the jet and k is the parameter of the anti- k_t method fixed to -1;

- for each cluster i the distance from the beam line is evaluated:

$$d_{iB} = p_{T,i}^{2k}; \quad (3.6)$$

- the minimum distance between d_{ij} and d_{iB} is found out;
- if the minimum values is represented by d_{ij} , then combine i and j into a single proto-jet and repeat from the first step. Otherwise i is considered as a final state and do no consider it in further iterations.

The anti- k_T algorithm is used in case of jet clusterization around hard seeds, while for soft particles the k_T ($k = 1$) [114] or for the energy independent clustering the Cambridge/Aachen [115] ($k = 0$) are used.

Pile-Up Corrections

During pp interactions, a huge variety of particles not belonging to the primary interaction vertex are produced (the so called *pile-up* (μ)). These secondary objects produced by the pile-up, can interfere or overlap with the objects of physics interest, requiring additional calibration corrections [116]. This contribution is accounted by subtracting the average energy due to pile-up and soft energy deposits in the calorimeter, from the energy measured, to guarantee precise jet energy measurements. Pile-up events can be divided into two classed of events: *in-time*, inside the same bunch-crossing, or *out-of-time*, from signals originating from previous bunch crossings (typically when the electronics integration time is larger than 25 ns). The correction constants used for this method are taken by *in situ* studies depending on the number of reconstructed PVs (N_{PV}), the jet pseudo-rapidity η and the bunch-spacing¹:

$$p_T^{corr} = p_T^{jet} - \langle f^{jet}(\langle \mu \rangle, N_{PV}, \eta) \rangle \quad (3.7)$$

where $\langle f^{jet} \rangle$ is measured from in-situ measurements or with MC simulation and represents an average offset applied to the jet p_T . Being applied as a mean value,

¹Due to the fast response of the silicon tracking detectors, N_{PV} is mostly unaffected by out-of-time pile-up.

such methods do not fully capture the fluctuations of the pile-up energy added to the calorimeter on an event-by-event basis but it is only indirectly estimated looking at its dependence on N_{PV} . To reject any jets not coming from hard-scattering interactions, the matching between the tracks and each jets is required.

To identify carefully pile-up jets, ATLAS has developed in Run 2, for particle flow jets, the Jet Vertex Tagger (JVT) algorithm [116], derived from variables based on the sum of transverse momentum of jet ID tracks and the N_{PV} , providing optimal performances.

Jet Vertex Tagger

The JVT is a discriminant derived by a pile-up correction (corrJVF) and a variable defined on hard-scatter observables R_{pT} . The corrJVF variables is defined as:

$$\text{corrJVF} = \frac{\sum_m p_{T,m}^{\text{track}}(\text{PV}_0)}{\sum_l p_{T,l}^{\text{track}}(\text{PV}_0) + \frac{\sum_{n \geq 1} \sum_l p_{T,l}^{\text{track}}(\text{PV}_n)}{k \cdot n_{\text{track}}^{\text{PU}}}} \quad (3.8)$$

where $\sum_m p_{T,m}^{\text{track}}(\text{PV}_0)$ is the scalar sum of the transverse momenta of the tracks associated to a jet originated from the hard-scatter vertex.

The $\sum_{n \geq 1} \sum_l p_{T,l}^{\text{track}}(\text{PV}_n) = p_T^{\text{PU}}$ term, is the scalar sum of the p_T associated to a jet originated from any pile-up vertex and k is equal to 0.01. The corrJVF variables aims to improve the efficiency of b -quark jets.

The variable R_{pT} is defined as the scalar sum of the p_T of the tracks that are associated with the jet and originate from the hard-scatter vertex divided by the fully calibrated jet momentum, which includes pile-up subtraction:

$$R_{pT} = \frac{\sum_k p_{T,k}^{\text{track}}(\text{PV}_0)}{p_T^{\text{jet}}}, \quad (3.9)$$

which is peaked at 0 and is steeply falling for pile-up jets while has a larger distribution for hard-scatter jets.

The JVT discriminant is based on a two-dimensional likelihood, using R_{pT} and corrJVF obtained from dijet events, exploiting the k-nearest neighbour (kNN) method [107]. In the corrJVF- R_{pT} plane, the relative probability for a jet to be of signal type is calculated as the ratio of the number of hard-scatter jets to the number of hard-scatter plus pile-up jets around the point. Signal and pile-up jets are required to have $20 < p_T < 50$ GeV and $|\eta| < 2.4$.

The JVT algorithm provides the best performance in term of signal efficiency and fake rates, giving a signal efficiencies of about 80%, 90% and 95% for pile-up fakes rates of 0.4%, 1.0% and 1.3% respectively.

Jet energy scale and resolution

To take into account the non-linear response of the calorimeter, energy from particles outside the detector acceptance, energy losses due to both jet misreconstruction and inactive regions of the detector, the jet energy scale (JES) correction is applied in the jet energy calibration stage [119]. After the pile-up subtraction step, already explained before, an origin correction is applied to jets to recalculate each topo-cluster using the new set of coordinates, unchanging the energy. Then, looking at the truth particle jet, a correction factor depending on p_T and $|\eta|$ is applied to improve the calibration. Finally, an *in situ* measurement is used to fill the gap in the data-MC differences. Additionally, the jet energy resolution (JER) is an important systematic uncertainty for measurements involving final states with the presence of jets and/or neutrinos since JER affects also the missing transverse energy reconstruction [120].

The dependence of the JER on the p_T of the jet can be parameterized exploiting a calorimeter-based resolution as function of three independent contributions just like the noise (N), stochastic (S) and constant (C) [121]:

$$\frac{\sigma(p_T)}{p_T} = \frac{N}{p_T} \oplus \frac{S}{\sqrt{p_T}} \oplus C. \quad (3.10)$$

The noise term is due to the electronic noise of the front-end electronics, as well as that due to pile-up. This term is expected to contribute in the p_T region less than 30 GeV. The stochastic term is affected by the statistical fluctuations in the amount of energy deposited, representing the limited resolution for jet p_T up to several hundred GeV. The constant term corresponds to the fluctuations due to the starting point of the hadron showers, the non-uniform response of the calorimeter and energy depositions in passive material. It is dominant in high- p_T region (above ~ 400 GeV).

In Figure 3.10a and 3.10b, the data-to-MC ratio and the jet energy resolution as function of the jet p_T for particle flow jets are shown.

b -tagging algorithms

During the reconstruction of jets, an important role is played by the flavour identification, which classifies jets depending on its composition: hadrons with b -quarks (b -jets), hadrons with c -quarks and no b -quarks (c -jets) and hadrons with neither b - or c -quarks (light-flavour jets). The identification procedure is called b -tagging [122]. Hadrons containing b -quarks are characterized by a long lifetime (about 1.5 ps and $c\tau \sim 450 \mu\text{m}$) with a significant mean flight path length, travelling few mm in the transverse direction inside the detectors before decaying. This phenomena involves events with at least one displaced vertex from the

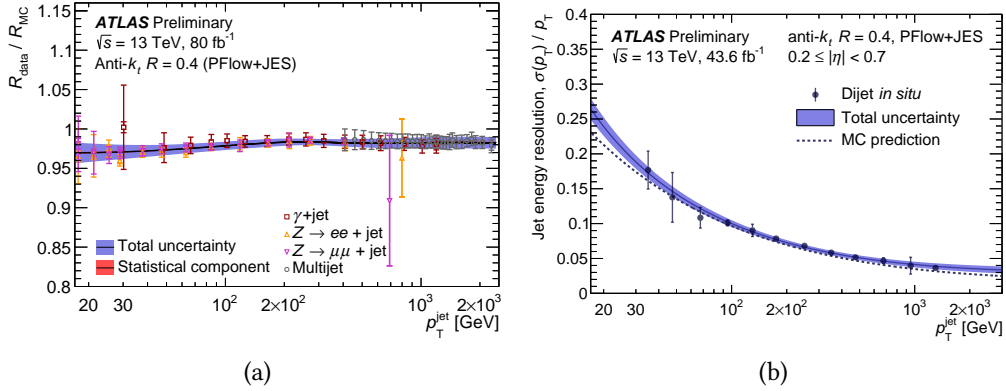


Figure 3.9: (a) Data-to-simulation ratio of the average jet p_T response as a function of jet p_T . The errors represent the statistical (inner error bars and small inner band) and the total uncertainty (statistical and systematic uncertainties added in quadrature, outer error bars and outer band) [117]. The relative jet energy resolution $\sigma(p_T)/p_T$ as a function of p_T . The expectation from Monte Carlo simulation is compared with the relative resolution as evaluated in data through the *in situ* techniques using the momentum balance of dijet events (triangles). The error bars on points indicate the total uncertainties on the derivation of the relative resolution in dijet events, adding in quadrature statistical and systematic components [118].

point where the hard-scatter occurred. The b -quark is also the heaviest quark that can form hadrons, which results in a heavy hadronic signature.

Two main classes of b -tagging techniques, divided into several categories, are used to identify b -jets: low-level and high-level algorithms. The taggers of the first class exploit physical observables as the track impact parameters, the secondary vertices and the topological features of the hadron decays inside the jet; while the second one combines algorithms of low-level using an MVA approach.

An inclusive approach based on the impact parameter of the charged particle track is used by two complementary algorithms: IP2D uses d_0/σ_{d_0} to construct a discriminating variable, while IP3D exploits both d_0/σ_{d_0} and $z_0 \sin \theta/\sigma_{z_0 \sin \theta}$ in a two-dimensional template taking into account their possible correlation. Ratios of b -jets, c -jets and light-flavour jets is calculated using probability density functions derived from MC simulations. A log-likelihood ratio discriminant is then defined as the sum of the per-track probability ratios for each jet-flavour hypothesis [123].

The secondary vertex tagging algorithm (SV) uses an exclusive approach, reconstructing the displaced secondary vertex within the jet. A two-track vertices hypothesis is built considering all the tracks associated with the jet, rejecting tracks from decay of long-lived particles or photon conversion. When two-track vertices are cleaned, SV1 algorithm runs iteratively on all the selected tracks to fit

one secondary vertex. A χ^2 test is used in each iteration to evaluate the goodness of fit [124].

The JetFitter [125] algorithm, exploits the topological features of weak b - and c -hadron decays within the jet to reconstruct the full b -hadron decay chain. A customized Kalman filter is used to find a common line where the PV, the b and c vertices lie, approximating the b -hadron flight path and the vertex positions. This method allows to resolve the b - and c -hadron vertices even if only a single track is attached to them.

In the high-level b -tagging algorithms, these three kinds of methods are combined exploiting a boost decision tree (BDT) and a deep feed-forward neural network (NN) defining the MV2 and the DL1 algorithms, respectively [123].

The MV2 is trained using the ROOT TMVA on the $t\bar{t}$ and Z' samples. The p_T and $|\eta|$ of the jets are included in the training to account the correlations with the other input variables. The b - and c -jets are reweighted in p_T and $|\eta|$ to match the spectrum of the light-flavour jets in order to discriminate between the different jet flavours. These weights are then removed at the evaluation stage of the MVA classifier. Three MV2 taggers have been developed by ATLAS, depending on the fraction of c -jets used in the training, with different light-flavour versus c -jet rejections: MV2c00, MV2c10 and MV2c20. The name of the tagger indicates the c -jet fraction in the training, e.g. in MV2c20, the background sample uses of 20% (80%) c - (light-flavour) jets. Different working points are defined as function of the average efficiency of the b -tagging of 60%, 70%, 77% and 85%.

The DL1 is based on a NN training using Keras [126] and Theano [127] backend and the Adam [128] optimiser. The DL1 NN has a multidimensional output corresponding to the probabilities for a jet to be a b -jet, a c -jet or a light-flavour jet [123]. Similar to the MV2 method, DL1 reweighs jet in p_T and $|\eta|$. In order to improve the performance of the algorithm, the c -jet fraction in the background training sample can be chosen a posteriori.

In Figure 3.10a, a comparison of the light-flavour jet rejection versus b -tagging efficiency for all the presented algorithms is shown. The b -tagging efficiency of the MV2 algorithm for the 77% working point as a function of jet p_T is displaced in Figure 3.10b.

3.5 Missing Transverse Energy

In collider experiments as ATLAS, momentum conservation in the plane transverse to the beam axis implies, in first approximation, that the vectorial sum of the transverse momentum of all the particles produced in the collision should be zero in the final states. A value different from zero may indicate the presence of SM neutrinos but also new particles predicted by Beyond the Standard Model

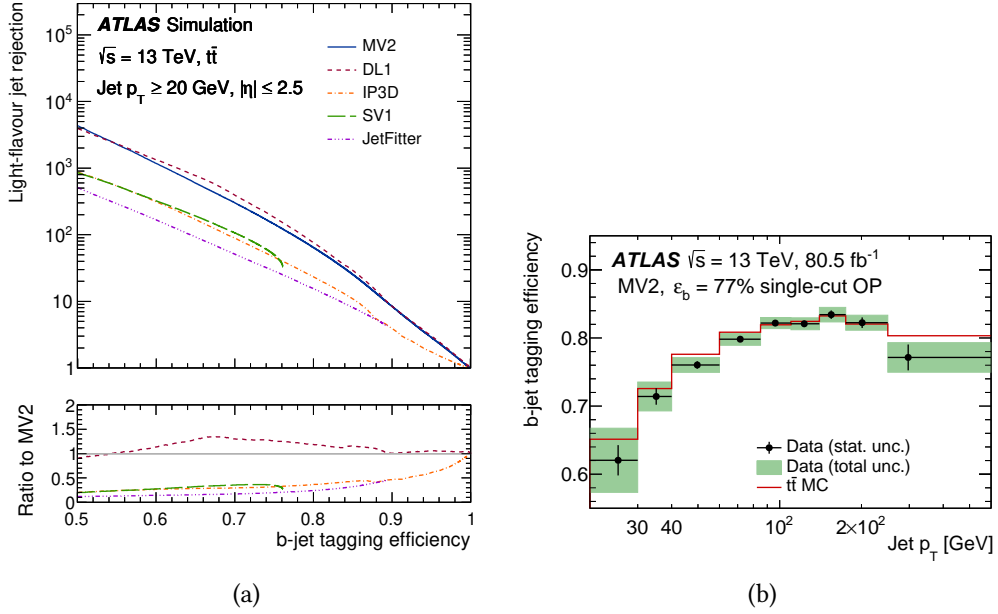


Figure 3.10: (a) The light-flavour jet rejections versus the b -jet tagging efficiency for the IP3D, SV1, JetFitter, MV2 and DL1 b -tagging algorithms evaluated on the baseline $t\bar{t}$ events. (b) b -tagging efficiency for the $\epsilon_b = 77\%$ single-cut OP of the MV2 tagger as a function of jet p_T . Vertical error bars include data statistical uncertainties only while the green bands correspond to the sum in quadrature of statistical and systematic uncertainties [122].

(BSM) mechanism which escape the detector without being detected [129]. This momentum imbalance is known as missing transverse energy (E_T^{miss}) [130].

E_T^{miss} is reconstructed combining information of all the detected particles, such as the reconstructed p_T , energy deposits in the calorimeters and tracks reconstructed in the ID. E_T^{miss} reconstruction is characterised by two main contributions: *hard objects*, considering fully reconstructed and calibrated leptons, photons and jets; *soft-term*, comprising reconstructed charged-particle tracks (soft signals) associated with the hard-scatter vertex but not with any of the reconstructed objects.

The missing transverse energy E_T^{miss} is the vectorial sum of missing transverse momentum terms of all the selected particles and jets reconstructed from the $\mathbf{p}_T = (p_x, p_y)$, and the soft term $E_T^{\text{miss,soft}}$ from the soft-events signals:

$$\begin{aligned}
 E_T^{\text{miss}} = & - \underbrace{\sum_{\text{selected electrons}} p_T^e}_{E_T^{\text{miss,e}}} - \underbrace{\sum_{\text{selected muons}} p_T^\mu}_{E_T^{\text{miss,\mu}}} - \underbrace{\sum_{\text{selected } \tau\text{-leptons}} p_T^{\text{had}}}_{E_T^{\text{miss,\tau had}}} - \underbrace{\sum_{\text{selected photons}} p_T^\gamma}_{E_T^{\text{miss,\gamma}}} - \underbrace{\sum_{\text{accepted jets}} p_T^{\text{jet}}}_{E_T^{\text{miss,jet}}} - \underbrace{\sum_{\text{unused tracks}} p_T^{\text{track}}}_{E_T^{\text{miss,soft}}}. \quad (3.11)
 \end{aligned}$$

To minimise double-counting of detector signals, topoclusters are associated with the reconstructed objects following a strict order: muons, electrons, photons, τ -leptons decaying hadronically, and jets. As final step, signals not associated with reconstructed objects are included in the soft term. Signals from neutral particles provided by the calorimeter are strongly affected by pile-up, then are not included in the soft term.

The vector $\mathbf{E}_T^{\text{miss}}$ leads the information of the amount of the missing transverse energy via its magnitude E_T^{miss} and its direction in the transverse plane via the azimuthal angle ϕ^{miss} .

Different E_T^{miss} working points have been provided by ATLAS depending on the characteristics of the jet, since they are the objects with the higher impact on E_T^{miss} performance:

- *Loose* E_T^{miss} WP includes jets with p_T more than 20 GeV . Jets with $|\eta| < 2.4$ and $p_T < 60$ GeV , must also satisfy the JVT criteria
- *Tight* E_T^{miss} WP is calculated excluding forward jets ($|\eta| > 2.4$ and $20 < p_T < 60$ GeV) to reduce the pile-up dependency
- fJVT E_T^{miss} WP is provided to suppress the E_T^{miss} tails. Forward jets failing the Loose fJVT criteria are removed. The JVT requirement is applied to jets with $|\eta| < 2.4$ and $p_T < 60$ GeV .

3.5.1 Missing Transverse Energy Significance

To distinguish real E_T^{miss} due to undetected particles from E_T^{miss} due to resolution smearing, E_T^{miss} significance $\mathcal{S}(E_T^{\text{miss}})$ must be evaluated. High values of $\mathcal{S}(E_T^{\text{miss}})$ suggest that the observed E_T^{miss} in the event cannot be due to momentum resolution effects but to undetected objects such as neutrinos or more exotic weakly interacting particles [131].

In several experiments including ATLAS, $\mathcal{S}(E_T^{\text{miss}})$ was previously defined as:

$$\mathcal{S}(E_T^{\text{miss}}) = \frac{E_T^{\text{miss}}}{\sqrt{H_T}} \quad \text{or} \quad \mathcal{S}(E_T^{\text{miss}}) = \frac{E_T^{\text{miss}}}{\sqrt{\sum E_T}} \quad (3.12)$$

where E_T^{miss} is the reconstructed magnitude of the missing transverse energy, H_T is the scalar sum of events transverse momenta and $\sqrt{E_T}$ and $\sqrt{H_T}$ are event-based approximations to the total E_T^{miss} resolution. These definitions had the limit to assume that E_T^{miss} was entirely calculated using calorimeter signals. To improve the performance of the reconstructed objects exploiting the measurements provided by all the ATLAS sub-detectors, a new approach was required. Then, an object-based E_T^{miss} significance variable was developed extending the

calculation to an event by event measurements considering the expected resolutions and likelihood of mismeasurement of all the objects present in the Equation 3.11.

The extended $\mathcal{S}(E_T^{\text{miss}})$ is defined to test the hypothesis that the total transverse momentum carried by invisible particles ($\mathbf{p}_T^{\text{inv}}$) equal to zero against the hypothesis that $\mathbf{p}_T^{\text{inv}}$ is different from zero. Given the likelihood function of the 2D parameter $\mathbf{p}_T^{\text{inv}}$ for the corresponding measured $\mathbf{E}_T^{\text{miss}}$ ($\mathcal{L}(\mathbf{E}_T^{\text{miss}}|\mathbf{p}_T^{\text{inv}})$), the log-likelihood ratio and the square of the significance \mathcal{S} are defined as:

$$\mathcal{S}(E_T^{\text{miss}})^2 = 2 \ln \left(\frac{\max_{\mathbf{p}_T^{\text{inv}} \neq 0} \mathcal{L}(\mathbf{E}_T^{\text{miss}}|\mathbf{p}_T^{\text{inv}})}{\max_{\mathbf{p}_T^{\text{inv}} = 0} \mathcal{L}(\mathbf{E}_T^{\text{miss}}|\mathbf{p}_T^{\text{inv}})} \right), \quad (3.13)$$

where the likelihood function depends on the multiplicities, types, and kinematics of the objects measured in each event.

Considering an $x - y$ coordinate system which is rotated parallel (longitudinal L) and perpendicular (transverse T) to the direction of the total missing transverse energy E_T^{miss} the significance \mathcal{S} can be written in a synthetic form:

$$\mathcal{S}(E_T^{\text{miss}})^2 = \frac{|\mathbf{E}_T^{\text{miss}}|^2}{\sigma_L^2 (1 - \rho_{LT}^2)}, \quad (3.14)$$

where σ_L^2 is total variance in the longitudinal direction to $\mathbf{E}_T^{\text{miss}}$ and ρ_{LT} is the correlation factor of the longitudinal L and transverse T measurements. This form shows the intrinsic meaning of the $\mathcal{S}(E_T^{\text{miss}})$, where the measured variable is in the numerator and the information of the variance is embedded in the denominator. The Equation 3.14 is also linked to the Equation 3.12, in which the $\sqrt{\sum E_T}$ is the approximated $\mathbf{E}_T^{\text{miss}}$ resolution.

The object-based $\mathcal{S}(E_T^{\text{miss}})$ is a powerful variable to suppress the background rejection while guaranteeing good signal selection efficiency in events with high values of E_T^{miss} .

The ROCs (Receiver Operating Characteristic) [132] in Figure 3.11a - 3.11c show the performance of the different types of $\mathcal{S}(E_T^{\text{miss}})$ in different E_T^{miss} ranges.

3.6 Overlap Removal

The *overlap removal* (OR) technique guarantees that the same particle leaving its signature in the detector, is not reconstructed as two different objects in the same event [133]. This procedure is typically used to avoid duplication (reconstruction of one object as two different objects) and isolation (two separate but close-by objects). Several steps compose the OR method and its performance depends on the quality and on the object selection. To guarantee the discrimination between

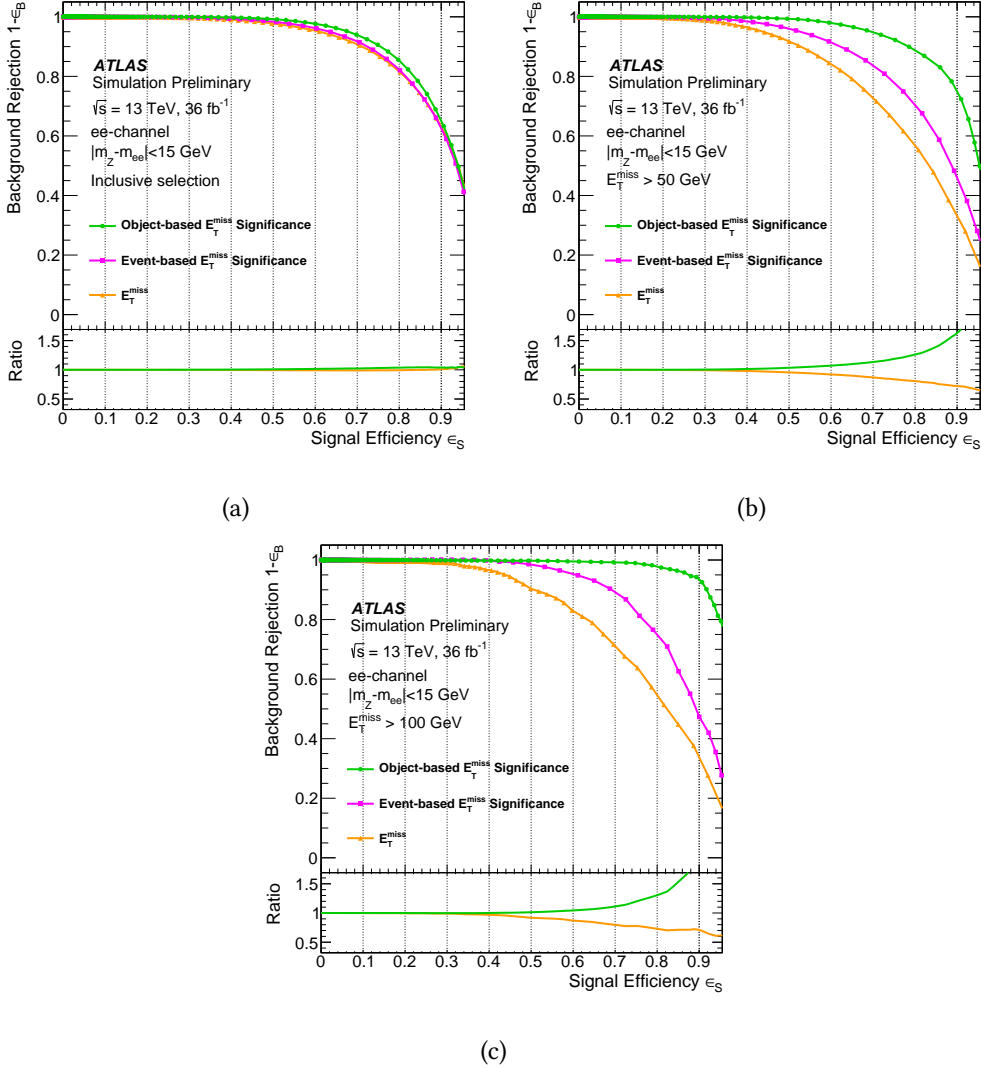


Figure 3.11: Background rejection versus signal efficiency in simulated $Z \rightarrow ee$ and $ZZ \rightarrow eee\nu\nu$ samples with a $Z \rightarrow ee$ selection. The performance is shown for E_T^{miss} , event-based $\mathcal{S}(E_T^{\text{miss}})$ and object-based $\mathcal{S}(E_T^{\text{miss}})$ as discriminants in events with (a) the entire E_T^{miss} range, (b) $E_T^{\text{miss}} > 50$ GeV, and (c) $E_T^{\text{miss}} > 100$ GeV. The lower panel of the figures shows the ratio of other definitions/event-based E_T^{miss} significance [131].

different objects, the ΔR variable defined in the $\eta - \phi$ space is used (see Equation 2.8).

- Electron-jet OR: It is used to remove reconstructed jets which are identical to reconstructed prompt electron and to reject events (or objects) where they are close to each other, to avoid bias on the position or energy mea-

surements. The duplication of electrons as jets can be efficiently removed excluding the region in $\Delta R(e, j)$. On the other side, the $0.2 < \Delta R < 0.6$ regions is enriched of real hadronic jets close to electrons, providing an increase of the jet energy due to the electron cluster merge

- Muon-jet OR: The goal is to separate prompt muons from muons originating from the hadron decay within a jet and to remove jets from final state radiation (FSR) or bremsstrahlung-photons. Due to pile-up, jet and muon can be produced in the same area of the detector either from the same or different bunch-crossings. Decays of light or heavy flavour meson can lead to close-by muons. FSR and bremsstrahlung can produce photons (which can be misreconstructed as a jet) very close to the muon track of muons reconstructed as jets. Muon duplication can be removed rejecting jets with a number of associated tracks less than 2 when $\Delta R(\mu, j) < 0.2$. Also, inside a cone of $\Delta R(\mu, j) < 0.4$ if the number of associated track to a jet is more than 2 and it overlaps with a muon, this latter is removed. For high- p_T muons, the cone size is variable following: $\Delta R(\mu, j) < 0.4 + 10 \text{ GeV} / p_T(\mu)$.
- Lepton-lepton OR: Duplication of standard electrons with soft electrons can be addressed by requiring a $\Delta R > 0.05$ between the second lepton and the most energetic lepton of the same flavour or the one with shares a track with the leading lepton. To avoid bias in the simulation or reconstruction steps, some performance groups requires a $\Delta R < 0.2$ or larger. Duplication of a muons as an electron can happen when the muon radiates a hard photon, in this case objects are usually closer than 0.01 in ΔR or share the same ID track. Also for this kind of overlap, the ID track sharing provides a better discrimination power. In this OR procedure, electron is removed if the muon has at least one associated track in the MS.

The OR process is very important in all the analysis performed in particle physics experiments. The recommended OR sequence is strongly based on the objects selection applied in each analysis. The suggested removal order is: ID and isolation of electrons and muons, same flavour leptons, opposite flavour leptons and finally lepton-jet.

3.7 Lepton Triggers

All the objects described in this section can be collected by using several triggers depending on the requirements imposed by the different analyses. Since the

work described in this thesis exploits only lepton triggers, only these ones are discussed in this section.

The rate of recorded events is reduced using triggers. These select events based on online reconstruction of objects, collecting interesting events for the analysis, and discarding uninteresting events. The choice of triggers is a compromise between the acceptance of the signal candidates and the rejection of background events.

Typically, a trigger name is self-explanatory, meaning that it contains the main information directly in its name. Considering for example an electron-trigger (but this description is the same for muons) as `e24_lhvloose_nod0`: it is clearly a single electron-trigger by the presence of the only “e” in the name; the p_T threshold is in GeV unit and it is represented by the number after the “e” (in this case 24 GeV); to pass this trigger electron must satisfy at least the likelihood identification level very loose (lhvloose) and no information on the impact parameter d_0 are used in this particular trigger, as denoted by the “nod0” at the end of the name.

Depending on the trigger used, all of these requirements can be changed: such as the p_T threshold, the lepton quality and the information used by the trigger itself.

For instance the di-electron trigger `HLT_2e12_lhloose_L12EM10VH` requires two electron, passing the LH ID loose, with at least $p_T > 12$ GeV requiring also to be identified at the first level trigger (L1). In such case, the L1 information may not be required (noL1).

Final rates for recorded events cannot go beyond the limits reported in Section 2.2.6. To keep the trigger rates at a reasonable level one can increase the momentum thresholds, tighten the quality of the reconstructed object at trigger level or prescale the trigger. A prescale is a factor N that can be applied to each trigger item and in those cases, only 1 event out of N particular events is recorded, discarding all the others. Prescales are constant inside each Luminosity Block.

For a particular case as the *fakes estimation* presented in this thesis in Section 5.2.2, to avoid trigger bias selecting a sample of isolated leptons, prescaled lepton triggers have been used, with a lower momentum threshold and a looser reconstructed quality. Also the additional request on another reconstructed object will decrease the trigger rates as for example the dilepton triggers.

In Figures 3.12 and 3.13 triggers efficiency for a certain set of trigger for muons and electrons is shown, respectively.

In Section 5.1 additional details on the triggers used in the analysis are reported.

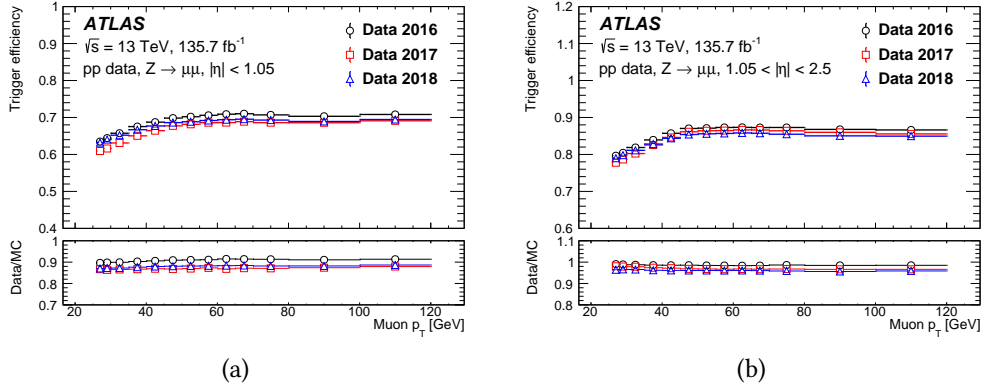


Figure 3.12: Efficiency of passing either the HLT_mu26_ivarmedium or the HLT_mu50 trigger in the barrel (3.12a) and endcaps (3.12b) as a function of the muon p_T , computed using data taken in 2016-2018. The error bars show the statistical uncertainties only [134].

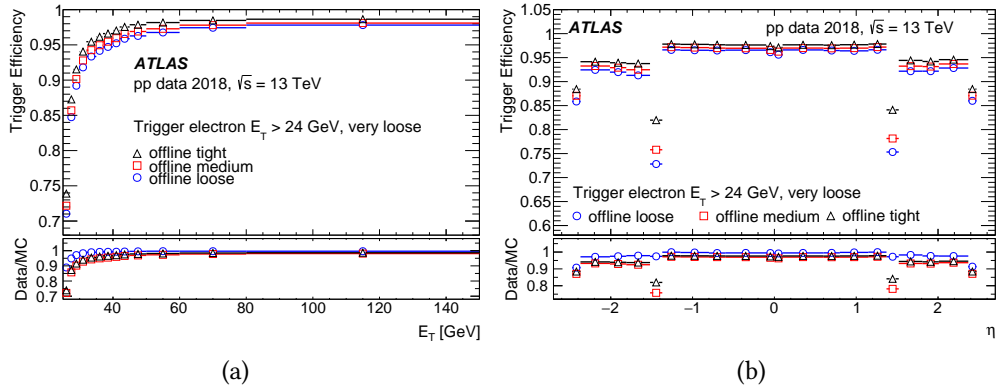


Figure 3.13: Efficiencies of the e24_lhvloose_nod0 trigger as a function of the offline electron (3.13a) E_T and (3.13b) η with respect to offline tight, medium, and loose identification, and no isolation requirements. The efficiencies are measured in data and shown with corresponding statistical and systematic uncertainties. The ratios of data to MC simulation are also shown. For (3.13b), only offline candidates with $E_T > 25$ GeV are used. [135].

Chapter 4

ATLAS Offline Software

4.1	Data Analysis Tools	93
4.2	Data Samples	103
4.3	Simulated Signal Samples	103
4.4	Simulated Background Samples	103

The analysis presented in this thesis has been performed using the full Run 2 dataset collected by the ATLAS detector in 2015-2018 period, at $\sqrt{s} = 13$ TeV, corresponding to an integrated luminosity of 139 fb^{-1} . To take into account all the physics processes for both signal and background, Monte Carlo samples have been used. A good description of the SM background processes is fundamental for a successful analysis, where a data-MC ratio as close as possible to one is required in each region.

4.1 Data Analysis Tools

To produce MC samples considering the detector response for all the different physics scenarios, a detailed simulation by the ATLAS simulation infrastructure is performed [136]. The simulation software chain involves three steps: *generation* of the event and immediate decays, *simulation* of the detector and physics interactions, and *digitization* of the energy deposited in the sensitive regions of the detector into voltages and currents to simulate the readout of the ATLAS detector. The result of this work-flow is provided in an object-based format or a specific format identical to the output of the ATLAS DAQ system. The simulation program, Athena [137], is implemented in the ATLAS software framework

and uses GEANT4 simulation toolkit to account the passage of particles through matter [138].

When the digitisation is completed, the simulated detector response looks like the raw data from the real detector, and after this step the process for the simulated events is the same as for real data. After this stage, MC and real data are the same, except that in MC the original generated events (called “truth”) are available as well as the reconstructed objects. Finally, the *derivation* framework is used to reduce the size of the original format selecting only the information needed by a specific analysis group [139].

Generation Framework

An overview of the ATLAS simulation data flow can be seen in Figure 4.1. The first stage is to *generate* all the physics processes of interest using MC generators software, which produce events in standard HepMC format [140]. At the genera-

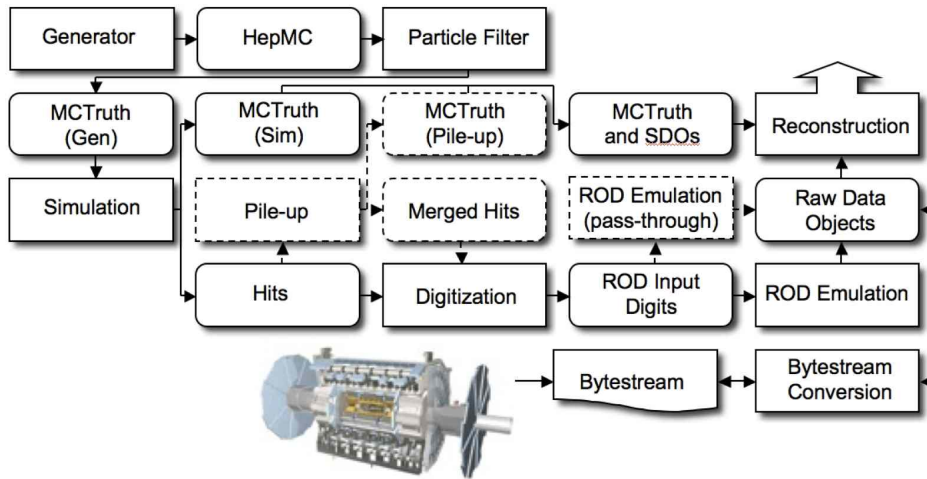


Figure 4.1: The flow of the ATLAS simulation software, from event generators (top left) through reconstruction (top right). Algorithms are placed in square-cornered boxes and persistent data objects are placed in rounded boxes [136].

tor level, pp interaction can be seen as the interaction between two partons of the protons using specific parton distribution functions (PDFs). In this way, the pp deep inelastic cross-section can be expressed in term of the parton-parton cross-section. The *QCD factorization theorem* [141] is used in this stage to remove singularities from the parton cross-section and to absorb them into the PDFs of the incoming hadrons at all orders in the perturbative expansion. Depending on the partons transverse momenta with respect to the *factorization* scale μ_F , they are considered: to be part of hadron structure and absorbed in the PDF ($p_T^{\text{parton}} < \mu_F$),

participants of the hard scattering process with a short-distance partonic cross-section ($p_T^{\text{parton}} > \mu_F$). The hard-scattering process is simulated using a Matrix Element (ME) calculation with different correction orders: Leading Order (LO), Next-to-Leading Order (NLO) and Next-to-Next-to-Leading Order (NNLO). High orders corrections (NLO and NNLO) allow to fix the renormalisation scheme ambiguities in QCD, for instance, adding virtual loops with quarks or gluons, or to provide accurate theoretical predictions calculating radiative corrections within the perturbative electroweak adding, for example, a virtual photon interaction between two charged particles or virtual loops of W/Z or Higgs bosons.

Different set of PDFs are used in proton collider experiments, depending on the input dataset used, on the correction orders or on the parametrization choice. The PDFs used in the MC samples for the analysis presented in this thesis are range from leading to next-to-leading order: NNPDF2.3LO [142], NNPDF3.0LO, NNPDF3.0NNLO and MEN3.0NLO [143]. In Sections 4.3 and 4.4 additional information on the MC samples used, are provided.

After the generation of the outgoing partons, the *parton shower* (PS) is used for simulating the cascades of radiation produced from QCD processes and interactions in high-energy particle collisions. PS is based on the parton model proposed by Richard Feynman in 1969, and describes the generation of two partons from a single parton conserving flavour, four momentum and respecting unitarity. Parton radiation is described as successive parton emissions from the hard interaction scale to the hadronization scale up to 1 GeV. The shower development depends on the different choice for the splitting variable and the scattering approach, requiring several MC generator to cover all the analyses needs: HERWIG (and HERWIG++) [144, 145] uses angular ordering as evolution variable and fully includes the spin correlation effects; PYTHIA [146] focuses on soft emission and averages the azimuthal correlation between two successive splitting over the polarizations; SHERPA [147] exploits an algorithm based on Catani-Seymour [148] dipole factorisation for both QCD and QED processes.

The PS algorithms based on collinear and soft approximation, low angle and low energy respectively, can not guarantee accurate predictions for hard and large-angle emissions. For this processes, the full ME amplitudes are needed. To avoid double counting of the final states configurations by ME generations and PS simulations, the *matching scale* is introduced. This arbitrary scale defines a threshold below which the additional radiation is modelled by the parton shower, while above it is simulated using the full ME calculations.

Two different matching methods are adopted to improve the PS description: the Matrix Element and Parton Shower matching (ME + PS) and the matching of the NLO calculation and Parton Shower (NLO + PS). The ME + PS technique exploits the three-level ME for large angle and hard emissions for the production of the basic process, with an additional number of partons. A minimum separation

angle is imposed on the produced partons requiring a p_T in any pair of partons more than a given threshold Q_{cut} (the matching scale). The Q_{cut} value must be small enough to guarantee an accurate PS emission, but large enough to allow fixed-order perturbation theory. On the other side, the NLO + PS method extends the accuracy of the generation of the basic process at the NLO level in QCD. It includes the radiation of an extra parton with tree-level accuracy and also the NLO virtual corrections. The ME + PS approach uses the existing LO generators for the ME calculation, like MADGRAPH [149], and feeds the partonic events to a general-purpose MC like PYTHIA or HERWIG. Other generators as SHERPA and HERWIG++ also include their own ME generators. The NLO + PS processes are implemented in the POWHEG framework [150–153] and in aMC@NLO [154]. In HERWIG++ is included its own POWHEG implementation, adapted in order to consider also vetoed and truncated showers; while SHERPA has a variant of the MC@NLO method [155].

In the final step of the PS, the *hadronization* process takes place. Since it is a non-perturbative model, the perturbation theory is not valid anymore and the dynamics can not be described by first-principle models. Two phenomenological iterative mechanisms are used to describe the hadronization mechanism: the Lund string model [156] and the cluster fragmentation model [157, 158]. In the former, the linear confinement potential leads to a linear relationship between the energy-momentum and space-time pictures of a simple $q\bar{q}$ fragmenting system. Gluons between the $q\bar{q}$ pairs are considered as color field lines and they are attracted to each other due to the gluon self-interaction. When the quarks pair separates, the gluon color field lines are stretched until it is more energetically favorable for them to fragment and create an additional $q\bar{q}$ pair. This procedure continues until all the color field lines are too light for further fragmentation. In the cluster fragmentation model, gluons are divided into $q\bar{q}$ pairs clustered and the hadronization occurs via preconfinement of colour singlet hadrons, which decay according to a simple phase-space scheme. Clusters are fragmented until stable hadrons are formed. If the cluster is not big enough to fragment into a hadron, a light hadron replaces the cluster. For a good description of the physics process, the decay modelling has to account also the unstable particles, as the primary hadrons, which further decay into a set of stable particles¹.

Commonly, MC generators contain MEs only for selected (generator-specific) classes of hadron and τ decays, that are coupled with a Breit-Wigner smearing of the masses, truncated at the edges of the physical decay phase space. Some generators, as SHERPA and HERWIG++, also include helicity-dependence in τ decays and spin correlations between hadronic decays for which ME are used. HER-

¹In this context, particles are considered stables if they have a minimum flight path distance of $c\tau \geq 10$ mm.

WIG++ and PYTHIA additionally include the probability for B mesons to oscillate into \bar{B} ones before decay. SHERPA takes into account also the CP-violating effects and the direct decay and oscillation followed by decay [9]. Models which describe hadronization are parameterizations of the physics processes, which depend on free parameters which need to be determined by experiments: this mechanism is called *tuning of parameters* in MC event generators. The MC tuning also takes into account the dependencies of some of these processes to the PDFs setting. Several MC generators, as SHERPA and HERWIG 7.1, have a dedicated set of tuned PS parameters developed by their authors; while for other MC generators different tunes are provided, such as ATLAS 2014 (A14) [159], AZ and AZNLO [160] and Perugia 2021 [161].

Detector Simulation

After the generation of the physics process, the interactions of the particles in the final states with the detector materials have to be simulated to compare directly simulated and real events. The GEANT4 software, used in the simulation stage, provides several models for physics and infrastructure for particle transportation through a given geometry. For this reason a detailed description of the ATLAS detector geometry and of the trigger system is mandatory to obtain a simulated process as close as possible to the reality. The geometry is constructed in the GEANT4 format and all the particles interactions are done on the Athena side, in the so-called *sensitive detector*. An exhaustive explanation of this mechanism is given in Appendix B.

The Framework for ATLAS Detector Simulation (FADS) [162] directly envelops GEANT4 classes for volumes, materials and sensitive detectors to process *hits*² and GEANT4 physics process definitions. These wraps are useful to easily connect Athena and GEANT4 information, and, on the user side, to load only the configuration related to the detector parts and physics processes of interest without recompiling the whole framework. This approach is convenient to add particles or processes not included in the GEANT4 tool-kit but included in the FADS catalogue. FADS provides a Python [163] interface for configurations and dictionaries in order to be translated into their GEANT4 equivalents and loaded. In order to have readable results by Athena, a service for GEANT4 called during the event loop have been implemented by the ATLAS Collaboration [164]. This simulation procedure is called in ATLAS, Full Simulation (FS).

Due to the complicated detector geometry and the detailed physics description used during the FS by the ATLAS GEANT4 simulation, many physics analysis or performance studies can not achieve the required simulated statistics without

²A hit represents the energies deposited in the sensitive materials of the detectors containing the total energy deposition, time and position.

faster simulation strategies. For this reason, several fast simulation techniques have been developed to integrate the FS. A huge part of the FS time ($\sim 80\%$) is spent to simulate particles traversing the calorimetry, mainly due to the electrons and photons which produce many secondary particles in the electromagnetic showers. The *Fast G4 Simulation* [165] has been developed to speed up this slowest part of the FS by using pre-simulated *frozen showers* stored in memory as library which replace the low energy electromagnetic particles. This approach guarantee a CPU time reduced by a factor of three in hard-scattering events.

Alternatively to the Fast G4 Simulation, FS time can be reduced by using the ATLAS Fast II simulation (AFII) [166], which exploits the Fast Calorimeter Simulation (FastCaloSim) [167]. It has been developed to simulate and reconstruct events including detector effects, but saving computing resources by the parameterizations of the longitudinal and lateral energy profile of the single particle showers. The reconstructed AFII output includes all the properties associated with a reconstructed object and the energies in the calorimeter cells. FastCaloSim uses the truth information of all interacting particles at the end of the inner detector volume as input to the calorimeter simulation. Because the standard reconstruction is used, it is possible to work with a combination of events obtained from GEANT4 and AF-II without modifying the analysis code. The FastCaloSim approach provides less accurate results, then the parameterizations are tuned with real data. It has been used since 2011 for the production of large MC samples (for both new physics searches and precise measurements) and it has been validated comparing results for electrons, jets and missing transverse energy to the ones obtained in the GEANT4 FS.

Similar to AFII, ATLAS Fast II simulation Fatras (AFIIF) has been developed by the ATLAS Collaboration using the Fast ATLAS Tracking Simulation (Fatras) for the inner detector and muon system [168, 169]. In Fatras, the reconstruction geometry is a simplified description of the full detector geometry. It preserve the descriptive accuracy for sensitive detector parts, while approximating all other detector components as simplified layers that carry a high-granularity density map. As the AFII, AFIIF includes all the properties associated to the reconstructed object with the addition of the hits in the inner detector and muon system. Fatras uses HepMC format as input, it performs a smearing of the primary vertex position to display the luminous region inside ATLAS, and save truth information similarly to the FS. Fatras can also be tuned against real data. Combining Fatras with FastCaloSim, AFIIF shows a high level of agreement with the GEANT4 FS, reducing the computing time of about two orders of magnitude.

In Figure 4.2 the CPU time required to simulate 500 $t\bar{t}$ events in ATLAS using the three different simulation techniques is shown [170].

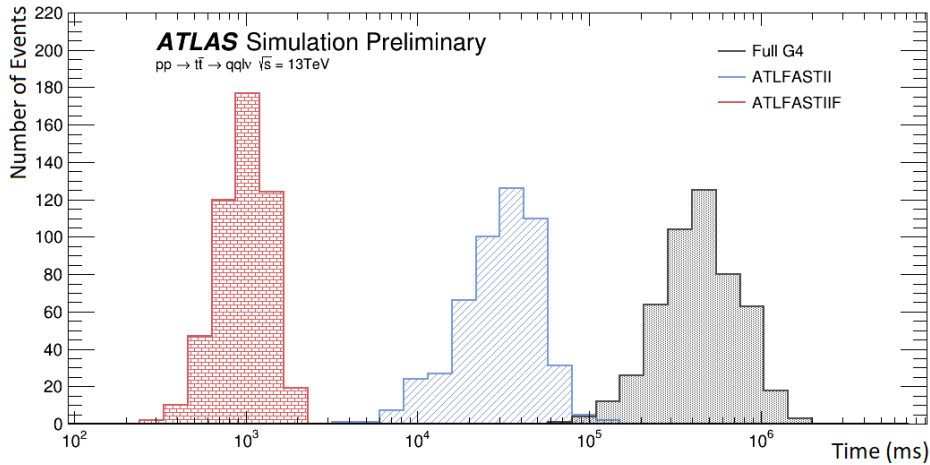


Figure 4.2: Comparison between GEANT4 and two fast simulators, the fast calorimeter simulation (labelled as ATLFASITII) and the fast chain (labelled as ATLFASITIF), in the CPU performance of event processing time. Simulations were performed in Athena release 21.3.8 on semi-leptonic $t\bar{t}$ events. Simulation benchmarks were performed using the BNL USATLAS Tier-3 Cluster which consists of 300 nodes, each with 8 2.6GHz CPUs and 16 GB of memory. 500 events were produced in a single run. No pile-up is simulated [170, 171].

Digitisation and Pile-up

The ATLAS digitization software is used to convert the hits produced during the simulation step into detector response objects, called *digits*. A digit is commonly produced when the current or voltage on a particular readout channel rises above a pre-configured threshold within a particular time-window. The digit format depends on the detector functionality: some sub-detectors contain information on the signal shape over this time, while others record only that the threshold has been exceeded. The digitization algorithm characteristics were tuned to reproduce the detector response seen during test beam data or laboratory tests. The digits of each sub-detector are written out as Raw Data Objects (RDOs). Additionally to RDOs, the digitization algorithms also produce Simulated Data Objects (SDOs). The SDOs contain information about all the particles and noise that contributed to the signal produced in the given sensor and the amount of energy contributed to the signal by each. The relation between SDOs and RDOs depends on the sub-detector structure.

To have a simulation as close as possible to reality, the detector response must include the additional pile-up interactions for any given hard scattering interaction. These events are simulated separately at the generation and simulation steps, and during the digitization stage hits from hard scattering are combined

with the pile-up ones before the calculation of the detector response. Given the average pile-up value for Run 2 data taking ($\langle\mu\rangle = 34$), more than 1000 simulated *minimum bias* events have to be selected randomly and processed. These events involve two main limitations in the current digitization workflow (shown in Figure 4.3a): large random I/O³ due to random event selection, and a long time in the digitization step to process large μ values, since the digitization of pile-up events is repeated for each hard-scatter process. For these reasons, a new

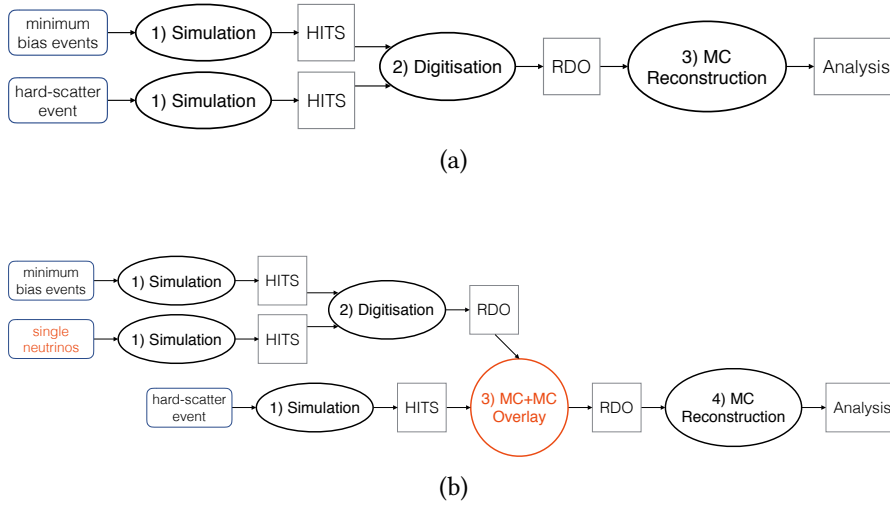


Figure 4.3: Diagrams illustrating the difference between (a) the standard digitisation and (b) the MC overlay pile-up methods [173].

MC + MC overlay method is proposed to be used instead of the current digitization [172], based on the data overlay technique already used for heavy-ion collisions simulations. As shown in Figure 4.3b, the new method introduces an additional step where pile-up events are pre-mixed. In *single neutrinos* events (representing zero-hard-scatter events) the standard pile-up digitization is considered, where additional digits are stored to bring the total information. In the *overlay* stage, each hard-scatter event is digitized and overlaid on pre-mixed pile-up digits. Using the new proposed method, the CPU and I/O requirements are lower and less dependent on μ values, and the background dataset can be digitized once per production campaign. On the other side, two signals from different events which are under threshold involving in a signal above threshold are now lost, and in some cases different dataset can have the same set of merged pile-up events.

³In random I/O, the time spent waiting for disk seeks and rotational latency dominates I/O service time, which can lead to damage to hard drivers.

Derivation Framework

After all the steps described previously, reconstruction provides both data and MC events in the Analysis Object Data (AOD) format. This kind of file has a huge size which is not practical for the user actions, then a less size data format satisfying the following characteristics is required:

- its size should be around a few per thousand of the original size;
- all the variables of interest need to be stored allowing calibration and performance studies by the so-called Combined Performance (CP) groups;
- all information necessary to perform the different analysis selections have to be present.

It was noted that during Run 1, almost all physics analyses went through the step of reducing PB of data down to a size of a few GB or smaller in the final ROOT [174] file (called *ntuple*) used to make plots and statistical analyses [175]. All this production process was done by users, via a complex procedure involving a large number of grid [176] jobs submitted. Furthermore, the final formats were defined by single analysis team depending on the analysis code developed, which caused difficulties in cross-team analyses where different tools were used.

To provide a common file format and to speed up the production avoiding the grid congestion, in Run 2 new intermediate formats (from now called *derivations*) have been made with the implementation of a centralized offline software, known as *Derivation Framework* [177]. The framework takes as input file a new ROOT-readable format, named xAOD, produced directly by Athena in the reconstruction step and which replaces the old AOD. The derivation framework is then used to remove and add information in the xAOD while maintaining the same structure of the original xAOD. The output file has a reduced size and it is called Derived-xAOD (DxAOD).

The derivation procedure is composed by four different steps:

- *skimming*: events which do not satisfy derivation requirements are removed;
- *thinning*: objects are removed from the event, according to some criteria, but keeping the rest of the event;
- *slimming*: removing not needed information from objects and keeping the interesting ones. Unlike the previous operations, slimming does not depend on event or object properties;

- augmentation: new containers of reconstructed objects and new variables to existing objects that are not available in the primary xAOD are implemented.

In Figure 4.4, a scheme of the whole ntuple production in ATLAS is shown. Derivations have been defined by individual physics analysis teams or subgroups

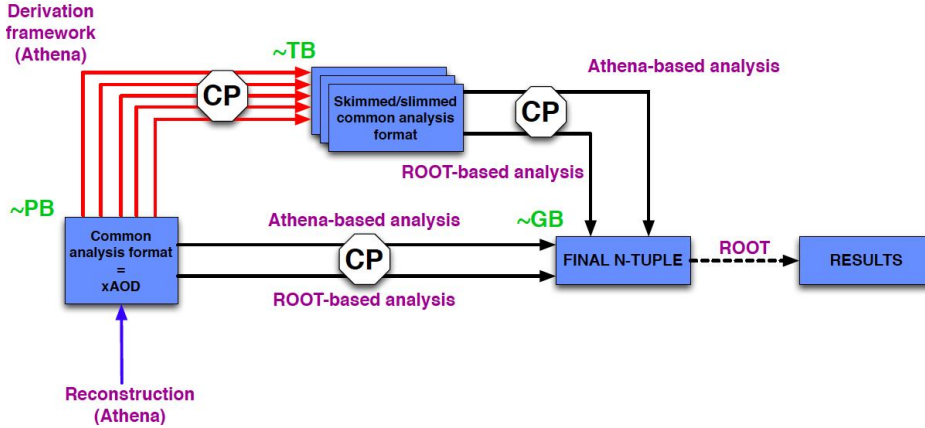


Figure 4.4: The ATLAS analysis model for Run 2 [177].

(e.g. Standard Model, Exotics, SUSY, Higgs, etc.) according to the specific analyses requirements.

For the analysis presented in this thesis, four different kinds of derivation was used:

EXOT12 : events are selected if they contain at least two leptons (in any flavour or charge combination) with an individual $p_T > 20$ GeV . Electrons are required to be LHLoose, while muons must be CB. This derivation is used in the Type-III SeeSaw analysis presented in the next chapter, in the Section 5.

EXOT19/22 : events contain at least one electron/muon with $p_T > 20$ GeV and passing LHLoose/combined identification. With this derivation, the fake estimation in the high- p_T ($p_T > 20$ GeV) electron/muon channel is performed, as explained in detailed in the Section 5.2.2.

SUSY17 : requires events containing at least one lepton (in any flavour and charge combination) with p_T more than 4.5 GeV . Muons are required to satisfy VeryLoose identification and $|\eta| < 2.7$, while electrons must be LHLoose with $|\eta| < 2.6$. This derivation is used to evaluate the fake lepton contribution in the low- p_T region ($p_T \in [10,20]$ GeV) for both electrons and muons.

4.2 Data Samples

The data used in this analysis were collected during the 2015-2018 data taking period at $\sqrt{s} = 13$ TeV . The combined 2015-2018 integrated luminosity amount to $\mathcal{L}_{\text{int}} \approx 139 \text{ fb}^{-1}$ with the uncertainty of 1.7% [178], obtained using the LUCID-2 detector [179] for the primary luminosity measurements.

All the data collected by the ATLAS detector are grouped into Luminosity Blocks (LBs), which are usually one minute long. In each LB, data have approximately constant instantaneous luminosity and the same data taking conditions. Only LB which are declared stable by LHC and all of the sub-detectors are used. These information are stored into the Good Run Lists (GRLs). Four of them are used in this analysis providing data collected in: 2015 with a $\mathcal{L}_{\text{int}} \approx 3.2 \text{ fb}^{-1}$, 2016 with a $\mathcal{L}_{\text{int}} \approx 33.0 \text{ fb}^{-1}$, 2017 with a $\mathcal{L}_{\text{int}} \approx 44.3 \text{ fb}^{-1}$, and 2018 with a $\mathcal{L}_{\text{int}} \approx 58.4 \text{ fb}^{-1}$.

4.3 Simulated Signal Samples

The MADGRAPH5_aMC@NLO framework is used to generate signal samples of this analysis following the simplified Type-III SeeSaw model [26] at LO using FEYNRULES [180]. For the simulated signal production, MADGRAPH5_aMC@NLO is interfaced to PYTHIA 8.230 for parton showering tuned with the A14 parameter set. The NNPDF3.0LO PDF set enters in the matrix element calculation, while the NNPDF2.3LO one is used in the parton shower. The signal cross-section and its uncertainty are calculated at NLO plus next-to-leading logarithmic (NLL) accuracy from $SU(2)$ triplet production in an electroweak chargino-neutralino model [181, 182]. The calculated cross-sections are compatible within uncertainties with the Type-III SeeSaw heavy leptons NLO implementation [183, 184].

Mass hypotheses for L^\pm and N^0 are considered in the 400-1200 GeV range with a mass step of 100 GeV . For each mass points, samples are sliced by lepton multiplicity requiring either two, three and four light leptons (electrons and muons) without hadronic tau decays. The fast simulation using GEANT4 toolkit and FastCaloSim is used for each slices. The generated mass hypotheses with their cross-sections at LO and at NLO+NLL are listed in Table 4.1.

4.4 Simulated Background Samples

Due to the topology presented in Figure 1.10b, the irreducible background events which involve in this final states are mainly diboson (WW, WZ, ZZ), Drell-Yan ($Z/\gamma^* \rightarrow e^+e^-/\mu^+\mu^-/\tau^+\tau^-$) and processes with the presence of top quarks.

Mass hypothesis [GeV]	$\sigma_{\text{NLO+NLL}}$ [fb]
400	180 \pm 14
500	69 \pm 6
600	29.6 \pm 3.0
700	13.9 \pm 1.5
800	7.0 \pm 0.8
900	3.7 \pm 0.4
1000	1.97 \pm 0.25
1100	1.08 \pm 0.15
1200	0.61 \pm 0.08

Table 4.1: Cross-sections of signal MC samples for each mass hypothesis considered in the analysis. Leading order cross-sections are computed by the generator and are re-weighted at the next-to-leading ($\sigma_{\text{NLO+NLL}}$) with their corresponding uncertainties using k-factors from [185, 186].

They also provide a source of reducible background due to charge misidentification in channels that contain electrons, as described in the next chapter. For this latter kind of background, a dedicated data-driven technique is used to estimate its contribution. The generators used for the MC samples, the cross-section calculation used for their normalisation and information on parton shower and matrix element PDF, are provided in Table 4.2.

Physics process	Event generator	ME PDF set	Cross-section normalization	Parton shower	Parton shower tune
Signal	MADGRAPH5_aMC@NLO	NNPDF3.0LO	LO	PYTHIA 8.230 & EVTGEN1.6.0	A14
Drell-Yan $Z/\gamma^* \rightarrow e^+e^-/\mu^+\mu^-/\tau^+\tau^-$	SHERPA 2.2.1	NNPDF3.0NNLO	NLO	SHERPA	SHERPA default
Top physics					
$t\bar{t}$	POWHEG-Box v2	NNPDF3.0NNLO	NNLO		A14
Single t	POWHEG-Box v2	NNPDF3.0NNLO	NNLO	PYTHIA 8.230	A14
$3t, 4t$	MADGRAPH5_aMC@NLO	NNPDF2.3LO	LO	& EVTGEN1.6.0	A14
$t\bar{t} + W/Z/H, tWZ$	MADGRAPH5_aMC@NLO	MEN3.0NLO	NNLO		A14
Diboson					
ZZ, WZ, WW	SHERPA 2.2.1 & 2.2.2	NNPDF3.0NNLO	NLO	SHERPA	SHERPA default
Multiboson					
WWW, WWZ, WZZ, ZZZ	SHERPA 2.2.1 & 2.2.2	NNPDF3.0NNLO	NNLO	SHERPA	SHERPA default

Table 4.2: Simulated signal and background samples. The event generator, PDF set used for the Matrix Element (ME) calculation, cross-section normalization, parton shower and parton shower tune are shown for each sample. The generator cross-section is used where not specifically stated otherwise.

The SM Drell–Yan processes were simulated using SHERPA 2.2.1 accounting the decay into e^+e^- , $\mu^+\mu^-$, $\tau^+\tau^-$. NLO and LO calculations for matrix ele-

ment are provided for events with up to 2 and up to 4 jets respectively, using Comix [187] and OpenLoops [188, 189] libraries. The default SHERPA parton shower based on Catani–Seymour dipoles and the cluster hadronization model are used with the default SHERPA and NNPDF3.0NNLO set for tuning.

For a given jet-multiplicity, the NLO matrix elements were matched to the parton shower using a colour-exact variant of the MC@NLO algorithm. Several jet multiplicities were merged into an inclusive sample exploiting a CKKW matching procedure [190, 191], extended to NLO accuracy using the MEPS@NLO prescription. The $Z + \text{jets}$ samples are normalised to NNLO calculation [192].

Diboson processes (VV) with one of the bosons decaying hadronically and the other leptonically are simulated with the SHERPA 2.2.1 generator, while processes where both bosons decay leptonically were simulated using SHERPA 2.2.2. Off-shell effects and Higgs boson contributions were also included where appropriate. Matrix elements are calculated for up to one or zero partons (zero partons are considered only in final states with three leptons and one neutrino) at NLO and up to three partons at LO using Comix and OpenLoops, and merged with the Sherpa parton shower, based on Catani–Seymour dipoles, according to the MEPS@NLO prescription.

Samples for the loop-induced processes ($gg \rightarrow VV$) were generated using LO-accurate matrix elements for emission of up to one additional parton for both the fully leptonic and semileptonic final states. The NNPDF3.0NNLO PDF set is used in conjunction with dedicated parton shower tuning developed by SHERPA authors. The event generator cross sections are used in this case (already at NLO).

Electroweak production of a diboson in association with two jets, $VVjj$, processes are generated using LO-accurate matrix elements for the inclusive process only. These samples include triboson contributions where one boson decays hadronically. Higgs diagrams with the Higgs decaying to two vector bosons are also included.

The production of multiboson (VVV) events are simulated using factorised gauge boson decays. Matrix elements are accurate at NNLO for the inclusive process and at LO for up to two additional parton emissions. These samples are limited to on-shell contributions only.

Seven variations of the QCD factorisation and renormalisation scales in the matrix elements by factors of 0.5 and 2 avoiding variations in opposite directions are used to evaluate the uncertainties from missing higher orders in all SHERPA samples [193].

Uncertainties in the nominal PDF set are evaluated from 100 replica variations. Furthermore, the results are cross-checked using the central values of the CT14NNLO and MMHT2014 NNLO PDF sets.

The production of single- t and $t\bar{t}$ events is modelled using the POWHEG-Box v2 generator at NNLO with the NNPDF3.0NNLO PDF set and the h_{damp} parameter set to $1.5 m_{top}$ [194]. The events are interfaced to PYTHIA 8.230 to model the parton shower, hadronization, and underlying event, using A14 as tune. The decays of bottom and charm hadrons are performed by EVTGEN1.6.0. For the $t\bar{t}$ sample, the computed cross-section at NNLO in QCD, includes the resummation of next-to-next-to-leading-logarithmic (NNLL) soft-gluon terms calculated with TOP++ 2.0 [195–197]. At $\sqrt{s} = 13$ TeV in pp collisions, this cross-section corresponds to $\sigma(t\bar{t})_{\text{NNLO+NNLL}} = 832 \pm 51$ pb, considering a top quark mass of $m_{top} = 172.5$ GeV. The cross-section uncertainties due to α_s and the PDF set were calculated with the PDF4LHC prediction [198] with the MSTW2008 68% CL NNLO [199], CT10 NNLO [200] and NNPDF2.3lo 5f FFN [142] PDF sets, which were added in quadrature to the scale uncertainty.

The production of $3t$, $4t$, $t\bar{t}V$ and tWZ events is modelled using the MADGRAPH5_aMC@NLO at NNLO for $t\bar{t}V$ and tWZ , and LO for the other ones. The events are interfaced to PYTHIA 8.230 using A14 tune and the NNPDF2.3LO PDF set for $3t$ and $4t$, while the MEN3.0NLO one is considered for $t\bar{t}V$ and tWZ . The decays of bottom and charm hadrons are performed by EVTGEN1.6.0.

A full simulation of the ATLAS detector response using the GEANT4 toolkit was performed for all the samples. Multiple interactions in the same and neighbouring bunch crossings was taken into account by overlaying the original hard-scattering event with simulated inelastic pp events generated with PYTHIA 8.186 using the NNPDF2.3lo set of PDFs and the A3 set of tuned parameters [201]. The MC events are weighted to reproduce the distribution of the average pile-up observed in the data by a rescaling factor of 1.03 ± 0.07 [202].

Chapter 5

Search for Type-III SeeSaw heavy leptons

5.1	Analysis Strategy	108
5.1.1	Objects Definition	110
5.1.2	Analysis Regions	113
5.2	Background Estimation	127
5.2.1	Background from electron charge misidentification	127
5.2.2	Background from fake leptons	130
5.3	Systematic Uncertainties	160
5.3.1	Theoretical Uncertainties	160
5.3.2	Experimental Uncertainties	162
5.4	Signal Extraction Technique	164
5.4.1	Likelihood-based test	166
5.4.2	Hypothesis test	167
5.4.3	Background extrapolation and error propagation	169
5.5	Results	170

The analysis presented in this thesis is aimed to search for possible signals of Type-III SeeSaw heavy leptons, described in Section 1.3, with respect the Standard Model prediction, in the data taken by the ATLAS Experiment.

This search is performed using data collected in the 2015-2018 period, corresponding to the full Run 2 dataset, at $\sqrt{s} = 13$ TeV with an integrated luminosity

of 139 fb^{-1} . This chapter describes the analysis strategy with the definition of the objects used and analysis regions (Section 5.1), the background estimation (Section 5.2), the signal extraction technique (Section 5.4) and the results (5.5).

5.1 Analysis Strategy

To search for events compatible with the prediction of the Type-III SeeSaw model, all possible decays involving the presence of three and four leptons are considered. Data and Monte Carlo samples described in Sections 4.2, 4.3 and 4.4, are then filtered to isolate only final states coherent with the interested heavy leptons decay modes. Final states with more than five leptons have cross-sections too low for being useful for discovery at the current integrated luminosity values [203], therefore they are not considered. Examples of the principle Feynman diagrams of the production and decay processes used in the analysis are shown in Figure 5.1a and 5.1b.

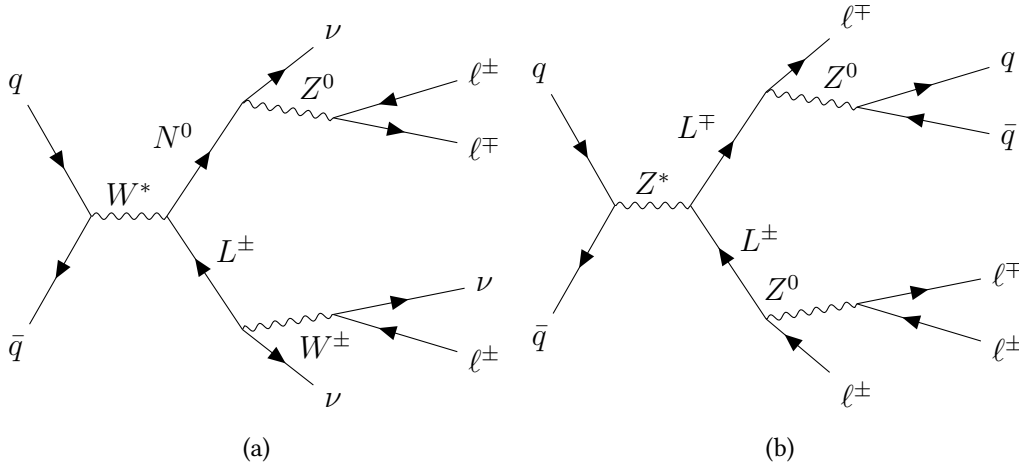


Figure 5.1: Example of Feynman diagrams for the considered Type-III SeeSaw heavy leptons pair production in the three- (a) and four-lepton (b) final states.

Selected events are then categorised into exclusive phase space regions, called *analysis regions*, fulfilling different sets of requirements on event- and object-level. Three kinds of analysis regions are provided, according to their purpose in the analysis: *signal regions* (SRs), *control regions* (CRs) and *validation regions* (VRs).

In the SRs a particular signal is expected to produce an excess over the SM expectation. SRs are enriched with signal events and are defined maximizing the sensitivity of the target models exploiting the signal-to-background ratio. In

the signal extraction step, they are used to compare data with the signal plus background hypothesis for each mass point of the considered mechanism.

CRs and VRs are constructed to evaluate and validate the main backgrounds affecting the SRs. Ideally, a CR and a VR are needed for each type of background. In order to have a good description of the SM events, these analysis regions must be enriched of background events minimizing the contribution of signal events. CRs and VRs are usually topologically close to the SRs due to one or more modified kinematics requirements which also guarantee orthogonality among all of them. CRs are specifically used to constrain and study the dominant backgrounds by comparing its shape and normalization to data using the background-only hypothesis. Using the background normalization as a free-floating parameter, a normalization factor can be extracted depending, as a first approximation, by the ratio of the background-MC/data yields. Once established, the goodness of the background estimation performed in the CRs should be tested in additional regions, the VRs, before being applied to the SRs. A scheme illustrating how this procedure operates is reported in Figure 5.2. It is important to point out that

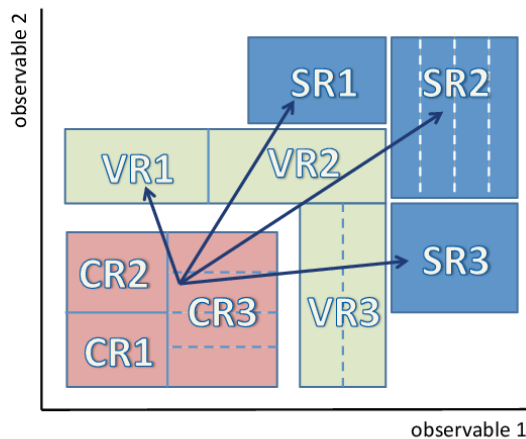


Figure 5.2: Schematic view of a template analysis strategy using several control, validation and signal regions. Each region can have single or multiple bins. As shown, the background estimation is performed in the controls regions, validated in the validation regions and the applied to the signal regions [204].

the SRs definition is performed in a *blinded* mode, i.e. without the presence of the data to avoid biases during the search for signal candidates. Once the background predictions are estimated and validated, data can be added to the SRs to finalize the analysis. Also for this reason CRs and VRs are designed to have negligible signal contamination.

The figure of merit used for the optimization of the SR is the signal-to-background significance \mathcal{S} , which allows to maximize the signal events while rejecting the backgrounds contribution [205]. \mathcal{S} is defined as:

$$\mathcal{S} = \sqrt{2 \left[(S + B) \ln \left(1 + \frac{S}{B} \right) - S \right]}, \quad (5.1)$$

where S is the number of signal events and B the total backgrounds contribution, based only on Monte Carlo predictions.

All the analysis regions defined in this work are obtained using a *cut-and-count* approach looking at the values of \mathcal{S} in several kinematic distributions. At least one of the cuts applied to define an analysis region guarantees the orthogonality among the others.

Data and MC samples are filtered, as described in Chapter 3 and 4, to satisfy good quality requirements rejecting events with large noise or due to non-collision backgrounds.

All the events for both data and MC samples are then pre-selected requiring exactly three leptons with a total charge equal to 1, and exactly four leptons with a total charge equal to 0 or 2. The inclusive flavour combination is considered in all the channels in order to increase the signal statistic. In Section 5.1.2, the definition of the CRs, VRs and SRs for both three- and four-lepton channel will be explained in detail.

To ensure the selection of good quality leptons, events must pass a set of dilepton triggers according to the flavour combination of the two leading leptons and data taking year. Despite finale states are composed by more than two leptons, dilepton triggers were chosen to guarantee enough signal events after this selection step. All the triggers used are unrescaled High Level Triggers (HLT), and they are reported in Table 5.1. No L1 requirement is imposed on the second muon in the $\mu\mu$ channel. Electron triggers require electrons passing at least `lhloose` and `lhvloose` offline reconstruction level, depending on the tag in trigger name, and do not require any isolation level on the electrons. Furthermore, for the 2016, 2017 and 2018 triggers no information on the impact parameter d_0 was used. For the muon triggers, an isolation requirement on the muon according to a medium working point of the muon reconstruction algorithm at trigger level with a $p_{\text{T}}^{\text{varcone30}}/p_{\text{T}}(\mu) < 0.07$ is required. For the mixed channel, the 2015 trigger does not use d_0 information while a loose requirement the electron according to the trigger level identification algorithm is applied.

5.1.1 Objects Definition

In ATLAS, physical objects like leptons and jets are reconstructed using several requirements, the so-called *working points*, corresponding to different efficiency

	2015	2016	2017-2018
ee	HLT_2e12_lhloose_L12EM10VH	HLT_2e17_lhvloose_nod0	HLT_2e24_lhvloose_nod0
$e\mu$	HLT_e17_lhloose_mu14	HLT_e17_lhloose_nod0_mu14	HLT_e17_lhloose_nod0_mu14
$\mu\mu$	HLT_mu18_mu8noL1	HLT_mu22_mu8noL1	HLT_mu22_mu8noL1

Table 5.1: Summary of the trigger requirements divided per lepton multiplicity and data taking year.

and purity levels with algorithms described in Chapter 3. The main motivation of the analysis object selection is to select WPs which provide the highest quality and reconstruction efficiencies, rejecting as much as possible the background events while not removing too much of the expected signal. To be able to apply the data-driven techniques for fake lepton estimation, two types of lepton definition, called *loose* and *tight*, are needed. This method, described in Section 5.2.2, is based on the measurement of the transition probability of leptons among these two categories. It is important to underline that these loose and tight definitions are not related to the WPs with a similar name. Tight leptons are considered as signal candidates while loose leptons are used to identify *fakes*, originated by misidentified particles or a non-prompt leptons.

The basic electrons requirements applied in this analysis are reported in Table 5.2. The electrons candidates must pass the `LHTight` identification selection with a $p_T > 10$ GeV and they are required to be in the $|\eta| < 2.47$ region, corresponding to the fiducial volume of the inner detector. The `FCLoose` isolation criterion must also be satisfied requiring $E_T^{\text{cone20}}/p_T < 0.2$ and $p_T^{\text{varcone30}}/p_T < 0.15$, for calorimeter-based and track-based selection respectively. The crack region between the barrel and the endcap of the calorimeter ($1.37 < |\eta| < 1.52$) is excluded due to the limited detector acceptance because of the service area. The track associated with the electron signal must satisfy requirements on the longitudinal and transverse impact parameter, which are required to be $|z_0 \sin(\theta)| < 0.5$ mm and $|d_0|/\sigma_{d_0} < 5.0$ respectively. The bad cluster veto is also applied to remove bad quality calorimeter clusters and fake clusters originating from calorimeter defects. For loose electron candidates, the `LHLoose` identification WP is applied with an exclusive OR between the identification and isolation requirements, corresponding to the exclusion of non-prompt non-isolated electrons. The other requirements on p_T , η and impact parameters are the same of the signal electron candidates.

The basic muons requirements applied in this analysis are reported in Table 5.3. The signal and background muons must have a $p_T > 10$ GeV and satisfy the `Medium` quality if their p_T is lower than 300 GeV, otherwise the `High- p_T` identification WP is considered. They have to pass (or fail in the case of loose

Requirement	Signal electrons (tight)	Background electrons (loose)
Identification	LHTight	LHLoose
Isolation	FCLoose	fail FCLoose or fail tight selection
p_T cut	$p_T > 10$ GeV	$p_T > 10$ GeV
η cut	$ \eta < 2.47$ and veto $1.37 < \eta < 1.52$	$ \eta < 2.47$ and veto $1.37 < \eta < 1.52$
$ d_0 /\sigma_{d_0}$ cut	$ d_0 /\sigma_{d_0} < 5.0$	$ d_0 /\sigma_{d_0} < 5.0$
$ z_0 \sin(\theta) $ cut	$ z_0 \sin(\theta) < 0.5$ mm	$ z_0 \sin(\theta) < 0.5$ mm
Bad cluster veto	yes	yes

Table 5.2: A summary of the baseline electron definitions in the analysis.

muons) also the `FixedCutTightTrackOnly` isolation requirement with $p_T^{\text{varcone20}} < 0.06$ for $p_T < 50$ GeV and $p_T^{\text{cone20}} < 0.06$ for p_T above 50 GeV. To avoid muons with a bad reconstructed momentum, the bad muon veto is applied. Constraints on the topological space are imposed requiring $|\eta| < 2.5$, a d_0 significance of $|d_0|/\sigma_{d_0} < 3.0$ and a longitudinal impact parameter of $|z_0 \sin(\theta)| < 0.5$ mm.

Requirement	Signal muons (tight)	Background muons (loose)
Quality	HighPt if $p_T > 300$ GeV else Medium	HighPt if $p_T > 300$ GeV else Medium
Bad muon veto	yes	yes
Isolation	FixedCutTightTrackOnly	fail FixedCutTightTrackOnly
p_T cut	$p_T > 10$ GeV	$p_T > 10$ GeV
η cut	$ \eta < 2.5$	$ \eta < 2.5$
$ d_0 /\sigma_{d_0}$ cut	$ d_0 /\sigma_{d_0} < 3.0$	$ d_0 /\sigma_{d_0} < 3.0$
$ z_0 \sin(\theta) $ cut	$ z_0 \sin(\theta) < 0.5$ mm	$ z_0 \sin(\theta) < 0.5$ mm

Table 5.3: Summary of the baseline muon definitions in the analysis.

Jets properties used in this analysis are reported in Table 5.4. They are reconstructed using the new particle flow algorithm requiring a `Medium` jet-vertex-tagger WP which provides an average efficiency of 92%. The base jet selection consists of $p_T > 20$ GeV with $|\eta| < 2.5$ for signal candidates (due to limitations of b -jets identification for higher values) and $|\eta| < 4.5$ for baseline jets. Jets satisfying all these requirements can contain b -hadrons, then the `MV2c10` algorithm is used providing a b -tagging efficiency of 77% and a background rejection against jets originated by light quarks and gluon jets by a factor of 134, a factor 6 against those from c -quarks and a factor of 22 for τ -leptons decaying hadronically.

After electron, muon and jet reconstruction, possible objects duplication is resolved using the dedicated overlap removal procedure (as described in Section

Requirement	Signal jets	Baseline jets
Jet type	AntiKt4EMPFLOWJETS	AntiKt4EMPFLOWJETS
JVT working point	Medium	Medium
fJVT working point	–	–
p_T cut	$p_T > 20 \text{ GeV}$	$p_T > 20 \text{ GeV}$
η_{cut}	$ \eta < 2.5$	$ \eta < 4.5$
b -tagging	MV2c10 with FixedCutBEff_77	

Table 5.4: Summary of the signal and baseline jet definitions in the analysis.

3.6), which is summarized in Table 5.5

Keep	Remove	ΔR cone size or tracks
electron	muon	sharing an ID track (no MS track)
muon	electron	sharing an ID track
electron	jet	0.2
jet	electron	0.4
muon	jet	0.2 and (jet tracks ≤ 2 or $p_T(\mu)/p_T(\text{jet}) > 0.5$)
jet	muon	0.4 and (jet tracks ≥ 2 or $p_T(\mu)/p_T(\text{jet}) < 0.5$)

Table 5.5: Summary of the overlap removal steps performed on electrons, muons, and jets.

5.1.2 Analysis Regions

The analysis strategy is based on the separate optimisation of each lepton multiplicity final state, containing three or four leptons. Then several CRs, VRs and SRs are used for each final state. The selection is optimised by looking at both signal significance (Equation 5.1) and efficiency mainly using the 800 GeV mass hypothesis as reference as it was the one close to the previous exclusion limit [36].

Three-lepton Channel

For the three-lepton channel, three kinds of analysis regions are build to categorise different event topologies based on all the possible signal Feynman diagrams:

- Z-Lepton Region (**ZL**): includes all the cases in which at least one of the heavy lepton decays in a Z boson decaying leptonically. In Figure 5.3 an example of the Feynman diagram which contributes in this region is shown ;

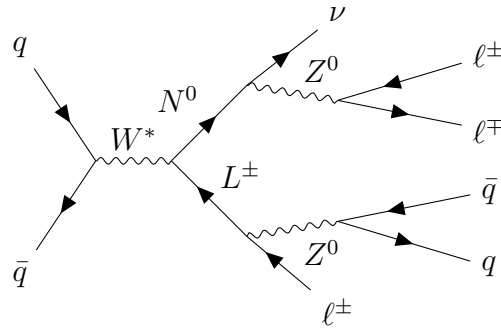


Figure 5.3: Example of Feynman diagram for ZL region.

- Z-Lepton Veto (**ZLVeto**): considers all the cases in which the Z boson produced by at least one of the heavy lepton does no decay leptonically. In Figure 5.4 an example of the Feynman diagram process in this region is shown;

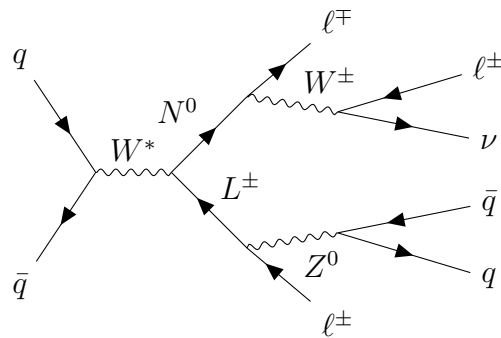


Figure 5.4: Example of Feynman diagram for ZL Veto region.

- Low Number of Jets (**JNLow**): includes all the Feynman diagrams in which no jets are present. Since the LO signal MC samples are reweighted at the NLO, and the number of jets is a quantity very sensitive to the NLO corrections, this requirement can lead to an overestimation of the signal efficiency. For this reason, the possibility of one jet emission is considered requiring no more than 1 jet. In Figure 5.5 an example of Feynman diagram for the JNLow region is shown.

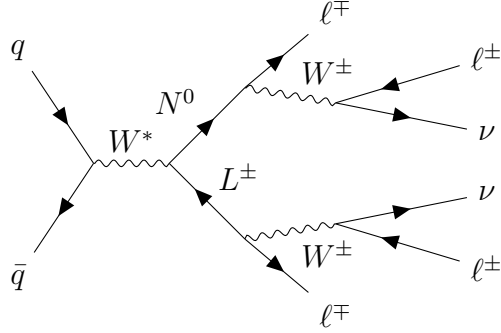


Figure 5.5: Example of Feynman diagram for JNLow region.

For the ZL and ZLVeto regions, at least two additional jets are required to take into account the possibility that the other EW boson could decay hadronically.

The selection criteria for all the possible three-lepton topologies with the corresponding analysis regions are reported in Table 5.6.

As the signal process is expected to produce leptons with a higher momentum with respect to the SM counterpart, a first common preselection is performed requiring a $p_T > 40$ GeV for the first two leading leptons and a $p_T > 15$ GeV for the third more energetic lepton. Signal events also contain high-energy neutrino in the final state, which are selected with another cut at the preselection level requiring $\mathcal{S}(E_T^{\text{miss}}) > 5$ GeV. The E_T^{miss} significance, $\mathcal{S}(E_T^{\text{miss}})$, is used to account also for the uncertainties of all objects that enter in the calculation of E_T^{miss} . This is done because backgrounds that have large E_T^{miss} contributions from misreconstructed objects should have low $\mathcal{S}(E_T^{\text{miss}})$ value. As a consequence, this cut is inverted in the Fake-VR, which is used to validate the fake contribution estimated using a data-driven technique.

The ZL SR is characterized by the presence of a Z boson decaying leptonically, then events are expected to contain lepton pairs with invariant mass close to the Z mass and a cut on the invariant mass of the opposite sign same flavour (OSSF) lepton pair is imposed between 80 and 100 GeV. If no OSSF events are present, the event is rejected. To suppress events coming from WZ processes, the invariant mass of the system formed by all the 3 leptons considered, $m_{\ell\ell\ell}$, must be higher than 300 GeV and the transverse masses of the leading and subleading leptons ($m_T(\ell_1, \ell_2)$) are required to be more than 200 GeV. The last optimization is performed looking at the ΔR distribution between the two leading leptons which provides a good separation power between signal and background events in the 1.2-3.5 interval.

The ZLVeto SR requires events without a leptonically decays of the Z boson imposing a veto for OSSF lepton pair with mass below 115 GeV. If no OSSF leptons pair is present, the event is included in this SR. As for the ZL SR, the $m_{\ell\ell}$ must be higher than 300 GeV. Since signal processes are characterised by high- p_T objects and neutrinos, the scalar sum of the selected leptons and jets in the event, H_T , plus the missing energy transverse, E_T^{miss} , is required to be more than 600 GeV. Since the presence of same-sign leptons in this region is mainly due to rare top events and fake non-prompt (FNP) leptons, the H_T of this pair is used as discriminating variable looking for values of $H_T(\text{SS}) \geq 300$ GeV. To account for possible hadronic decays of the EW bosons, an upper limit is placed on the dijet invariant mass ($m_{jj} < 300$ GeV).

The JNLow SR targets heavy leptons decays where the produced EW bosons decay leptonically, and events with a small jet multiplicity are selected. A lower bound on the invariant mass of the OSSF lepton pair is imposed (> 80 GeV) to reject contributions from soft-leptons which are not expected to be produced by heavy leptons. Also, a large value of H_T of the three leptons is required to be $H_T(\ell\ell\ell) > 230$ GeV, in this case the H_T includes only leptonic terms since the Feynman diagram of this topology does not provide any other visible objects. Similar to the ZL SR, the transverse masses of the leading and subleading leptons are used to distinguish signal from background processes ($m_T(\ell_1) > 240$ GeV and $m_T(\ell_2) > 150$ GeV), removing an important fraction of the FNP contribution. The angular separation between leading and subleading leptons is used to reject the remaining background events considering values higher than 1.3.

The dominant SM backgrounds in the three-lepton SRs are the diboson events and the rare top processes. The first ones are present in all the three defined SRs with a percentage of about 60%, 80% and 40% in ZL, JNLow and ZLVeto, respectively; the seconds contribute only in the ZL and ZLVeto, amounting to about 40% and 50% respectively.

Since the diboson contribution in all the SRs comes from the same kind of processes, it is evaluated in a single CR defined from the ZL topology, the ZL CR, inverting the cut on the transverse mass of the subleading lepton used for the corresponding SR. The rare top background is estimated using a dedicated CR from the four-lepton channel due to its higher purity.

To validate the background estimation, several VRs are introduced. For the diboson contribution, the ZL DB-VR is obtained by requiring zero b -jet, to suppress events from top quarks, and inverting the ΔR selection used in ZL SR, while the JNLow VR is defined considering the phase space not covered by the JNLow SR containing values of $m_T(\ell_1) < 240$ GeV. The rare top process is validated

in the ZL RT-VR which have at least one b -jet and $\Delta R(\ell_1, \ell_2)$ values up to 1.2. Moreover, the Fake-VR is enriched of FNP events and it assesses the goodness of fake lepton estimation, explained in detail in Section 5.2.2 .

To show the optimization carried from each cut applied, the so-called N-1 distributions are shown. It is important to underline that the cut choice is performed looking for a compromise between the signal significance and the signal efficiency. N-1 plots consist in special distributions where each variable used in the signal selection is plotted with the corresponding cut omitted. The plots for all the three-lepton SRs are shown in Figures 5.6, 5.7 and 5.8. All these figures contain a sub-plot panel showing the integrated significance of the corresponding variable distribution. This signal significance is defined as in Equation 5.1, and it is evaluated considering the integrated number of events from a certain bin to the last bin of the distribution.

	Fake-VR	ZL				ZLveto	JNLow	
		CR	DB-VR	RT-VR	SR	SR	VR	SR
				$p_T(\ell_1) > 40 \text{ GeV}$ $p_T(\ell_2) > 40 \text{ GeV}$ $p_T(\ell_3) > 15 \text{ GeV}$				
$\mathcal{S}(E_T^{\text{miss}})$	< 5			≥ 5				
$N(\text{jet})$	-			≥ 2				≤ 1
$N(\text{bjet})$	-	-	0	≥ 1	-	-	-	-
$m_{\ell\ell}(\text{OSSF}) [\text{GeV}]$	-		80 – 100			≥ 115	≥ 80	
$H_T + E_T^{\text{miss}} [\text{GeV}]$	-	-	-	-	-	≥ 600	-	-
$m_{\ell\ell\ell} [\text{GeV}]$	-	-		≥ 300		≥ 300	-	-
$H_T(\text{SS}) [\text{GeV}]$	-	-	-	-	-	≥ 300	-	-
$m_{jj} [\text{GeV}]$	-	-	-	-	-	< 300	-	-
$H_T(\ell\ell\ell) [\text{GeV}]$	-	-	-	-	-	-	≥ 230	
$m_T(\ell_1) [\text{GeV}]$	-	-		≥ 200		-	< 240	≥ 240
$m_T(\ell_2) [\text{GeV}]$	-	< 200		≥ 200		-	≥ 150	
$\Delta R(\ell_1, \ell_2)$	-	-	< 1.2	1.2 – 3.5		-	≥ 1.3	

Table 5.6: Summary of the selection criteria used to define analysis regions in the three-lepton channel.

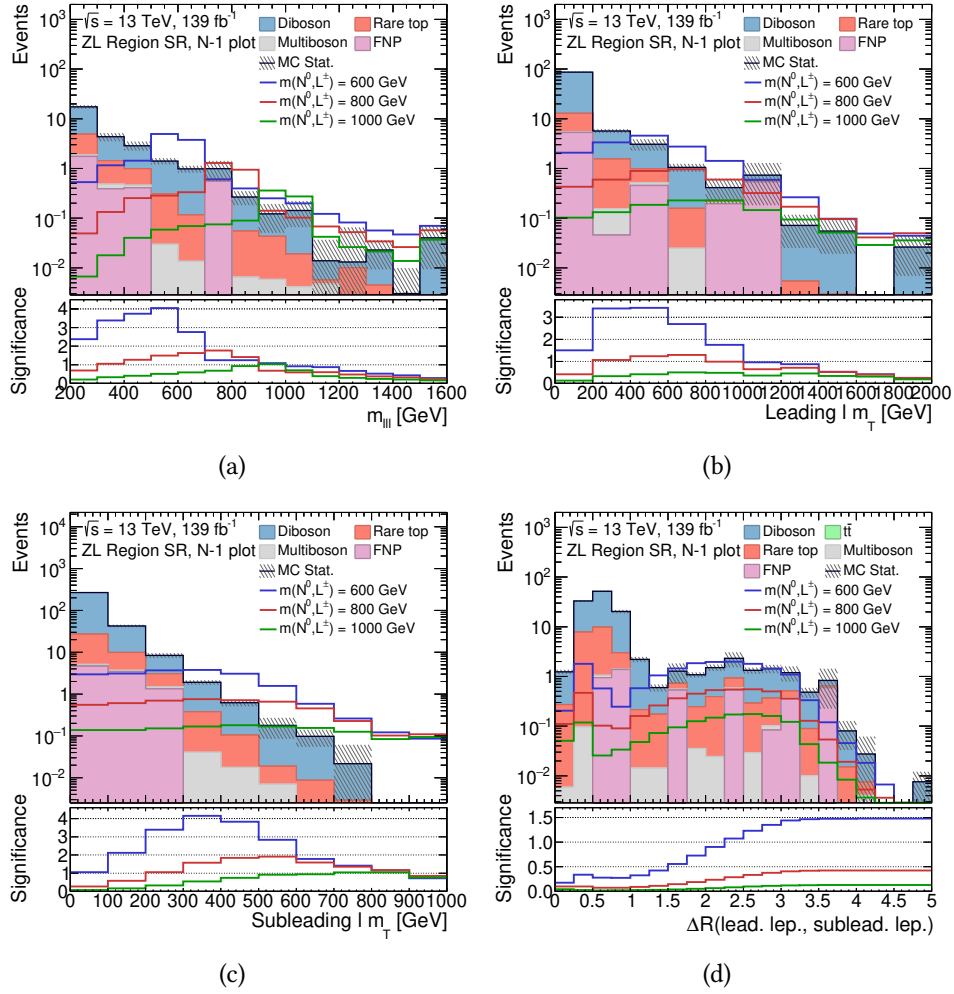


Figure 5.6: N-1 plots including expected signal and background events in the ZL SR in log-scale, data are not considered in this step. Only statistical uncertainties are shown. Each of the observables is plotted with the cut on it omitted: invariant mass of the three-lepton system 5.6a, transverse mass of the leading lepton 5.6b, transverse mass of the subleading lepton 5.6c, angular separation between leading and subleading leptons 5.6d.

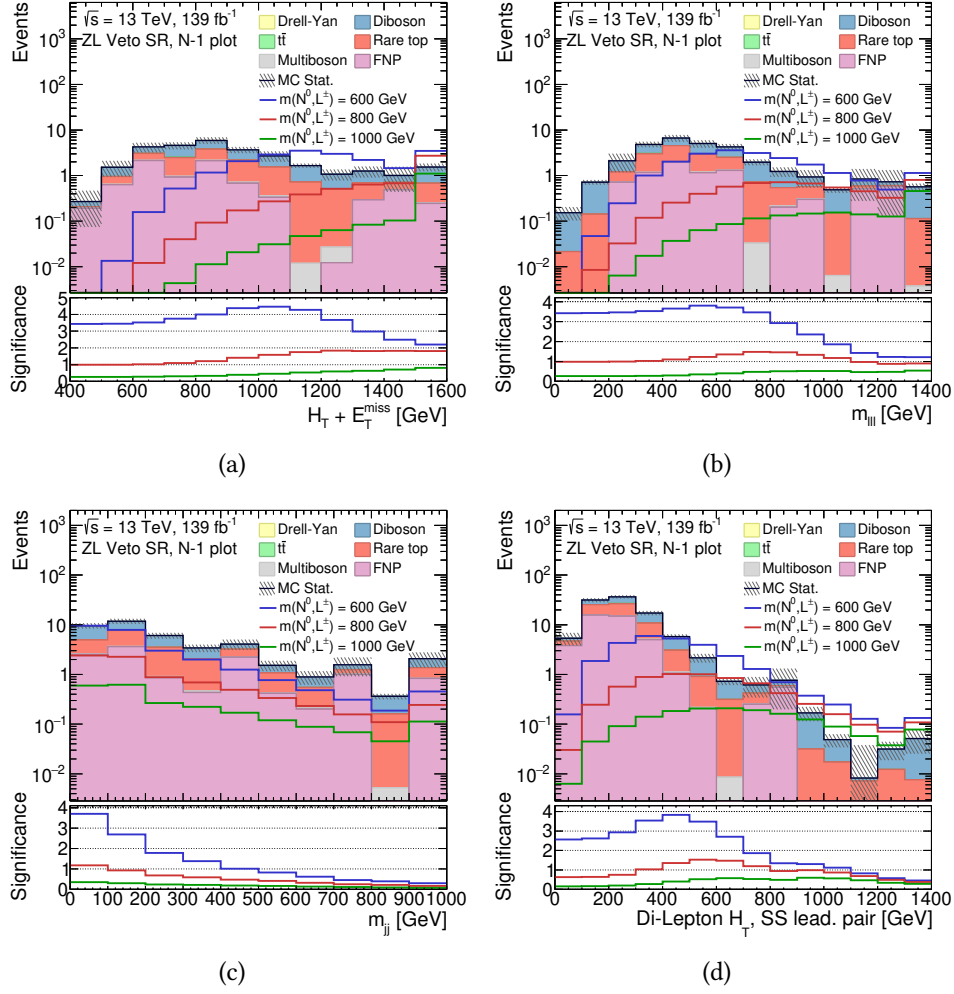


Figure 5.7: N-1 plots including expected signal and background events in the ZLVeto SR in log-scale., data are not considered in this step. Only statistical uncertainties are shown. Each of the observables is plotted with the cut on it omitted: $H_T + E_T^{\text{miss}}$ 5.7a, invariant mass of the three-lepton system 5.7b, invariant mass of the two leading jets 5.7c, H_T of the same-sign lepton pair 5.7d.

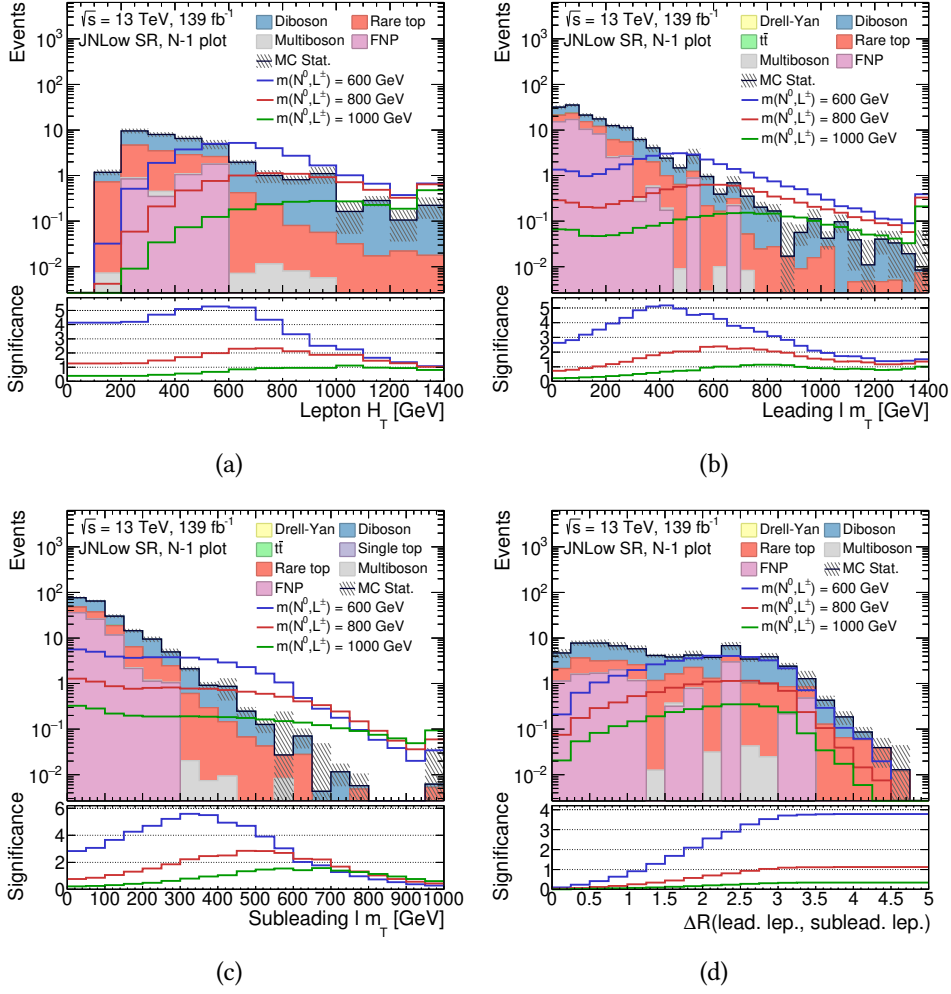


Figure 5.8: N-1 plots including expected signal and background events in the JNLow SR in log-scale, data are not considered in this step. Only statistical uncertainties are shown. Each of the observables is plotted with the cut on it omitted: H_T of the three-lepton system 5.8a, transverse mass of the leading lepton 5.8b, transverse mass of the subleading lepton 5.8c, angular separation between leading and subleading leptons 5.8d.

Four-lepton Channel

The four-lepton channel is defined requiring exactly four leptons in the final states. Looking at all the possible topologies provided by the Feynman diagrams, two kinds of analysis regions, depending by the total charge of the final states, are considered:

- Total charge 0 (**Q0**): includes events with two leptons pairs of the same charge, leading to a zero charge of the system. In Figure 5.9 an example of Feynman diagram which contributes to the Q0 region is shown;

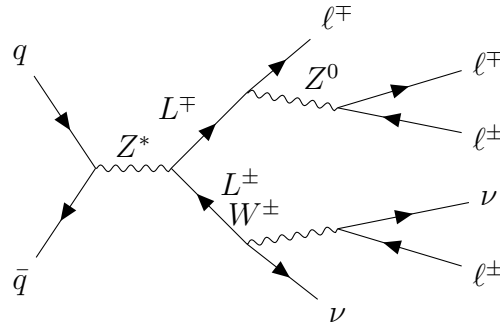


Figure 5.9: Example of Feynman diagram for the Q0 region.

- Total charge 2 (**Q2**): considers events with one lepton of different charge with respect to the others, leading to a system charge equal to 2. In Figure 5.10 an example of Feynman diagram process in the Q2 region is shown.

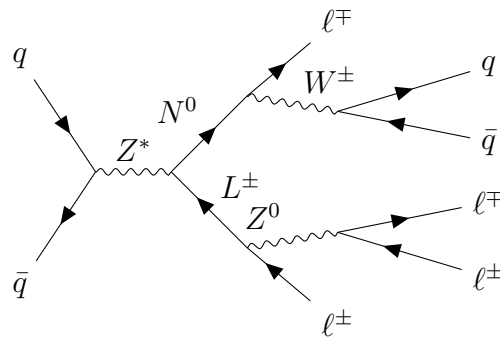


Figure 5.10: Example of Feynman diagram for the Q2 region.

Similar to the three-lepton channel, the two leading leptons are required to have a p_T larger than 40 GeV , while the third and fourth leptons must satisfy the basic

p_T requirement applied to the object definition ($p_T > 10$ GeV). The selection criteria for all the four-lepton analysis regions are reported in Table 5.7.

The main backgrounds affecting the four-lepton channel are the diboson, mainly with ZZ processes, and rare top where the electric charge of one of the electrons is mismeasured. However, the Q2 regions have very low background events since it is very rare for a SM process to produce a doubly charged final state, and few requirements have to be imposed to reduce the presence of SM contributions.

In the Q0 SR, rare top events are substantially removed by vetoing the presence of any b -jet in the final state, while the ZZ contribution is reduced with the request of at maximum one OSSF lepton pair compatible with a Z leptonic decay. The same Z window used for the three-lepton channel is considered for these events. Since signal events are produced in a boosted regions with also high momentum neutrino in the final state, high values of $H_T + E_T^{\text{miss}}$ and invariant mass of the four-lepton system are imposed for both Q0 and Q2 SRs. Since more SM processes with a null-charge in the final states are produced, an additional selection on the E_T^{miss} significance is applied in the Q0 SR. Events with four leptons can be easily affected by the presence of charge-flipped electrons (see Section 5.2.1 for details). For this reason, the $\mathcal{S}(E_T^{\text{miss}})$ guarantees better discrimination with respect to the E_T^{miss} variable.

Given the low background contribution in the Q2 regions, CRs for dedicated to diboson and rare top events are built looking at the Q0 final states. This is possible as the background composition in the Q2 SR is the same of the Q0 final states.

A CR targeting diboson backgrounds is defined by selecting four leptons with an invariant mass in the window $170 \text{ GeV} < m_{\ell\ell\ell\ell} < 300 \text{ GeV}$ and requiring zero b -jet to increase the purity of ZZ events. Rare top processes are estimated in a second CR obtained by the presence of at least two b -jets and $m_{\ell\ell\ell\ell} < 500 \text{ GeV}$. The Q0 VRs guarantee the orthogonality with the CRs, selecting events with exactly one b -jet. To increase the contribution of the corresponding background, DB-VR and RT-VR use the same $m_{\ell\ell\ell\ell}$ requirement of the diboson and rare top CR, respectively. To evaluate the backgrounds estimation also in the Q2 final state, a dedicated VR is defined by requiring $m_{\ell\ell\ell\ell}$ to be less than 200 GeV or $H_T + E_T^{\text{miss}}$ less than 300 GeV. The logical OR in this region is used to increase the yields of the different contributions in order to have enough events in the validation step.

The N-1 distributions are shown in Figures 5.11, 5.12 and 5.13.

	Q0					Q2	
	DB-CR	RT-CR	DB-VR	RT-VR	SR	VR	SR
	$p_T(\ell_{1,2}) > 40 \text{ GeV}$ $p_T(\ell_3) > 15 \text{ GeV}$ $p_T(\ell_4) > 10 \text{ GeV}$						
$ \sum q_\ell $	0					2	
$N_{b\text{-jet}}$	0	≥ 2	1	1	0	-	-
$m_{\ell\ell\ell} [\text{GeV}]$	170 – 300	< 500	170 – 300	300 – 500	≥ 300	< 200 OR	≥ 300
$H_T + E_T^{\text{miss}} [\text{GeV}]$	-	-	-	≥ 400	≥ 300	< 300	≥ 300
N_Z	-	-	-	-	≤ 1	-	-
$\mathcal{S}(E_T^{\text{miss}})$	-	-	-	≥ 5	≥ 5	-	-

Table 5.7: Summary of the selection criteria used to define analysis regions in the four-lepton channel.

During the fitting procedure, described in Section 5.4, the main backgrounds considered as free-floating parameters are: WZ diboson contribution in the three-lepton channel, ZZ diboson contribution in the four-lepton channel and rare top processes in both the channels. For all the analysis regions containing four leptons, $H_T + E_T^{\text{miss}}$ is used as a fit variable, while for the three-lepton channel the transverse mass of the three-lepton system, $m_{T,3\ell}$, is considered¹. These fit variables were chosen as they provide the better signal versus background discrimination power in most of the variable range. The $m_{T,3\ell}$ observable is defined as the the magnitude of the vector sum of the three-lepton p_T and the E_T^{miss} , as:

$$m_{T,3\ell} = \left| \sum_i^{3\ell} \vec{p}_{T,i} + E_T^{\text{miss}} \right|. \quad (5.2)$$

In Table 5.8, the signal percentage in the CRs and VRs for two signal mass hypothesis above the values already excluded by previous analyses are reported. In all regions the signal contamination is below 1%.

The signal efficiency for each mass point considered in the analysis is shown in Figure 5.14, divided per SR and per channel. The results are obtained comparing yields in the SRs with the total number of generated events.

¹The generic transverse mass of one or multiple objects N_{obj} is defined as: $m_T(N_{obj}) = \sum_i^{N_{obj}} E_{T,i} + E_T^{\text{miss}} - \left| \sum_i^{N_{obj}} \vec{p}_{T,i} + \vec{p}_T^{\text{miss}} \right|$.

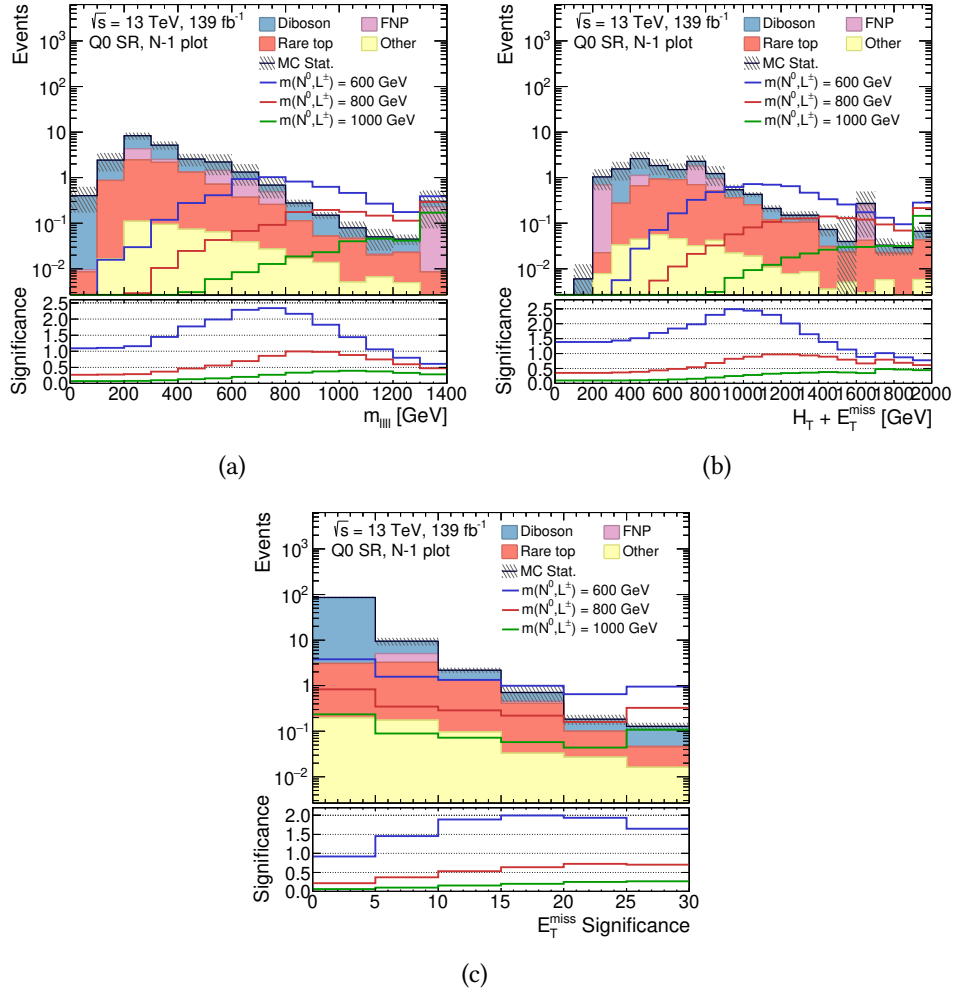


Figure 5.11: N-1 plots including expected signal and background events in the Q0 SR in log-scale, data are not considered in this step. Only statistical uncertainties are shown. Each of the observables is plotted with the cut on it omitted: invariant mass of the four leptons 5.11a, $H_T + E_T^{\text{miss}}$ 5.11b, E_T^{miss} significance 5.11c.

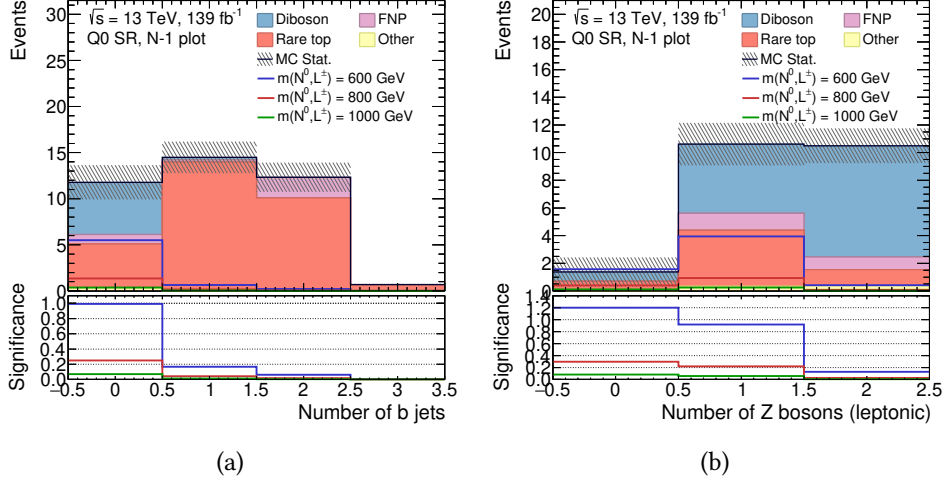


Figure 5.12: N-1 plots including expected signal and background events in the Q0 SR, data are not considered in this step. Only statistical uncertainties are shown. Each of the observables is plotted with the cut on it omitted: number of b -jets 5.12a, number of Z bosons 5.12b.

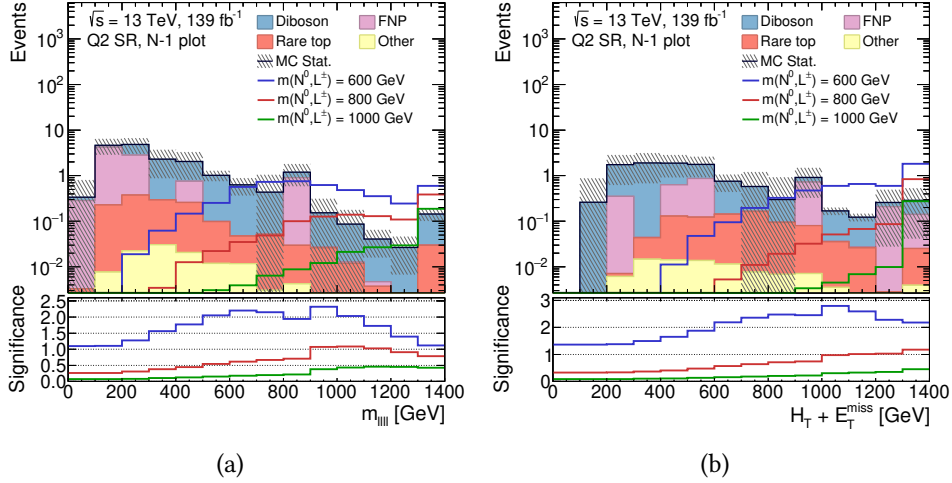


Figure 5.13: N-1 plots including expected signal and background events in the Q2 SR in log scale, data are not considered in this step. Only statistical uncertainties are shown. Each of the observables is plotted with the cut on it omitted: invariant mass of the four leptons 5.13a, $H_T + E_T^{\text{miss}}$ 5.13b.

Region	Signal mass point 800 GeV	Signal mass point 1200 GeV
ZL CR	0.04%	< 0.01%
ZL VR	1.00%	0.08%
JNLow VR	0.01%	< 0.01%
Fakes VR	0.07%	0.03%
DB-CR	< 0.01%	< 0.01%
DB-VR	< 0.01%	< 0.01%
RT-CR	< 0.01%	< 0.01%
RT-VR	0.04%	0.01%
Q2 VR	0.01%	< 0.01%

Table 5.8: Signal contamination fraction in CRs and VRs for the 800 GeV and 1200 GeV signal mass points.

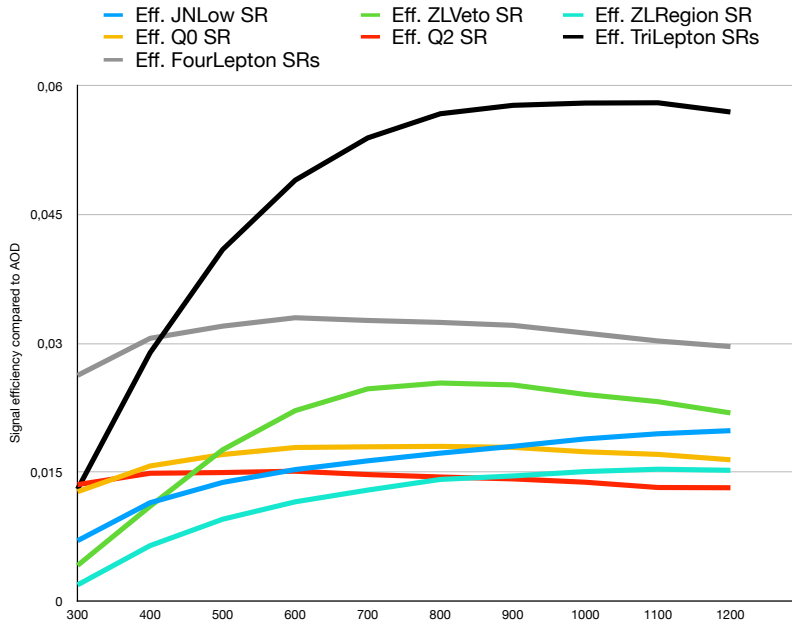


Figure 5.14: Signals efficiency for different SR as a function of the mass points of the Type-III SeeSaw heavy leptons.

5.2 Background Estimation

The sources of irreducible backgrounds are prompt leptons which are estimated using Monte Carlo samples and coming from SM processes, such as decays of Z , W and Higgs bosons, or from prompt leptonic τ -lepton and t quark decays. To remove possible overlap with the fake-factor method described in this section, they are identified using truth-reco object matching. This kind of background is obtained from the MC samples described in Section 4.4.

Still using these MC simulations, the source of another kind of background is evaluated. Charge misidentified (charge-flipped) electrons are taken into account by applying a dedicated scale factor in regions that contain electrons. This SF is derived by using a data-driven technique from the deviation of the modelling of charge misidentification in MC samples from data, as described in Section 5.2.1.

The most important source of reducible background is given by events with the presence of at least one fake or non-prompt lepton, commonly called *fakes*. This contribution mainly comes from in-flight decays of mesons, jets reconstructed as leptons and electron produced by photon-conversion. Due to the large uncertainties affecting jets and hadronization processes, fake leptons can not be estimated using MC predictions, but a dedicated data-driven method have to be performed. The fake factor is calculated separately for electrons and muons. In both cases, a fake factor estimations is performed independently in the low and high regions of the lepton p_T spectrum.

5.2.1 Background from electron charge misidentification

The misidentification of charge of prompt electrons is responsible for the largest background in events with a same-sign electrons pair. This background consists of events with two opposite-sign (OS) electrons among which one has its charge misidentified. This source of background affects mainly the Q2 SR, where two SS lepton pairs are present. By far the most probable mechanism of electron charge misidentification is bremsstrahlung and it can be divided into two categories: the so-called *trident events* and *stiff tracks*. A simplified sketch of the misidentification process is illustrated in Figure 5.15. Trident events arise when an electron undergoes bremsstrahlung and the radiated photon converts into a pair of electron-positron due to interactions with the detector material. It can happen that the calorimeter is matched to a track with the opposite charge compared to the original electron or that the photon transfers all of the energy to the opposite sign electron and the original charge is lost. Stiff tracks are a special case of bremsstrahlung where the radiated photon does not convert into a pair

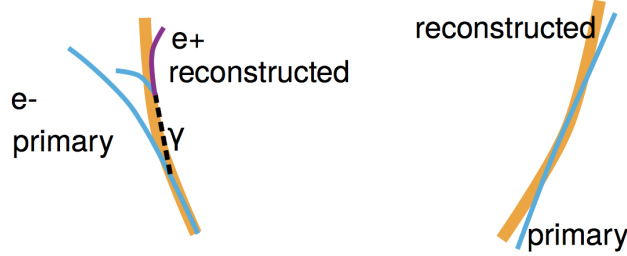


Figure 5.15: Simplified representation of the electron charge misidentification process due to electron interaction with the detector material.

of electron-positron. The energy of the electron is correctly reconstructed from the calorimeter information, however, the matched track has very few hits in the silicon pixel layers, corresponding to the original electron, and its curvature is not well defined. Since the electron charge is derived from the track curvature, it could be incorrectly determined while the electron energy is likely appropriate. These tracks can have very high momenta and are therefore called stiff tracks. The probability to have one of these effects depends by the object energy in the considered region.

The effect of muon charge misidentification is negligible because muons undergo bremsstrahlung in the inner detector very rarely. Furthermore, their tracks are measured also in the muon spectrometer, complementary to the inner detector, which provides a much larger lever arm for the curvature measurement.

Charge misidentification is simulated by GEANT4 in Monte Carlo samples but it is not reliable to use it immediately. Misidentification due to trident events is caused by interactions of particles with the detector material and such processes are hard to simulate with an accurately precision. Furthermore, a very accurate description of the detector material would be needed to reliably predict these events. A data-driven approach was used to avoid this problem: the probability of an electron undergoing charge misidentification was measured from the data and compared to the Monte Carlo prediction. From this, a SF is derived as a correction factor for the charge misidentification modelling in the simulation and is then applied to simulated events involving in same-sign pairs.

The charge-flip probability is estimated by performing a likelihood fit on a dedicated $Z \rightarrow ee$ data and MC Samples [104]. The first quantity to measure is the probability ϵ for one electron to be reconstructed with incorrect charge. Considering an event with an OS electron pair, the final state can involve one of the

following category:

- no charge misidentification, with a probability of $(1 - \epsilon)^2$;
- both electron misidentified, with a probability of ϵ^2 ;
- only one electron with a wrong reconstructed charge, with probability $2\epsilon(e\epsilon)$.

Given an initial number of real OS events, the reconstructed ones can be divided by charge as:

$$N^{OS} = (1 - 2\epsilon + 2\epsilon^2) N \quad (5.3)$$

$$N^{SS} = 2\epsilon(1 - \epsilon) \simeq 2\epsilon N \quad (5.4)$$

where the last approximation is possible if ϵ^2 is negligible. Taken two electrons i and j with different probabilities in the (p_T, η) plane, the number of SS event is:

$$N_{SS}^{ij} = N^{ij} (\epsilon_i + \epsilon_j). \quad (5.5)$$

If these SS events are produced by charge-flip in the Z peak, N_{SS}^{ij} follows a poissonian probability:

$$f(N_{SS}^{ij}; \lambda) = \frac{\lambda^{N_{SS}^{ij}} e^{-\lambda}}{N_{SS}^{ij}!} \quad (5.6)$$

where λ is the expected number of SS events in bin (i, j) and it is defined as:

$$\lambda = (\epsilon_i (1 - \epsilon_j) + \epsilon_j (1 - \epsilon_i)). \quad (5.7)$$

Then, the probability for both electrons to produce a charge-flip is expressed by the following equation:

$$P(\epsilon_i, \epsilon_j | N_{SS}^{ij}, N^{ij}) = \frac{[N^{ij} (\epsilon_i + \epsilon_j)]^{N_{SS}^{ij}} e^{-N^{ij}(\epsilon_i + \epsilon_j)}}{N_{SS}^{ij}!}. \quad (5.8)$$

The likelihood function \mathcal{L} for all the events is expressed as:

$$\mathcal{L}(\epsilon | N_{SS}, N) = \prod_{i,j} P(\epsilon_i, \epsilon_j | N_{SS}^{ij}, N^{ij}) \quad (5.9)$$

and the ϵ parameter can be obtained by the minimization of the negative logarithm likelihood which can be written as:

$$-\ln \mathcal{L}(\epsilon | N_{SS}, N) \approx \sum_{i,j,k,l} \ln [N^{i,j,k,l} (\epsilon_{i,k} + \epsilon_{j,l})]^{N_{SS}^{i,j,k,l}} e^{-N^{i,j,k,l}(\epsilon_{i,k} + \epsilon_{j,l})} \quad (5.10)$$

where k and l indexes indicate the p_T and $|\eta|$ dependencies of ϵ . As already said, this likelihood method is performed on a pure Z sample, for which the subtraction of the backgrounds is needed. For this reason, the Z peak is divided into three regions, for convenience named A , B and C , where B is the central region and A and C the *side-bands*. The number of events in the side-bands n_A and n_C is removed from B region and then the final number of signal Z events is given by:

$$N_Z = n_B - \frac{n_A + n_C}{2}. \quad (5.11)$$

Using the parameterization in electron p_T and η , which express the misidentification probability P , a set of scale factors is obtained as:

- prompt electrons: $SF = \frac{1-P(CF;data)}{1-P(CF;;MC)}$,
- charge flip electrons: $SF = \frac{P(CF;data)}{P(CF;;MC)}$.

Two different mass intervals are used to define an opposite-charge (OC) and a same-charge (SC) peak: $|m(ee) - m_{OC}(Z)| = 11.8$ GeV and $|m(ee) - m_{SC}(Z)| = 13.6$ GeV, while the side-bands are defined in 11.8 GeV - 17.7 GeV and 13.6 GeV - 27.2 GeV interval for the OC and SC regions, respectively. As shown in Figure 5.16, the Z peak in the SC region is shifted by approximately 1.5 GeV to lower energies and the width is slightly broader compared to the Z peak in the OC region. This is due to electron charge-flip events coming from an electron radiating a photon which converts into an electron-positron pair. The particle with the wrong charge is reconstructed with a lower energy than the parent electron.

5.2.2 Background from fake leptons

Leptons can be produced from secondary decays into light leptons of light-flavour or heavy-flavour mesons, embedded within jets, as illustrated in Figure 5.17. It was already discussed and explained that MC simulations can not well describe the non-prompt leptons contribution, then a data-driven method is used to estimate it to be considered into the analysis regions. Due to the low events involving in this kind of processes, dedicated samples with a lot of simulated processes are need to an accurate and precise measurement. Electron and muon fake background estimation approach used in this analysis is called the *fake-factor* method [209].

The fake factor method is an extrapolation technique for lepton fakes which are taken from a dedicated control region with large statistics enriched with this kind of contribution. A weight is calculated for each fake lepton, the *fake factor*,

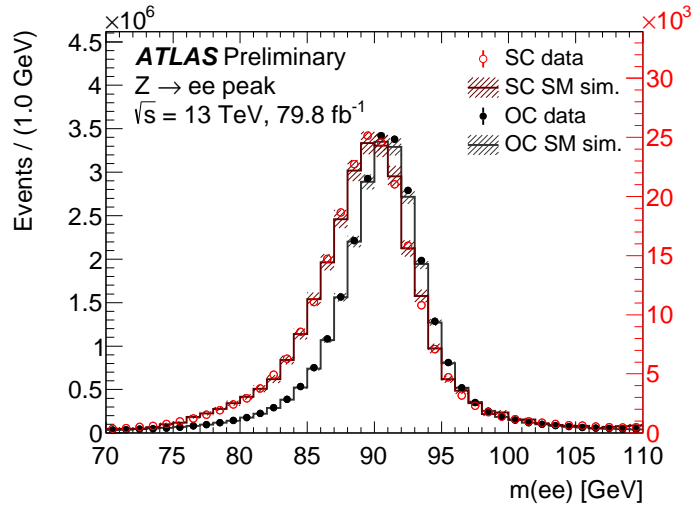


Figure 5.16: Dielectron invariant mass distributions for opposite-charge (OC, black) and same-charge (SC, red) pairs for data (circles) and MC simulation (continuous line). The latter includes a correction for charge misidentification. The hatched band indicates the statistical error and the luminosity uncertainty summed in quadrature applied to MC simulated events. Please note that the scales for OC and SC are different and given at the left side (OC) and right side (SC), respectively [208].

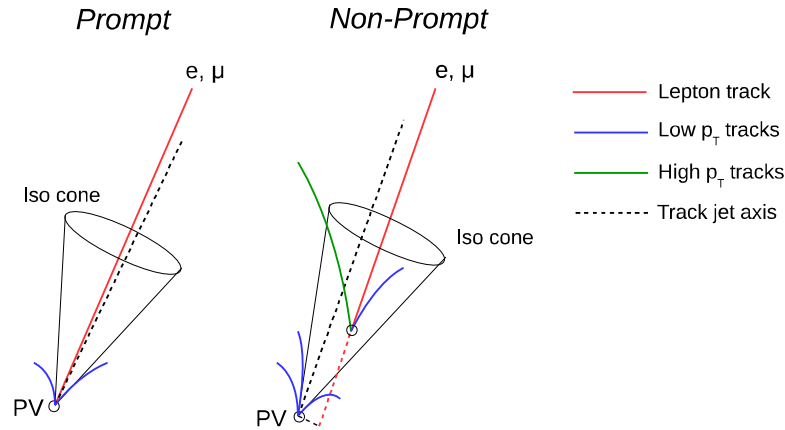


Figure 5.17: Representation of an event containing a prompt lepton (left) and non-prompt lepton (right). Electrons or muons are originated from a secondary vertex and are selected as fake leptons coming from the primary vertex.

which is the ratio in which a fake particle passes the signal selection criteria (the ID or *tight* selection) relative to another closely related, but with different se-

lection (the anti-ID or *loose* selection). These weights are then applied to events containing at least one fake lepton.

The selection requirements for tight and loose leptons applied for the fake estimation are the same as for the analysis leptons, reported in Table 5.2 and 5.3. As described in Chapter 3, the tighter selections for all the objects are, by definition, a subset of the loose selection. Then, to guarantee the orthogonality between the two kind of object definitions, the loose lepton is required to fail the tight criteria, as schematically illustrated in Figure 5.18. Also the control regions used to estimate the fake contribution must be orthogonal to all the CRs, VRs and SRs defined inside the analysis. The *fake rate*, representing the misidentification

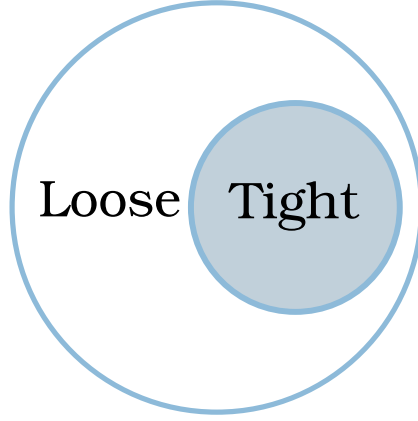


Figure 5.18: The loose and the tight regions in the MM. The tight region must be a subset of the loose region (i.e. tight leptons should also pass all of the loose requirements).

probability, is defined as:

$$f = \frac{N_{\text{Tight}}}{N_{\text{Tight}} + N_{\text{Loose}}} \quad (5.12)$$

where N_{Tight} and N_{Loose} are the number of non-prompt leptons satisfying the tight and loose identification conditions previously imposed. Exploiting the 5.12, the *fake-factor* can be written as:

$$F = \frac{f}{1 - f} = \frac{N_{\text{Tight}}}{N_{\text{Loose}}}. \quad (5.13)$$

The fake-factor is measured as a function of one or more kinematic variables, in this analysis p_T and η . Only loose leptons contribute to the final number of fake leptons and to avoid double counting, the prompt contribution estimated with MC events needs to be subtracted from data:

$$N_{\text{fakes}} = \left[\sum_{\text{events}}^{n_{\text{loose}}} (-1)^{n-1} \prod_i^n f_i \right]_{\text{data}} - \left[\sum_{\text{events}}^{n_{\text{loose}}} (-1)^{n-1} \prod_i^n f_i \right]_{\text{MC}}. \quad (5.14)$$

For the two-lepton channel the 5.14 becomes:

$$N_{fakes}^{Dilepton} = \left[\sum_{TL} F_2 + \sum_{LT} F_1 - \sum_{LL} F_1 F_2 \right]_{data} - \left[\sum_{TL} F_2 + \sum_{LT} F_1 - \sum_{LL} F_1 F_2 \right]_{MC}, \quad (5.15)$$

while for the three-lepton channel:

$$\begin{aligned} N_{fakes}^{Trilepton} = & \left[\sum_{TTL} F_3 + \sum_{TTL} F_2 + \sum_{LTT} F_1 - \sum_{TLL} F_2 F_3 \right. \\ & \left. - \sum_{LTL} F_1 F_3 - \sum_{LLT} F_1 F_2 + \sum_{LLL} F_1 F_2 F_3 \right]_{data} \\ & - \left[\sum_{TTL} F_3 + \sum_{TTL} F_2 + \sum_{LTT} F_1 - \sum_{TLL} F_2 F_3 \right. \\ & \left. - \sum_{LTL} F_1 F_3 - \sum_{LLT} F_1 F_2 + \sum_{LLL} F_1 F_2 F_3 \right]_{MC}, \end{aligned}$$

and for the four-lepton channel:

$$\begin{aligned} N_{fakes}^{Fourlepton} = & \left[\sum_{TTTL} F_4 + \sum_{TTTL} F_3 + \sum_{TLTT} F_2 + \sum_{LTTT} F_1 - \sum_{TTLL} F_3 F_4 \right. \\ & - \sum_{TLTL} F_2 F_4 - \sum_{LTTL} F_1 F_4 - \sum_{LTLT} F_1 F_3 - \sum_{LLTT} F_1 F_2 - \sum_{TLLT} F_2 F_3 \\ & + \sum_{TLLL} F_2 F_3 F_4 + \sum_{LTLL} F_1 F_3 F_4 + \sum_{LLTL} F_1 F_2 F_4 + \sum_{LLLT} F_1 F_2 F_3 \\ & \left. - \sum_{LLLL} F_1 F_2 F_3 F_4 \right]_{data} \\ & - \left[\sum_{TTTL} F_4 + \sum_{TTTL} F_3 + \sum_{TLTT} F_2 + \sum_{LTTT} F_1 - \sum_{TTLL} F_3 F_4 \right. \\ & - \sum_{TLTL} F_2 F_4 - \sum_{LTTL} F_1 F_4 - \sum_{LTLT} F_1 F_3 - \sum_{LLTT} F_1 F_2 - \sum_{TLLT} F_2 F_3 \\ & + \sum_{TLLL} F_2 F_3 F_4 + \sum_{LTLL} F_1 F_3 F_4 + \sum_{LLTL} F_1 F_2 F_4 + \sum_{LLLT} F_1 F_2 F_3 \\ & \left. - \sum_{LLLL} F_1 F_2 F_3 F_4 \right]_{MC}. \end{aligned}$$

A special note for the negative contributions in both the equation which are needed to prevent double counting of events with exactly two and four loose leptons.

Electron Fake-Factor Estimation

Electron fake-factors are estimated in a single electron + jets control region. The method relies on the assumption that the probability for reconstructing fake leptons is assumed to be independent on the number of leptons in the event. Two different p_T regions are studied to estimate fake leptons with low- p_T ($10 \text{ GeV} < p_T < 30 \text{ GeV}$) and high- p_T ($> 30 \text{ GeV}$) in order to have enough events in each one to estimate both contributions. In all these p_T regions, the following selection is applied:

- Exactly one electron and zero muons;
- $E_T^{\text{miss}} < 40 \text{ GeV}$;
- b -jet veto;
- At least 1 jet.

A second control region is defined with exactly the same cut above plus the requirement of at least 2 jets in the event. This requirement is particularly useful because it is also present in some of the analysis signal and control regions. The reason for this selection is twofold:

- checking the stability of the fake factor that should be in principle independent from the number of jets in the events;
- use the difference in the two regions as a source of systematic of the method.

The trigger selection for single-electron events could artificially bias the sample, enhancing isolated electrons with respect to non-isolated ones. To avoid this problem, prescaled low threshold single-lepton triggers are used instead of the dilepton-trigger used in the analysis or the nominal single-electron triggers which have much tighter requirements on electron identification compared with the needs of this analysis. The average prescale is lower with the increase of the trigger p_T threshold. Each electron in the event is assigned to its own trigger corresponding to its p_T . The list of triggers used for this study is reported in Table 5.9. If a trigger with lower prescale and higher p_T threshold is available, it is used instead. If the electron is matched to the corresponding trigger and the trigger fired, then it is included in the region.

The dijet fakes-enriched regions are shown in Figures 5.19 and 5.20 for the high- p_T regions with at least 1 and at least 2 jets, and in Figures 5.21 and 5.22 for the low- p_T region considering also in this case two sets of plots depending on the number of jets in the final state. Selected events still contain prompt electrons

	Trigger	Average prescale	Periods
Low- p_T region	HLT_e5_lhvloose	78151	2015
	HLT_e5_lhvloose_nod0	99497	2016-2018
	HLT_e10_lhvloose_L1EM7	34175	2015
	HLT_e10_lhvloose_nod0_L1EM7	85354	2018
	HLT_e12_lhvloose_L1EM10VH	2199.9	2015
	HLT_e12_lhvloose_nod0_L1EM10VH	8981.7	2016-2018
	HLT_e15_lhvloose_L1EM13VH	760.01	2015
	HLT_e15_lhvloose_nod0_L1EM7	15361	2018
	HLT_e17_lhvloose	480.00	2015
	HLT_e17_lhvloose_nod0	1963.5	2016-2018
	HLT_e20_lhvloose	400.00	2015
	HLT_e20_lhvloose_nod0	1599.9	2016-2018
	HLT_e24_lhvloose_nod0_L1EM18VH	2274.7	2016
Both p_T regions	HLT_e26_lhvloose_nod0_L1EM20VH	111.23	2015-2016
	HLT_e28_lhvloose_nod0_L1EM20VH	367.62	2017
	HLT_e28_lhvloose_nod0_L1EM22VH	384.54	2018
High- p_T region	HLT_e60_lhvloose_nod0	32.935	2015-2018
	HLT_e70_lhvloose_nod0	64.131	2018
	HLT_e80_lhvloose_nod0	40.430	2018
	HLT_e100_lhvloose_nod0	19.453	2018
	HLT_e120_lhvloose_nod0	12.150	2016, 2018
	HLT_e140_lhvloose_nod0	2.6370	2017-2018
	HLT_e160_lhvloose_nod0	1.6010	2017-2018
	HLT_e200_etcut	/	2015
HLT_e300_etcut	/	2016-2018	

Table 5.9: A summary of the fake-factor estimation trigger requirements for electrons.

after all selection requirements are applied, coming from W +jets, Drell-Yan, di-boson and multiboson, rare top, $t\bar{t}$ and single top decays. They are subtracted from data before the calculation of fake-factors. The fake electron composition is reported in Appendix A.1 to show events producing non-prompt leptons. The MC subtraction is much larger in the tight region compared with the loose region and amounts for up to 50% of all electrons. The fake-factor is parameterized in p_T with a variable binning which is driven by the uncertainty in a specific bin², and η accounting four slices ($0 < |\eta| < 0.7$, $0.7 < |\eta| < 1.37$, $1.52 < |\eta| < 2.01$ and $2.01 < |\eta| < 2.47$) excluding the crack-region.

Looking at the high- p_T loose electrons p_T distributions, in Figures 5.19b and

²The last p_T bin includes the overflow and is extended to infinity and no extrapolation of the fake factor is performed.

5.20b, a discontinuity around 300 GeV is observed. This effect is due to the different online ID requirements on triggers, as `HLT_e300_etcut` does not have any ID requirements and its efficiency is around 100%.

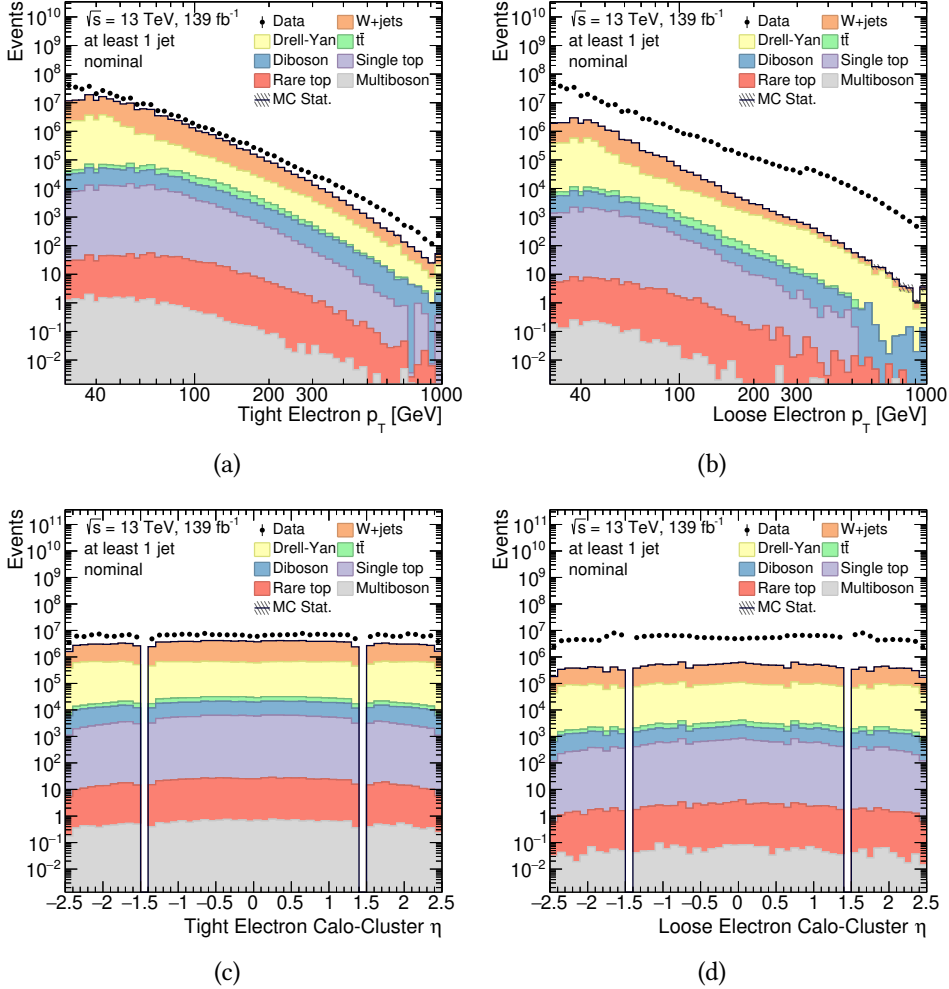


Figure 5.19: Fakes-enriched regions in the nominal high- p_T selection with at least 1 jet: 5.19a p_T distribution of tight electrons, 5.19b p_T distribution of loose electrons, 5.19c η distribution of tight electrons, 5.19d η distribution of loose electrons. All the distributions show data events and the prompt MC component subtracted from data, to ensure a fake dominated region.

The main sources of the systematic uncertainties of the fake-factor come from Monte Carlo modelling of the subtracted leptons, from different composition of fake electrons in the fake enriched region compared to the signal region, and

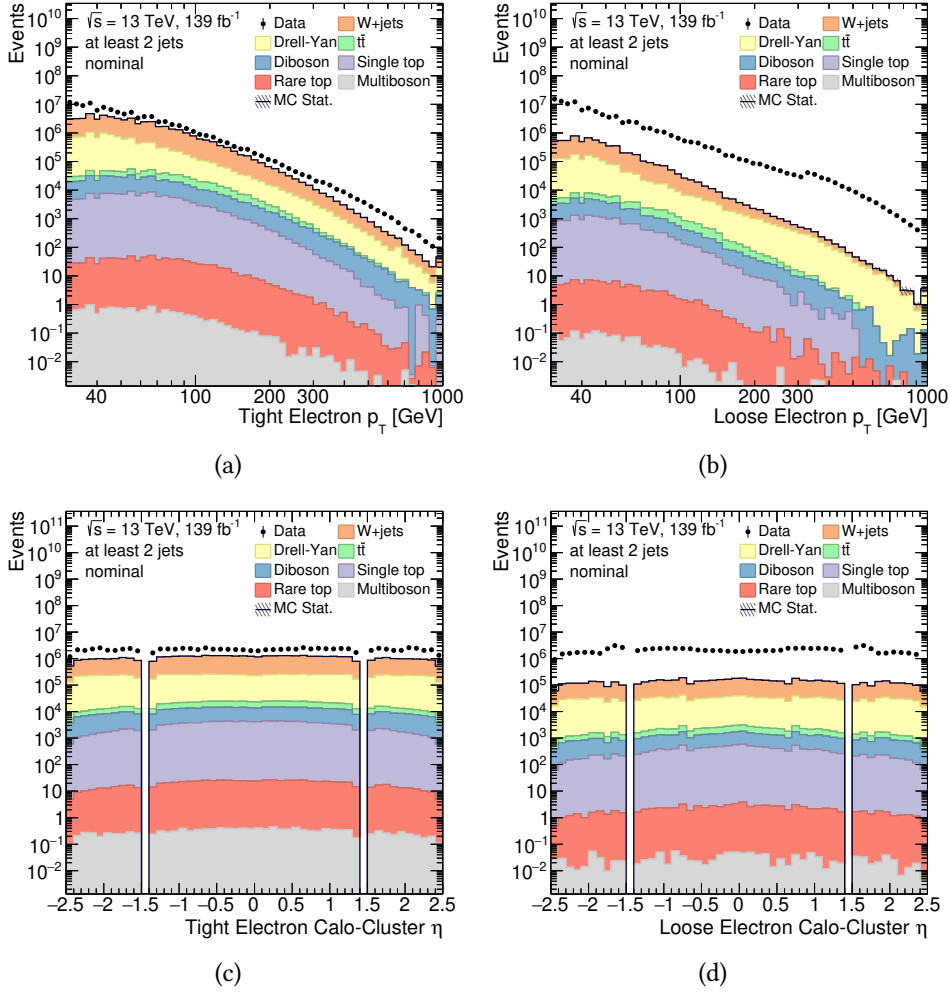


Figure 5.20: Fakes-enriched regions in the nominal high- p_T selection with at least 2 jets: [5.20a](#) p_T distribution of tight electrons, [5.20b](#) p_T distribution of loose electrons, [5.20c](#) η distribution of tight electrons, [5.20d](#) η distribution of loose electrons. All the distributions show data events and the prompt MC component subtracted from data, to ensure a fake dominated region.

from the normalisation of Monte Carlo samples in the fakes-enriched region. The fake factor is independently measured for each of those variations and all of them are presented in Table 5.10. In addition, all MC samples were varied by 10 % to account for cross-section and luminosity uncertainties as well as the modelling of the prompt MC used in the subtraction procedure.

The resulting fake-factors for each variation are shown in Figure 5.23 and 5.24

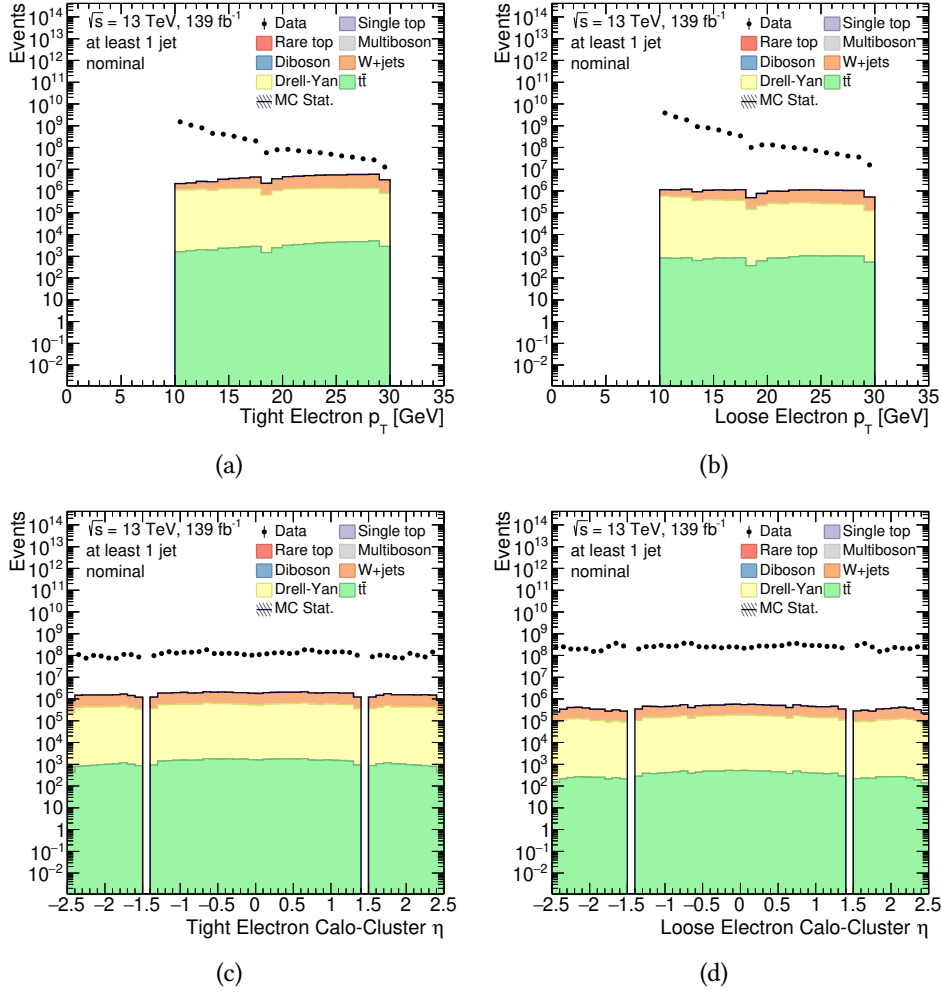


Figure 5.21: Fakes-enriched regions in the nominal high- p_T selection with at least 1 jet: [5.21a](#) p_T distribution of tight electrons, [5.21b](#) p_T distribution of loose electrons, [5.21c](#) η distribution of tight electrons, [5.21d](#) η distribution of loose electrons. All the distributions show data events and the prompt MC component subtracted from data, to ensure a fake dominated region.

for the high- p_T region with at least 1 and at least 2 jets, while for low- p_T region they are reported in Figure 5.25 and 5.26, also divided per jets multiplicity. Combined fake-factors systematic is calculated by adding all variations and the statistical uncertainty in quadrature. As shown by these sets of plots, the largest contribution to the uncertainty is due to the MC scaling.

The extrapolated fake-factors are validated by performing closure tests in the

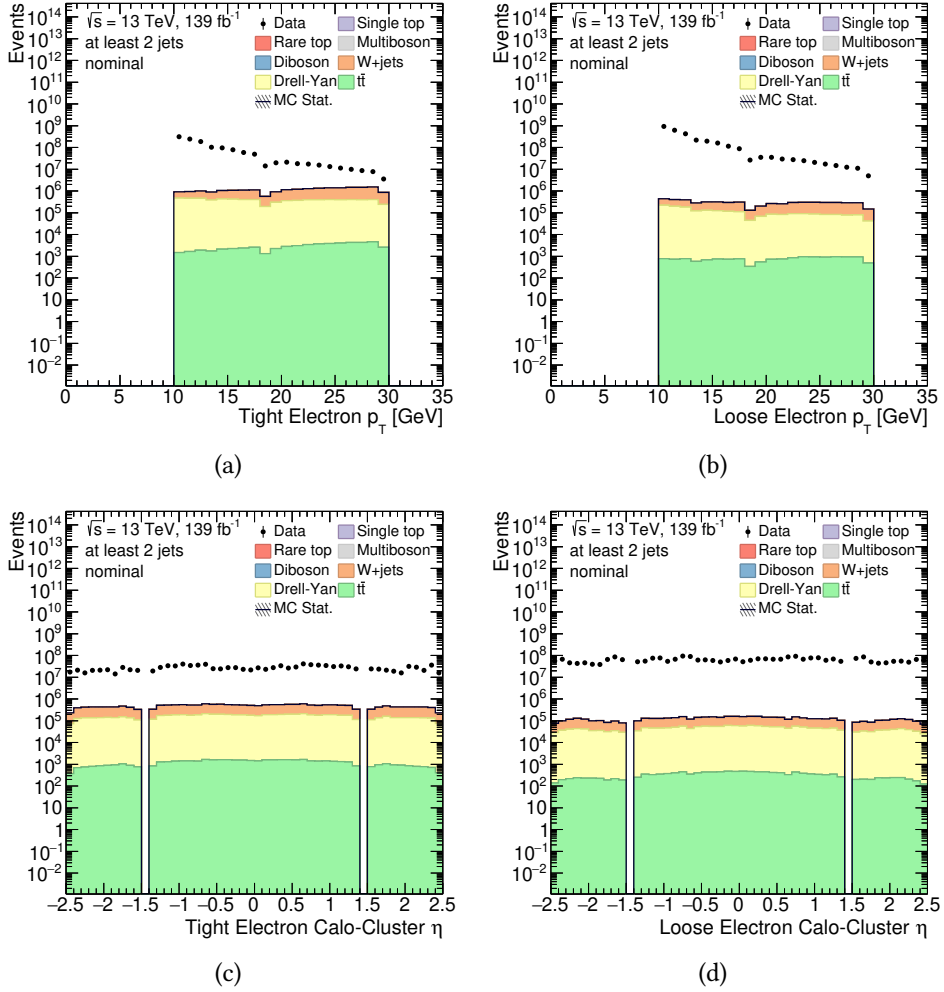


Figure 5.22: Fakes-enriched regions in the nominal high- p_T selection with at least 2 jets: [5.22a](#) p_T distribution of tight electrons, [5.22b](#) p_T distribution of loose electrons, [5.22c](#) η distribution of tight electrons, [5.22d](#) η distribution of loose electrons. All the distributions show data events and the prompt MC component subtracted from data, to ensure a fake dominated region.

fakes-enriched region using exactly the same selection as for the fake-factors measurement for data events and comparing them to the combined prediction of MC and the fake-factor method. Also the object selection is the same as the nominal event selection.

Prompt MC processes considered in the closure tests are the same as for the fake-factors derivation, while the remaining events are well described by the esti-

Variation	Purpose
Flipped requirement on number of jets	fakes composition
Removed E_T^{miss} requirement	fakes composition
Removed b -jet veto	fakes composition
MC scaled up by 10 %	MC modelling, cross-section and luminosity
MC scaled down by 10 %	MC modelling, cross-section and luminosity

Table 5.10: Summary of the variations used for the determination of the systematic uncertainty of the fake factors.

mated fake-factors contribution, as shown in Figure 5.27 and 5.28 for the high- p_T region and in Figure 5.29 and 5.30 for the low- p_T one. For both p_T regions the at least 1 and at least 2 jets selection are shown. Only the systematic uncertainty related to the fake-factor is considered. Overall the agreement is good even up to very high electron energies.

In the low- p_T closure tests, an asymmetric systematic band can be seen. This effect is attributable to the different pre-selection at the generation level which is present in the SUSY17 DAOD between data and MC samples. Due to the huge size of the data in this DAOD set, a number of jet more or equal than two was imposed by the Derivation Production Team. This requirement was not applied to the MC predictions. For this reason, the asymmetry of the uncertainty is more evident in the region with at least one jet with respect to the one where more than two jets are present.

As clearly visible in the sub-plots of Figures 5.25 and 5.26, this effect does not involve the nominal fake-factor value, but it affects only the systematic uncertainty. This is mainly due to events coming from the number of jets variation.

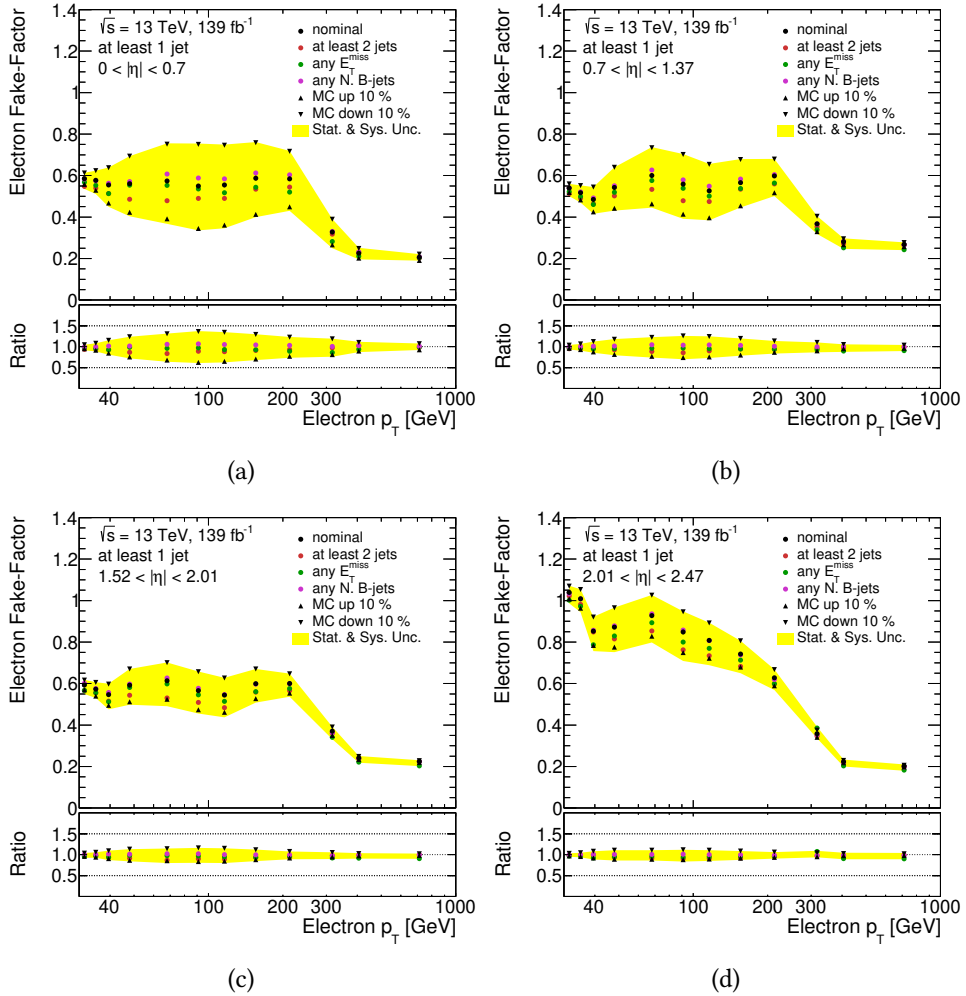


Figure 5.23: Measured fake-factors for an electron in the high- p_T region with at least 1 jet, with systematic variation applied. First η bin in 5.23a, second in 5.23b, third in 5.23c and last in 5.23d.

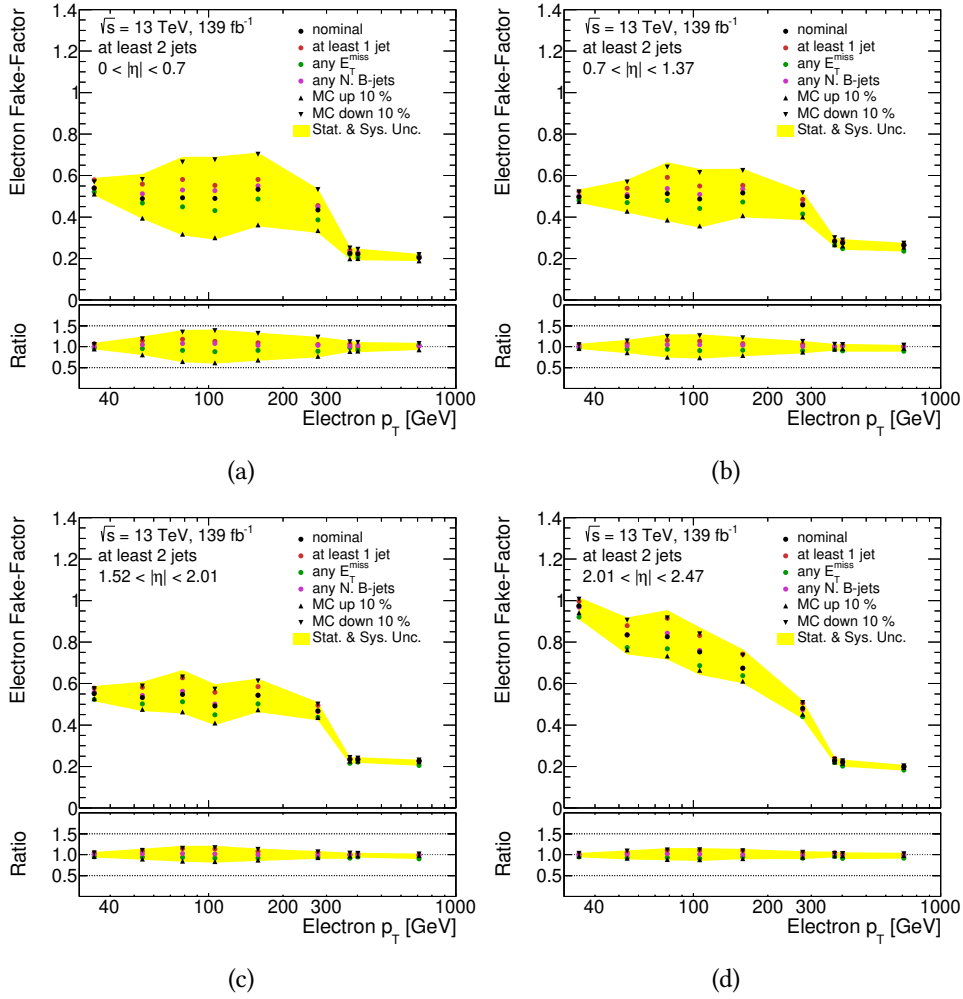


Figure 5.24: Measured fake-factors for an electron in the high- p_T region with at least 2 jets, with systematic variation applied. First η bin in 5.24a, second in 5.24b and last in 5.24d.

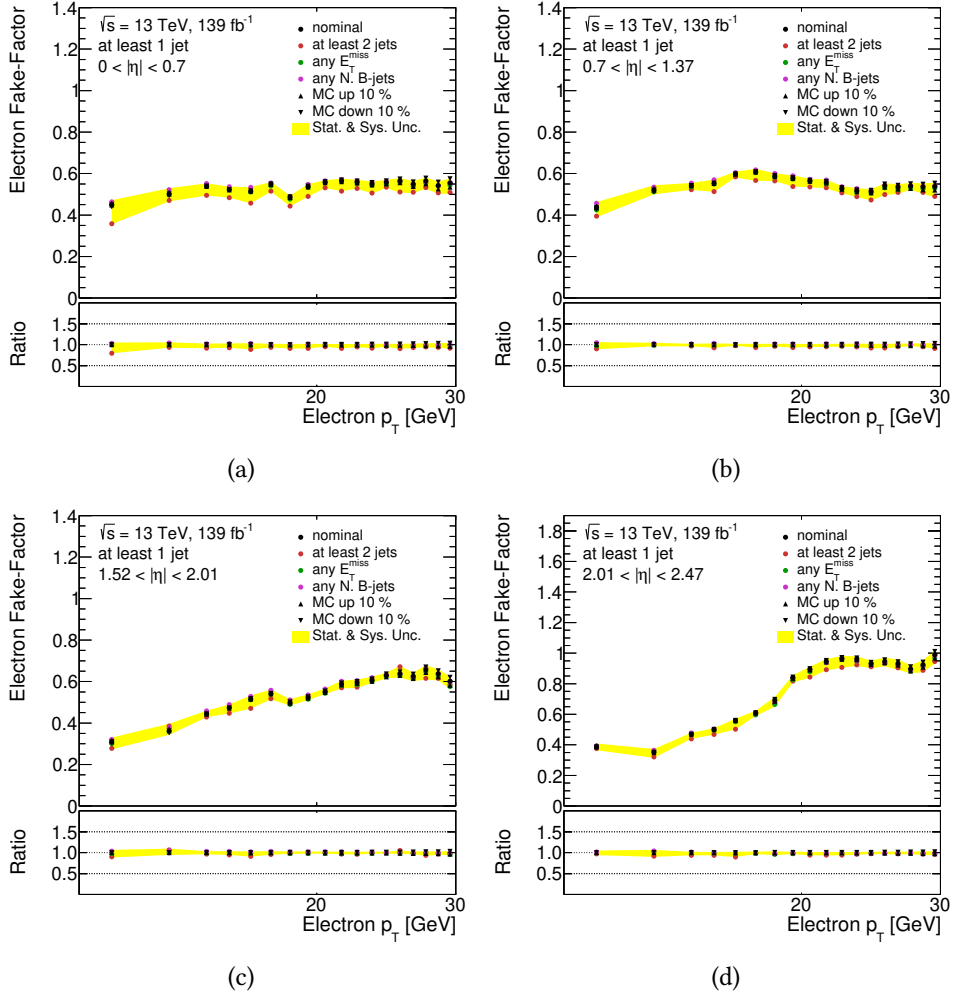


Figure 5.25: Measured fake-factors for an electron in the low- p_T region with at least 1 jet, with systematic variation applied. First η bin in 5.25a, second in 5.25b, third in 5.25c and last in 5.25d.

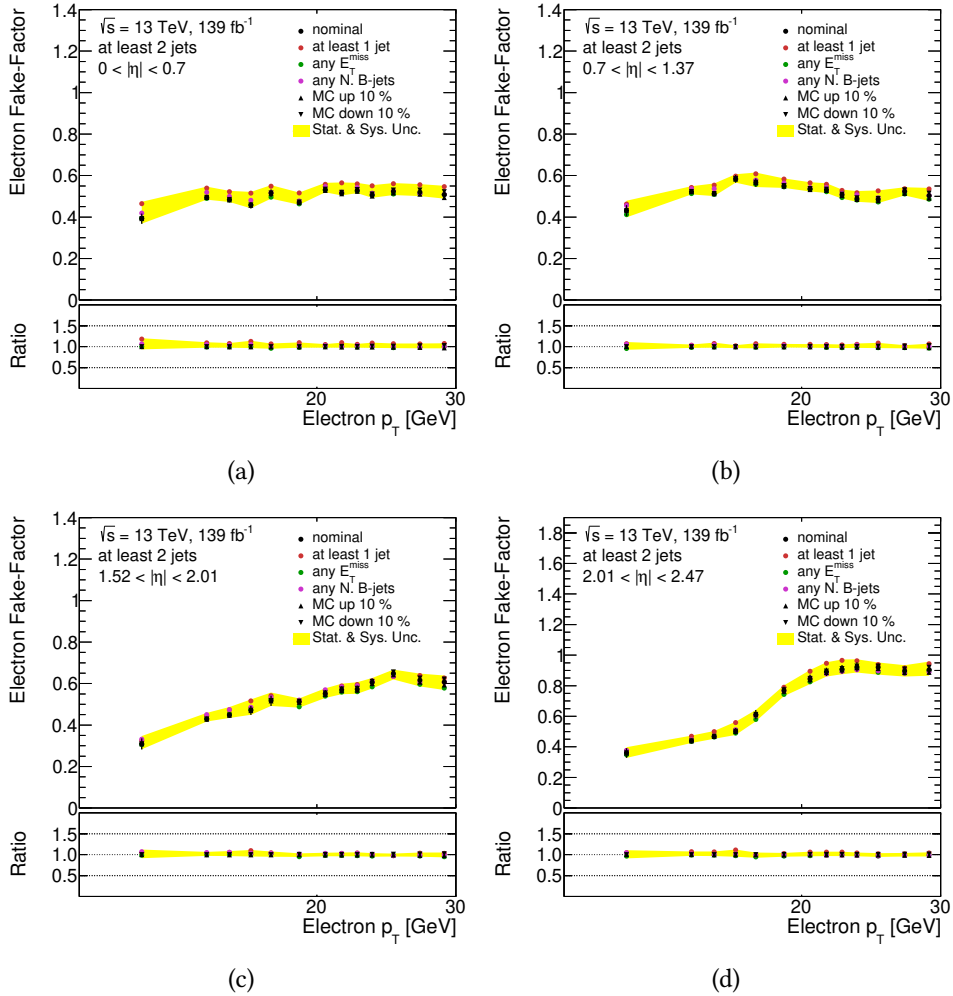


Figure 5.26: Measured fake-factors for an electron in the low- p_T region with at least 2 jets, with systematic variation applied. First η bin in 5.26a, second in 5.26b and last in 5.26d.

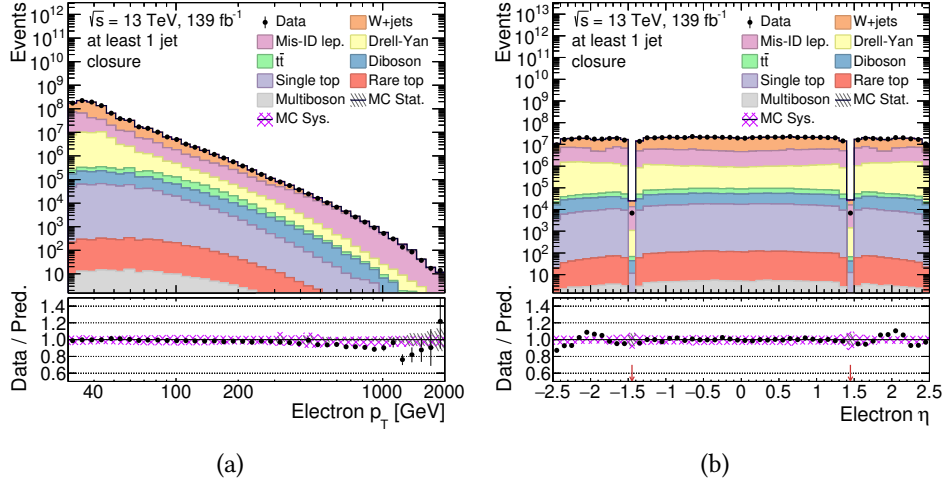


Figure 5.27: The electron fake-factors closure test in high- p_T region with at least 1 jet. In 5.27a the p_T distribution is shown, while in 5.27b the η one. The pink band shows the systematic uncertainty associated to the fake-factor measurement.

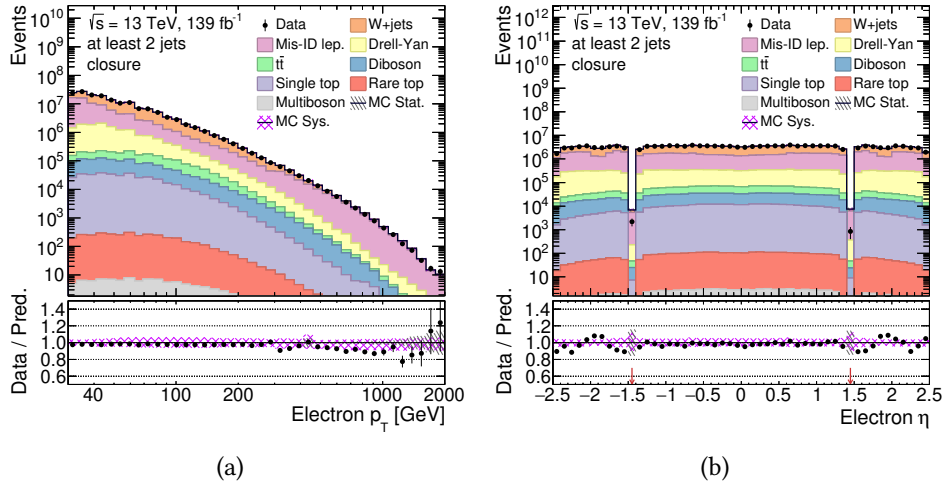


Figure 5.28: The electron fake-factors closure test in high- p_T region with at least 2 jets. In 5.28a the p_T distribution is shown, while in 5.28b the η one. The pink band shows the systematic uncertainty associated to the fake-factor measurement.

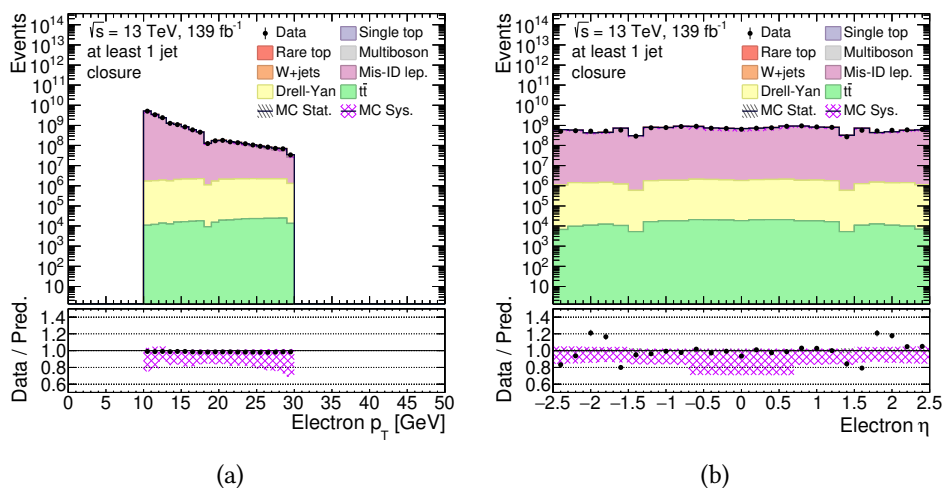


Figure 5.29: The electron fake-factors closure test in low- p_T region with at least 1 jet. In 5.29a the p_T distribution is shown, while in 5.29b the η one. The pink band shows the systematic uncertainty associated to the fake-factor measurement.

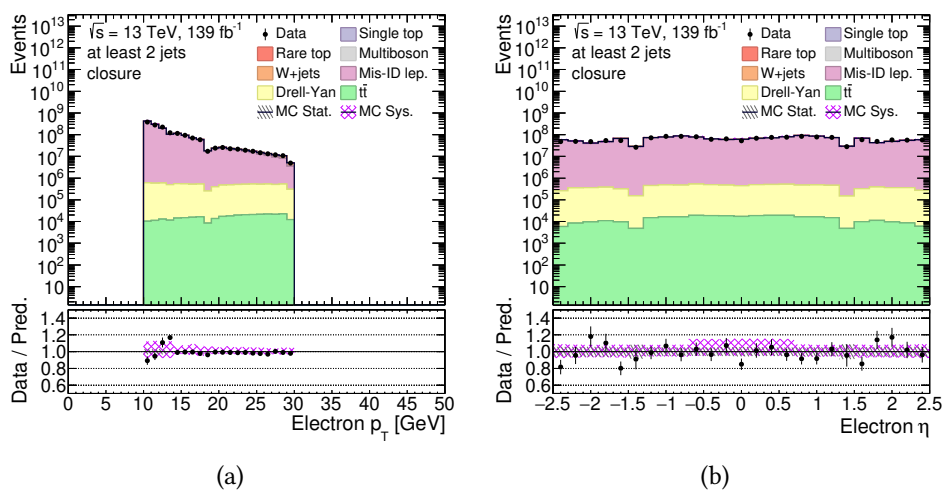


Figure 5.30: The electron fake-factors closure test in low- p_T region with at least 2 jets. In 5.30a the p_T distribution is shown, while in 5.30b the η one. The pink band shows the systematic uncertainty associated to the fake-factor measurement.

Muon Fake-Factor Estimation

Fake muons might arise from in-flight decays of mesons inside jets with the semi-leptonic decay of B meson as one of the largest contributions, as illustrated in Figure 5.31. Combinations of prompt and fake muons can contribute to the signal region if the fake muon satisfies tight isolation and impact parameter requirements.

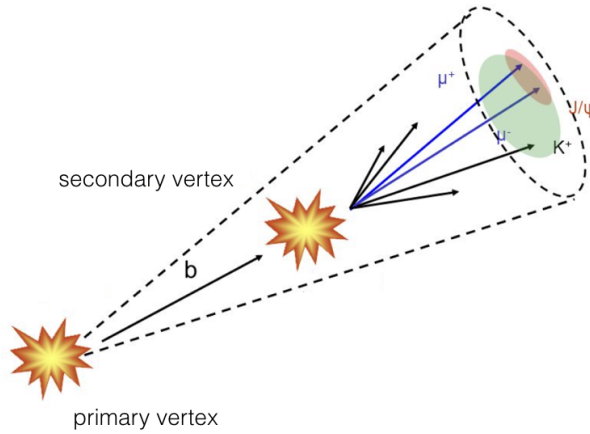


Figure 5.31: Representation of an event containing a non-prompt muon: a b -hadron is produced in the IP with consequent decay into light quarks jets in secondary displaced vertex. Muons originate from the b -hadron secondary decay and can fake leptons coming directly from the PV [210].

As for the electron fake-factor estimation, also for muons a dedicated dijet CR is defined, considering both high- p_T and low- p_T regions. Selected events still contain prompt electrons after all selection requirements are applied, coming from W +jets, Drell-Yan, diboson and multiboson, rare top, $t\bar{t}$ and single top decays. They are subtracted from data before the calculation of fake-factors. The fake muon composition is reported in Appendix A.1 to show events producing non-prompt leptons. Since high momenta fake muons are usually produced with an associated jet, in the high- p_T phase-space region fake-factors are measured using a tag-and-probe (T&P) technique having a better performance with respect to the standard single-lepton approach. the following selection is applied:

- Exactly one muon and zero electron;

- b -jet veto to avoid fakes from heavy flavour decay;
- $E_T^{\text{miss}} < 40$ GeV to reduce the $W \rightarrow \mu\nu$ events;
- At least 1 jet.

Also in this case, the *at least 2 jets* region is studied. Using the T& P method, a jet is considered as the *tag* and a reconstructed muon as the *probe*. Tag and probe objects are assumed to travel in the opposite directions, then an angular requirement on the ϕ angle is imposed as $\Delta\phi > 2.7$, requiring also a jet with $p_T > 35$ GeV. Similar to electrons prescaled non-isolated single-muon triggers have to be used and are listed in Table 5.11.

	Trigger	Average prescale	Periods
Low- p_T region	HLT_mu6	43434	2015–2018
	HLT_mu10	4832.0	2015–2016
	HLT_mu14	2143.2	2015–2018
	HLT_mu18	546.81	2015–2016
	HLT_mu20	1426.1	2016–2018
	HLT_mu22	1170.7	2016–2018
Both p_T regions	HLT_mu24	49.363	2015–2018
High- p_T region	HLT_mu50	/	2015–2018

Table 5.11: A summary of the fake-factor estimation trigger requirements for muons.

The p_T and η distributions after the selection requirements are shown in Figure 5.32 and 5.32 for the high- p_T region and in Figure 5.34d and 5.34d for the low- p_T one, for both tight and loose muons.

Systematic uncertainties in the measurement of muon fake-factors are estimated by altering the selection of dijet events. For the low- p_T region, the same variations as for the electron fake-factor estimation are accounted, as reported in Table 5.10. For the high- p_T region, several variations are instead performed due to the different effects in T& P method:

- E_T^{miss} is varied, independently, upward and downward by 10 GeV for both tight and loose muons. With these requirements, the subtracted W +jets events (i.e. the fraction of prompt muons) are varied looking at different phase-space;

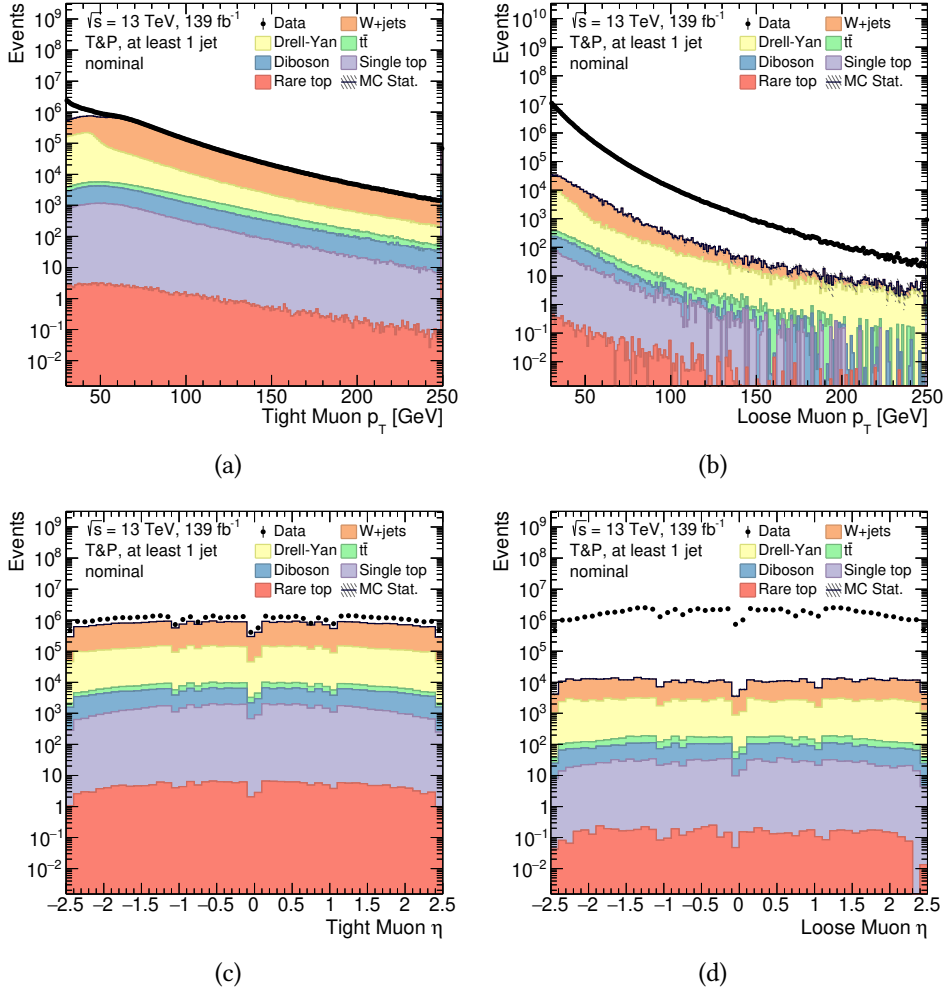


Figure 5.32: Fakes-enriched regions in the nominal high- p_T selection with at least 1 jet: [5.19a](#) p_T distribution of tight muons, [5.19b](#) p_T distribution of loose muons, [5.19c](#) η distribution of tight muons, [5.19d](#) η distribution of loose muons. All the distributions show data events and the prompt MC component subtracted from data, to ensure a fake dominated region.

- p_T of recoiling jet is increased up to 40 GeV (hence altering the collimation of the fake jet) for the same reason, since the isolation distribution of the fake muon might differ between the dijet selection and the sidebands;
- The kinematic balance of the muon and the recoiling jet, which affects the isolation, can also be altered varying the back-to-back requirement $\Delta\phi(\mu, \text{jet})$ by 0.1 upward and downward.

The fake-factor is parameterized in p_T with a variable binning, and η considering

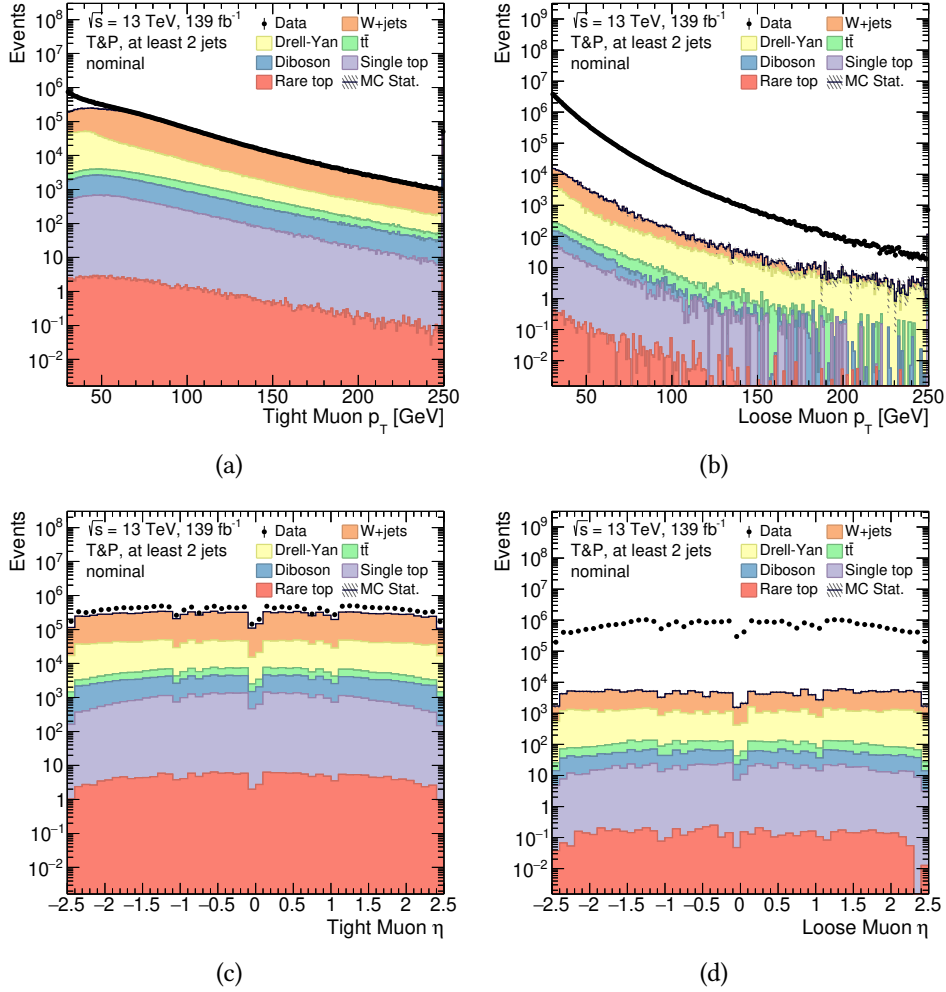


Figure 5.33: Fakes-enriched regions in the nominal high- p_T selection with at least 2 jets: [5.20a](#) p_T distribution of tight muons, [5.20b](#) p_T distribution of loose muons, [5.20c](#) η distribution of tight muons, [5.20d](#) η distribution of loose muons. All the distributions show data events and the prompt MC component subtracted from data, to ensure a fake dominated region.

5 slices, including also the crack-region. The measured fake-factors for muons and the effect of each systematic alteration on the nominal measurement can be seen for the high- p_T region in [Figure 5.36](#) for at least 1 jet and [Figure 5.37](#) for at least 2 jets, while for the low- p_T one in [Figure 5.38](#) considering at least 1 jet and [Figure 5.38](#) for at least 2 jets. The total uncertainty is estimated by comparing the statistical uncertainty on the nominal measurement with the maximum deviation between the nominal fake-factor and each systematically altered measurement.

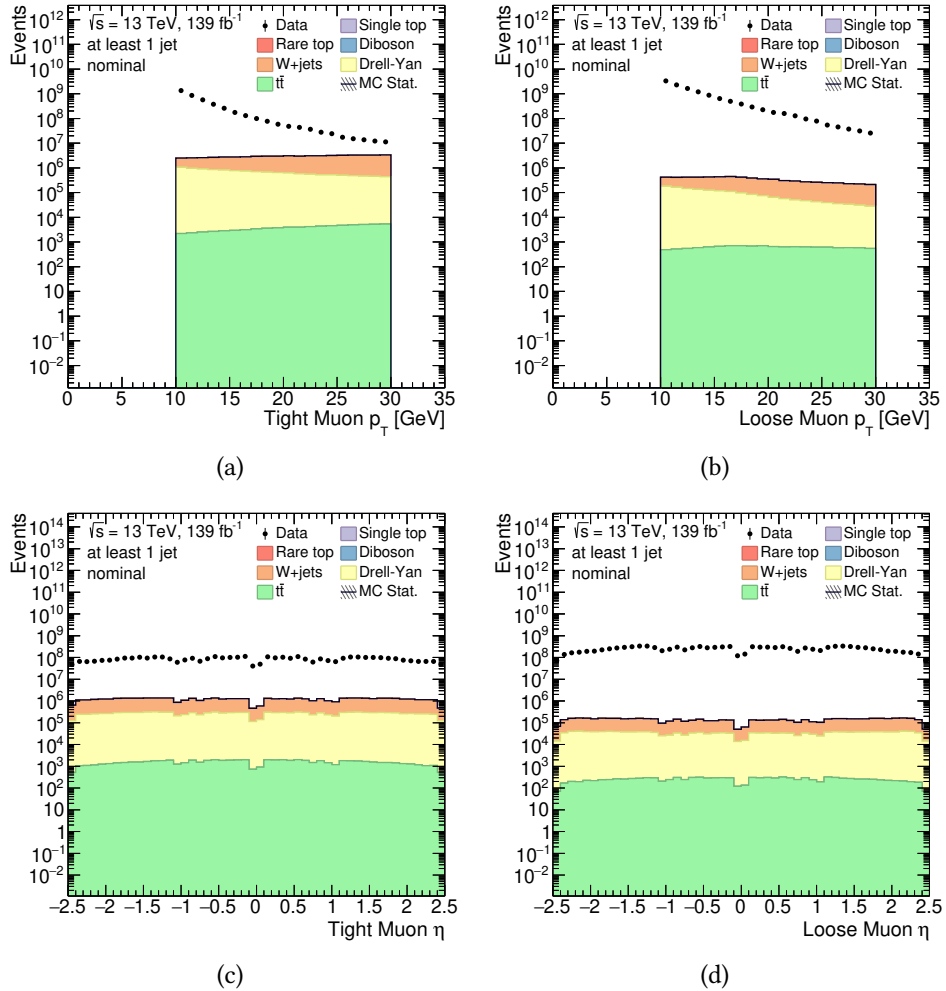


Figure 5.34: Fakes-enriched regions in the nominal low- p_T selection with at least 1 jet: [5.21a](#) p_T distribution of tight muons, [5.21b](#) p_T distribution of loose muons, [5.21c](#) η distribution of tight muons, [5.21d](#) η distribution of loose electrons. All the distributions show data events and the prompt MC component subtracted from data, to ensure a fake dominated region.

The largest signed deviation is taken to be the total uncertainty for lower bounds and upper bounds in turn. An uncertainty ranging between $\approx 10\%$ and $\approx 50\%$ is achieved across p_T intervals.

The deviation of the at least 1 jet case with respect to the at least 2 jets one is clearly visible in the fake-factors distributions is due to different pre-selection in data and MC simulations of the SUSY17 derivations, as mentioned in the

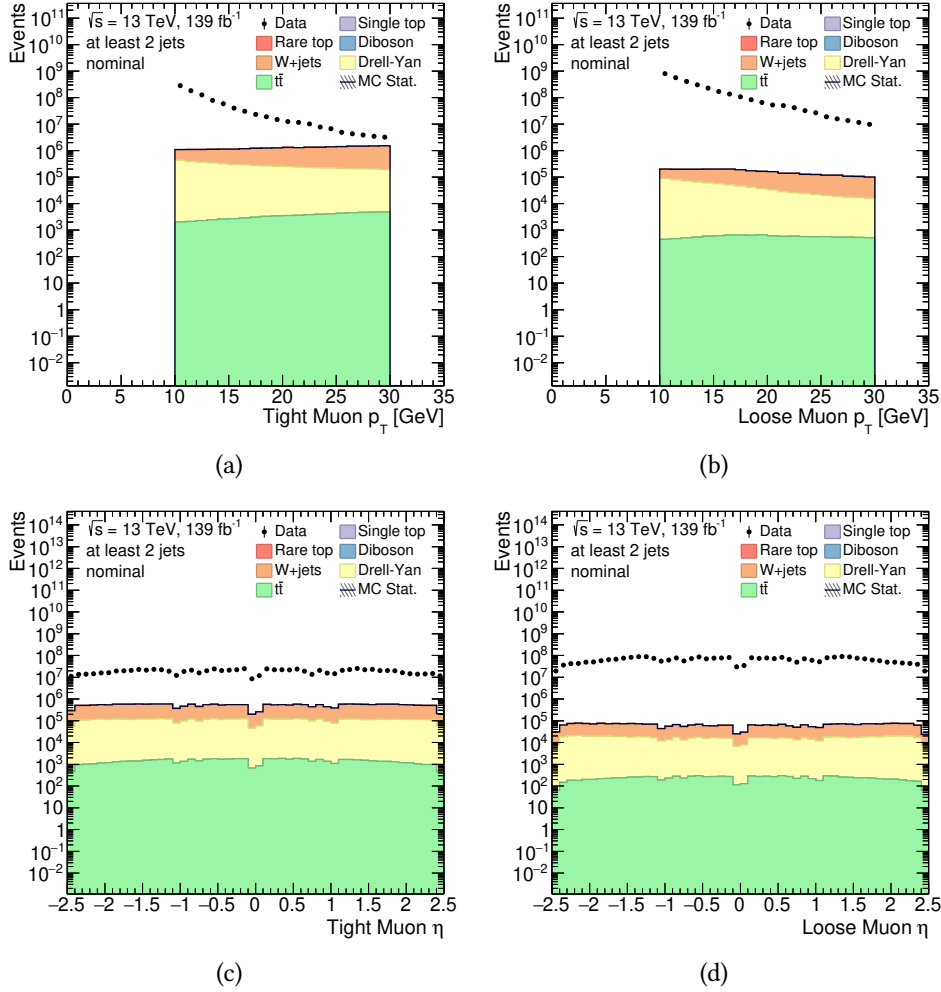


Figure 5.35: Fakes-enriched regions in the nominal low- p_T selection with at least 2 jets: [5.22a](#) p_T distribution of tight muons, [5.22b](#) p_T distribution of loose muons, [5.22c](#) η distribution of tight muons, [5.22d](#) η distribution of loose muons. All the distributions show data events and the prompt MC component subtracted from data, to ensure a fake dominated region.

previous sub-section.

The extrapolated fake-factors are validated by performing closure tests in the fake-enriched regions for each p_T region in the at least 1 and at least 2 jets phase-space. The closure test CRs have similar event selection to fake-factor derivation but removing, for the high- p_T range, the jet angular requirements.

Prompt MC processes considered in the closure tests are the same as for the

fake-factors derivation, while the remaining events are well described by the estimated fake-factors contribution, as shown in Figure 5.40 and 5.41 for the high- p_T region and in Figure 5.42 and 5.43 for the low- p_T one. For both p_T regions the at least 1 and at least 2 jets selection are shown. Only the systematic uncertainty related to the fake-factor is considered. As for the electron low- p_T case, the asymmetry in the systematic bands for low- p_T muons is due to the pre-selection at the derivation level.

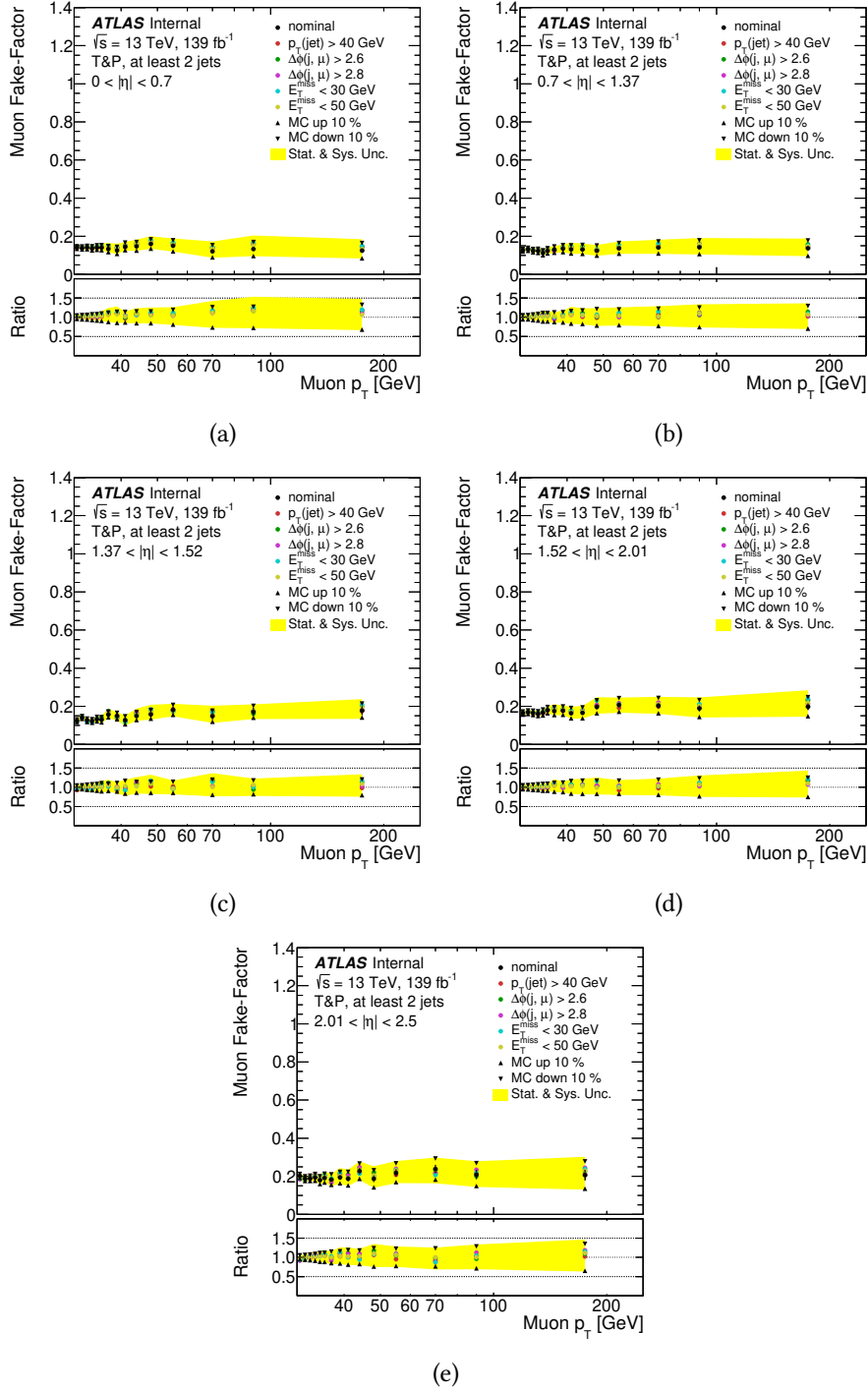


Figure 5.36: Measured fake-factors for a muon in the high- p_T region with at least 1 jet, with systematic variation applied. First η bin in 5.36a, second in 5.36b, third in 5.36c, the fourth in 5.36d and the last in 5.36e.

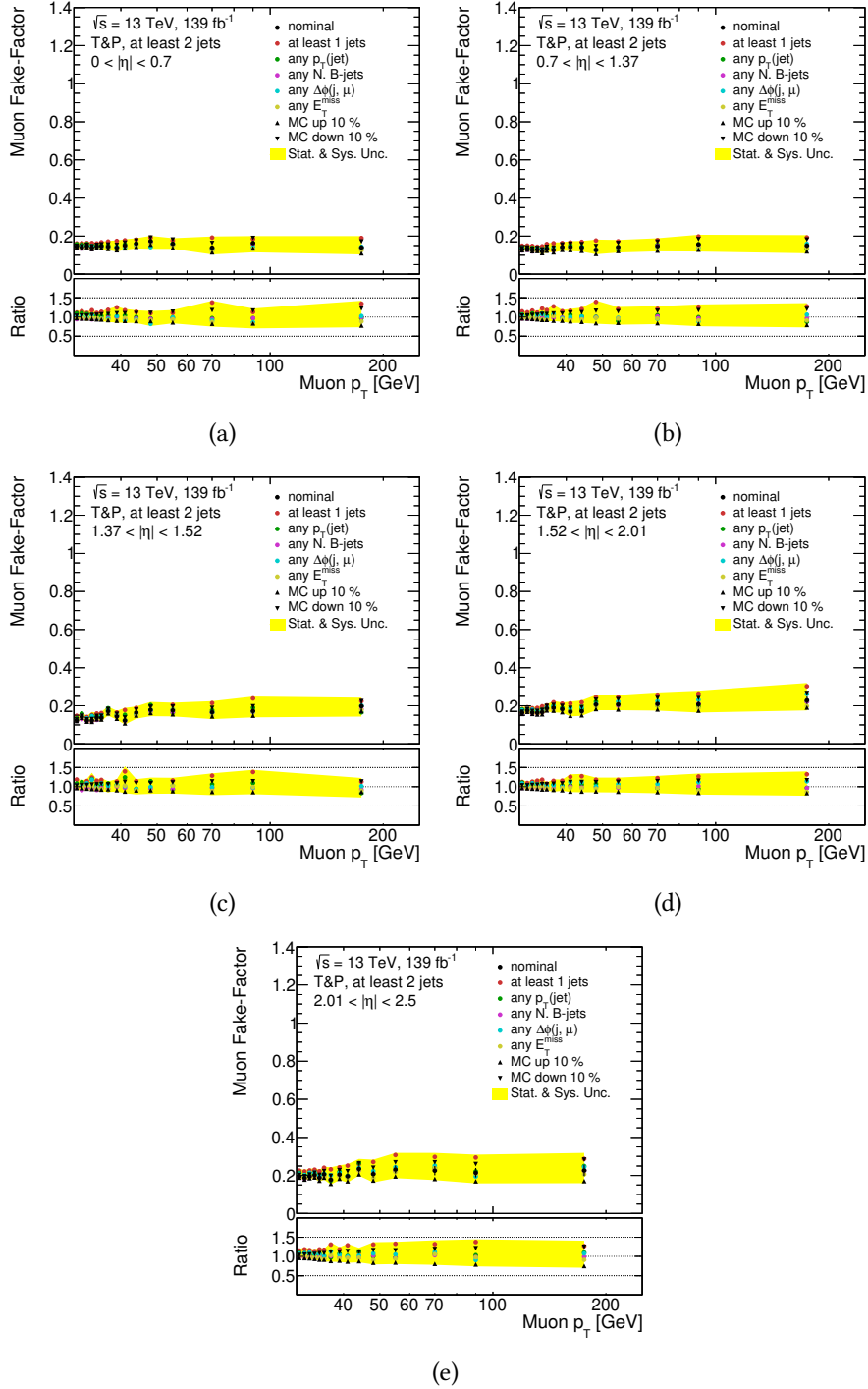


Figure 5.37: Measured fake-factors for a muon in the high- p_T region with at least 2 jets, with systematic variation applied. First η bin in 5.37a, second in 5.37b, third in 5.37c, the fourth in 5.37d and last in 5.37e.

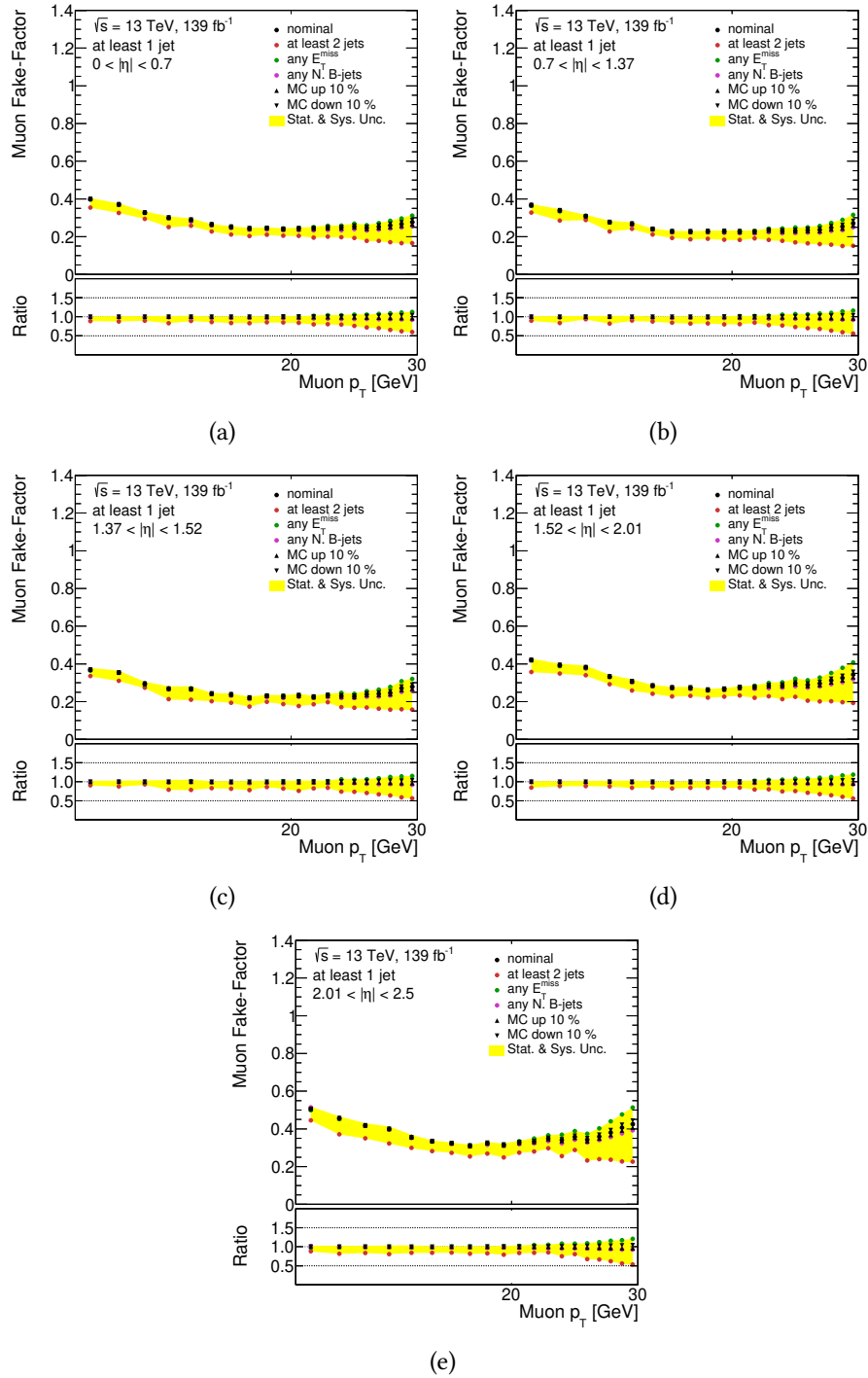


Figure 5.38: Measured fake-factors for a muon in the low- p_T region with at least 1 jet, with systematic variation applied. First η bin in 5.38a, second in 5.38b, third in 5.38c, the fourth in 5.38d and last in 5.38e.

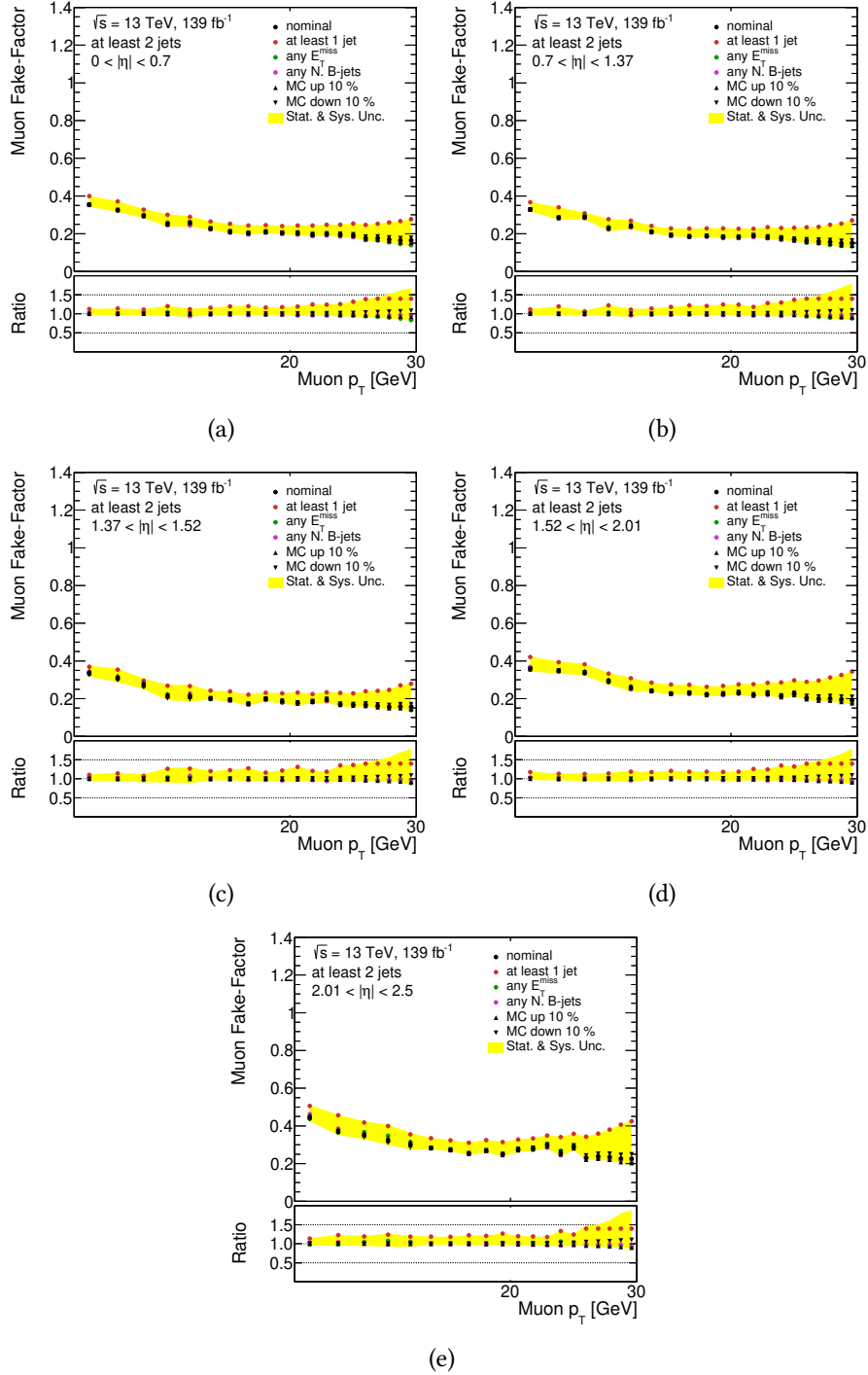


Figure 5.39: Measured fake-factors for a muon in the low- p_T region with at least 2 jets, with systematic variation applied. First η bin in 5.39a, second in 5.39b, third in 5.39c, the fourth in 5.39d and last in 5.39e.

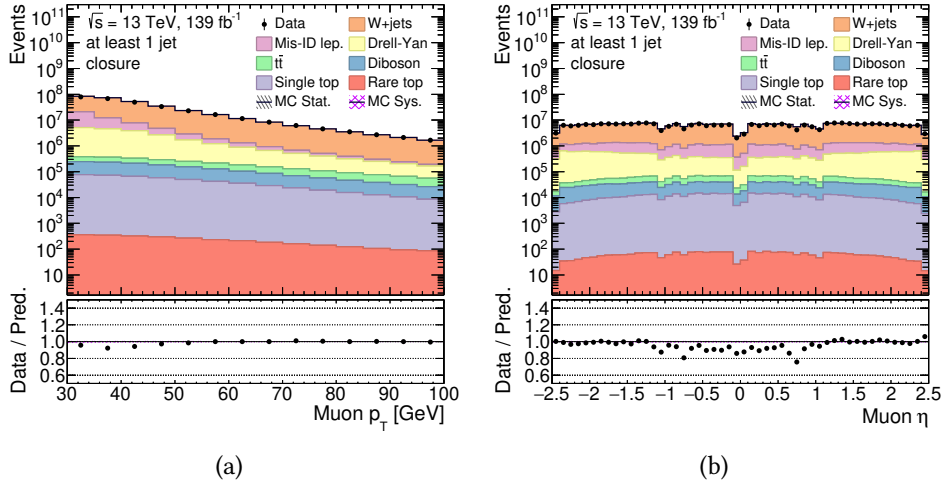


Figure 5.40: The muon fake-factors closure test in high- p_T region with at least 1 jet. In 5.40a the p_T distribution is shown, while in 5.40b the η one. The pink band shows the systematic uncertainty associated to the fake-factor measurement.

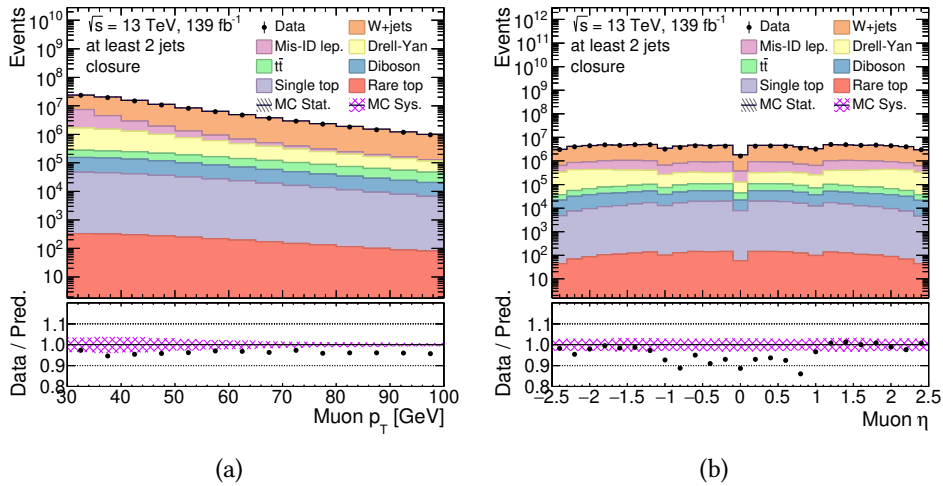


Figure 5.41: The muon fake-factors closure test in high- p_T region with at least 2 jets. In 5.41a the p_T distribution is shown, while in 5.41b the η one. The pink band shows the systematic uncertainty associated to the fake-factor measurement.

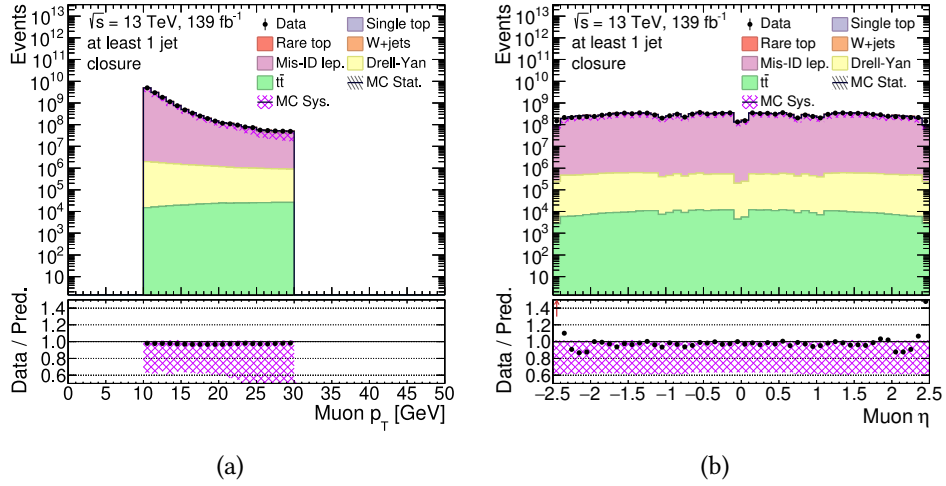


Figure 5.42: The muon fake-factors closure test in low- p_T region with at least 1 jet. In 5.42a the p_T distribution is shown, while in 5.42b the η one. The pink band shows the systematic uncertainty associated to the fake-factor measurement.

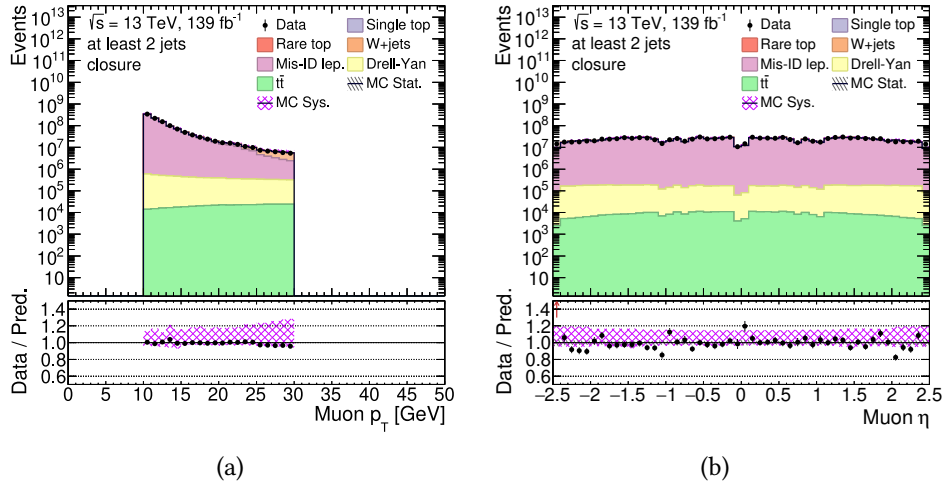


Figure 5.43: The muon fake-factors closure test in low- p_T region with at least 2 jets. In 5.43a the p_T distribution is shown, while in 5.43b the η one. The pink band shows the systematic uncertainty associated to the fake-factor measurement.

5.3 Systematic Uncertainties

In the statistical analysis, several sets of systematic uncertainties are taken into account to cover all the detector and simulation limitations. Despite the very powerful and precise tools used to generate Monte Carlo samples, they exploit theoretical models which are as close as possible to reality but still an approximation of the real Nature. On the other side, as discussed in Chapter 3, the ATLAS detector provides optimal measurements of all the physical objects detected even with a certain level of approximation. For these reasons, theoretical and experimental systematic uncertainty sources have to be considered in every analysis for both background and signal predictions. Usually each systematic uncertainty in the signal strength is evaluated by varying the corresponding nuisance parameter (NP) by one standard deviation (σ) and reweighting accordingly all the events. This leads to two shifted distributions for each variable of interest representing the fluctuation ($\pm 1\sigma$) with respect to the nominal distribution. In cases where both shifted distributions produce a defect or an excess with respect to the nominal distribution, the resulting variation is symmetrized assuming that is of the same size in both directions. Some systematic uncertainties can not be treated in this way and require a specific case dependent approach.

Systematic uncertainties may affect the normalization of the samples, the shape of the distributions or both. Even if they come from different sources of systematics, during the fit procedure possible correlated effects can appear in the measurement.

All the systematics, both theoretical and experimental, which are considered in this analysis are reported in Table 5.13 with the corresponding number of NP. In Appendix A.2 the magnitudes of systematic and normalisation uncertainties after the background-only fit are summarised.

5.3.1 Theoretical Uncertainties

Monte Carlo generators allows variations of theoretical models used to produce the samples. The schematically representation of an inclusive cross-section $\sigma^{(n)}$ for $pp \rightarrow X$ calculated at n -th order in perturbation theory is given by:

$$\sigma^{(n)} = \text{PDF}(x_1, \mu_F) \otimes \text{PDF}(x_2, \mu_F) \otimes \hat{\sigma}^{(n)}(x_1, x_2, \mu_R) \quad (5.16)$$

with

$$\hat{\sigma}^{(n)} = \alpha_s \hat{\sigma}^{(0)} + \alpha_s^2 \hat{\sigma}^{(1)} + \dots + \alpha_s^n \hat{\sigma}^{(n)} + \mathcal{O}(\alpha_s^{n+1}), \quad (5.17)$$

where x_1 and x_2 are the fractions of momentum coming from each of the two partons, and μ_F and μ_R are factorisation and renormalisation scales, respectively. Scale variation uncertainties, PDF uncertainties and α_s uncertainties are estimated for the main background, the diboson, and for the signal samples. Also

the effect of the choice of generator software used for the hard process and for showering is estimated.

Additionally, a systematic uncertainty to cover the different number of jets requirement between the ZL and the JNLow regions is taken into account. This was needed since the background estimation evaluated in a CR with at least two jets applied to a SR with maximum one jets can not account the mis-modelling of the MC generators. The variation applied to this systematic is the normalization factor obtained by performing a background-only fit considering the JNLow VR as a CR. For the second main background, the rare top process, a theoretical systematic is applied considering only the higher scale uncertainties due to ttW and ttZ processes following the recommendations provided by the Top Physics Modelling Group of the ATLAS Collaboration [206]. These last two systematics are equal to: ± 1.1 for the diboson modelling, $+13.3 - 11.7$ for the rare top contribution.

The choice of the QCD renormalisation scale μ_R and factorisation scale μ_F is taken as an uncertainty. The conventional approach is to vary these scales upwards and downwards by a factor of two, both individually and then together. The uncertainty is evaluated by taking an asymmetric envelope of seven variations obtained by varying scales up and down by a factor of two, but excluding the variations where one is varied up and the other varied down. This leads to the inclusion of the variations as they are shown in Table 5.12.

In addition at the missing higher order uncertainties there are several sources

$\mu_R \backslash \mu_F$	0.5	1	2
0.5	✱	✱	✱
1	✱	✓	✱
2	✱	✱	✱

Table 5.12: Applied renormalisation and factorisation scale variations. Variations marked in green are taken as uncertainties, while the ones in red are not used. In black the is the nominal choice.

of uncertainty that affect the determination of PDFs, mainly experimental uncertainties entering the datasets used in the PDF fits and the uncertainty on functional form used in the PDF fits. Other theory uncertainties such as the nuclear effects or the flavour scheme are not explicitly taken into account, but some of these effects are indirectly probed when comparing different PDF sets.

The LHAPDF6 toolkit [207] is used to calculate the PDF uncertainties.

The strong coupling constant α_s is determined experimentally from the combination of a different datasets and its value is quoted at the scale of the Z boson mass. Two main sources of uncertainty are taken into account: the truncation of the cross-section calculation at a fixed order in perturbation theory and the experimental errors in the determination of α_s . To estimate the effect of the computation of the strong coupling constant α_s of 0.118 the event weights are recomputed using PDFs where α_s is scaled downwards and upwards to 0.117 and 0.119, respectively. The nominal value is compared with the scaled values by using:

$$\delta^{\alpha_s} \sigma = \frac{\sigma(\alpha_s^{\text{down}}) - \sigma(\alpha_s^{\text{up}})}{2}. \quad (5.18)$$

Since the value of α_s affects the cross-sections of the processes used in the PDF fits, there is an interplay between the α_s and PDF uncertainties, however the correlation is small. To reduce the impact the two uncertainties are added in quadrature

$$\delta^{\alpha_s + \text{PDF}} \sigma = \sqrt{(\delta^{\text{PDF}} \sigma)^2 + (\delta^{\alpha_s} \sigma)^2}. \quad (5.19)$$

5.3.2 Experimental Uncertainties

The main reason to use experimental systematics is due to differences between reconstruction results of data and simulated events. Two kinds of uncertainties affect the experimental contribution:

- *Calibration* uncertainties change particle momenta to account for uncertainties in momentum scale and track reconstruction;
- *Efficiencies* uncertainties are the result of different reconstruction, object identification, charge identification, isolation, and trigger efficiencies of leptons in data compared to Monte Carlo and are estimated by varying the corresponding scale-factors (SF).

Both of them are applied to signal and background MC predictions but not to data.

Since the fake-lepton contribution is estimated by a data-driven technique, an additional uncertainty is assigned for both the lepton flavours accounted. Fake-factors are varied to improve the modelling of the fake background as discussed in Section 5.2.2.

The experimental systematics considered in this analysis are:

- Luminosity: which is the uncertainty on the total integrated luminosity recorded by ATLAS during the full Run 2 period, from 2015 to 2018. It is accounted as a variation of 1.7%;
- Pile-up reweighting: comes from the SF used to control the pile-up value which scales data before the assignment of pile-up weights;
- Electron calibration: considers both uncertainties in the electron momentum resolution and scale;
- Electron efficiencies: due to the uncertainty on each SF calculated for the electron trigger, reconstruction, identification and isolation steps. The charge identification efficiency SF is also included in this set which is obtained using a BDT to reduce the numbers of electrons that are reconstructed with a wrong charge. This uncertainty includes one term for the systematic effects and another one to account the limited statistics available in the bins where the SF was obtained;
- Muon calibration: includes uncertainties for momentum measurements provided by the Inner Detector and Muon Spectrometer and the muon momentum scale accounting also the residual charge-dependent bias due to the muon track sagitta correction;
- Muon efficiencies: as for the electron case, a set of uncertainties on the efficiency SFs of the muon are provided. All of these systematics have two nuisance parameters (three for the muon reconstruction step since also the bad muon uncertainty is considered), accounting both systematic and statistical effects. Additionally, the uncertainty on the muon track-to-vertex association (TTVA) efficiency is part of this set with two NPs;
- Jet Calibration: this set of systematics includes uncertainties for both JER and JES. The JES uncertainties come from several primary sources: the standard calibration which have 14 NPs, the flavour dependence by the jet composition, the pile-up uncertainty due to the number of primary vertexes and μ values, the punch-through uncertainty depending by the number of muon segments behind the jet and the MC non-closure which affects samples where kinematic observables of the calibrated jet are not restored to that of the corresponding truth jet. JER systematic has instead 9 NPs due to the difference between data and MC and the noise term evaluation from random cones in zero bias data;
- Jet efficiency: considers a single NP which encodes the efficiency of the Jet Vertex Tagger algorithm and a set of 6 NPs accounting the SFs that correct the flavour tagging rate of the various jet flavours;

- E_T^{miss} soft term: includes uncertainties parameterized as parallel and perpendicular components to the hard term. Both offset and smearing contribution are taken into account;
- Fake factor: to cover the uncertainties on the data-drive method used to estimate the fake factors, two additional systematics are added, one for electron and one for muon. Each systematic covers the phase-spaces not considered during this evaluation.

5.4 Signal Extraction Technique

Data can be interpreted following two kind of hypotheses: they can be consistent with the SM prediction only (usually called *background-only*) or check if a match with the background plus signal hypothesis is possible at a certain *confidence level* [211]. To study these statistical interpretations, each hypothesis needs to be included in a likelihood (LH) function, which encodes the probability distributions for different regions defined in the analysis fitted simultaneously. The LH function uses several parameters commonly divided into *parameters of interest* (POI) and *nuisance parameters* (NPs). The POI is represented by the signal strength μ , which is a free parameter in the fit to perform an extrapolation indicating the best match hypothesis. A $\mu = 0$ indicates the background only hypothesis while $\mu = 1$ represents the signal plus background hypothesis. The NPs correspond to the uncertainties entering in the fit and are estimated by maximizing the LH, returning their most likely values based on the observations from data.

The `HistFitter` statistical framework [204] is used to perform the fit, based on ROOT and RooFit [212] frameworks. First, a background-only fit is performed in all the CRs, considering as floating parameters the yields of the main backgrounds affecting the analysis regions. With this procedure, a normalization factor (NF) can be extrapolated for each process. Then, an exclusion fit is executed using both signal and background yields to find possible excess of the signal with respect to the SM predictions, if not present, an upper bound on the production cross-section of the new physics process is set. The validity and performance of the fit is estimated in VRs where the NFs are applied. A summary of the fit procedure considered in this analysis is reported in Table 5.14

Signal Extraction Technique Search for Type-III SeeSaw heavy leptons

Category	Type	Nuisance Parameters
Luminosity		1
Pile-up reweighting		1
Theory uncertainties	SHERPA 2.2.1 PDF variation	1
	SHERPA 2.2.1 QCD scale variation	1
	SHERPA 2.2.1 PDF choice	1
	Diboson Njet Modelling	1
	Rare Top ttW/ttZ	1
	MADGRAPH5_aMC@NLO PDF variation	1
	MADGRAPH5_aMC@NLO QCD scale variation	1
Data-driven background	Electron fake factors	1
	Muon fake factors	1
Electron calibration	Resolution	1
	Momentum scale	2
Electron efficiencies	ID	1
	Reconstruction	1
	Isolation	1
	Trigger	2
	Charge identification	2
Muon calibration	Smearing of the ID and MS track	2
	Momentum scale	3
Muon efficiencies	Reconstruction	3
	Isolation	2
	TTVA	2
	Trigger	2
Jet calibration	Jet energy scale calibration	14
	Jet energy scale flavour dependence	3
	Jet energy scale pile-up dependence	4
	Jet energy scale calorimeter punch-through	2
	Jet energy scale MC non-closure	2
	Jet energy resolution	9
Jet efficiencies	JVT	1
	Flavour tagging	6
E_T^{miss} soft track	Offset along the pt_{Hard} axis	1
	Smearing by resolution uncertainty along and perpendicular to pt_{Hard} axis	2

Table 5.13: Summary of the sources of systematic uncertainty considered in the analysis with the corresponding number of nuisance parameters.

Search for Type-III SeeSaw heavy leptons Signal Extraction Technique

	3 leptons				4 leptons			
	ZL CR	ZL SR	ZL veto SR	JNLow SR	Q0 Diboson CR	Q0 Rare Top CR	Q0 SR	Q2 SR
Diboson-3l (WZ)	✓	✱	✱	✱	-	-	-	-
Diboson-4l (ZZ)	-	-	-	-	✓	✱	✱	✱
RareTop	✱	✱	✱	✱	✱	✓	✱	✱
background-only fit	✓	-	-	-	✓	✓	-	-
exclusion fit	✓	✓	✓	✓	✓	✓	✓	✓

Table 5.14: Upper part shows the summary of the regions used to fit the yields of the largest SM background predictions. Regions used to extrapolate the normalization factor for a certain SM prediction are marked with a black check-mark (✓), while regions where this NF is only applied are marked with a green check-mark (✱). Regions where the NF is neither extrapolated and neither applied are instead marked with a dash(-). The lower part shows which regions are used in the fit depending on the fit configuration (background-only or exclusion).

5.4.1 Likelihood-based test

A *likelihood function* (\mathcal{L}) is constructed in the fit, containing the POI, the NFs for background processes and the NPs. The likelihood is defined as:

$$\mathcal{L}(\mathbf{n}, \boldsymbol{\theta}_0 | \mu_{sig}, \boldsymbol{\mu}_b, \boldsymbol{\theta}) = P_{SR} \times P_{CR} \times G_{NP} \quad (5.20)$$

$$= P \left(n_{SR} | \mu_{sig} \cdot S(\boldsymbol{\theta}) + \sum_b^{bkg} \mu_b B(\boldsymbol{\theta}) \right) \quad (5.21)$$

$$\times \prod_{i \in CR}^{n_{bins}} P_i \left(n_{CR} | \sum_b^{bkg} \mu_b B(\boldsymbol{\theta}) \right) \quad (5.22)$$

$$\times G_{NPs}(\boldsymbol{\theta}_0 | \boldsymbol{\theta}). \quad (5.23)$$

The first term 5.21 is the poissonian probability to observe n events given the signal plus background hypothesis:

$$n = \mu_{sig} \cdot S(\boldsymbol{\theta}) + \mu_b \cdot B(\boldsymbol{\theta}). \quad (5.24)$$

The number of observed events in the signal region is n_{SR} while $S(\boldsymbol{\theta})$ and $B(\boldsymbol{\theta})$ are the expected signal and background yields as function of the NPs $\boldsymbol{\theta}$, respectively. The parameter $\boldsymbol{\mu}_b$ is a vector describing the NF for each background process which is constrained exploiting the 5.22. To increase the experimental power and to constrain the values of NPs, in this analysis CRs use binned distributions, then a multi-bin Poisson distribution is considered. Since CRs are poor in signal events, n_{SR} is assumed to be null and only the total background yields of an individual bin in the CR are accounted in the i index. Both the signal and the

background expected yields depend on NP, accounting for the impact of systematic uncertainties on the expected yields. Not all the NPs are common for both CR and SR, but they are correlated across the regions if the same background process is present. The term in 5.23 is referred to the parameterization of the NPs and constrains the values of auxiliary measurements θ_0 to its measured value θ . Depending on the NP considered, the G can be a Gaussian or a Poisson distribution. Luminosity, cross-sections or experimental systematic uncertainties require a Gaussian auxiliary measurements, such as most of the systematic uncertainties; while to account the limited number of events in the samples used in the analysis a poissonian treatment is needed. Each systematic uncertainty can either affect the overall normalization of the sample, or its shape, or both. Commonly, the θ are scaled to have a nominal value equal to 0 and systematic uncertainty variation corresponding to $\pm x\sigma$ for $\theta = \pm x$.

5.4.2 Hypothesis test

To test a hypothesised value of signal strength μ , the *profile likelihood ratio* q_μ is used as test statistic. It is defined as:

$$q_\mu = -2 \cdot \ln \frac{\mathcal{L}(\mu, \hat{\theta}_\mu)}{\mathcal{L}(\hat{\mu}, \hat{\theta})} \quad (5.25)$$

where $\hat{\mu}$ and $\hat{\theta}$ maximize the unconditional LH function, while $\hat{\theta}_\mu$ maximizes the LH for the specific value of μ . The test-statistic is positive-defined. A q_μ value close to zero suggests a signal-like data distribution while a larger q_μ a background-like data distribution.

The probability value assigned to a hypothesis test, commonly named *p-value*, is calculated using a distribution of test statistic, the probability density function (PDF), $f(q_\mu|\mu, \theta)$. It is determined using a MC generation of pseudo-experiments (called *toys*) to randomize the observed events and the the central values of the auxiliary measurements. Following the Wilks' theorem [213], the distribution of $f(q_\mu|\mu, \theta)$ can be approached with the asymptotic formula [214], when data sample is large enough. In this case it is distributed as a χ^2 with one degree of freedom and it is independent of the actual values of the auxiliary measurements. This theorem holds true for as few as $\sim \mathcal{O}(10)$ events and can be used to save time by forgoing the need to run computationally expensive toys. The *p-value* for a given observation can be defined, under the μ hypothesis, as the level of agreement of data with the same hypothesis. Considering an observed value of test statistic q_μ^{obs} , the *p-values* is defined as:

$$p_\mu = \int_{q_\mu^{obs}}^{\infty} f(q_\mu|\mu) dq_\mu, \quad (5.26)$$

and can be converted into equivalent normal significance Z : by convention a discovery is made when the background-only hypothesis is rejected at 5σ . If x is a Gaussian distributed variable with mean m_x , \hat{x} ($\hat{x} > m_x$) is defined as the value of x which has an upper-tail probability equal to the p -value p . The significance Z is defined as the number of standard deviations of \hat{x} with respect to m_x :

$$Z = \Phi^{-1}(1 - p), \quad (5.27)$$

where Φ^{-1} is the quantile (that is the inverse of the cumulative distribution) of the standard Gaussian.

The *CLs* [215] method is used to ascertain upper limits on the signal regions. When considering upper limits, it is quoted the value of μ for which the median p -value is equal to 0.05, as this gives the median upper limit on μ at 95% confidence level. To define it, both the p -values for the signal plus background hypothesis p_{S+B} and for the background-only hypothesis p_B need to be computed. Once the PDFs are known, the probability p_{S+B} can be defined that a signal plus background hypothesis gives a test-statistic above an observed value q_μ^{obs} . Likewise, the probability p_B is defined that a background-only hypothesis exhibits a test-statistic lower than the observed value:

$$p_B = P(q_\mu < q_\mu^{obs} | B) = \int_{-\infty}^{q_\mu^{obs}} f(q_\mu | B) dq_\mu, \quad (5.28)$$

$$p_{S+B} = P(q_\mu > q_\mu^{obs} | S + B) = \int_{q_\mu^{obs}}^{\infty} f(q_\mu | S + B) dq_\mu. \quad (5.29)$$

Then, the final confidence level *CLs* is computed as the ratio:

$$CLs = \frac{p_{S+B}}{1 - p_B}, \quad (5.30)$$

and if below 5%, allows to exclude a hypothesis at 95% CL.

Since NPs are usually used in this kind of computation, the fitted $\hat{\mu}$ parameters is affected also by uncertainty, which depends on the one of the NPs Δ_θ . For simplicity, considering only one NP on $\hat{\mu}$, its impact can be evaluated as:

$$\Delta_{\hat{\mu}} = \hat{\mu}(\hat{\theta} \pm \Delta_\theta) - \hat{\mu}(\hat{\theta}). \quad (5.31)$$

As a result, the NP can be *over-constrained* which means that the post-fit uncertainty Δ_θ is smaller than the pre-fit one or *pulled*, showing the difference between pre- and post-fit NP values (θ). In both cases, the predicted rates of signal and background process and the corresponding systematic uncertainties are modified.

It is also important to point out that the sensitivity of an experiment is characterized by the expected median significance to reject different values of μ . In

this way is it possible to find also a measure of how much one would expect this to vary as a result of statistical fluctuations in the data. Usually, this estimation is performed by replacing the ensemble of simulated datasets by a single representative one, the so called *Asimov* dataset, which is generated depending on the distributions of the MC samples and to the chosen test statistic. Considering the Asimov dataset, data are set, in each bin, to the corresponding background predictions value and this is used to evaluate the effects of systematics on the fit, looking for possible pulled or over constrained NPs.

5.4.3 Background extrapolation and error propagation

As previously mentioned, the normalization factor for the corresponding background hypothesis μ_B is performed in the CR and then applied to VRs and SRs. A single PDF is constructed including all the NPs shared between CRs and SRs to consider information from both signal and background events, as well as systematic uncertainties. In this procedure, only the CRs are used as a constrain in the fit, while in SRs and VRs only the corresponding modification to the PDF can be applied. Taking for simplicity only one NF extracted by a single CR and applied to a single SR (or VR), the estimated background yields are computed as:

$$\begin{aligned} N_p (SR, \text{est.}) &= N_p (CR, \text{obs.}) \cdot \left[\frac{MC_p (SR, \text{unnorm})}{MC_p (CR, \text{unnorm})} \right] \\ &= \mu_p \cdot MC_p (SR, \text{unnorm}), \end{aligned}$$

where p indicates the background process, $N_p (CR, \text{obs.})$ the observed number (data) of events in the CR and $MC_p (CR, \text{unnorm})$ and $MC_p (SR, \text{unnorm})$ the not normalized (MC simulation) events in CR and SR, respectively. With this mechanism, the total uncertainty on the background events in the SR is a combination of the statistical and systematic uncertainties of the extrapolation. The uncertainty is then propagated as:

$$\sigma_{B,\text{tot}}^2 = \sum_i^n \left(\frac{\partial B}{\partial \eta_i} \right)^2 + \sigma_{\eta_i}^2 + \sum_i^n \sum_{j \neq i}^n \rho_{ij} \left(\frac{\partial B}{\partial \eta_i} \right) \left(\frac{\partial B}{\partial \eta_j} \right) \sigma_{\eta_i} \sigma_{\eta_j} \quad (5.32)$$

where $\eta_{i,j}$ are the floating parameters in the fit, both NFs and NPs, ρ_{ij} is the correlation between the floating parameters and $\sigma_{\eta_{i,j}}$ are the standard deviations of $\eta_{i,j}$. In the pre-fit step, correlations and errors on the NFs are set to zero, since they are not known before the fit.

5.5 Results

As detailed explained in the previous Sections of this Chapter, the final normalization of diboson and rare top backgrounds are obtained in the simultaneous fit comparing data with MC expectations in the ZL Region CR, Q0 Diboson CR and Q0 RareTop CR. It is important to remind that diboson contributions are considered independently in the three- and four-lepton channels since their composition is different, then two different normalization factors are derived for the WZ and ZZ processes, called from now *diboson-3l* and *diboson-4l*. To increase the fit power and to reduce the number of parameter given as input, the backgrounds with the minor contributions are grouped all together in the *other* category. The strategy to use in the three-lepton channel the rare top NF derived from the four-lepton channel does not affect the fit results, but helps, during the combined fit procedure, in having less pulled nuisance parameters.

The derived normalization scale factors for all the main backgrounds with the corresponding uncertainty are listed in Table 5.15. Pre- and post-fit distribution for each analysis region defined in this work are reported in Figure 5.44-5.51. In CRs, the extrapolated NFs lead the Monte Carlo yields to a perfect match with the data, producing a data on MC ratio equal to one which show a optimal agreement in the bottom panel of each post-fit plot. The obtained NFs are validated in the several VRs, which have a very good agreement between data and MC within the uncertainty bands. Additional post-fit distributions are shown in Appendix A.3. Event yields after the likelihood fitting procedure for all the analysis

Normalization Factor	$\mu_{norm} - 3lep$	$\mu_{norm} - 4lep$
diboson-3l	0.85 ± 0.03	-
diboson-4l	-	1.08 ± 0.03
raretop	-	1.4 ± 0.2

Table 5.15: A table listing the normalisation factors with the corresponding uncertainty for normalisation of the floating MC contributions, as extracted from the background-only fit for the separate lepton multiplicity channels, three and four.

regions in the three- and four-lepton channels are shown in Figure 5.52. Good agreement within statistical and systematic uncertainties between data and MC expectations is observed in all regions, demonstrating the validity of the background estimation procedure. The total number of yields in each analysis region is listed in Tables 5.16-5.18. For SRs only, also the number of signal events for three mass hypotheses is included. In Appendix A.4 the so-called *cutflow* tables listing the number of yields in each analysis region after each selection cut are reported.

	Three lepton channel			Four lepton channel	
	JNLow SR	ZL SR	ZLVeto SR	Q0-SR	Q2-SR
Data	25	7	16	25	17
Total background	24.4 ± 2.3	6.25 ± 0.52	25.2 ± 2.8	19.0 ± 1.6	10.3 ± 1.9
Diboson	18.0 ± 2.1	2.62 ± 0.27	7.64 ± 0.95	7.70 ± 0.78	8.5 ± 1.6
Rare top	1.82 ± 0.32	3.23 ± 0.46	11.2 ± 1.7	9.4 ± 1.4	1.63 ± 0.35
FNP	4.3 ± 0.5	0.29 ± 0.05	5.98 ± 0.85	1.37 ± 0.36	0.07 ± 0.37
Other	0.33 ± 0.03	0.11 ± 0.01	0.36 ± 0.12	0.49 ± 0.04	0.10 ± 0.01
$m(N^0, L^\pm) = 600$ GeV	15.0 ± 0.12	9.90 ± 0.09	20.5 ± 0.14	5.67 ± 0.04	4.80 ± 0.04
$m(N^0, L^\pm) = 800$ GeV	3.99 ± 0.03	2.82 ± 0.02	5.55 ± 0.04	1.37 ± 0.01	1.11 ± 0.01
$m(N^0, L^\pm) = 1000$ GeV	1.24 ± 0.01	0.83 ± 0.01	1.48 ± 0.01	0.38 ± 0.01	0.30 ± 0.01

Table 5.16: Observed data and background and signals yields in the three- and four-lepton signal regions after the background only fit.

	ZL-CR	JNLow VR	Fake VR	ZL Diboson VR	ZL Rare Top VR
Data	1959	121	8353	43	23
Total background	1960 ± 44	111.9 ± 8.9	8540 ± 600	34.2 ± 1.9	25.4 ± 2.8
Diboson	1348 ± 77	90.1 ± 9.1	4490 ± 430	28.7 ± 2.1	3.81 ± 0.47
Rare top	432 ± 60	3.99 ± 0.63	1200 ± 180	3.92 ± 0.66	21.6 ± 3.0
FNP	176 ± 18	17.4 ± 2.2	2730 ± 290	1.40 ± 0.56	< 0.001
Other	3.0 ± 1.3	0.39 ± 0.09	114 ± 11	0.128 ± 0.009	0.042 ± 0.005

Table 5.17: Observed data and background yields in the three-lepton control and validation regions after the background only fit.

	Q2 VR	Q0 Diboson CR	Q0 Rare Top CR	Q0 Diboson VR	Q0 Rare Top VR
Data	10	1642	67	79	20
Total background	14.3 ± 2.4	1642 ± 41	66.2 ± 7.8	91 ± 20	20.6 ± 2.7
Diboson	10.2 ± 2.1	1578 ± 41	5.37 ± 0.72	47.8 ± 4.5	0.56 ± 0.11
Rare Top	0.32 ± 0.06	12.3 ± 2.0	60.6 ± 7.8	38 ± 19	19.3 ± 2.7
FNP	3.76 ± 0.52	50.8 ± 3.3	0.06 ± 0.14	5.58 ± 0.78	0.76 ± 0.22
Other	0.026 ± 0.003	0.79 ± 0.05	0.11 ± 0.01	0.077 ± 0.008	0.012 ± 0.003

Table 5.18: Observed data and background yields in the four-lepton control and validation regions after the background only fit.

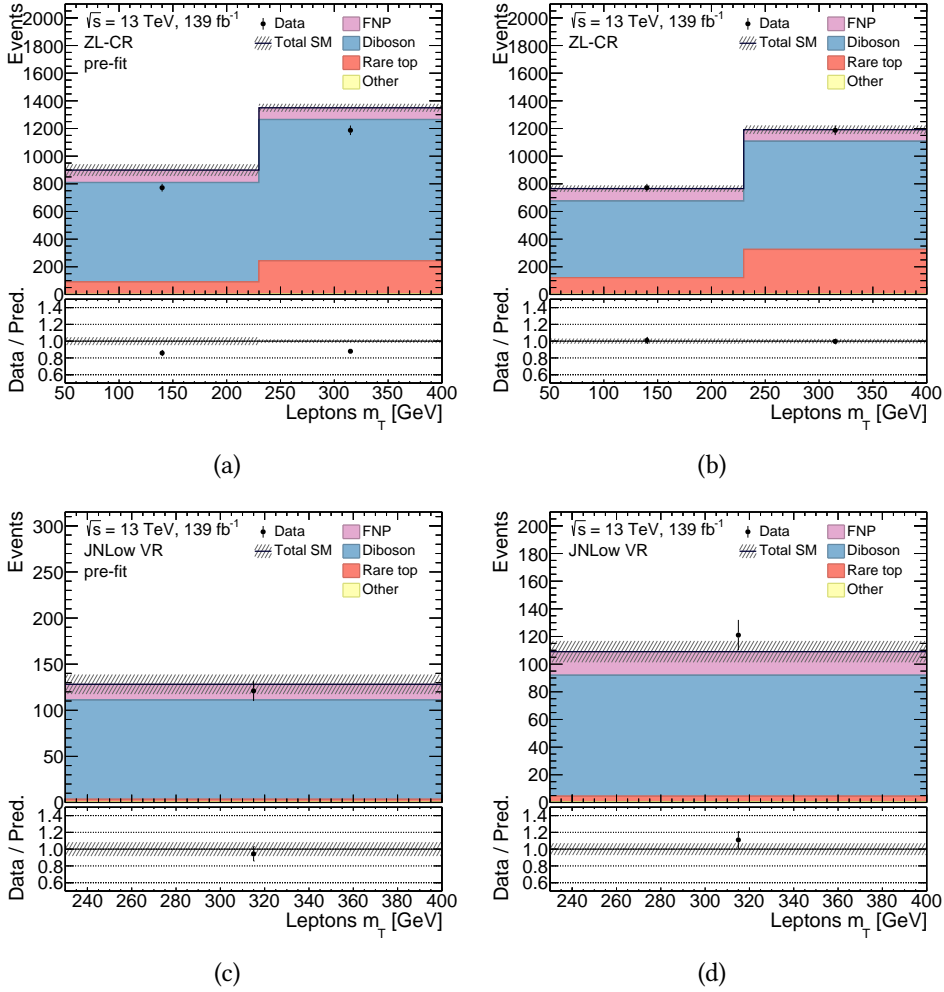


Figure 5.44: Pre- (left) and post-fit (right) distributions of $m_{T,3\ell}$ in ZL Region CR in 5.44a and 5.44b and in JNLow VR in 5.44c and in 5.44d. The uncertainty bands include both statistical and systematic uncertainties after the background-only fit taking into account all the correlation.

The final assessment of systematic uncertainties as determined by the fit is given by the so-called *pull plots*, in units of standard deviations, where uncertainties are constrained using data from only the control region in the background-only fit and from control and signal regions in the exclusion fit. As explained by Equation 5.31, NPs should not be significantly distant by the predicted values. If a NP is not centered at $\Delta_\theta = 0$, it means that has been shifted to a better value by the fit. In Figure 5.53, the pull plots for the combined fit considering three- and four-lepton analysis regions together, are shown. In the background only-fit with real

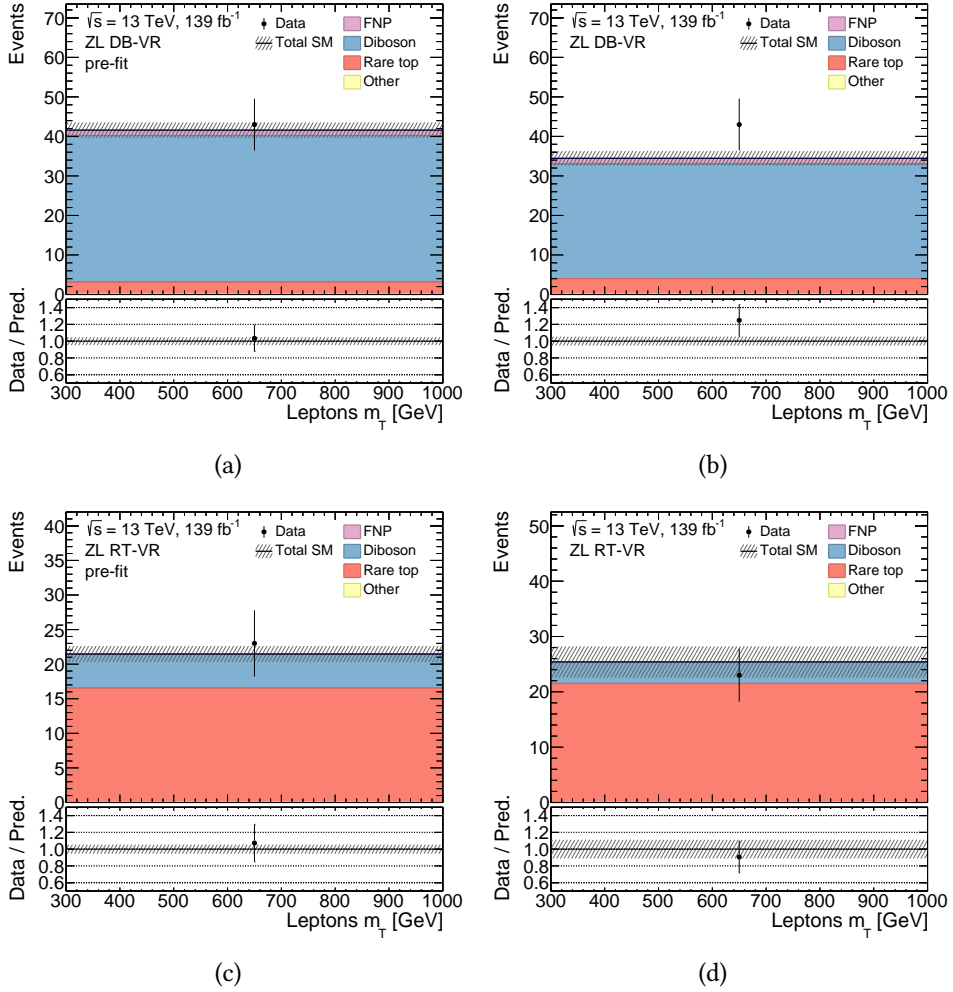


Figure 5.45: Pre- (left) and post-fit (right) distributions of $m_{T,3\ell}$ in ZL Diboson VR in 5.45a and 5.45b and in ZL Rare Top VR in 5.45c and in 5.45d. The uncertainty bands include both statistical and systematic uncertainties after the background-only fit taking into account all the correlation.

data in CR (Figure 5.53a), only the theory systematic uncertainty related to the diboson QCD scale is a bit pulled and constrained but without significant deviations. The same for the exclusion fit with Asimov dataset in Figure 5.53b. Using real data in both CRs and SRs in the exclusion fit, Figure 5.53c, the muon sagitta systematic is slightly pulled ($< 0.5 \sigma$) as well as the statistical term of the charge-flip NP ($> -0.5 \sigma$), while the systematic term of this NP results outside -1σ due to the data excess present in the second bin of the Q2 SR (Figure 5.51d) which pull this systematic trying to cover this discrepancy. The effect of the nuisance

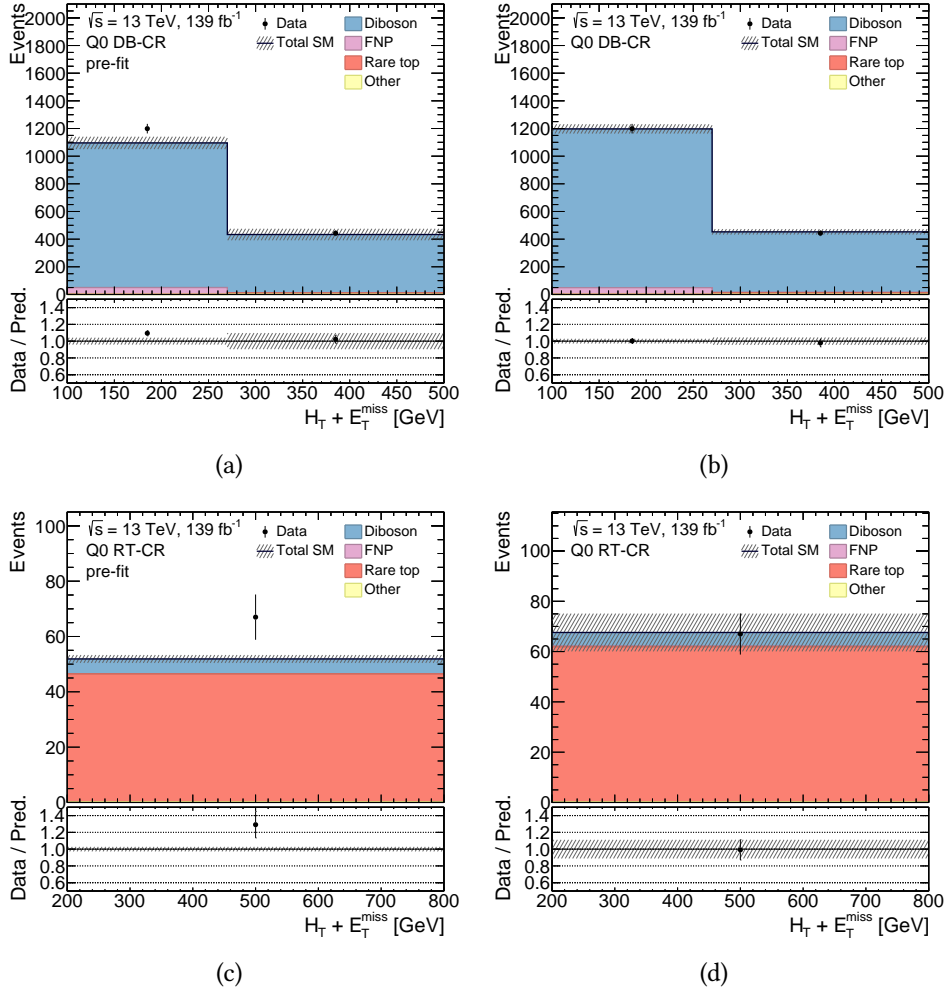


Figure 5.46: Pre- (left) and post-fit (right) distributions of $H_T + E_T^{\text{miss}}$ in Q0 Diboson CR in 5.46a and 5.46b and in Q0 Rare Top CR in 5.46c and in 5.46d. The uncertainty bands include both statistical and systematic uncertainties after the background-only fit taking into account all the correlation.

parameters, both systematics and statistics, on the signal POI μ_{SIG} is evaluated by fixing one nuisance parameter at the time to its $\pm 1\sigma$ variations and minimizing the likelihood function. After the fit, the impact on μ_{SIG} is compared with post-fit one to show its contribution. Furthermore, statistical uncertainty from limited number of MC events used to build the histograms for both predicted signal and background results in independent uncertainties in each bin, referred as γ parameters. One γ parameter per bin is considered, with a scaled Poisson prior. The so-called *ranking plots* are used to show the effects of the uncertainties

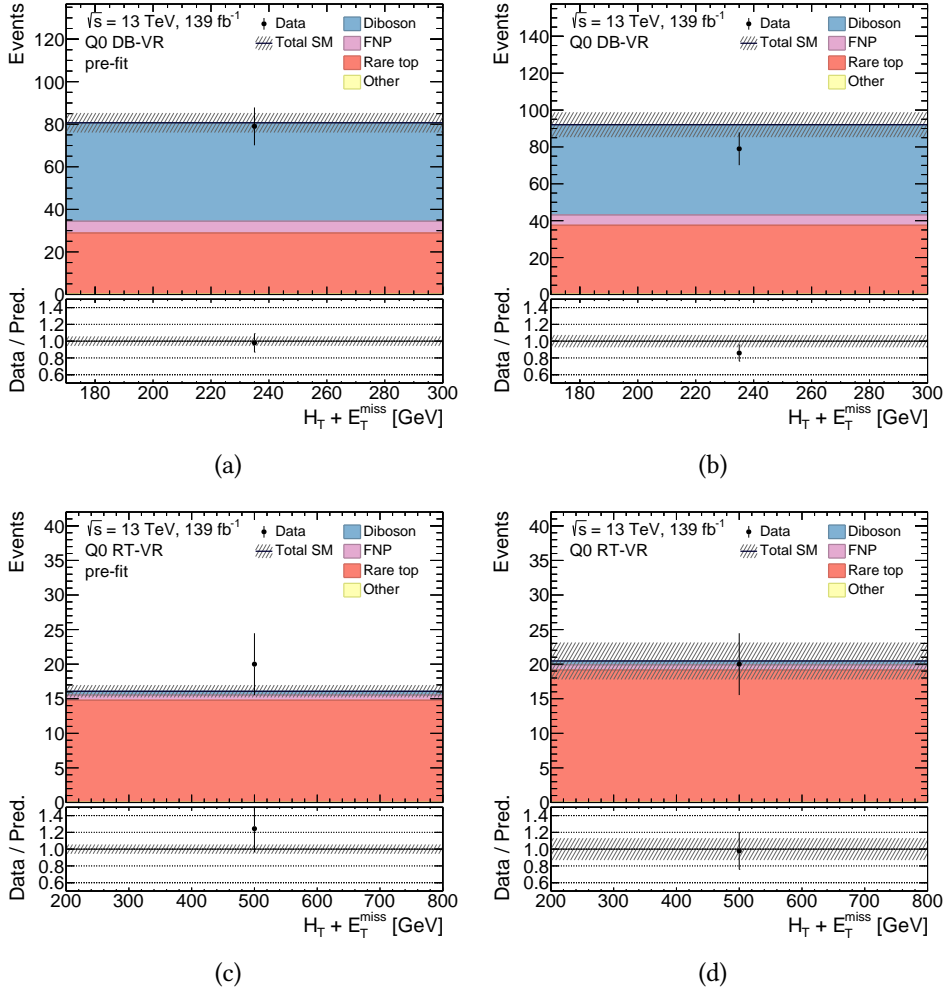


Figure 5.47: Pre- (left) and post-fit (right) distributions of $H_T + E_T^{\text{miss}}$ in Q0 Diboson VR in 5.47a and 5.47b and in Q0 Rare Top VR in 5.47c and in 5.47d. The uncertainty bands include both statistical and systematic uncertainties after the background-only fit taking into account all the correlation.

on μ_{SIG} , they are presented in Figures 5.54 and 5.55. As expected, the dominant uncertainty in this analysis is the statistical one which affects the signal yield for about 15%, while the dominant systematic is the electron identification efficiency with a 5% effect.

To have an overview of the different systematics effects in each analysis regions, in Figure 5.56 the relative uncertainties in the background yields are shown. The dominant uncertainty is, as said, the statistical one. The corresponding statistical uncertainty in data, depending on the signal region, varies from 20% to

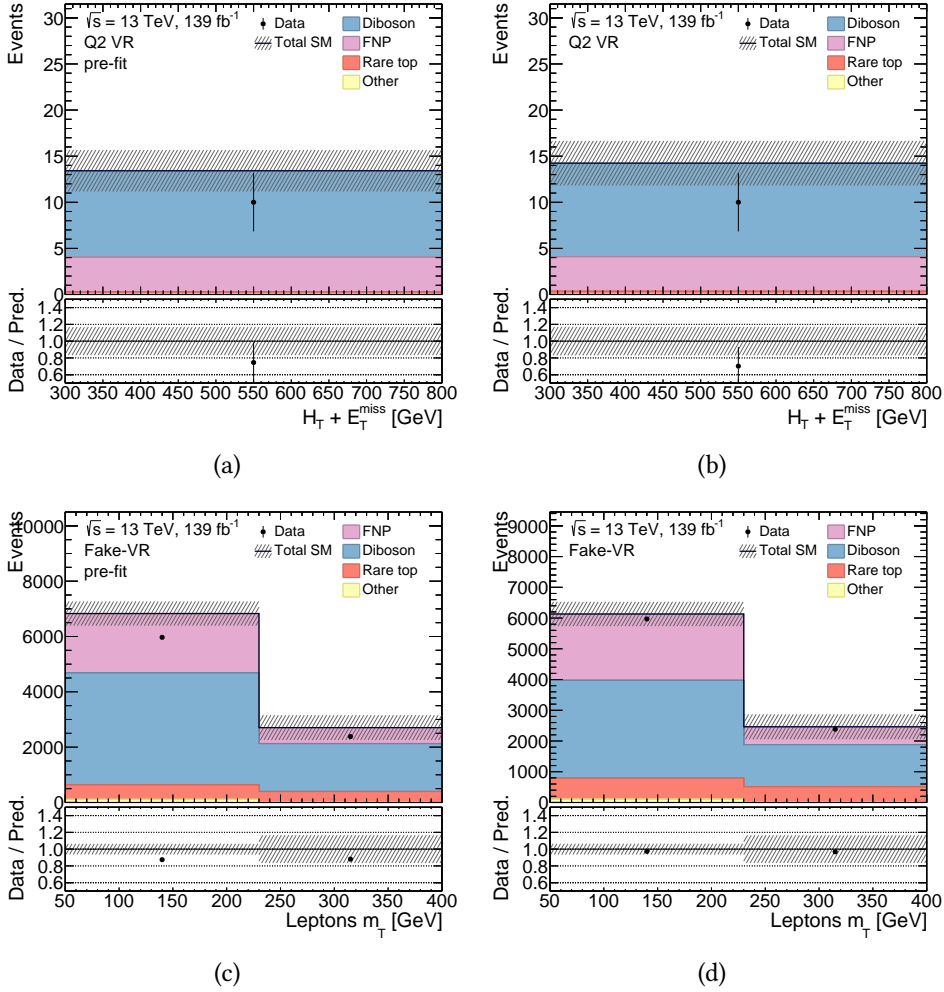


Figure 5.48: Pre- (left) and post-fit (right) distributions of $H_T + E_T^{\text{miss}}$ in Q2 VR in 5.48a and 5.48b and of $m_{T,3\ell}$ in the three-lepton Fakes VR in 5.48c and in 5.48d. The uncertainty bands include both statistical and systematic uncertainties after the background-only fit taking into account all the correlation.

37%, while the MC statistical uncertainty varies from 2% up to 7%. Since no significant deviations from the Standard Model expectations within uncertainties are found, 95% confidence level upper limits on the signal production cross-section are derived using the CL_s method. The upper limit on the production cross-section of the Type-III SeeSaw heavy leptons processes are evaluated at 95% CL as a function of the heavy lepton mass using the three- and four-lepton channels. By comparing the upper limits on the cross-section with the theoretical cross-section calculation as a function of the heavy-lepton mass, the lower mass

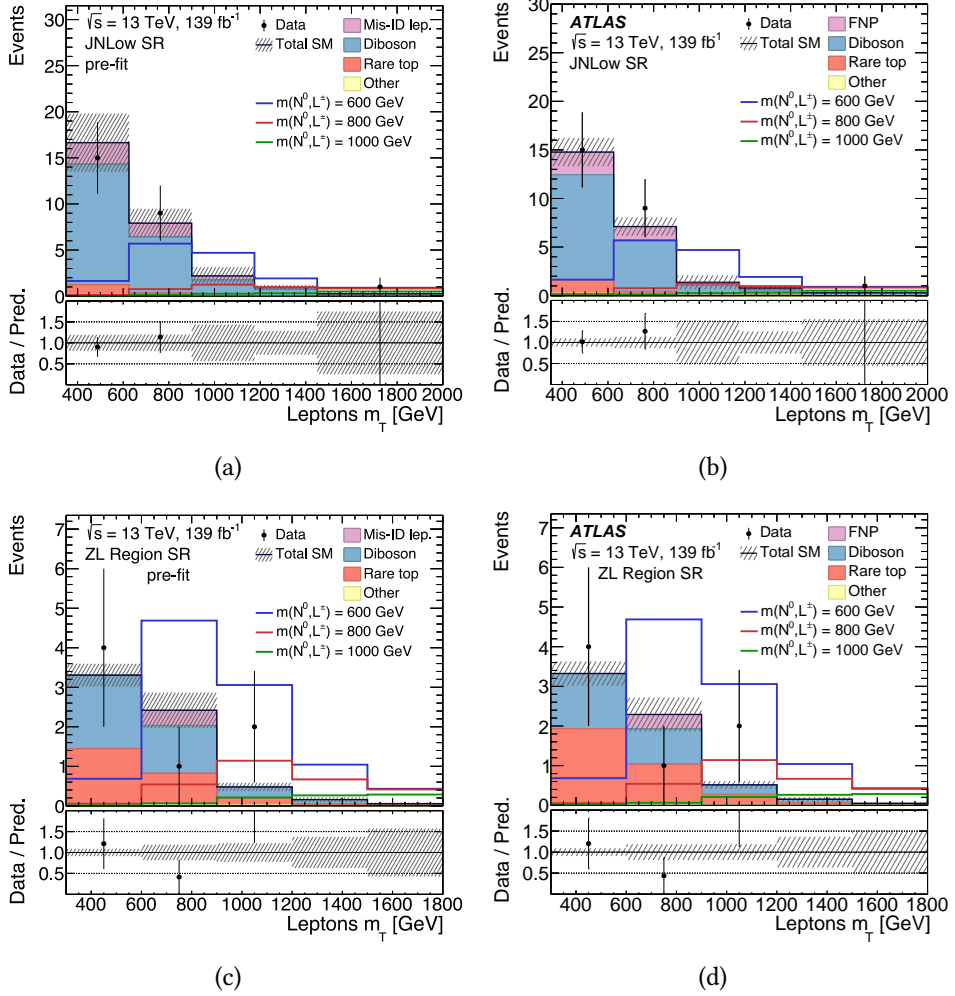


Figure 5.49: Pre- (left) and post-fit (right) distributions of $m_{T,3l}$ in JNLow SR in 5.49a and 5.49b and in ZL Region SR in 5.49c and in 5.49d. The uncertainty bands include both statistical and systematic uncertainties after the background-only fit taking into account all the correlation. The post-fit distributions in 5.49b and 5.49d were published in [216].

limit on the mass of the Type-III SeeSaw heavy leptons N^0 and L^\pm is derived, excluding the mass values below this point. The observed (expected) exclusion limit is 870 GeV ($900_{-80}^{+80} \text{ GeV}$) [216], shown in Figure 5.57.

In Appendix A.5, some results are shown also for three- and four-lepton channel separately.

The signal hypothesis in the multi-lepton channel is also tested in a combination with the same mechanism but in the two leptons plus two jets channel [36].

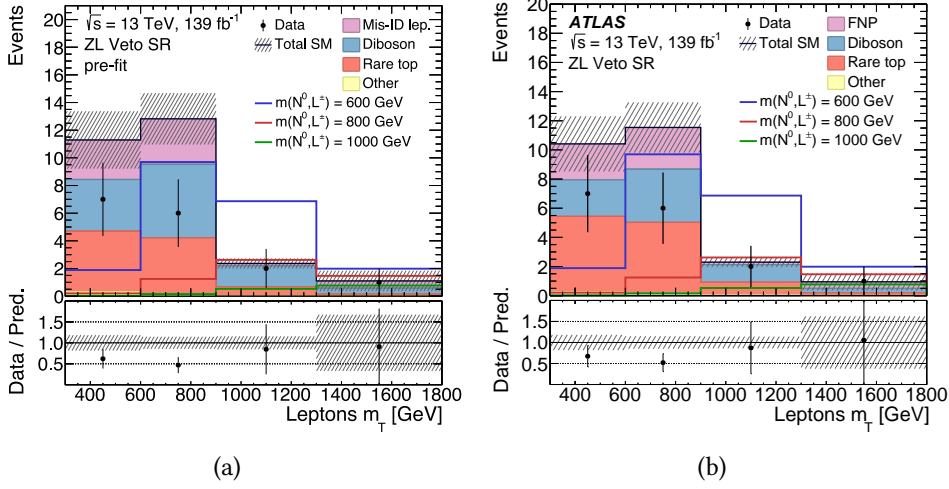


Figure 5.50: Pre- (left) and post-fit (right) distributions of $m_{T,3\ell}$ in ZL Veto SR in 5.50a and 5.50b. The uncertainty bands include both statistical and systematic uncertainties after the background-only fit taking into account all the correlation. The post-fit distribution in 5.50b was published in [216].

All the analysis regions with the various lepton multiplicity regions are statistically independent and orthogonal. The same object definitions, fake leptons estimation (except the low- p_T regions and the at least 1 jet phase-space which are not accounted in the two-lepton channel) and systematic uncertainties are used in the two analyses. For the two-lepton final states, six analysis channels depending on lepton flavour (ee , $\mu\mu$, $e\mu$) and charge combination (OS,SS) are defined. All regions used in the dilepton analysis, with the corresponding selection criteria, are summarised in Table 5.19. The signal sensitivity is optimised independently among OS and SS channels, as the background compositions and

	OS ($\ell^+\ell^- = e^+e^-, e^\pm\mu^\mp, \mu^+\mu^-$)			SS ($\ell^\pm\ell^\pm = e^\pm e^\pm, e^\pm\mu^\pm, \mu^\pm\mu^\pm$)		
	Top CR	m_{jj} VR	SR	Diboson CR	m_{jj} VR	SR
$N(\text{jet})$	≥ 2	≥ 2	≥ 2	≥ 2	≥ 2	≥ 2
$N(b\text{-jet})$	≥ 2	0	0	0	0	0
m_{jj} [GeV]	(60, 100)	$(35, 60) \cup (100, 125)$	(60, 100)	$(0, 60) \cup (100, 300)$	$(0, 60) \cup (100, 300)$	(60, 100)
$m_{\ell\ell}$ [GeV]	≥ 110	≥ 110	≥ 110	≥ 100	≥ 100	≥ 100
$\mathcal{S}(E_T^{\text{miss}})$	≥ 5	≥ 10	≥ 10	≥ 5	≥ 5	≥ 7.5
$\Delta\phi(E_T^{\text{miss}}, \ell)_{\min}$	—	—	≥ 1	—	—	—
$p_T(jj)$ [GeV]	—	—	≥ 100	—	—	≥ 60
$p_T(\ell\ell)$ [GeV]	—	—	≥ 100	—	—	≥ 100
$H_T + E_T^{\text{miss}}$ [GeV]	≥ 300	≥ 300	≥ 300	(300, 500)	≥ 500	≥ 300

Table 5.19: Summary of the selection criteria used to define analysis regions in the two-lepton channel [36].

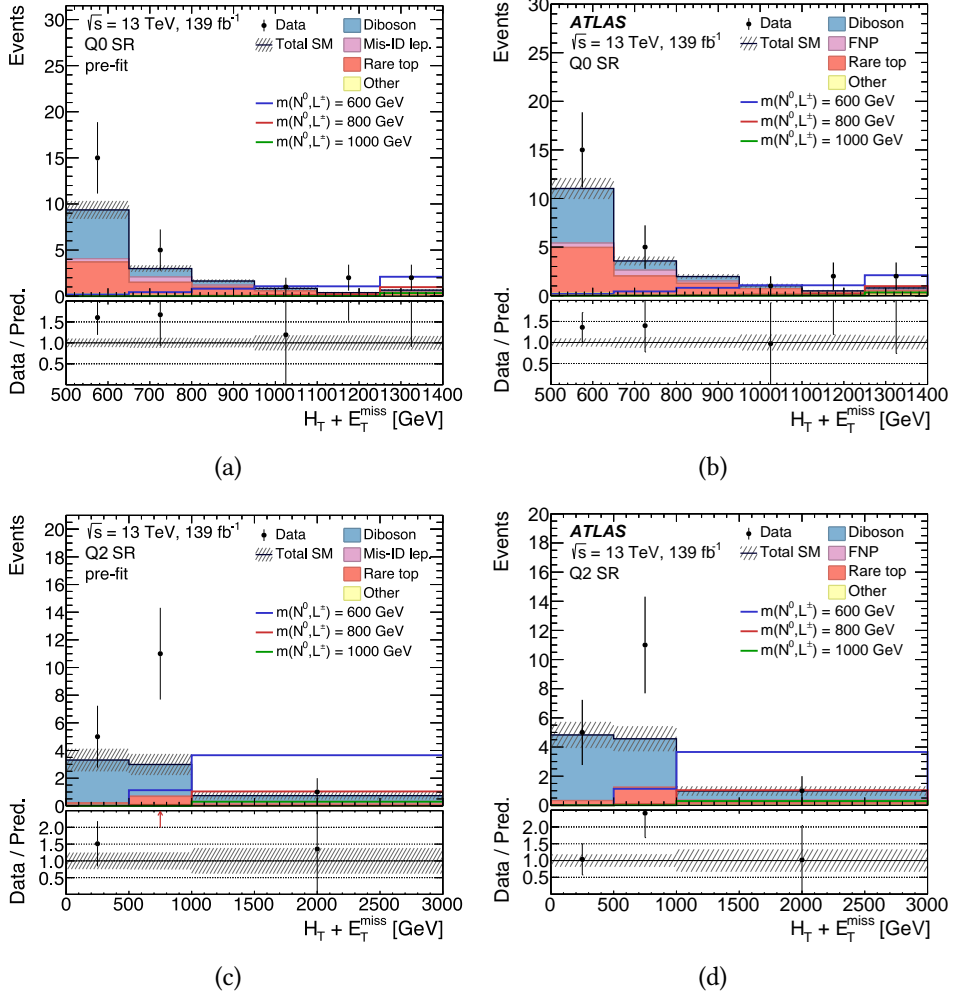


Figure 5.51: Pre- (left) and post-fit (right) distributions of $H_T + E_T^{\text{miss}}$ in Q0 SR in 5.51a and 5.51b and in Q2 SR in 5.51c and in 5.51d. The uncertainty bands include both statistical and systematic uncertainties after the background-only fit taking into account all the correlation. The post-fit distributions in 5.51b and 5.51d were published in [216].

associated event topologies are different. Due to the presence of neutrinos in the final states, one of the most important requirement is based on the $\mathcal{S}(E_T^{\text{miss}})$ which must be larger than 10 for the OS channels and than 7.5 for the SS ones.

All jets passing the selection criteria must not be b -jets to suppress the top quark processes. Since signal candidates are expected to be produced by a W boson, the dijet invariant mass is imposed in the window $60 \text{ GeV} < m_{jj} < 100 \text{ GeV}$, considering the two leading jets.

Drell-Yan events can affect greatly affect this analysis, leading also a large

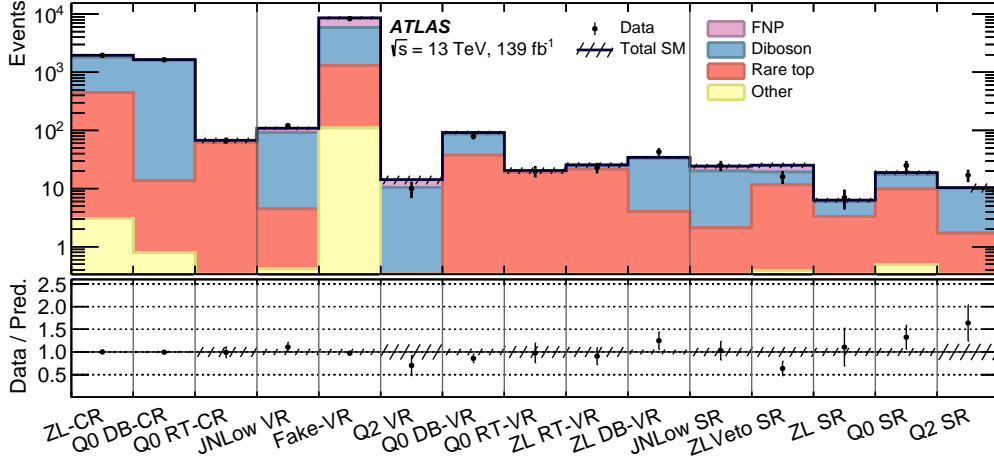


Figure 5.52: Observed and expected event yields the CRs, VRs and SRs for the three- and four-lepton channels after the fit procedure described in the text. Diboson indicates background from diboson processes. Rare top indicates background from $t\bar{t}+V$ and tWZ processes. Other indicates all other background that contribute less than 2%. The hatched bands include systematic uncertainties with the correlations between various sources taken into account and also statistical uncertainty. The lower panel shows the ratio of the observed data to the predicted SM background after the likelihood fit [216].

contribution of charge-flip electron. For this reason, a lower bound on the invariant mass of the lepton pair is set to 110 GeV and 100 GeV in the OS and SS region, respectively.

Diboson (WW) and $t\bar{t}$ processes are reduced in the OS SR by looking at the angle $\Delta\phi(E_T^{\text{miss}}, \ell)_{\text{min}}$ between the directions of E_T^{miss} and the closest lepton, which ensure a good separation between signal and background events. This selection operates well in this region due to the spurious component of misreconstructed jets coming from WW and $t\bar{t}$ events.

Additional cuts of dijet and dilepton p_T are applied to further increase the expected signal significance looking for high-energy phase-space. For this purpose, also a requirement on the $H_T + E_T^{\text{miss}} > 300$ GeV is imposed to account the high- p_T activity of the neutrinos.

The dominant contributions in the two leptons plus two jets analysis are $t\bar{t}$ production which produces two W bosons decaying leptonically, and diboson events mainly due to WW processes where at least one of the EW boson decays into a lepton-neutrino pair. In the OS channel $t\bar{t}$ is almost 50% of the total, while in the SS is at the level of 25%. This source of background is estimated in a dedicated OS CR (Top CR), requiring only b -jets in the final states to ensure orthogonality with respect to the OS SR. Other cuts applied in the SR are omit-

ted to increase the statistical significance, except the $\mathcal{S}(E_T^{\text{miss}})$ which is relaxed to $\mathcal{S}(E_T^{\text{miss}}) > 5$. The SS Diboson CR is defined to constrain the WW contribution by requiring zero b -jets to suppress the top quark events and an $H_T + E_T^{\text{miss}}$ value in the 300-500 GeV interval. To remove events with a Z boson, the invariant mass of the lepton pair must be larger than 100 GeV. The diboson contribution is slightly less than the $t\bar{t}$ one in the OS SR (about 45%) and more than half (55%) of the total in the SS SR.

In addition to the background contributions described in the three- and four-lepton analysis, also $t\bar{t}$ events and WW processes are considered as floating parameters in the fit procedure. The former is normalised in the OS Top CR, while the latter in the SS Diboson CR. The RareTop background is a minor background for this analysis, and it is included into the *other* category. All the two-lepton regions use $H_T + E_T^{\text{miss}}$ as fit variable due to its higher discriminating power. The fitted normalization factors with their corresponding uncertainties are listed in Table 5.20. Event yields after the likelihood fitting procedure for all the analysis

Normalization Factor	μ_{norm}
diboson-2l	1.03 ± 0.19
$t\bar{t}$	0.96 ± 0.02

Table 5.20: A table listing the normalisation factors with the corresponding uncertainty for normalisation of the floating MC contributions, as extracted from the background-only fit for the separate lepton multiplicity channels, three and four.

regions in the two-lepton plus two jets channels are shown in Figure 5.58, while in Appendix A.6, the post-fit SRs distributions of this analysis are reported.

With this implementation, this is the first analysis which shows an exclusion limit considering all the most important decay modes of the Type-III SeeSaw heavy leptons. The combined exclusion limit is shown in Figure 5.59. The observed (expected) exclusion limit is 910 GeV (960_{-90}^{+90} GeV) [216]. In Appendix A.7, pull and ranking plots and exclusion limits obtained with toys for this combined fit are reported.

The results of this analysis, together with the combination of those obtained by the dilepton channel search [36], were already published in June 2021 [216].

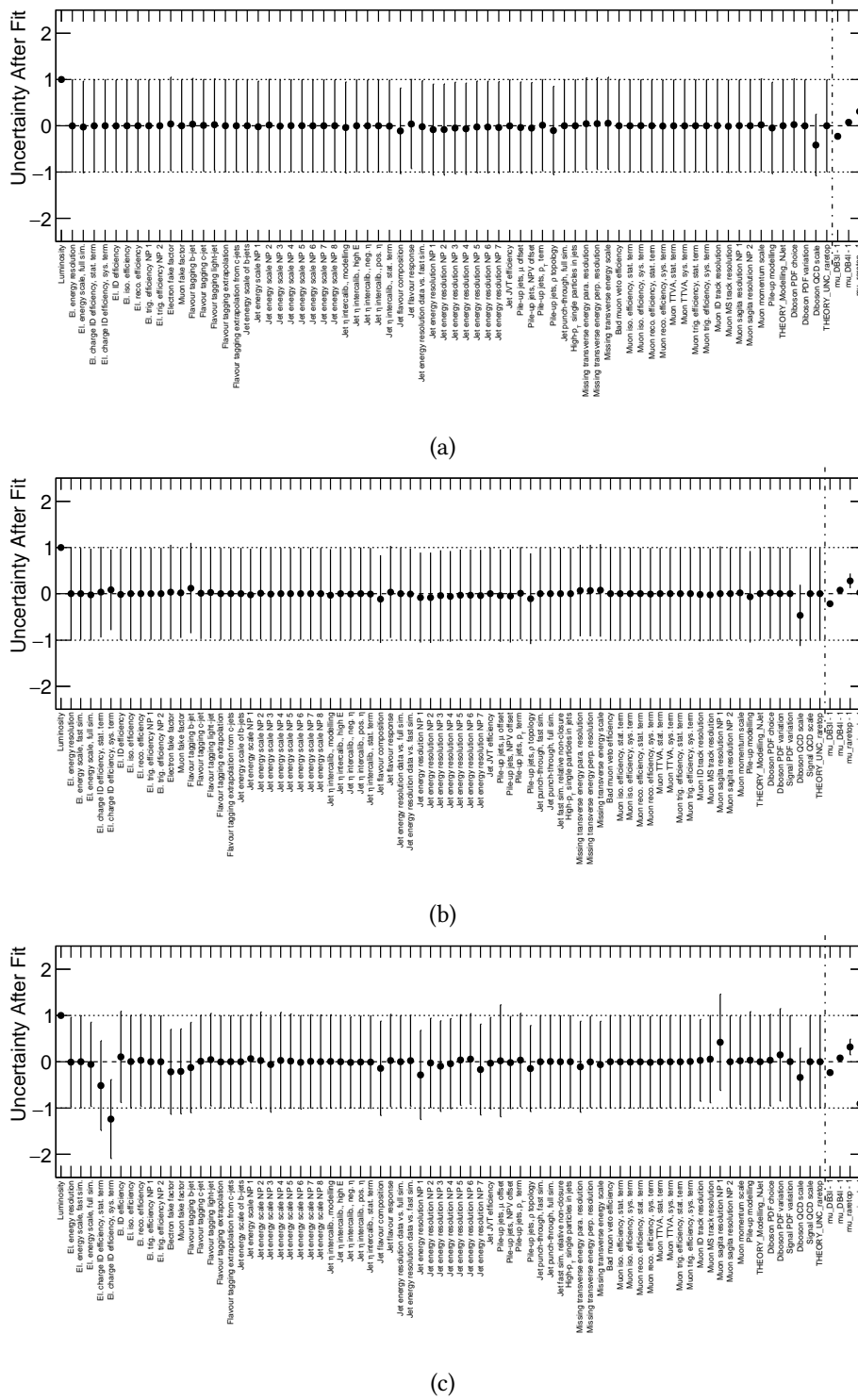


Figure 5.53: Post-fit nuisance parameters of the background-only fit with real data in control regions 5.53a, exclusion fit with Asimov dataset 5.53b and exclusion fit with real data in both control and signal regions 5.53c. These plots are related to the combined fit with three and four leptons. 182

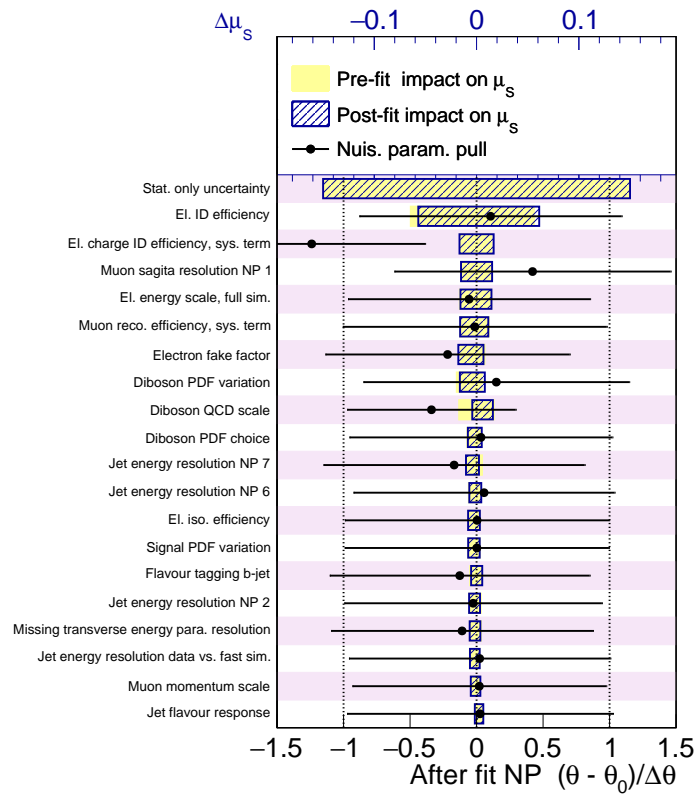


Figure 5.54: Impact of MC statistical uncertainty and systematic uncertainties on μ_{SIG} constructed by fixing one nuisance parameter to its $\pm 1\sigma$ variations at the time and minimizing the rest. Pre-fit impact are shown with a yellow box, post-fit with a dashed blue box while α with black points. This plot is related to the combined fit with three and four leptons.

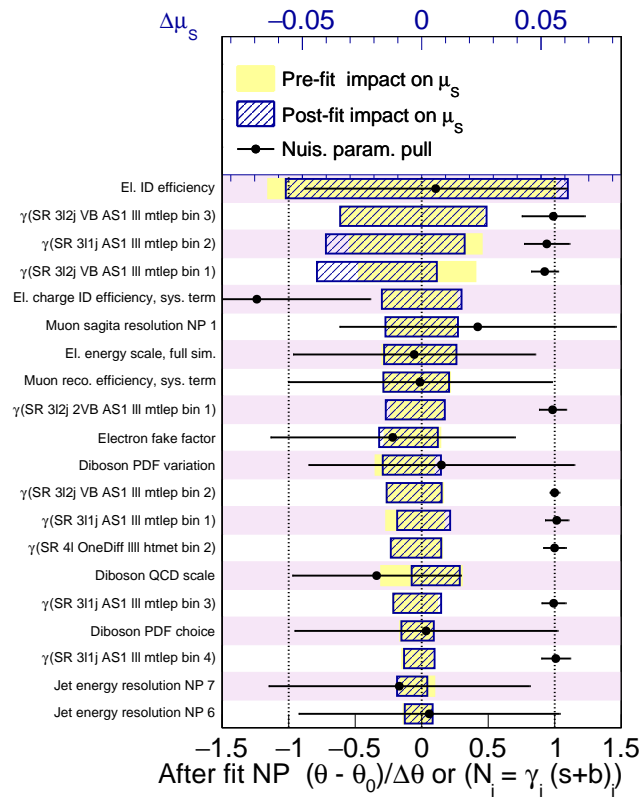


Figure 5.55: Gamma parameters corresponding to each bin in the analysis regions and impact of systematic uncertainties on μ_{SIG} constructed by fixing one nuisance parameter to its $\pm 1\sigma$ variations at the time and minimizing the rest. Pre-fit impact are shown with a yellow box, post-fit with a dashed blue box while α with black points. This plot is related to the combined fit with three and four leptons

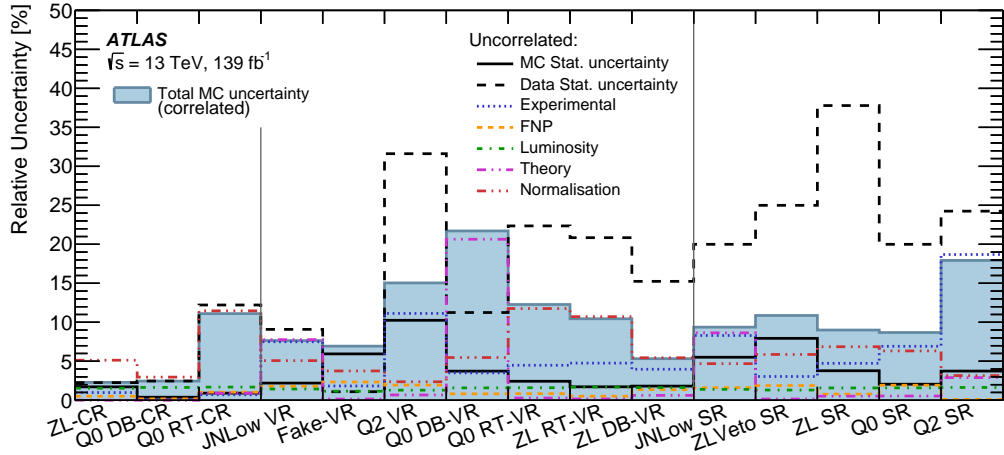


Figure 5.56: Relative contributions of different sources of statistical and systematic uncertainty in the total background yield estimates after the fit. *Experimental* uncertainties are related to the lepton, jet and E_T^{miss} selection and reconstruction. *Misidentified leptons* are related to the FNP and lepton charge misidentification. *Luminosity* is related to the luminosity uncertainty that affect the background simulation yields. *Theory* affects the theoretical uncertainties connected to the theory uncertainties like PDF, α_s , normalization and factorization scale. *Normalization* is related to the diboson and rare top normalization factor extracted by the likelihood fit. Systematic uncertainties are calculated in an uncorrelated way by changing each nuisance parameter from its fit value by one standard deviation, keeping all the other parameters at their central values, and comparing the resulting event yield with the nominal yield. Individual uncertainties can be correlated, and do not necessarily add in quadrature to the total background uncertainty, which is indicated by 'Total uncertainty' [216].

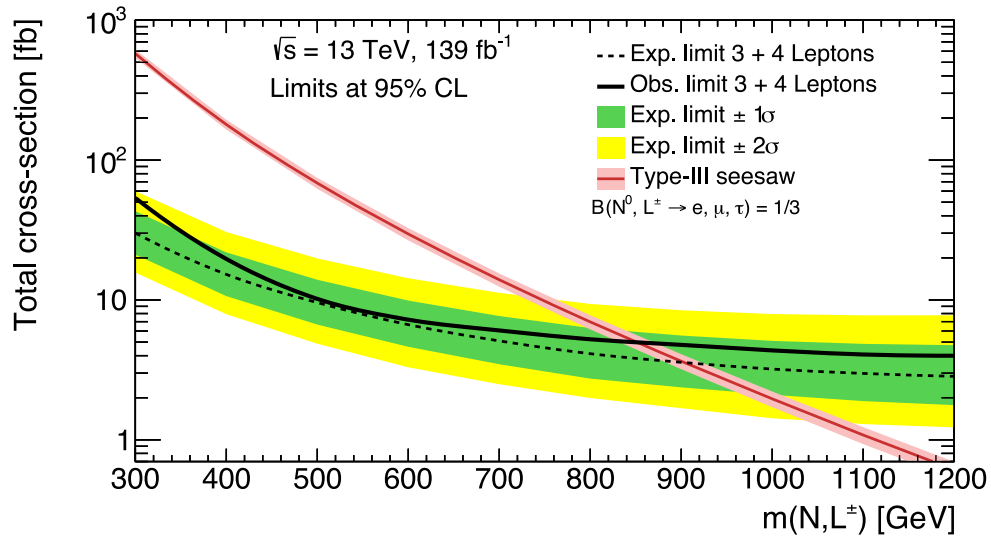


Figure 5.57: Expected and observed 95% CLs exclusion limits in the three- and four-lepton channels for the Type-III SeeSaw process with the corresponding one- and two-standard-deviation uncertainty bands, showing the 95% CL upper limit on the cross-section. The theoretical signal cross-section prediction, given by the NLO calculation, with its corresponding uncertainty band is also shown.

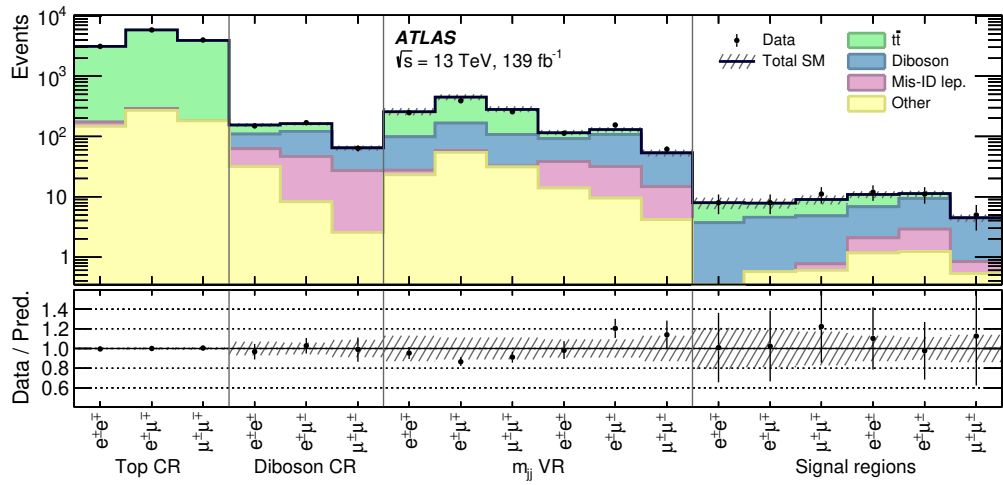


Figure 5.58: Observed and expected event yields the CRs, VRs and SRs for the two-lepton plus two jets channel after the fit procedure described in the text. Regions are divided per flavour and electric charge combination. Diboson indicates background from diboson processes (WW), while $t\bar{t}$ considers $t\bar{t}$ pair production in which the two W bosons in the final state decay leptonically. Other indicates all other background that contribute less than 2%. The hatched bands include systematic uncertainties with the correlations between various sources taken into account and also statistical uncertainty. The lower panel shows the ratio of the observed data to the predicted SM background after the likelihood fit [36].

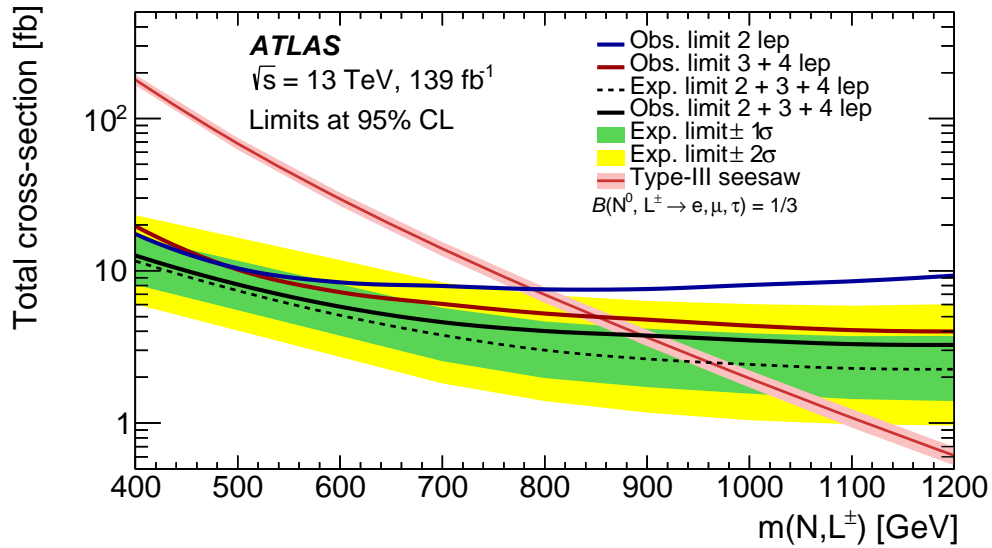


Figure 5.59: Expected and observed 95% CLs exclusion limits in the two (from [36]), three- and four-lepton channels for the Type-III SeeSaw process with the corresponding one- and two-standard-deviation uncertainty bands, showing the 95% CL upper limit on the cross-section. The theoretical signal cross-section prediction, given by the NLO calculation, with its corresponding uncertainty band is also shown [216].

Conclusions

Neutrino physics presents some of the biggest puzzles yet to be addressed in modern particle physics. The Standard Model (SM) of particle physics does not contain massive neutrinos, while experiments observed neutrino flavour oscillations implying non-null masses for these particles. Their extremely small masses compared to the ones of the other fermions appear unnatural in the theory.

In this context, the Type-III SeeSaw is one of the most reliable Beyond the Standard Model mechanism aiming to accommodate in a natural way the smallness of the neutrinos masses. It introduces at least one extra heavy fermionic $SU(2)_L$ triplet field coupled to electroweak gauge bosons that is expected to be produced by electroweak processes at the LHC energy.

The analysis presented in this thesis describes the search for these heavy leptons using data collected by the ATLAS detector during the full Run 2 period at a $\sqrt{s} = 13$ TeV, corresponding to an integrated luminosity of 139 fb^{-1} . This work targets final states with three and four light leptons (electrons and muons) and large energy produced by the collision, which have low contribution from SM events and low systematic uncertainties associated with objects reconstruction.

Multiple regions enriched of signal candidates are defined based on the expected signal significance, which separates heavy leptons from background events searching for energetic objects, looking at high values of kinematic observables such as $H_T + E_T^{\text{miss}}$ or invariant mass of the leptonic system. Despite the lower cross-section of the signal with respect to the SM expectations, the full Run 2 luminosity ensures a large enough number of events to be sensitive to heavy leptons masses at the TeV energy.

The main irreducible backgrounds affecting these channels are simulated through Monte Carlo generators which provide a good description of diboson events (WZ and ZZ processes) and top quarks associated with vector boson production and Higgs boson decaying leptonically. The reducible background coming from misreconstructed objects, such as leptons from wrongly reconstructed objects or electrons with wrongly reconstructed charge, is investigated via an *ad hoc* data-driven technique. Both these kinds of backgrounds are estimated and validated in specific control and validation regions.

Conclusions

All the analysis regions are considered in a statistical likelihood fit to check their compatibility with the Standard Model hypotheses. As expected, the fit procedure showed a very low contribution of systematics on the total uncertainty, which is dominated by the statistical uncertainty at the level of 15%. No significant excesses over the SM predictions are observed and a lower limit on the mass of the Type-III SeeSaw heavy leptons is set at 870 GeV at 95% of confidence level. This result is combined with the one already published by the ATLAS Collaboration, for the same model, in the two leptons plus two jets channel, showing for the first time measurements on these heavy leptons considering all the most important decay channels. In this case, the observed lower limit on the mass is 910 GeV. This is the highest exclusion limit on the Type-III SeeSaw heavy leptons masses ever observed up today.

The next LHC Run 3 will provide an integrated luminosity of about 300 fb^{-1} leading to a better precision on the presented results. In the Run 4, planned for the 2027, the collider will reach a center-of-mass energy $\sqrt{s} = 14 \text{ TeV}$, with an integrated luminosity of about 4000 fb^{-1} , opening the possibility to explore uncovered phase-space regions and allowing to improve the current exclusion limit and its uncertainties.

The analysis sensitivity can be further increased with the implementation of hadronic tau decays in the final states, which needs an additional background estimation to separate such processes from standard hadronic jets, with a consequently extension of the considered topologies and heavy leptons branching ratios.

The analysis can also benefit by the usage of new techniques based on a multivariate approach. Using these methods instead of the cut-and-count one, several requirements can be reduced increasing the signal contribution while rejecting more background events. With these machine learning (MLs) algorithms or multiple neural networks (NNs), final states would be individually optimised by dedicated NNs or ML methods, improving the analyses sensitivity to new physics phenomena and reducing, even more, the uncertainties on the measure.

Appendix A

Analysis details

A.1 Fake Lepton Composition	192
A.2 Systematics Tables	201
A.3 Post-fit distributions	210
A.4 Cutflows	226
A.5 Results for separated channels	236
A.6 Signal regions post-fit distributions Dilepton channel	243
A.7 Pull and ranking plots, and exclusion limit with toys for the combined fit with two-, three- and four-lepton channels	246

In this Appendix a series of additional results related to the analysis described in Chapter 5, are presented:

- Fake Lepton Composition in Section [A.1](#);
- Systematics tables showing the impact of each systematic in each analysis region in Section [A.2](#);
- Post-fit distribution of several observables in Section [A.3](#);
- Cutflow tables in Section [A.4](#);
- Separated results obtained studying independently the three- and four-leptons channels in Section [A.5](#);
- Systematic uncertainties and exclusion limit with toys for the combination of the two-, three- and four lepton channels in Section [A.7](#).

A.1 Fake Lepton Composition

Fake composition can be studied for the fake enriched regions and the analysis regions to ensure compatibility between them. The fake composition can be studied analysing the origin of the fake leptons in Monte Carlo simulation through truth particle information.

In this Appendix, the fake composition for both electrons and muons and for each fake-enriched CR and analysis region is shown. Fake lepton background can be classified in the following categories:

- Unknown or KnownUnknown lepton;
- Prompt isolated electron: which includes also electron that originates from an FSR photon (or bremsstrahlung) that subsequently converted;
- Charge-Flip Isolated Electron, where electrons originating from FSR are excluded;
- Prompt muon;
- Prompt photon conversion: categorizes electrons originating from the conversion of prompt photons if it corresponds to background electron and it originates from a photon conversion or an electromagnetic process;
- Electron from Muon: an electron is classified as a muon being reconstructed as electron if the truth-type of the electron corresponds to a non-isolated electron or photon;
- Tau decay: non-isolated electrons and muons from hadronic τ -decays;
- b -Hadron decay;
- c -Hadron decay;
- Light-Flavor decay.

The fake composition of the electron and muon fake estimation region is shown in Figures A.1 and A.2, respectively. Analysis regions composition are shown in Figure A.3-A.8, in some regions only electrons or muons are present as fake leptons. In the ZL Regions SR and the Q2 VR, fake events are not enough to perform studies on the fake composition.

The main sources of fake leptons in both fake enriched CRs and analysis regions are light hadron and b -hadron decays. The dominant contribution of fake leptons is due to dijet, $t\bar{t}$ and single-top events.

Analysis regions match well with the fake estimation composition since a very small fraction of events come from categories not accounted by the fake enriched CRs. It is also important to look at the statistical uncertainty in some plots which implicitly indicates the small contribution of fake leptons.

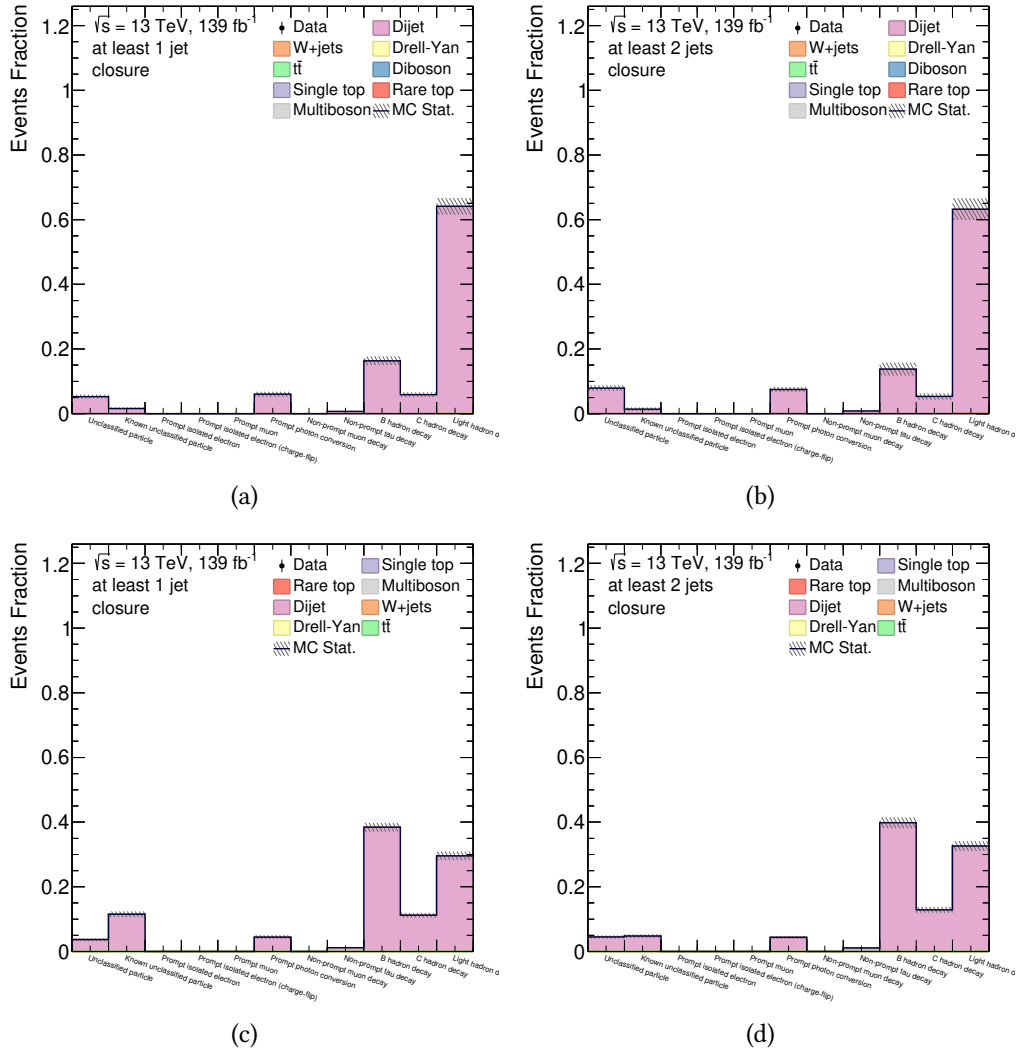


Figure A.1: Fake composition of the electron fake-factor estimation regions for: high- p_T at least 1 jet region [A.1a](#), high- p_T at least 2 jets region [A.1b](#), low- p_T at least 1 jet region [A.1c](#), low- p_T at least 2 jets region [A.1c](#).

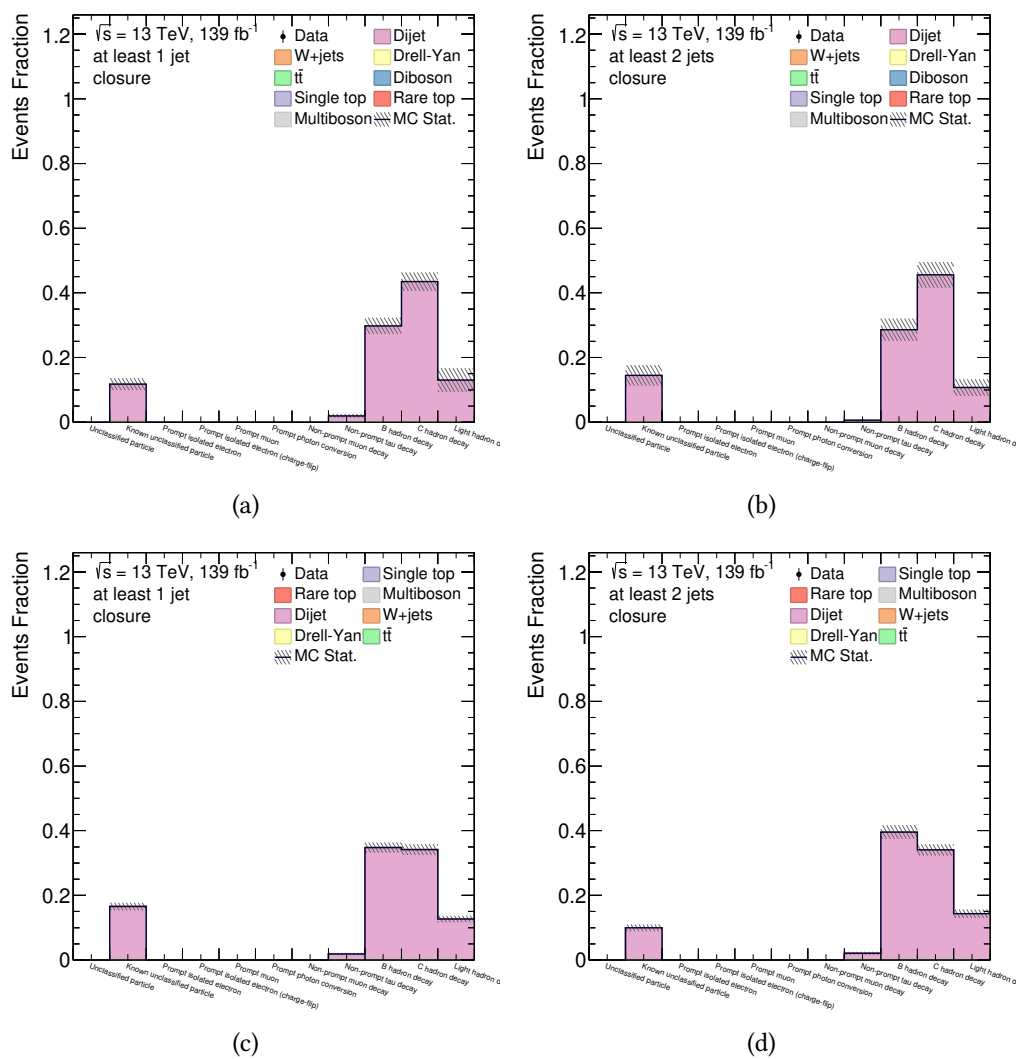


Figure A.2: Fake composition of the muon fake-factor estimation regions for: high- p_T at least 1 jet region A.2a, high- p_T at least 2 jets region A.2b, low- p_T at least 1 jet region A.2c, low- p_T at least 2 jets region A.2d.

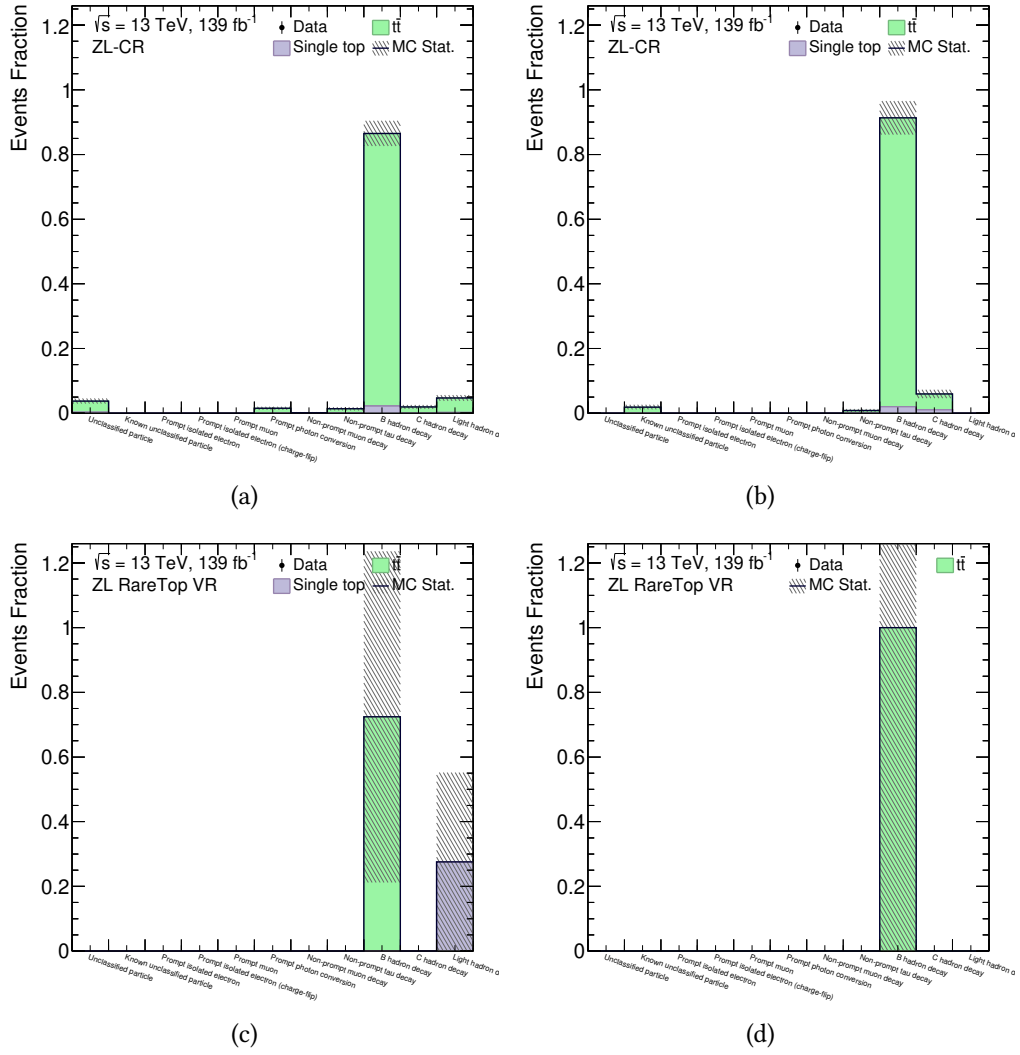


Figure A.3: Fake composition of the ZL CR on the top for fake electrons in A.3a and fake muons in A.3b, and of the ZL-RT-VR on the bottom for fake electrons in A.3c and fake muons in A.3d.

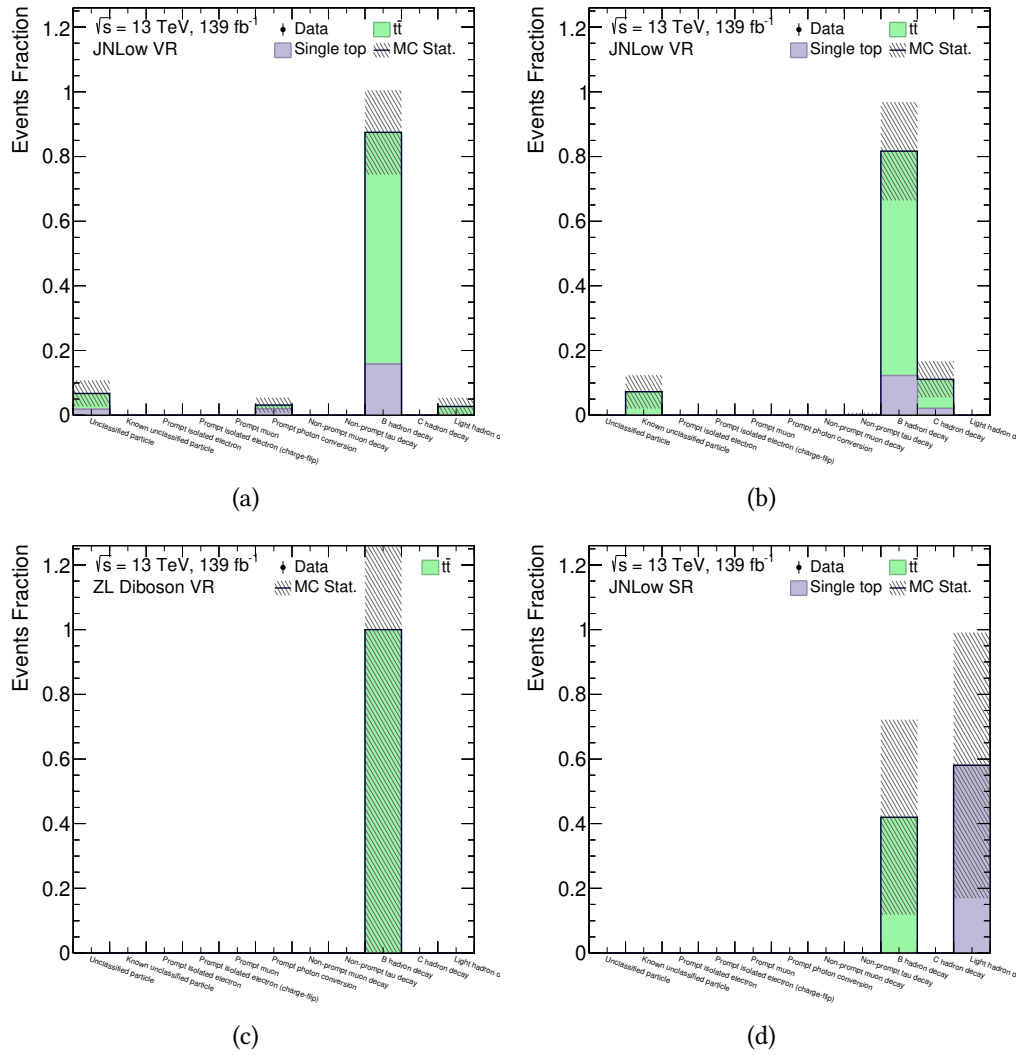


Figure A.4: Fake composition of the JNLow VR on the top for fake electrons in A.4a and fake muons in A.4b. On the bottom, electrons fake composition for both ZL-DB-VR in A.4c and JNLow SR in A.4d.

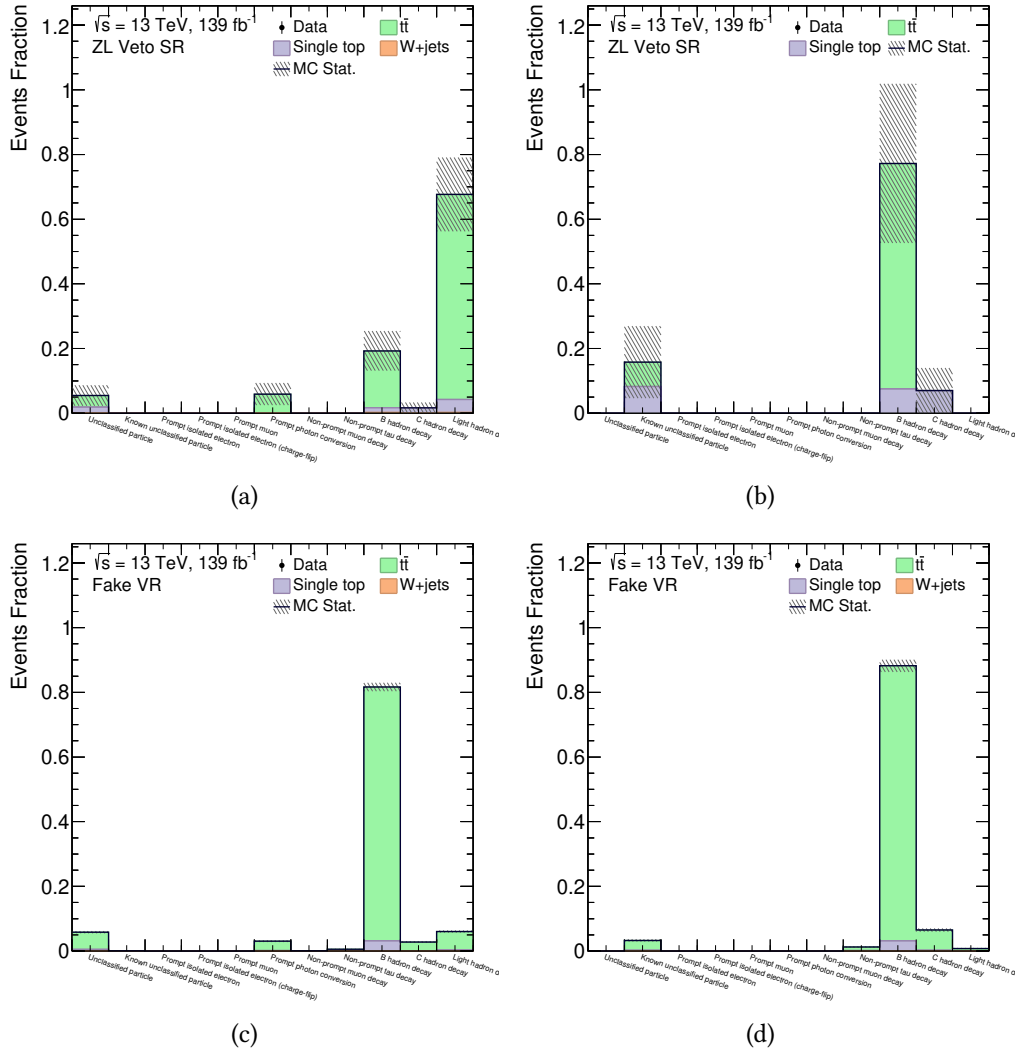


Figure A.5: Fake composition of the ZL Veto SR on the top for fake electrons in A.5a and fake muons in A.5b, and of the Fakes VR on the bottom for fake electrons in A.5c and fake muons in A.5d.

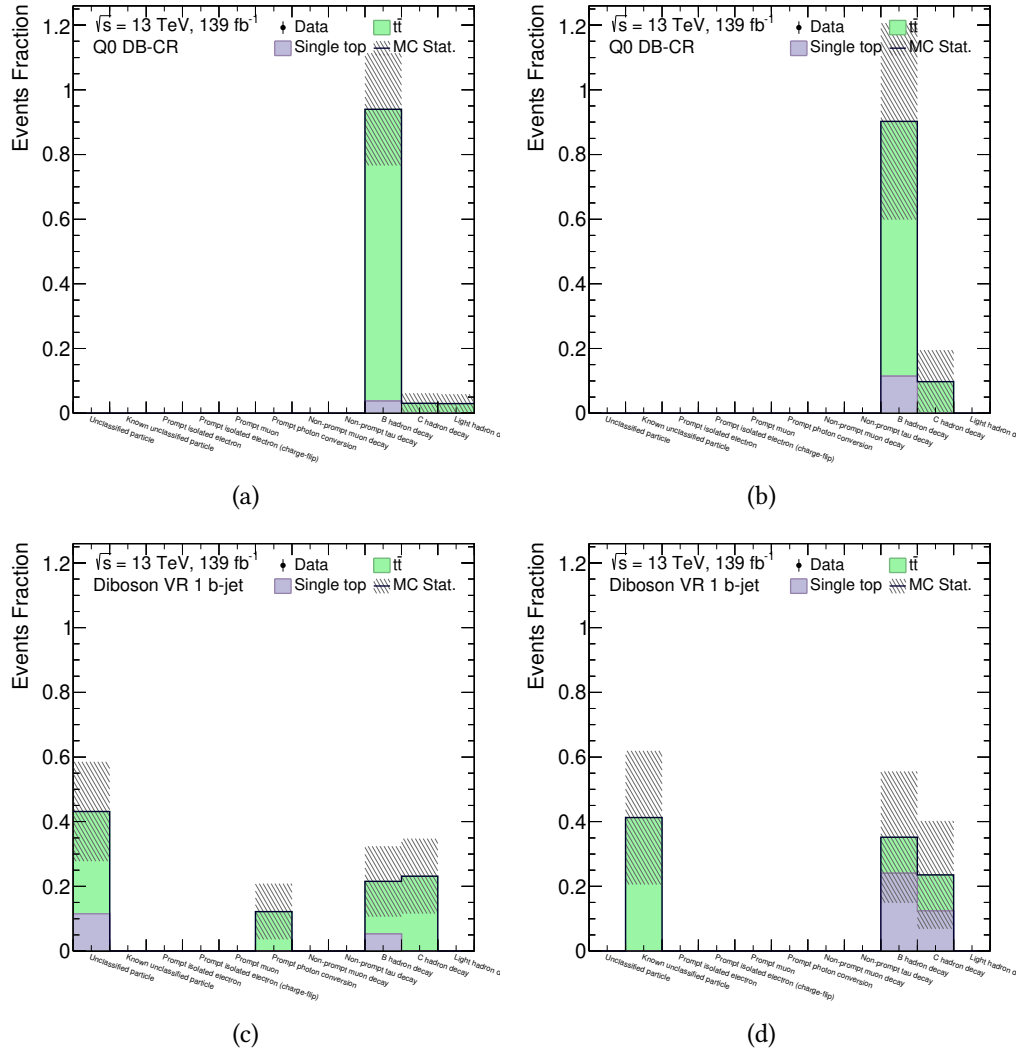


Figure A.6: Fake composition of the Q0 Diboson CR on the top for fake electrons in A.6a and fake muons in A.6b, and of the Q0 Diboson VR on the bottom for fake electrons in A.6c and fake muons in A.6d.

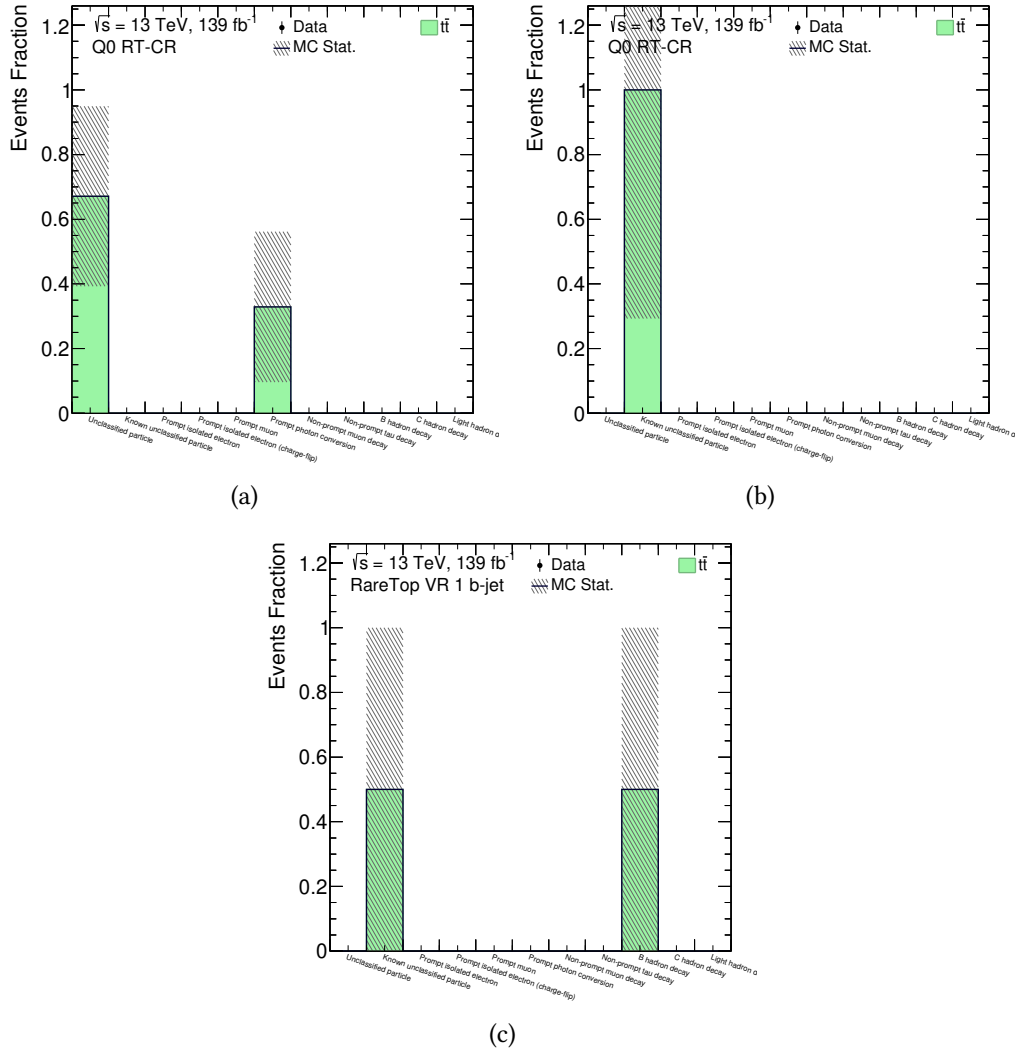


Figure A.7: Fake composition of the Q0 RareTop CR on the top for fake electrons in A.7a and fake muons in A.7b, and of the Q0 RareTop VR on the bottom for fake muons in A.7c.

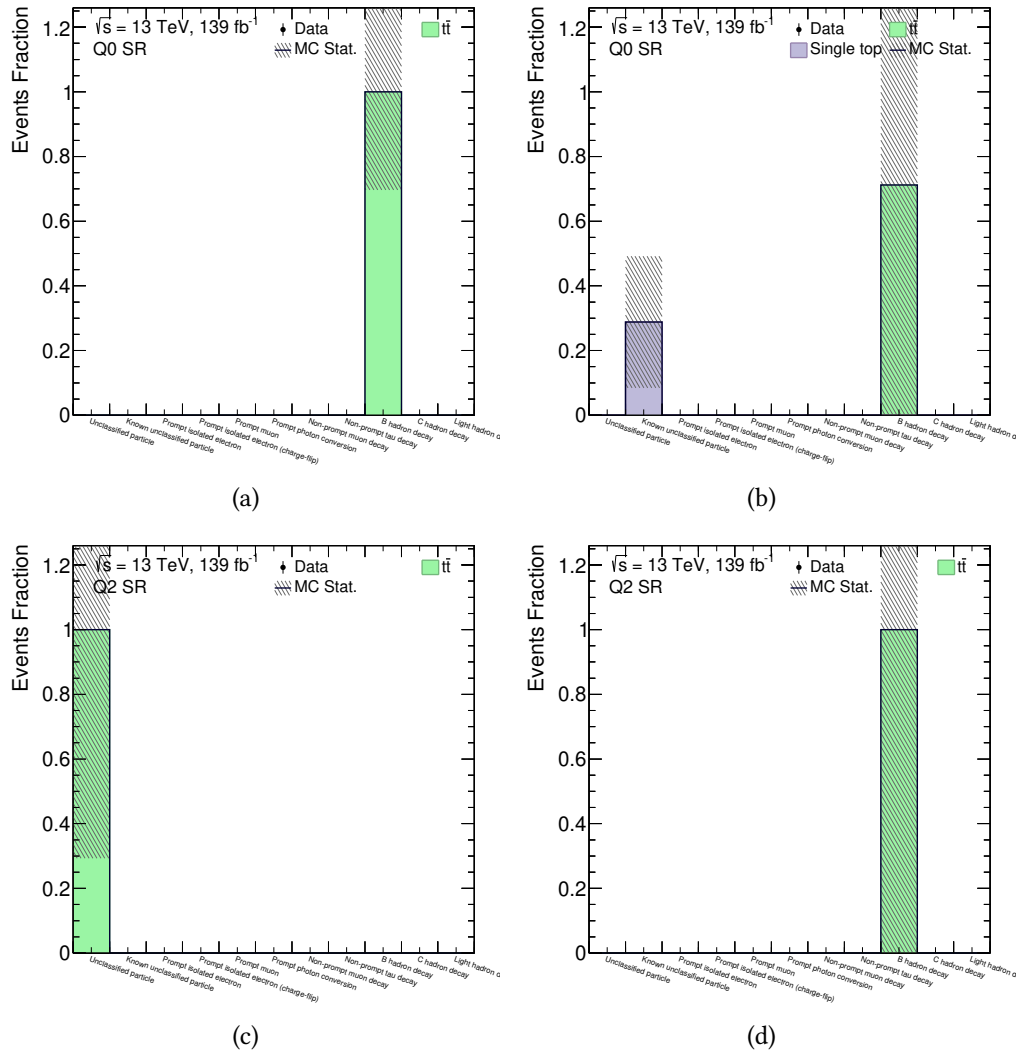


Figure A.8: Fake composition of the Q0 SR on the top for fake electrons in A.8a and fake muons in A.8b, and of the Q2 SR on the bottom for fake electrons in A.8c and fake muons in A.8d.

A.2 Systematics Tables

The magnitudes of systematic and normalisation uncertainties after the background-only fit are summarised for all the regions in Tables [A.2](#) - [A.5](#). Uncertainties in these tables correspond to categories (reported in the first column of each table) in Table [A.1](#).

Category	Type	Label
Luminosity		Lumi
Pile-up reweighting		PileUp
Theory uncertainties	SHERPA 2.2.1 QCD scale variation SHERPA 2.2.1 PDF variation SHERPA 2.2.1 PDF choice Diboson Njet Modelling Rare Top ttW/ttZ	THEORY_SCALE_diboson THEORY_PDF_VARIATION_diboson THEORY_PDF_CHOICE_diboson THEORY_Modelling_NJet THEORY_UNC_raretop
Data-driven background	Electron fake factors Muon fake factors	FAKES_Electron FAKES_Muons
Electron calibration	Resolution Momentum scale Momentum scale (AF2)	EG_RESOLUTION_ALL EG_SCALE_ALL EG_SCALE_AF2
Electron efficiencies	ID Reconstruction Isolation Trigger Charge-flip Charge-flip (stat.)	EL_EFF_ID_TOTAL_1NPCOR_PLUS_UNCOR EL_EFF_Reco_TOTAL_1NPCOR_PLUS_UNCOR EL_EFF_Iso_TOTAL_1NPCOR_PLUS_UNCOR EL_EFF_Trig_TOTAL_1NPCOR_PLUS_UNCOR EL_CHARGEID_SYStotal EL_CHARGEID_STAT
Muon calibration	Smearing of the ID track Smearing of the MS track Momentum scale Momentum scale based on the recombination of the corrections Momentum scale based on residual charge-dependent bias	MUON_ID MUON_MS MUON_SCALE MUON_SAGITTA_RHO MUON_SAGITTA_RESBIAS
Muon efficiencies	Reconstruction Reconstruction (stat.) Isolation Isolation (stat.) TTVA TTVA (stat.) Trigger Trigger (stat.)	MUON_EFF_RECO_SYS MUON_EFF_RECO_STAT MUON_EFF_ISO_SYS MUON_EFF_ISO_STAT MUON_EFF_TTVA_SYS MUON_EFF_TTVA_STAT MUON_EFF_TrigStatUncertainty MUON_EFF_TrigSystUncertainty
Jet calibration	Jet energy scale Jet energy resolution	JET_* JET_JER*
Jet efficiencies	JVT Flavour tagging	JET_JvtEfficiency FT_EFF_B_systematics FT_EFF_C_systematics FT_EFF_Light_systematics FT_EFF_extrapolation FT_EFF_extrapolation_from_charm
E_{Γ}^{miss} soft track	Offset along the pt_{Hard} axis Smearing by resolution uncertainty along pt_{Hard} axis Smearing by resolution uncertainty perpendicular to pt_{Hard} axis	MET_SoftTrk_Scale MET_SoftTrk_ResoPara MET_SoftTrk_ResoPerp

Table A.1: Summarised list of all used systematic uncertainties with the corresponding name as α variables.

Systematics Tables

Analysis details

Uncertainty of channel	JNLow VR	ZL CR	Fakes VR
Total background expectation	111.94	1959.75	8540.56
Total statistical ($\sqrt{N_{\text{exp}}}$)	± 10.58	± 44.27	± 92.42
Total background systematic	± 8.91 [7.96%]	± 44.28 [2.26%]	± 595.93 [6.98%]
alpha_THEORY_SCALE_diboson	± 8.93 [8.0%]	± 0.01 [0.00%]	± 3.39 [0.04%]
mu_DB3l	± 5.84 [5.2%]	± 87.36 [4.5%]	± 291.29 [3.4%]
alpha_JET_Pileup_RhoTopology	± 4.57 [4.1%]	± 2.02 [0.10%]	± 17.26 [0.20%]
alpha_JET_Flavor_Composition	± 3.90 [3.5%]	± 1.59 [0.08%]	± 29.13 [0.34%]
alpha_JET_Flavor_Response	± 2.45 [2.2%]	± 0.49 [0.03%]	± 43.21 [0.51%]
alpha_JET_JER_EffectiveNP_4	± 1.80 [1.6%]	± 2.99 [0.15%]	± 24.72 [0.29%]
alpha_JET_JER_EffectiveNP_2	± 1.78 [1.6%]	± 5.78 [0.30%]	± 50.66 [0.59%]
alpha_FAKES_Electron	± 1.70 [1.5%]	± 12.48 [0.64%]	± 208.91 [2.4%]
alpha_JET_Pileup_OffsetNPV	± 1.65 [1.5%]	± 0.72 [0.04%]	± 14.30 [0.17%]
Lumi	± 1.60 [1.4%]	± 30.18 [1.5%]	± 98.28 [1.2%]
alpha_JET_JER_EffectiveNP_7restTerm	± 1.55 [1.4%]	± 3.17 [0.16%]	± 29.34 [0.34%]
alpha_JET_EffectiveNP_1	± 1.52 [1.4%]	± 0.05 [0.00%]	± 22.46 [0.26%]
alpha_JET_JER_EffectiveNP_6	± 1.42 [1.3%]	± 2.78 [0.14%]	± 26.49 [0.31%]
alpha_FAKES_Muon	± 1.36 [1.2%]	± 12.35 [0.63%]	± 143.71 [1.7%]
alpha_JET_JER_EffectiveNP_5	± 1.30 [1.2%]	± 2.05 [0.10%]	± 22.47 [0.26%]
alpha_JET_EtaIntercalibration_Modelling	± 1.23 [1.1%]	± 0.59 [0.03%]	± 9.90 [0.12%]
alpha_JET_JER_EffectiveNP_3	± 1.07 [0.95%]	± 3.70 [0.19%]	± 21.34 [0.25%]
alpha_PRW_DATASF	± 0.92 [0.82%]	± 1.35 [0.07%]	± 15.66 [0.18%]
alpha_JET_JER_EffectiveNP_1	± 0.77 [0.69%]	± 4.13 [0.21%]	± 50.03 [0.59%]
alpha_THEORY_PDF_CHOICE_diboson	± 0.53 [0.48%]	± 0.00 [0.00%]	± 12.91 [0.15%]
mu_raretop	± 0.52 [0.46%]	± 56.29 [2.9%]	± 156.17 [1.8%]
alpha_MET_SoftTrk_ResoPara	± 0.49 [0.44%]	± 2.99 [0.15%]	± 53.71 [0.63%]
alpha_MUON_SAGITTA_RESBIAS	± 0.49 [0.44%]	± 0.04 [0.00%]	± 0.04 [0.00%]
alpha_JET_JvtEfficiency	± 0.45 [0.40%]	± 0.98 [0.05%]	± 3.30 [0.04%]
alpha_JET_Pileup_OffsetMu	± 0.38 [0.34%]	± 0.45 [0.02%]	± 7.96 [0.09%]
alpha_JET_EffectiveNP_2	± 0.37 [0.33%]	± 0.38 [0.02%]	± 4.98 [0.06%]
alpha_JET_JER_DataVsMC_MC16	± 0.36 [0.32%]	± 0.99 [0.05%]	± 9.57 [0.11%]
alpha_MET_SoftTrk_ResoPerp	± 0.34 [0.30%]	± 2.38 [0.12%]	± 54.89 [0.64%]
alpha_THEORY_PDF_VARIATION_diboson	± 0.33 [0.30%]	± 0.00 [0.00%]	± 3.02 [0.04%]
alpha_JET_EtaIntercalibration_TotalStat	± 0.30 [0.27%]	± 0.00 [0.00%]	± 1.89 [0.02%]
alpha_MUON_SCALE	± 0.27 [0.24%]	± 0.12 [0.01%]	± 4.58 [0.05%]
alpha_MUON_ID	± 0.23 [0.21%]	± 0.13 [0.01%]	± 0.50 [0.01%]
alpha_EL_EFF_ID_TOTAL_1NPCOR_PLUS_UNCOR	± 0.21 [0.19%]	± 3.39 [0.17%]	± 6.86 [0.08%]
alpha_MET_SoftTrk_Scale	± 0.20 [0.18%]	± 2.92 [0.15%]	± 64.43 [0.75%]
alpha_EL_CHARGEID_SYStotal	± 0.18 [0.16%]	± 0.25 [0.01%]	± 4.10 [0.05%]
alpha_JET_EffectiveNP_3	± 0.16 [0.15%]	± 0.32 [0.02%]	± 5.81 [0.07%]
alpha_EG_SCALE_ALL	± 0.15 [0.13%]	± 0.41 [0.02%]	± 1.64 [0.02%]
alpha_MUON_EFF_RECO_SYS	± 0.14 [0.13%]	± 0.43 [0.02%]	± 0.64 [0.01%]
alpha_FT_EFF_Light_systematics	± 0.14 [0.13%]	± 2.17 [0.11%]	± 9.12 [0.11%]
alpha_EG_RESOLUTION_ALL	± 0.14 [0.12%]	± 0.25 [0.01%]	± 2.25 [0.03%]
alpha_JET_EffectiveNP_4	± 0.10 [0.09%]	± 0.04 [0.00%]	± 0.86 [0.01%]
alpha_FT_EFF_B_systematics	± 0.09 [0.08%]	± 14.45 [0.74%]	± 40.15 [0.47%]
alpha_JET_Pileup_PtTerm	± 0.08 [0.07%]	± 1.01 [0.05%]	± 7.70 [0.09%]
alpha_MUON_EFF_ISO_SYS	± 0.07 [0.06%]	± 0.85 [0.04%]	± 2.86 [0.03%]
alpha_JET_EtaIntercalibration_NonClosure_posEta	± 0.06 [0.06%]	± 0.02 [0.00%]	± 0.30 [0.00%]
alpha_MUON_MS	± 0.05 [0.05%]	± 0.65 [0.03%]	± 0.50 [0.01%]
alpha_FT_EFF_C_systematics	± 0.05 [0.04%]	± 0.53 [0.03%]	± 2.12 [0.02%]
alpha_JET_EffectiveNP_8restTerm	± 0.04 [0.04%]	± 0.03 [0.00%]	± 0.70 [0.01%]
alpha_EL_EFF_Iso_TOTAL_1NPCOR_PLUS_UNCOR	± 0.04 [0.04%]	± 0.18 [0.01%]	± 0.38 [0.00%]
alpha_MUON_EFF_TTVA_SYS	± 0.04 [0.03%]	± 0.21 [0.01%]	± 0.43 [0.01%]
alpha_EL_CHARGEID_STAT	± 0.03 [0.03%]	± 0.05 [0.00%]	± 1.14 [0.01%]
alpha_MUON_EFF_TTVA_STAT	± 0.03 [0.02%]	± 0.20 [0.01%]	± 0.48 [0.01%]
alpha_MUON_EFF_TrigSystUncertainty	± 0.02 [0.02%]	± 0.76 [0.04%]	± 2.46 [0.03%]
alpha_JET_PunchThrough_MC16	± 0.02 [0.01%]	± 0.04 [0.00%]	± 0.26 [0.00%]
alpha_MUON_EFF_ISO_STAT	± 0.02 [0.01%]	± 0.11 [0.01%]	± 0.28 [0.00%]
alpha_JET_EtaIntercalibration_NonClosure_negEta	± 0.01 [0.01%]	± 0.02 [0.00%]	± 0.02 [0.00%]
alpha_FT_EFF_extrapolation	± 0.01 [0.01%]	± 0.03 [0.00%]	± 0.34 [0.00%]
alpha_JET_EffectiveNP_6	± 0.01 [0.01%]	± 0.05 [0.00%]	± 0.15 [0.00%]
alpha_JET_EffectiveNP_7	± 0.01 [0.01%]	± 0.03 [0.00%]	± 0.25 [0.00%]
alpha_JET_EffectiveNP_5	± 0.01 [0.01%]	± 0.01 [0.00%]	± 0.63 [0.01%]
alpha_FT_EFF_extrapolation_from_charm	± 0.01 [0.01%]	± 0.12 [0.01%]	± 0.17 [0.00%]
alpha_MUON_EFF_RECO_SYS_LOWPT	± 0.00 [0.00%]	± 0.32 [0.02%]	± 0.90 [0.01%]
alpha_MUON_EFF_TrigStatUncertainty	± 0.00 [0.00%]	± 0.09 [0.00%]	± 0.30 [0.00%]
alpha_EL_EFF_Trigger_TOTAL_1NPCOR_PLUS_UNCOR	± 0.00 [0.00%]	± 0.04 [0.00%]	± 0.18 [0.00%]
alpha_MUON_EFF_RECO_STAT	± 0.00 [0.00%]	± 0.12 [0.01%]	± 0.28 [0.00%]
alpha_MUON_EFF_RECO_STAT_LOWPT	± 0.00 [0.00%]	± 0.11 [0.01%]	± 0.31 [0.00%]
alpha_EL_EFF_Reco_TOTAL_1NPCOR_PLUS_UNCOR	± 0.00 [0.00%]	± 1.15 [0.06%]	± 2.78 [0.03%]
alpha_EL_EFF_TriggerEff_TOTAL_1NPCOR_PLUS_UNCOR	± 0.00 [0.00%]	± 0.00 [0.00%]	± 0.02 [0.00%]
alpha_MUON_EFF_BADMUON_SYS	± 0.00 [0.00%]	± 0.00 [0.00%]	± 0.00 [0.00%]
alpha_JET_EtaIntercalibration_NonClosure_highE	± 0.00 [0.00%]	± 0.00 [0.00%]	± 0.00 [0.00%]
mu_DB4l	± 0.00 [0.00%]	± 0.00 [0.00%]	± 0.00 [0.00%]
alpha_THEORY_Modelling_NJet	± 0.00 [0.00%]	± 0.00 [0.00%]	± 0.00 [0.00%]
alpha_JET_SingleParticle_HighPt	± 0.00 [0.00%]	± 0.00 [0.00%]	± 0.00 [0.00%]
alpha_JET_BJES_Response	± 0.00 [0.00%]	± 0.00 [0.00%]	± 0.00 [0.00%]
alpha_MUON_SAGITTA_RHO	± 0.00 [0.00%]	± 0.00 [0.00%]	± 0.00 [0.00%]

alpha_THEORY_UNC_raretop	± 0.00 [0.00%]	± 0.00 [0.00%]	± 0.00 [0.00%]
--------------------------	--------------------	--------------------	--------------------

Table A.2: Breakdown of the dominant uncertainties on background estimates. The given total statistical error is a quadratic sum of individual statistical errors of each bin in the region. Note that the individual uncertainties can be correlated, and do not necessarily add up quadratically to the total background uncertainty. Uncertainties are ordered from the largest to smallest depending by the impact on the region in the second column.

Uncertainty of channel	JNLow SR	ZLVeto SR	ZL SR
Total background expectation	24.32	25.20	6.33
Total statistical ($\sqrt{N_{\text{exp}}}$)	± 4.93	± 5.02	± 2.52
Total background systematic	± 2.28 [9.36%]	± 2.74 [10.89%]	± 0.57 [9.08%]
alpha_THEORY_SCALE_diboson	± 2.08 [8.6%]	± 0.00 [0.01%]	± 0.01 [0.14%]
alpha_JET_Flavor_Composition	± 1.31 [5.4%]	± 0.19 [0.75%]	± 0.12 [1.9%]
mu_DB3l	± 1.12 [4.6%]	± 0.48 [1.9%]	± 0.17 [2.6%]
alpha_JET_Pileup_RhoTopology	± 1.00 [4.1%]	± 0.12 [0.48%]	± 0.06 [1.0%]
alpha_JET_Flavor_Response	± 0.60 [2.5%]	± 0.27 [1.1%]	± 0.13 [2.0%]
alpha_FAKES_Electron	± 0.39 [1.6%]	± 0.41 [1.6%]	± 0.05 [0.77%]
alpha_PRW_DATASF	± 0.34 [1.4%]	± 0.14 [0.54%]	± 0.02 [0.24%]
Lumi	± 0.34 [1.4%]	± 0.33 [1.3%]	± 0.10 [1.6%]
alpha_JET_Pileup_OffsetNPV	± 0.33 [1.3%]	± 0.07 [0.26%]	± 0.05 [0.84%]
alpha_JET_EffectiveNP_1	± 0.31 [1.3%]	± 0.16 [0.62%]	± 0.07 [1.1%]
alpha_JET_EtaIntercalibration_Modelling	± 0.27 [1.1%]	± 0.04 [0.16%]	± 0.03 [0.46%]
alpha_THEORY_PDF_CHOICE_diboson	± 0.27 [1.1%]	± 0.00 [0.02%]	± 0.01 [0.13%]
alpha_JET_Pileup_OffsetMu	± 0.27 [1.1%]	± 0.06 [0.25%]	± 0.01 [0.17%]
alpha_MET_SoftTrk_ResoPara	± 0.24 [0.99%]	± 0.02 [0.09%]	± 0.02 [0.24%]
alpha_JET_JER_EffectiveNP_3	± 0.24 [0.97%]	± 0.02 [0.08%]	± 0.00 [0.06%]
alpha_JET_JER_EffectiveNP_6	± 0.23 [0.94%]	± 0.01 [0.03%]	± 0.04 [0.63%]
mu_raretop	± 0.22 [0.92%]	± 1.40 [5.6%]	± 0.40 [6.4%]
alpha_JET_JER_EffectiveNP_1	± 0.21 [0.84%]	± 0.12 [0.46%]	± 0.01 [0.20%]
alpha_EL_EFF_ID_TOTAL_1NPCOR_PLUS_UNCOR	± 0.20 [0.83%]	± 0.23 [0.91%]	± 0.03 [0.42%]
alpha_EG_SCALE_ALL	± 0.20 [0.82%]	± 0.29 [1.1%]	± 0.08 [1.2%]
alpha_JET_JER_EffectiveNP_7restTerm	± 0.20 [0.81%]	± 0.21 [0.82%]	± 0.02 [0.24%]
alpha_JET_JER_DataVsMC_MC16	± 0.19 [0.78%]	± 0.03 [0.10%]	± 0.07 [1.1%]
alpha_JET_JER_EffectiveNP_4	± 0.18 [0.74%]	± 0.00 [0.02%]	± 0.03 [0.44%]
alpha_JET_JER_EffectiveNP_5	± 0.17 [0.71%]	± 0.03 [0.12%]	± 0.06 [0.92%]
alpha_JET_JER_EffectiveNP_2	± 0.16 [0.67%]	± 0.05 [0.21%]	± 0.05 [0.86%]
alpha_MET_SoftTrk_ResoPerp	± 0.15 [0.60%]	± 0.01 [0.05%]	± 0.07 [1.1%]
alpha_THEORY_PDF_VARIATION_diboson	± 0.14 [0.58%]	± 0.04 [0.17%]	± 0.03 [0.51%]
alpha_MUON_SAGITTA_RESBIAS	± 0.14 [0.57%]	± 0.19 [0.77%]	± 0.03 [0.49%]
alpha_JET_JvtEfficiency	± 0.09 [0.35%]	± 0.02 [0.08%]	± 0.01 [0.20%]
alpha_MET_SoftTrk_Scale	± 0.07 [0.31%]	± 0.01 [0.04%]	± 0.03 [0.54%]
alpha_MUON_SCALE	± 0.07 [0.28%]	± 0.06 [0.25%]	± 0.04 [0.66%]
alpha_JET_EtaIntercalibration_TotalStat	± 0.06 [0.26%]	± 0.01 [0.05%]	± 0.00 [0.02%]
alpha_MUON_EFF_RECO_SYS	± 0.06 [0.26%]	± 0.06 [0.25%]	± 0.01 [0.22%]
alpha_JET_EffectiveNP_2	± 0.05 [0.22%]	± 0.00 [0.02%]	± 0.01 [0.17%]
alpha_FAKES_Muon	± 0.05 [0.21%]	± 0.24 [0.97%]	± 0.00 [0.04%]
alpha_MUON_ID	± 0.05 [0.19%]	± 0.02 [0.07%]	± 0.01 [0.12%]
alpha_EL_CHARGEID_SYStotal	± 0.04 [0.18%]	± 0.15 [0.59%]	± 0.00 [0.02%]
alpha_FT_EFF_B_systematics	± 0.04 [0.17%]	± 0.36 [1.4%]	± 0.12 [1.9%]
alpha_JET_EtaIntercalibration_NonClosure_negEta	± 0.04 [0.16%]	± 0.00 [0.00%]	± 0.00 [0.03%]
alpha_JET_Pileup_PtTerm	± 0.04 [0.15%]	± 0.02 [0.07%]	± 0.01 [0.14%]
alpha_FT_EFF_Light_systematics	± 0.03 [0.14%]	± 0.06 [0.22%]	± 0.02 [0.38%]
alpha_EL_EFF_Iso_TOTAL_1NPCOR_PLUS_UNCOR	± 0.02 [0.09%]	± 0.03 [0.13%]	± 0.01 [0.08%]
alpha_JET_EtaIntercalibration_NonClosure_posEta	± 0.01 [0.05%]	± 0.00 [0.01%]	± 0.01 [0.10%]
alpha_EG_RESOLUTION_ALL	± 0.01 [0.05%]	± 0.00 [0.02%]	± 0.01 [0.21%]
alpha_FT_EFF_C_systematics	± 0.01 [0.04%]	± 0.01 [0.03%]	± 0.00 [0.07%]
alpha_EL_CHARGEID_STAT	± 0.01 [0.04%]	± 0.07 [0.27%]	± 0.00 [0.02%]
alpha_MUON_EFF_ISO_STAT	± 0.01 [0.03%]	± 0.01 [0.03%]	± 0.00 [0.03%]
alpha_MUON_EFF_TTVA_SYS	± 0.01 [0.03%]	± 0.00 [0.00%]	± 0.00 [0.00%]
alpha_MUON_EFF_ISO_SYS	± 0.01 [0.03%]	± 0.04 [0.15%]	± 0.01 [0.15%]
alpha_JET_EffectiveNP_8restTerm	± 0.01 [0.02%]	± 0.01 [0.02%]	± 0.00 [0.04%]
alpha_MUON_EFF_TTVA_STAT	± 0.00 [0.02%]	± 0.00 [0.01%]	± 0.00 [0.00%]
alpha_MUON_EFF_TrigSystUncertainty	± 0.00 [0.02%]	± 0.01 [0.04%]	± 0.00 [0.04%]
alpha_JET_EffectiveNP_3	± 0.00 [0.02%]	± 0.01 [0.06%]	± 0.01 [0.19%]
alpha_MUON_MS	± 0.00 [0.01%]	± 0.03 [0.13%]	± 0.01 [0.10%]
alpha_JET_EffectiveNP_5	± 0.00 [0.01%]	± 0.01 [0.03%]	± 0.00 [0.02%]
alpha_FT_EFF_extrapolation	± 0.00 [0.01%]	± 0.00 [0.01%]	± 0.00 [0.01%]
alpha_JET_EffectiveNP_7	± 0.00 [0.01%]	± 0.00 [0.01%]	± 0.00 [0.06%]
alpha_EL_EFF_Reco_TOTAL_1NPCOR_PLUS_UNCOR	± 0.00 [0.01%]	± 0.02 [0.09%]	± 0.01 [0.11%]
alpha_JET_EffectiveNP_6	± 0.00 [0.01%]	± 0.01 [0.02%]	± 0.00 [0.05%]
alpha_JET_EffectiveNP_4	± 0.00 [0.01%]	± 0.01 [0.05%]	± 0.00 [0.01%]
alpha_MUON_EFF_RECO_STAT	± 0.00 [0.01%]	± 0.00 [0.00%]	± 0.00 [0.01%]

alpha_MUON_EFF_RECO_SYS_LOWPT	±0.00 [0.01%]	±0.01 [0.03%]	±0.00 [0.04%]
alpha_FT_EFF_extrapolation_from_charm	±0.00 [0.00%]	±0.00 [0.00%]	±0.01 [0.09%]
alpha_EL_EFF_Trigger_TOTAL_1NPCOR_PLUS_UNCOR	±0.00 [0.00%]	±0.00 [0.01%]	±0.00 [0.00%]
alpha_JET_PunchThrough_MC16	±0.00 [0.00%]	±0.00 [0.01%]	±0.00 [0.02%]
alpha_MUON_EFF_TrigStatUncertainty	±0.00 [0.00%]	±0.00 [0.00%]	±0.00 [0.01%]
alpha_MUON_EFF_RECO_STAT_LOWPT	±0.00 [0.00%]	±0.00 [0.01%]	±0.00 [0.01%]
alpha_EL_EFF_TriggerEff_TOTAL_1NPCOR_PLUS_UNCOR	±0.00 [0.00%]	±0.00 [0.00%]	±0.00 [0.00%]
alpha_MUON_EFF_BADMUON_SYS	±0.00 [0.00%]	±0.00 [0.00%]	±0.00 [0.00%]
alpha_JET_EtaIntercalibration_NonClosure_highE	±0.00 [0.00%]	±0.00 [0.00%]	±0.00 [0.00%]
alpha_THEORY_Modelling_NJet	±0.00 [0.00%]	±0.00 [0.00%]	±0.00 [0.00%]
alpha_JET_SingleParticle_HighPt	±0.00 [0.00%]	±0.00 [0.00%]	±0.00 [0.00%]
alpha_JET_BJES_Response	±0.00 [0.00%]	±0.00 [0.00%]	±0.00 [0.00%]
alpha_MUON_EFF_SAGITTA_RHO	±0.00 [0.00%]	±0.00 [0.00%]	±0.00 [0.00%]
mu_DB4l	±0.00 [0.00%]	±0.00 [0.00%]	±0.00 [0.00%]
alpha_THEORY_UNC_raretop	±0.00 [0.00%]	±0.00 [0.00%]	±0.00 [0.00%]

Table A.3: Breakdown of the dominant uncertainties on background estimates. The given total statistical error is a quadratic sum of individual statistical errors of each bin in the region. Note that the individual uncertainties can be correlated, and do not necessarily add up quadratically to the total background uncertainty. Uncertainties are ordered from the largest to smallest depending by the impact on the region in the second column.

Uncertainty of channel	ZL RT VR	ZL DB VR
Total background expectation	25.43	34.20
Total statistical ($\sqrt{N_{\text{exp}}}$)	±5.04	±5.85
Total background systematic	±2.82 [11.08%]	±1.86 [5.44%]
mu_raretop	±2.81 [11.1%]	±0.51 [1.5%]
alpha_FT_EFF_B_systematics	±0.51 [2.0%]	±0.37 [1.1%]
alpha_JET_Flavor_Composition	±0.50 [2.0%]	±0.54 [1.6%]
alpha_JET_Flavor_Response	±0.45 [1.8%]	±0.53 [1.6%]
Lumi	±0.43 [1.7%]	±0.55 [1.6%]
alpha_JET_Pileup_RhoTopology	±0.35 [1.4%]	±0.33 [0.95%]
alpha_FT_EFF_Light_systematics	±0.28 [1.1%]	±0.32 [0.95%]
mu_DB3l	±0.25 [0.97%]	±1.86 [5.4%]
alpha_JET_JER_EffectiveNP_2	±0.24 [0.95%]	±0.21 [0.63%]
alpha_JET_JER_EffectiveNP_4	±0.23 [0.92%]	±0.10 [0.30%]
alpha_JET_JER_EffectiveNP_3	±0.23 [0.89%]	±0.29 [0.84%]
alpha_JET_EffectiveNP_1	±0.22 [0.86%]	±0.27 [0.79%]
alpha_EG_SCALE_ALL	±0.21 [0.82%]	±0.30 [0.89%]
alpha_JET_JER_DataVsMC_MC16	±0.19 [0.75%]	±0.13 [0.39%]
alpha_JET_JER_EffectiveNP_7restTerm	±0.18 [0.72%]	±0.17 [0.51%]
alpha_JET_EtaIntercalibration_Modelling	±0.17 [0.68%]	±0.13 [0.38%]
alpha_JET_JER_EffectiveNP_1	±0.17 [0.66%]	±0.23 [0.66%]
alpha_JET_JER_EffectiveNP_5	±0.16 [0.62%]	±0.21 [0.61%]
alpha_JET_JER_EffectiveNP_6	±0.10 [0.41%]	±0.20 [0.59%]
alpha_FT_EFF_C_systematics	±0.10 [0.39%]	±0.11 [0.31%]
alpha_JET_Pileup_OffsetNPV	±0.09 [0.36%]	±0.17 [0.50%]
alpha_MET_SoftTrk_Scale	±0.08 [0.31%]	±0.20 [0.58%]
alpha_FAKES_Electron	±0.07 [0.26%]	±0.55 [1.6%]
alpha_MUON_EFF_ISO_SYS	±0.07 [0.26%]	±0.04 [0.11%]
alpha_PRW_DATASF	±0.07 [0.26%]	±0.07 [0.19%]
alpha_MET_SoftTrk_ResoPerp	±0.06 [0.25%]	±0.20 [0.58%]
alpha_MET_SoftTrk_ResoPara	±0.06 [0.23%]	±0.26 [0.77%]
alpha_EL_EFF_Reco_TOTAL_1NPCOR_PLUS_UNCOR	±0.06 [0.22%]	±0.01 [0.03%]
alpha_MUON_EFF_RECO_SYS	±0.05 [0.21%]	±0.09 [0.27%]
alpha_MUON_SCALE	±0.05 [0.19%]	±0.06 [0.18%]
alpha_THEORY_SCALE_diboson	±0.04 [0.15%]	±0.06 [0.17%]
alpha_MUON_SAGITTA_RESBIAS	±0.03 [0.12%]	±0.01 [0.03%]
alpha_JET_Pileup_OffsetMu	±0.03 [0.12%]	±0.04 [0.12%]
alpha_JET_JvtEfficiency	±0.03 [0.10%]	±0.01 [0.03%]
alpha_FT_EFF_extrapolation	±0.02 [0.09%]	±0.02 [0.05%]
alpha_MUON_MS	±0.02 [0.09%]	±0.02 [0.05%]
alpha_FT_EFF_extrapolation_from_charm	±0.02 [0.09%]	±0.01 [0.04%]
alpha_JET_EtaIntercalibration_TotalStat	±0.02 [0.08%]	±0.01 [0.03%]
alpha_JET_EffectiveNP_4	±0.02 [0.07%]	±0.03 [0.09%]
alpha_EL_EFF_ID_TOTAL_1NPCOR_PLUS_UNCOR	±0.02 [0.07%]	±0.18 [0.54%]
alpha_MUON_EFF_RECO_SYS_LOWPT	±0.02 [0.06%]	±0.00 [0.01%]
alpha_EL_CHARGEID_STAT	±0.02 [0.06%]	±0.02 [0.05%]
alpha_EL_EFF_Iso_TOTAL_1NPCOR_PLUS_UNCOR	±0.02 [0.06%]	±0.02 [0.07%]
alpha_JET_Pileup_PtTerm	±0.01 [0.05%]	±0.07 [0.20%]
alpha_MUON_EFF_TrigSystUncertainty	±0.01 [0.04%]	±0.03 [0.09%]
alpha_FAKES_Muon	±0.01 [0.04%]	±0.08 [0.23%]
alpha_JET_EffectiveNP_2	±0.01 [0.03%]	±0.08 [0.22%]

alpha_THEORY_PDF_VARIATION_diboson	±0.01 [0.03%]	±0.00 [0.00%]
alpha_JET_EffectiveNP_5	±0.01 [0.03%]	±0.01 [0.03%]
alpha_JET_EtaIntercalibration_NonClosure_posEta	±0.01 [0.03%]	±0.01 [0.04%]
alpha_JET_EffectiveNP_8restTerm	±0.01 [0.03%]	±0.01 [0.02%]
alpha_JET_EffectiveNP_3	±0.01 [0.03%]	±0.05 [0.15%]
alpha_THEORY_PDF_CHOICE_diboson	±0.01 [0.03%]	±0.20 [0.59%]
alpha_MUON_EFF_RECO_STAT_LOWPT	±0.01 [0.02%]	±0.00 [0.00%]
alpha_MUON_EFF_RECO_STAT	±0.01 [0.02%]	±0.00 [0.00%]
alpha_MUON_EFF_ISO_STAT	±0.01 [0.02%]	±0.01 [0.04%]
alpha_MUON_ID	±0.01 [0.02%]	±0.04 [0.12%]
alpha_MUON_EFF_TTVA_STAT	±0.00 [0.01%]	±0.01 [0.02%]
alpha_JET_EffectiveNP_7	±0.00 [0.01%]	±0.00 [0.00%]
alpha_MUON_EFF_TrigStatUncertainty	±0.00 [0.01%]	±0.00 [0.00%]
alpha_JET_PunchThrough_MC16	±0.00 [0.01%]	±0.00 [0.00%]
alpha_EL_CHARGEID_SYStotal	±0.00 [0.01%]	±0.00 [0.01%]
alpha_MUON_EFF_TTVA_SYS	±0.00 [0.01%]	±0.01 [0.03%]
alpha_JET_EtaIntercalibration_NonClosure_highE	±0.00 [0.01%]	±0.00 [0.00%]
alpha_JET_EtaIntercalibration_NonClosure_negEta	±0.00 [0.01%]	±0.00 [0.00%]
alpha_EL_EFF_Trigger_TOTAL_1NPCOR_PLUS_UNCOR	±0.00 [0.01%]	±0.00 [0.00%]
alpha_JET_EffectiveNP_6	±0.00 [0.00%]	±0.01 [0.01%]
alpha_EG_RESOLUTION_ALL	±0.00 [0.00%]	±0.00 [0.00%]
alpha_EL_EFF_TriggerEff_TOTAL_1NPCOR_PLUS_UNCOR	±0.00 [0.00%]	±0.00 [0.00%]
alpha_MUON_EFF_BADMUON_SYS	±0.00 [0.00%]	±0.00 [0.00%]
mu_DB4l	±0.00 [0.00%]	±0.00 [0.00%]
alpha_THEORY_Modelling_NJet	±0.00 [0.00%]	±0.00 [0.00%]
alpha_JET_SingleParticle_HighPt	±0.00 [0.00%]	±0.00 [0.00%]
alpha_JET_BJES_Response	±0.00 [0.00%]	±0.00 [0.00%]
alpha_MUON_SAGITTA_RHO	±0.00 [0.00%]	±0.00 [0.00%]
alpha_THEORY_UNC_raretop	±0.00 [0.00%]	±0.00 [0.00%]

Table A.4: Breakdown of the dominant uncertainties on background estimates. The given total statistical error is a quadratic sum of individual statistical errors of each bin in the region. Note that the individual uncertainties can be correlated, and do not necessarily add up quadratically to the total background uncertainty. Uncertainties are ordered from the largest to smallest depending by the impact on the region in the second column.

Uncertainty of channel	Q0 DB CR	Q0 RT CR	Q2 VR
Total background expectation	1642.12	66.18	14.27
Total statistical ($\sqrt{N_{\text{exp}}}$)	±40.52	±8.14	±3.78
Total background systematic	±40.52 [2.47%]	±7.79 [11.76%]	±2.42 [16.97%]
mu_DB4l	±48.78 [3.0%]	±0.17 [0.25%]	±0.31 [2.2%]
Lumi	±26.93 [1.6%]	±1.12 [1.7%]	±0.18 [1.2%]
alpha_FAKES_Electron	±3.30 [0.20%]	±0.03 [0.04%]	±0.29 [2.1%]
mu_raretop	±1.60 [0.10%]	±7.90 [11.9%]	±0.04 [0.29%]
alpha_FT_EFF_B_systematics	±1.06 [0.06%]	±0.23 [0.35%]	±0.00 [0.01%]
alpha_JET_Pileup_RhoTopology	±0.24 [0.01%]	±0.15 [0.23%]	±0.04 [0.25%]
alpha_JET_Flavor_Composition	±0.23 [0.01%]	±0.16 [0.24%]	±0.04 [0.29%]
alpha_FAKES_Muon	±0.17 [0.01%]	±0.13 [0.20%]	±0.20 [1.4%]
alpha_JET_JER_EffectiveNP_2	±0.17 [0.01%]	±0.06 [0.09%]	±0.04 [0.25%]
alpha_JET_JER_EffectiveNP_4	±0.14 [0.01%]	±0.05 [0.07%]	±0.00 [0.02%]
alpha_JET_Flavor_Response	±0.13 [0.01%]	±0.08 [0.12%]	±0.03 [0.18%]
alpha_FT_EFF_Light_systematics	±0.12 [0.01%]	±0.26 [0.40%]	±0.02 [0.11%]
alpha_JET_JER_EffectiveNP_3	±0.12 [0.01%]	±0.05 [0.07%]	±0.01 [0.10%]
alpha_JET_JER_EffectiveNP_1	±0.11 [0.01%]	±0.03 [0.05%]	±0.04 [0.31%]
alpha_JET_JER_EffectiveNP_7restTerm	±0.09 [0.01%]	±0.05 [0.07%]	±0.03 [0.18%]
alpha_JET_EffectiveNP_1	±0.08 [0.00%]	±0.05 [0.08%]	±0.02 [0.12%]
alpha_JET_EtaIntercalibration_Modelling	±0.07 [0.00%]	±0.05 [0.07%]	±0.01 [0.04%]
alpha_JET_Pileup_OffsetNPV	±0.07 [0.00%]	±0.07 [0.10%]	±0.02 [0.12%]
alpha_JET_JER_EffectiveNP_5	±0.06 [0.00%]	±0.06 [0.09%]	±0.02 [0.11%]
alpha_EL_EFF_ID_TOTAL_1NPCOR_PLUS_UNCOR	±0.05 [0.00%]	±0.02 [0.02%]	±0.25 [1.8%]
alpha_JET_JER_EffectiveNP_6	±0.05 [0.00%]	±0.05 [0.08%]	±0.02 [0.14%]
alpha_JET_JvtEfficiency	±0.05 [0.00%]	±0.02 [0.04%]	±0.00 [0.02%]
alpha_JET_JER_DataVsMC_MC16	±0.05 [0.00%]	±0.03 [0.04%]	±0.02 [0.13%]
alpha_PRW_DATASF	±0.04 [0.00%]	±0.03 [0.05%]	±0.02 [0.11%]
alpha_FT_EFF_C_systematics	±0.03 [0.00%]	±0.08 [0.12%]	±0.01 [0.09%]
alpha_JET_Pileup_OffsetMu	±0.03 [0.00%]	±0.03 [0.04%]	±0.00 [0.00%]
alpha_JET_EtaIntercalibration_TotalStat	±0.02 [0.00%]	±0.01 [0.02%]	±0.00 [0.03%]
alpha_JET_EffectiveNP_2	±0.02 [0.00%]	±0.01 [0.02%]	±0.00 [0.02%]
alpha_JET_Pileup_PtTerm	±0.02 [0.00%]	±0.00 [0.01%]	±0.00 [0.01%]
alpha_JET_EffectiveNP_3	±0.01 [0.00%]	±0.00 [0.01%]	±0.00 [0.01%]
alpha_MUON_ID	±0.01 [0.00%]	±0.00 [0.00%]	±0.01 [0.07%]
alpha_EL_EFF_Reco_TOTAL_1NPCOR_PLUS_UNCOR	±0.01 [0.00%]	±0.01 [0.01%]	±0.06 [0.39%]
alpha_MUON_EFF_RECO_STAT	±0.01 [0.00%]	±0.00 [0.01%]	±0.02 [0.16%]

alpha_MUON_MS	±0.01 [0.00%]	±0.00 [0.00%]	±0.02 [0.15%]
alpha_MUON_SCALE	±0.01 [0.00%]	±0.00 [0.01%]	±0.00 [0.01%]
alpha_JET_EffectiveNP_4	±0.00 [0.00%]	±0.00 [0.01%]	±0.00 [0.01%]
alpha_EG_SCALE_ALL	±0.00 [0.00%]	±0.00 [0.00%]	±0.02 [0.11%]
alpha_EG_RESOLUTION_ALL	±0.00 [0.00%]	±0.00 [0.00%]	±0.01 [0.04%]
alpha_MUON_EFF_ISO_SYS	±0.00 [0.00%]	±0.00 [0.00%]	±0.03 [0.22%]
alpha_MUON_EFF_TTVA_SYS	±0.00 [0.00%]	±0.00 [0.00%]	±0.00 [0.03%]
alpha_EL_EFF_Iso_TOTAL_1NPCOR_PLUS_UNCOR	±0.00 [0.00%]	±0.00 [0.00%]	±0.01 [0.08%]
alpha_EL_CHARGEID_SYStotal	±0.00 [0.00%]	±0.00 [0.00%]	±1.81 [12.7%]
alpha_FT_EFF_extrapolation	±0.00 [0.00%]	±0.01 [0.01%]	±0.00 [0.00%]
alpha_MUON_EFF_RECO_SYS_LOWPT	±0.00 [0.00%]	±0.00 [0.00%]	±0.00 [0.00%]
alpha_MUON_EFF_TrigSysUncertainty	±0.00 [0.00%]	±0.00 [0.00%]	±0.00 [0.02%]
alpha_JET_EffectiveNP_5	±0.00 [0.00%]	±0.00 [0.00%]	±0.00 [0.00%]
alpha_MUON_SAGITTA_RESBIAS	±0.00 [0.00%]	±0.00 [0.00%]	±0.00 [0.01%]
alpha_JET_EffectiveNP_8restTerm	±0.00 [0.00%]	±0.00 [0.00%]	±0.00 [0.00%]
alpha_MUON_EFF_TTVA_STAT	±0.00 [0.00%]	±0.00 [0.00%]	±0.00 [0.02%]
alpha_FT_EFF_extrapolation_from_charm	±0.00 [0.00%]	±0.00 [0.00%]	±0.00 [0.01%]
alpha_JET_EtaIntercalibration_NonClosure_negEta	±0.00 [0.00%]	±0.00 [0.00%]	±0.00 [0.00%]
alpha_MUON_EFF_ISO_STAT	±0.00 [0.00%]	±0.00 [0.00%]	±0.00 [0.01%]
alpha_JET_EffectiveNP_6	±0.00 [0.00%]	±0.00 [0.00%]	±0.00 [0.00%]
alpha_MUON_EFF_RECO_STAT_LOWPT	±0.00 [0.00%]	±0.00 [0.00%]	±0.00 [0.00%]
alpha_MUON_EFF_RECO_STAT	±0.00 [0.00%]	±0.00 [0.00%]	±0.01 [0.05%]
alpha_MUON_EFF_TrigStatUncertainty	±0.00 [0.00%]	±0.00 [0.00%]	±0.00 [0.00%]
alpha_JET_EtaIntercalibration_NonClosure_posEta	±0.00 [0.00%]	±0.00 [0.00%]	±0.00 [0.00%]
alpha_EL_EFF_Trigger_TOTAL_1NPCOR_PLUS_UNCOR	±0.00 [0.00%]	±0.00 [0.00%]	±0.00 [0.01%]
alpha_EL_CHARGEID_STAT	±0.00 [0.00%]	±0.00 [0.00%]	±0.38 [2.7%]
alpha_JET_EffectiveNP_7	±0.00 [0.00%]	±0.00 [0.00%]	±0.00 [0.00%]
alpha_EL_EFF_TriggerEff_TOTAL_1NPCOR_PLUS_UNCOR	±0.00 [0.00%]	±0.00 [0.00%]	±0.00 [0.00%]
alpha_JET_PunchThrough_MC16	±0.00 [0.00%]	±0.00 [0.00%]	±0.00 [0.00%]
alpha_MUON_EFF_BADMUON_SYS	±0.00 [0.00%]	±0.00 [0.00%]	±0.00 [0.00%]
alpha_MET_SoftTrk_Scale	±0.00 [0.00%]	±0.00 [0.00%]	±0.01 [0.04%]
alpha_JET_EtaIntercalibration_NonClosure_highE	±0.00 [0.00%]	±0.00 [0.00%]	±0.00 [0.00%]
alpha_THEORY_PDF_CHOICE_diboson	±0.00 [0.00%]	±0.11 [0.17%]	±0.02 [0.17%]
alpha_THEORY_SCALE_diboson	±0.00 [0.00%]	±0.62 [0.94%]	±0.09 [0.65%]
alpha_THEORY_Modelling_Njet	±0.00 [0.00%]	±0.00 [0.00%]	±0.00 [0.00%]
alpha_JET_SingleParticle_HighPt	±0.00 [0.00%]	±0.00 [0.00%]	±0.00 [0.00%]
alpha_JET_BJES_Response	±0.00 [0.00%]	±0.00 [0.00%]	±0.00 [0.00%]
alpha_THEORY_PDF_VARIATION_diboson	±0.00 [0.00%]	±0.03 [0.04%]	±0.02 [0.15%]
alpha_MET_SoftTrk_ResoPara	±0.00 [0.00%]	±0.00 [0.00%]	±0.04 [0.31%]
alpha_MUON_SAGITTA_RHO	±0.00 [0.00%]	±0.00 [0.00%]	±0.00 [0.00%]
alpha_MET_SoftTrk_ResoPerp	±0.00 [0.00%]	±0.00 [0.00%]	±0.02 [0.16%]
mu_DB3l	±0.00 [0.00%]	±0.00 [0.00%]	±0.00 [0.00%]
alpha_THEORY_UNC_raretop	±0.00 [0.00%]	±0.00 [0.00%]	±0.00 [0.00%]

Table A.5: Breakdown of the dominant uncertainties on background estimates. The given total statistical error is a quadratic sum of individual statistical errors of each bin in the region. Note that the individual uncertainties can be correlated, and do not necessarily add up quadratically to the total background uncertainty. Uncertainties are ordered from the largest to smallest depending by the impact on the region in the second column.

Uncertainty of channel	Q0 SR	Q2 SR
Total background expectation	18.88	10.37
Total statistical ($\sqrt{N_{\text{exp}}}$)	±4.34	±3.22
Total background systematic	±1.64 [8.66%]	±1.86 [17.97%]
mu_raretop	±1.17 [6.2%]	±0.20 [2.0%]
alpha_FT_EFF_B_systematics	±0.78 [4.1%]	±0.05 [0.48%]
alpha_JET_JER_EffectiveNP_1	±0.47 [2.5%]	±0.01 [0.13%]
alpha_JET_JER_EffectiveNP_2	±0.40 [2.1%]	±0.02 [0.22%]
alpha_FAKES_Muon	±0.36 [1.9%]	±0.00 [0.03%]
alpha_MET_SoftTrk_Scale	±0.33 [1.7%]	±0.01 [0.11%]
Lumi	±0.30 [1.6%]	±0.17 [1.7%]
alpha_JET_JER_EffectiveNP_4	±0.28 [1.5%]	±0.01 [0.11%]
alpha_JET_JER_EffectiveNP_6	±0.27 [1.4%]	±0.00 [0.02%]
alpha_MET_SoftTrk_ResoPerp	±0.26 [1.4%]	±0.00 [0.02%]
alpha_JET_JER_EffectiveNP_3	±0.26 [1.4%]	±0.02 [0.20%]
mu_DB4l	±0.24 [1.3%]	±0.26 [2.5%]
alpha_JET_JER_EffectiveNP_7restTerm	±0.24 [1.3%]	±0.00 [0.01%]
alpha_JET_JER_EffectiveNP_5	±0.23 [1.2%]	±0.02 [0.18%]
alpha_MET_SoftTrk_ResoPara	±0.22 [1.2%]	±0.04 [0.41%]
alpha_JET_Pileup_RhoTopology	±0.17 [0.92%]	±0.01 [0.06%]
alpha_MUON_MS	±0.12 [0.66%]	±0.01 [0.05%]
alpha_JET_Flavor_Composition	±0.12 [0.63%]	±0.01 [0.05%]
alpha_JET_JER_DataVsMC_MC16	±0.12 [0.62%]	±0.02 [0.15%]

alpha_MUON_SAGITTA_RESBIAS	±0.11 [0.60%]	±0.01 [0.08%]
alpha_PRW_DATASF	±0.11 [0.59%]	±0.09 [0.85%]
alpha_FT_EFF_Light_systematics	±0.11 [0.56%]	±0.05 [0.45%]
alpha_THEORY_SCALE_diboson	±0.10 [0.55%]	±0.30 [2.9%]
alpha_MUON_ID	±0.09 [0.47%]	±0.00 [0.02%]
alpha_JET_JvEfficiency	±0.08 [0.45%]	±0.00 [0.04%]
alpha_EL_EFF_ID_TOTAL_1NPCOR_PLUS_UNCOR	±0.08 [0.42%]	±0.33 [3.2%]
alpha_JET_Pileup_OffsetMu	±0.08 [0.41%]	±0.01 [0.06%]
alpha_MUON_SCALE	±0.07 [0.38%]	±0.01 [0.08%]
alpha_EG_SCALE_ALL	±0.07 [0.38%]	±0.07 [0.66%]
alpha_JET_Flavor_Response	±0.07 [0.38%]	±0.01 [0.07%]
alpha_JET_EffectiveNP_1	±0.06 [0.34%]	±0.01 [0.08%]
alpha_JET_EtaIntercalibration_Modelling	±0.05 [0.26%]	±0.01 [0.14%]
alpha_FAKES_Electron	±0.05 [0.25%]	±0.01 [0.11%]
alpha_MUON_EFF_RECO_SYS	±0.04 [0.22%]	±0.01 [0.09%]
alpha_JET_EffectiveNP_2	±0.04 [0.19%]	±0.01 [0.06%]
alpha_FT_EFF_C_systematics	±0.03 [0.15%]	±0.01 [0.06%]
alpha_JET_EtaIntercalibration_TotalStat	±0.02 [0.11%]	±0.01 [0.07%]
alpha_THEORY_PDF_VARIATION_diboson	±0.02 [0.10%]	±0.01 [0.14%]
alpha_JET_Pileup_PtTerm	±0.02 [0.09%]	±0.00 [0.01%]
alpha_JET_EffectiveNP_4	±0.02 [0.09%]	±0.00 [0.00%]
alpha_JET_EffectiveNP_3	±0.02 [0.08%]	±0.00 [0.00%]
alpha_THEORY_PDF_CHOICE_diboson	±0.01 [0.07%]	±0.02 [0.19%]
alpha_EL_EFF_Iso_TOTAL_1NPCOR_PLUS_UNCOR	±0.01 [0.05%]	±0.03 [0.25%]
alpha_EL_CHARGEID_STAT	±0.01 [0.05%]	±0.77 [7.4%]
alpha_JET_EffectiveNP_8restTerm	±0.01 [0.04%]	±0.00 [0.00%]
alpha_MUON_EFF_ISO_SYS	±0.01 [0.04%]	±0.04 [0.35%]
alpha_JET_EffectiveNP_5	±0.01 [0.04%]	±0.00 [0.00%]
alpha_JET_EtaIntercalibration_NonClosure_negEta	±0.01 [0.04%]	±0.00 [0.00%]
alpha_EL_EFF_Reco_TOTAL_1NPCOR_PLUS_UNCOR	±0.01 [0.03%]	±0.04 [0.43%]
alpha_MUON_EFF_TTVA_SYS	±0.01 [0.03%]	±0.00 [0.01%]
alpha_JET_PunchThrough_MC16	±0.01 [0.03%]	±0.00 [0.00%]
alpha_JET_EffectiveNP_6	±0.01 [0.03%]	±0.00 [0.00%]
alpha_MUON_EFF_TTVA_STAT	±0.00 [0.02%]	±0.00 [0.02%]
alpha_EG_RESOLUTION_ALL	±0.00 [0.02%]	±0.02 [0.16%]
alpha_EL_CHARGEID_SYStotal	±0.00 [0.02%]	±1.74 [16.8%]
alpha_JET_EffectiveNP_7	±0.00 [0.02%]	±0.00 [0.00%]
alpha_MUON_EFF_ISO_STAT	±0.00 [0.02%]	±0.00 [0.01%]
alpha_FT_EFF_extrapolation	±0.00 [0.02%]	±0.00 [0.01%]
alpha_JET_Pileup_OffsetNPV	±0.00 [0.01%]	±0.01 [0.09%]
alpha_MUON_EFF_TrigSystUncertainty	±0.00 [0.01%]	±0.00 [0.04%]
alpha_MUON_EFF_RECO_STAT	±0.00 [0.01%]	±0.01 [0.06%]
alpha_MUON_EFF_RECO_SYS_LOWPT	±0.00 [0.00%]	±0.00 [0.03%]
alpha_JET_EtaIntercalibration_NonClosure_posEta	±0.00 [0.00%]	±0.00 [0.00%]
alpha_MUON_EFF_TrigStatUncertainty	±0.00 [0.00%]	±0.00 [0.01%]
alpha_MUON_EFF_RECO_STAT_LOWPT	±0.00 [0.00%]	±0.00 [0.01%]
alpha_EL_EFF_Trigger_TOTAL_1NPCOR_PLUS_UNCOR	±0.00 [0.00%]	±0.00 [0.01%]
alpha_FT_EFF_extrapolation_from_charm	±0.00 [0.00%]	±0.00 [0.00%]
alpha_EL_EFF_TriggerEff_TOTAL_1NPCOR_PLUS_UNCOR	±0.00 [0.00%]	±0.00 [0.00%]
alpha_MUON_EFF_BADMUON_SYS	±0.00 [0.00%]	±0.00 [0.00%]
alpha_JET_EtaIntercalibration_NonClosure_highE	±0.00 [0.00%]	±0.00 [0.00%]
alpha_THEORY_Modelling_Njet	±0.00 [0.00%]	±0.00 [0.00%]
alpha_JET_SingleParticle_HighPt	±0.00 [0.00%]	±0.00 [0.00%]
alpha_JET_BJES_Response	±0.00 [0.00%]	±0.00 [0.00%]
alpha_MUON_SAGITTA_RHO	±0.00 [0.00%]	±0.00 [0.00%]
mu_DB3l	±0.00 [0.00%]	±0.00 [0.00%]
alpha_THEORY_UNC_raretop	±0.00 [0.00%]	±0.00 [0.00%]

Table A.6: Breakdown of the dominant uncertainties on background estimates. The given total statistical error is a quadratic sum of individual statistical errors of each bin in the region. Note that the individual uncertainties can be correlated, and do not necessarily add up quadratically to the total background uncertainty. Uncertainties are ordered from the largest to smallest depending by the impact on the region in the second column.

Uncertainty of channel	Q0 DB VR	Q0 RT VR
Total background expectation	92.65	21.17
Total statistical ($\sqrt{N_{\text{exp}}}$)	±9.63	±4.60
Total background systematic	±20.12 [21.71%]	±2.60 [12.30%]
alpha_THEORY_UNC_raretop	±18.94 [20.4%]	±0.00 [0.00%]
mu_raretop	±4.85 [5.2%]	±2.49 [11.7%]
alpha_FT_EFF_Light_systematics	±2.76 [3.0%]	±0.13 [0.60%]
alpha_THEORY_SCALE_diboson	±2.64 [2.9%]	±0.06 [0.26%]
mu_DB4l	±1.49 [1.6%]	±0.02 [0.08%]

Lumi	± 1.47 [1.6%]	± 0.34 [1.6%]
alpha_FT_EFF_B_systematics	± 1.00 [1.1%]	± 0.79 [3.7%]
alpha_FT_EFF_C_systematics	± 0.73 [0.79%]	± 0.03 [0.15%]
alpha_FAKES_Muon	± 0.73 [0.78%]	± 0.16 [0.74%]
alpha_JET_Flavor_Composition	± 0.62 [0.67%]	± 0.21 [0.98%]
alpha_THEORY_PDF_CHOICE_diboson	± 0.61 [0.66%]	± 0.01 [0.05%]
alpha_JET_Pileup_RhoTopology	± 0.55 [0.60%]	± 0.20 [0.96%]
alpha_JET_JER_EffectiveNP_4	± 0.42 [0.45%]	± 0.16 [0.75%]
alpha_JET_JER_EffectiveNP_2	± 0.33 [0.36%]	± 0.22 [1.0%]
alpha_JET_JER_EffectiveNP_3	± 0.27 [0.29%]	± 0.19 [0.89%]
alpha_PRW_DATASF	± 0.25 [0.27%]	± 0.03 [0.12%]
alpha_JET_JER_EffectiveNP_7restTerm	± 0.24 [0.26%]	± 0.05 [0.25%]
alpha_FAKES_Electron	± 0.22 [0.23%]	± 0.08 [0.38%]
alpha_JET_Flavor_Response	± 0.21 [0.23%]	± 0.10 [0.48%]
alpha_JET_JER_EffectiveNP_1	± 0.21 [0.22%]	± 0.11 [0.54%]
alpha_JET_EtaIntercalibration_Modelling	± 0.21 [0.22%]	± 0.08 [0.37%]
alpha_THEORY_PDF_VARIATION_diboson	± 0.15 [0.16%]	± 0.00 [0.01%]
alpha_JET_EffectiveNP_1	± 0.13 [0.14%]	± 0.07 [0.33%]
alpha_JET_Pileup_OffsetNPV	± 0.13 [0.14%]	± 0.05 [0.24%]
alpha_JET_Pileup_OffsetMu	± 0.13 [0.14%]	± 0.00 [0.01%]
alpha_JET_JER_EffectiveNP_5	± 0.12 [0.13%]	± 0.01 [0.04%]
alpha_JET_JER_EffectiveNP_6	± 0.11 [0.12%]	± 0.02 [0.10%]
alpha_MUON_MS	± 0.09 [0.10%]	± 0.03 [0.15%]
alpha_MUON_SAGITTA_RESBIAS	± 0.08 [0.09%]	± 0.04 [0.18%]
alpha_JET_EffectiveNP_2	± 0.08 [0.08%]	± 0.02 [0.10%]
alpha_MUON_SCALE	± 0.07 [0.08%]	± 0.03 [0.12%]
alpha_EG_SCALE_ALL	± 0.07 [0.07%]	± 0.05 [0.22%]
alpha_EL_EFF_ID_TOTAL_INPCOR_PLUS_UNCOR	± 0.06 [0.07%]	± 0.01 [0.04%]
alpha_JET_EtaIntercalibration_TotalStat	± 0.06 [0.06%]	± 0.02 [0.07%]
alpha_JET_JvtEfficiency	± 0.04 [0.05%]	± 0.04 [0.19%]
alpha_EL_EFF_Reco_TOTAL_INPCOR_PLUS_UNCOR	± 0.02 [0.03%]	± 0.01 [0.07%]
alpha_EG_RESOLUTION_ALL	± 0.02 [0.02%]	± 0.02 [0.11%]
alpha_JET_EtaIntercalibration_NonClosure_posEta	± 0.02 [0.02%]	± 0.00 [0.00%]
alpha_MUON_ID	± 0.02 [0.02%]	± 0.01 [0.06%]
alpha_FT_EFF_extrapolation	± 0.01 [0.01%]	± 0.00 [0.00%]
alpha_MUON_EFF_RECO_SYS	± 0.01 [0.01%]	± 0.01 [0.07%]
alpha_JET_EtaIntercalibration_NonClosure_negEta	± 0.01 [0.01%]	± 0.00 [0.01%]
alpha_MUON_EFF_RECO_SYS_LOWPT	± 0.01 [0.01%]	± 0.00 [0.02%]
alpha_JET_EffectiveNP_4	± 0.01 [0.01%]	± 0.01 [0.03%]
alpha_JET_EffectiveNP_3	± 0.01 [0.01%]	± 0.01 [0.05%]
alpha_JET_JER_DataVsMC_MC16	± 0.01 [0.01%]	± 0.06 [0.29%]
alpha_JET_Pileup_PtTerm	± 0.01 [0.01%]	± 0.01 [0.02%]
alpha_MUON_EFF_TrigSystUncertainty	± 0.00 [0.00%]	± 0.01 [0.03%]
alpha_MUON_EFF_TTVA_STAT	± 0.00 [0.00%]	± 0.00 [0.01%]
alpha_MUON_EFF_RECO_STAT_LOWPT	± 0.00 [0.00%]	± 0.00 [0.00%]
alpha_JET_EffectiveNP_7	± 0.00 [0.00%]	± 0.00 [0.01%]
alpha_JET_EffectiveNP_5	± 0.00 [0.00%]	± 0.01 [0.03%]
alpha_JET_EffectiveNP_6	± 0.00 [0.00%]	± 0.01 [0.05%]
alpha_EL_EFF_Iso_TOTAL_INPCOR_PLUS_UNCOR	± 0.00 [0.00%]	± 0.00 [0.01%]
alpha_MUON_EFF_TTVA_SYS	± 0.00 [0.00%]	± 0.00 [0.01%]
alpha_MUON_EFF_ISO_SYS	± 0.00 [0.00%]	± 0.01 [0.05%]
alpha_EL_CHARGEID_STAT	± 0.00 [0.00%]	± 0.00 [0.02%]
alpha_MUON_EFF_RECO_STAT	± 0.00 [0.00%]	± 0.00 [0.00%]
alpha_MUON_EFF_TrigStatUncertainty	± 0.00 [0.00%]	± 0.00 [0.00%]
alpha_EL_CHARGEID_SYStotal	± 0.00 [0.00%]	± 0.00 [0.02%]
alpha_JET_EffectiveNP_8restTerm	± 0.00 [0.00%]	± 0.00 [0.02%]
alpha_MUON_EFF_ISO_STAT	± 0.00 [0.00%]	± 0.00 [0.00%]
alpha_FT_EFF_extrapolation_from_charm	± 0.00 [0.00%]	± 0.00 [0.00%]
alpha_EL_EFF_Trigger_TOTAL_INPCOR_PLUS_UNCOR	± 0.00 [0.00%]	± 0.00 [0.00%]
alpha_EL_EFF_TriggerEff_TOTAL_INPCOR_PLUS_UNCOR	± 0.00 [0.00%]	± 0.00 [0.00%]
alpha_MET_SoftTrk_ResoPara	± 0.00 [0.00%]	± 0.04 [0.19%]
alpha_JET_PunchThrough_MC16	± 0.00 [0.00%]	± 0.00 [0.00%]
alpha_MET_SoftTrk_Scale	± 0.00 [0.00%]	± 0.08 [0.36%]
alpha_MUON_EFF_BADMUON_SYS	± 0.00 [0.00%]	± 0.00 [0.00%]
alpha_THEORY_Modelling_Njet	± 0.00 [0.00%]	± 0.00 [0.00%]
alpha_JET_SingleParticle_HighPt	± 0.00 [0.00%]	± 0.00 [0.00%]
alpha_JET_BJES_Response	± 0.00 [0.00%]	± 0.00 [0.00%]
alpha_JET_EtaIntercalibration_NonClosure_highE	± 0.00 [0.00%]	± 0.00 [0.00%]
alpha_MUON_SAGITTA_RHO	± 0.00 [0.00%]	± 0.00 [0.00%]
alpha_MET_SoftTrk_ResoPerp	± 0.00 [0.00%]	± 0.07 [0.33%]
mu_DB3l	± 0.00 [0.00%]	± 0.00 [0.00%]

Table A.7: Breakdown of the dominant uncertainties on background estimates. The given total statistical error is a quadratic sum of individual statistical errors of each bin in the region. Note that the individual uncertainties can be correlated, and do not necessarily add up quadratically to the total background uncertainty. Uncertainties are ordered from the largest to smallest depending by the impact on the region in the second column.

A.3 Post-fit distributions

Additional kinematic distributions for observables not used as discriminating variables in the fit are shown in this appendix for all the analysis regions in the three- and four-lepton channels after the fit procedure. They show an overall good agreement between data and scaled MC prediction in each region. The variable reported are $H_T + E_T^{\text{miss}}$, E_T^{miss} , p_T and invariant mass of the three-lepton system $m_{(\ell\ell\ell)}$ for the three-lepton channel and E_T^{miss} , p_T and invariant mass of the four-lepton system $m_{(\ell\ell\ell\ell)}$ and $m_{(\ell\ell\ell\ell)} + E_T^{\text{miss}}$.

These variables are shown for:

- ZL CR in Figure [A.9](#);
- Fakes VR in Figure [A.10](#);
- JNLow VR in Figure [A.11](#);
- ZL Diboson VR in Figure [A.12](#);
- ZL RareTop VR in Figure [A.13](#);
- JNLow SR in Figure [A.14](#)
- ZL SR in Figure [A.15](#);
- ZL Veto SR in Figure [A.16](#);
- Q0 Diboson CR in Figure [A.17](#);
- Q0 RareTop CR in Figure [A.18](#);
- Q0 Diboson VR in Figure [A.19](#);
- Q0 RareTop VR in Figure [A.20](#);
- Q2 VR in Figure [A.21](#);
- Q0 SR in Figure [A.22](#)
- Q2 SR in Figure [A.23](#).

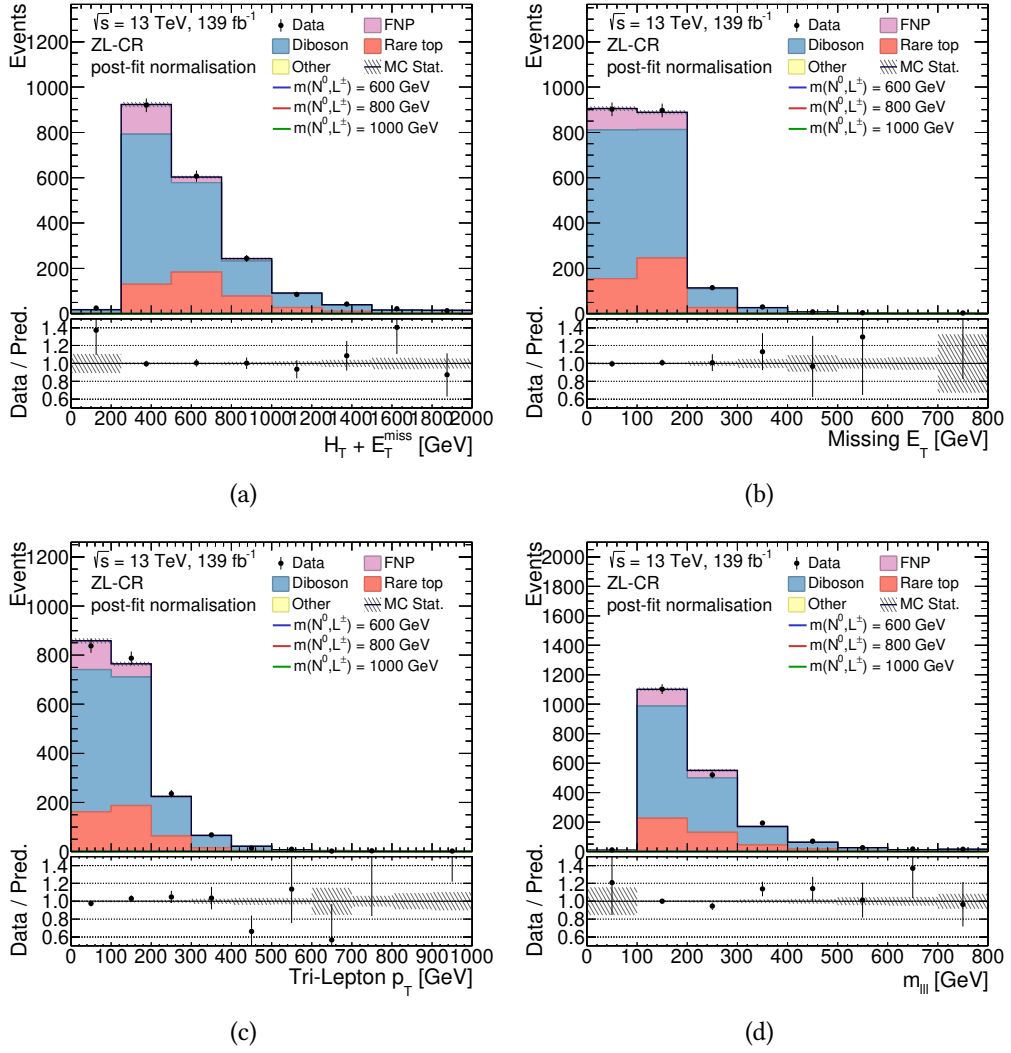
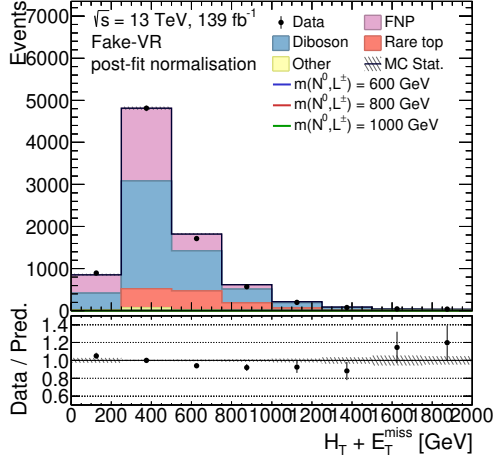
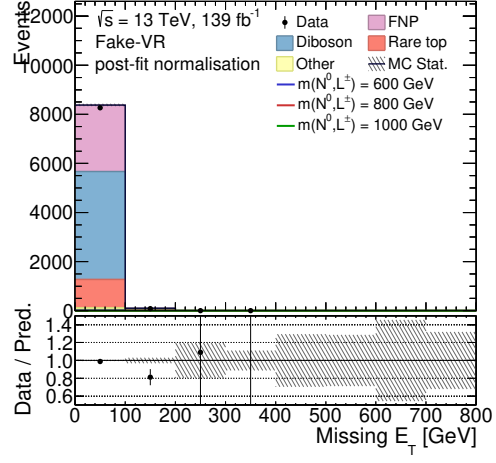


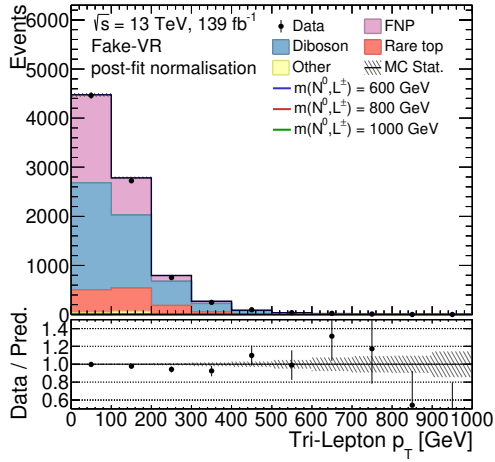
Figure A.9: Post-fit distribution for the ZL CR: $H_T + E_T^{\text{miss}}$ in A.9a, E_T^{miss} in A.9c, tri-lepton system p_T in A.9c and $m_{\ell\ell\ell}$ in A.9d.



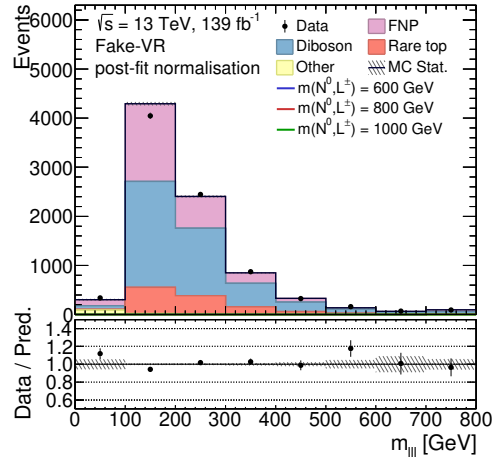
(a)



(b)



(c)



(d)

Figure A.10: Post-fit distribution for the Fakes VR: $H_T + E_T^{\text{miss}}$ in A.10a, E_T^{miss} in A.10b, tri-lepton system p_T in A.10c and $m_{\ell\ell}$ in A.10d.

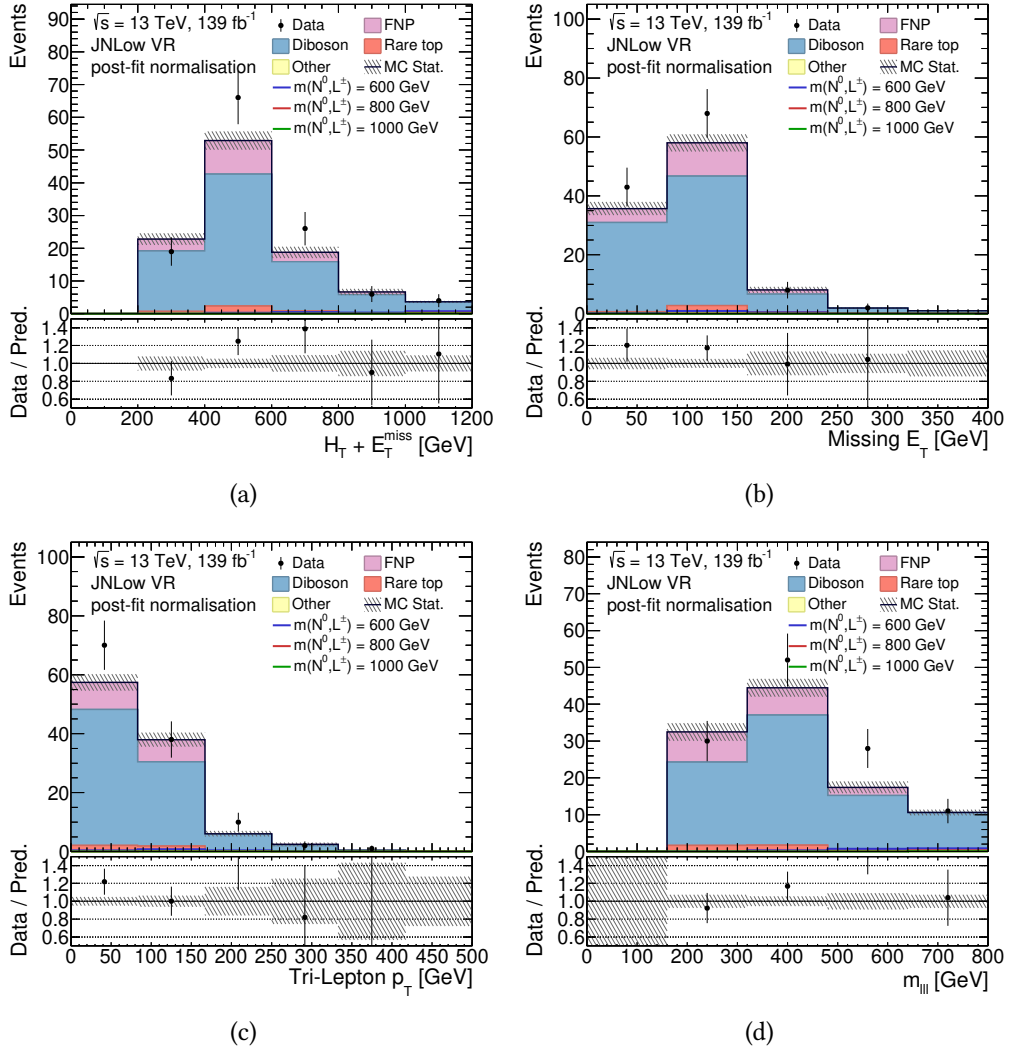
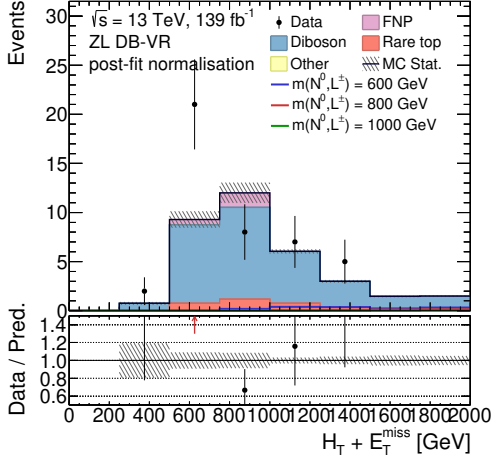
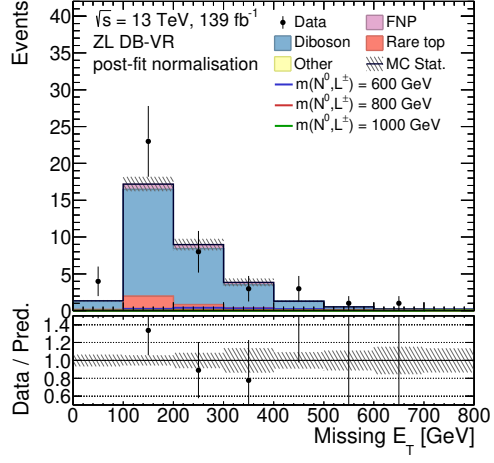


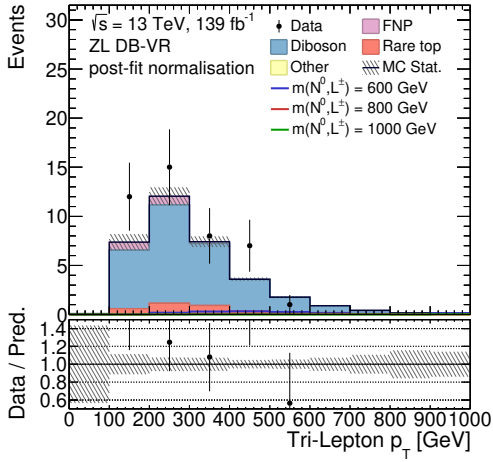
Figure A.11: Post-fit distribution for the JNLow VR: $H_T + E_T^{\text{miss}}$ in A.11a, E_T^{miss} in A.11b, tri-lepton system p_T in A.11c and $m_{\ell\ell}$ in A.11d.



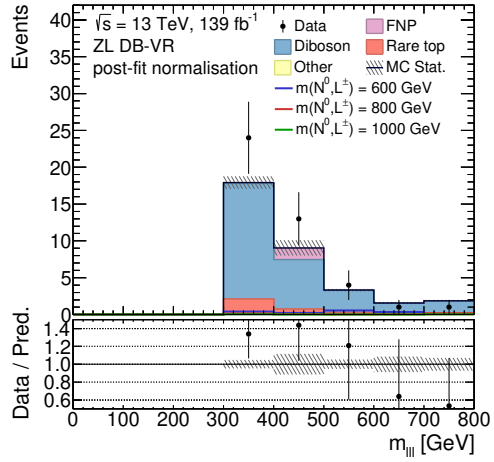
(a)



(b)



(c)



(d)

Figure A.12: Post-fit distribution for the ZL Diboson VR: $H_T + E_T^{\text{miss}}$ in A.12a, E_T^{miss} in A.12b, tri-lepton system p_T in A.12c and $m_{\ell\ell}$ in A.12d.

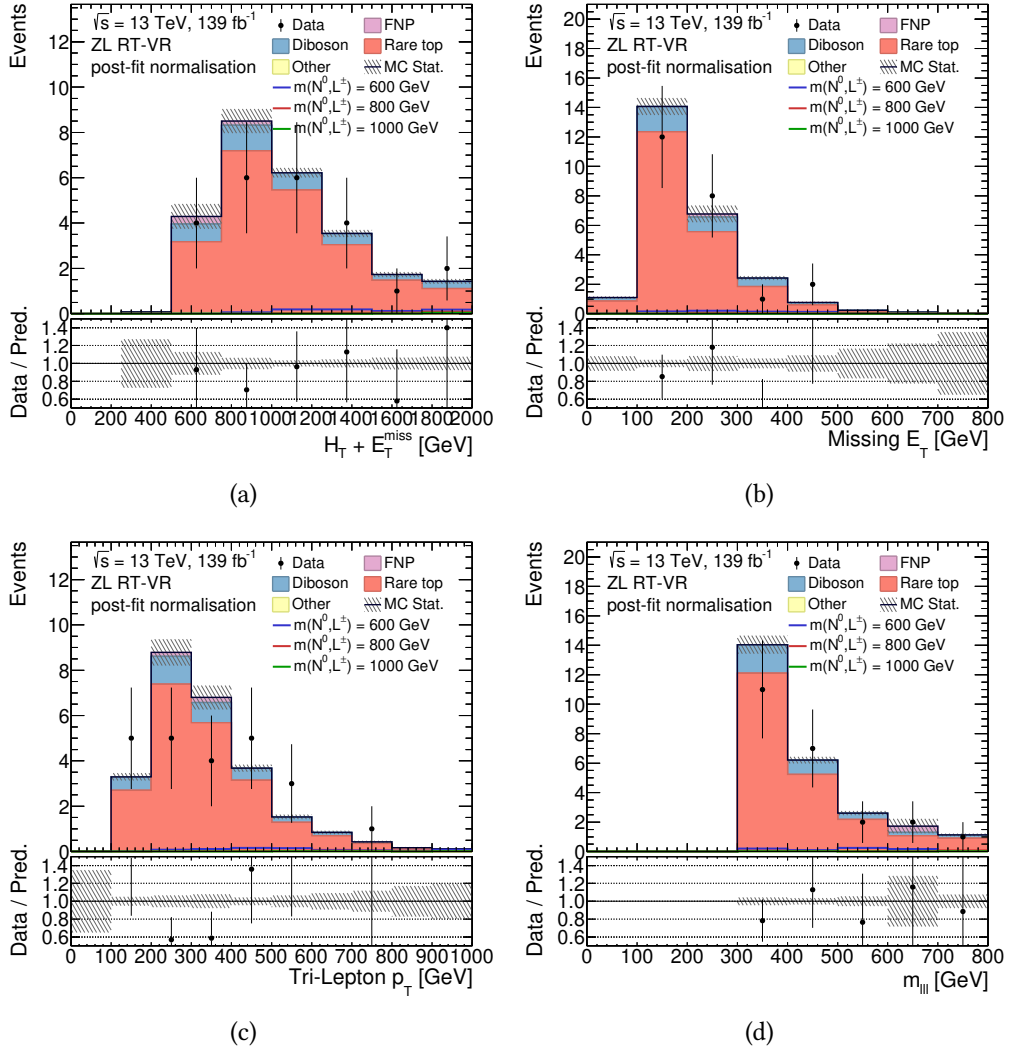
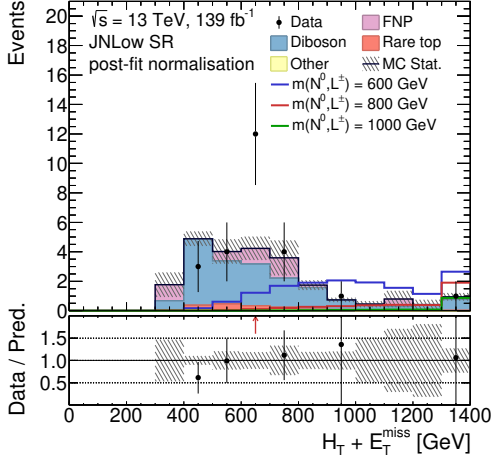
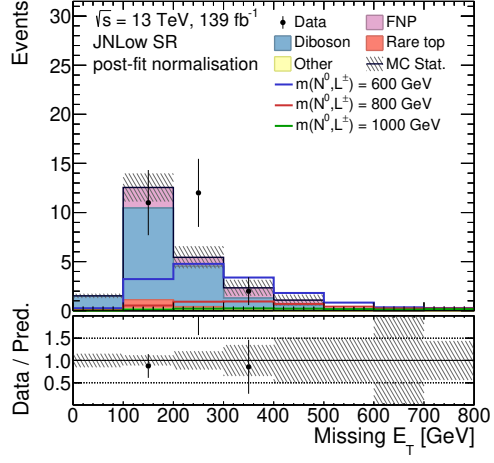


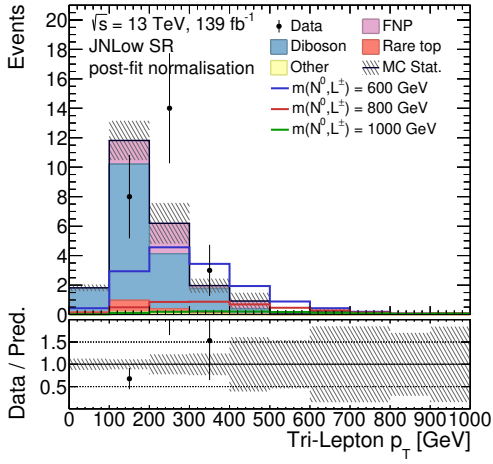
Figure A.13: Post-fit distribution for the ZL RareTop VR: $H_T + E_T^{\text{miss}}$ in A.13a, E_T^{miss} in A.13b, tri-lepton system p_T in A.13c and $m_{(\ell\ell)}$ in A.13d.



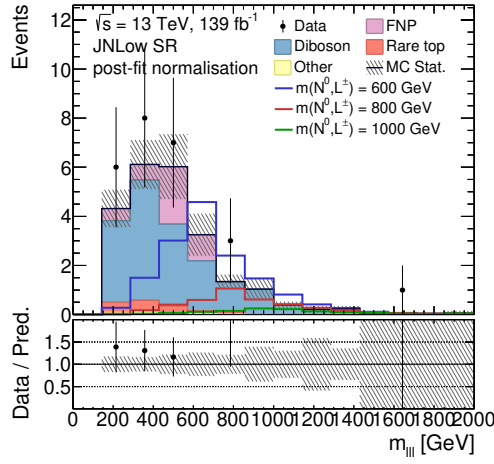
(a)



(b)



(c)



(d)

Figure A.14: Post-fit distribution for the JNLow SR: $H_T + E_T^{\text{miss}}$ in A.14a, E_T^{miss} in A.14b, tri-lepton system p_T in A.14c and $m_{(\ell\ell)}$ in A.14d.

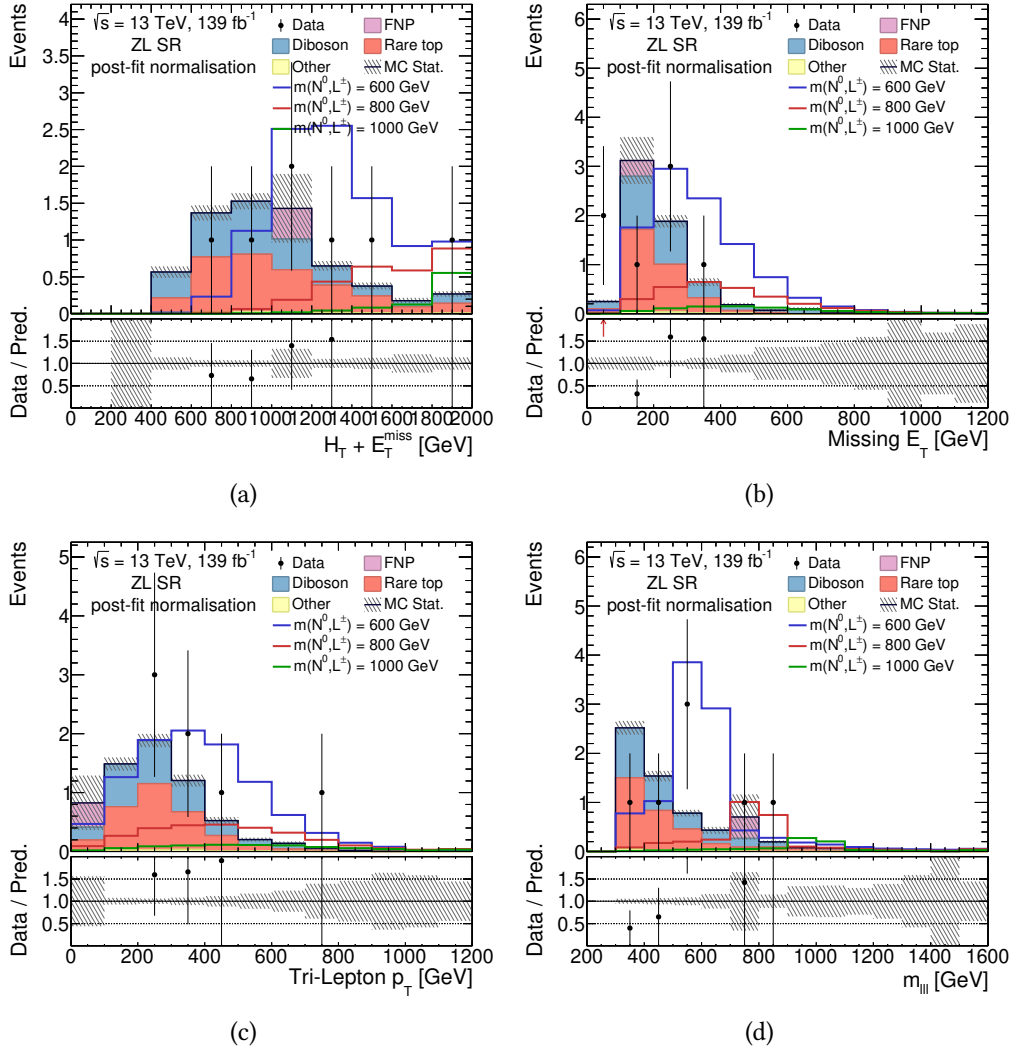
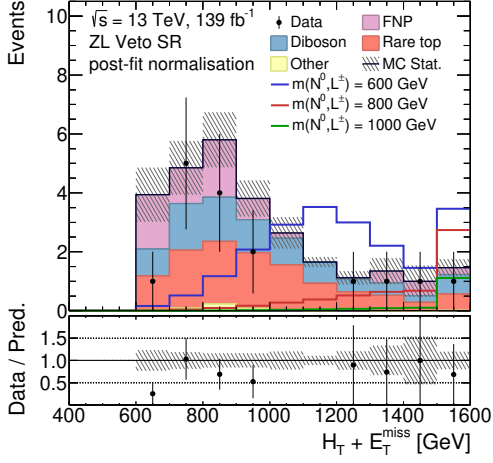
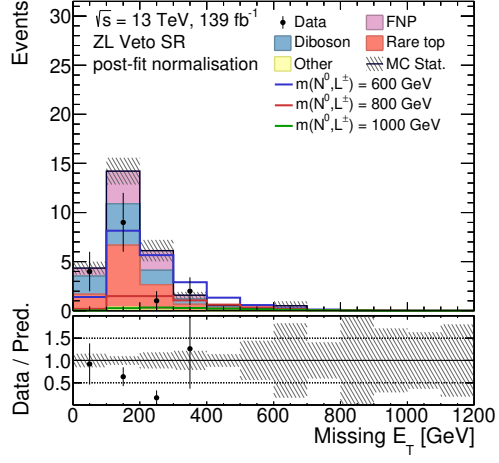


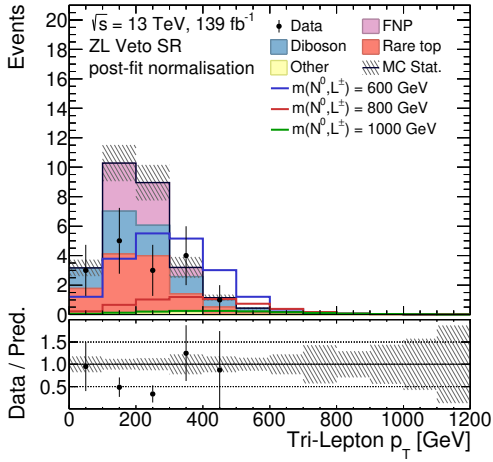
Figure A.15: Post-fit distribution for the ZL SR: $H_T + E_T^{\text{miss}}$ in A.15a, E_T^{miss} in A.15b, tri-lepton system p_T in A.15c and $m_{\ell\ell}$ in A.15d.



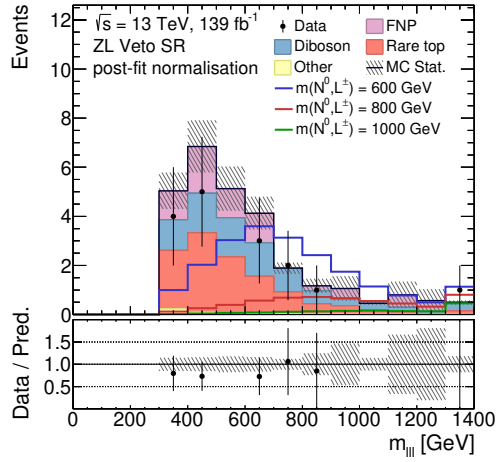
(a)



(b)



(c)



(d)

Figure A.16: Post-fit distribution for the ZL Veto SR: $H_T + E_T^{\text{miss}}$ in A.16a, E_T^{miss} in A.16b, tri-lepton system p_T in A.16c and $m_{\ell\ell}$ in A.16d.

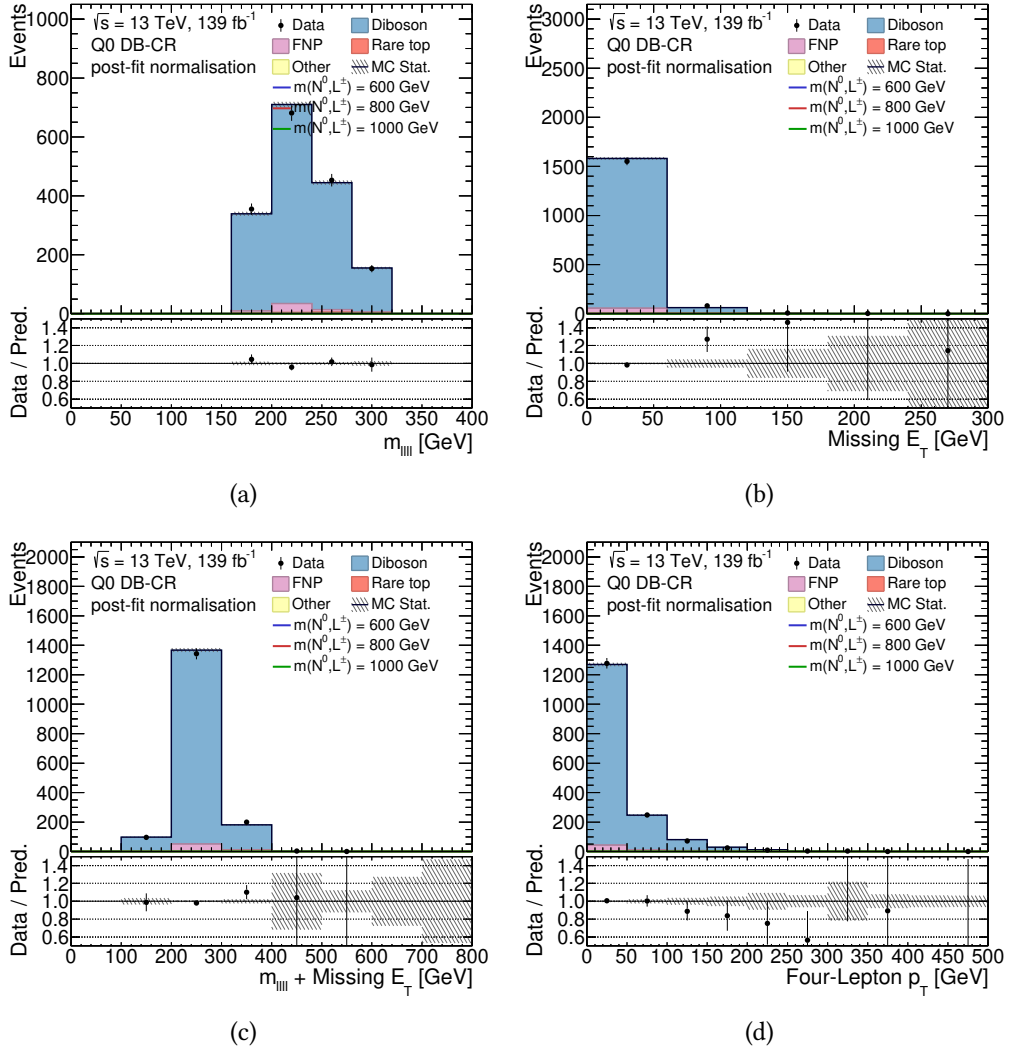


Figure A.17: Post-fit distribution for the Q0 Diboson CR: $m_{(\ell\ell\ell)}$ in A.17a, E_T^{miss} in A.17b, $m_{(\ell\ell\ell)} + E_T^{\text{miss}}$ in A.17c and four-lepton system p_T in A.17d.

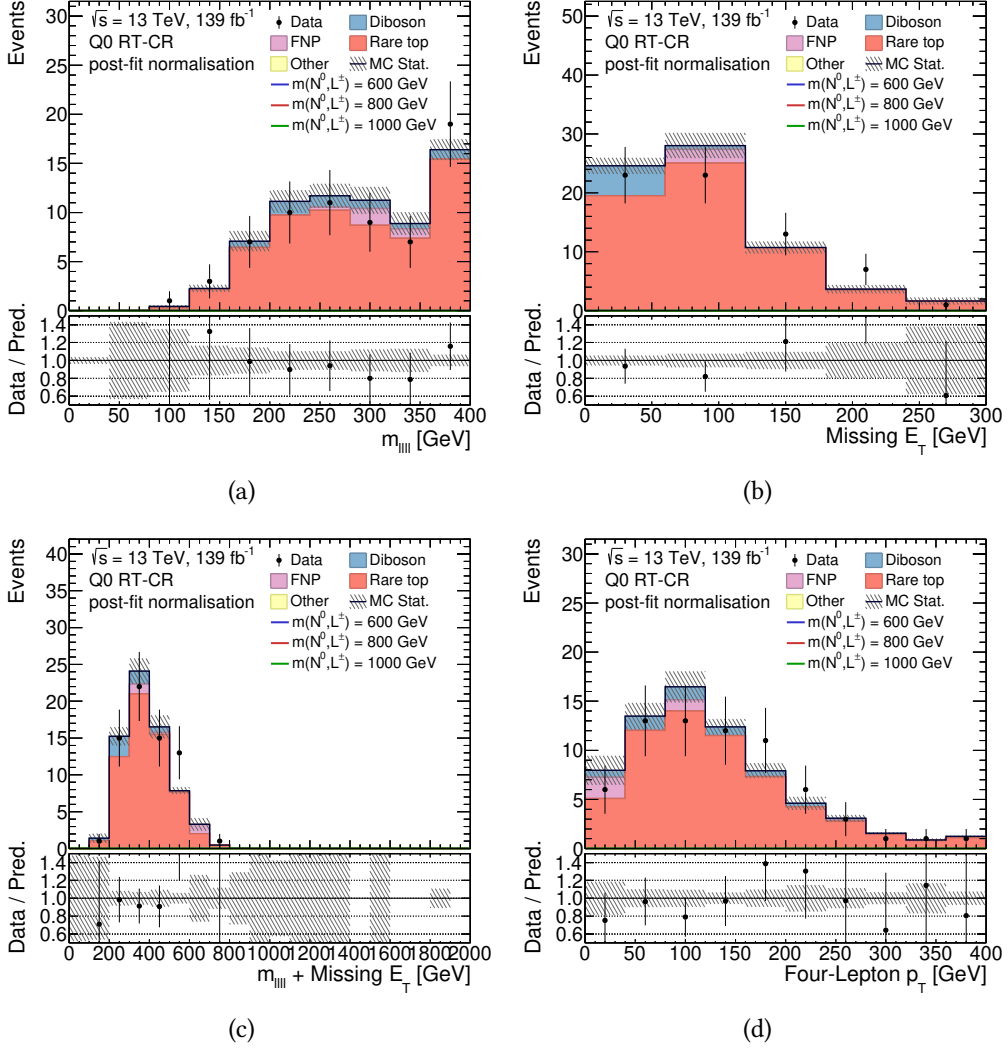


Figure A.18: Post-fit distribution for the Q0 RareTop CR: $m_{(\ell\ell\ell)}$ in A.18a, E_T^{miss} in A.18b, $m_{(\ell\ell\ell)} + E_T^{\text{miss}}$ in A.18c and four-lepton system p_T in A.18d.

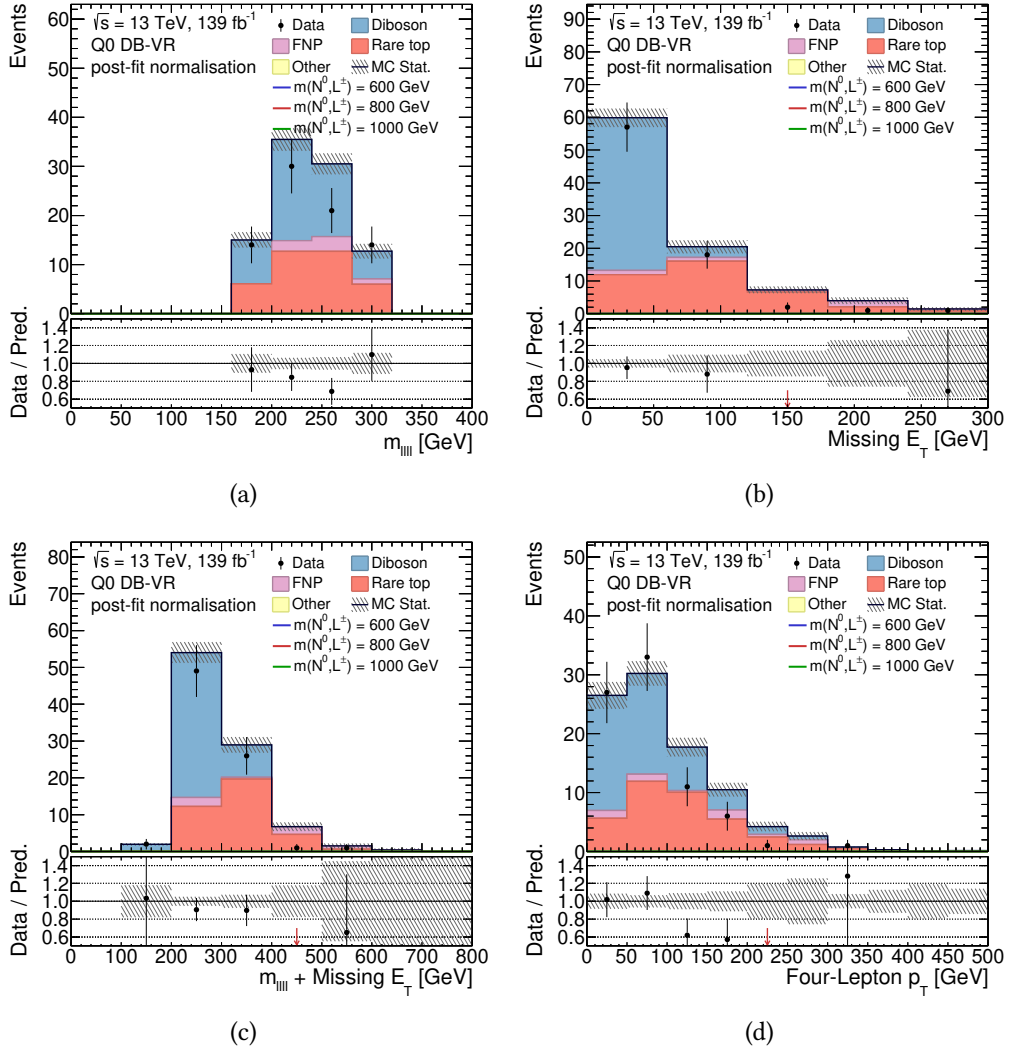


Figure A.19: Post-fit distribution for the Q0 Diboson VR: $m_{(\ell\ell)}$ in A.19a, E_T^{miss} in A.19b, $m_{(\ell\ell)} + E_T^{\text{miss}}$ in A.19c and four-lepton system p_T in A.19d.

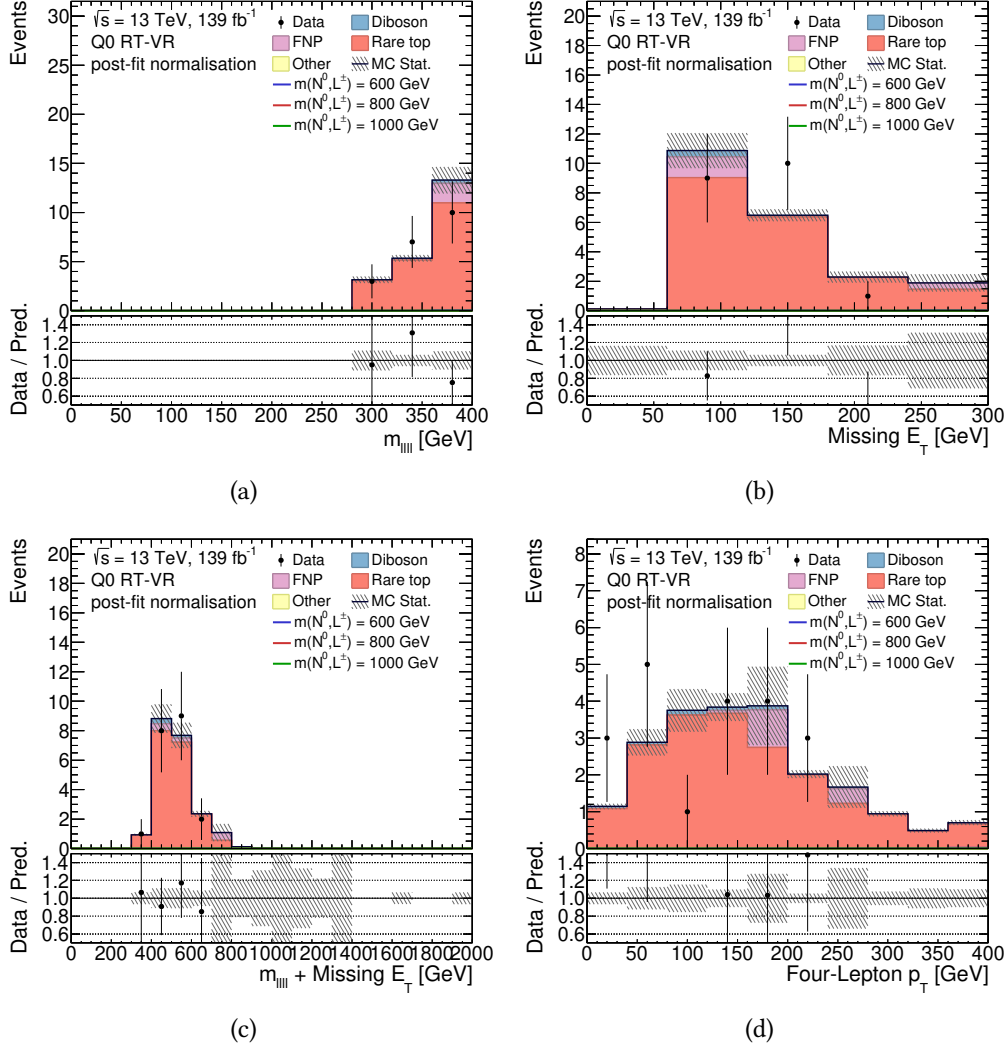


Figure A.20: Post-fit distribution for the Q0 RareTop VR: $m_{(\ell\ell\ell)}$ in A.20a, E_T^{miss} in A.20b, $m_{(\ell\ell\ell)} + E_T^{\text{miss}}$ in A.20c and four-lepton system p_T in A.20d.

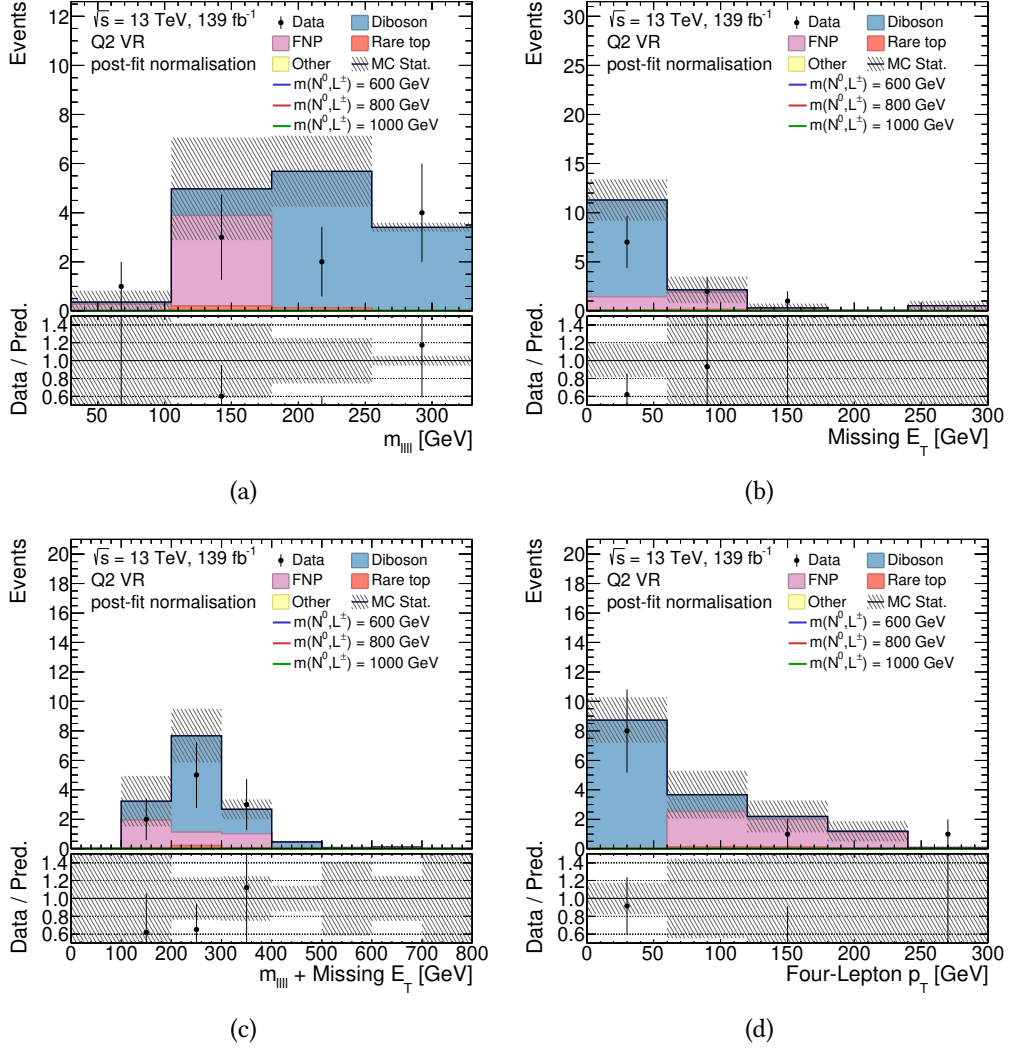
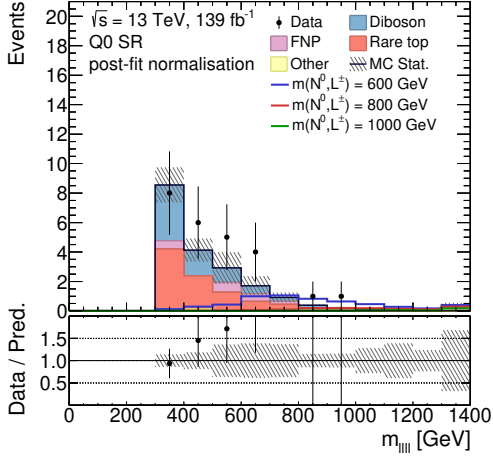
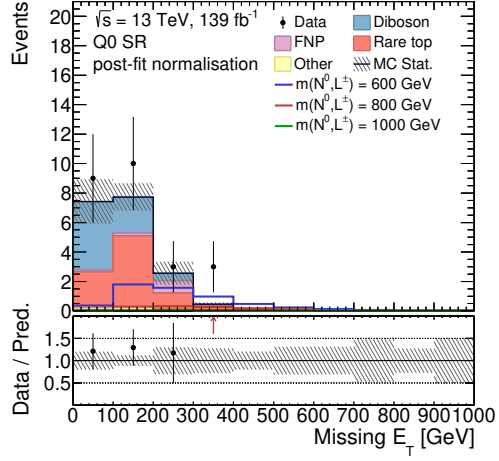


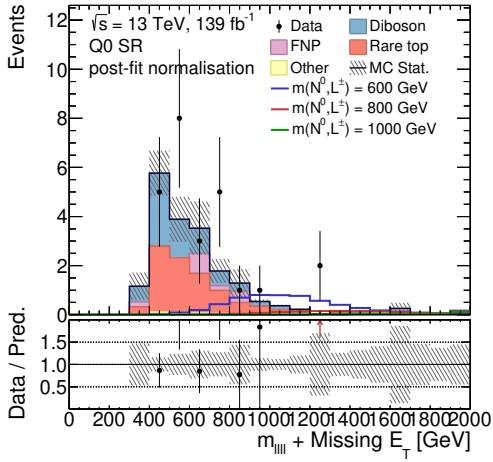
Figure A.21: Post-fit distribution for the Q2 VR: $m_{(\ell\ell\ell)}$ in A.21a, E_T^{miss} in A.21b, $m_{(\ell\ell\ell)} + E_T^{\text{miss}}$ in A.21c and four-lepton system p_T in A.21d.



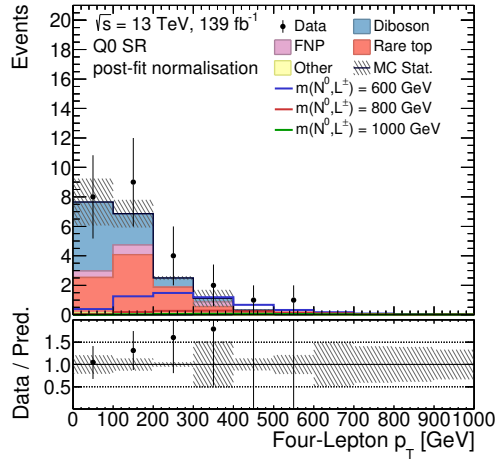
(a)



(b)



(c)



(d)

Figure A.22: Post-fit distribution for the Q0 SR: $m_{(\ell\ell\ell)}$ in A.22a, E_T^{miss} in A.22b, $m_{(\ell\ell\ell)} + E_T^{\text{miss}}$ in A.22c and four-lepton system p_T in A.22d.

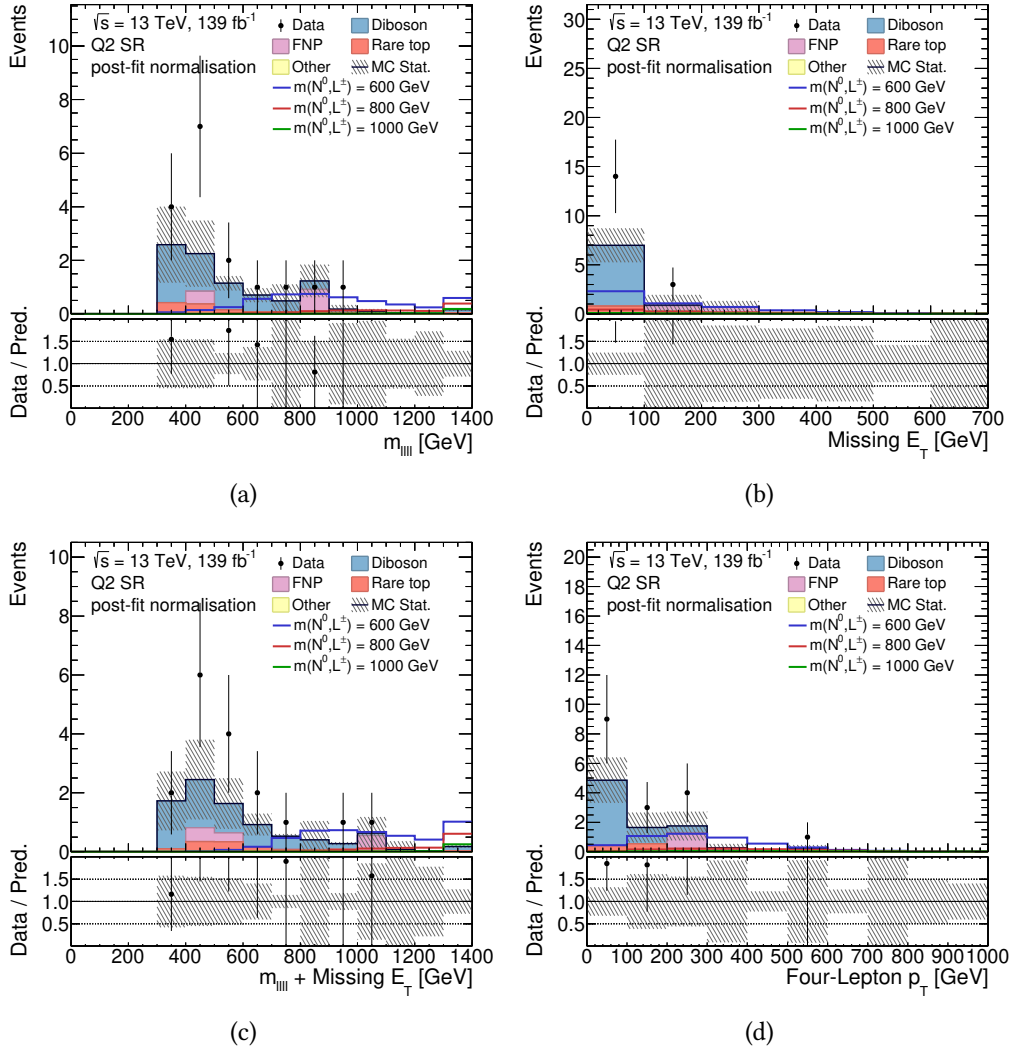


Figure A.23: Post-fit distribution for the Q2 SR: $m_{(\ell\ell\ell)}$ in A.23a, E_T^{miss} in A.23b, $m_{(\ell\ell\ell)} + E_T^{\text{miss}}$ in A.23c and four-lepton system p_T in A.23d.

A.4 Cutflows

In this Appendix, several tables listing the number of yields in each analysis region after each selection cut, the so-called *cutflow*, are reported. These yields are obtained before the fit procedure. The *Preselection* level corresponds to the request for at least three leptons.

These cutflows are presented for:

- ZL SR in Table [A.8](#);
- ZLVeto SR in Table [A.9](#);
- JNLow SR in Table [A.10](#);
- Q0 SR in Table [A.11](#);
- Q2 SR in Table [A.12](#);
- ZL CR in Table [A.13](#);
- Q0 Diboson CR in Table [A.14](#);
- Q0 RareTop CR in Table [A.15](#);
- Fake VR in Table [A.16](#);
- JNLow VR in Table [A.17](#);
- ZL Diboson VR in Table [A.18](#);
- ZL RareTop VR in Table [A.19](#);
- Q0 Diboson VR in Table [A.20](#);
- Q0 RareTop VR in Table [A.21](#);
- Q2 VR in Table [A.22](#).

ZL SR				
Cut	Signal	Other	RT	DB
Preselection	39.7	3.27e+03	2.28e+04	3.45e+04
Number of jets	28.3	1.48e+03	2.2e+04	1.25e+04
Three loose leptons	28.3	1.48e+03	3.28e+03	1.25e+04
Triggers	28.3	1.48e+03	3.27e+03	1.25e+04
Trigger matching	28.3	1.48e+03	3.21e+03	1.25e+04
Bad muon veto	28.3	1.48e+03	3.21e+03	1.25e+04
Three tight leptons	23.7	236	2.41e+03	9.29e+03
Analysis channel	23.7	236	1.7e+03	9.29e+03
Charge	20.4	232	1.69e+03	8.75e+03
Third lepton p_T	19.8	134	1.57e+03	8.08e+03
E_T^{miss} significance	15	18.1	656	2.3e+03
Number of Z bosons (leptonic)	5.38	4.04	408	1.95e+03
m_{ll}	4.92	1.05	89.1	362
Leading lepton m_T	4.49	0.778	61	191
Subleading lepton T	3.53	0.29	22	45.6
$\Delta R(\text{lead.lep.}, \text{sublead.lep.})$	2.82	0.116	2.41	3.49

Table A.8: Signal and MC events at different stage of the applied event section. Events are reweighted using the proper reconstruction weighs. The signal sample considered is generated with a heavy lepton mass hypothesis of 800 GeV.

ZLVeto SR				
Cut	Signal	Other	RT	DB
Preselection	39.7	3.27e+03	2.28e+04	3.45e+04
Number of jets	28.3	1.48e+03	2.2e+04	1.25e+04
Three loose leptons	28.3	1.48e+03	3.28e+03	1.25e+04
Triggers	28.3	1.48e+03	3.27e+03	1.25e+04
Trigger matching	28.3	1.48e+03	3.21e+03	1.25e+04
Bad muon veto	28.3	1.48e+03	3.21e+03	1.25e+04
Three tight leptons	23.7	236	2.41e+03	9.29e+03
Analysis channel	23.7	236	1.7e+03	9.29e+03
Charge	20.4	232	1.69e+03	8.75e+03
Third lepton p_T	19.8	134	1.57e+03	8.08e+03
E_T^{miss} significance	15	18.1	656	2.3e+03
Number of Z bosons (leptonic)	9.32	12	192	195
$H_T + E_T^{\text{miss}}$	9.28	3.84	108	89.4
m_{ll}	9.09	1.84	50.9	38.5
m_{jj}	6.38	1.27	31.9	27.2
Di-lepton H_T , SS lead. pair	5.53	0.482	9.24	11

Table A.9: Signal and MC events at different stage of the applied event section. Events are reweighted using the proper reconstruction weighs. The signal sample considered is generated with a heavy lepton mass hypothesis of 800 GeV.

JNLow SR				
Cut	Signal	Other	RT	DB
Preselection	39.7	3.27e+03	2.28e+04	3.45e+04
Number of jets	11.4	1.79e+03	842	2.21e+04
Three loose leptons	9.22	1.78e+03	303	1.95e+04
Triggers	9.22	1.78e+03	302	1.95e+04
Trigger matching	9.22	1.78e+03	298	1.95e+04
Bad muon veto	9.22	1.78e+03	298	1.95e+04
Three tight leptons	7.87	297	227	1.51e+04
Analysis channel	7.87	297	147	1.51e+04
Charge	7.73	296	147	1.51e+04
Third lepton p_T	7.5	166	137	1.39e+04
E_T^{miss} significance	6.75	9.58	66.7	3.99e+03
Number of Z bosons (leptonic)	6.68	8.58	62.8	3.75e+03
Lepton H_T	6.63	3.2	22.3	897
Subleading lepton T	5.34	1.23	9.32	310
Leading lepton m_T	4.92	0.771	5.06	160
$\Delta R(\text{lead.lep.}, \text{sublead.lep.})$	3.98	0.319	1.3	21.9

Table A.10: Signal and MC events at different stage of the applied event section. Events are reweighted using the proper reconstruction weighs. The signal sample considered is generated with a heavy lepton mass hypothesis of 800 GeV.

Q0 SR				
Cut	Signal	Other	RT	DB
Preselection	39.7	3.27e+03	2.28e+04	3.45e+04
Number of jets	39.7	3.27e+03	2.28e+04	3.45e+04
Four loose leptons	5.18	18.7	269	3.43e+03
Triggers	5.18	18.7	269	3.43e+03
Trigger matching	5.18	18.7	268	3.43e+03
Bad muon veto	5.18	18.7	268	3.43e+03
Four tight leptons	4.07	14.7	179	2.27e+03
Analysis channel	4.07	14.7	146	2.27e+03
Charge	2.95	14.6	145	2.25e+03
Number of b -jets	2.28	14.2	23	2.17e+03
$H_T + E_T^{\text{miss}}$	2.28	2.72	21.4	726
m_{lll}	2.27	1.12	12.2	426
Number of Z bosons (leptonic)	2.21	0.762	11	136
E_T^{miss} significance	1.37	0.49	6.84	7.26

Table A.11: Signal and MC events at different stage of the applied event section. Events are reweighted using the proper reconstruction weighs. The signal sample considered is generated with a heavy lepton mass hypothesis of 800 GeV.

Q2 SR				
Cut	Signal	Other	RT	DB
Preselection	39.7	3.27e+03	2.28e+04	3.45e+04
Number of jets	39.7	3.27e+03	2.28e+04	3.45e+04
Four loose leptons	5.18	18.7	269	3.43e+03
Triggers	5.18	18.7	269	3.43e+03
Trigger matching	5.18	18.7	268	3.43e+03
Bad muon veto	5.18	18.7	268	3.43e+03
Four tight leptons	4.07	14.7	179	2.27e+03
Analysis channel	4.07	14.7	146	2.27e+03
Charge	1.11	0.137	1.54	17.2
m_{lll}	1.11	0.0941	0.891	7.49
$H_T + E_T^{\text{miss}}$	1.11	0.0878	0.889	5.85

Table A.12: Signal and MC events at different stage of the applied event section. Events are reweighted using the proper reconstruction weighs. The signal sample considered is generated with a heavy lepton mass hypothesis of 800 GeV.

ZL CR				
Cut	Signal	Other	RT	DB
Preselection	39.7	3.27e+03	2.28e+04	3.45e+04
Number of jets	28.3	1.48e+03	2.2e+04	1.25e+04
Three loose leptons	28.3	1.48e+03	3.28e+03	1.25e+04
Triggers	28.3	1.48e+03	3.27e+03	1.25e+04
Trigger matching	28.3	1.48e+03	3.21e+03	1.25e+04
Bad muon veto	28.3	1.48e+03	3.21e+03	1.25e+04
Three tight leptons	23.7	236	2.41e+03	9.29e+03
Analysis channel	23.7	236	1.7e+03	9.29e+03
Charge	20.4	232	1.69e+03	8.75e+03
Third lepton p_T	19.8	134	1.57e+03	8.08e+03
E_T^{miss} significance	15	18.1	656	2.3e+03
Number of Z bosons (leptonic)	5.38	4.04	408	1.95e+03
Subleading lepton T	1.1	3.18	331	1.74e+03

Table A.13: Signal and MC events at different stage of the applied event section. Events are reweighted using the proper reconstruction weighs. The signal sample considered is generated with a heavy lepton mass hypothesis of 800 GeV.

Q0 Diboson CR				
Cut	Signal	Other	RT	DB
Preselection	39.7	3.27e+03	2.28e+04	3.45e+04
Number of jets	39.7	3.27e+03	2.28e+04	3.45e+04
Four loose leptons	5.18	18.7	269	3.43e+03
Triggers	5.18	18.7	269	3.43e+03
Trigger matching	5.18	18.7	268	3.43e+03
Bad muon veto	5.18	18.7	268	3.43e+03
Four tight leptons	4.07	14.7	179	2.27e+03
Analysis channel	4.07	14.7	146	2.27e+03
Charge	2.95	14.6	145	2.25e+03
Number of b -jets	2.28	14.2	23	2.17e+03
m_{llll}	0.00662	0.787	9.4	1.47e+03

Table A.14: Signal and MC events at different stage of the applied event section. Events are reweighted using the proper reconstruction weighs. The signal sample considered is generated with a heavy lepton mass hypothesis of 800 GeV.

Q0 RareTop CR				
Cut	Signal	Other	RT	DB
Preselection	39.7	3.27e+03	2.28e+04	3.45e+04
Number of jets	39.7	3.27e+03	2.28e+04	3.45e+04
Four loose leptons	5.18	18.7	269	3.43e+03
Triggers	5.18	18.7	269	3.43e+03
Trigger matching	5.18	18.7	268	3.43e+03
Bad muon veto	5.18	18.7	268	3.43e+03
Four tight leptons	4.07	14.7	179	2.27e+03
Analysis channel	4.07	14.7	146	2.27e+03
Charge	2.95	14.6	145	2.25e+03
Number of b -jets	0.208	0.113	53.2	6.05
m_{llll}	0.0026	0.112	46.3	5.39

Table A.15: Signal and MC events at different stage of the applied event section. Events are reweighted using the proper reconstruction weighs. The signal sample considered is generated with a heavy lepton mass hypothesis of 800 GeV.

Fake VR				
Cut	Signal	Other	RT	DB
Preselection	39.7	3.27e+03	2.28e+04	3.45e+04
Number of jets	28.3	1.48e+03	2.2e+04	1.25e+04
Three loose leptons	28.3	1.48e+03	3.28e+03	1.25e+04
Triggers	28.3	1.48e+03	3.27e+03	1.25e+04
Trigger matching	28.3	1.48e+03	3.21e+03	1.25e+04
Bad muon veto	28.3	1.48e+03	3.21e+03	1.25e+04
Three tight leptons	23.7	236	2.41e+03	9.29e+03
Analysis channel	23.7	236	1.7e+03	9.29e+03
Charge	20.4	232	1.69e+03	8.75e+03
Third lepton p_T	19.8	134	1.57e+03	8.08e+03
E_T^{miss} significance	4.83	116	915	5.78e+03

Table A.16: Signal and MC events at different stage of the applied event section. Events are reweighted using the proper reconstruction weighs. The signal sample considered is generated with a heavy lepton mass hypothesis of 800 GeV.

JNLow VR				
Cut	Signal	Other	RT	DB
Preselection	39.7	3.27e+03	2.28e+04	3.45e+04
Number of jets	11.4	1.79e+03	842	2.21e+04
Three loose leptons	9.22	1.78e+03	303	1.95e+04
Triggers	9.22	1.78e+03	302	1.95e+04
Trigger matching	9.22	1.78e+03	298	1.95e+04
Bad muon veto	9.22	1.78e+03	298	1.95e+04
Three tight leptons	7.87	297	227	1.51e+04
Analysis channel	7.87	297	147	1.51e+04
Charge	7.73	296	147	1.51e+04
Third lepton p_T	7.5	166	137	1.39e+04
E_T^{miss} significance	6.75	9.58	66.7	3.99e+03
Number of Z bosons (leptonic)	6.68	8.58	62.8	3.75e+03
Leading lepton m_T	0.532	6.54	45.3	3.26e+03
Lepton H_T	0.503	1.41	9.72	486
Subleading lepton T	0.424	0.463	3.84	150
$\Delta R(\text{lead.lep.}, \text{sublead.lep.})$	0.405	0.377	3	108

Table A.17: Signal and MC events at different stage of the applied event section. Events are reweighted using the proper reconstruction weighs. The signal sample considered is generated with a heavy lepton mass hypothesis of 800 GeV.

ZL Diboson VR				
Cut	Signal	Other	RT	DB
Preselection	39.7	3.27e+03	2.28e+04	3.45e+04
Number of jets	28.3	1.48e+03	2.2e+04	1.25e+04
Three loose leptons	28.3	1.48e+03	3.28e+03	1.25e+04
Triggers	28.3	1.48e+03	3.27e+03	1.25e+04
Trigger matching	28.3	1.48e+03	3.21e+03	1.25e+04
Bad muon veto	28.3	1.48e+03	3.21e+03	1.25e+04
Three tight leptons	23.7	236	2.41e+03	9.29e+03
Analysis channel	23.7	236	1.7e+03	9.29e+03
Charge	20.4	232	1.69e+03	8.75e+03
Third lepton p_T	19.8	134	1.57e+03	8.08e+03
E_T^{miss} significance	15	18.1	656	2.3e+03
Number of b -jets	9.61	8.24	101	2.08e+03
Number of Z bosons (leptonic)	3.56	2.95	68.2	1.76e+03
m_{ll}	3.3	0.926	15.1	326
Leading lepton m_T	3.01	0.676	9.98	171
Subleading lepton T	2.35	0.234	3.38	40.2
$\Delta R(\text{lead.lep.}, \text{sublead.lep.})$	0.435	0.129	3.01	37.1

Table A.18: Signal and MC events at different stage of the applied event section. Events are reweighted using the proper reconstruction weighs. The signal sample considered is generated with a heavy lepton mass hypothesis of 800 GeV.

ZL RareTop VR				
Cut	Signal	Other	RT	DB
Preselection	39.7	3.27e+03	2.28e+04	3.45e+04
Number of jets	28.3	1.48e+03	2.2e+04	1.25e+04
Three loose leptons	28.3	1.48e+03	3.28e+03	1.25e+04
Triggers	28.3	1.48e+03	3.27e+03	1.25e+04
Trigger matching	28.3	1.48e+03	3.21e+03	1.25e+04
Bad muon veto	28.3	1.48e+03	3.21e+03	1.25e+04
Three tight leptons	23.7	236	2.41e+03	9.29e+03
Analysis channel	23.7	236	1.7e+03	9.29e+03
Charge	20.4	232	1.69e+03	8.75e+03
Third lepton p_T	19.8	134	1.57e+03	8.08e+03
E_T^{miss} significance	15	18.1	656	2.3e+03
Number of b -jets	5.4	9.87	555	221
Number of Z bosons (leptonic)	1.82	1.09	340	187
m_{ll}	1.71	0.134	73.9	36.6
Leading lepton m_T	1.56	0.108	51	19.7
Subleading lepton T	1.24	0.0569	18.6	5.43
$\Delta R(\text{lead.lep.}, \text{sublead.lep.})$	0.212	0.042	16.5	4.92

Table A.19: Signal and MC events at different stage of the applied event section. Events are reweighted using the proper reconstruction weights. The signal sample considered is generated with a heavy lepton mass hypothesis of 800 GeV.

Q0 Diboson VR				
Cut	Signal	Other	RT	DB
Preselection	39.7	3.27e+03	2.28e+04	3.45e+04
Number of jets	39.7	3.27e+03	2.28e+04	3.45e+04
Four loose leptons	5.18	18.7	269	3.43e+03
Triggers	5.18	18.7	269	3.43e+03
Trigger matching	5.18	18.7	268	3.43e+03
Bad muon veto	5.18	18.7	268	3.43e+03
Four tight leptons	4.07	14.7	179	2.27e+03
Analysis channel	4.07	14.7	146	2.27e+03
Charge	2.95	14.6	145	2.25e+03
Number of b -jets	0.461	0.308	68.3	76.3
m_{ll}	0.000643	0.077	28.7	46.3

Table A.20: Signal and MC events at different stage of the applied event section. Events are reweighted using the proper reconstruction weights. The signal sample considered is generated with a heavy lepton mass hypothesis of 800 GeV.

Q0 RareTop VR				
Cut	Signal	Other	RT	DB
Preselection	39.7	3.27e+03	2.28e+04	3.45e+04
Number of jets	39.7	3.27e+03	2.28e+04	3.45e+04
Four loose leptons	5.18	18.7	269	3.43e+03
Triggers	5.18	18.7	269	3.43e+03
Trigger matching	5.18	18.7	268	3.43e+03
Bad muon veto	5.18	18.7	268	3.43e+03
Four tight leptons	4.07	14.7	179	2.27e+03
Analysis channel	4.07	14.7	146	2.27e+03
Charge	2.95	14.6	145	2.25e+03
Number of b -jets	0.461	0.308	68.3	76.3
$H_T + E_T^{\text{miss}}$	0.461	0.186	57.5	32.4
m_{lll}	0.00643	0.0325	24.7	12.9
E_T^{miss} significance	0.00589	0.0121	14.8	0.569

Table A.21: Signal and MC events at different stage of the applied event section. Events are reweighted using the proper reconstruction weighs. The signal sample considered is generated with a heavy lepton mass hypothesis of 800 GeV.

Q2 VR				
Cut	Signal	Other	RT	DB
Preselection	39.7	3.27e+03	2.28e+04	3.45e+04
Number of jets	39.7	3.27e+03	2.28e+04	3.45e+04
Four loose leptons	5.18	18.7	269	3.43e+03
Triggers	5.18	18.7	269	3.43e+03
Trigger matching	5.18	18.7	268	3.43e+03
Bad muon veto	5.18	18.7	268	3.43e+03
Four tight leptons	4.07	14.7	179	2.27e+03
Analysis channel	4.07	14.7	146	2.27e+03
Charge	1.11	0.137	1.54	17.2
m_{lll}				
OR	1.07e-04	0.026	0.313	10.1
$H_T + E_T^{\text{miss}}$				

Table A.22: Signal and MC events at different stage of the applied event section. Events are reweighted using the proper reconstruction weighs. The signal sample considered is generated with a heavy lepton mass hypothesis of 800 TeV.

A.5 Results for separated channels

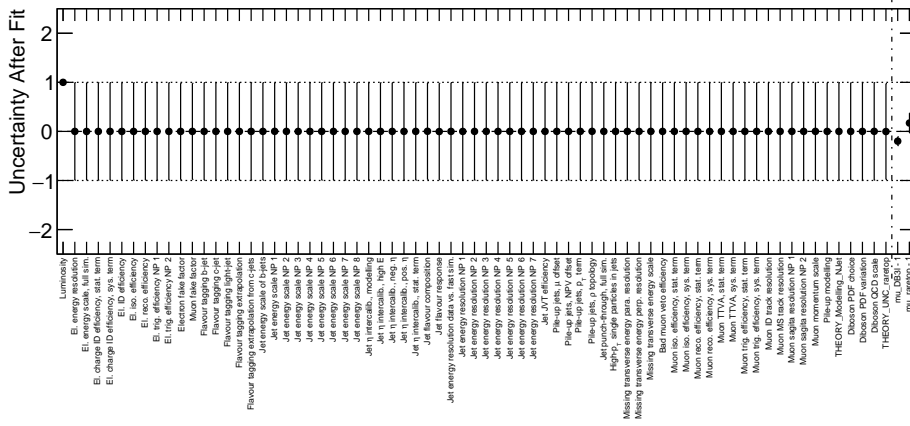
In this Appendix results obtained studying three- and four-channel separately are reported.

By performing a fit with the three-lepton channel only:

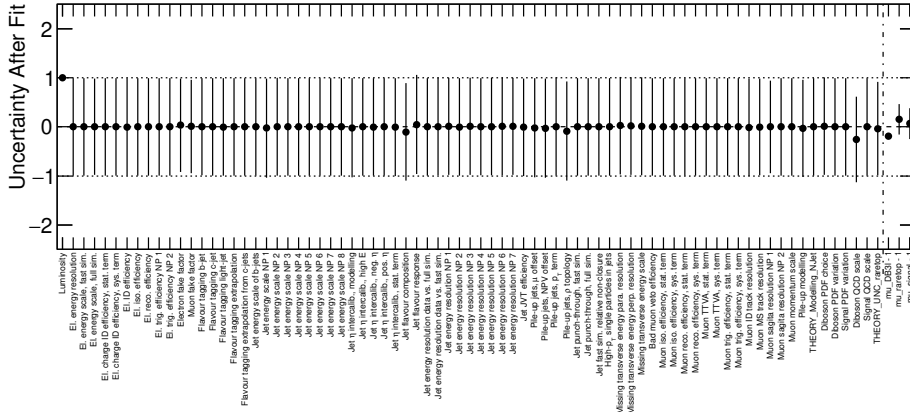
- pull-plots are in Figure [A.24](#);
- ranking plots are in Figure [A.25](#);
- exclusion limit is in Figure [A.26](#). The observed (expected) excluded limit is 860 GeV (885^{+84}_{-89} GeV).

Considering only the four-lepton channel:

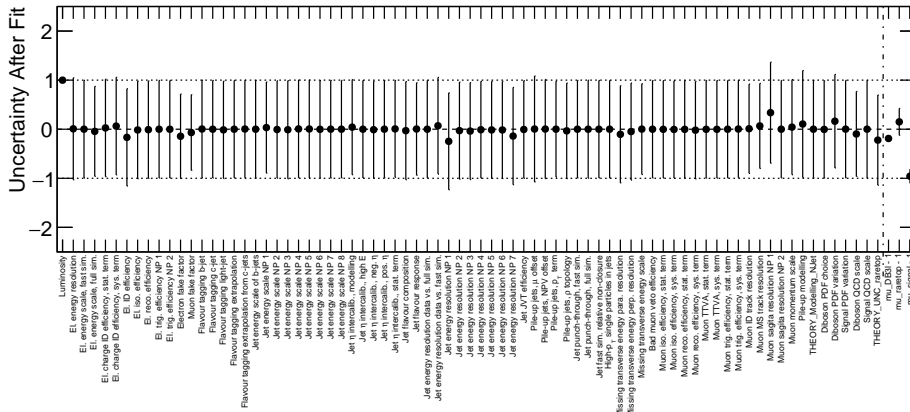
- pull-plots are in Figure [A.27](#);
- ranking plots are in Figure [A.28](#);
- exclusion limit is in Figure [A.29](#). The observed (expected) excluded limit is 580 GeV (690^{+68}_{-75} GeV).



(a)



(b)



(c)

Figure A.24: Post-fit nuisance parameters of the background-only fit with real data in control regions A.24a, exclusion fit with Asimov dataset A.24b and exclusion fit with real data in both control and signal regions A.24c. These plots are related to the three-lepton channel.

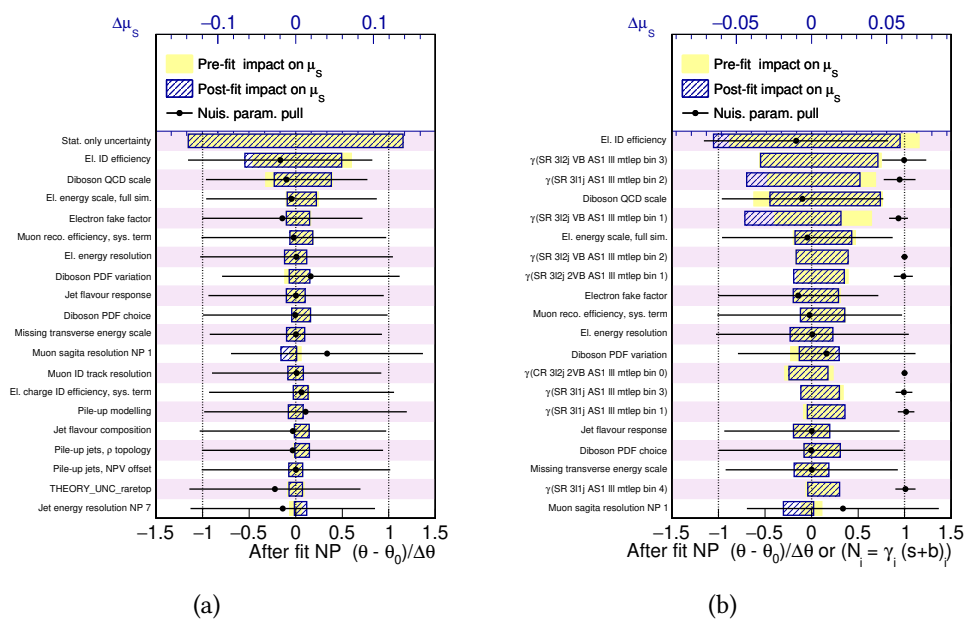


Figure A.25: Impact of systematic uncertainties on μ_{SIG} constructed by fixing one nuisance parameter to its $\pm 1\sigma$ variations at the time and minimizing the rest. In A.25a the impact of the dominant systematic source and MC statistical uncertainty, in A.25b only dominant systematic sources and gamma parameters corresponding to each bin in the analysis regions. Pre-fit impact are shown with a yellow box, post-fit with a dashed blue box while α with black points. These plots are related to three-lepton channel.

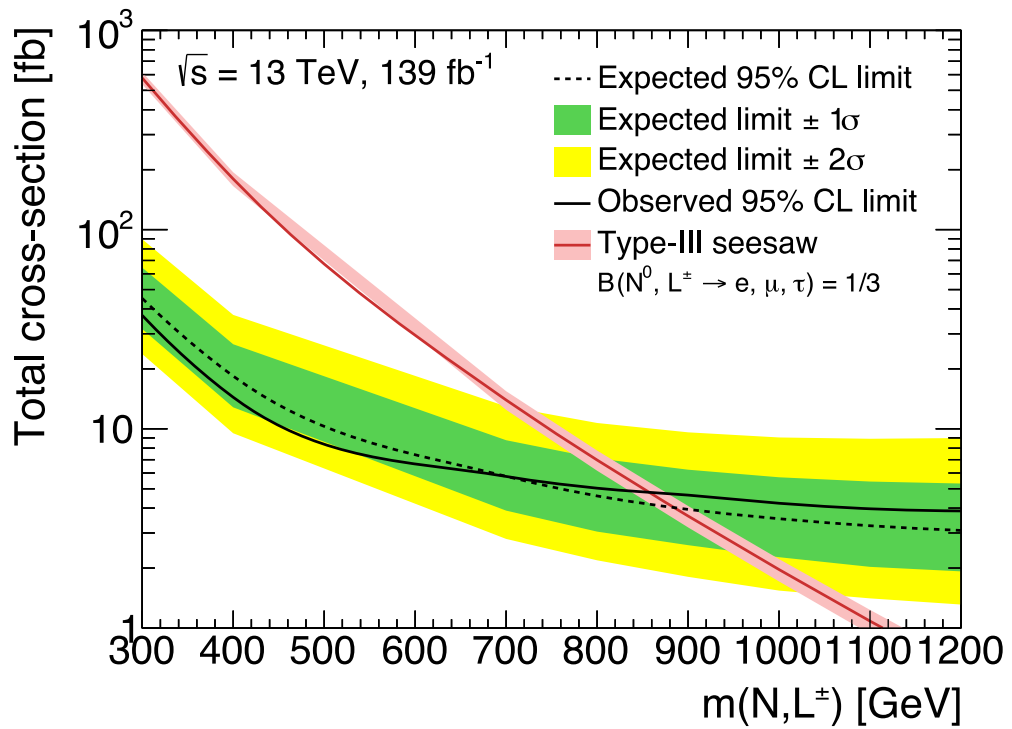


Figure A.26: Expected and observed 95% CLs exclusion limits in the three-lepton channel for the Type-III SeeSaw process with the corresponding one- and two-standard-deviation uncertainty bands, showing the 95% CL upper limit on the cross-section. The theoretical signal cross-section prediction, given by the NLO calculation, with its corresponding uncertainty band is also shown.

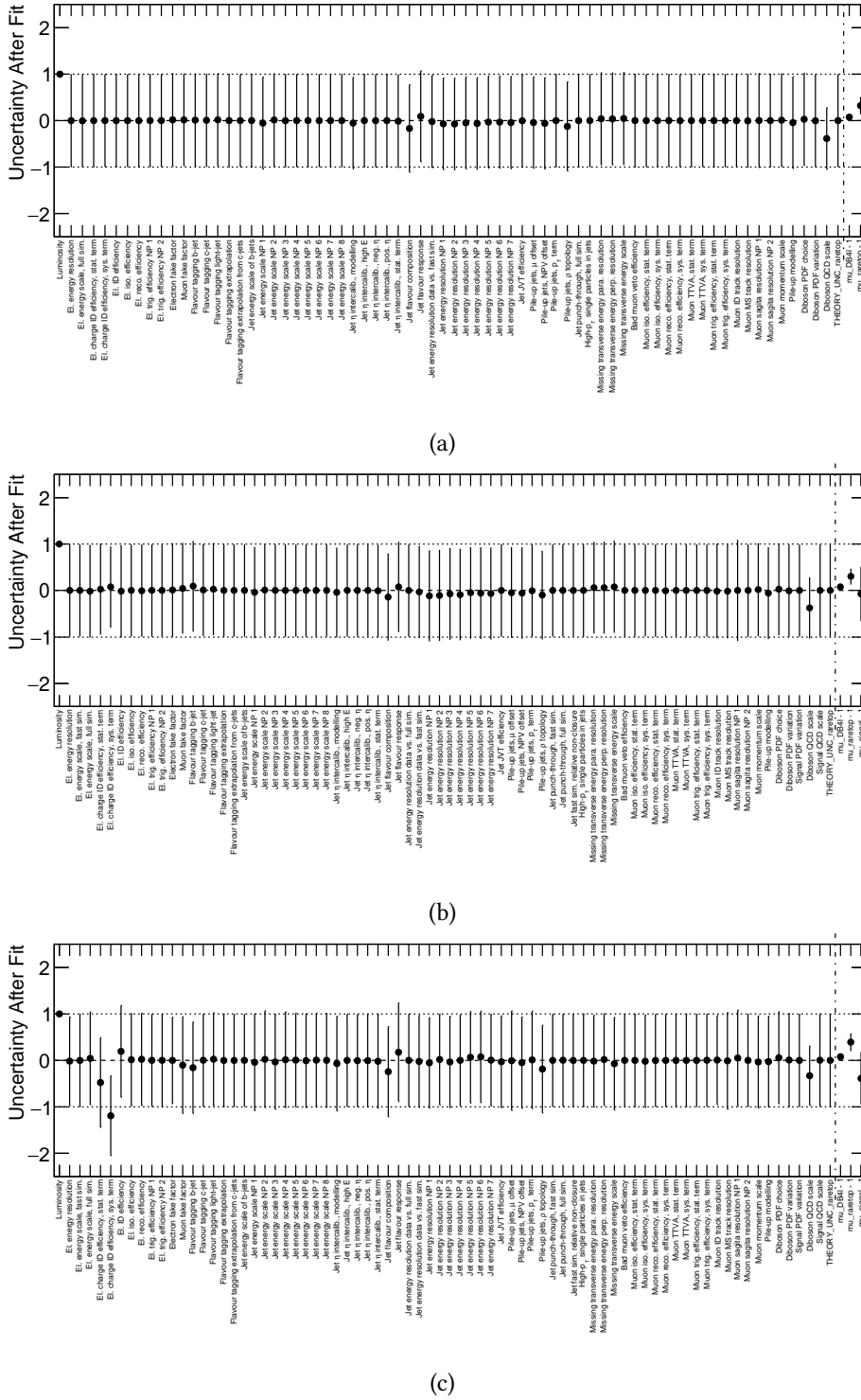


Figure A.27: Post-fit nuisance parameters of the background-only fit with real data in control regions [A.24a](#), exclusion fit with Asimov dataset [A.24b](#) and exclusion fit with real data in both control and signal regions [A.24c](#). These plots are related to the four-lepton channel.

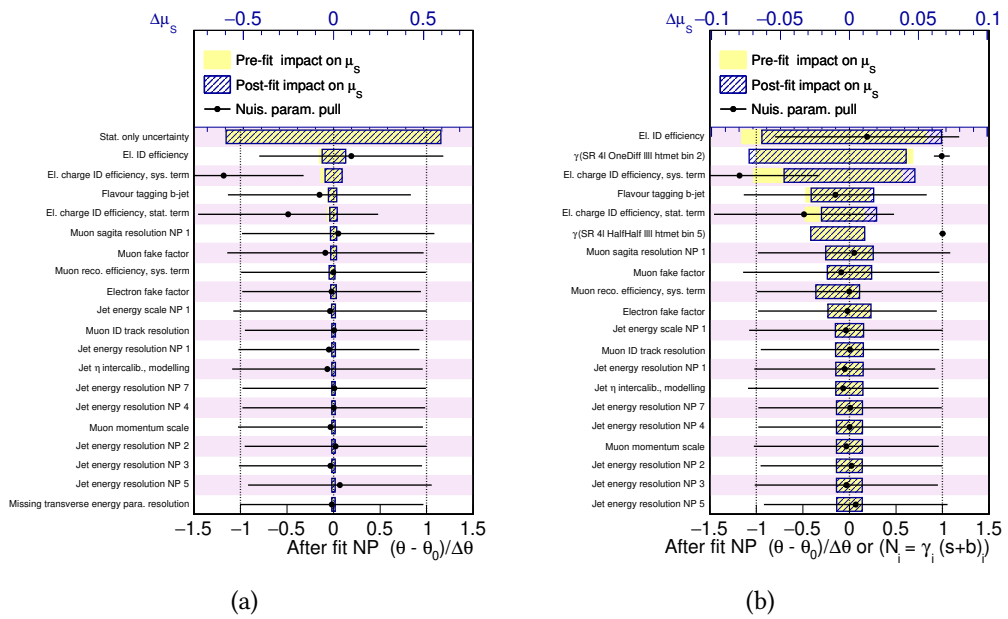


Figure A.28: Impact of systematic uncertainties on μ_{SIG} constructed by fixing one nuisance parameter to its $\pm 1\sigma$ variations at the time and minimizing the rest. In A.28a the impact of the dominant systematic source and MC statistical uncertainty, in A.28b only dominant systematic sources and gamma parameters corresponding to each bin in the analysis regions. Pre-fit impact are shown with a yellow box, post-fit with a dashed blue box while α with black points. These plots are related to four-lepton channel.

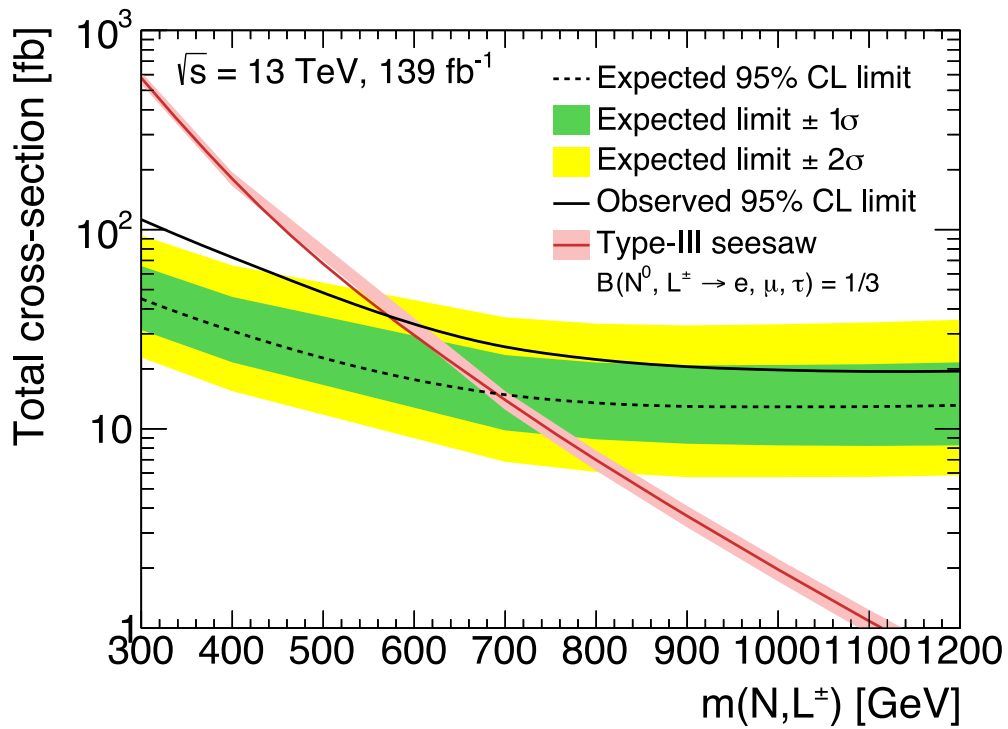


Figure A.29: Expected and observed 95% CLs exclusion limits in the four-lepton channel for the Type-III SeeSaw process with the corresponding one- and two-standard-deviation uncertainty bands, showing the 95% CL upper limit on the cross-section. The theoretical signal cross-section prediction, given by the NLO calculation, with its corresponding uncertainty band is also shown. This plot is related to the four-lepton channel.

A.6 Signal regions post-fit distributions Dilepton channel

In this Appendix the post-fit SRs distributions for the two-lepton plus two jets analysis are shown:

- Opposite-Sign Signal Regions in Figure [A.30](#);
- Same-Sign Signal Regions in Figure [A.30](#).

Analysis details Signal regions post-fit distributions Dilepton channel

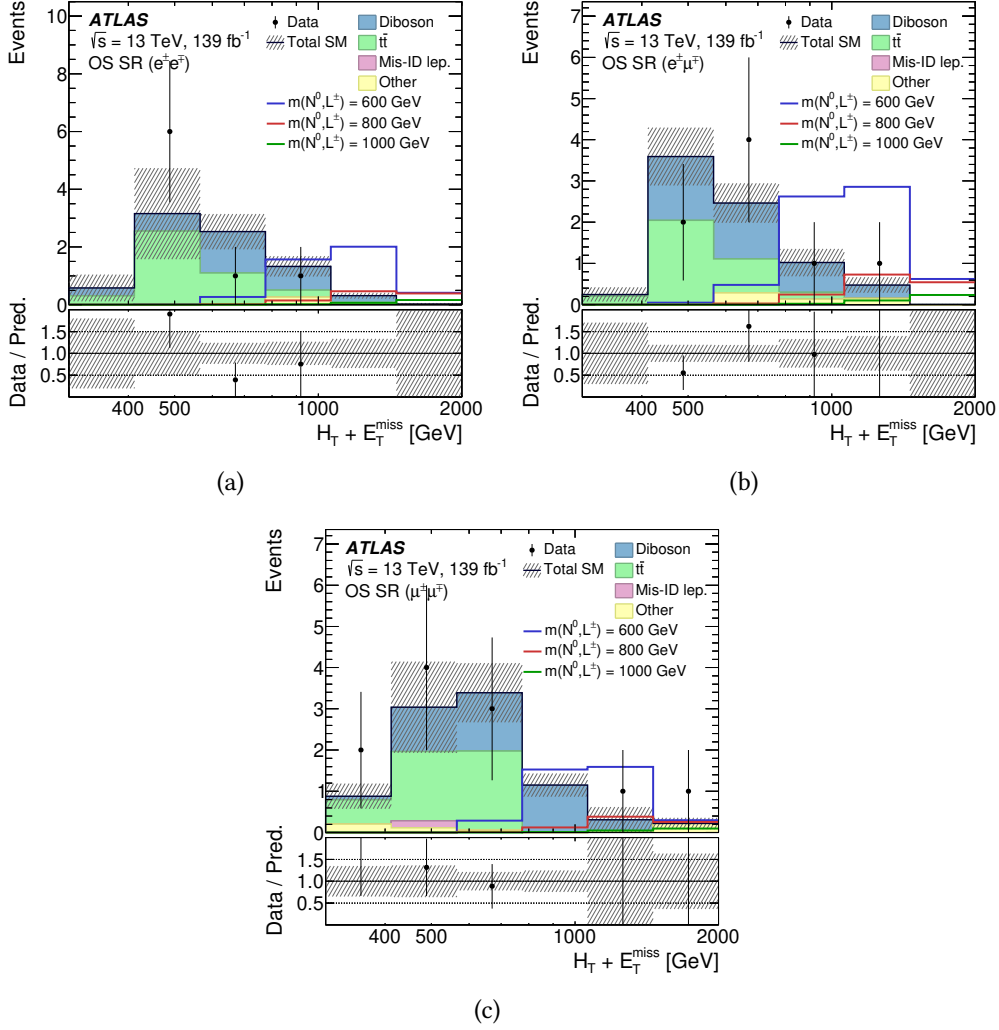


Figure A.30: Distributions of $H_T + E_T^{\text{miss}}$ in opposite-sign signal regions, namely **a** the electron–electron signal region, **b** the electron–muon signal region, and **c** the muon–muon signal region after the background-only fit. The hatched bands include all systematic uncertainties post-fit with the correlations between various sources taken into account. Errors on data are statistical only. The lower panel shows the ratio of the observed data to the estimated SM background [36].

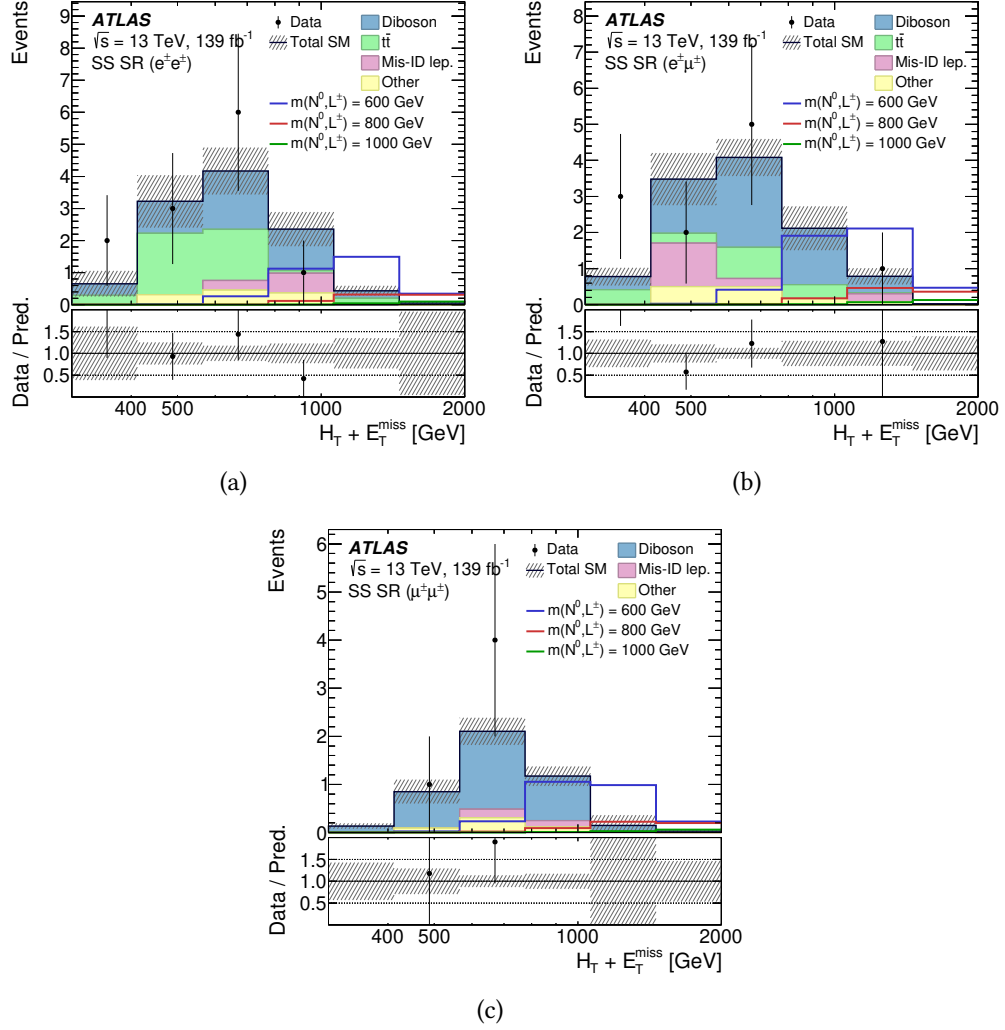


Figure A.31: Distributions of $H_T + E_T^{\text{miss}}$ in same-sign signal regions, namely **a** the electron–electron signal region, **b** the electron–muon signal region, and **c** the muon–muon signal region after the background-only. The hatched bands include all systematic uncertainties post-fit with the correlations between various sources taken into account. Errors on data are statistical only. The lower panel shows the ratio of the observed data to the estimated SM background [36].

A.7 Pull and ranking plots, and exclusion limit with toys for the combined fit with two-, three- and four-lepton channels

In this Appendix are shown the pull, in Figure [A.32](#), and the ranking plots, in Figure [A.33](#), for the combination of the two-, three- and four lepton channels.

Some NPs are a bit pulled, mainly related to the jets and $t\bar{t}$ backgrounds. As clear looking at the Appendix [A.5](#) and the Figures in [5.53](#), the main source of these pulled NPs is the two-lepton plus two jets channel, while the three- and four-lepton channels cause the deviation of the electron charge ID efficiency systematic.

Toys are also used to check the sensitivity of the analysis increasing the number of events during the fit procedure with a frequentist approach. The final results is consistent with the asymptotic calculation showing, in Figure [A.34](#), the same expected and observed limit with uncertainty bands reduced due to the larger statistic.

Pull and ranking plots, and exclusion limit with toys for the combined fit with two-, three- and four-lepton channels Analysis details

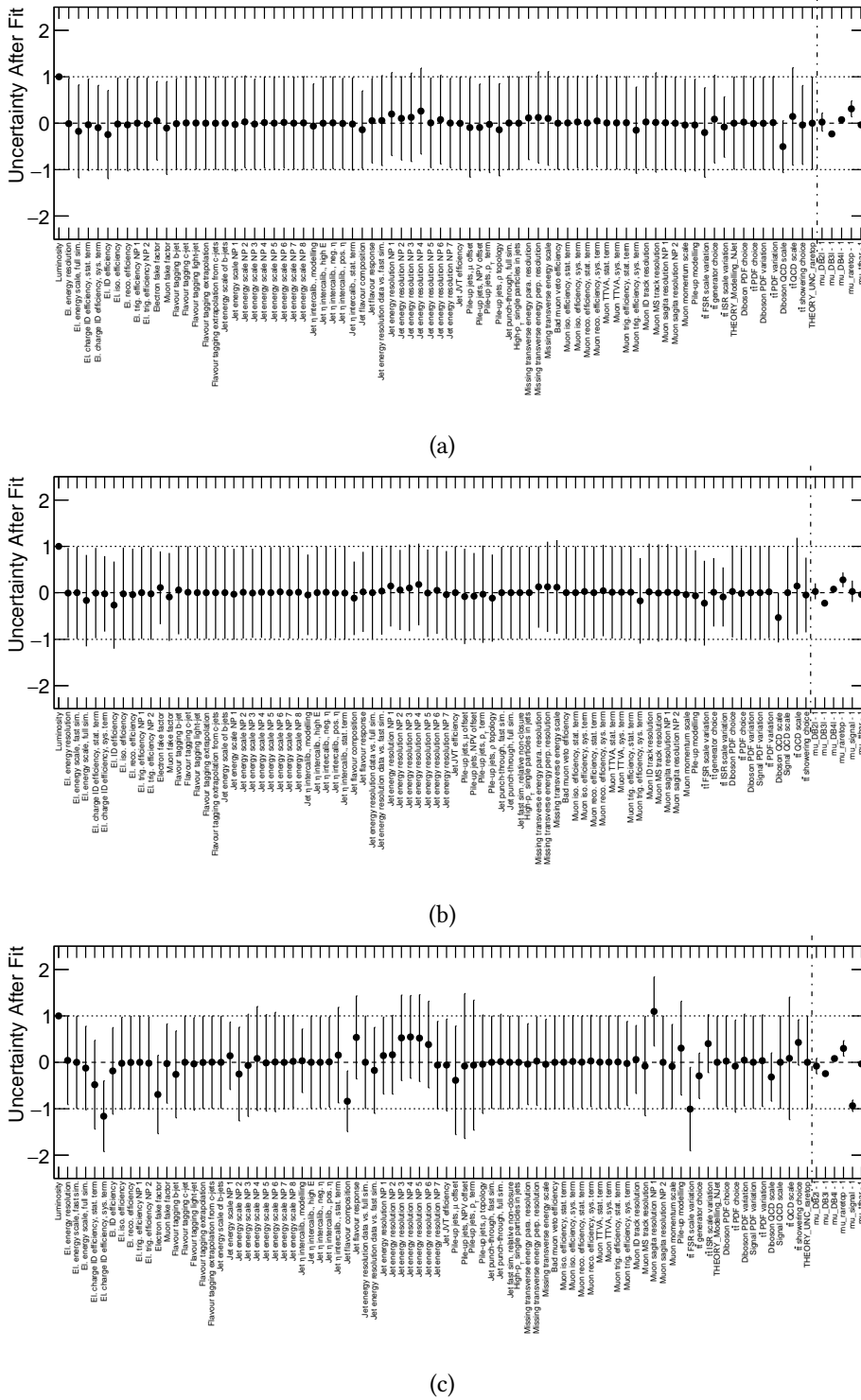


Figure A.32: Post-fit nuisance parameters of the background-only fit with real data in control regions [A.32a](#), exclusion fit with Asimov dataset [A.32b](#) and exclusion fit with real data in both control and signal regions [A.32c](#). These plots are related to the combination of two-, three- and four-lepton channels. 247

Pull and ranking plots, and exclusion limit with toys for the combined Analysis details fit with two-, three- and four-lepton channels

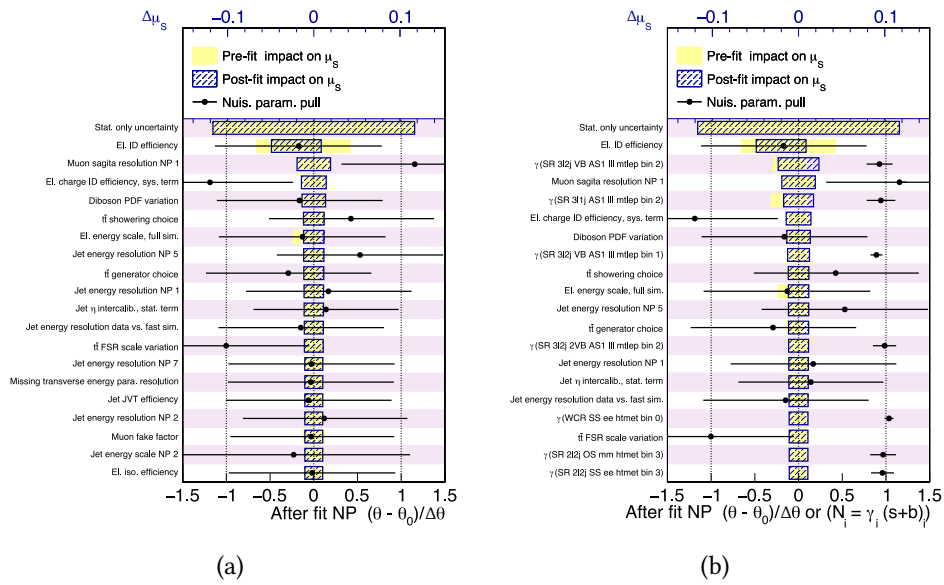


Figure A.33: Impact of systematic uncertainties on μ_{SIG} constructed by fixing one nuisance parameter to its $\pm 1\sigma$ variations at the time and minimizing the rest. In A.33a the impact of the dominant systematic source and MC statistical uncertainty, in A.33b also gamma parameters corresponding to each bin in the analysis regions are added. Pre-fit impact are shown with a yellow box, post-fit with a dashed blue box while α with black points. These plots are related to the combination of two-, three- and four-lepton channels.

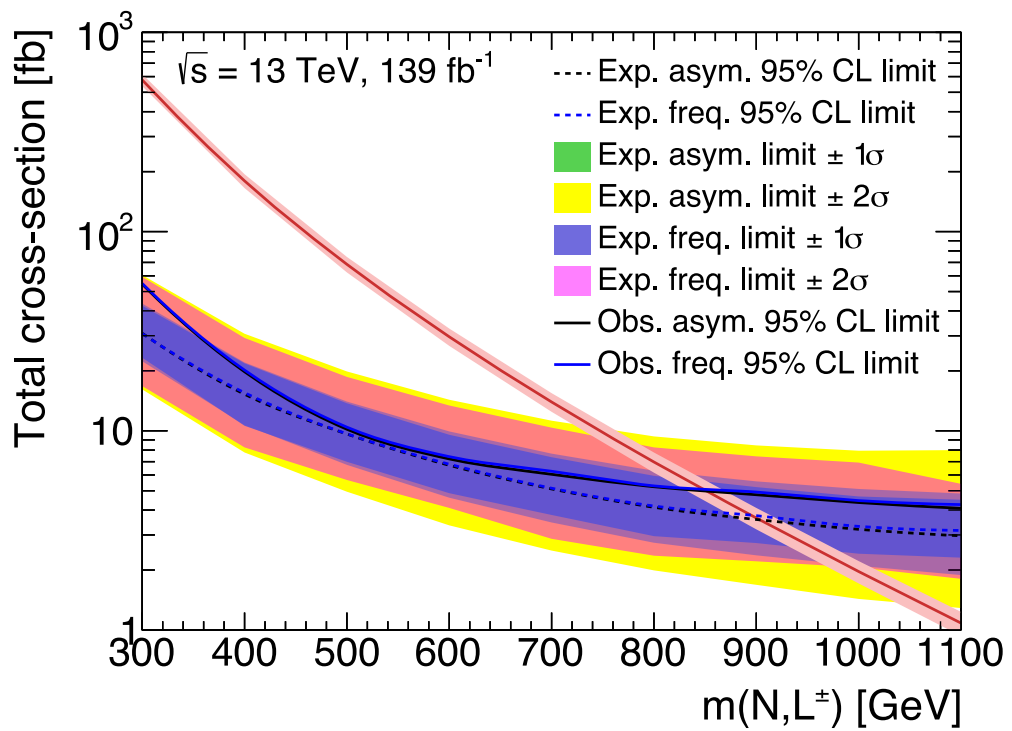


Figure A.34: Comparison of expected and observed 95% CLs exclusion limits using toys with a frequentist approach and the standard asymptotic formulae. Toys are overlaid with observed and expected limit in blue and uncertainty bands in pink and violet

**Pull and ranking plots, and exclusion limit with toys for the combined
Analysis details fit with two-, three- and four-lepton channels**

Appendix B

The LUCID Detector

B.1	Luminosity Measurement	252
B.2	The LUCID-2 Detector	256
B.2.1	The LUCID-2 Design	257
B.2.2	The Calibration System	259
B.2.3	LUCID Electronics	262
B.2.4	LUCID-3 Test and Installation	265
B.3	LUCID-3 Design	268
B.4	LUCID Simulations	270
B.5	Conclusions and perspectives	274

Luminosity is a fundamental parameter since it reflects the capability of a collider to produce a significant statistical sample of rare events. A reliable and precise measurement of the luminosity is necessary both for beam and performance monitoring purpose and for offline analysis. The uncertainty on luminosity measurement represents the largest systematic uncertainty in many SM physics analyses and for this reason it is required to be kept at the order of few %, while, on the other side, searches for new physics phenomena beyond the SM also rely on accurate information about the delivered and collected luminosity.

The ATLAS approach is redundant, exploiting several detectors and multiple algorithms, to increase the precision of the luminosity measurements and correctly estimate the related systematic uncertainty.

Since 2015, LUCID (*LU*minosity measurements using *Cherenkov Integrating Detectors*) is the reference detector for offline and online ATLAS luminosity measurements. In this Appendix, the description of the detector is presented. The upgraded design for the future Run 3 and Run 4 will be described also as an important part of my activity on the simulation and technical work side.

B.1 Luminosity Measurement

A description of the LHC main features is given in Section 2.1, together with the definition of the luminosity in terms of the collider parameters. The luminosity can be also re-written as function of the average number of inelastic interactions per bunch crossing (μ^{inel}) (called pile-up parameter):

$$\mathcal{L} = \frac{\mu^{\text{inel}} f_r n_b}{\sigma^{\text{inel}}} \quad (\text{B.1})$$

where f_r is the beam-revolution frequency, n_b number of bunches and σ^{inel} the pp inelastic cross-section.

Any luminosity detector can only measure a relative μ parameter, called μ^{vis} , connected to the inelastic μ parameter by the detector acceptance and efficiency: $\mu^{\text{vis}} = \epsilon \mu^{\text{inel}}$. The Equation B.1 can then be re-written as:

$$\mathcal{L} = \frac{\mu^{\text{inel}} f_r n_b}{\sigma^{\text{inel}}} = \frac{\mu^{\text{vis}} f_r n_b}{\epsilon \sigma^{\text{inel}}} = \frac{\mu^{\text{vis}} f_r n_b}{\sigma^{\text{vis}}} \quad (\text{B.2})$$

where σ^{vis} is the calibration constant measured through dedicated LHC runs, called van der Meer scans. A van der Meer scan is a general calibration method, performed in a beam-separation scan, where the absolute luminosity can be inferred from direct measurements of beam parameters, through the relation [179]:

$$\mathcal{L} = \frac{n_b f_r n_1 n_2}{2\pi \Sigma_x \Sigma_y}. \quad (\text{B.3})$$

Under the assumption of Gaussian beams, Σ_x (Σ_y) corresponds to the standard deviations σ_x (σ_y) of the horizontal (vertical) distribution.

Luminosity Algorithms

Looking at the Equation B.1, the instantaneous luminosity can be clearly determined measuring the ratio $\frac{\mu^{\text{inel}}}{\sigma^{\text{inel}}}$ or $\frac{\mu^{\text{vis}}}{\sigma^{\text{vis}}}$. Since μ follows the beam degradation formula $\mathcal{L} = \mathcal{L} \cdot e^{-t/\tau}$, the luminosity is evaluated in short time periods, called *Luminosity Blocks* (LB), in which it can be considered constant [217]. In ATLAS this time interval is about 60 s. Several methods for luminosity measurement can be used:

- *Event counting* algorithms are based on the determination of bunch crossing fraction in which a detector registers an event satisfying a given selection criterion required to observe one or more interactions. Those algorithms are mainly divided into EventOR (inclusive counting) and EventAND (coincidence counting);
- *Hit counting* algorithms count the number of signals above a certain threshold (a *hit*) in a set of electronic channels of a luminosity detector;
- *Particle counting* algorithms are based on the measurement of quantities proportional to the instantaneous particle flux in the detector (such as number of tracks, energy deposits in the calorimeter).

Once the absolute calibration constant σ^{vis} is determined, to measure the luminosity \mathcal{L} within each LB, the μ^{vis} value is needed. Two assumptions must be valid to perform this estimation:

1. the number of pp interactions follows a Poissonian statistics;
2. the efficiency ϵ_1 to detect a single inelastic pp interaction is independent of the number of interactions which occur in the same bunch crossing.

Then, the efficiency for detecting n interactions in the same bunch crossing is:

$$\epsilon_n = 1 - (1 - \epsilon_1)^n. \quad (\text{B.4})$$

Most of the luminosity detectors consist of two symmetric arms with respect to the interaction point, in order to perform coincidence counting. In ATLAS, Forwards and Backwards sides are labelled “A” and “C”, respectively. According to the request on the hits recorded in the two sides, two different categories of Event counting algorithms can be used.

In the case of the EventOR class, a bunch crossing is counted if at least one hit is observed in either A and B side. Under the Poissonian assumption, the probability to observe an (OR) event can be computed as:

$$P_{\text{EventOR}}(\mu_{\text{vis}}^{\text{OR}}) = \frac{N_{\text{OR}}}{N_{\text{BC}}} = 1 - e^{-\mu_{\text{vis}}^{\text{OR}}} \quad (\text{B.5})$$

where $\mu_{\text{vis}}^{\text{OR}} = \mu \epsilon_{\text{OR}}$ being ϵ_{OR} the single interaction detection efficiency of the detector, N_{OR} is the number of bunch crossings in a certain LB in which at least one pp interaction satisfies the event-selection requirement for the OR algorithm, and N_{BC} is the total number of bunch crossings, during the same interval.

Solving the Equation in B.5 for $\mu_{\text{vis}}^{\text{OR}}$, it returns:

$$\mu_{\text{vis}}^{\text{OR}} = -\ln\left(1 - \frac{N_{\text{OR}}}{N_{\text{BC}}}\right). \quad (\text{B.6})$$

Event-OR algorithms can be single-side or double-side, if they distinguish or not between the detector sides in which the hit is detected.

In the case of EventAND algorithm (coincidence method), a bunch crossing will be counted if there is at least one hit on both the A or C side of the detector, a condition that can be satisfied from both single pp interaction or different pp interactions occurring in the same bunch crossing. Considering an equal acceptance in both the detector sides, the probability of recording a coincidence event can be expressed as:

$$\begin{aligned} P_{\text{EventAND}}(\mu_{\text{vis}}^{\text{AND}}) &= \frac{N_{\text{AND}}}{N_{\text{BC}}} \\ &= 1 - 2e^{-(1+\sigma_{\text{vis}}^{\text{OR}}/\sigma_{\text{vis}}^{\text{AND}})\mu_{\text{vis}}^{\text{AND}}/2} + e^{-(\sigma_{\text{vis}}^{\text{OR}}/\sigma_{\text{vis}}^{\text{AND}})\mu_{\text{vis}}^{\text{AND}}}. \end{aligned} \quad (\text{B.7})$$

This relationship cannot be inverted analytically to determine $\mu_{\text{vis}}^{\text{AND}}$ as a function of $N_{\text{AND}}/N_{\text{BC}}$, then a numerical inversion has to be performed.

Event counting algorithms loose their sensitivity for $\mu_{\text{vis}} \gg 1$ due to the absence of bunch-crossings with the observed interactions on a LB ($N_{\text{OR}} = N_{\text{BC}}$) leading to the failure of Equation B.6. This effect is called *algorithm saturation*. Different algorithms must be used should this limit be reached. Hit-counting algorithms are a reliable option. In Hit-counting algorithms, a new set of assumptions must be considered: the number of hits in one pp interaction follows a Binomial distribution while the number of interactions per bunch crossing the Poisson one. Then, the probability to have a hit per bunch crossing is calculated as:

$$P_{\text{HIT}}(\mu_{\text{vis}}^{\text{HIT}}) = \frac{N_{\text{HIT}}}{N_{\text{BC}}N_{\text{CH}}} = 1 - e^{-\mu_{\text{vis}}^{\text{HIT}}}, \quad (\text{B.8})$$

where N_{HIT} and N_{BC} are the total number of hits and bunch crossings in a LB, respectively, and N_{CH} is the number of detector channels, each having an independent probability to record a hit. The mean number of interactions μ_{vis} can be calculated by the following expression:

$$\mu_{\text{vis}}^{\text{HIT}} = -\ln\left(1 - \frac{N_{\text{HIT}}}{N_{\text{BC}}N_{\text{CH}}}\right). \quad (\text{B.9})$$

Online and Offline Luminosity

LUCID provides luminosity information for machine tuning independently of the ATLAS detector state (meaning also when ATLAS is not taking data). The calculation and publication of instantaneous luminosity measurements are provided

by the *ATLAS Luminosity Calculator* (OLC) analysing raw data (such as hits and event counts), with a frequency of about 0.5 Hz for fast feedback on accelerator tuning. The OLC gives also information on the number of colliding bunches, number of LHC orbits in the LB and finally it determines μ and luminosity. Due to the short time interval allowed for online luminosity calculation, no background subtraction is performed. The Bunch Crossing Identifier (BCID) is the detector main time unit, that identifies each bunch of protons from 0 to 3564. The LUCID detector is the only one able to provide BCID luminosity for each LB, as well as per BCID LB-averaged, as shown in Figure B.1. The OLC calculates

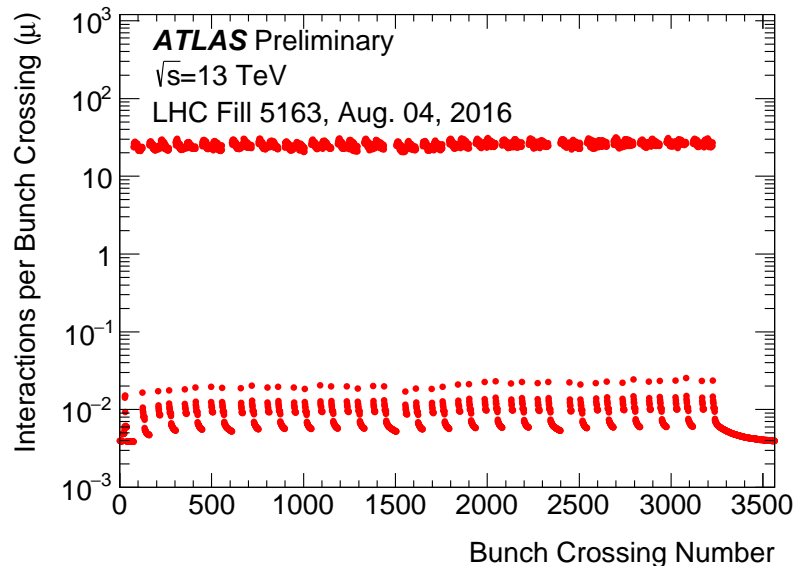


Figure B.1: Measured pile-up parameter μ as a function of the bunch-crossing number averaged over the duration of the run, in a physics fill in 2016. The plot shows more than 3 orders of magnitude between the μ measured in colliding BCIDs (upper points) and the background in the non-colliding BCIDs (lower points) [218].

the bunch-integrated luminosity using the following sum over all the colliding BCIDs:

$$\mathcal{L} = \sum_{i \in BCID} \frac{\mu_i^{\text{vis}} f_r}{\sigma_{\text{vis}}}. \quad (\text{B.10})$$

The offline analysis uses the same algorithms for the online measurement, with the possibility to perform background subtraction and update with a more precise calibration constants (σ_{vis}) and offline corrections, when available.

B.2 The LUCID-2 Detector

Among all the sub-detectors installed in ATLAS, LUCID is the only one entirely dedicated to luminosity measurements. The LUCID-1 [219] was installed in 2008 and was used by the ATLAS Experiment as the main luminosity detector for Run 1 (2009-2010) and in combination with other detectors in the period 2011-2013.

It consisted of two stations placed symmetrically with respect to the IP (side A and side C), at a distance from the beam axis of $z = 17$ m. Each station consisted in twenty 150 cm long Cherenkov detectors mostly made of aluminium tubes with 14 mm diameter, pointing towards the interaction region, filled with a radiation gas C_4F_{10} , and read-out by photomultiplier PMTs. This first LUCID detector was designed to measure luminosity with a 5% precision up to a $\mu \leq 10$. Due to the increased μ values up to 20 in 2011, the migration effects [179] were observed leading to more linearity with μ and spoiling the luminosity determination. On the other hand, it was observed that particles crossing only the PMT quartz windows (1.2 mm deep thick) produced enough Cherenkov light to have sizeable signal and less affected by migration. For these reasons, LUCID-1 operated without gas for the 2011 and 2012 operations.

In this way the foundations for the future LUCID-2 were laid. A new complete design was needed in view of LHC Run 2 (2015-2018) due to the following motivations:

- In Run 2 the instantaneous luminosity increased by almost a factor of 3, causing a larger expected pile-up with a consequent increase of non linearity due to migration. In addition, as already explained before, some event-counting algorithms were close to saturation or already saturated in Run 1 operations;
- The LHC beam pipe material was changed from stainless steel to aluminium and Monte Carlo simulations showed an expected increase in the particle fluxes in LUCID by a factor ~ 4 , with an impact on luminosity algorithm saturation;
- The bunch spacing was halved from 50 ns to 25 ns.

To fulfil the new physical requirements, during the long shutdown in the period 2013 and 2015, the LUCID-1 has been removed to build and install the new LUCID-2 detector [220]. The first two problems described above were solved reducing the acceptance of the detector by using PMTs with a smaller diameter (from 15 mm to 10 mm). The third effect, related to the data taking condition, was solved with by developing a new electronic system (the LUCROD board) composed by a set of VME boards to digitize the signals close to the detector

to optimize discriminator performances and avoid distortions of analog signals from the PMTs.

B.2.1 The LUCID-2 Design

LUCID-2 consists in two modules on either side of the interaction point at about 17 meter from it, named A and C corresponding to the two ATLAS sides, placed symmetrically around the beam pipe. Each module is installed on a carbon fibre cylindrical support tube surrounding the LHC beam-pipe, at a radial distance of about 10 cm from it. In Figure B.2, a sketch of one LUCID-2 module using the 2016 configuration is illustrated. Two active detector groups are shown: the *PMT detector* and the *Fiber detector*. The first one is composed of four groups of

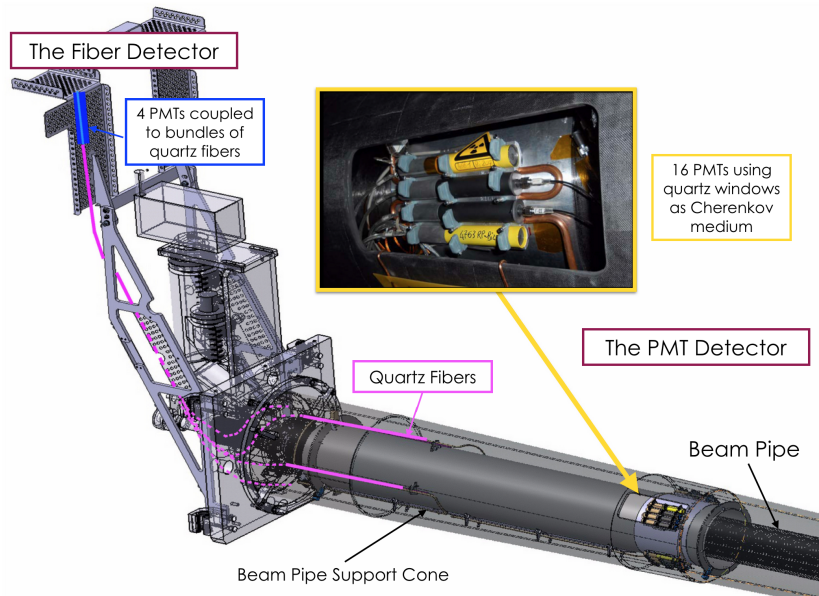


Figure B.2: View of one of the two LUCID-2 detector modules using the 2016 configuration, with its main component highlighted [179].

4 PMTs per side, for a total of 16 Hamamatsu R760 photomultipliers, acting like independent detectors. Each group is composed by four different types of PMTs, as shown in Figure B.4:

- Bi-detector: 4 PMTs with quartz window acting as Cherenkov medium, with a diameter of 10 mm and equipped with a small amount of radioactive source, liquid ^{207}Bi , for gain monitoring (described in Section B.2.2);
- LED-detector: similar to the Bi-detector but calibrated with LED signals;

- Modified-detector (MOD): 4 PMTs with a reduced acceptance (7 mm instead of 10 mm) obtained through the deposition of a thin aluminium ring in order to mask a part of the photo-cathode (see Figure B.3);
- SPARE-detector, containing PMTs with a radius of 10 mm, which is identical to the LED-detector but not turned on. The PMTs were used as spares in case of malfunctioning of the main ones.

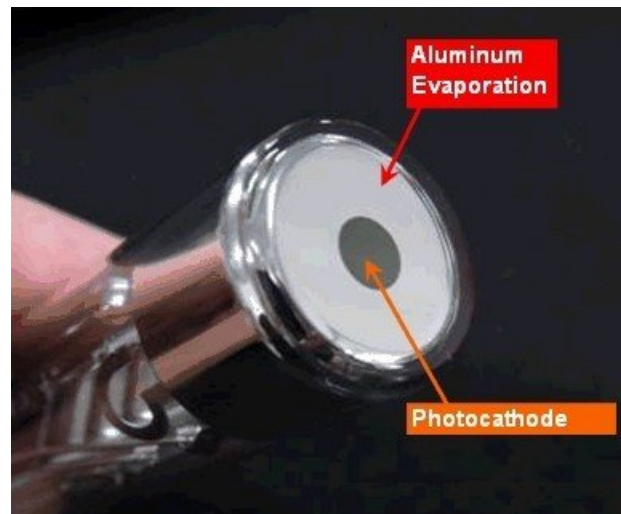


Figure B.3: Photo of a modified Hamamatsu photomultiplier. The acceptance of the photo-cathode has been reduced by a thin aluminium layer on the window [179].

During the 2015 data-taking period, it was clear that the ^{207}Bi system guaranteed a gain stability at 1% while the LED system at 10% and the photomultipliers in the SPARE sub-detector were therefore equipped with ^{207}Bi at the start of 2016, while the LED and MODIFIED detectors were likewise equipped with ^{207}Bi at the start of 2017. Eventually all PMTs were monitored with the radioactive source.

The Fiber-detector exploits four bundles of quartz fiber used as a Cherenkov medium, read out by a set of four PMTs located in a lower radiation area. For gain monitoring, the subsystem is connected to a LED and a Laser systems, while the read out is provided by PMTs of the same type as the PMT detector. For the fiber-detector the LED system was kept also after the 2015 data-taking.

Given the quartz windows with a thickness of 1.2 mm, the Cherenkov kinetic energy threshold in the LUCID-2 is about 175 keV. Charged particles crossing the quartz produce light, which is converted in the PMT cathode in an electric signal (current) and then amplified by the dynode chain with a certain gain ($G \sim 10^5$). At the end of this process, a measurable signal is produced and

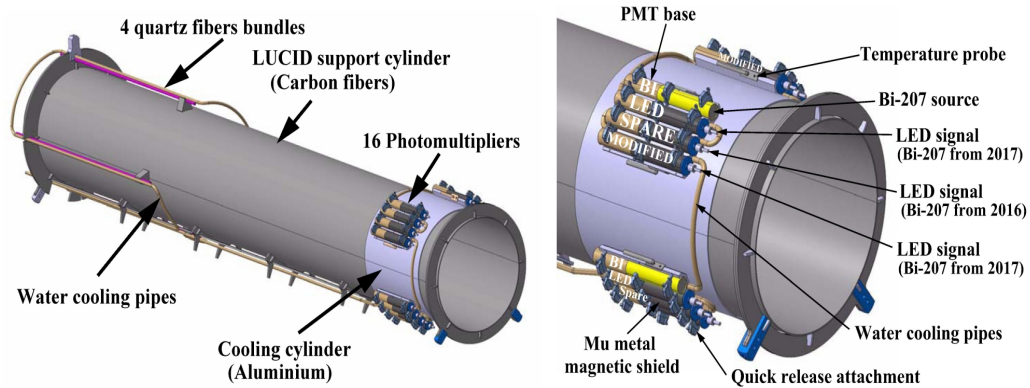


Figure B.4: The left drawing shows the LUCID support cylinder with the four quartz bundles at the back and the 16 photomultipliers at the front. The right drawing shows the support and cooling structure of the photomultipliers, with also the different PMTs types [179].

elaborated in the readout electronics (see Section B.2.3). For the quartz fiber an analogous mechanism occurs, acting as Cherenkov radiator for charged particles and as light-guide for the Cherenkov light. The number of generated Cherenkov photons depends on the property of the incident charged particle following the Frank-Tamm formula [221], and it is consequently transformed into the number of photoelectrons (named p.e.). A hit is defined when the number of photoelectrons recorded in the event is larger than a given threshold, which is chosen in such a way to separate signal from noise and background, as shown in Figure B.5. A threshold of 15 p.e. was chosen resulting from previous considerations.

B.2.2 The Calibration System

An important part of the luminosity measurements is the monitoring of the gain stability and ageing, both affecting the PMTs during the data taking. Three kinds of calibration systems were developed, each exploiting a different technique and applied to a different set of PMTs. At the beginning, 4 + 4 PMTs were equipped with ^{207}Bi radioactive sources producing internal conversion electrons (1 MeV) above the Cherenkov threshold in the quartz windows, while 16 + 16 were fed with both LED and laser light, carried by quartz optical fibers. Figure B.6 shows a schematic view of the two systems for one detector module in 2015.

These calibrations are performed at the of each LHC fill, since the gain is found to be lower up to 5% due to the charge produced in the dynode chain. A change of 5% in gain reflects in a 1% change in the luminosity measured by hit-algorithms and in a 5% change for the charge-algorithms.

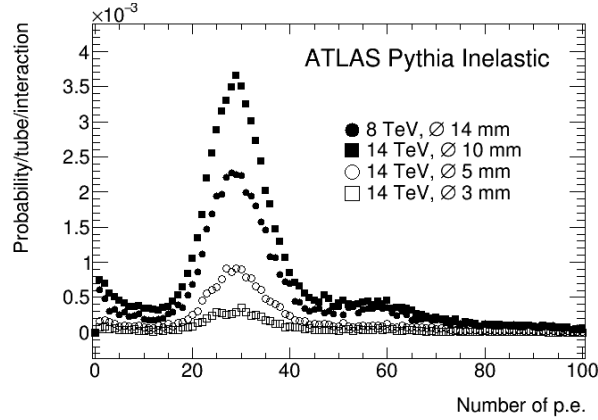


Figure B.5: Typical photoelectron distribution obtained from a PMT in single pp collisions at different center of mass energies (8 and 14 TeV) and for different diameter of the PMT window (14 mm, 10 mm, 5 mm, 3 mm) [179].

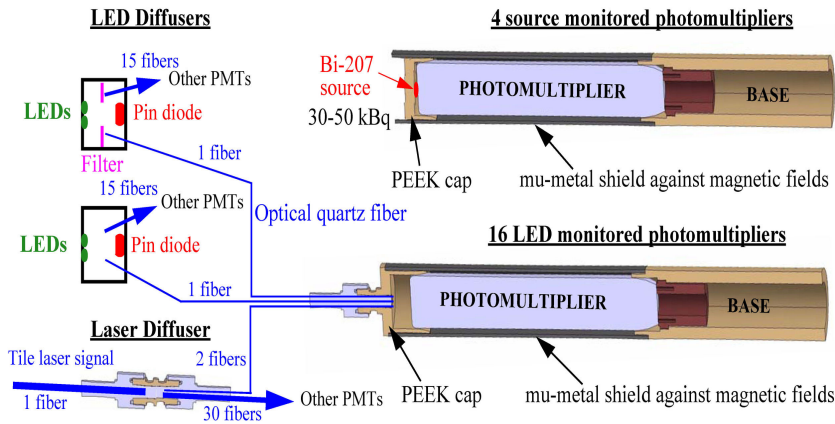


Figure B.6: Schematic view of the LUCID-2 relative calibration system for one detector module in 2015 [179].

The LUCID-2 calibration system is mainly based on the ^{207}Bi sources which is completely new and it was used for the first time in LUCID. The radioactive source produces electrons from about 500 keV up to 1 MeV, all above the Cherenkov threshold, but only electrons above 900 keV can penetrate the full quartz window before being stopped. ^{207}Bi is directly deposited on the PMT window avoiding degradation of the optical fibers transporting light. Figure B.7 shows the similar amplitude spectra of electrons produced by the ^{207}Bi source and the signal from LHC interactions, which is a very important feature for the calibration step. A peak in the distributions is clearly visible, whose value depends on the PMT gain and needs to be stable since it is used to monitor the gain

stability and with a precision of few percent and to calibrate the PMT. This peak does not follow the electron monochromatic emission due to the path travelled by electrons inside the PMT quartz window causing a certain width in the ^{207}Bi spectrum. Figure B.8b shows the variation in percent of the mean charge value as a function of time for the year 2016. With the calibration procedure, the mean charge was kept constant over the whole running period of several months. After long LHC fills the charge can decrease up to 5% but it is recovered by the high-voltage adjustments.

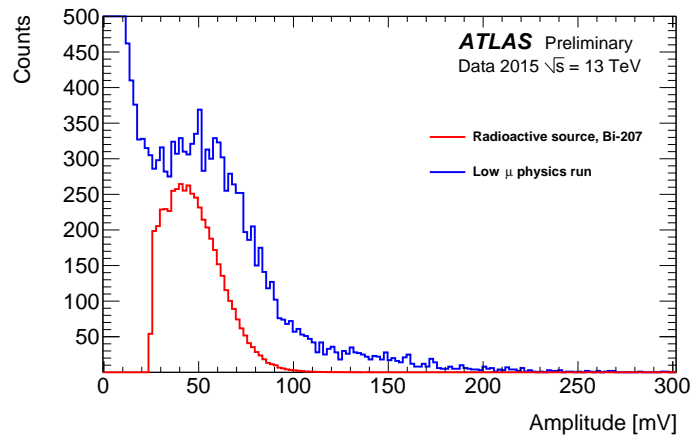


Figure B.7: Amplitude spectrum of LUCID photomultiplier recorded in a 13 TeV run (blue) and of ^{207}Bi internal conversion electron in a calibration run (red) [222].

The LED signals provide calibrations for PMTs which do not use the radioactive source. The LED are pulsed at the LHC orbit frequency of about 11 kHz and can produce large signals in the photomultiplier. An automatic correction on the PMT high-voltage is performed by looking at the mean value of the amplitude and the charge of the signals collected during calibration runs. The LED stability is monitored by PIN-diodes, as well as possible light fluctuations, ensuring the correction of the observed signals in the PMT. Since the PIN-diode is less sensitive to the LED light with respect to the PMTs, it is placed in front of the LED source. The produced light is transported to all photomultipliers via 4.5 m long, 240 μm diameter quartz fibers. Several tests for radiation damage were performed via irradiation with neutrons and gammas at doses equivalent to those expected after 2 years of LHC exposure. Figure B.8a shows the LED light stability monitored by a PIN-diode as a function of time in 2016. An initial drop of about 4% is present, with a consequently good stability for the rest of the data-taking period. Fiber connectors are used to connect LED fibers to the front of the PMTs. During the data acquisition, the activation of the material induced

by the large particle fluxes caused a source of background coming from these connectors, which is absent in the ^{207}Bi -calibrated PMTs.

A similar approach is used for the laser calibration. In this case, laser light is provided by the ATLAS Tile calorimeter calibration system [223] with also a monitoring of the light stability. The PIN-diode monitoring is not needed for this purpose. Since the laser light is collimated, contrary to the LED one, a cylindrical diffuser was designed to distribute the light to all PMTs. It is used to connect the single larger fiber coming from the laser source to a bundle of smaller fibers going to PMTs. To have a homogeneous illumination among PMTs, two fibers for each PMT are used: one placed in the peripheral part of the bundle and one in the more central part.

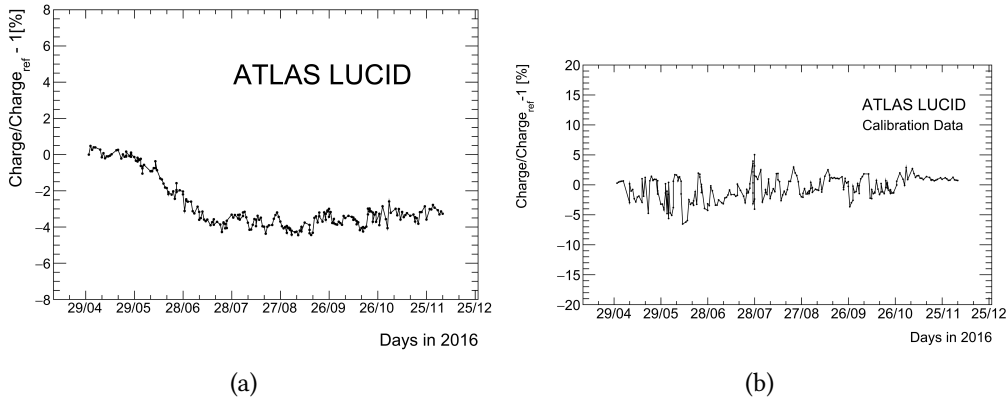


Figure B.8: Figure B.8a shows the variation in percent of the measured mean charge relative a reference run for the LED calibration signal, while in Figure B.8b the ^{207}Bi source is considered [179].

Starting from the 2017 data taking, only photomultipliers in the FIBER detector have been calibrated with laser or LED signals, while for the other the ^{207}Bi -based calibration system has been used.

B.2.3 LUCID Electronics

The electronic system of the LUCID-2 is composed by four (two per side) custom-made VME boards, called LUCid ReadOut Driver (LUCROD), as shown in Figure B.9. These boards were fully designed in the Electronic Laboratories of the INFN Bologna Unit. The readout boards were placed close to the detectors in the experimental cavern in order to reduce the path of the analog signals from the PMTs and cope with the 25 ns bunch separation time. The LUCRODs were in fact placed only 15 m away from the PMTs, to minimize PMT signal distortion and broadening, and the cables connecting the electronics with the photomultipliers

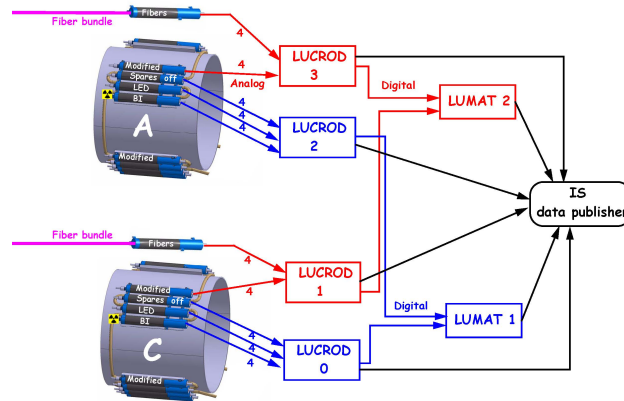


Figure B.9: Block diagram of the electronics for the LUCID-2 detector [179].

are thick and fast high-performance cables so that the signals do not deteriorate before being digitized preserving also the original shape of the signal and avoiding pole-zero compensation circuitry. Due to the position of the LUCRODs, close to the PMTs, they are not accessible during LHC run periods. A dedicated firmware has been developed to allow reloading and problem solving without intervention, a feature necessary to recover from Single Event Upset (SEU) occurring at a typical rate of few cases per week.

Two different boards, called LUMAT, are positioned in the electronics cavern and receive hit patterns from the LUCROD boards over a 100m optical fiber. They perform coincidence algorithms synchronizing and combining side A and side C hits. Both the LUCROD and the LUMAT board cumulate hits and events (the LUCROD integrates charges as well) over LB periods, with BCID granularity, on internal FIFOs (First In First Out) that are read via VME interface by the TDAQ software at the end of each integration period. LUCROD only can also integrate charge used as additional luminosity algorithm.

LUCROD Board

The LUCROD board is a custom 9U VME board which features 16 lemo analog inputs, each one associated with one of the installed PMTs, 16 lemo analog outputs amplifying the signal of the inputs, four lemo digital I/O channels for triggering and debugging purposes, a TTCrq¹ to receive external synchronization signals and optical transceivers to deliver digital information to the LUMAT. Exploiting the TTCrq, the LUCROD internal clock can be aligned with the ATLAS 40

¹A mezzanine card developed by the CERN microelectronics group to handle Timing, Trigger and Control systems for the LHC.

MHz main clock. Each LUCROD input is pre-amplified by a programmable factor (with a gain of up to a factor of 16), and digitized by a 320 MHz FADC (Flash Analog-to-Digital Converter) with a 12-bit resolution for a 1.5 V dynamic range. Each LUCROD board hosts one group of eight channel FPGAs and another group of two main FPGAs. The first one is directly connected to the inputs, each receiving the digitized data of two channels. The digitized inputs are summed over the time window of a BCID period (8 clock samples, corresponding to 25 ns), to provide charge information, and are compared to a programmable threshold to identify hits. While information for both charge and hits are accumulated in 3564-slot FIFOs (the depth corresponds to an LHC orbit), 64 samples of the digitized waveforms are made available for VME readout upon the presence of a trigger, selectable between a programmable portion of the LHC orbit, or the presence of a hit. This slow VME readout is used during data-taking to provide a monitoring data stream, representing a hardware sampling of each PMT waveform. The second set of two FPGAs, receive charge and hits from a selectable combination of inputs, in order to provide hit sums, charge sums and events sums per BCID basis, where an event is selected if it has at least a hit in the bunch-crossing. In addition, they transmit hits to the output transceiver that feeds optical fibers connected to the LUMAT board.

LUMAT Board

The LUMAT boards are 9U VME boards equipped with FTK Input Mezzanines (FTK IM) [224], which allows to receive optical data containing both hits and synchronization data. The FTK IM host two Spartan IV (Xilinx) FPGAs and were programmed to have as input two streams of hit data from two LUCROD boards from both side A and C (see Figure B.9). These FPGAs manage bidirectional optical channels and use the the 8b/10b protocol implemented in the FPGAs to read the LUCROD information. The input connectors are characterized by four optical fiber links, with an input bit-rate of 25 Gbit/s, while the total input/output rate is 12.4 Gbit/s. The two streams of hit coming from the two LUCID sides, are synchronised before sending the hit data to the main FPGA of the LUMAT board, a Stratix II from Altera, where the luminosity algorithms are implemented. For a quick luminosity information, as needed by LHC for luminosity levelling and beam monitoring, the LUMAT board provides a few counters of events and hits, evaluated on short intervals of time (less then 0.1 s). The actual integration time is 2 s and counts (converted into luminosity information) are sent to the LHC control room for an immediate feedback on beam settings. While the LUCROD board implements the evaluation of luminosity algorithms for single channels and the OR on one side of ATLAS at a time, the LUMAT board can perform luminosity algorithms on both sides with the advantage of a correlation among

the two sides by counting events where hits have been observed in both sides.

B.2.4 LUCID-3 Test and Installation

In order to test the detector conditions and the assembled prototypes for the future LHC runs, a pilot beam was scheduled for the end of October 2021. In this context also the LUCID Collaboration performed several tasks and tests to check the stability and the performance of the current detector and to prepare the upgrades planned to be installed for the LUCID-3 [225] (see Section B.3 for details).

To prepare the detector for the pilot beam, both LUCID sides were disassembled from the ATLAS detector and brought to the ATLAS surface building (SX1). A photo of the Side-A of the LUCID detector in the SX1 building is shown in Figure B.10. Due to the stress suffered by the PMTs during the whole LHC Run

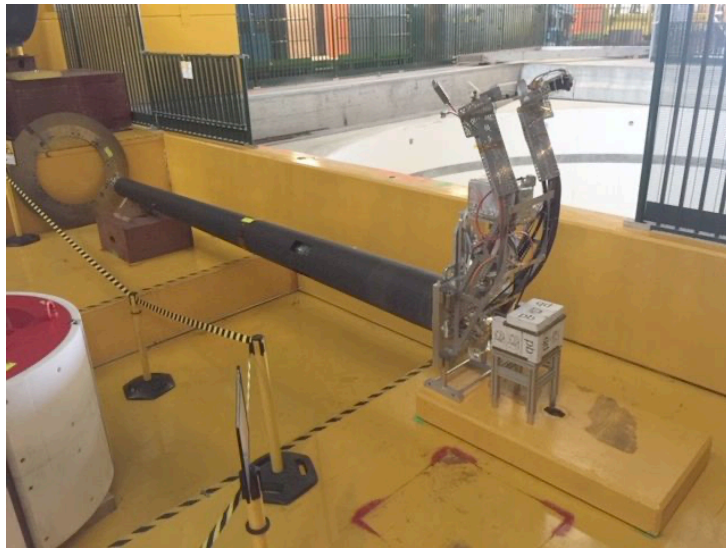


Figure B.10: LUCID Side-A in the ATLAS surface building, SX1.

2, the photomultipliers were first removed from the detector, and I measured the gain of each one to select the best set for re-installation into LUCID. I powered the PMTs through a CAEN mainframe a high-voltage of 1000 V and I acquired the signals coming from the ^{207}Bi source with a trigger threshold of -4 mV. Figure B.11a shows a problematic PMT because of a too low amplitude of signals. This PMT was therefore excluded. In Figure B.11b the behaviour of a selected PMT is shown. As a second step, I tested also a set of 40 new purchased PMTs to measure the mean amplitude with the same configuration of the first measurements. Then I tuned the high voltage of each PMT so that all signals (and thus all gains) were equalized to the same amplitude, needed for data acquisition.

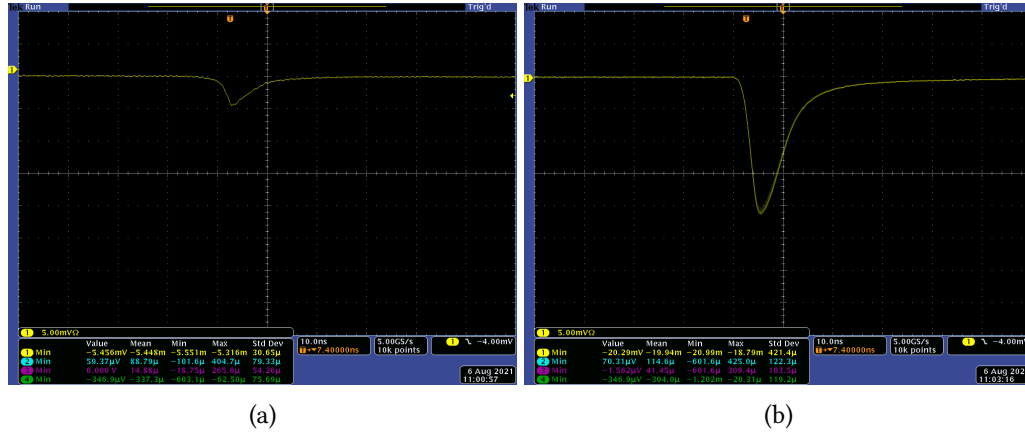


Figure B.11: Measured voltage of two tested PMTs using the same configuration. In B.11a a PMT which has not been selected to the installation, while in B.11b one that has been chosen.

After the selection, I installed the best performing PMTs in LUCID (see Figure B.12) and I tested them with their ^{207}Bi source again. Connection and cabling system were checked as well. I also developed a new python script to determine the high voltage needed on each dynode, including boosters, of each PMT to produce a non-zero current also during no-collisions period. The determination of high-voltage values is crucial in order to avoid the PMTs in the so called *sleeping mode*. In Table B.1, the high-voltage and current values obtained during this stage for the selected PMTs installed on the LUCID Side A, are reported. Finally,

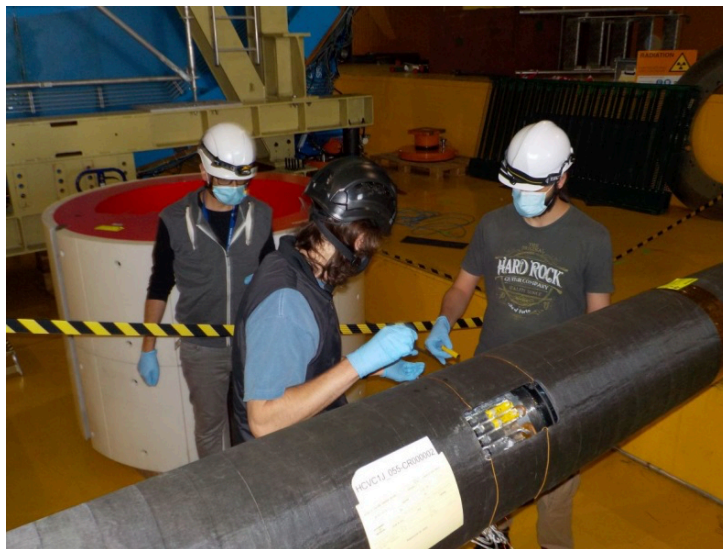


Figure B.12: Installation of the selected PMTs on the LUCID side-A in SX1.

PMT	Source	Activation (kBq)	HV ₀ (V)	HV ₁ (V)	HV ₂ (V)	HV ₃ (V)	I ₀ (mA)	I ₁ (mA)	I ₂ (mA)	I ₃ (mA)
EA3430	4769RP	41.95	770	228	156	81	205.5	14.0	10	12.5
XN1846	4901RP	31.70	810	240	164	85	217.0	13.0	12.5	12.0
EA3482	RP5045	146.00	780	231	158	81	208.5	13.0	12.5	11.5
EA3490	RP5052	134.00	810	240	164	84	216.0	14.5	11.5	13.0
EA3387	4935RP	39.21	800	236	163	83	214.0	12.0	13.0	14.0
EA3451	4918RP	56.40	860	254	173	89	230.5	12.0	13.0	14.5
EA3457	RP5024	115.00	760	225	154	80	203.0	11.5	13.0	12.0
EA3485	RP5048	127.00	770	228	156	79	205.5	13.5	11.5	10.5
EA3438	4910RP	46.90	910	267	184	93	243.0	13.5	14.0	13.5
EA3453	4919RP	52.50	800	237	162	83	214.0	12.5	11.5	13.5
EA3484	RP5047	123.00	760	225	154	79	203.5	12.0	13.0	9.5
EA3474	RP5038	109.00	800	237	162	83	214.0	14.0	12.0	13.0
EA3441	4912RP	47.10	930	271	187	95	248.5	12.0	13.0	12.5
XN1853	4902RP	31.10	950	277	189	97	254.0	12.0	12.0	12.5
EA3494	RP5056	127.00	780	231	158	82	208.5	12.0	12.5	14.5
EA3477	RP5051	105.00	800	237	163	84	214.0	11.0	14.5	14.5
EA3487	RP5050	123.00	800	237	163	83	213.5	13.0	14.0	12.5
EA3461	RP5027	121.00	800	237	162	83	213.5	11.5	13.0	13.5

Table B.1: PMTs installed on the LUCID Side-A with their corresponding high-voltage (HV) and current (I) for each dynode.

a new set of HV boards has been installed in the ATLAS service cavern to connect the PMTs into LUCID-Side A to the whole ATLAS electronic system. Then, all the channels were also connected to the LUCROD, inside the ATLAS detector cavern, to be ready for new data takings.

B.3 LUCID-3 Design

The next LHC runs, the so-called Run 4 for High-Luminosity LHC (HL-LHC), will see increased pile-up effects causing algorithm saturation (it is already described in the previous sections). For the luminosity measurements, avoiding any kind of saturation in each used algorithm is essential, either hit-counting and event-counting.

Considering the hit-counting algorithms, the so called μ -correction has to be applied to the logarithmic formula used to calculate luminosity from the number of hits to correct for non-linearity due to migrations. The correction is proportional to μ values, that will be large in LHC Run 4 since the average μ is expected to increase by a factor of 2.5 to 3.8. To avoid the HIT-saturation effect, the first proposal is to use the already described MOD-PMTs. They were produced by Hamamatsu starting from the standard R760, upon request of the LUCID group, in order to reduce the detector acceptance to about a half. Lowering the geometrical acceptance of the detector means reducing the active area of the sensors while increasing the size of the required mu-correction.

The first option for LUCID-3 could be a copy of the current LUCID-2 [179], using a different PMT configuration. In this case, as for LUCID-2, the detector would be attached to the vacuum forward shielding (VJ) and to beam-pipe and placed inside the new beam-pipe support cone. The main complication of this project, will be the new vacuum equipment (VAX) that will be installed in the LUCID-2 location for the LHC Run 4. In Figure B.13, the forward area around the beam-pipe comparing Run 2 and 3 with Run 4 is illustrated.

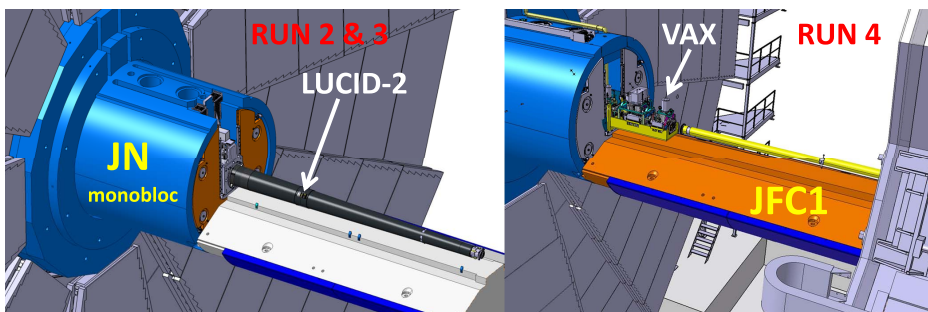


Figure B.13: On the left the location of the present LUCID-2 detector in the beam-pipe support cone is shown. In this illustration only the bottom part of the forward shielding (named JFC1) is installed. On the right the new vacuum equipment (VAX) that will be installed in Run 4 is shown. For this one, the beam-pipe support cone is not reported since it has not been designed yet [225].

The other strategy would be to attach a new detector to one of the forward shield-

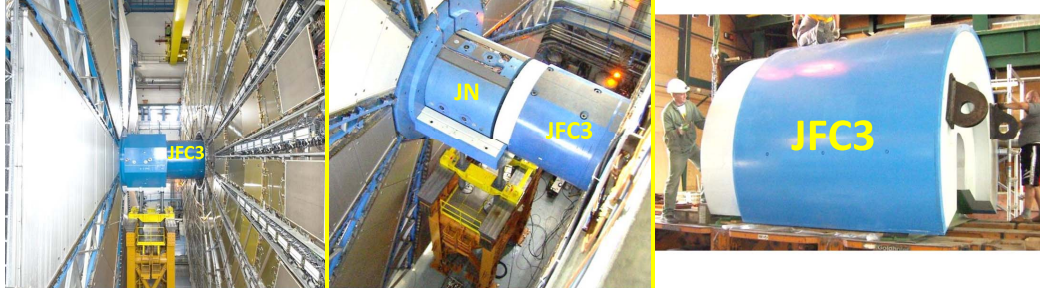


Figure B.14: Photos of the forward shielding piece JFC3 during different stages of an ATLAS opening. The left photo shows the situation when all shielding is installed. The top octagonal shielding piece has been removed in the middle photo. The JFC3 shielding piece after removal from ATLAS is shown in the photo on the right [225].

ing pieces (JF). The cylindrical forward shielding (JFC3) (see Figure B.14), was chosen. Using this shielding, the new detector would be available for maintenance in the SX1 every winter, since the shielding (like all forward shielding pieces) is removed during each end-of-year-shutdown and it will be at a larger distance from the beam-pipe thus reducing particle flux (i.e. acceptance) and radiation levels (i.e. ageing). Also a FIBER detector is still under consideration, but it will not be discussed in this section. Several advantages (As) and few disadvantages (Ds) are to be taken into account when it comes to attaching the detector on the JFC3 instead of to the beam-pipe:

- As** The detector and services will be more accessible in SX1 during shutdowns;
- As** No interference with the VAX or the beam-pipe design;
- As** Less radiation and saturation at a longer distance from the to beam-pipe;
- As** No need for water cooling during beam-pipe bake-out (if JFC3 is not installed);
- As** When compared to a FIBER detector, more channels are possible in a PMT detector;
- Ds** The detector has to be disconnected and connected in every shutdown;
- Ds** The location of JFC3 and LUCID might change slightly every year;
- Ds** Some additional machining to the shielding will be needed.

An illustration and a photo of the LUCID-3 PMT prototype attached to the JFC3 are shown in Figure B.15. Eight photomultipliers would be placed on the beam-pipe

hole attached in each one of the two JFC3 shielding pieces. As shown in Figure B.15b, a rail system is used to pull out the PMTs during the maintenance work. This kind of detector would require eight signal cables and eight HV cables to connect all PMTs.

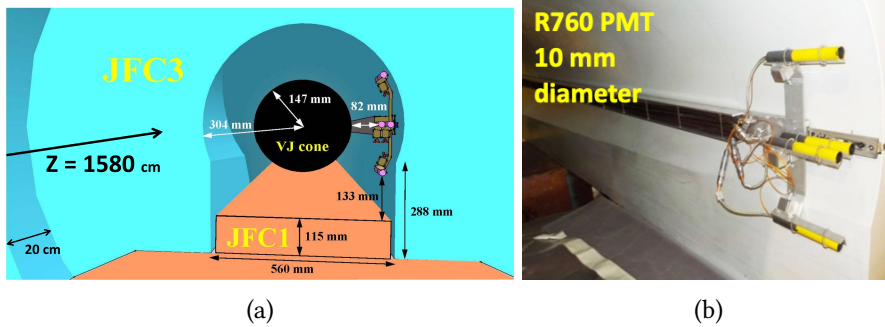


Figure B.15: Drawing of the prototype detector attached to the JFC3 forward shielding piece with the clearance to the VJ cone at a distance of 1600 cm from the IP (Figure B.15a). In B.15b, photo of the PMTs installed on the JFC3 shielding [225].

B.4 LUCID Simulations

Several simulations of the LUCID detectors were performed in order to estimate its efficiency using the different detector configurations described in the previous sections.

I carried out this work using the Athena framework [137] to simulate inelastic processes detected by LUCID. Since the ATLAS sub-detectors were upgraded almost every year, different ATLAS geometries were considered exploiting the information provided by the ATLAS Detector Description Database [226], in order to have a complete overview of the whole detector configurations. In Table B.2, all the geometry tags considered are reported. Since the LUCID area is mainly affected by changes on the beam-pipe and the Muon Spectrometer, only tags with differences in these sub-detectors were taken into account.

The historical detector description tool used by the ATLAS experiment is *GeoModel* [227], which describes standard shapes and nodes, that are then customized with parameters taken from the geometry database. In addition, a standalone GEANT4 based simulation of the full ATLAS detector, *FullSimLight* [228], was used to test activities and possible overlaps among all the sub-detectors involved in the simulation stage. FullSimLight was not used to perform the complete simulation since sensitive detectors are not implemented and it can not be

Geometry tag	LUCID Configuration
ATLAS-R2-2015-03-00-00	LUCID-1
ATLAS-R2-2016-01-00-01	LUCID-2
ATLAS-R3-2021-01-00-02	LUCID-3
ATLAS-R3S-2021-01-00-02	LUCID-3

Table B.2: ATLAS Geometry tags used during the simulation step with the corresponding LUCID detector version.

used as a replacement of the full Monte Carlo simulation.

The first step of my work was to update the LUCID sensitive detector from the Run 1 geometry to the Run 2 one. As explained in Section B.2, the main changes from the LUCID-1 to the LUCID-2 detector were the removal of the gas, and consequently of the cone-shaped vessel, and the replacement of the Cherenkov tubes with four sets of four PMTs each, attached to the aluminium PMT support around the metallic support cylinder. All this new structure was placed inside the carbon-fiber VJ cone. Exploiting the GeoModel framework, a 3D view of the simulated detectors can be obtained and visualized as shown in Figure B.16 for both LUCID-1 and LUCID-2. To check if the implemented geometry follows the real detector features, the PMT hits can be plotted in the x - y plane looking at the positions values of each photomultiplier. Hits can also be shown as a function of the ϕ angles to be compared with the angular positions of the LUCID PMTs. These observables are reported in Figure B.17, showing the same configuration of the real LUCID-2 detector features which are reported in [179]. The efficiencies for both LUCID sides and for the OR and AND algorithms were calculated as:

$$\epsilon_i = \frac{\text{Number of } i \text{ events}}{\text{Total number of events}}, \quad (\text{B.11})$$

where the i indicates the A and C sides, or the OR and AND logical conditions. Also these values were in agreement with the LUCID-2 results of about: $\epsilon_A = 38\%$, $\epsilon_C = 38\%$, $\epsilon_{\text{OR}} = 60\%$ and $\epsilon_{\text{AND}} = 18\%$.

The last step of my work was the simulation of particles interacting with the LUCID-3 PMT detector, to have a comparison between the efficiency of the new detector and the old one. Following the information provided by the LUCID-3 Initial Design Report, such as the ones in Figure B.15a, all the geometry details of the prototype were implemented in the simulation framework in order to provide the first expected results using PMTs attached to the JFC3 shielding. In Figure B.18, an illustration of the simulated detector and the hits in the x - y plane for

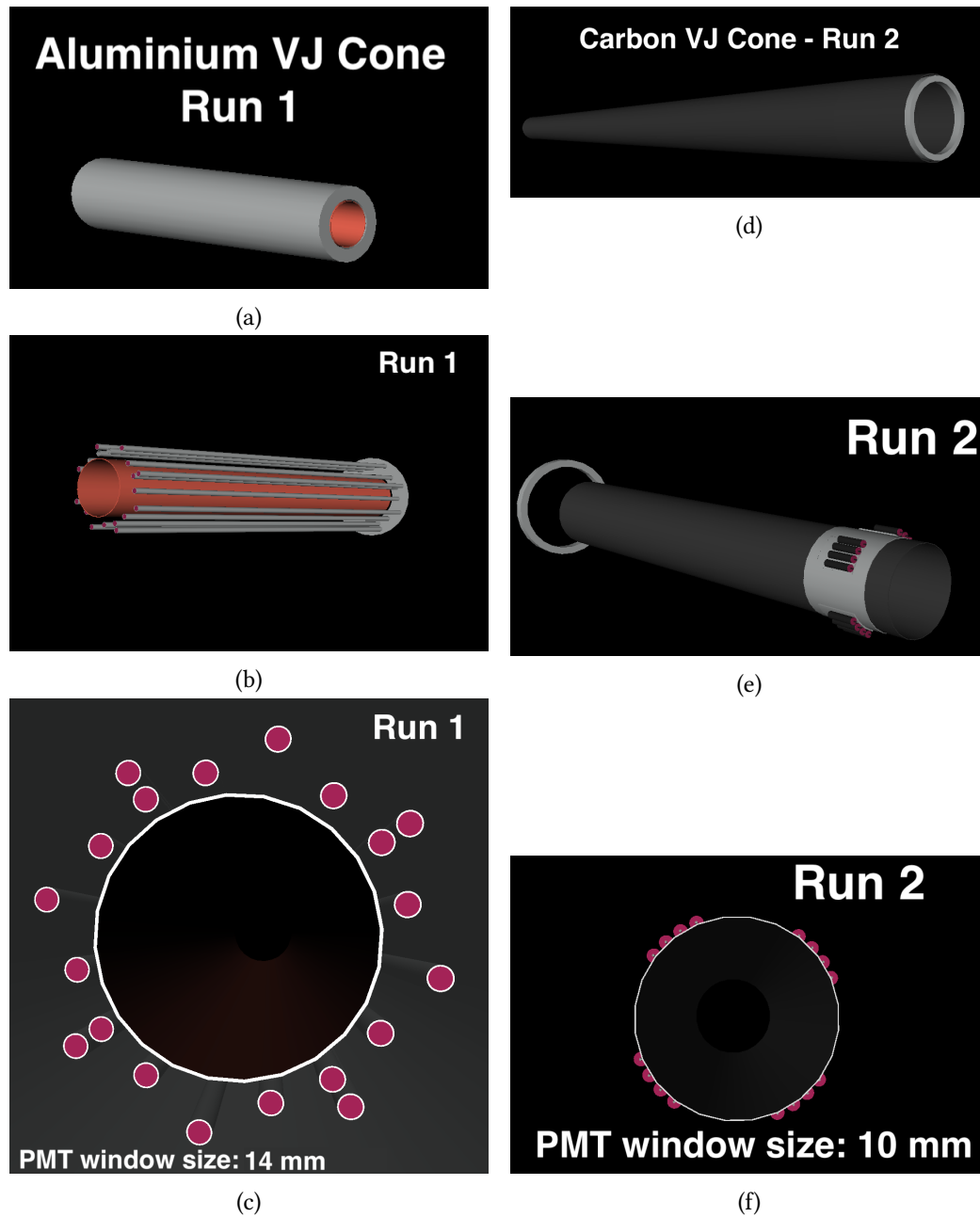


Figure B.16: Illustrations of LUCID-1 (left) and LUCID-2 (right) detector simulations. From top to bottom different parts of the detectors are shown. Top: Aluminium (B.16a) and Carbon (B.16d) VJ Cones. Middle: Cherenkov tubes (B.16b) and PMT support cylinder (B.16e), located inside the respective VJ cone. Bottom: frontal view of the PMTs.

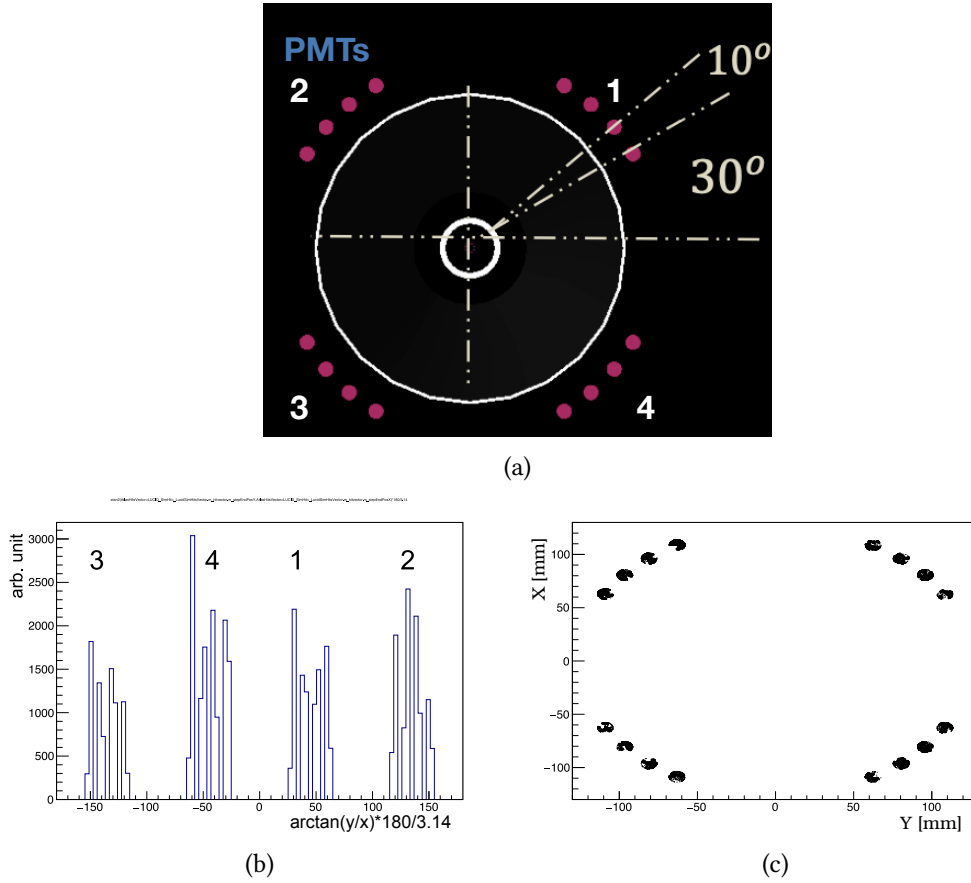


Figure B.17: Sketch of the LUCID-2 PMTs (Figure B.17a). Figures B.17b and B.17c plot the ϕ position of each PMT and the x vs. y position, respectively.

each PMT are reported. As shown in Table B.2, two different kinds of ATLAS Geometry tags were considered for this simulation: ATLAS-R3-2021-01-00-02 and ATLAS-R3S-2021-01-00-02. This was due to the difference in the New Small Wheel (NSW) [229] layout, which is taken as symmetric in the R3S, and asymmetric in the R3. Final results obtained by using independently both the Run 3 tags showed that the NSW layout does not strongly affect the LUCID-3 performances.

The simulated detector has the same characteristic as the proposed prototype, as close as possible to reality. The number of hits in the LUCID-3 PMTs showed a reduction of the acceptance by $\sim 30\%$ with respect to LUCID-2 location. The lower acceptance of the detector is what it takes to perform measurements at high luminosity without saturation effects on the hit-algorithms. This result is in agreement with the one obtained by the ATLAS Radiation Simulation Working Group which performed an independent simulation using a different tool-

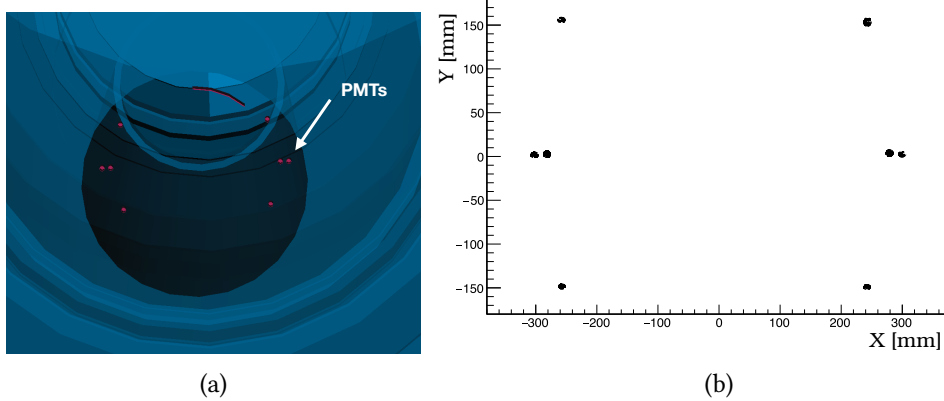


Figure B.18: Simulates LUCID-3 PMT detector (Figure B.18a), following the proposal illustrated in Figure B.15a, is shown. In B.18b, the PMTs position in the $x-y$ plane is presented.

kit [230], whose outcome is reported in Figure B.19, in terms of integrated dose and electron flux in the LUCID-2 and LUCID-3 regions. Five points as function of r and z (see Section 2.2 for ATLAS coordinate system) are reported. LUCID-3 detector attached to the beam-pipe (same location as LUCID-2) would experience a dose that is 15-48% larger (depending on the position in z), while a detector attached to the JFC3 shielding would have a dose reduced by a third compared to the LUCID-2 location.

B.5 Conclusions and perspectives

Among the several detectors that can measure the luminosity in ATLAS, LUCID has been chosen as the main luminometer for both online and offline measurements, due to its excellent performance, fast front-end electronics and optimal calibration procedures. The whole Run 2 data-taking period confirmed the success of its results.

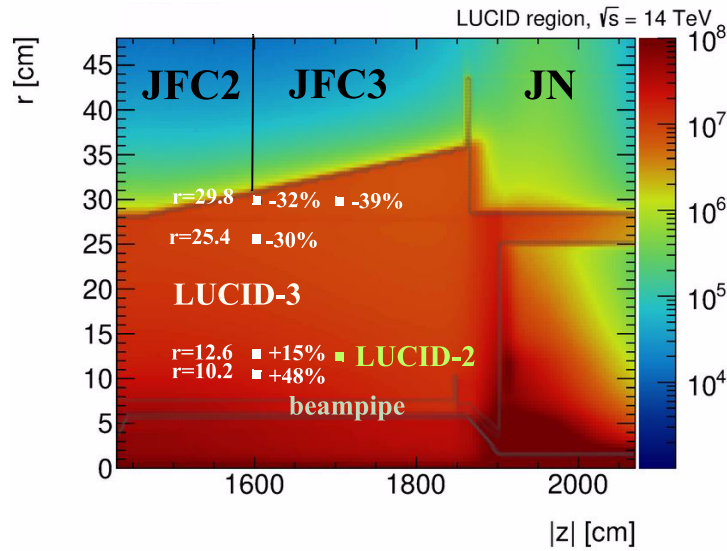
My contributions inside the collaboration can be divided into technical and software. For the former, I tested and calibrated, with a ^{207}Bi source, both old and new PMTs in order to measure the signal amplitude values to determine the gain. Then, I installed a set of PMTs directly on the LUCID detector performing additional checks to ensure the good quality of the signal sensors. To finalize this task, I wrote a script to determine the high-voltage needed on the dynodes, including boosters, of each PMT to produce a non-zero current also during no-collisions periods to avoid the PMTs in the sleeping mode. After the LUCID installation in the ATLAS detector, I installed several HV boards in the ATLAS

service cavern to connect LUCID to the whole ATLAS electronic system. To have a working readout system, I also connected all the channels to the LUCROD board, to be able to perform final tests with the DCS system to monitor PMTs currents, crate temperature and calibration data.

In the second half of October 2021 a pilot beam is scheduled in ATLAS, when the upgraded LUCID detector will be used.

On the simulation side I replaced the old LUCID-1 structure with the current LUCID-2 one in order to have an updated geometry into the official ATLAS simulation framework. Then, I started to implement LUCID-3 PMT prototype to have the first preliminary results which are essential for the project validation. This work will be continued in the near future to test the performance of the new fiber prototype which is considered as a possible alternative for the LUCID-3 detector.

Dose in Gray per 4000 fb⁻¹



Electron flux per cm²

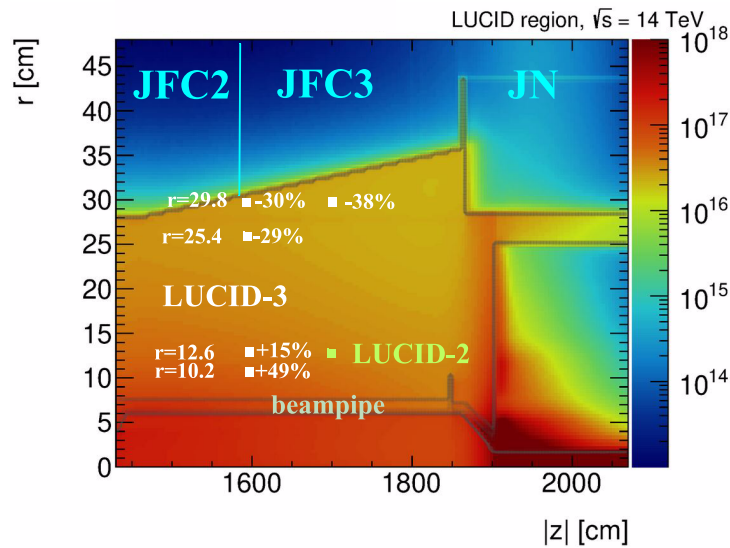


Figure B.19: Results of a simulation performed by the ATLAS Radiation Simulation Working Group in the region around the beam-pipe in ATLAS [230]. Figure B.19a shows the dose corresponding to 4000 fb⁻¹ expected in Run 4. The relative change in dose with respect to the present LUCID-2 location is given in five points with different position along the beam-pipe (z) and distance (r). Figure B.19b shows a map of the electron flux. The change in electron plus charged hadron flux with respect to the current LUCID-2 location is given in five different points.

Appendix C

The ATLAS Inner Tracker

C.1	High-Luminosity LHC	277
C.2	The ITk Design	280
C.2.1	ITk Pixel Detector	281
C.3	Database system	284
C.4	Conclusions	288

LHC experiments are aimed to search extremely rare processes, in particular new physics phenomena, as well as to provide very precise measurements of Standard Model physics. All of them would benefit from a rise in the number of collisions, meaning an increase in the available statistics, and energy in center-of-mass. For this reason, the LHC physics programme will be first extended in Run 3, when ATLAS will have collected more than 300 fb^{-1} , and then with and upgrade of the accelerator in 2025 to reach highest levels of luminosity and to deliver more pp collisions to the experiments starting operations in 2027 [77]. This new running phase, corresponding to the LHC Run 4, is the so-called High-Luminosity LHC (HL-LHC).

C.1 High-Luminosity LHC

As a consequence of the increase in luminosity for the HL-LHC, the number of protons in the bunches will be about $2.2 \cdot 10^{11}$, compared to $1.5 \cdot 10^{11}$ in LHC, with an instantaneous luminosity of about $7.5 \cdot 10^{34} \text{ cm}^{-2} \text{ s}^{-1}$ (more than five times the actual value of the LHC). The HL-LHC is planned to run for about 10 years with the goal to deliver an integrated luminosity up to 4000 fb^{-1} (more

than ten times the luminosity reach of the first 10 years of the LHC lifetime) at a $\sqrt{s} = 14$ TeV.

As already explained describing Equation 2.2, the luminosity depends on different input parameters only related to the beam properties. Then, the upgrade should provide the potential for good performance over a wide range of these parameters [231]:

Number of protons: The almost double number of protons in the bunches will result in a beam current over the 30% of the so-called *ultimate beam current* (0.86 A), laying hard challenges to the systems involved, such as RF power system and RF cavities, collimation and cryogenics systems, kickers.

Beam beta function β^* : A classical route for a luminosity upgrade with head-on collisions is to reduce β^* by using stronger and larger aperture quadrupole magnets. The plan is to reduce β^* from 0.55 m to 0.2 m, which reduces the transverse size of the luminous region resulting in the gain in peak luminosity.

Geometrical reduction factor F : Since the F factor decreases as the crossing angle between the two beams increases, with the increase of the luminosity the geometrical factor would be reduced to about 0.31, down from 0.84 in the LHC. To mitigate this effect novel crab cavities will be used, in order to rotate longitudinally the bunches and therefore improve the overlap between them. With this implementation, HL-LHC will ensure this parameter to a value of 0.83.

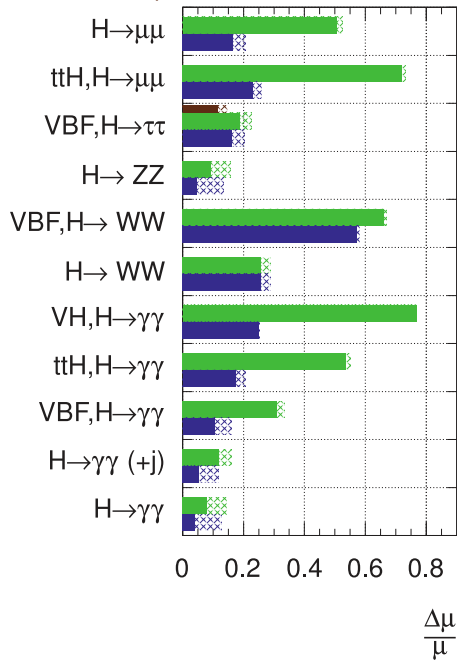
Geometric emittance ϵ_{xy} : The beam brightness is defined as the ratio of the bunch intensity to its geometric emittance, and it is a beam property that must be maximized at the beginning of beam generation and in the whole accelerator chain, including LHC. For this reason, the emittance has to be reduced at the beginning of the acceleration process by replacing the current LINAC2 with LINAC4 to provide a doubled beam brightness.

From a physics point of view, HL-LHC will contribute to measuring Standard Model processes with even higher precision due to the large amount of data collect. Also Beyond the Standard Model phenomena, such as exotic particles or supersymmetry theories, will benefit from the LHC upgrade increasing the accuracy and the sensitivity of the analyses. For example, during the last HL-LHC runs the Higgs boson mass is expected to be measured with a precision of one order of magnitude better than the current results. In Figure C.1a the expected uncertainty on the Higgs boson signal-strength for different channels are

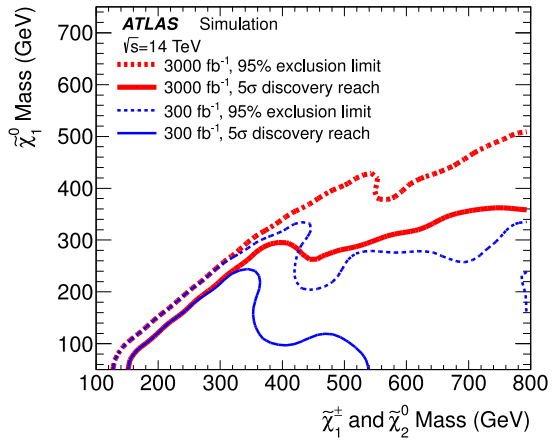
reported, showing an important improvement on the measurements precision. On the other hand, Figure C.1b shows the discovery reach and exclusion limits for the chargino and neutralino search with an extended discovery power for chargino masses above 800 GeV, to be compared with the reach of 350 GeV for the Run 3 dataset. This simulated result is also important for exotic particles such as the Type-III SeeSaw heavy leptons, whose cross-sections can be calculated exploiting the electroweak chargino-neutralino model, as described in Section 4.3.

ATLAS Simulation

$\sqrt{s} = 14 \text{ TeV}$: $\int \text{Ldt}=300 \text{ fb}^{-1}$; $\int \text{Ldt}=3000 \text{ fb}^{-1}$
 $\int \text{Ldt}=300 \text{ fb}^{-1}$ extrapolated from 7+8 TeV



(a)



(b)

Figure C.1: Figure C.1a shows the uncertainty on the signal strength of Higgs analyses with with 300 fb^{-1} and 3000 fb^{-1} at $\sqrt{s} = 14 \text{ TeV}$ for a SM Higgs boson with a mass of 125 GeV. Figure C.1b shows the discovery reach (solid lines) and exclusion limits (dashed lines) for charginos and neutralinos in $\tilde{\chi}_1^\pm \tilde{\chi}_2^0 \rightarrow W^{(*)} \tilde{\chi}_1^0 Z^{(*)} \chi_1^0$ decays. The results are shown for the 300 fb^{-1} and 3000 fb^{-1} datasets [232].

The HL-LHC upgrade will lead to huge improvements for the physics analyses but also hard challenges on the detector side. One of the biggest will be related to the rise of the average pile-up up to 200 (from the average of 24 in 2016), as well as the higher radiation levels will be present in the inner regions of the de-

tectors. To cope the new requirements coming from this challenge, the ATLAS experiment developed the so-called ATLAS Phase-2 Upgrade programme [233]. In this programme the main sub-detectors (as the inner tracker, the calorimeters and the muon spectrometer) are planned to be upgraded, with also the Trigger and Data Acquisition system. Since the tracker is placed in the inner region of ATLAS where the tracks are the most dense and where radiation is the largest, it is strongly sensitive to these changes and a full replacement by a new system, the ATLAS Inner Tracker (ITk), is needed.

Since the ATLAS ITk detector was the topic of my qualification task inside the ATLAS Collaboration, only this upgrade will be discussed in this Appendix.

C.2 The ITk Design

The ATLAS ITk detector was designed to address the demanding requirements and hard challenges coming from the HL-LHC project. For this purpose, ITk will be a full-silicon tracking detector in order to provide the required tracking resolution as expected by the huge pile-up levels. A cross-sectional view of ITk is shown in Figure C.2. Two different subsystems compose the ITk structure: a sil-

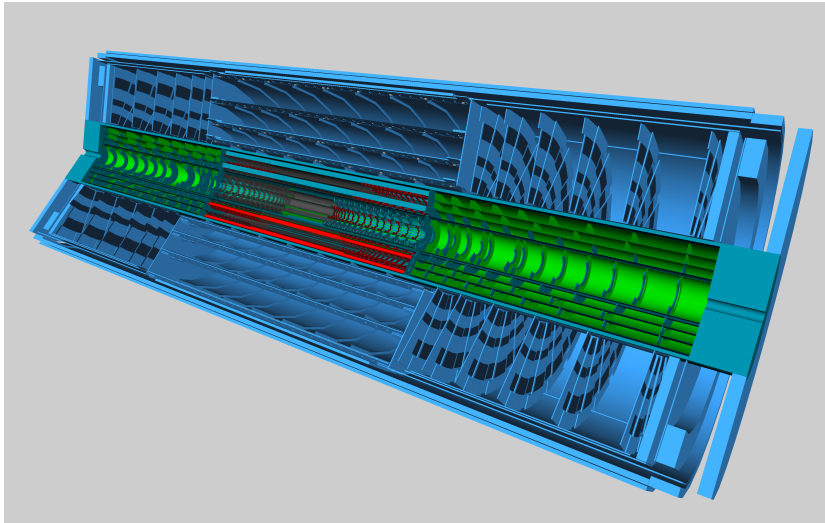


Figure C.2: Display of the ATLAS Phase-II Inner Tracker ITk with the Inclined Duals detector layout [234].

icon pixel detector in the region closest to the beam-pipe and a silicon microstrip detector at higher radii from the beam-line. A sketch of the sensor layout of the ITk is shown in Figure C.3, where the Pixel Detector is coloured in red and green while the Strip Detector in blue. Each detector is further divided into a *barrel* region, placed centrally around the Interaction Point, and an *end-cap* part covering

the forward regions of ITk. This separation into two different subsystems was designed to provide a higher granularity of the detector minimizing the number of readout channels when resolving nearby tracks. Comparing the new subsystems

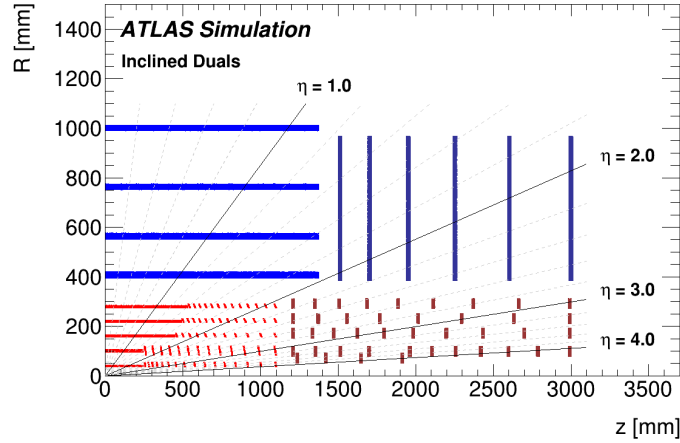


Figure C.3: A schematic layout of the ITk Inclined Duals layout for the HL-LHC phase with the Pixel Detector in red and the Strip Detector in blue [234].

tems with the current ones inside the Inner Detector, the main differences are that: the ITk Strip detector will replace the SCT covering a much larger region up to the TRT area; the TRT needed to be removed due to its saturation in presence of a large value of pile-up; the ITk Pixel Detector will be an extension of the current Pixel Detector covering a larger region up to η of 4.0 (from the 2.5 of the ID).

Another great improvements of ITk with respect to the ID is the minimization of the material budget. The low presence of material is essential to reduce the effect on the tracking performance, as an excess of material induces more particle interactions which can cause track deflection, multiple scattering, create photon conversions or modify the particle momentum. The radiation length X_0 versus the pseudorapidity η is used to compare the material budget in the ATLAS ITk and in the ATLAS ID, where X_0 represents the average path a particle needs to travel to reduce its initial energy by a factor $1/e$. As shown in Figure C.4, the lightweight materials used by ITk reduce the material budget by about 30% for $|\eta| < 4$ and even more for higher values.

C.2.1 ITk Pixel Detector

To have a very fine granularity, the ITk Pixel Detector [234] exploits silicon pixel modules with a pixel sizes of $50 \times 50 \mu\text{m}^2$. It covers 14 m^2 of silicon area with

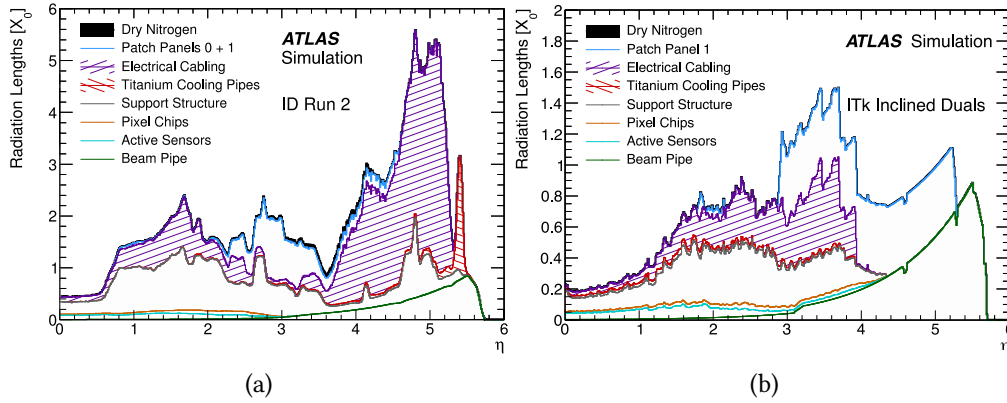


Figure C.4: Radiation length X_0 versus the pseudorapidity η in the Inner Detector (Figure C.4a) and in the Inner Tracker. The figures show only positive η , negative η is expected to look the same [234]. Note the different scale of these plots.

580 million readout channels. Two kind of technologies are considered for the sensors, both using n-implant in p-substrate with a thin active thickness of $200 \mu\text{m}$:

- 3D sensors in triplet modules in the innermost layer. They have pixel size of $50 \times 50 \mu\text{m}^2$ (end-cap) and $25 \times 100 \mu\text{m}^2$ (barrel) with a single collection electrode in the centre providing a hit efficiency more than 97%, as shown in Figure C.5. These sensors consist of $150 \mu\text{m}$ active thickness with $100 \mu\text{m}$ support wafer in addition with a low operational bias voltage of 80 - 140 V. Due to their high level of radiation tolerance are used close to the beam at only 34 mm. In the baseline scenario, they are expected to be replaced after 2000 fb^{-1} with an expected expected fluence of $1.3 \cdot 10^{16} \text{ neq/cm}^2$.
- Planar sensors in quad modules in all other layers. All of them have pixel size of $50 \times 50 \mu\text{m}^2$ with a thickness of $100 \mu\text{m}$ in the inner layer and $150 \mu\text{m}$ in the outer layers. Also these sensors provide efficiency higher than 97% and a bias voltage at the end of life up 600 V (inner layer) and 400 V (outer layer). They are designed using different bias structures as punch-through, temporary metal and bias rail and bias resistor. A planar sensor with a punch-trough bias structure is shown in Figure C.6.

Also a new front-end chip is being developed by the RD53 Collaboration [237], to be used as common readout chip for both ATLAS and CMS pixel detectors, in 65 nm CMOS technology. The prototype developed for the ATLAS Collaboration is the ITkPix [238] consisting of 400×384 pixels using differential front-end with a pixel bump pitch of $50 \times 50 \mu\text{m}^2$. The chip is specified to be radiation hard to

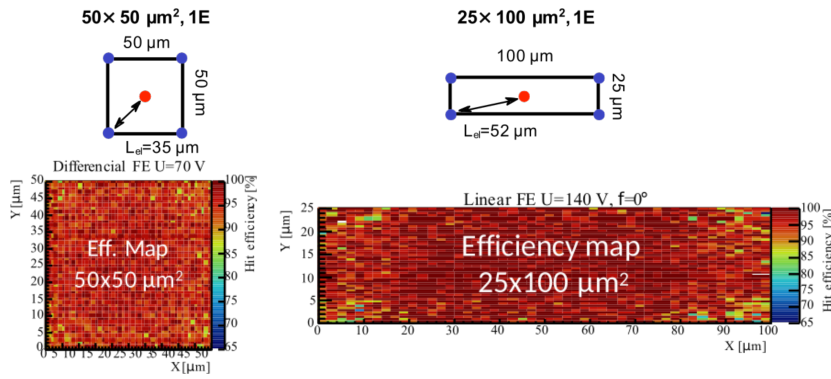


Figure C.5: Top figures show the pixel sizes used in 3D sensors with a single collection electrode (point in red), while the bottom ones the efficiency maps for different pixel sizes [236].

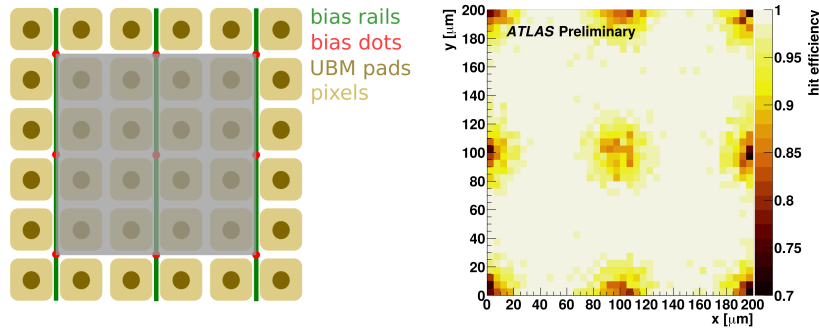


Figure C.6: Pixel matrix structure with punch-through bias structure is shown on the left, while on the right the efficiency map of the grey area corresponding to 4×4 pixels of a planar sensor before irradiation [236].

more than 5 MGy with an in-time threshold of less than 1 ke. It is designed to support a hit rate of up to 3 GHz/cm² with a trigger rate of 1 MHz.

On the geometrical point of view, the Pixel Detector is divided into an inner system, with two barrel layers and three groups of rings (two in correspondence of the barrel layer radii and one in between the two) and an outer system composed by three barrel layers with three corresponding groups of rings. Two half-rings with a carbon core with electrical and cooling services are used to build the each ring. The number of rings per layer and their location has been designed to cover the pseudorapidity region up to $|\eta| = 4.0$ and to provide at least nine points per track. An innovative feature of the ITk Pixel Detector in the forward part of the barrel layers where an *Inclined Duals* layout is implemented. This allows the material traversed by particles at large η to be minimised and at the same time requires less silicon surface to cover the full pseudorapidity range. In addition, these inclined sensors provide two or more hits in the first layer, providing redundancy for the local track finding close to the IP even at large pseudorapidity.

As the radiation damage will be up to $2 \cdot 10^{16}$ neq/cm², the detectors was designed to allow the replacement of the two innermost barrel layers as well as the innermost end-cap ring layer.

C.3 Database system

My qualification task (QT) was focused on the development of an interface to get data from external sources and a framework to perform quality control (QC) using data taken from this interface. These data (such as current as function of voltage (IV), temperature, low-voltage) had to be stored in a local database to be visualized and used in a second stage.

I choose to join this project given the large contribution of the ATLAS Italian community in the production and testing phase of the readout chip that will be used in the new electronics of the ITk detector.

To perform this task I used a RD53A prototype (see Figure C.7), which has a similar structure of the ITkPix chip already described. RD53A has three blocks of pixels with different types of front-end circuits and has three programmable output lanes up to 1.28 Gbps, with Aurora 64/66 protocol. The chip is controlled with 160 Mbps single differential serial inputs.

The YARR software [241] was used as readout system for the RD53A front-end chip since it can run on XpressK7 as well as commercial FPGA boards. This software system aims to simulate on the software side almost all the functionalities of a firmware in a DAQ system. The display port present on the RD53A was connected to the XpressK7 board via a FPGA Mezzanine Card (Ohio card). Exploiting a Peripheral Component Interconnect Express (PCIe), the FPGA board



Figure C.7: Single chip card with RD53A. The readout chip is located at the bottom in the center of the picture and the display ports for communication are located on top of the picture. [240].

mounted on a PC can communicate with the software. In this way all the quality assurance (QA) and quality control tests can be performed.

QA/QC tests are essential during the production and checking phase to ensure a high reliability of all on-detector components. QC tests are performed to validate the chip performance in conformance with its specifications, as well as to assess thermal performance and its behavior after a suffered stress (for example due to travel between two institutes, several hours under high current). On the other hand, QA is used to study component quality during the research and development stage to improve the reliability and validate the component design. All the QA/QC measurements have to be considered to search for possible changes in device performances compared to before, which can indicate possible defeat on the chip.

A large fraction of the institutes involved in the ATLAS Collaboration are working on the production and testing stage of the ATLAS ITk detector modules. For this reason, a database hosting all the measurements performed among the community can increase the precision and the quality of this project. Then, the ITk community developed a simple but effective structure to connect the results coming from all the institutes. The idea is to use the YARR system to readout the

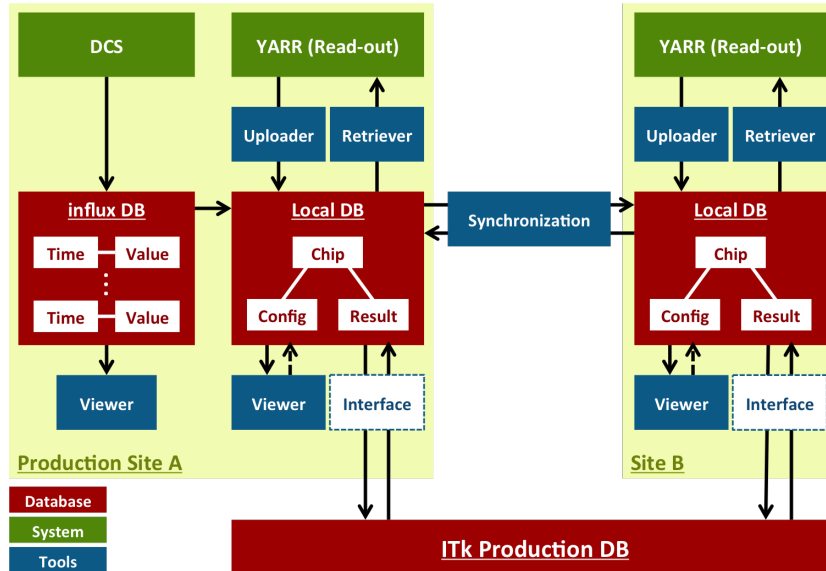


Figure C.8: Schematic view of the readout and database systems [242].

modules and build a so-called *local database*, mainly composed of json format files storing results and information regarding the configuration and the chip as well. Each production site has its own local database able to communicate with other local databases and with the *ITk Production Database*, used as final step of the production and testing chain. A schematic view of the readout chain is reported in Figure C.8. Also a *Master Database* can be implemented to store measurements of national sections.

I first created a prototype of Master Database in the Bologna INFN section to be used as Italian national database. To allow accesses only to the involved people I first developed several scripts to ensure the connection only from INFN domain with a login system based on the MD5 message-digest algorithm producing a 128-bit hash value.

I maintained the database structure inside the Bologna section exploiting the YARR framework to test the RD53A chip uploading the results of all the different scans in the local database. An example is shown in Figure C.9.

On the detector control system side, I developed different scripts to upload and store QA/QC measurements. Since DCS for module QA/QC was fast evolving, I decided to assume that DCS measurements were stored in text or csv format to be converted in dat files with current, voltage and time values. The dat files have been chosen to be coherent with the current database structure already implemented in the YARR system. Then, I converted these analysed results in .json format and I created a dedicated section inside the database to store and manage QC and DCS results. In Figures C.10 and C.11 an example of the web-browser

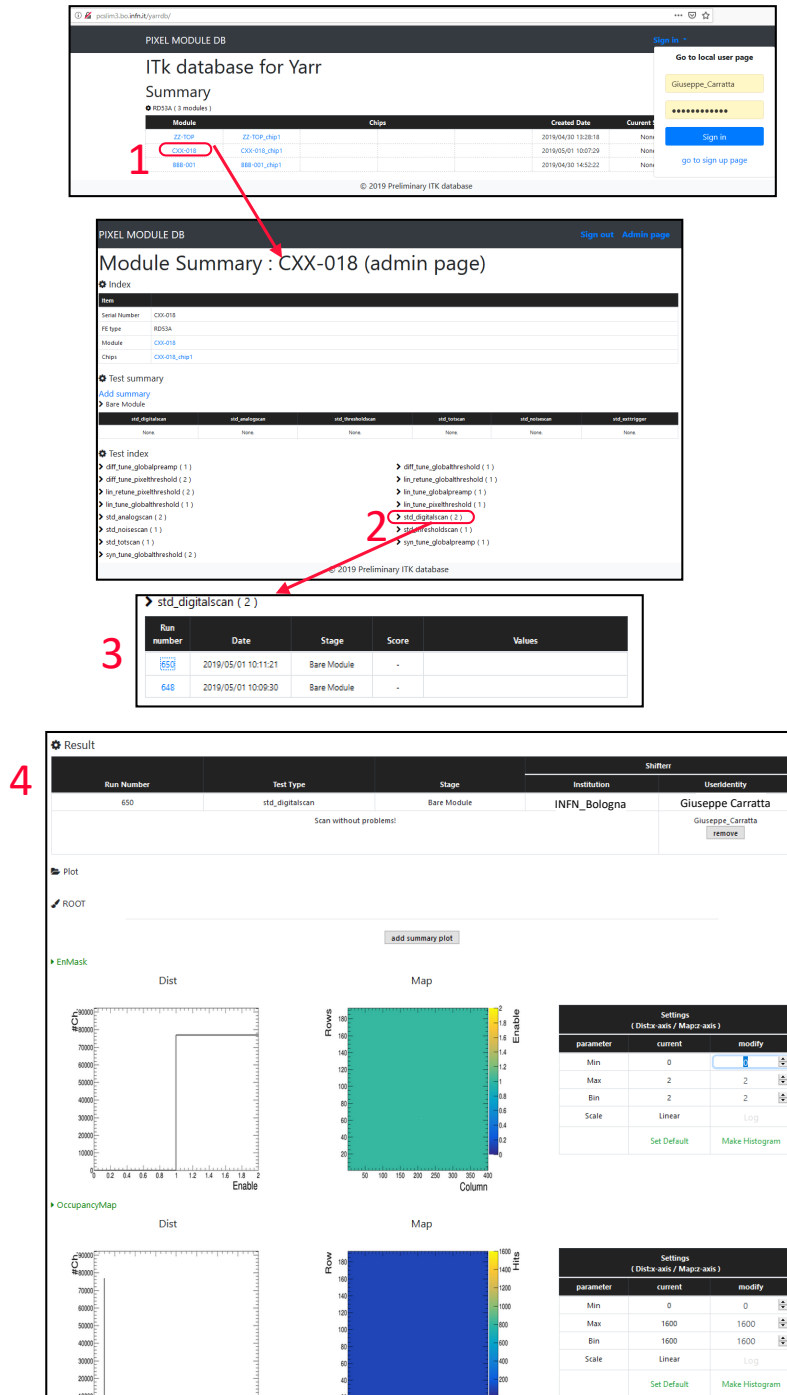


Figure C.9: Scheme of the visualization of an uploaded result on the database. 1. is the top page with all the scanned modules with also the login window; 2. is the chip providing information as the serial number front-end type and also the scans performed, 3. choosing a certain scan, the several run performed a shown, 4. results of the selected scan.

visualization for QC and DCS scans are shown.

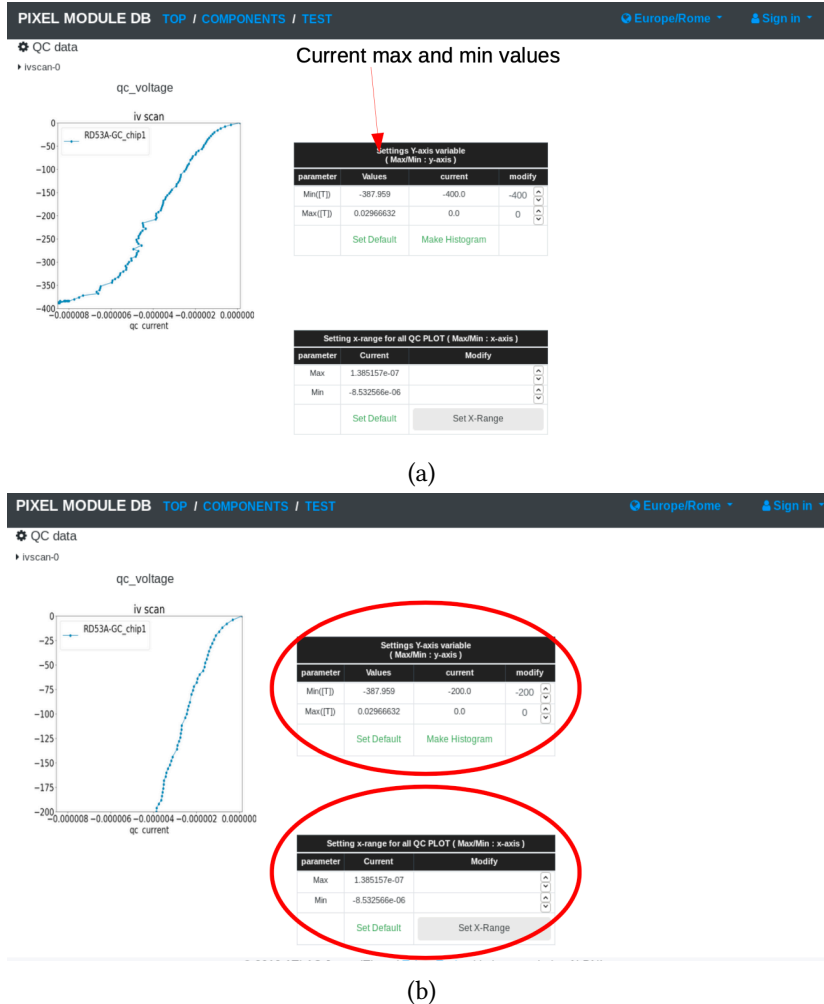
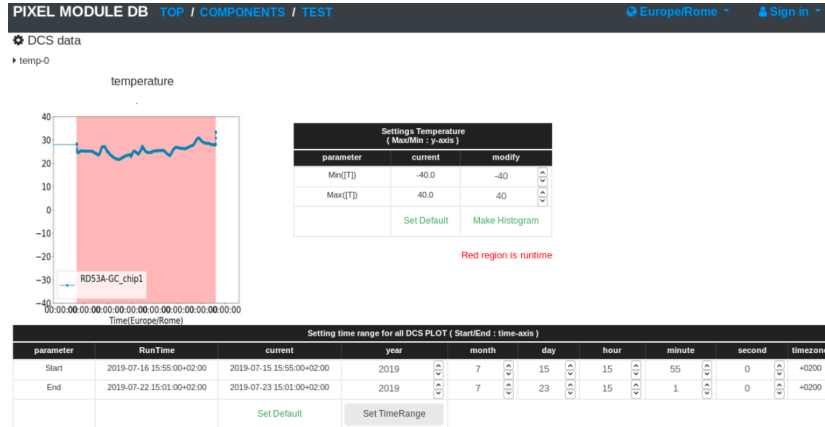


Figure C.10: View of the QC results stored on the local database (Figure C.10a). The histogram is directly displayed based on the x and y values. Two different interacting tables were implemented in order to manage the axes (Figure C.10b) and to restore default values.

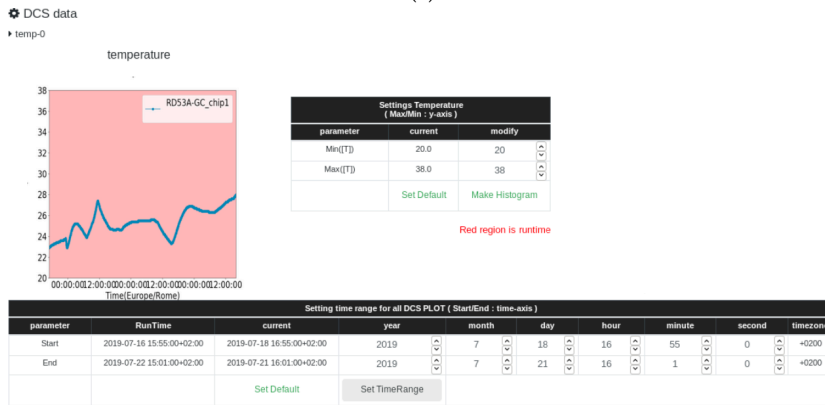
C.4 Conclusions

The QC and DCS data implementation in the local database framework was a preliminary work to be refined in the next future, but already operative.

During the testing phase of the RD53A front-end chip in Bologna, it was important to store the collected data and to compare the results under different chip



(a)



(b)

Figure C.11: View of the DCS results (temperature) stored on the local database (Figure C.11a). The histogram is directly displayed based on the x and y values. Two different interacting tables were implemented in order to manage the axes (Figure C.11b) and to restore default values.

conditions. At the end of 2019, several modules arrived in Bologna from other institutes and the developed DCS interface has been used to take into account the travel environment and to compare the performance with those before shipment.

Exploiting the QA/QC database functionalities different issues affecting the modules were noted and fixed, as well as the ultimate conditions to which they can be stressed.

Bibliography

- [1] C. Quigg, “Gauge Theories of the Strong, Weak and Electromagnetic Interactions”, Westview Press (1983).
- [2] H. Fritzsch, M. Gell-Mann, H. Leutwyler, “Advantages of the color octet gluon picture”, *Phys. Lett. B* **47**, 365-368 (1973). ISSN: 0370-2693. DOI: [10.1016/0370-2693\(73\)90625-4](https://doi.org/10.1016/0370-2693(73)90625-4)
- [3] L.S. Glashow, “The renormalizability of vector meson interactions”, *Nuclear Physics* **10**, 107-117 (1959). ISSN: 0029-5582. DOI: [10.1016/0029-5582\(59\)90196-8](https://doi.org/10.1016/0029-5582(59)90196-8)
- [4] S. Weinberg, J. C. Ward, “A Model of Leptons”, *Phys. Rev. Lett.* **19**, 1264-1266 (1967). ISSN: 1079-7114. DOI: [10.1103/PhysRevLett.19.1264](https://doi.org/10.1103/PhysRevLett.19.1264)
- [5] A. Salam, “Weak and electromagnetic interactions”, *Il Nuovo Cimento* **11**, 568-577 (1959). ISSN: 1827-6121. DOI: [10.1007/BF02726525](https://doi.org/10.1007/BF02726525)
- [6] P. W. Higgs, “Spontaneous Symmetry Breakdown without Massless Bosons”, *Phys. Rev.* **145**, 1156-1163 (1966). ISSN: 1536-6065. DOI: [10.1103/PhysRev.145.1156](https://doi.org/10.1103/PhysRev.145.1156)
- [7] C. Burgard, “Example: Standard model of physics”. URL: <https://example.net/tikz/examples/model-physics/>
- [8] W. Pauli, “Wissenschaftlicher Briefwechsel mit Bohr, Einstein, Heisenberg u.a. - Band II: 1930-1939”, edited by Karl von Meyenn *Springer-Verlag Berlin Heidelberg New York Tokyo*, pp. 39-41 (1985).
- [9] C. Patrignani et al. , “Particle Data Group”, *Chinese Phys. C* **40**, 100001 (2006). DOI: [10.1088/1674-1137/40/10/100001](https://doi.org/10.1088/1674-1137/40/10/100001)
- [10] E. Fermi, “Tentativo di una teoria dei raggi β ”, *Il Nuovo Cimento, Societ 'a Italiana di Fisica* (1934).

- [11] K. Kleinknecht, “CP Violation and K Decays”, *Annual Review of Nuclear Science* **26**, 1-50 (1976). DOI: [10.1146/annurev.ns.26.120176.000245](https://doi.org/10.1146/annurev.ns.26.120176.000245)
- [12] N. Cabibbo, “Unitary Symmetry and Leptonic Decays”, *Phys. Rev. Lett.*, **101**, 531-533 (1963). DOI: [10.1103/PhysRevLett.10.531](https://doi.org/10.1103/PhysRevLett.10.531)
- [13] M. Kobayashi, T. Maskawa, “CP-Violation in the Renormalizable Theory of Weak Interaction”, *Progress of Theoretical Physics* **49**, 652-657 (1973). DOI: [10.1143/PTP.49.652](https://doi.org/10.1143/PTP.49.652)
- [14] M. E. Peskin, D. V. Schroeder, “An Introduction to Quantum Field Theory”, Perseus Books (1995).
- [15] B. Pontecorvo, “Electron and Muon Neutrinos”, *Journal of Experimental and Theoretical Physics* **10**, 1236–1240 (1960).
- [16] Super-Kamiokande Collaboration, Fukuda Y. et al., “Evidence for oscillation of atmospheric neutrinos”, *Phys. Rev. Lett.* **81**, 1562-1567 (1998). DOI: [10.1103/PhysRevLett.81.1562](https://doi.org/10.1103/PhysRevLett.81.1562)
- [17] N. Arkani-Hamed, M. Schmaltz, “Hierarchies without symmetries from extra dimensions”, *Phys. Rev. D* **61**, 033005 (2000). DOI: [10.1103/PhysRevD.61.033005](https://doi.org/10.1103/PhysRevD.61.033005)
- [18] A. De Gouvea, “Neutrinos have mass: So what?”, *Mod. Phys. Lett. A* **19**, 2799-2813 (2004). DOI: [10.1142/S0217732304016032](https://doi.org/10.1142/S0217732304016032)
- [19] E. Majorana, “Teoria simmetrica dell’elettrone e del positrone”, *Il Nuovo Cimento* **14**, 171 (1937). DOI: [10.1007/BF02961314](https://doi.org/10.1007/BF02961314)
- [20] M. Drewes, “The phenomenology of right handed neutrinos”, *International Journal of Modern Physics E* **22** (2013). DOI: [10.1142/S02183013133300191](https://doi.org/10.1142/S02183013133300191)
- [21] F. Bonnet, D. Hernandez, T. Ota, W. Winter, “Neutrino masses from higher than d = 5 effective operators”, *Journal of High Energy Physics* (2009). DOI: [10.1088/1126-6708/2009/10/076](https://doi.org/10.1088/1126-6708/2009/10/076)
- [22] B. Adhikary, P. Roy, “Neutrino Yukawa textures within type-I see-saw”, *Advanced High Energy Physics* (2013). DOI: [10.1155/2013/324756](https://doi.org/10.1155/2013/324756)
- [23] A. Melfo et al., “Type II Seesaw at LHC: The Roadmap”, *Phys.Rev. D* **85** (2012). DOI: [10.1103/PhysRevD.85.055018](https://doi.org/10.1103/PhysRevD.85.055018)
- [24] S.M. Barr, I. Dorsner, “A Prediction from the type III see-saw mechanism”, *Physics Letter B* **632**, 527-531 (2006). DOI: [10.1016/j.physletb.2005.10.080](https://doi.org/10.1016/j.physletb.2005.10.080)

- [25] P.F. Pérez, “Type III Seesaw and left-right symmetry”, *Journal of High Energy Physics* **03**, 142 (2009). DOI: [10.1088/1126-6708/2009/03/142](https://doi.org/10.1088/1126-6708/2009/03/142)
- [26] C. Biggio, F. Bonnet, “Implementation of the Type III Seesaw Model in FeynRules/MadGraph and Prospects for Discovery with Early LHC Data” *Eur. Phys. J. C* **72**, 1899 (2012). DOI: [10.1140/epjc/s10052-012-1899-z](https://doi.org/10.1140/epjc/s10052-012-1899-z)
- [27] Arindam Das, “Searching for the Minimal Seesaw Models at the LHC and Beyond”, *Advances in High Energy Physics* 2018, pp.16 (2018). DOI: [10.1155/2018/9785318](https://doi.org/10.1155/2018/9785318)
- [28] F. del Aguila, J. de Blas, M. Perez-Victoria, “Effects of new leptons in Electroweak Precision Data”, *Phys. Rev. D* **78**, 013010 (2008). DOI: [10.1103/PhysRevD.78.013010](https://doi.org/10.1103/PhysRevD.78.013010)
- [29] A. Abada, C. Biggio, F. Bonnet, M. B. Gavela, T. Hambye, “ $\mu \rightarrow e\gamma$ and $\tau \rightarrow \ell\gamma$ in the fermion triplet seesaw model”, *Phys. Rev. D* **78**, 033007 (2008). DOI: [10.1103/PhysRevD.78.033007](https://doi.org/10.1103/PhysRevD.78.033007)
- [30] A. Abada, C. Biggio, F. Bonnet, M. B. Gavela, T. Hambye, “Low energy effects of neutrino masses”, *JHEP* **12**, 061 (2007). DOI: [10.1088/1126-6708/2007/12/061](https://doi.org/10.1088/1126-6708/2007/12/061)
- [31] R. Franceschini *et al.*, “Type-III seesaw mechanism at CERN LHC”, *Phys. Rev. D* **78**, no.3 033002 (2008). DOI: [10.1103/PhysRevD.78.033002](https://doi.org/10.1103/PhysRevD.78.033002)
- [32] ATLAS Collaboration, “Search for Type-III SeeSaw heavy leptons in pp collisions at $\sqrt{s} = 8$ TeV with the ATLAS Detector”, *Phys. Rev. D* **92**, p. 032001 (2015). DOI: [10.1103/PhysRevD.92.032001](https://doi.org/10.1103/PhysRevD.92.032001)
- [33] ATLAS Collaboration, “Search for heavy lepton resonances decaying to a Z boson and a lepton in pp collisions at $\sqrt{s} = 8$ TeV with the ATLAS detector”, *High Energ. Phys.* **2015**, 108 (2015). DOI: [10.1007/JHEP09\(2015\)108](https://doi.org/10.1007/JHEP09(2015)108)
- [34] CMS Collaboration, “Search for Heavy Lepton Partners of Neutrinos in Proton-Proton Collisions in the Context of the Type III Seesaw Mechanism”, *Phys. Lett. B* **718**, 348-368 (2012). DOI: [10.1016/j.physletb.2012.10.070](https://doi.org/10.1016/j.physletb.2012.10.070)
- [35] CMS Collaboration. “Search for physics beyond the standard model in multilepton final states in proton-proton collisions at $\sqrt{s} = 13$ TeV”, *High Energ. Phys.* **2020**, 51 (2020). DOI: [10.1007/JHEP03\(2020\)051](https://doi.org/10.1007/JHEP03(2020)051)
- [36] ATLAS Collaboration, “Search for type-III seesaw heavy leptons in dilepton final states in pp collisions at $\sqrt{s} = 13$ TeV with the ATLAS detector”, *Eur. Phys. J. C* **81**, 218 (2021). DOI: [10.1140/epjc/s10052-021-08929-9](https://doi.org/10.1140/epjc/s10052-021-08929-9)

- [37] G. Carratta [ATLAS Collaboration], “Search for Type-III SeeSaw heavy leptons in dileptonic final states using 139 fb^{-1} of pp collision at $\sqrt{s} = 13 \text{ TeV}$ with the ATLAS detector”, *PoS ICHEP2020*, 297 (2021). DOI:[10.22323/1.390.0297](https://doi.org/10.22323/1.390.0297)
- [38] S. Alekhin *et al.*, “A facility to Search for Hidden Particles at the CERN SPS: the SHiP physics case”, *Rept. Prog. Phys.* **79** no.12, 124201 (2016). DOI: [10.1088/0034-4885/79/12/124201](https://doi.org/10.1088/0034-4885/79/12/124201)
- [39] G. Cottin, “Searches for long-lived particles and Heavy Neutral Leptons: Theory perspective”, *PoS LHCP2021*, 003 (2021). DOI: [10.22323/1.397.0003](https://doi.org/10.22323/1.397.0003)
- [40] ATLAS Collaboration, “Summary plots for heavy-particle searches and long-lived particle searches”, ATL-PHYS-PUB-2021-033 (2021). URL: <https://inspirehep.net/literature/1920639>
- [41] CMS Collaboration, “Long Lived Particle summary plots”. URL: https://twiki.cern.ch/twiki/bin/view/CMSPublic/SummaryPlot-sEXO13TeV#Long_lived_particle_summary_plot
- [42] M. Borsato *et al.*, “Unleashing the full power of LHCb to probe Stealth New Physics”, *Rept. Prog. Phys.* (2022). DOI: <https://doi.org/10.1088/1361-6633/ac4649>
- [43] A. Usachov, “Long-lived particles results from LHCb”, presented at *Search for long-lived particles at the LHC and beyond 9th workshop of the LLP community*, virtual conference (2021). URL: <https://cds.cern.ch/record/2770581>
- [44] F. F. Deppisch *et al.*, “Neutrinos and Collider Physics”, *New J. Phys.* **17** no.7, 075019 (2015). DOI: [10.1088/1367-2630/17/7/075019](https://doi.org/10.1088/1367-2630/17/7/075019)
- [45] D. Gorbunov and M. Shaposhnikov, “How to find neutral leptons of the ν MSM?”, *JHEP* **10**, 015 (2007). DOI: [10.1007/JHEP11\(2013\)101](https://doi.org/10.1007/JHEP11(2013)101)
- [46] O. Ruchayskiy and A. Ivashko, “Restrictions on the lifetime of sterile neutrinos from primordial nucleosynthesis”, *JCAP* **10**, 014 (2012). DOI: [10.1088/1475-7516/2012/10/014](https://doi.org/10.1088/1475-7516/2012/10/014)
- [47] A. Boyarsky *et al.*, “The Role of sterile neutrinos in cosmology and astrophysics”, *Ann. Rev. Nucl. Part. Sci.* **59**, 191-214 (2009). DOI: [10.1146/annurev.nucl.010909.083654](https://doi.org/10.1146/annurev.nucl.010909.083654)
- [48] S. Antusch and O. Fischer, “Testing sterile neutrino extensions of the Standard Model at future lepton colliders”, *JHEP* **05**, 053 (2015). DOI: [10.1007/JHEP05\(2015\)053](https://doi.org/10.1007/JHEP05(2015)053)

- [49] D. I. Britton *et al.* “Improved search for massive neutrinos in $\pi^+ \rightarrow e^+$ neutrino decay”, *Phys. Rev. D* **46**, R885-R887 (1992). DOI: [10.1103/PhysRevD.46.R885](https://doi.org/10.1103/PhysRevD.46.R885)
- [50] M. Aoki *et al.* [PIENU], “Search for Massive Neutrinos in the Decay $\pi \rightarrow e\nu$ ”, *Phys. Rev. D* **84**, 052002 (2011). DOI: [10.1103/PhysRevD.84.052002](https://doi.org/10.1103/PhysRevD.84.052002)
- [51] Britton, D. I *et al.*, “Measurement of the $\pi^+ \rightarrow e^+\nu$ branching ratio”, *Phys. Rev. Lett.* **68**, 3000-3003 (1992). DOI: [10.1103/PhysRevLett.68.3000](https://doi.org/10.1103/PhysRevLett.68.3000)
- [52] T. Yamazaki *et al.*, “Search for Heavy Neutrinos in Kaon Decay”, *Conf. Proc. C* **840719**, 262 (1984). <https://inspirehep.net/literature/211342>
- [53] G. Bernardi *et al.*, “FURTHER LIMITS ON HEAVY NEUTRINO COUPLINGS”, *Phys. Lett. B* **203**, 332-334 (1988). DOI: [10.1016/0370-2693\(88\)90563-1](https://doi.org/10.1016/0370-2693(88)90563-1)
- [54] F. Bergsma *et al.* [CHARM], “A Search for Decays of Heavy Neutrinos in the Mass Range 0.5-GeV to 2.8-GeV”, *Phys. Lett. B* **166**, 473-478 (1986). DOI: [10.1016/0370-2693\(86\)91601-1](https://doi.org/10.1016/0370-2693(86)91601-1)
- [55] J. Badier *et al.* [NA3], “Direct Photon Production From Pions and Protons at 200-GeV/c”, *Z. Phys. C* **31**, 341 (1986). DOI: [10.1007/BF01588030](https://doi.org/10.1007/BF01588030)
- [56] S. A. Baranov *et al.*, “Search for heavy neutrinos at the IHEP-JINR neutrino detector”, *Phys. Lett. B* **302**, 336-340 (1993). DOI: [10.1016/0370-2693\(93\)90405-7](https://doi.org/10.1016/0370-2693(93)90405-7)
- [57] A. Atre, T. Han, S. Pascoli and B. Zhang, “The Search for Heavy Majorana Neutrinos”, *JHEP* **05**, 030 (2009). DOI: [10.1088/1126-6708/2009/05/030](https://doi.org/10.1088/1126-6708/2009/05/030)
- [58] D. Liventsev *et al.* [Belle], “Search for heavy neutrinos at Belle”, *Phys. Rev. D* **87** no.7, 071102 (2013). DOI: <https://doi.org/10.1103/PhysRevD.87.071102>.
- [59] O. Adriani *et al.* [L3], “Search for isosinglet neutral heavy leptons in Z0 decays”, *Phys. Lett. B* **295**, 371-382 (1992). DOI: [10.1016/0370-2693\(92\)91579-X](https://doi.org/10.1016/0370-2693(92)91579-X)
- [60] P. Abreu *et al.* [DELPHI], “Search for neutral heavy leptons produced in Z decays”, *Z. Phys. C* **74**, 57-71 (1997). DOI: [10.1007/s002880050370](https://doi.org/10.1007/s002880050370)
- [61] P. Achard *et al.* [L3], “Search for heavy isosinglet neutrino in e^+e^- annihilation at LEP”, *Phys. Lett. B* **517**, 67-74 (2001). DOI: [10.1016/S0370-2693\(01\)00993-5](https://doi.org/10.1016/S0370-2693(01)00993-5)

- [62] ATLAS Collaboration, “Search for heavy Majorana neutrinos with the ATLAS detector in pp collisions at $\sqrt{s} = 8$ TeV”, *JHEP* **07**, 162 (2015). DOI: [10.1007/JHEP07\(2015\)162](https://doi.org/10.1007/JHEP07(2015)162)
- [63] S. Banerjee *et al.*, “Prospects of Heavy Neutrino Searches at Future Lepton Colliders”, *Phys. Rev. D* **92**, 075002 (2015). DOI: [10.1103/PhysRevD.92.075002](https://doi.org/10.1103/PhysRevD.92.075002)
- [64] C. Adams *et al.* [LBNE], “The Long-Baseline Neutrino Experiment: Exploring Fundamental Symmetries of the Universe”, BNL-101354-2013-JA (2013). URL: <https://inspirehep.net/literature/1245018>
- [65] A. Blondel *et al.* [FCC-ee study Team], “Search for Heavy Right Handed Neutrinos at the FCC-ee”, *Nucl. Part. Phys. Proc.* **273-275**, 1883-1890 (2016). DOI: [10.1016/j.nuclphysbps.2015.09.304](https://doi.org/10.1016/j.nuclphysbps.2015.09.304)
- [66] W. Bonivento *et al.*, “Proposal to Search for Heavy Neutral Leptons at the SPS”, CERN-SPSC-2013-024 (2013). URL: <https://inspirehep.net/literature/1257391>
- [67] E. Graverini, “SHiP sensitivity to Heavy Neutral Leptons”, CERN-SHiP-NOTE-2016-003 (2016). URL: <https://cds.cern.ch/record/2214085>
- [68] A. V. Artamonov *et al.* [E949], “Search for heavy neutrinos in $K^+ \rightarrow \mu^+ \nu_H$ decays”, *Phys. Rev. D* **91** no.5, 052001 (2015). DOI: [10.1103/PhysRevD.91.052001](https://doi.org/10.1103/PhysRevD.91.052001)
- [69] A. M. Cooper-Sarkar *et al.* [WA66], “Search for Heavy Neutrino Decays in the BEBC Beam Dump Experiment”, *Phys. Lett. B* **160**, 207-211 (1985). DOI: [10.1016/0370-2693\(85\)91493-5](https://doi.org/10.1016/0370-2693(85)91493-5)
- [70] FMMF Collaboration, “Search for neutral weakly interacting massive particles in the Fermilab Tevatron wideband neutrino beam”, *Phys. Rev. D* **52**, 6–14 (1995). DOI: [10.1103/PhysRevD.52.6](https://doi.org/10.1103/PhysRevD.52.6)
- [71] A. Vaitaitis *et al.* [NuTeV and E815], “Search for neutral heavy leptons in a high-energy neutrino beam”, *Phys. Rev. Lett.* **83**, 4943-4946 (1999). DOI: [10.1103/PhysRevLett.83.4943](https://doi.org/10.1103/PhysRevLett.83.4943)
- [72] R. Aaij *et al.* [LHCb], “Search for Majorana neutrinos in $B^- \rightarrow \pi^+ \mu^- \mu^-$ decays”, *Phys. Rev. Lett.* **112** no.13, 131802 (2014). DOI: [10.1103/PhysRevLett.112.131802](https://doi.org/10.1103/PhysRevLett.112.131802)
- [73] P. Vilain *et al.* [CHARM II], “Search for heavy isosinglet neutrinos”, *Phys. Lett. B* **343**, 453-458 (1995). DOI: [10.1016/0370-2693\(94\)01422-9](https://doi.org/10.1016/0370-2693(94)01422-9)

- [74] V. Khachatryan *et al.* [CMS], “Search for heavy Majorana neutrinos in $\mu^\pm\mu^\pm + \text{jets}$ events in proton-proton collisions at $\sqrt{s} = 8 \text{ TeV}$ ”, *Phys Lett. B* **748**, 144-166 (2015). DOI: [10.1016/j.physletb.2015.06.070](https://doi.org/10.1016/j.physletb.2015.06.070)
- [75] P. Mouche, “Overall view of the LHC. Vue d’ensemble du LHC”, OPEN-PHO-ACCEL-2014-001 (2014). URL: <https://cds.cern.ch/record/1708847>
- [76] R. Bruce *et al.* “LHC Run 2: Results and challenges” (2016). URL: <https://hb2016.esss.se/prepress/papers/moam5p50.pdf>
- [77] High Luminosity LHC project. URL: <https://project-hl-lhc-industry.web.cern.ch/content/project-schedule>
- [78] LHC Commissioning, “LHC 2017 Performance”. URL: <https://lhc-commissioning..2017-performance.htm>
- [79] ATLAS Collaboration, Luminosity Public Results Run-2: Luminosity summary plots for 2015 pp data taking. URL: https://twiki.cern.ch/twiki/bin/view/AtlasPublic/LuminosityPublicResultsRun2#Luminosity_summary_plots_for_AN5
- [80] ATLAS Collaboration, Luminosity Public Results Run-2: Luminosity summary plots for 2018 pp data taking. URL: https://twiki.cern.ch/twiki/bin/view/AtlasPublic/LuminosityPublicResultsRun2#Luminosity_summary_plots_for_201
- [81] ATLAS Collaboration, Luminosity Public Results Run-2: 2018 pp Collisions, Pileup Interactions and Data Taking Efficiency. URL: https://twiki.cern.ch/twiki/bin/view/AtlasPublic/LuminosityPublicResultsRun2#Pileup_Interactions_and_Data_Tak
- [82] ATLAS Collaboration, Luminosity Public Results Run-2: Multiple Year Collision Plots. URL: https://twiki.cern.ch/twiki/bin/view/AtlasPublic/LuminosityPublicResultsRun2#Multiple_Year_Collision_Plots
- [83] ATLAS Collaboration “ATLAS data quality operations and performance for 2015-2018 data-taking”, *IOP Publishing* vol. 15 Nr. 4 pp.P04003 (2020). DOI: [10.1088/1748-0221/15/04/p04003](https://doi.org/10.1088/1748-0221/15/04/p04003)
- [84] E. Mobs, “The CERN accelerator complex - 2019. Complexe des accélérateurs du CERN - 2019”, CERN-GRAPHICS-2019-002 (2019). URL: <https://cds.cern.ch/record/2684277>

- [85] J. Pequeno and P. Schaffner, “How ATLAS detects particles: diagram of particle paths in the detector”, CERN-EX-1301009 (2013). URL: <https://cds.cern.ch/record/1505342>
- [86] ATLAS Collaboration, “The ATLAS Experiment at the CERN Large Hadron Collider”, *JINST* **3**, S08003 (2008). DOI: [10.1088/1748-0221/3/08/S08003](https://doi.org/10.1088/1748-0221/3/08/S08003)
- [87] J. Pequeno “Computer generated image of the whole ATLAS detector”, CERN-GE-0803012 (2008). URL: <https://cds.cern.ch/record/1095924>
- [88] ATLAS Collaboration, “Muon reconstruction performance of the ATLAS detector in proton-proton collision data at $\sqrt{s}=13$ TeV”, *Eur. Phys. J. C* **76** no.5, 292 (2016). DOI: [10.1140/epjc/s10052-016-4120-y](https://doi.org/10.1140/epjc/s10052-016-4120-y)
- [89] ATLAS Collaboration, “Insertable B-Layer Technical Design Report”, ATLAS-TDR-019. URL: <https://inspirehep.net/literature/1609508>
- [90] F. Hugging, “The ATLAS Pixel Insertable B-Layer (IBL)”. URL: [arXiv:1012.2742](https://arxiv.org/abs/1012.2742).
- [91] ATLAS Collaboration, “Particle Identification Performance of the ATLAS Transition Radiation Tracker”, ATLAS-CONF-2011-128. URL: <https://inspirehep.net/literature/1204154>
- [92] ATLAS Collaboration, “Impact Parameter Resolution”, IDTR-2015-007. URL: <https://atlas.web.cern.ch/Atlas/GROUPS/PHYSICS/PLOTS/IDTR-2015-007/>
- [93] ATLAS Collaboration, “Electron and photon energy calibration with the ATLAS detector using 2015–2016 LHC proton-proton collision data”, *JINST* **14** no.03, P03017 (2019). DOI: <https://doi.org/10.1088/1748-0221/14/03/P03017>
- [94] P. Amal, “Physics prospects with the ALFA and AFP detectors”, ATL-LUM-SLIDE-2013-251 (2013). URL: <https://cds.cern.ch/record/1548109>
- [95] M. Bruschi, “Diffraction and Forward Physics in ATLAS: results and perspectives”, *EPJ Web Conf.* **90**, 06003 (2015). DOI: [10.1051/epj-conf/20159006003](https://doi.org/10.1051/epj-conf/20159006003)
- [96] ATLAS Collaboration, “The ATLAS Data Acquisition and High Level Trigger system”, *JINST* **11** no.06, P06008 (2016). DOI: [10.1088/1748-0221/11/06/P06008](https://doi.org/10.1088/1748-0221/11/06/P06008)

- [97] ATLAS Collaboration, “Performance of the ATLAS Trigger System in 2015”, *Eur. Phys. J. C* **77** no.5, 317 (2017). DOI: [10.1140/epjc/s10052-017-4852-3](https://doi.org/10.1140/epjc/s10052-017-4852-3)
- [98] ATLAS Collaboration, “Performance of the ATLAS Track Reconstruction Algorithms in Dense Environments in LHC Run 2”, *Eur. Phys. J. C* **77** 673 (2017). DOI: [10.1140/epjc/s10052-017-5225-7](https://doi.org/10.1140/epjc/s10052-017-5225-7)
- [99] ATLAS Collaboration, “Performance of the ATLAS Silicon Pattern Recognition Algorithm in Data and Simulation at $\sqrt{s}7$ TeV”, ATLAS-CONF-2010-072. URL: <https://inspirehep.net/literature/1204016>
- [100] ATLAS Collaboration, “Reconstruction of primary vertices at the ATLAS experiment in Run 1 proton–proton collisions at the LHC”, *Eur. Phys. J. C* **77**, 332 (2017). DOI: [10.1140/epjc/s10052-017-4887-5](https://doi.org/10.1140/epjc/s10052-017-4887-5)
- [101] ATLAS Collaboration “Electron reconstruction and identification in the ATLAS experiment using the 2015 and 2016 LHC proton-proton collision data at $\sqrt{s} = 13$ TeV”, *Eur. Phys. J. C* **79**, 639 (2019). DOI: [10.1140/epjc/s10052-019-7140-6](https://doi.org/10.1140/epjc/s10052-019-7140-6)
- [102] ATLAS Collaboration, ‘Electron efficiency measurements with the ATLAS detector using the 2015 LHC proton-proton collision data’, ATLAS-CONF-2016-024. URL: <https://inspirehep.net/literature/1467063>
- [103] W. Lampl et al., “Calorimeter clustering algorithms: Description and performance”, ATL-LARG-PUB-2008-002. URL: <https://inspirehep.net/literature/807147>
- [104] ATLAS Collaboration, “Electron and photon performance measurements with the ATLAS detector using the 2015-2017 LHC proton-proton collision data”, *JINST* **14** P12006 (2019). DOI: [10.1088/1748-0221/14/12/p12006](https://doi.org/10.1088/1748-0221/14/12/p12006)
- [105] T.G. Cornelissen et al., “The global χ^2 track fitter in ATLAS”, *J. Phys.: Conf. Ser.* **119** 032013 (2008). DOI: [10.1088/1742-6596/119/3/032013](https://doi.org/10.1088/1742-6596/119/3/032013)
- [106] ATLAS Collaboration, “Improved electron reconstruction in ATLAS using the Gaussian Sum Filter-based model for bremsstrahlung”, ATLAS-CONF-2012-047. URL: <https://inspirehep.net/literature/1204271>
- [107] A. Hoecker et al., “TMVA - Toolkit for Multivariate Data Analysis”, CERN-OPEN-2007-007 (2007). URL: [arXiv:0703039](https://arxiv.org/abs/0703039)
- [108] ATLAS Collaboration, “Muon reconstruction performance of the ATLAS detector in proton–proton collision data at $\sqrt{s} = 13$ TeV”, *Eur. Phys. J. C* **76**, 292 (2016). DOI: [10.1140/epjc/s10052-016-4120-y](https://doi.org/10.1140/epjc/s10052-016-4120-y)

- [109] J. Illingworth and J. Kittler, "A survey of the hough transform", *Computer Vision, Graphics, and Image Processing* **44** 1, pp.87-116 (1988). DOI: [10.1016/S0734-189X\(88\)80033-1](https://doi.org/10.1016/S0734-189X(88)80033-1)
- [110] ATLAS Collaboration, "Muon reconstruction and identification efficiency in ATLAS using the full Run 2 pp collision data set at $\sqrt{s} = 13$ TeV", *Eur. Phys. J. C.* **81**, 578 (2021). DOI: [10.1140/epjc/s10052-021-09233-2](https://doi.org/10.1140/epjc/s10052-021-09233-2)
- [111] N.M Koehler, "ATLAS Muon Reconstruction Performance in LHC Run 2", ATL-PHYS-PROC-2015-186. URL: <https://inspirehep.net/literature/1678370>
- [112] ATLAS Collaboration, "Jet reconstruction and performance using particle flow with the ATLAS Detector", *Eur. Phys. J. C.* **77** 466 (2017). DOI: [10.1140/epjc/s10052-017-5031-2](https://doi.org/10.1140/epjc/s10052-017-5031-2)
- [113] M. Cacciari, G. P. Salam and G. Soyez, "The anti- k_t jet clustering algorithm", *JHEP* **04** 063 (2008). DOI: <https://doi.org/10.1088/1126-6708/2008/04/063>
- [114] S. Catani, Yu.L. Dokshitzer, M.H. Seymour and B.R. Webber, "Longitudinally-invariant k_T -clustering algorithms for hadron-hadron collisions", *Nuclear Physics B* **B406**, pp. 187-224 (1993). DOI: [10.1016/0550-3213\(93\)90166-M](https://doi.org/10.1016/0550-3213(93)90166-M)
- [115] Yu.L. Dokshitzer, G.D. Leder, S. Moretti and B.R. Webber, "Better jet clustering algorithms", *JHEP* **08**, pp.001 (1997). DOI: [10.1088/1126-6708/1997/08/001](https://doi.org/10.1088/1126-6708/1997/08/001)
- [116] ATLAS Collaboration, "Performance of pile-up mitigation techniques for jets in pp collisions at $\sqrt{s} = 8$ TeV using the ATLAS detector", *Eur. Phys. J. C.* **76**, 581 (2016). DOI: [10.1140/epjc/s10052-016-4395-z](https://doi.org/10.1140/epjc/s10052-016-4395-z)
- [117] ATLAS Collaboration, "Jet energy scale and uncertainties in 2015-2017 data and simulation" (2018). URL: <https://atlas.web.cern.ch/Atlas/GROUPS/PHYSICS/PLOTS/JETM-2018-006>
- [118] ATLAS Collaboration, "Jet energy resolution in 2017 data and simulation" (2018). URL: <https://atlas.web.cern.ch/Atlas/GROUPS/PHYSICS/PLOTS/JETM-2018-005>
- [119] ATLAS Collaboration, "Jet energy scale measurements and their systematic uncertainties in proton-proton collisions at $\sqrt{s} = 13$ TeV with the ATLAS detector", *Phys. Rev. D.* **96** 072002 (2017). DOI: [10.1103/PhysRevD.96.072002](https://doi.org/10.1103/PhysRevD.96.072002)

- [120] ATLAS Collaboration, “Jet energy scale and resolution measured in proton-proton collisions at $\sqrt{s} = 13$ TeV with the ATLAS detector”, CERN-EP-2020-083. URL: <https://inspirehep.net/literature/1805279>
- [121] R. Wigmans, “Calorimetry: Energy Measurement in Particle Physics”, *Oxford Scholarship Online* (2018). DOI: [10.1093/oso/9780198786351.001.0001](https://doi.org/10.1093/oso/9780198786351.001.0001)
- [122] ATLAS Collaboration, “ATLAS b -jet identification performance and efficiency measurement with $t\bar{t}$ events in pp collisions at $\sqrt{s} = 13$ TeV”, *Eur. Phys. J. C* **79** 970 (2019). DOI: [10.1140/epjc/s10052-019-7450-8](https://doi.org/10.1140/epjc/s10052-019-7450-8)
- [123] ATLAS Collaboration, “Optimisation and performance studies of the ATLAS b -tagging algorithms for the 2017-18 LHC run”, ATL-PHYS-PUB-2017-013. URL: <https://inspirehep.net/literature/1795306>
- [124] ATLAS Collaboration, “Secondary vertex finding for jet flavour identification with the ATLAS detector”, ATL-PHYS-PUB-2017-011. URL: <https://inspirehep.net/literature/1795302>
- [125] ATLAS Collaboration, “Topological b -hadron decay reconstruction and identification of b -jets with the JetFitter package in the ATLAS experiment at the LHC”, ATL-PHYS-PUB-2018-025. URL: <https://inspirehep.net/literature/1795264>
- [126] F. Chollet et al, “Keras” (2015). URL: <https://keras.io/>
- [127] The Theano Development Team, “Theano: A Python framework for fast computation of mathematical expressions” (2016). URL: [arXiv:1605.02688](https://arxiv.org/abs/1605.02688)
- [128] D. P. Kingma, J. Ba, “Adam: A method for stochastic optimization” (2014). URL: [arXiv: 1412.6980](https://arxiv.org/abs/1412.6980)
- [129] ATLAS Collaboration, “Performance of missing transverse momentum reconstruction with the ATLAS detector using proton-proton collisions at $\sqrt{s} = 13$ TeV”, *Eur. Phys. J. C*. **78** 903 (2018). DOI: [10.1140/epjc/s10052-018-6288-9](https://doi.org/10.1140/epjc/s10052-018-6288-9)
- [130] ATLAS Collaboration, “ E_T^{miss} performance in the ATLAS detector using 2015-2016 LHC p-p collisions”, ATLAS-CONF-2018-023. URL: <https://inspirehep.net/literature/1679132>
- [131] ATLAS Collaboration, “Object-based missing transverse momentum significance in the ATLAS detector”, ATLAS-CONF-2018-038. URL: <https://inspirehep.net/literature/1682356>

- [132] T. Fawcett, “An introduction to ROC analysis”, *Pattern Recognition Letters* **27** 8 (2006). DOI: [10.1016/j.patrec.2005.10.010](https://doi.org/10.1016/j.patrec.2005.10.010)
- [133] D. Adams et al. ,“Recommendations of the Physics Objects and Analysis Harmonisation Study Groups 2014”, ATL-PHYS-INT-2014-018 (2014). URL: <https://cds.cern.ch/record/1743654>
- [134] ATLAS Collaboration, “Performance of the ATLAS muon triggers in Run 2”, *JINST* **15** no.09, P09015 (2020). DOI: [10.1088/1748-0221/15/09/p09015](https://doi.org/10.1088/1748-0221/15/09/p09015)
- [135] ATLAS Collaboration, “Performance of electron and photon triggers in ATLAS during LHC Run 2”, *Eur. Phys. J. C* **80** no.1, 47 (2020). DOI: [10.1140/epjc/s10052-019-7500-2](https://doi.org/10.1140/epjc/s10052-019-7500-2)
- [136] ATLAS Collaboration, “The ATLAS Simulation Infrastructure”, *Eur. Phys. J. C.* **70**, 823–874 (2010). DOI: [10.1140/epjc/s10052-010-1429-9](https://doi.org/10.1140/epjc/s10052-010-1429-9)
- [137] ATLAS Collaboration, “ATLAS computing: Technical design report”, CERN-LHCC-2005-022 (2005). URL: <https://inspirehep.net/literature/689029>
- [138] GEANT4 Collaboration, “GEANT4—a simulation toolkit”, *Nucl. Instrum. Meth. A* **506**, 250-303 (2003). DOI: [10.1016/S0168-9002\(03\)01368-8](https://doi.org/10.1016/S0168-9002(03)01368-8)
- [139] J. Catmore, “Introduction to ATLAS data preparation and analysis”, *Joint Oslo/Bergen/NBI ATLAS Software Tutorial* (2016). URL: <https://indico.cern.ch/event/472469/contributions/1982677/>
- [140] M. Dobbs and J. B. Hansen, “The HepMC C++ Monte Carlo event record for High Energy Physics”, *Comput. Phys. Commun.* **134**, 41-46 (2001). DOI: [10.1016/S0010-4655\(00\)00189-2](https://doi.org/10.1016/S0010-4655(00)00189-2)
- [141] J. C. Collins, D. E. Soper and G. F. Sterman, “Factorization of Hard Processes in QCD”, *Adv. Ser. Direct. High Energy Phys.* **5**, 1-91 (1989). DOI: [10.1142/9789814503266_0001](https://doi.org/10.1142/9789814503266_0001)
- [142] R. D. Ball et al., “Parton distributions with LHC data”, *Nucl. Phys. B* **867**, 244-289 (2013). DOI: [10.1016/j.nuclphysb.2012.10.003](https://doi.org/10.1016/j.nuclphysb.2012.10.003)
- [143] R. D. Ball et al., “Parton distributions for the LHC Run II”, *JHEP* **04** 040 (2015). DOI: [10.1007/JHEP04\(2015\)040](https://doi.org/10.1007/JHEP04(2015)040)
- [144] M. Bähr, S. Gieseke, M.A. Gigg, et al., “Herwig++ physics and manual”, *Eur. Phys. J. C* **58**, 639-707 (2008). DOI: [10.1140/epjc/s10052-008-0798-9](https://doi.org/10.1140/epjc/s10052-008-0798-9)

- [145] J. Bellm et al., “Herwig 7.0/Herwig++ 3.0 release note”, *Eur. Phys. J. C* **76**, 196 (2016). DOI: [10.1140/epjc/s10052-016-4018-8](https://doi.org/10.1140/epjc/s10052-016-4018-8)
- [146] T. Sjöstrand, S. Mrenna, P. Skands, “PYTHIA 6.4 physics and manual”, *Journal of High Energy Physics* **2006** 05, 026 (2006). DOI: [10.1088/1126-6708/2006/05/026](https://doi.org/10.1088/1126-6708/2006/05/026)
- [147] T. Gleisberg, S. Höche, F. Krauss, M. Schönherr, S. Schumann, F. Siegert and J. Winter, “Event generation with SHERPA 1.1”, *Journal of High Energy Physics* **02**, 007 **2009**. DOI: [10.1088/1126-6708/2009/02/007](https://doi.org/10.1088/1126-6708/2009/02/007)
- [148] S. Catani, M. H. Seymour, “A General algorithm for calculating jet cross-sections in NLO QCD”, *Nucl. Phys. B* **485**, 291-419 (1998). DOI: [10.1016/S0550-3213\(96\)00589-5](https://doi.org/10.1016/S0550-3213(96)00589-5)
- [149] J. Alwall, R. Frederix, S. Frixione, V. Hirschi, F. Maltoni, O. Mattelaer, H. S. Shao, T. Stelzer, P. Torrielli, M. Zaro, “The automated computation of tree-level and next-to-leading order differential cross sections, and their matching to parton shower simulations”, *JHEP* **07** 079 (2014). DOI: [10.1007/JHEP07\(2014\)079](https://doi.org/10.1007/JHEP07(2014)079)
- [150] S. Frixione, P. Nason, G. Ridolfi, “A Positive-weight next-to-leading-order Monte Carlo for heavy flavour hadroproduction”, *JHEP* **09**, 126 (2007). DOI: [10.1088/1126-6708/2007/09/126](https://doi.org/10.1088/1126-6708/2007/09/126)
- [151] P. Nason, “A New method for combining NLO QCD with shower Monte Carlo algorithms”, *JHEP* **11**, 040 (2004). DOI: [10.1088/1126-6708/2004/11/040](https://doi.org/10.1088/1126-6708/2004/11/040)
- [152] S. Frixione, P. Nason, C. Oleari, “Matching NLO QCD computations with Parton Shower simulations: the POWHEG method”, *JHEP* **11**, 070 (2007). DOI: [10.1088/1126-6708/2007/11/070](https://doi.org/10.1088/1126-6708/2007/11/070)
- [153] S. Alioli, P. Nason, C. Oleari, E. Re, “A general framework for implementing NLO calculations in shower Monte Carlo programs: the POWHEG BOX”, *JHEP* **06**, 043 (2010). DOI: [10.1007/JHEP06\(2010\)043](https://doi.org/10.1007/JHEP06(2010)043)
- [154] S. Höche et al, “QCD matrix elements + parton showers. The NLO case”, *J. High Energ. Phys* **2013**, 27 (2013). DOI: [10.1007/JHEP04\(2013\)027](https://doi.org/10.1007/JHEP04(2013)027)
- [155] S. Frixione, F. Stoeckli, P. Torrielli, B. R. Webber, C. D. White, “The MCanLO 4.0 Event Generator”, CERN-TH-2010-216. URL: <https://inspire-hep.net/literature/872031>

- [156] B. Andersson, G. Gustafson, G. Ingelman, T. Sjöstrand, “Parton fragmentation and string dynamics”, *Physics Reports* **97** 2, 31-145 (1983). DOI: [10.1016/0370-1573\(83\)90080-7](https://doi.org/10.1016/0370-1573(83)90080-7)
- [157] B. R. Webber, “A QCD model for jet fragmentation including soft gluon interference”, *Nuclear Physics B* **238** 3, 492-528 (1984). DOI: [10.1016/0550-3213\(84\)90333-X](https://doi.org/10.1016/0550-3213(84)90333-X)
- [158] G. Marchesini, B. R. Webber, “Monte Carlo simulation of general hard processes with coherent QCD radiation”, *Nuclear Physics B* **310** 3, 461-526 (1988). DOI: [10.1016/0550-3213\(88\)90089-2](https://doi.org/10.1016/0550-3213(88)90089-2)
- [159] ATLAS Collaboration, “ATLAS Pythia 8 tunes to 7 TeV data”, ATL-PHYS-PUB-2014-021. URL: <https://inspirehep.net/literature/1795399>
- [160] ATLAS Collaboration, “Measurement of the Z/γ^* boson transverse momentum distribution in pp collisions at $\sqrt{s} = 7$ TeV with the ATLAS detector”, *JHEP* **09**, 145 (2014). DOI: [10.1007/JHEP09\(2014\)145](https://doi.org/10.1007/JHEP09(2014)145)
- [161] P. Z. Skands, “Tuning Monte Carlo Generators: The Perugia Tunes”, *Phys. Rev. D* **82**, 074018 (2010). DOI: [10.1103/PhysRevD.82.074018](https://doi.org/10.1103/PhysRevD.82.074018)
- [162] A. Dell’Acqua et al., “Development of the ATLAS Simulation Framework”, *Computing in High Energy and Nuclear Physics 2001 Conference (CHEP2001)* **34081859**. URL: https://inis.iaea.org/search/search.aspx?orig_q=RN:34081859
- [163] Python Software Foundation, “Python Package Index - PyPI”. URL: <https://pypi.org>
- [164] A. Dell’Acqua, A. Di Simone, M. Gallas, Z. Marshall, A. Rimoldi, V. Tsulaia, I. Ueda, S. Vahsen, “ATLAS Simulation readiness for first data at LHC”, ATL-SOFT-CONF-2007-001. URL: <https://inspirehep.net/literature/1196556>
- [165] E. Barberio et al., “The Geant4-Based ATLAS Fast Electromagnetic Shower Simulation”, ATL-SOFT-CONF-2007-002. DOI: [10.1142/9789812819093_0133](https://doi.org/10.1142/9789812819093_0133)
- [166] W. Lukas, “Fast Simulation for ATLAS: Atlfast-II and ISF”, *J. Phys. Conf. Ser.* **396**, 022031 (2012). DOI: [10.1088/1742-6596/396/2/022031](https://doi.org/10.1088/1742-6596/396/2/022031)
- [167] T. Yamanaka, “The ATLAS calorimeter simulation FastCaloSim”, *J. Phys. Conf. Ser.* **331**, 032053 (2011). DOI: [10.1088/1742-6596/331/3/032053](https://doi.org/10.1088/1742-6596/331/3/032053)

- [168] K. Edmonds et al., “The fast ATLAS track simulation (FATRAS)”, ATL-SOFT-PUB-2008-001. URL: <https://inspirehep.net/literature/807206>
- [169] S. Hamilton, “The ATLAS Fast Track Simulation Project”, ATL-SOFT-PROC-2011-038. URL: <https://inspirehep.net/literature/1196761>
- [170] J. Chapman et al., “Fast simulation methods in ATLAS: from classical to generative models”, *EPJ Web Conf.* **245**, 02035 (2020). DOI: [10.1051/epjconf/202024502035](https://doi.org/10.1051/epjconf/202024502035)
- [171] ATLAS Collaboration, “ATLAS Simulation CPU performance”. URL: <https://atlas.web.cern.ch/Atlas/GROUPS/PHYSICS/PLOTS/SIM-2019-002/>
- [172] T. Novak, “New techniques for pile-up simulation in ATLAS”, *EPJ Web Conf.* **214** 02044 (2019). DOI: [10.1051/epjconf/201921402044](https://doi.org/10.1051/epjconf/201921402044)
- [173] ATLAS Collaboration, “MC+MC Pile-up Overlay Performance Plots” (2018). URL: <https://atlas.web.cern.ch/Atlas/GROUPS/PHYSICS/PLOTS/SIM-2018-002>
- [174] R. Brun and F. Rademakers, “ROOT - An object oriented data analysis framework”, *Nucl. Inst. & Meth. in Phys. Res. A* **389**, 81-86 (1997). DOI: [10.1016/S0168-9002\(97\)00048-X](https://doi.org/10.1016/S0168-9002(97)00048-X)
- [175] ATLAS Collaboration, “Derivation Framework”. URL: <https://twiki.cern.ch/twiki/bin/view/AtlasProtected/DerivationFramework>
- [176] WLCG Organisation, “Worldwide LHC Computing Grid”. URL: <https://wlcg.web.cern.ch/>
- [177] J. Catmore et al., “A new petabyte-scale data derivation framework for ATLAS”, *J. Phys. Conf. Ser.* **664** no.7, 072007 (2015). DOI: [10.1088/1742-6596/664/7/072007](https://doi.org/10.1088/1742-6596/664/7/072007)
- [178] ATLAS Collaboration, “Luminosity determination in pp collisions at $\sqrt{s} = 13$ TeV using the ATLAS detector at the LHC”, ATL-CONF-2019-021. URL: <https://inspirehep.net/literature/1737864>
- [179] G. Avoni et al., “The new LUCID-2 detector for luminosity measurement and monitoring in ATLAS”, *JINST* **13** no.07, P07017 (2018). DOI: [10.1088/1748-0221/13/07/P07017](https://doi.org/10.1088/1748-0221/13/07/P07017)

- [180] A. Alloul, “FeynRules 2.0 - A complete toolbox for tree-level phenomenology”, *Comput. Phys. Commun.* **185**, 2250-2300 (2014). DOI: [10.1016/j.cpc.2014.04.012](https://doi.org/10.1016/j.cpc.2014.04.012)
- [181] B. Fuks et al., “Gaugino production in proton-proton collisions at a center-of-mass energy of 8 TeV”, *JHEP* **10**, 081 (2012). DOI: [10.1007/JHEP10\(2012\)081](https://doi.org/10.1007/JHEP10(2012)081)
- [182] B. Fuks et al., “Precision predictions for electroweak superpartner production at hadron colliders with Resummino”, *Eur. Phys. J. C* **73**, 2480 (2013). DOI: [10.1140/epjc/s10052-013-2480-0](https://doi.org/10.1140/epjc/s10052-013-2480-0)
- [183] R. Ruiz, “QCD Corrections to Pair Production of Type III Seesaw Leptons at Hadron Colliders”, *JHEP* **12**, 165 (2015). DOI: [10.1007/JHEP12\(2015\)165](https://doi.org/10.1007/JHEP12(2015)165)
- [184] Y. Cai et al., “Lepton Number Violation: Seesaw Models and Their Collider Tests”, *Front. in Phys.* **6**, 40 (2018). DOI: [10.3389/fphy.2018.00040](https://doi.org/10.3389/fphy.2018.00040)
- [185] LHC SUSY Cross Section Working Group, “NLO-NLL wino-like chargino-chargino (C1C1) cross sections” (2017). URL: <https://twiki.cern.ch/twiki/bin/view/LHCPhysics/SUSYCrossSections13TeVx1x1wino>
- [186] LHC SUSY Cross Section Working Group, “NLO-NLL wino-like chargino-neutralino (N2C1) cross sections” (2017). URL: <https://twiki.cern.ch/twiki/bin/view/LHCPhysics/SUSYCrossSections13TeVn2x1wino>
- [187] T. Gleisberg, S. Hoeche, “Comix, a new matrix element generator”, *JHEP* **12**, 039 (2008). DOI: <https://doi.org/10.1088/1126-6708/2008/12/039>
- [188] F. Cascioli et al., “Scattering Amplitudes with Open Loops”, *Phys. Rev. Lett.* **108**, 111601 (2012). DOI: [10.1103/PhysRevLett.108.111601](https://doi.org/10.1103/PhysRevLett.108.111601)
- [189] A. Denner et al., “Collier: a fortran-based Complex One-Loop Library in Extended Regularizations”, *Comput. Phys. Commun.* **212**, 220-238 (2017). DOI: [10.1016/j.cpc.2016.10.013](https://doi.org/10.1016/j.cpc.2016.10.013)
- [190] S. Catani et al., “QCD matrix elements + parton showers”, *JHEP* **11**, 063 (2001). DOI: [10.1088/1126-6708/2001/11/063](https://doi.org/10.1088/1126-6708/2001/11/063)
- [191] S. Hoeche et al., “QCD matrix elements and truncated showers”, *JHEP* **05**, 053 (2009). DOI: [10.1088/1126-6708/2009/05/053](https://doi.org/10.1088/1126-6708/2009/05/053)

- [192] C. Anastasiou et al., “High precision QCD at hadron colliders: Electroweak gauge boson rapidity distributions at NNLO”, *Phys. Rev. D* **69**, 094008 (2004). DOI: [10.1103/PhysRevD.69.094008](https://doi.org/10.1103/PhysRevD.69.094008)
- [193] E. Bothmann et al., “Reweighting QCD matrix-element and parton-shower calculations”, *Eur. Phys. J. C* **76** no.11, 590 (2016). DOI: [10.1140/epjc/s10052-016-4430-0](https://doi.org/10.1140/epjc/s10052-016-4430-0)
- [194] ATLAS Collaboration, “Studies on top-quark Monte Carlo modelling for Top2016”, ATL-PHYS-PUB-2016-020. URL: <https://inspirehep.net/literature/1795321>
- [195] M. Beneke et al., “Hadronic top-quark pair production with NNLL threshold resummation”, *Nucl. Phys. B* **855**, 695-741 (2012). DOI: [10.1016/j.nuclphysb.2011.10.021](https://doi.org/10.1016/j.nuclphysb.2011.10.021)
- [196] M. Cacciari et al., “Top-pair production at hadron colliders with next-to-next-to-leading logarithmic soft-gluon resummation”, *Phys. Lett. B* **710**, 612-622 (2012). DOI: [10.1016/j.physletb.2012.03.013](https://doi.org/10.1016/j.physletb.2012.03.013)
- [197] M. Czakon, A. Mitov, “Top++: A Program for the Calculation of the Top-Pair Cross-Section at Hadron Colliders”, *Comput. Phys. Commun.* **185**, 2930 (2014). DOI: [10.1016/j.cpc.2014.06.021](https://doi.org/10.1016/j.cpc.2014.06.021)
- [198] M. Botje et al., “The PDF4LHC Working Group Interim Recommendations” (2011) URL: [arXiv:1101.0538](https://arxiv.org/abs/1101.0538)
- [199] A. D. Martin et al., “Uncertainties on $\alpha(S)$ in global PDF analyses and implications for predicted hadronic cross sections”, *Eur. Phys. J. C* **64**, 653-680 (2009). DOI: [10.1140/epjc/s10052-009-1164-2](https://doi.org/10.1140/epjc/s10052-009-1164-2)
- [200] J. Gao et al., “CT10 next-to-next-to-leading order global analysis of QCD”, *Phys. Rev. D* **89** no.3, 033009 (2014). DOI: [10.1103/PhysRevD.89.033009](https://doi.org/10.1103/PhysRevD.89.033009)
- [201] ATLAS Collaboration, “The Pythia 8 A3 tune description of ATLAS minimum bias and inelastic measurements incorporating the Donnachie-Landshoff diffractive model”, ATL-PHYS-PUB-2016-017. URL: <https://inspirehep.net/literature/1795311>
- [202] ATLAS Collaboration, “Measurement of the Inelastic Proton-Proton Cross Section at $\sqrt{s} = 13$ TeV with the ATLAS Detector at the LHC”, *Phys. Rev. Lett.* **117** no.18, 182002 (2016). DOI: [10.1103/PhysRevLett.117.182002](https://doi.org/10.1103/PhysRevLett.117.182002)

- [203] F. del Aguila and J. A. Aguilar-Saavedra, “Distinguishing seesaw models at LHC with multi-lepton signals”, *Nucl. Phys. B* **813**, 22-90 (2009). DOI: [10.1016/j.nuclphysb.2008.12.029](https://doi.org/10.1016/j.nuclphysb.2008.12.029)
- [204] M. Baak et al., “HistFitter software framework for statistical data analysis”, *Eur. Phys. J. C* **75**, 153 (2015). DOI: [10.1140/epjc/s10052-015-3327-7](https://doi.org/10.1140/epjc/s10052-015-3327-7)
- [205] G. Cowan et al., “Asymptotic formulae for likelihood-based tests of new physics”, *Eur. Phys. J. C* **71**, 1554 (2011). DOI: [10.1140/epjc/s10052-011-1554-0](https://doi.org/10.1140/epjc/s10052-011-1554-0)
- [206] ATLAS collaboration, PmgTopProcesses twiki. URL: <https://twiki.cern.ch/twiki/bin/viewauth/AtlasProtected/PmgTopProcesses>
- [207] A. Buckley et al., “LHAPDF6: parton density access in the LHC precision era”, *Eur. Phys. J. C* **75** 132 (2015). DOI: [10.1140/epjc/s10052-015-3318-8](https://doi.org/10.1140/epjc/s10052-015-3318-8)
- [208] ATLAS Collaboration, “Search for type-III seesaw heavy leptons in proton-proton collisions at $\sqrt{s} = 13$ TeV with the ATLAS detector”, ATLAS-CONF-2018-020. URL: <https://inspirehep.net/literature/1676308>
- [209] ATLAS Collaboration, “Search for doubly charged Higgs boson production in multi-lepton final states with the ATLAS detector using proton-proton collisions at $\sqrt{s} = 13$ TeV”, *Eur. Phys. J. C* **78** no.3, 199 (2018). DOI: [10.1140/epjc/s10052-018-5661-z](https://doi.org/10.1140/epjc/s10052-018-5661-z)
- [210] Y. Lee, “Recent Open Heavy Flavor Results from ATLAS and CMS Experiment at LHC”, RHIC & AGS Annual Users’ Meeting (2014). URL: https://www.bnl.gov/aum2014/content/workshops/workshop_6/140618-bnl_yenjie-v2.pdf
- [211] L. Lista, “Statistical Methods for Data Analysis in Particle Physics”, *Lect. Notes Phys.* **909**, pp.1-172 (2016). DOI: [10.1007/978-3-319-20176-4](https://doi.org/10.1007/978-3-319-20176-4)
- [212] W. Verkerke and D. Kirkby, “The RooFit toolkit for data modeling”. URL: <https://arxiv.org/abs/physics/0306116>
- [213] S. S. Wilks, “The Large-Sample Distribution of the Likelihood Ratio for Testing Composite Hypotheses”, *Annals Math. Statist.* **9** no.1, 60-62 (1938). DOI: [10.1214/aoms/1177732360](https://doi.org/10.1214/aoms/1177732360)
- [214] G. Cowan et al. “Asymptotic formulae for likelihood-based tests of new physics”, *Eur. Phys. J. C* **71**, 1554 (2011). DOI: [10.1140/epjc/s10052-011-1554-0](https://doi.org/10.1140/epjc/s10052-011-1554-0)

- [215] A. L. Read, “Presentation of search results: The CL(s) technique”, *J. Phys. G* **28**, 2693-2704 (2002). DOI: [10.1088/0954-3899/28/10/313](https://doi.org/10.1088/0954-3899/28/10/313)
- [216] ATLAS Collaboration, “Search for type-III seesaw heavy leptons in leptonic final states in pp collisions at $\sqrt{s} = 13$ TeV with the ATLAS detector”, *CERN-EP-2021-211* (2022). URL: [arXiv:2202.02039](https://arxiv.org/abs/2202.02039)
- [217] ATLAS Collaboration, “Luminosity Determination in pp Collisions at $\sqrt{s} = 7$ TeV using the ATLAS Detector in 2011”, ATLAS-CONF-2011-116. URL: <https://inspirehep.net/literature/1204166>
- [218] ATLAS Collaboration, Luminosity Public Results Run 2. URL: <https://twiki.cern.ch/twiki/bin/view/AtlasPublic/LuminosityPublicResultsRun2>
- [219] ATLAS Collaboration, “Improved luminosity determination in pp collisions at $\sqrt{s} = 7$ TeV using the ATLAS detector at the LHC”, *Eur. Phys. J. C* **73** no.8, 2518 (2013). DOI: [10.1140/epjc/s10052-013-2518-3](https://doi.org/10.1140/epjc/s10052-013-2518-3)
- [220] G. L. Alberghi et al., “Choice and characterization of photomultipliers for the new ATLAS LUCID detector,” *JINST* **11** no.05, P05014 (2016). DOI: [10.1088/1748-0221/11/05/P05014](https://doi.org/10.1088/1748-0221/11/05/P05014)
- [221] I. Tamm, “Radiation emitted by uniformly moving electrons”, *J. Phys. USSR* **1**, 439 (1939).
- [222] O. Viazlo [ATLAS], “ATLAS LUCID detector upgrade for LHC Run 2”, *PoS EPS-HEP2015*, 275 (2015). DOI: [10.22323/1.234.0275](https://doi.org/10.22323/1.234.0275)
- [223] ATLAS Tile Calorimeter group, “The Laser calibration of the Atlas Tile Calorimeter during the LHC run 1”, *JINST* **11** no.10, T10005 (2016). DOI: [10.1088/1748-0221/11/10/T10005](https://doi.org/10.1088/1748-0221/11/10/T10005)
- [224] A. Annovi et al., “The EDRO Board Connected to the Associative Memory: a “Baby” FastTracKer Processor for the ATLAS Experiment”, *Phys. Procedia* **37**, 1772-1780 (2012). DOI: [10.1016/j.phpro.2012.02.502](https://doi.org/10.1016/j.phpro.2012.02.502)
- [225] ATLAS Collaboration, “The LUCID 3 detector for the ATLAS Phase-II Upgrade”, CERN-LHCC-2021-016, LHCC-P-018. URL: <https://cds.cern.ch/record/2780604>
- [226] ATLAS Collaboration, *ATLAS Detector Description Database*. URL: <https://atlas-geometry-db.web.cern.ch/atlas-geometry-db/>

- [227] M. Bandieramonte et al., “FullSimLight: ATLAS standalone Geant4 simulation”, *EPJ Web Conf.* **245**, 02029 (2020). DOI: [10.1051/epjconf/202024502029](https://doi.org/10.1051/epjconf/202024502029)
- [228] *FullSimLight*. URL: <https://gitlab.cern.ch/GeoModelDev/FullSimLight>
- [229] B. Stelzer, “The New Small Wheel Upgrade Project of the ATLAS Experiment”, *Nucl. Part. Phys. Proc.* **273-275**, 1160-1165 (2016). DOI: [10.1016/j.nuclphysbps.2015.09.182](https://doi.org/10.1016/j.nuclphysbps.2015.09.182)
- [230] ATLAS Collaboration, Radiation Simulation Public Results. URL: <https://twiki.cern.ch/twiki/bin/view/AtlasPublic/RadiationSimulationPublicResults>
- [231] G. Apollinari et al., “High-Luminosity Large Hadron Collider (HL-LHC): Technical Design Report V. 0.1”, CERN Yellow Reports: Monographs, 4/2017 (2017). DOI: [10.23731/CYRM-2017-004](https://doi.org/10.23731/CYRM-2017-004)
- [232] A. Liss et al. “Physics at a High-Luminosity LHC with ATLAS”, ATL-PHYS-PUB-2013-007. URL: <https://inspirehep.net/literature/1245017>
- [233] ATLAS Collaboration, “ATLAS Phase-II Upgrade Scoping Document”, CERN-LHCC-2015-020. URL: <https://cds.cern.ch/record/2055248/>
- [234] ATLAS Collaboration, “Technical Design Report for the ATLAS Inner Tracker Pixel Detector”, CERN-LHCC-2017-021, ATLAS-TDR-030 (2017). URL: <https://cds.cern.ch/record/2285585>
- [235] ATLAS Collaboration, “Technical Design Report for the ATLAS Inner Tracker Strip Detector”, CERN-LHCC-2017-005, ATLAS-TDR-025 (2017). URL: <https://cds.cern.ch/record/2257755>
- [236] L. Meng, “ATLAS ITk Pixel Detector Overview”, ATL-COM-ITK-2021-017. URL: <https://inspirehep.net/literature/1864641>
- [237] RD53 Collaboration (2021). URL: <https://rd53.web.cern.ch/>
- [238] M. Garcia-Sciveres, “RD53B Manual”, CERN-RD53-PUB-19-002 (2019). URL: <http://cds.cern.ch/record/2665301>
- [239] Science and Technology Facilities Council Particle Physics Department, “ATLAS Inner Tracker Upgrade (ITk)”. URL: <https://www.ppd.stfc.ac.uk/Pages/ATLAS-SLHC-Upgrade.aspx>
- [240] K. Todome, “Data-acquisition system developments for ATLAS pixel QA and QC test toward High-Luminosity LHC”, *Nucl. Instrum. Meth. A*, **986** 164413 (2021). DOI: [10.1016/j.nima.2020.164413](https://doi.org/10.1016/j.nima.2020.164413)

- [241] T. Heim, “YARR - A PCIe based readout concept for current and future ATLAS Pixel modules”, *J. Phys. Conf. Ser.* **898** no.3, 032053 (2017). DOI: [10.1088/1742-6596/898/3/032053](https://doi.org/10.1088/1742-6596/898/3/032053)
- [242] ATLAS Local Database Community, *Local DB*. URL: <https://localdb-docs.readthedocs.io/en/master/>

List of Figures

1.1	Constituents of the SM. Starting from left: fermions, divided into quarks (upper part) and leptons (bottom part), gauge bosons, including the Higgs boson, and particles outside the SM as the graviton or the heavy leptons predicted by the SeeSaw mechanism. Adapted from [7].	3
1.2	The diagrams illustrate basic processes that may occur in positron and electron interactions with a photon. They are: fundamental QED vertex (<i>top left</i>); electron-positron annihilation (<i>top right</i>); emission of a photon by a positron (<i>bottom left</i>); pair production by a photon (<i>bottom right</i>). .	8
1.3	Feynman diagrams for: the β -decay (<i>left</i>); fundamental vertex of weak interaction in CC (<i>center</i>) and in NC (<i>right</i>). .	9
1.4	Masses of all known fundamental fermions. A normal mass-hierarchy has been assumed - $m^2\nu_1 < m^2\nu_2 < m^2\nu_3$ - together with a rather conservative upper bound $m^2\nu_i < 1 \text{ eV}$ $\forall i = 1, 2, 3$. The light, hatched region indicates the six-orders-of-magnitude “desert” between the largest possible neutrino mass and the electron mass [18].	14
1.5	Generation of neutrino Majorana mass terms for the three versions of the SeeSaw mechanism.	17
1.6	Branching ratios of the neutral component of the fermionic triplet as a function of its mass considering the following lepton mixing matrix elements: $V_e=V_\tau=0$ and $V_\mu=0.063$. Since the heavy leptons are assumed to be degenerate in mass, BRs into W , Z and H bosons are the same for the charged component [27].	19

1.7	Expected and observed 95% CLs exclusion limits for the Type-III SeeSaw process with the corresponding one- and two-standard-deviation uncertainty bands, showing the 95% CL upper limit on the cross-section. The theoretical signal cross-section prediction with its corresponding uncertainty band is also shown. Top: two-lepton channel plus two jets performed by ATLAS [36]. Bottom: three- and four-lepton channel performed by CMS [35].	24
1.8	Limits on the mixing between the electron neutrino and a heavy neutral lepton in the mass range 100 MeV - 500 GeV [38].	25
1.9	Limits on the mixing between the muon neutrino and a heavy neutral lepton in the mass range 100 MeV - 500 GeV [38].	25
1.10	Example of Feynman diagrams for the considered Type-III SeeSaw heavy leptons pair production in the three- (a) and four-lepton (b) final states.	26
2.1	The LHC system in the underground of Geneva [75].	28
2.2	Time schedule of LHC, from Run-1 to last upgrade to High Luminosity LHC [77].	30
2.3	The mean number of interactions per filled bunch crossing per lumi-block versus day during the pp runs of (a) 2015 [79] and (b) 2018 [80]. For this calculation, the on-line luminosity measurement is used. Only the maximum value during stable beam periods is shown.	31
2.4	Left: Luminosity distribution as function of the mean number of interaction per crossing (pile-up) for the 2015-2018 pp collision data recorded by ATLAS at $\sqrt{s}=13$ TeV [81]. Right: Total integrated luminosity versus time delivered by LHC (green), recorded by the ATLAS detector (yellow) and certified to be good quality data (blue) during stable beams for pp collisions at 13 TeV centre-of-mass energy in 2015-2018 [82].	32
2.5	Scheme of the CERN accelerator complex [84].	34
2.6	Different reconstruction of particles in ATLAS according to their different interactions with materials [85].	35
2.7	Cut-away view of the ATLAS detector. The dimensions of the detector are 25 m in height and 44 m in length. The overall weight of the detector is approximately 7000 tonnes. Adapted from [87].	37

2.8	Left: ATLAS detector coordinate system. Right: Coordinate system in the transverse momentum plane.	38
2.9	Top: Schematic layout of the Inner Detector including the new Insertable B-Layer [86]. The distances to the interaction point are also shown. Bottom: Cut-away view of the ATLAS inner detector [86].	40
2.10	Cut-away view of the ATLAS pixel detector [86].	43
2.11	The HT fraction for electrons from photon conversions and pion candidates in the momentum range $4 \text{ GeV} < p_T < 20 \text{ GeV}$, in the barrel region (left) and in the end-cap region (right) [91].	45
2.12	Unfolded transverse impact parameter resolution measured from data in 2015, $\sqrt{s} = 13 \text{ TeV}$, with the Inner Detector including the IBL, as a function of p_T , for values of $0.0 < \eta < 0.2$, compared to that measured from data in 2012, $\sqrt{s} = 8 \text{ TeV}$. The data in 2015 is collected with a minimum bias trigger. The data in 2012 is derived from a mixture of jet, tau and E_T^{miss} triggers. Figure 2.12a shows the distribution for $\sigma(d_0)$, while Figure 2.12b for $\sigma(z_0)$ [92].	46
2.13	Geometry of magnet windings and tile calorimeter steel [86]. The eight barrel toroid coils, with the end-cap coils interleaved are visible. The solenoid winding lies inside the calorimeter volume.	46
2.14	Cut-away view of the ATLAS calorimeter system [86].	48
2.15	Sketch of a barrel module with the accordion geometry. The granularity in η and ϕ cells of each of the three layers and of the trigger towers is also shown [86].	50
2.16	Energy resolution, $\sigma_{E_{\text{calib}}}/E_{\text{gen}}$, estimated from the interquartile range of $E_{\text{calib}}/E_{\text{gen}}$ as a function of $ \eta $ for 2.16a electrons and 2.16b unconverted photons, for different E_T ranges [93].	51
2.17	Schematic diagram showing the three FCal modules located in the end-cap cryostat [86]. The material in front of the FCal and the shielding plug behind it are also shown. The black regions are structural parts of the cryostat. The diagram has a larger vertical scale for clarity.	53
2.18	Cut-away view of the ATLAS muon system [86].	54
2.19	Schematics of the muon trigger system [86]. RPC2 and TGC3 are the reference (pivot) planes for barrel and end-cap, respectively.	55
2.20	ATLAS Forward Detectors and their relative positions with respect to the IP [94].	58

2.21	Particle flow (left) and energy flow (right) as a function of rapidity as obtained by DPMJET generator for pp interactions at \sqrt{s} 14TeV [95].	58
2.22	Block diagram of the L1 trigger. The overall L1 decision is made by the central trigger processor, taking input from calorimeter and muon trigger results. The paths to the detector front-ends, L2 trigger, and data acquisition system are shown from left to right in red, blue and black, respectively [97].	61
3.1	Illustration of (a) single-particle pixel clusters on a pixel sensor and (b) a merged pixel cluster due to very collimated charged particles. Different colours represent energy deposits from different charged particles traversing the sensor and the particles trajectories are shown as arrows [98].	65
3.2	A sketch of the technique used to estimate the track parameters of the seeds [99].	66
3.3	A schematic illustration of the path of an electron through the detector. The red trajectory shows the hypothetical path of an electron, which first traverses the tracking system (pixel detectors, then silicon-strip detectors and lastly the TRT) and then enters the electromagnetic calorimeter. The dashed red trajectory indicates the path of a photon produced by the interaction of the electron with the material in the tracking system [101].	67
3.4	The total reconstruction efficiency for simulated electrons in a single-electron sample is shown in (a) as a function of the true (generator) transverse energy E_T for each step of the electron-candidate formation [104]. The reconstruction efficiency relative to reconstructed clusters, ϵ_{reco} , as a function of electron transverse energy E_T for $Z \rightarrow ee$ events is shown in (b) [102].	68
3.5	The electron identification efficiency in $Z \rightarrow ee$ events as a function of E_T (a) and as a function of η (b) for the Loose, Medium and Tight working points. The lower panels show the ratio of the efficiencies measured in data and in MC simulations. The total uncertainties include both statistical and systematic components. [104].	71

3.6	The electron isolation efficiency in $Z \rightarrow ee$ events as a function of E_T (a) and as a function of η (b) for different working points. The electrons are required to fulfil the Medium selection from the LH-based electron identification. The lower panels show the ratio of the efficiencies measured in data and in MC simulations. The total uncertainties include both statistical and systematic components [104].	73
3.7	Schematic drawing of the detector parts used for muon reconstruction. Several muon types are defined depending on the detector parts used for the reconstruction [111]. . .	74
3.8	Muon reconstruction and identification efficiencies for the <i>Loose</i> , <i>Medium</i> , and <i>Tight</i> criteria. The efficiencies measured in $J/\Psi \rightarrow \mu\mu$ events as function of p_T and in $Z \rightarrow \mu\mu$ events as function of η are shown in (a) and (b) respectively. The predicted efficiencies are depicted as open markers, while filled markers illustrate the result of the measurement in collision data. When not negligible, the statistical uncertainty in the efficiency measurement is indicated by the error bars. The panel at the bottom shows the ratio of the measured to predicted efficiencies, with statistical and systematic uncertainties. [110].	77
3.9	(a) Data-to-simulation ratio of the average jet p_T response as a function of jet p_T . The errors represent the statistical (inner error bars and small inner band) and the total uncertainty (statistical and systematic uncertainties added in quadrature, outer error bars and outer band) [117]. The relative jet energy resolution $\sigma(p_T)/p_T$ as a function of p_T . The expectation from Monte Carlo simulation is compared with the relative resolution as evaluated in data through the <i>in situ</i> techniques using the momentum balance of dijet events (triangles). The error bars on points indicate the total uncertainties on the derivation of the relative resolution in dijet events, adding in quadrature statistical and systematic components [118].	83

3.10	(a) The light-flavour jet rejections versus the b -jet tagging efficiency for the IP3D, SV1, JetFitter, MV2 and DL1 b -tagging algorithms evaluated on the baseline $t\bar{t}$ events. (b) b -tagging efficiency for the $\epsilon_b = 77\%$ single-cut OP of the MV2 tagger as a function of jet p_T . Vertical error bars include data statistical uncertainties only while the green bands correspond to the sum in quadrature of statistical and systematic uncertainties [122].	85
3.11	Background rejection versus signal efficiency in simulated $Z \rightarrow ee$ and $ZZ \rightarrow eev\nu$ samples with a $Z \rightarrow ee$ selection. The performance is shown for E_T^{miss} , event-based $\mathcal{S}(E_T^{\text{miss}})$ and object-based $\mathcal{S}(E_T^{\text{miss}})$ as discriminants in events with (a) the entire E_T^{miss} range, (b) $E_T^{\text{miss}} > 50$ GeV, and (c) $E_T^{\text{miss}} > 100$ GeV. The lower panel of the figures shows the ratio of other definitions/event-based E_T^{miss} significance [131].	88
3.12	Efficiency of passing either the HLT_mu26_ivarmedium or the HLT_mu50 trigger in the barrel (3.12a) and endcaps (3.12b) as a function of the muon p_T , computed using data taken in 2016-2018. The error bars show the statistical uncertainties only [134].	91
3.13	Efficiencies of the e24_lhvloose_nod0 trigger as a function of the offline electron (3.13a) E_T and (3.13b) η with respect to offline tight, medium, and loose identification, and no isolation requirements. The efficiencies are measured in data and shown with corresponding statistical and systematic uncertainties. The ratios of data to MC simulation are also shown. For (3.13b), only offline candidates with $E_T > 25$ GeV are used. [135].	91
4.1	The flow of the ATLAS simulation software, from event generators (top left) through reconstruction (top right). Algorithms are placed in square-cornered boxes and persistent data objects are placed in rounded boxes [136].	94

4.2	Comparison between GEANT4 and two fast simulators, the fast calorimeter simulation (labelled as ATLEFASTII) and the fast chain (labelled as ATLEFASTIIF), in the CPU performance of event processing time. Simulations were performed in Athena release 21.3.8 on semi-leptonic $t\bar{t}$ events. Simulation benchmarks were performed using the BNL US-ATLAS Tier-3 Cluster which consists of 300 nodes, each with 8 2.6GHz CPUs and 16 GB of memory. 500 events were produced in a single run. No pile-up is simulated [170, 171].	99
4.3	Diagrams illustrating the difference between (a) the standard digitisation and (b) the MC overlay pile-up methods [173].	100
4.4	The ATLAS analysis model for Run 2 [177].	102
5.1	Example of Feynman diagrams for the considered Type-III SeeSaw heavy leptons pair production in the three- (a) and four-lepton (b) final states.	108
5.2	Schematic view of a template analysis strategy using several control, validation and signal regions. Each region can have single or multiple bins. As shown, the background estimation is performed in the controls regions, validated in the validation regions and the applied to the signal regions [204].	109
5.3	Example of Feynman diagram for ZL region.	114
5.4	Example of Feynman diagram for ZL Veto region.	114
5.5	Example of Feynman diagram for JNLow region.	115
5.6	N-1 plots including expected signal and background events in the ZL SR in log-scale, data are not considered in this step. Only statistical uncertainties are shown. Each of the observables is plotted with the cut on it omitted: invariant mass of the three-lepton system 5.6a, transverse mass of the leading lepton 5.6b, transverse mass of the subleading lepton 5.6c, angular separation between leading and sub-leading leptons 5.6d.	118
5.7	N-1 plots including expected signal and background events in the ZLVeto SR in log-scale., data are not considered in this step. Only statistical uncertainties are shown. Each of the observables is plotted with the cut on it omitted: $H_T + E_T^{\text{miss}}$ 5.7a, invariant mass of the three-lepton system 5.7b, invariant mass of the two leading jets 5.7c, H_T of the same-sign lepton pair 5.7d.	119

5.8	N-1 plots including expected signal and background events in the JNLow SR in log-scale, data are not considered in this step. Only statistical uncertainties are shown. Each of the observables is plotted with the cut on it omitted: H_T of the three-lepton system 5.8a, transverse mass of the leading lepton 5.8b, transverse mass of the subleading lepton 5.8c, angular separation between leading and subleading leptons 5.8d.	120
5.9	Example of Feynman diagram for the Q0 region.	121
5.10	Example of Feynman diagram for the Q2 region.	121
5.11	N-1 plots including expected signal and background events in the Q0 SR in log-scale, data are not considered in this step. Only statistical uncertainties are shown. Each of the observables is plotted with the cut on it omitted: invariant mass of the four leptons 5.11a, $H_T + E_T^{\text{miss}}$ 5.11b, E_T^{miss} significance 5.11c.	124
5.12	N-1 plots including expected signal and background events in the Q0 SR, data are not considered in this step. Only statistical uncertainties are shown. Each of the observables is plotted with the cut on it omitted: number of b -jets 5.12a, number of Z bosons 5.12b.	125
5.13	N-1 plots including expected signal and background events in the Q2 SR in log scale, data are not considered in this step. Only statistical uncertainties are shown. Each of the observables is plotted with the cut on it omitted: invariant mass of the four leptons 5.13a, $H_T + E_T^{\text{miss}}$ 5.13b.	125
5.14	Signals efficiency for different SR as a function of the mass points of the Type-III SeeSaw heavy leptons.	126
5.15	Simplified representation of the electron charge misidentification process due to electron interaction with the detector material.	128
5.16	Dielectron invariant mass distributions for opposite-charge (OC, black) and same-charge (SC, red) pairs for data (circles) and MC simulation (continuous line). The latter includes a correction for charge misidentification. The hatched band indicates the statistical error and the luminosity uncertainty summed in quadrature applied to MC simulated events. Please note that the scales for OC and SC are different and given at the left side (OC) and right side (SC), respectively [208].	131

5.17	Representation of an event containing a prompt lepton (left) and non-prompt lepton (right). Electrons or muons are originated from a secondary vertex and are selected as fake leptons coming from the primary vertex.	131
5.18	The loose and the tight regions in the MM. The tight region must be a subset of the loose region (i.e. tight leptons should also pass all of the loose requirements).	132
5.19	Fakes-enriched regions in the nominal high- p_T selection with at least 1 jet:5.19a p_T distribution of tight electrons, 5.19b p_T distribution of loose electrons, 5.19c η distribution of tight electrons, 5.19d η distribution of loose electrons. All the distributions show data events and the prompt MC component subtracted from data, to ensure a fake dominated region.	136
5.20	Fakes-enriched regions in the nominal high- p_T selection with at least 2 jets:5.20a p_T distribution of tight electrons, 5.20b p_T distribution of loose electrons, 5.20c η distribution of tight electrons, 5.20d η distribution of loose electrons. All the distributions show data events and the prompt MC component subtracted from data, to ensure a fake dominated region.	137
5.21	Fakes-enriched regions in the nominal high- p_T selection with at least 1 jet:5.21a p_T distribution of tight electrons, 5.21b p_T distribution of loose electrons, 5.21c η distribution of tight electrons, 5.21d η distribution of loose electrons. All the distributions show data events and the prompt MC component subtracted from data, to ensure a fake dominated region.	138
5.22	Fakes-enriched regions in the nominal high- p_T selection with at least 2 jets:5.22a p_T distribution of tight electrons, 5.22b p_T distribution of loose electrons, 5.22c η distribution of tight electrons, 5.22d η distribution of loose electrons. All the distributions show data events and the prompt MC component subtracted from data, to ensure a fake dominated region.	139
5.23	Measured fake-factors for an electron in the high- p_T region with at least 1 jet, with systematic variation applied. First η bin in 5.23a, second in 5.23b, third in 5.23c and last in 5.23d.	141

5.24 Measured fake-factors for an electron in the high-p_T region with at least 2 jets, with systematic variation applied. First η bin in 5.24a, second in 5.24b, third in 5.24c and last in 5.24d.	142
5.25 Measured fake-factors for an electron in the low-p_T region with at least 1 jet, with systematic variation applied. First η bin in 5.25a, second in 5.25b, third in 5.25c and last in 5.25d.	143
5.26 Measured fake-factors for an electron in the low-p_T region with at least 2 jets, with systematic variation applied. First η bin in 5.26a, second in 5.26b, third in 5.26c and last in 5.26d.	144
5.27 The electron fake-factors closure test in high-p_T region with at least 1 jet. In 5.27a the p_T distribution is shown, while in 5.27b the η one. The pink band shows the systematic uncertainty associated to the fake-factor measurement.	145
5.28 The electron fake-factors closure test in high-p_T region with at least 2 jets. In 5.28a the p_T distribution is shown, while in 5.28b the η one. The pink band shows the systematic uncertainty associated to the fake-factor measurement.	145
5.29 The electron fake-factors closure test in low-p_T region with at least 1 jet. In 5.29a the p_T distribution is shown, while in 5.29b the η one. The pink band shows the systematic uncertainty associated to the fake-factor measurement.	146
5.30 The electron fake-factors closure test in low-p_T region with at least 2 jets. In 5.30a the p_T distribution is shown, while in 5.30b the η one. The pink band shows the systematic uncertainty associated to the fake-factor measurement.	146
5.31 Representation of an event containing a non-prompt muon: a b-hadron is produced in the IP with consequent decay into light quarks jets in secondary displaced vertex. Muons originate from the b-hadron secondary decay and can fake leptons coming directly from the PV [210].	147
5.32 Fakes-enriched regions in the nominal high-p_T selection with at least 1 jet: 5.19a p_T distribution of tight muons, 5.19b p_T distribution of loose muons, 5.19c η distribution of tight muons, 5.19d η distribution of loose muons. All the distributions show data events and the prompt MC component subtracted from data, to ensure a fake dominated region.	149

5.33	Fakes-enriched regions in the nominal high- p_T selection with at least 2 jets:5.20a p_T distribution of tight muons, 5.20b p_T distribution of loose muons, 5.20c η distribution of tight muons, 5.20d η distribution of loose muons. All the distributions show data events and the prompt MC component subtracted from data, to ensure a fake dominated region.	150
5.34	Fakes-enriched regions in the nominal low- p_T selection with at least 1 jet:5.21a p_T distribution of tight muons, 5.21b p_T distribution of loose muons, 5.21c η distribution of tight muons, 5.21d η distribution of loose electrons. All the distributions show data events and the prompt MC component subtracted from data, to ensure a fake dominated region.	151
5.35	Fakes-enriched regions in the nominal low- p_T selection with at least 2 jets:5.22a p_T distribution of tight muons, 5.22b p_T distribution of loose muons, 5.22c η distribution of tight muons, 5.22d η distribution of loose muons. All the distributions show data events and the prompt MC component subtracted from data, to ensure a fake dominated region.	152
5.36	Measured fake-factors for a muon in the high- p_T region with at least 1 jet, with systematic variation applied. First η bin in 5.36a, second in 5.36b, third in 5.36c, the fourth in 5.36d and the last in 5.36e.	154
5.37	Measured fake-factors for a muon in the high- p_T region with at least 2 jets, with systematic variation applied. First η bin in 5.37a, second in 5.37b, third in 5.37c, the fourth in 5.37d and last in 5.37e.	155
5.38	Measured fake-factors for a muon in the low- p_T region with at least 1 jet, with systematic variation applied. First η bin in 5.38a, second in 5.38b, third in 5.38c, the fourth in 5.38d and last in 5.38e.	156
5.39	Measured fake-factors for a muon in the low- p_T region with at least 2 jets, with systematic variation applied. First η bin in 5.39a, second in 5.39b, third in 5.39c, the fourth in 5.39d and last in 5.39e.	157
5.40	The muon fake-factors closure test in high- p_T region with at least 1 jet. In 5.40a the p_T distribution is shown, while in 5.40b the η one. The pink band shows the systematic uncertainty associated to the fake-factor measurement.	158

5.41	The muon fake-factors closure test in high- p_T region with at least 2 jets. In 5.41a the p_T distribution is shown, while in 5.41b the η one. The pink band shows the systematic uncertainty associated to the fake-factor measurement. .	158
5.42	The muon fake-factors closure test in low- p_T region with at least 1 jet. In 5.42a the p_T distribution is shown, while in 5.42b the η one. The pink band shows the systematic uncertainty associated to the fake-factor measurement. .	159
5.43	The muon fake-factors closure test in low- p_T region with at least 2 jets. In 5.43a the p_T distribution is shown, while in 5.43b the η one. The pink band shows the systematic uncertainty associated to the fake-factor measurement. .	159
5.44	Pre- (left) and post-fit (right) distributions of $m_{T,3\ell}$ in ZL Region CR in 5.44a and 5.44b and in JNLow VR in 5.44c and in 5.44d. The uncertainty bands include both statistical and systematic uncertainties after the background-only fit taking into account all the correlation.	172
5.45	Pre- (left) and post-fit (right) distributions of $m_{T,3\ell}$ in ZL Diboson VR in 5.45a and 5.45b and in ZL Rare Top VR in 5.45c and in 5.45d. The uncertainty bands include both statistical and systematic uncertainties after the background-only fit taking into account all the correlation.	173
5.46	Pre- (left) and post-fit (right) distributions of $H_T + E_T^{\text{miss}}$ in Q0 Diboson CR in 5.46a and 5.46b and in Q0 Rare Top CR in 5.46c and in 5.46d. The uncertainty bands include both statistical and systematic uncertainties after the background-only fit taking into account all the correlation.	174
5.47	Pre- (left) and post-fit (right) distributions of $H_T + E_T^{\text{miss}}$ in Q0 Diboson VR in 5.47a and 5.47b and in Q0 Rare Top VR in 5.47c and in 5.47d. The uncertainty bands include both statistical and systematic uncertainties after the background-only fit taking into account all the correlation.	175
5.48	Pre- (left) and post-fit (right) distributions of $H_T + E_T^{\text{miss}}$ in Q2 VR in 5.48a and 5.48b and of $m_{T,3\ell}$ in the three-lepton Fakes VR in 5.48c and in 5.48d. The uncertainty bands include both statistical and systematic uncertainties after the background-only fit taking into account all the correlation.	176

5.49	Pre- (left) and post-fit (right) distributions of $m_{T,3\ell}$ in JN-Low SR in 5.49a and 5.49b and in ZL Region SR in 5.49c and in 5.49d. The uncertainty bands include both statistical and systematic uncertainties after the background-only fit taking into account all the correlation. The post-fit distributions in 5.49b and 5.49d were published in [216].	177
5.50	Pre- (left) and post-fit (right) distributions of $m_{T,3\ell}$ in ZL Veto SR in 5.50a and 5.50b. The uncertainty bands include both statistical and systematic uncertainties after the background-only fit taking into account all the correlation. The post-fit distribution in 5.50b was published in [216].	178
5.51	Pre- (left) and post-fit (right) distributions of $H_T + E_T^{\text{miss}}$ in Q0 SR in 5.51a and 5.51b and in Q2 SR in 5.51c and in 5.51d. The uncertainty bands include both statistical and systematic uncertainties after the background-only fit taking into account all the correlation. The post-fit distributions in 5.51b and 5.51d were published in [216].	179
5.52	Observed and expected event yields the CRs, VRs and SRs for the three- and four-lepton channels after the fit procedure described in the text. Diboson indicates background from diboson processes. Rare top indicates background from $t\bar{t}+V$ and tWZ processes. Other indicates all other background that contribute less than 2%. The hatched bands include systematic uncertainties with the correlations between various sources taken into account and also statistical uncertainty. The lower panel shows the ratio of the observed data to the predicted SM background after the likelihood fit [216].	180
5.53	Post-fit nuisance parameters of the background-only fit with real data in control regions 5.53a, exclusion fit with Asimov dataset 5.53b and exclusion fit with real data in both control and signal regions 5.53c. These plots are related to the combined fit with three and four leptons.	182
5.54	Impact of MC statistical uncertainty and systematic uncertainties on μ_{SIG} constructed by fixing one nuisance parameter to its $\pm 1\sigma$ variations at the time and minimizing the rest. Pre-fit impact are shown with a yellow box, post-fit with a dashed blue box while α with black points. This plot is related to the combined fit with three and four leptons.	183

5.55	Gamma parameters corresponding to each bin in the analysis regions and impact of systematic uncertainties on μ_{SIG} constructed by fixing one nuisance parameter to its $\pm 1\sigma$ variations at the time and minimizing the rest. Pre-fit impact are shown with a yellow box, post-fit with a dashed blue box while α with black points. This plot is related to the combined fit with three and four leptons	184
5.56	Relative contributions of different sources of statistical and systematic uncertainty in the total background yield estimates after the fit. <i>Experimental</i> uncertainties are related to the lepton, jet and E_T^{miss} selection and reconstruction. <i>Misidentified leptons</i> are related to the FNP and lepton charge misidentification. <i>Luminosity</i> is related to the luminosity uncertainty that affect the background simulation yields. <i>Theory</i> affects the theoretical uncertainties connected to the theory uncertainties like PDF, α_s , normalization and factorization scale. <i>Normalization</i> is related to the diboson and rare top normalization factor extracted by the likelihood fit. Systematic uncertainties are calculated in an uncorrelated way by changing each nuisance parameter from its fit value by one standard deviation, keeping all the other parameters at their central values, and comparing the resulting event yield with the nominal yield. Individual uncertainties can be correlated, and do not necessarily add in quadrature to the total background uncertainty, which is indicated by 'Total uncertainty' [216].	185
5.57	Expected and observed 95% CLs exclusion limits in the three- and four-lepton channels for the Type-III SeeSaw process with the corresponding one- and two-standard-deviation uncertainty bands, showing the 95% CL upper limit on the cross-section. The theoretical signal cross-section prediction, given by the NLO calculation, with its corresponding uncertainty band is also shown.	186

5.58	Observed and expected event yields the CRs, VRs and SRs for the two-lepton plus two jets channel after the fit procedure described in the text. Regions are divided per flavour and electric charge combination. Diboson indicates background from diboson processes (WW), while $t\bar{t}$ considers $t\bar{t}$ pair production in which the two W bosons in the final state decay leptonically. Other indicates all other background that contribute less than 2%. The hatched bands include systematic uncertainties with the correlations between various sources taken into account and also statistical uncertainty. The lower panel shows the ratio of the observed data to the predicted SM background after the likelihood fit [36].	187
5.59	Expected and observed 95% CLs exclusion limits in the two (from [36]), three- and four-lepton channels for the Type-III SeeSaw process with the corresponding one- and two-standard-deviation uncertainty bands, showing the 95% CL upper limit on the cross-section. The theoretical signal cross-section prediction, given by the NLO calculation, with its corresponding uncertainty band is also shown [216].	188
A.1	Fake composition of the electron fake-factor estimation regions for: high- p_T at least 1 jet region A.1a, high- p_T at least 2 jets region A.1b, low- p_T at least 1 jet region A.1c, low- p_T at least 2 jets region A.1c.	193
A.2	Fake composition of the muon fake-factor estimation regions for: high- p_T at least 1 jet region A.2a, high- p_T at least 2 jets region A.2b, low- p_T at least 1 jet region A.2c, low- p_T at least 2 jets region A.2d.	194
A.3	Fake composition of the ZL CR on the top for fake electrons in A.3a and fake muons in A.3b, and of the ZL-RT-VR on the bottom for fake electrons in A.3c and fake muons in A.3d.	195
A.4	Fake composition of the JNLow VR on the top for fake electrons in A.4a and fake muons in A.4b. On the bottom, electrons fake composition for both ZL-DB-VR in A.4c and JN-Low SR in A.4d.	196
A.5	Fake composition of the ZL Veto SR on the top for fake electrons in A.5a and fake muons in A.5b, and of the Fakes VR on the bottom for fake electrons in A.5c and fake muons in A.5d.	197

A.6 Fake composition of the Q0 Diboson CR on the top for fake electrons in A.6a and fake muons in A.6b, and of the Q0 Diboson VR on the bottom for fake electrons in A.6c and fake muons in A.6d.	198
A.7 Fake composition of the Q0 RareTop CR on the top for fake electrons in A.7a and fake muons in A.7b, and of the Q0 RareTop VR on the bottom for fake muons in A.7c.	199
A.8 Fake composition of the Q0 SR on the top for fake electrons in A.8a and fake muons in A.8b, and of the Q2 SR on the bottom for fake electrons in A.8c and fake muons in A.8d.	200
A.9 Post-fit distribution for the ZL CR: $H_T + E_T^{\text{miss}}$ in A.9a, E_T^{miss} in A.9c, tri-lepton system p_T in A.9c and $m_{(\ell\ell)}$ in A.9d.	211
A.10 Post-fit distribution for the Fakes VR: $H_T + E_T^{\text{miss}}$ in A.10a, E_T^{miss} in A.10b, tri-lepton system p_T in A.10c and $m_{(\ell\ell)}$ in A.10d.	212
A.11 Post-fit distribution for the JNLow VR: $H_T + E_T^{\text{miss}}$ in A.11a, E_T^{miss} in A.11b, tri-lepton system p_T in A.11c and $m_{(\ell\ell)}$ in A.11d.	213
A.12 Post-fit distribution for the ZL Diboson VR: $H_T + E_T^{\text{miss}}$ in A.12a, E_T^{miss} in A.12b, tri-lepton system p_T in A.12c and $m_{(\ell\ell)}$ in A.12d.	214
A.13 Post-fit distribution for the ZL RareTop VR: $H_T + E_T^{\text{miss}}$ in A.13a, E_T^{miss} in A.13b, tri-lepton system p_T in A.13c and $m_{(\ell\ell)}$ in A.13d.	215
A.14 Post-fit distribution for the JNLow SR: $H_T + E_T^{\text{miss}}$ in A.14a, E_T^{miss} in A.14b, tri-lepton system p_T in A.14c and $m_{(\ell\ell)}$ in A.14d.	216
A.15 Post-fit distribution for the ZL SR: $H_T + E_T^{\text{miss}}$ in A.15a, E_T^{miss} in A.15b, tri-lepton system p_T in A.15c and $m_{(\ell\ell)}$ in A.15d.	217
A.16 Post-fit distribution for the ZL Veto SR: $H_T + E_T^{\text{miss}}$ in A.16a, E_T^{miss} in A.16b, tri-lepton system p_T in A.16c and $m_{(\ell\ell)}$ in A.16d.	218
A.17 Post-fit distribution for the Q0 Diboson CR: $m_{(\ell\ell\ell)}$ in A.17a, E_T^{miss} in A.17b, $m_{(\ell\ell\ell)} + E_T^{\text{miss}}$ in A.17c and four-lepton system p_T in A.17d.	219
A.18 Post-fit distribution for the Q0 RareTop CR: $m_{(\ell\ell\ell)}$ in A.18a, E_T^{miss} in A.18b, $m_{(\ell\ell\ell)} + E_T^{\text{miss}}$ in A.18c and four-lepton system p_T in A.18d.	220
A.19 Post-fit distribution for the Q0 Diboson VR: $m_{(\ell\ell\ell)}$ in A.19a, E_T^{miss} in A.19b, $m_{(\ell\ell\ell)} + E_T^{\text{miss}}$ in A.19c and four-lepton system p_T in A.19d.	221

A.20 Post-fit distribution for the Q0 RareTop VR: $m_{(\ell\ell\ell)}$ in A.20a, E_T^{miss} in A.20b, $m_{(\ell\ell\ell)} + E_T^{\text{miss}}$ in A.20c and four-lepton system p_T in A.20d.	222
A.21 Post-fit distribution for the Q2 VR: $m_{(\ell\ell\ell)}$ in A.21a, E_T^{miss} in A.21b, $m_{(\ell\ell\ell)} + E_T^{\text{miss}}$ in A.21c and four-lepton system p_T in A.21d.	223
A.22 Post-fit distribution for the Q0 SR: $m_{(\ell\ell\ell)}$ in A.22a, E_T^{miss} in A.22b, $m_{(\ell\ell\ell)} + E_T^{\text{miss}}$ in A.22c and four-lepton system p_T in A.22d.	224
A.23 Post-fit distribution for the Q2 SR: $m_{(\ell\ell\ell)}$ in A.23a, E_T^{miss} in A.23b, $m_{(\ell\ell\ell)} + E_T^{\text{miss}}$ in A.23c and four-lepton system p_T in A.23d.	225
A.24 Post-fit nuisance parameters of the background-only fit with real data in control regions A.24a, exclusion fit with Asimov dataset A.24b and exclusion fit with real data in both control and signal regions A.24c. These plots are related to the three-lepton channel.	237
A.25 Impact of systematic uncertainties on μ_{SIG} constructed by fixing one nuisance parameter to its $\pm 1\sigma$ variations at the time and minimizing the rest. In A.25a the impact of the dominant systematic source and MC statistical uncertainty, in A.25b only dominant systematic sources and gamma parameters corresponding to each bin in the analysis regions. Pre-fit impact are shown with a yellow box, post-fit with a dashed blue box while α with black points. These plots are related to three-lepton channel.	238
A.26 Expected and observed 95% CLs exclusion limits in the three-lepton channel for the Type-III SeeSaw process with the corresponding one- and two-standard-deviation uncertainty bands, showing the 95% CL upper limit on the cross-section. The theoretical signal cross-section prediction, given by the NLO calculation, with its corresponding uncertainty band is also shown.	239
A.27 Post-fit nuisance parameters of the background-only fit with real data in control regions A.24a, exclusion fit with Asimov dataset A.24b and exclusion fit with real data in both control and signal regions A.24c. These plots are related to the four-lepton channel.	240

<p>A.28 Impact of systematic uncertainties on μ_{SIG} constructed by fixing one nuisance parameter to its $\pm 1\sigma$ variations at the time and minimizing the rest. In A.28a the impact of the dominant systematic source and MC statistical uncertainty, in A.28b only dominant systematic sources and gamma parameters corresponding to each bin in the analysis regions. Pre-fit impact are shown with a yellow box, post-fit with a dashed blue box while α with black points. These plots are related to four-lepton channel.</p>	<p>241</p>
<p>A.29 Expected and observed 95% CLs exclusion limits in the four-lepton channel for the Type-III SeeSaw process with the corresponding one- and two-standard-deviation uncertainty bands, showing the 95% CL upper limit on the cross-section. The theoretical signal cross-section prediction, given by the NLO calculation, with its corresponding uncertainty band is also shown. This plot is related to the four-lepton channel.</p>	<p>242</p>
<p>A.30 Distributions of $H_T + E_T^{miss}$ in opposite-sign signal regions, namely a the electron–electron signal region, b the electron–muon signal region, and c the muon–muon signal region after the background-only fit. The hatched bands include all systematic uncertainties post-fit with the correlations between various sources taken into account. Errors on data are statistical only. The lower panel shows the ratio of the observed data to the estimated SM background [36].</p>	<p>244</p>
<p>A.31 Distributions of $H_T + E_T^{miss}$ in same-sign signal regions, namely a the electron–electron signal region, b the electron–muon signal region, and c the muon–muon signal region after the background-only. The hatched bands include all systematic uncertainties post-fit with the correlations between various sources taken into account. Errors on data are statistical only. The lower panel shows the ratio of the observed data to the estimated SM background [36].</p>	<p>245</p>
<p>A.32 Post-fit nuisance parameters of the background-only fit with real data in control regions A.32a, exclusion fit with Asimov dataset A.32b and exclusion fit with real data in both control and signal regions A.32c. These plots are related to the combination of two-, three- and four-lepton channels.</p>	<p>247</p>

A.33	Impact of systematic uncertainties on μ_{SIG} constructed by fixing one nuisance parameter to its $\pm 1\sigma$ variations at the time and minimizing the rest. In A.33a the impact of the dominant systematic source and MC statistical uncertainty, in A.33b also gamma parameters corresponding to each bin in the analysis regions are added. Pre-fit impact are shown with a yellow box, post-fit with a dashed blue box while α with black points. These plots are related to the combination of two-, three- and four-lepton channels.	248
A.34	Comparison of expected and observed 95% CLs exclusion limits using toys with a frequentist approach and the standard asymptotic formulae. Toys are overlaid with observed and expected limit in blue and uncertainty bands in pink and violet	249
B.1	Measured pile-up parameter μ as a function of the bunch-crossing number averaged over the duration of the run, in a physics fill in 2016. The plot shows more than 3 orders of magnitude between the μ measured in colliding BCIDs (upper points) and the background in the non-colliding BCIDs (lower points) [218].	255
B.2	View of one of the two LUCID-2 detector modules using the 2016 configuration, with its main component highlighted [179].	257
B.3	Photo of a modified Hamamatsu photomultiplier. The acceptance of the photo-cathode has been reduced by a thin aluminium layer on the window [179].	258
B.4	The left drawing shows the LUCID support cylinder with the four quartz bundles at the back and the 16 photomultipliers at the front. The right drawing shows the support and cooling structure of the photomultipliers, with also the different PMTs types [179].	259
B.5	Typical photoelectron distribution obtained from a PMT in single pp collisions at different center of mass energies (8 and 14 TeV) and for different diameter of the PMT window (14 mm, 10 mm, 5 mm, 3 mm) [179].	260
B.6	Schematic view of the LUCID-2 relative calibration system for one detector module in 2015 [179].	260
B.7	Amplitude spectrum of LUCID photomultiplier recorded in a 13 TeV run (blue) and of ^{207}Bi internal conversion electron in a calibration run (red) [222].	261

B.8	Figure B.8a shows the variation in percent of the measured mean charge relative a reference run for the LED calibration signal, while in Figure B.8b the ^{207}Bi source is considered [179].	262
B.9	Block diagram of the electronics for the LUCID-2 detector [179].	263
B.10	LUCID Side-A in the ATLAS surface building, SX1.	265
B.11	Measured voltage of two tested PMTs using the same configuration. In B.11a a PMT which has not been selected to the installation, while in B.11b one that has been chosen.	266
B.12	Installation of the selected PMTs on the LUCID side-A in SX1.	266
B.13	On the left the location of the present LUCID-2 detector in the beam-pipe support cone is shown. In this illustration only the bottom part of the forward shielding (named JFC1) is installed. On the right the new vacuum equipment (VAX) that will be installed in Run 4 is shown. For this one, the beam-pipe support cone is not reported since it has not been designed yet [225].	268
B.14	Photos of the forward shielding piece JFC3 during different stages of an ATLAS opening. The left photo shows the situation when all shielding is installed. The top octagonal shielding piece has been removed in the middle photo. The JFC3 shielding piece after removal from ATLAS is shown in the photo on the right [225].	269
B.15	Drawing of the prototype detector attached to the JFC3 forward shielding piece with the clearance to the VJ cone at a distance of 1600 cm from the IP (Figure B.15a). In B.15b, photo of the PMTs installed on the JFC3 shielding [225].	270
B.16	Illustrations of LUCID-1 (left) and LUCID-2 (right) detector simulations. From top to bottom different parts of the detectors are shown. Top: Aluminium (B.16a) and Carbon (B.16d) VJ Cones. Middle: Cherenkov tubes (B.16b) and PMT support cylinder (B.16e), located inside the respective VJ cone. Bottom: frontal view of the PMTs.	272
B.17	Sketch of the LUCID-2 PMTs (Figure B.17a). Figures B.17b and B.17c plot the ϕ position of each PMT and the x vs. y position, respectively.	273
B.18	Simulates LUCID-3 PMT detector (Figure B.18a), following the proposal illustrated in Figure B.15a, is shown. In B.18b, the PMTs position in the x - y plane is presented.	274

<p>B.19 Results of a simulation performed by the ATLAS Radiation Simulation Working Group in the region around the beam-pipe in ATLAS [230]. Figure B.19a shows the dose corresponding to 4000 fb^{-1} expected in Run 4. The relative change in dose with respect to the present LUCID-2 location is given in five points with different position along the beam-pipe (z) and distance (r). Figure B.19b shows a map of the electron flux. The change in electron plus charged hadron flux with respect to the current LUCID-2 location is given in five different points.</p>	276
<p>C.1 Figure C.1a shows the uncertainty on the signal strength of Higgs analyses with with 300 fb^{-1} and 3000 fb^{-1} at $\sqrt{s} = 14 \text{ TeV}$ for a SM Higgs boson with a mass of 125 GeV. Figure C.1b shows the discovery reach (solid lines) and exclusion limits (dashed lines) for charginos and neutralinos in $\tilde{\chi}_1^\pm \tilde{\chi}_2^0 \rightarrow W^{(*)} \tilde{\chi}_1^0 Z^{(*)} \chi_1^0$ decays. The results are shown for the 300 fb^{-1} and 3000 fb^{-1} datasets [232].</p>	279
<p>C.2 Display of the ATLAS Phase-II Inner Tracker ITk with the Inclined Duals detector layout [234].</p>	280
<p>C.3 A schematic layout of the ITk Inclined Duals layout for the HL-LHC phase with the Pixel Detector in red and the Strip Detector in blue [234].</p>	281
<p>C.4 Radiation length X_0 versus the pseudorapidity η in the Inner Detector (Figure C.4a) and in the Inner Tracker. The figures show only positive η, negative η is expected to look the same [234]. Note the different scale of these plots. . .</p>	282
<p>C.5 Top figures show the pixel sizes used in 3D sensors with a single collection electrode (point in red), while the bottom ones the efficiency maps for different pixel sizes [236]. . .</p>	283
<p>C.6 Pixel matrix structure with punch-through bias structure is shown on the left, while on the right the efficiency map of the grey area corresponding to 4×4 pixels of a planar sensor before irradiation [236].</p>	283
<p>C.7 Single chip card with RD53A. The readout chip is located at the bottom in the center of the picture and the display ports for communication are located on top of the picture. [240].</p>	285
<p>C.8 Schematic view of the readout and database systems [242].</p>	286

C.9	Scheme of the visualization of an uploaded result on the database. 1. is the top page with all the scanned modules with also the login window; 2. is the chip providing information as the serial number front-end type and also the scans performed, 3. choosing a certain scan, the several run performed a shown, 4. results of the selected scan. . .	287
C.10	View of the QC results stored on the local database (Figure C.10a). The histogram is directly displayed based on the x and y values. Two different interacting tables were implemented in order to manage the axes (Figure C.10b) and to restore default values.	288
C.11	View of the DCS results (temperature) stored on the local database (Figure C.11a). The histogram is directly displayed based on the x and y values. Two different interacting tables were implemented in order to manage the axes (Figure C.11b) and to restore default values.	289

List of Tables

1.1	Main characteristics of the fundamental forces at the EW scale [1].	3
1.2	Comparison of Dirac and Majorana mass terms. Λ is a new physics mass scale where Majorana neutrinos could acquire its mass, y the Yukawa Coupling, v is the vacuum expectation value (vev). PMNS matrix is the equivalent of CKM matrix for the leptonic sector.	16
2.1	LHC performance during the operation of 2015-2017 compared to the machine design values [78].	30
2.2	Delivered and recorded integrated luminosity \mathcal{L} in 2010 and 2011 ($\sqrt{s} = 7$ TeV), 2012 ($\sqrt{s} = 8$ TeV), 2015 and 2016 ($\sqrt{s} = 13$ TeV), by the ATLAS detector. [83]	31
2.3	General performance goals [86] and obtained resolutions in 2015 [88] of the ATLAS detector. If not indicated, the units for E and p_T are in GeV.	38
2.4	Main performance of the ATLAS tracking detector.	41
2.5	Main features of the sampling calorimeters of the ATLAS detector. The interaction (λ) and radiation (X_0) lengths values refer to $ \eta = 0$ and $ \eta = 3.2$ for the barrel and the end-cap regions respectively.	48
2.6	Parameters of the four sub-systems of the muon detector [86]. The quoted spatial resolution (columns 2, 3) does not include chamber-alignment uncertainties. Column 4 lists the intrinsic time resolution of each chamber type, to which contributions from signal-propagation and electronics contributions need to be added.	54
3.1	Definition of the electron isolation working points and isolation efficiency ϵ . In the Gradient definition, the momenta is expressed in GeV [104].	72

3.2	Prompt-muon identification efficiencies ϵ_μ and light-hadron misidentification rates ϵ_{had} for the different selection WPs, evaluated in $t\bar{t}$ MC samples in different p_T regions for $ \eta < 2.5$. The p_T is expressed in GeV [110].	77
3.3	Prompt-muon isolation efficiencies ϵ_μ and heavy-flavour hadron semileptonic decays ϵ_{had} for the different isolation WPs, evaluated in $t\bar{t}$ MC samples in different p_T regions. The p_T is expressed in GeV [110].	78
4.1	Cross-sections of signal MC samples for each mass hypothesis considered in the analysis. Leading order cross-sections are computed by the generator and are re-weighted at the next-to-leading ($\sigma_{\text{NLO+NLL}}$) with their corresponding uncertainties using k-factors from [185, 186].	104
4.2	Simulated signal and background samples. The event generator, PDF set used for the Matrix Element (ME) calculation, cross-section normalization, parton shower and parton shower tune are shown for each sample. The generator cross-section is used where not specifically stated otherwise.	104
5.1	Summary of the trigger requirements divided per lepton multiplicity and data taking year.	111
5.2	A summary of the baseline electron definitions in the analysis.	112
5.3	Summary of the baseline muon definitions in the analysis.	112
5.4	Summary of the signal and baseline jet definitions in the analysis.	113
5.5	Summary of the overlap removal steps performed on electrons, muons, and jets.	113
5.6	Summary of the selection criteria used to define analysis regions in the three-lepton channel.	117
5.7	Summary of the selection criteria used to define analysis regions in the four-lepton channel.	123
5.8	Signal contamination fraction in CRs and VRs for the 800 GeV and 1200 GeV signal mass points.	126
5.9	A summary of the fake-factor estimation trigger requirements for electrons.	135
5.10	Summary of the variations used for the determination of the systematic uncertainty of the fake factors.	140
5.11	A summary of the fake-factor estimation trigger requirements for muons.	148

5.12	Applied renormalisation and factorisation scale variations. Variations marked in green are taken as uncertainties, while the ones in red are not used. In black the is the nominal choice.	161
5.13	Summary of the sources of systematic uncertainty considered in the analysis with the corresponding number of nuisance parameters.	165
5.14	Upper part shows the summary of the regions used to fit the yields of the largest SM background predictions. Regions used to extrapolate the normalization factor for a certain SM prediction are marked with a black check-mark (✓), while regions where this NF is only applied are marked with a green check-mark (☀). Regions where the NF is neither extrapolated and neither applied are instead marked with a dash(-). The lower part shows which regions are used in the fit depending on the fit configuration (background-only or exclusion).	166
5.15	A table listing the normalisation factors with the corresponding uncertainty for normalisation of the floating MC contributions, as extracted from the background-only fit for the separate lepton multiplicity channels, three and four.	170
5.16	Observed data and background and signals yields in the three- and four-lepton signal regions after the background only fit.	171
5.17	Observed data and background yields in the three-lepton control and validation regions after the background only fit.	171
5.18	Observed data and background yields in the four-lepton control and validation regions after the background only fit.	171
5.19	Summary of the selection criteria used to define analysis regions in the two-lepton channel [36].	178
5.20	A table listing the normalisation factors with the corresponding uncertainty for normalisation of the floating MC contributions, as extracted from the background-only fit for the separate lepton multiplicity channels, three and four.	181
A.1	Summarised list of all used systematic uncertainties with the corresponding name as α variables.	202

A.2	Breakdown of the dominant uncertainties on background estimates. The given total statistical error is a quadratic sum of individual statistical errors of each bin in the region. Note that the individual uncertainties can be correlated, and do not necessarily add up quadratically to the total background uncertainty. Uncertainties are ordered from the largest to smallest depending by the impact on the region in the second column.	204
A.3	Breakdown of the dominant uncertainties on background estimates. The given total statistical error is a quadratic sum of individual statistical errors of each bin in the region. Note that the individual uncertainties can be correlated, and do not necessarily add up quadratically to the total background uncertainty. Uncertainties are ordered from the largest to smallest depending by the impact on the region in the second column.	205
A.4	Breakdown of the dominant uncertainties on background estimates. The given total statistical error is a quadratic sum of individual statistical errors of each bin in the region. Note that the individual uncertainties can be correlated, and do not necessarily add up quadratically to the total background uncertainty. Uncertainties are ordered from the largest to smallest depending by the impact on the region in the second column.	206
A.5	Breakdown of the dominant uncertainties on background estimates. The given total statistical error is a quadratic sum of individual statistical errors of each bin in the region. Note that the individual uncertainties can be correlated, and do not necessarily add up quadratically to the total background uncertainty. Uncertainties are ordered from the largest to smallest depending by the impact on the region in the second column.	207
A.6	Breakdown of the dominant uncertainties on background estimates. The given total statistical error is a quadratic sum of individual statistical errors of each bin in the region. Note that the individual uncertainties can be correlated, and do not necessarily add up quadratically to the total background uncertainty. Uncertainties are ordered from the largest to smallest depending by the impact on the region in the second column.	208

A.7	Breakdown of the dominant uncertainties on background estimates. The given total statistical error is a quadratic sum of individual statistical errors of each bin in the region. Note that the individual uncertainties can be correlated, and do not necessarily add up quadratically to the total background uncertainty. Uncertainties are ordered from the largest to smallest depending by the impact on the region in the second column.	209
A.8	Signal and MC events at different stage of the applied event section. Events are reweighted using the proper reconstruction weighs. The signal sample considered is generated with a heavy lepton mass hypothesis of 800 GeV.	227
A.9	Signal and MC events at different stage of the applied event section. Events are reweighted using the proper reconstruction weighs. The signal sample considered is generated with a heavy lepton mass hypothesis of 800 GeV.	228
A.10	Signal and MC events at different stage of the applied event section. Events are reweighted using the proper reconstruction weighs. The signal sample considered is generated with a heavy lepton mass hypothesis of 800 GeV.	229
A.11	Signal and MC events at different stage of the applied event section. Events are reweighted using the proper reconstruction weighs. The signal sample considered is generated with a heavy lepton mass hypothesis of 800 GeV.	229
A.12	Signal and MC events at different stage of the applied event section. Events are reweighted using the proper reconstruction weighs. The signal sample considered is generated with a heavy lepton mass hypothesis of 800 GeV.	230
A.13	Signal and MC events at different stage of the applied event section. Events are reweighted using the proper reconstruction weighs. The signal sample considered is generated with a heavy lepton mass hypothesis of 800 GeV.	230
A.14	Signal and MC events at different stage of the applied event section. Events are reweighted using the proper reconstruction weighs. The signal sample considered is generated with a heavy lepton mass hypothesis of 800 GeV.	231
A.15	Signal and MC events at different stage of the applied event section. Events are reweighted using the proper reconstruction weighs. The signal sample considered is generated with a heavy lepton mass hypothesis of 800 GeV.	231

A.16	Signal and MC events at different stage of the applied event section. Events are reweighted using the proper reconstruction weighs. The signal sample considered is generated with a heavy lepton mass hypothesis of 800 GeV.	232
A.17	Signal and MC events at different stage of the applied event section. Events are reweighted using the proper reconstruction weighs. The signal sample considered is generated with a heavy lepton mass hypothesis of 800 GeV.	232
A.18	Signal and MC events at different stage of the applied event section. Events are reweighted using the proper reconstruction weighs. The signal sample considered is generated with a heavy lepton mass hypothesis of 800 GeV.	233
A.19	Signal and MC events at different stage of the applied event section. Events are reweighted using the proper reconstruction weighs. The signal sample considered is generated with a heavy lepton mass hypothesis of 800 GeV.	234
A.20	Signal and MC events at different stage of the applied event section. Events are reweighted using the proper reconstruction weighs. The signal sample considered is generated with a heavy lepton mass hypothesis of 800 GeV.	234
A.21	Signal and MC events at different stage of the applied event section. Events are reweighted using the proper reconstruction weighs. The signal sample considered is generated with a heavy lepton mass hypothesis of 800 GeV.	235
A.22	Signal and MC events at different stage of the applied event section. Events are reweighted using the proper reconstruction weighs. The signal sample considered is generated with a heavy lepton mass hypothesis of 800 TeV.	235
B.1	PMTs installed on the LUCID Side-A with their corresponding high-voltage (HV) and current (I) for each dynode. . .	267
B.2	ATLAS Geometry tags used during the simulation step with the corresponding LUCID detector version.	271

